BEILSTEIN JOURNAL OF ORGANIC CHEMISTRY

Molecular switches

Edited by Wiktor Szymanski and Stefan Hecht

Generated on 10 February 2026, 14:19

Imprint

Beilstein Journal of Organic Chemistry
www.bjoc.org
ISSN 1860-5397
Email: journals-support@beilstein-institut.de

The *Beilstein Journal of Organic Chemistry* is published by the Beilstein-Institut zur Förderung der Chemischen Wissenschaften.

Beilstein-Institut zur Förderung der Chemischen Wissenschaften
Trakehner Straße 7–9
60487 Frankfurt am Main
Germany
www.beilstein-institut.de

The copyright to this document as a whole, which is published in the *Beilstein Journal of Organic Chemistry*, is held by the Beilstein-Institut zur Förderung der Chemischen Wissenschaften. The copyright to the individual articles in this document is held by the respective authors, subject to a Creative Commons Attribution license.

BEILSTEIN JOURNAL OF ORGANIC CHEMISTRY

Reversible end-to-end assembly of selectively functionalized gold nanorods by light-responsive arylazopyrazole–cyclodextrin interaction

Maximilian Niehues, Patricia Tegeder and Bart Jan Ravoo*

Full Research Paper

Open Access

Address:
Organic Chemistry Institute and Center for Soft Nanoscience, Westfälische Wilhelms-Universität Münster, Corrensstraße 40, D-48149, Germany

Email:
Bart Jan Ravoo* - b.j.ravoo@uni-muenster.de

* Corresponding author

Keywords:
cyclodextrins; gold nanorods; host–guest chemistry; light-responsive materials; molecular switches; self-assembly

Beilstein J. Org. Chem. **2019,** *15,* 1407–1415.
doi:10.3762/bjoc.15.140

Received: 15 March 2019
Accepted: 12 June 2019
Published: 26 June 2019

This article is part of the thematic issue "Molecular switches".

Guest Editor: W. Szymanski

© 2019 Niehues et al.; licensee Beilstein-Institut.
License and terms: see end of document.

Abstract

We propose a two-step ligand exchange for the selective end-functionalization of gold nanorods (AuNR) by thiolated cyclodextrin (CD) host molecules. As a result of the complete removal of the precursor capping agent cetyltrimethylammonium bromide (CTAB) by a tetraethylene glycol derivative, competitive binding to the host cavity was prevented, and reversible, light-responsive assembly and disassembly of the AuNR could be induced by host–guest interaction of CD on the nanorods and a photoswitchable arylazopyrazole cross-linker in aqueous solution. The end-to-end assembly of AuNR could be effectively controlled by irradiation with UV and visible light, respectively, over four cycles. By the introduction of AAP, previous disassembly limitations based on the photostationary states of azobenzenes could be solved. The combination photoresponsive interaction and selectively end-functionalized nanoparticles shows significant potential in the reversible self-assembly of inorganic–organic hybrid nanomaterials.

Introduction

Metallic nanomaterials have received intense and interdisciplinary interest due to their unique optical [1], electronic [2,3] and sensing properties [4,5]. In particular, noble metal nanoparticles of sizes smaller than the wavelength of the incident light show interesting optical behavior as a result of collective oscillations of the valence electrons. This leads to surface plasmon resonance (SPR), which is highly dependent on size, shape and chemical environment giving rise to different SPR band wavelengths [6-8]. Especially gold nanorods (AuNR) are of interest because of their good synthetic availability and their unique optical properties. Due to their anisotropy AuNR possess a transversal SPR (TSPR) band in the visible and a longitudinal SPR (LSPR) band that can reach up to the near infrared (NIR) region [9]. The LSPR band can be tuned over a wider wavelength range than for isotropic nanoparticles by varying the aspect ratio of the AuNR or by the assembly of multiple AuNR into linear clusters [10]. These linear aggregates can be realized more or less efficiently through various approaches based on

supramolecular interactions like metal–metal and π–π interactions [11], DNA mediated [12] or by host–guest chemistry [13]. Most of these approaches require selective functionalization of the ends of the AuNR and take advantage of the different ligand exchange kinetics of CTAB on the ends and the side of the particles [14,15]. CTAB serves as a capping agent in AuNR synthesis by the seed-mediated growth process and is essential for the anisotropic growth. Due to the different crystallographic environments on the particle surface, weaker packing and binding forces enable the preferential exchange of ligands on the facets at the ends [16]. Removal of CTAB on the side facets is relatively slow and requires a higher ligand concentration. However, for biotechnological applications it might be advantageous to remove CTAB from the complete surface because of its cell toxicity [17], hence strategies for replacing this coating are desirable.

Host–guest chemistry is a supramolecular interaction that is tailor-made for self-assembly due to its lock–key mechanism and has been applied in our and other groups to various nanoparticle systems [18-24]. The host–guest interaction can be responsive to external stimuli such as redox, pH or light, with the latter being the most desirable for assembling nanoparticles by virtue of its noninvasive nature [25]. Prominent light-responsive guest molecules are azobenzenes that form inclusion complexes with α- or β-CD exclusively in the *trans* configuration, not in the *cis* configuration [26]. This light-responsive interaction has been recently applied by Ma et al. for the end-to-end assembly of AuNR [27]. However, the system showed some limitations as the assembly was only achieved when the CD ligand and the divalent azobenzene linker were premixed to generate the host–guest complex. This solution was then added to the AuNR leading to a ligand exchange preferentially at the ends and therefore to the linear arrangement of AuNR. If the AuNR were first end-functionalized with the CD, no assembly could be observed after addition of the divalent azobenzene linker. Moreover, the assemblies could only once be disassembled by the combination of UV irradiation and physical forces by sonication. The light-induced back-isomerization of azobenzenes did not form similar end-to-end aggregates. Ma et al. suggested that the host–guest interaction is not strong enough to assemble the particles if not preformed. Yet, this is not consistent with publications that report photoswitchable azobenzene–CD interaction on surfaces [28], in hydrogels [29], the assembly of CD vesicles [30] or the assembly of Au nanoparticles [31].

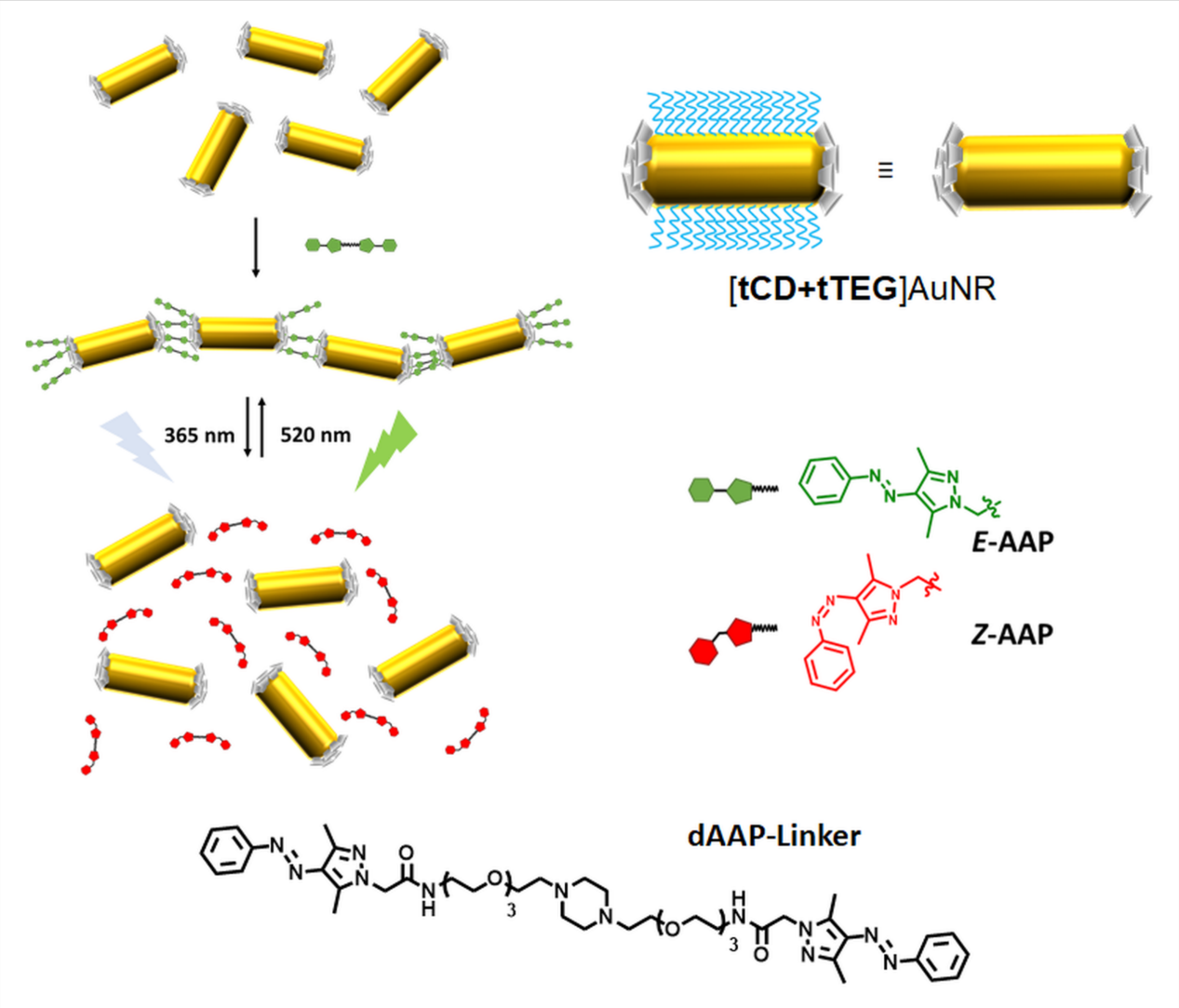
It is our hypothesis that CTAB, which serves as surfactant and is essential in the synthesis of AuNR in seed-mediated growth processes, acts as a competitive binder to the CD cavity and prevents the reversible self-assembly. In fact, CTAB has a more than 20-fold higher binding constant to β-CD (6.5×10^4 M^{-1}) [32] than unmodified azobenzenes (2.5×10^3 M^{-1}) [33]. Therefore, the competitive binding of CTAB to β-CD has been applied previously, e.g., in sensing applications [34] or to enhance the water solubility of a cyclodextrin polymer [35]. On account of the experimental conditions that lead to a CTAB double layer formation around the AuNR, a significant amount of unbound CTAB may remain in solution and interact with host molecules. Furthermore, the light-responsive dispersion of the AuNR was only possible by the combination of irradiation and sonication, whilst some dimers could not be fully dispersed. Possibly this observation can be explained from the limited photostationary states (PSS) of azobenzenes (*E* – *Z*: 80%, *Z* – *E*: 70%) [36].

Arylazopyrazoles (AAP) are a new class of molecular switches introduced by Fuchter et al. with excellent photophysical properties like nearly quantitative isomerization, straight forward synthesis in excellent yields and very long *Z*-isomer half-life times up to 1000 days due to less steric repulsion [37]. In previous reports we could show that the AAP guest inclusion properties to β-CD are comparable to azobenzenes leading due to the superior photophysical properties to fully reversible supramolecular systems, which showed limited feasibility with azobenzenes [20,38,39].

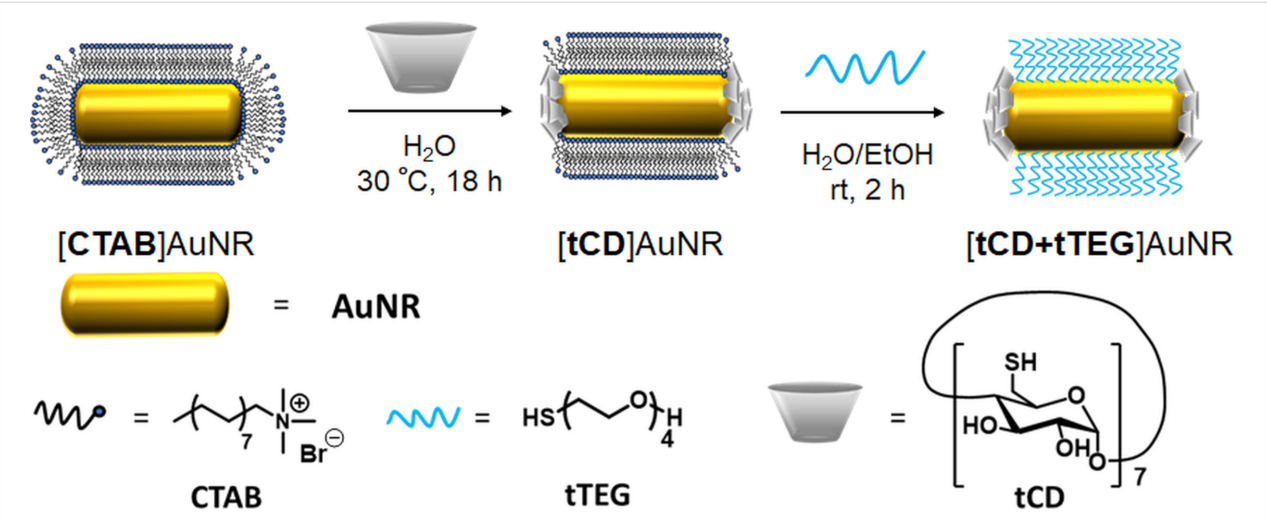
Herein, we present the application of a light-responsive CD–AAP host–guest system for the reversible end-to-end assembly of AuNR. The AuNR are functionalized selectively in a two-step ligand exchange reaction. The ends are capped with per-6-thio-β-cyclodextrin (tCD) and CTAB is removed from the remaining surface by monothiolated tetraethylene glycol (tTEG) enabling reversible host–guest chemistry. The addition of a divalent AAP linker molecule (dAAP) led to light-responsive reversible self-assembly of AuNR in an end-to-end manner as depicted in Scheme 1 to open up a novel strategy for the design of hybrid nanomaterials by supramolecular chemistry.

Results and Discussion

The AuNR (length: 58 nm, width: 25 nm, aspect-ratio: 2.3) were synthesized according to the seed-mediated growth procedure developed by Murphy [40] and El-Sayed [41]. CD-end functionalized AuNR were obtained in a two-step ligand exchange procedure as depicted in Scheme 2. For an efficient ligand exchange the primary alcohol groups of β-CD were replaced with thiols by a known two-step synthesis [42,43] to give a multivalent ligand (tCD) that is tightly bound to the gold surface and is not replaced by an excess of monothiolated tetraethylene glycol (tTEG). It is important to note the importance of the addition of ethanol during the ligand exchange to increase the solubility of CTAB and destabilize its double layer. Further-



Scheme 1: Light-responsive end-to-end assembly of host-functionalized gold nanorods (AuNR) by cyclodextrin–AAP interaction.



Scheme 2: Two-step ligand exchange reaction for the synthesis of water-soluble cyclodextrin end-functionalized gold nanorods.

more, ethanol weakens the hydrophobic effect of the solvent so that the inclusion of CTAB into β-CD is suppressed.

The ligand exchange was followed by ζ-potential measurements giving direct information about the surface charge potential and therefore about the capping agent (Figure 1a). CTAB-functionalized AuNR have a highly positive surface charge (+55 mV) due to the formation of CTAB double layers. The intermediate state [tCD]AuNR shows a decreased surface charge (+42 mV) indicating a reduction of the CTAB surface coverage. It is assumed by preliminary studies that the ligand exchange mainly emerges at the AuNR ends due to its high ligand exchange kinetics [10,15,16]. The addition of an excess of tTEG resulted in a negative surface charge (−32 mV) indicating a complete removal of CTAB from the gold surface. Furthermore, the high negative ζ-potential evidences electrostatic repulsion between the particles and thus good colloidal stability against uncontrolled aggregation. It is well known that PEGylated surfaces and particles show a negative ζ-potential in water due to the preferential absorption of hydroxide anions [44]. Furthermore, the ζ-potential is known to be highest in deionized water and highly pH-dependent [45].

The ligand exchange reaction was also analyzed by UV–vis spectroscopy (Figure 1b). The synthesized [CTAB]AuNR show the two expected absorption maxima at λ = 525 nm for the TSPR band and at λ = 690 nm for the LSPR band. After the ligand exchange the bands shift to λ = 528 nm TSPR and to λ = 721 nm LSPR accompanied by a general broadening of the SPR bands. This broadening can be explained by different chemical environments for diverse ligands and is a known characteristic for dual surfactant nanoparticle systems [46]. This interpretation is also supported by TEM images (Figure 4a, see below) indicating significant interparticle repulsion and no aggregation-induced absorption maxima broadening.

For further experiments the [tCD+tTEG]AuNR stock solution was diluted with ddH_2O. For the photoresponsive aggregation of isotropic nanoparticles, the 1,4-bis(2-(2-(2-(2-aminoethoxy)ethoxy)ethoxy)ethyl)piperazine-based AAP linker molecule (dAAP) has been successfully applied before and it was synthesized as described in detail in the literature [38]. This divalent linker molecule can form a light-responsive 1:2 complex with host-functionalized AuNR as shown in Scheme 1. The light-responsive AAP moiety isomerizes upon irradiation with λ = 365 nm to the *Z*-state and upon irradiation with λ = 520 nm back to the *E*-state. A non-ionic linker design was chosen to eliminate the possibility that the assembly is affected by changes of the ionic strength.

Shortly after the addition of dAAP to the AuNR solution, UV–vis spectra were recorded (Figure 2a) indicating a strong LSPR shift of λ = 36 nm to λ = 757 nm while the TSPR band change is negligible. This indicates selective end-to-end assembly, whereas side-to-side or uncontrolled aggregation would result in an additional shift of the TSPR band [15]. In the course of repeated photoswitching experiments, the spectra show a small but significant decrease of the overall nanoparticle absorbance which is most likely due to sedimentation of irreversible aggregates or size-dependent nanoparticle settling and is in agreement with other studies on linear assemblies of AuNR [12]. To visualize the AuNR end-to-end assemblies, TEM measurements have been conducted (Figure 4b and c, see below) showing chains of AuNR. Hardly any unselective side-by-side or random assemblies can be observed which are often seen in various publications and are due to unspecific drying

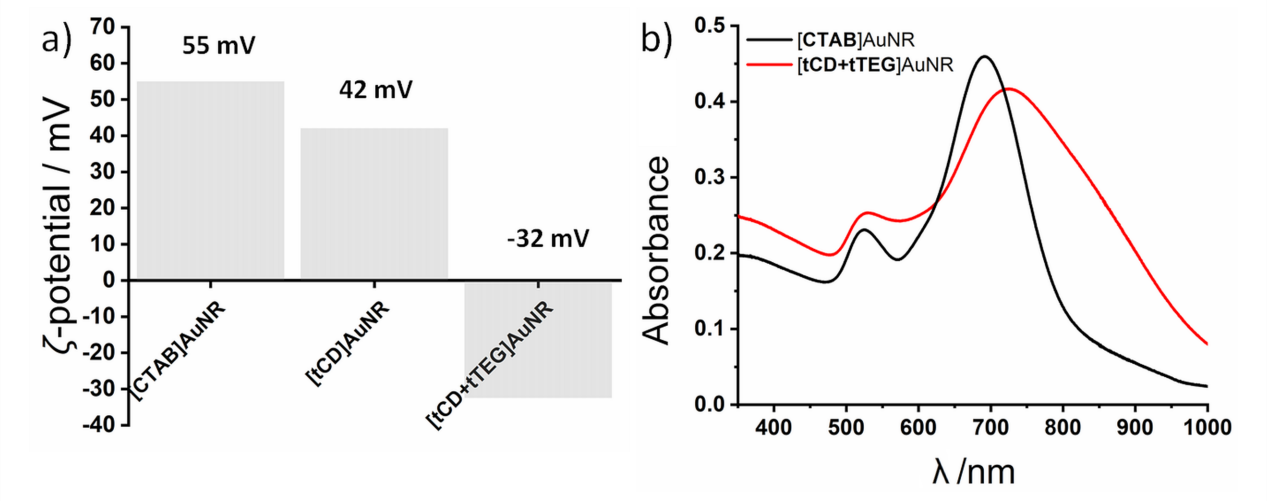


Figure 1: a) ζ-Potential measurement of different stages of the ligand exchange. b) UV–vis spectroscopy before (black) and after complete ligand exchange (red).

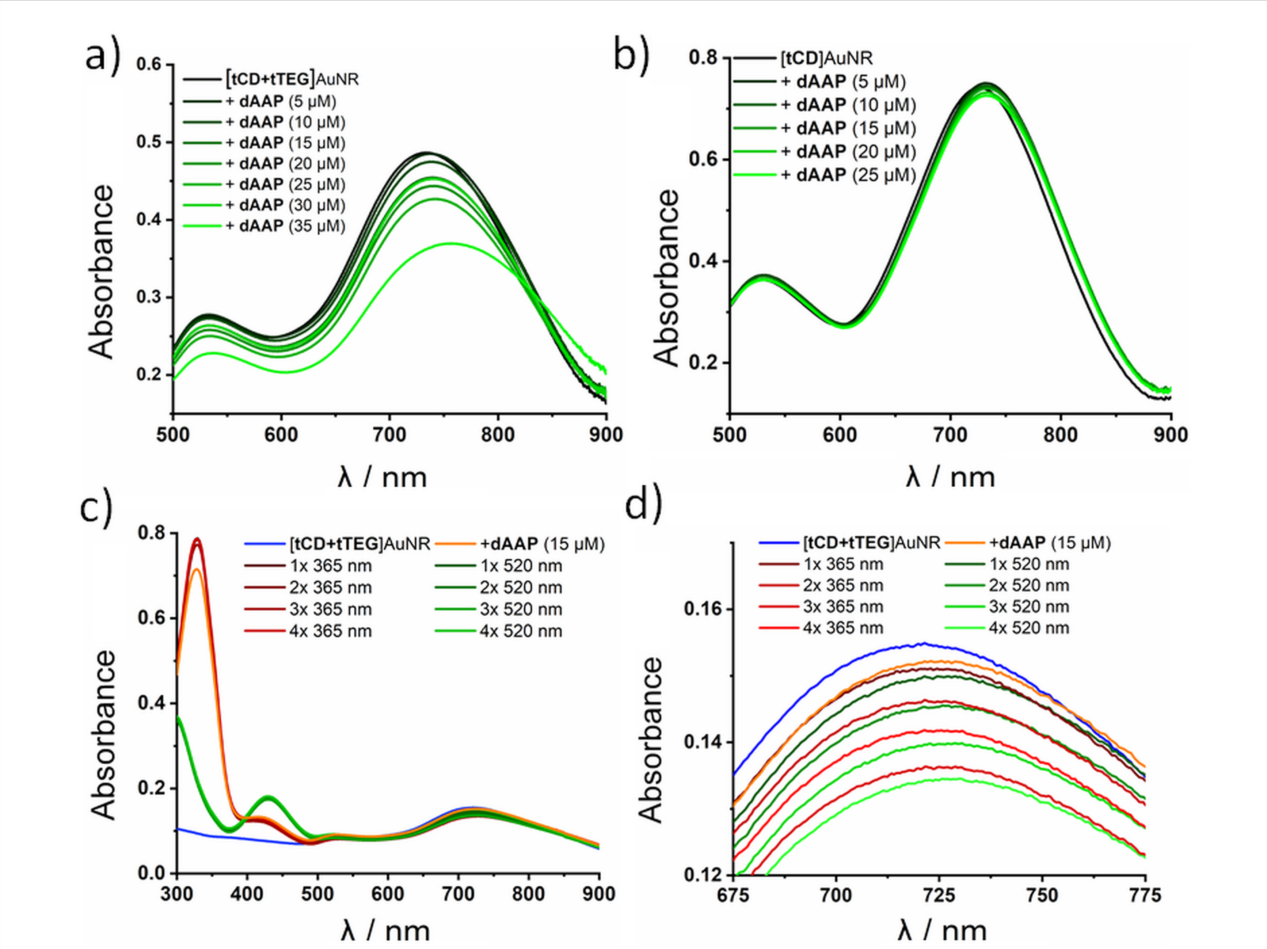


Figure 2: UV–vis spectroscopy of a) [tCD+tTEG]AuNR with different amount of dAAP (0-35 µM). b) [tCD]AuNR with dAAP (0–25 µM). c) [tCD+tTEG]AuNR with dAAP (15 µM). Assembly and disassembly by irradiation (5 min, 3 W lamp, λ = 360 nm and λ = 520 nm) over four cycles. d) Zoomed-in region of the LSPR.

effects during the TEM grid preparation [11,27]. Adding the dAAP to the intermediate state of the ligand exchange ([tCD]AuNR, with CTAB surface coating on the sides of the particles) showed no significant shift of the SPR maxima (Figure 2b). This observation is consistent with the results of Ma et al. and reinforces the assumption that CTAB behaves as a competitive guest molecule towards β-CD. Therefore, reversible host–guest chemistry was not possible unless CTAB is completely removed.

The reversibility of the light-responsive assembly was further investigated via UV–vis spectroscopy (Figure 2c and d). The spectrum measured after injection of dAAP shows a broadened LSPR maximum with a red shift of λ = 7 nm while the TSPR band remains unchanged. This indicates longitudinal coupling of AuNR as a result of the formation of end-to-end assemblies. Irradiation with UV light (λ = 365 nm, 5 min, 3 W) led to a sharpening of the LSPR band in addition to a blue-shifted maximum to λ = 721 nm, which is the same value recorded before the addition of dAAP. The LSPR and TSPR maxima have been plotted over four cycles showing only minor changes of the TSPR over the assembly (Figure 3). For reversible end-to-end assembly of AuNR, a shift λ < 10 nm is the expected range as it has been reported previously [18,38]. Longer irradiation times did not lead to stronger SPR band shifts and therefore all samples were irradiated for 5 min of the respective wavelength.

Via irradiation with visible light (λ = 520 nm, 5 min, 3 W), the LSPR band is again broadened and shifted to a higher wavelength indicating the assembly of AuNR. This procedure could be repeated over four cycles without any fatigue effect and shows the good reversibility of the switching behavior. The dispersion of AuNR assemblies after visible light irradiation can also be verified by TEM bright field images (Figure 4d) showing that the disassembly is possible without the combination of irradiation and sonication. This can be attributed to the favorable photostationary states of the AAP moiety in compari-

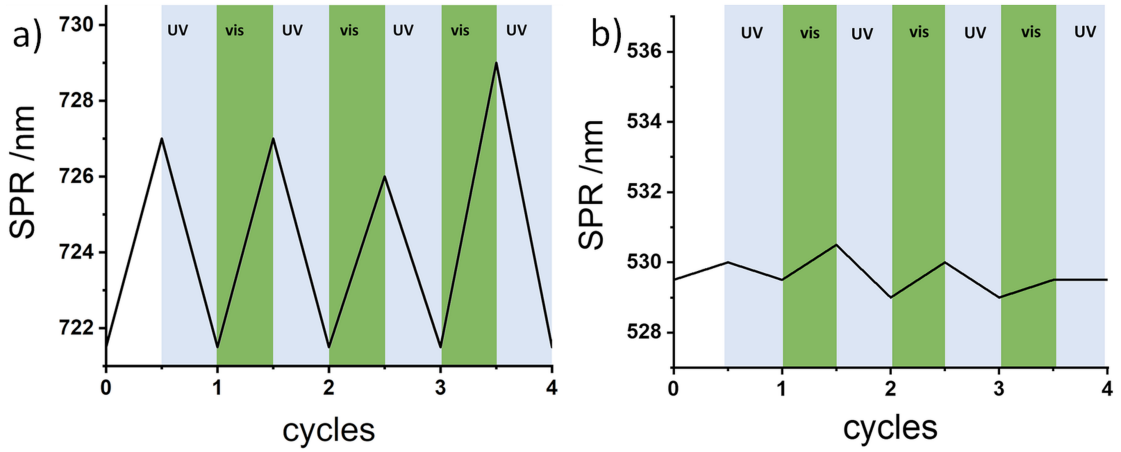


Figure 3: SPR maxima of [tCD+tTEG]AuNR with dAAP during four cycles of irradiation. a) Longitudinal SPR. b) Transversal SPR.

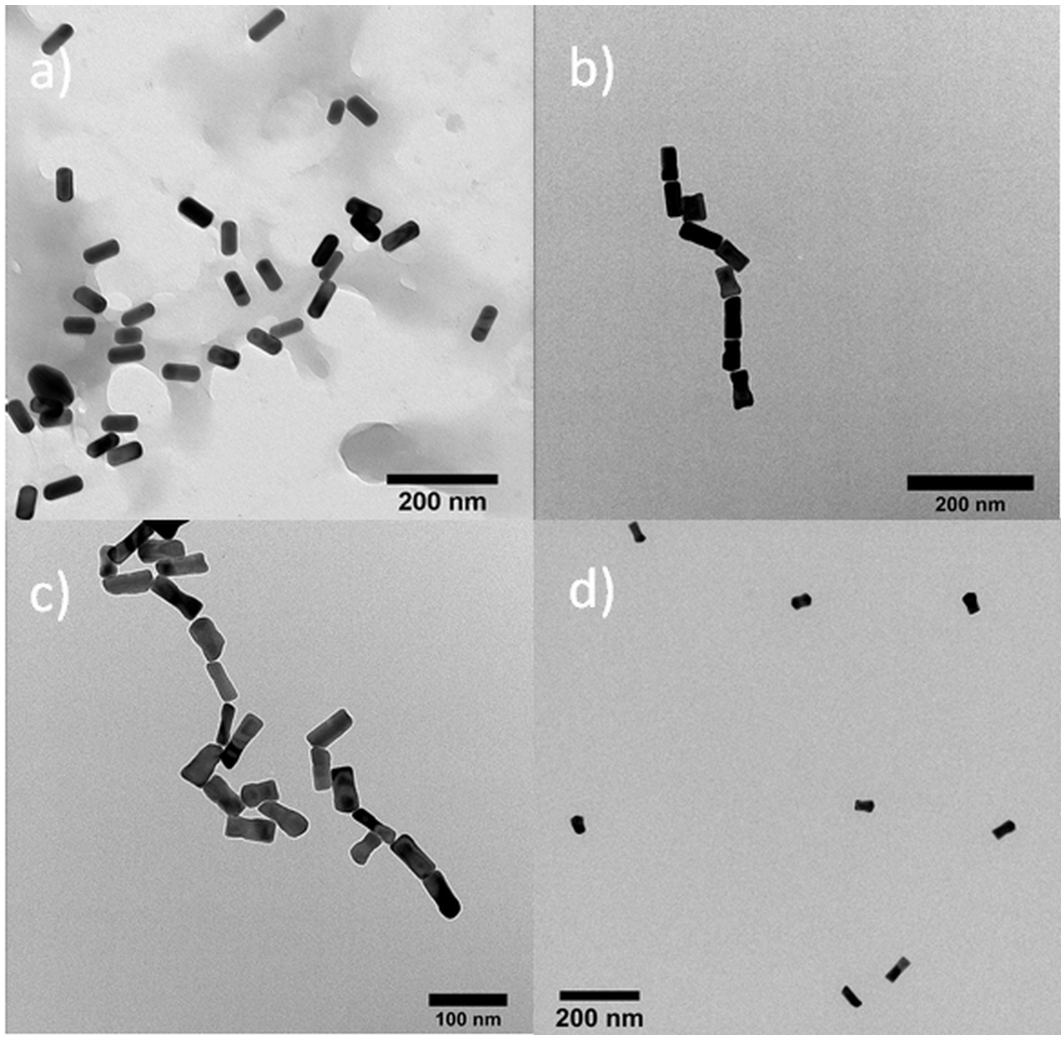


Figure 4: TEM-BF images of a) [tCD+tTEG]AuNR. b and c) AuNR end-to-end assemblies by dAAP (15 μM). d) Dissolved AuNR by UV irradiation (λ = 360 nm).

son to azobenzenes used in previous studies. Furthermore, dynamic light scattering was conducted to analyze the assembly in solution (Figure 5). The mean diameter increases upon dAAP addition from ca. 100 nm to ca. 230 nm. Upon UV-light irradiation, the mean diameter decreases to 120 nm. We note that for anisotropic particles, the hydrodynamic diameter values give only a rough overestimation of the nanoparticle diameter and are not suitable to characterize end-to-end assembly. However dynamic light scattering clearly confirms the light-responsive aggregation of the AuNR [47].

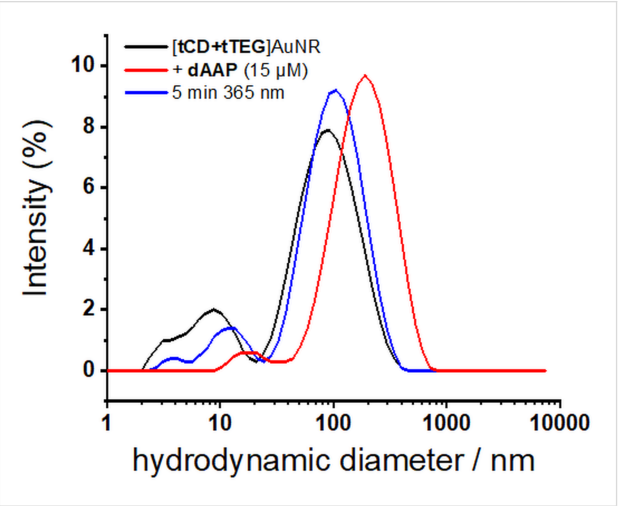


Figure 5: Reversible aggregation of [tCD+tTEG]AuNR by addition of dAAP (15 µM) monitored by dynamic light scattering.

Finally, to confirm that end-to-end assembly of AuNR occurs through the formation of a 2:1 complex of the [tCD+tTEG]AuNR and dAAP, a control experiment was performed by the addition of a monovalent AAP (mAAP) molecule (see Scheme S1 and Figure S3 in Supporting Information File 1). Even upon addition of rather high concentrations of mAAP (100 µM) no strong shift can be observed by UV–vis spectroscopy, indicating that supramolecular cross-linking is essential for end-to-end assembly of the AuNR.

Conclusion

In summary, we reported a supramolecular system based on the reversible light-responsive interaction between arylazopyrazoles and β-CD for the end-to-end assembly of AuNR. The substitution of azobenzenes by AAP as guest molecules, which feature nearly quantitative photostationary states, allows the control over assembled and disassembled states solely by irradiation. The divalent AAP linker forms a 1:2 complex with per-6-thiolated β-CD which is selectively located at the ends of the AuNR. This was achieved through a novel two-step ligand exchange reaction including the complete removal of CTAB by the addition of thiolated TEG. The removal of CTAB is crucial due to its competitive interaction with β-CD since it has a higher binding constant than the AAP moieties. The success of the consecutive ligand exchange strategy was verified by ζ-potential measurements. The selective end-to-end assembly of AuNR was evidenced by UV–vis and TEM measurements. The LSPR shift could reversibly be shifted back and forth ending at the original wavelength. Switching of the end-to-end assembly was possible over four cycles without fatigue appearance. Previously reported limited feasibilities of azobenzenes could be resolved by the implementation of arylazopyrazoles. This report shows a successful method for the fabrication of new hybrid nanomaterials by the application of light-responsive host–guest chemistry allowing for effective control over assembled and disassembled states of anisotropic nanoparticles over several cycles.

Experimental

Instrumentation and materials

All chemicals were purchased from Sigma-Aldrich, Acros Organics, Merck, VWR or TCI and used without further purification if not stated otherwise. UV–vis absorbance measurements were performed with a V-770 double beam spectrophotometer (JASCO) at 25 °C. Samples for spectroscopic measurements were prepared in disposable 1 mL semi-micro PMMA cuvettes (BRAND). Transmission electron microscopy was performed using a Titan Themis G3 300 TEM (FEI) operating at 300 kV or a Libra 200 FE electron microscope (Zeiss) operating at 200 kV. The ζ-potential measurements were carried out on a Nano ZS Zetasizer (Malvern Instruments) at 25 °C and samples were prepared in disposable DTS 1060 capillary cells (Malvern Instruments). The syntheses of the tCD and tTEG can be found in Supporting Information File 1.

AuNR seed-mediated growth

The CTAB-stabilized AuNR were synthesized according to a literature procedure [38,39]. All glassware used were rinsed with aqua regia before use. A 0.1 M aqueous solution of CTAB was prepared by gentle heating and sonication. Au seeds were prepared as follows: An aqueous solution of $HAuCl_4{\cdot}3H_2O$ (250 µL, 0.01 M) was added to an aqueous solution of CTAB (9.75 mL, 0.1 M) in a round-bottomed flask. The solution was stirred at 25 °C for 10 min. Then, a freshly prepared ice-cold aqueous solution of $NaBH_4$ (600 µL, 0.01 M, prepared by diluting an 0.1 M solution) was added in one portion under vigorous stirring. After 10 min, stirring was slowed down to 200 rpm and continued at 25 °C. The seeds were kept at this temperature until their further use.

Growth of AuNR: Aqueous solutions of CTAB (95 mL, 0.1 M), $HAuCl_4{\cdot}3H_2O$ (5 mL, 0.01 M), $AgNO_3$ (800 µL, 0.01 M) and ascorbic acid (800 µL, 0.1 M) were added in the given order to

a 100 mL Erlenmeyer flask and were mixed after every addition by stirring. The addition of ascorbic acid turned the yellow solution colourless due to Au^{3+} to Au^{+} reduction. The flask was placed into a water bath of 25 °C. After 10 min, seed solution (120 µL) was added and mixed by gentle stirring. Stirring was continued for 18 h. The obtained AuNR solution was separated into two falcon tubes (50 mL) and centrifuged (6000 rpm, 20 min). The AuNR pellet was redispersed in H_2O (50 mL each tube) and centrifuged again (6000 rpm, 20 min). The AuNR were dissolved in H_2O stock solution of a total amount of 10 mL and stored in the fridge.

[tCD+tTEG]AuNR ligand exchange

The isolated AuNR (1.9 mL of the stock solution) were diluted with H_2O (8.1 mL) and tCD (3 mL, 0.5 mM, freshly prepared) was added dropwise under sonication. The solution was further sonicated for 10 min and then stirred for 18 h at 30 °C. A fresh aqueous solution of tTEG (2 mL, 10 mM) was added under sonication. The solution was stirred for 1 h at 30 °C. After this, EtOH abs. (3 mL) was added and stirring was continued at 30 °C for 1.5 h. DMSO (10 mL) was added and the resulting solution was centrifuged (6000 rpm, 10 min). The AuNR pellet was redispersed in H_2O/EtOH 1:1 (10 mL) and centrifuged again (6000 rpm, 10 min). For final removal of excess ligands, the AuNR were purified by centrifugal filtration (2 × 3 mL H_2O, 6000 rpm, 10 min, 10 kDa MWCO).

Supporting Information

Supporting Information File 1

Experimental details and additional characterization data.
[https://www.beilstein-journals.org/bjoc/content/supplementary/1860-5397-15-140-S1.pdf]

Acknowledgements

We are grateful for financial support by the Deutsche Forschungsgemeinschaft (DFG Ra 1732/7-1 and INST 211/719-1 FUGG for TEM instrumentation). We thank Dr. Lucas Stricker for the synthesis of AAP. Dr. Sabrina Engel is acknowledged for inspiring discussions.

ORCID® iDs

Bart Jan Ravoo - https://orcid.org/0000-0003-2202-7485

References

1. Motl, N. E.; Smith, A. F.; DeSantis, C. J.; Skrabalak, S. E. *Chem. Soc. Rev.* **2014,** *43,* 3823–3834. doi:10.1039/c3cs60347d
2. Gschneidtner, T. A.; Diaz Fernandez, Y. A.; Moth-Poulsen, K. *J. Mater. Chem. C* **2013,** *1,* 7127–7133. doi:10.1039/c3tc31483a
3. Makarenko, K. S.; Liu, Z.; de Jong, M. P.; Zwanenburg, F. A.; Huskens, J.; van der Wiel, W. G. *Adv. Mater. (Weinheim, Ger.)* **2017,** *29,* 1702920. doi:10.1002/adma.201702920
4. Howes, P. D.; Chandrawati, R.; Stevens, M. M. *Science* **2014,** *346,* 1247390. doi:10.1126/science.1247390
5. Polavarapu, L.; Pérez-Juste, J.; Xu, Q.-H.; Liz-Marzán, L. M. *J. Mater. Chem. C* **2014,** *2,* 7460–7467. doi:10.1039/c4tc01142b
6. Willets, K. A.; Van Duyne, R. P. *Annu. Rev. Phys. Chem.* **2007,** *58,* 267–297. doi:10.1146/annurev.physchem.58.032806.104607
7. Eustis, S.; El-Sayed, M. A. *Chem. Soc. Rev.* **2006,** *35,* 209–217. doi:10.1039/b514191e
8. Jensen, T. R.; Malinsky, M. D.; Haynes, C. L.; Van Duyne, R. P. *J. Phys. Chem. B* **2000,** *104,* 10549–10556. doi:10.1021/jp002435e
9. Chen, H.; Shao, L.; Li, Q.; Wang, J. *Chem. Soc. Rev.* **2013,** *42,* 2679–2724. doi:10.1039/c2cs35367a
10. Liu, K.; Nie, Z.; Zhao, N.; Li, W.; Rubinstein, M.; Kumacheva, E. *Science* **2010,** *329,* 197–200. doi:10.1126/science.1189457
11. Leung, F. C.-M.; Leung, S. Y.-L.; Chung, C. Y.-S.; Yam, V. W.-W. *J. Am. Chem. Soc.* **2016,** *138,* 2989–2992. doi:10.1021/jacs.6b01382
12. Ma, W.; Kuang, H.; Xu, L.; Ding, L.; Xu, C.; Wang, L.; Kotov, N. A. *Nat. Commun.* **2013,** *4,* No. 2689. doi:10.1038/ncomms3689
13. Jones, S. T.; Zayed, J. M.; Scherman, O. A. *Nanoscale* **2013,** *5,* 5299–5302. doi:10.1039/c3nr01454a
14. Carbó-Argibay, E.; Rodríguez-González, B.; Gómez-Graña, S.; Guerrero-Martínez, A.; Pastoriza-Santos, I.; Pérez-Juste, J.; Liz-Marzán, L. M. *Angew. Chem., Int. Ed.* **2010,** *49,* 9397–9400. doi:10.1002/anie.201004910
15. Nepal, D.; Park, K.; Vaia, R. A. *Small* **2012,** *8,* 1013–1020. doi:10.1002/smll.201102152
16. Katz-Boon, H.; Rossouw, C. J.; Weyland, M.; Funston, A. M.; Mulvaney, P.; Etheridge, J. *Nano Lett.* **2011,** *11,* 273–278. doi:10.1021/nl103726k
17. Indrasekara, A. S. D. S.; Wadams, R. C.; Fabris, L. *Part. Part. Syst. Charact.* **2014,** *31,* 819–838. doi:10.1002/ppsc.201400006
18. Engel, S.; Möller, N.; Stricker, L.; Peterlechner, M.; Ravoo, B. J. *Small* **2018,** *14,* 1704287. doi:10.1002/smll.201704287
19. Möller, N.; Hellwig, T.; Stricker, L.; Engel, S.; Fallnich, C.; Ravoo, B. J. *Chem. Commun.* **2017,** *53,* 240–243. doi:10.1039/c6cc08321h
20. Sagebiel, S.; Stricker, L.; Engel, S.; Ravoo, B. J. *Chem. Commun.* **2017,** *53,* 9296–9299. doi:10.1039/c7cc04594h
21. Krings, J. A.; Vonhören, B.; Tegeder, P.; Siozios, V.; Peterlechner, M.; Ravoo, B. J. *J. Mater. Chem. A* **2014,** *2,* 9587–9593. doi:10.1039/c4ta01359j
22. Han, K.; Go, D.; Tigges, T.; Rahimi, K.; Kuehne, A. J. C.; Walther, A. *Angew. Chem., Int. Ed.* **2017,** *56,* 2176–2182. doi:10.1002/anie.201612196
Angew. Chem., **2017,** *129,* 2208–2214. doi:10.1002/ange.201612196
23. Liu, J.; Mendoza, S.; Román, E.; Lynn, M. J.; Xu, R.; Kaifer, A. E. *J. Am. Chem. Soc.* **1999,** *121,* 4304–4305. doi:10.1021/ja990330n
24. de laRica, R. M.; Fratila, R. M.; Szarpak, A.; Huskens, J.; Velders, A. H. *Angew. Chem., Int. Ed.* **2011,** *50,* 5704–5707. doi:10.1002/anie.201008189
Angew. Chem. **2011,** *123,* 5822–5825. doi:10.1002/ange.201008189
25. Engel, S.; Möller, N.; Ravoo, B. J. *Chem. – Eur. J.* **2018,** *24,* 4741–4748. doi:10.1002/chem.201705540
26. Bandara, H. M. D.; Burdette, S. C. *Chem. Soc. Rev.* **2012,** *41,* 1809–1825. doi:10.1039/c1cs15179g
27. Wu, J.; Xu, Y.; Li, D.; Ma, X.; Tian, H. *Chem. Commun.* **2017,** *53,* 4577–4580. doi:10.1039/c7cc01678f

28. Klajn, R. *Pure Appl. Chem.* **2010,** *82,* 2247–2279. doi:10.1351/pac-con-10-09-04
29. Zhao, Y.-L.; Stoddart, J. F. *Langmuir* **2009,** *25,* 8442–8446. doi:10.1021/la804316u
30. Schenkel, J. H.; Samanta, A.; Ravoo, B. J. *Adv. Mater. (Weinheim, Ger.)* **2014,** *26,* 1076–1080. doi:10.1002/adma.201304689
31. Liu, Z.; Jiang, M. *J. Mater. Chem.* **2007,** *17,* 4249–4254. doi:10.1039/b707910a
32. Samanta, A.; Ravoo, B. J. *Chem. – Eur. J.* **2014,** *20,* 4966–4973. doi:10.1002/chem.201304658
33. Dharmawardana, U. R.; Christian, S. D.; Tucker, E. E.; Taylor, R. W.; Scamehorn, J. F. *Langmuir* **1993,** *9,* 2258–2263. doi:10.1021/la00033a003
34. Afkhami, A.; Khalafi, L. *J. Chin. Chem. Soc.* **2007,** *54,* 431–436. doi:10.1002/jccs.200700060
35. Dwivedi, A. K.; Singh, R.; Singh, A.; Wei, K.-H.; Wu, C.-Y.; Lyu, P.-C.; Lin, H.-C. *Macromolecules* **2016,** *49,* 5587–5598. doi:10.1021/acs.macromol.6b00789
36. Nalluri, S. K. M.; Voskuhl, J.; Bultema, J. B.; Boekema, E. J.; Ravoo, B. J. *Angew. Chem., Int. Ed.* **2011,** *50,* 9747–9751. doi:10.1002/anie.201103707
Angew. Chem. **2011,** *123* 9921–9925. doi:10.1002/ange.201103707
37. Weston, C. E.; Richardson, R. D.; Haycock, P. R.; White, A. J. P.; Fuchter, M. J. *J. Am. Chem. Soc.* **2014,** *136,* 11878–11881. doi:10.1021/ja505444d
38. Stricker, L.; Fritz, E.-C.; Peterlechner, M.; Doltsinis, N. L.; Ravoo, B. J. *J. Am. Chem. Soc.* **2016,** *138,* 4547–4554. doi:10.1021/jacs.6b00484
39. Chu, C.-W.; Ravoo, B. J. *Chem. Commun.* **2017,** *53,* 12450–12453. doi:10.1039/c7cc07859e
40. Jana, N. R.; Gearheart, L.; Murphy, C. J. *J. Phys. Chem. B* **2001,** *105,* 4065–4067. doi:10.1021/jp0107964
41. Nikoobakht, B.; El-Sayed, M. A. *Chem. Mater.* **2003,** *15,* 1957–1962. doi:10.1021/cm020732l
42. Gadelle, A.; Defaye, J. *Angew. Chem., Int. Ed. Engl.* **1991,** *30,* 78–80. doi:10.1002/anie.199100781
Angew. Chem. **1991,** *103,* 94–95. doi:10.1002/ange.19911030121
43. Rojas, M. T.; Koeniger, R.; Stoddart, J. F.; Kaifer, A. E. *J. Am. Chem. Soc.* **1995,** *117,* 336–343. doi:10.1021/ja00106a036
44. Chan, Y.-H. M.; Schweiss, R.; Werner, C.; Grunze, M. *Langmuir* **2003,** *19,* 7380–7385. doi:10.1021/la0343977
45. Jokerst, J. V.; Lobovkina, T.; Zare, R. N.; Gambhir, S. S. *Nanomedicine (London, U. K.)* **2011,** *6,* 715–728. doi:10.2217/nnm.11.19
46. Henson, C. B.; Harris, J. T.; Homan, K. A. *Mater. Matters* **2017,** *12,* 26–30.
47. Wang, Y.; Li, Y. F.; Wang, J.; Sang, Y.; Huang, C. Z. *Chem. Commun.* **2010,** *46,* 1332–1334. doi:10.1039/b921464j

License and Terms

This is an Open Access article under the terms of the Creative Commons Attribution License (http://creativecommons.org/licenses/by/4.0). Please note that the reuse, redistribution and reproduction in particular requires that the authors and source are credited.

The license is subject to the *Beilstein Journal of Organic Chemistry* terms and conditions: (https://www.beilstein-journals.org/bjoc)

The definitive version of this article is the electronic one which can be found at: doi:10.3762/bjoc.15.140

BEILSTEIN JOURNAL OF ORGANIC CHEMISTRY

Diazocine-functionalized TATA platforms

Roland Löw[1], Talina Rusch[2], Fynn Röhricht[1], Olaf Magnussen[2] and Rainer Herges[*1]

Full Research Paper

Open Access

Address:
[1]Otto Diels Institute of Organic Chemistry, University of Kiel, Otto-Hahn-Platz 4, 24118 Kiel, Germany and [2]Institute for Experimental and Applied Physics, University of Kiel, Leibnizstraße 19, 24098 Kiel, Germany

Email:
Rainer Herges[*] - rherges@oc.uni-kiel.de

* Corresponding author

Keywords:
cis–trans isomerization; diazocine; molecular switch; photochrome; self-assembled monolayers; TATA platform

Beilstein J. Org. Chem. **2019,** *15,* 1485–1490.
doi:10.3762/bjoc.15.150

Received: 17 April 2019
Accepted: 28 June 2019
Published: 05 July 2019

This article is part of the thematic issue "Molecular switches".

Guest Editor: W. Szymanski

© 2019 Löw et al.; licensee Beilstein-Institut.
License and terms: see end of document.

Abstract

Recently, it has been shown that the thermochemical *cis*→*trans* isomerization of azobenzenes is accelerated by a factor of more than 1000 by electronic coupling to a gold surface via a conjugated system with 11 bonds and a distance of 14 Å. The corresponding molecular architecture consists of a platform (triazatriangulenium (TATA)) which adsorbs on the gold surface, with an acetylene spacer standing upright, like a post in the middle of the platform and the azobenzene unit mounted on top. The rate acceleration is due to a very peculiar thermal singlet–triplet–singlet mechanism mediated by bulk gold. To investigate this mechanism further and to examine scope and limitation of the "spin-switch catalysis" we now prepared analogous diazocine systems. Diazocines, in contrast to azobenzenes, are stable in the *cis*-configuration. Upon irradiation with light of 405 nm the *cis*-configuration isomerizes to the *trans*-form, which slowly returns back to the stable *cis*-isomer. To investigate the thermal *trans*→*cis* isomerization as a function of the conjugation to the metal surface, we connected the acetylene spacer in *meta* (weak conjugation) and in *para* (strong conjugation) position. Both isomers form ordered monolayers on Au(111) surfaces.

Introduction

Catalysts increase chemical reaction rates by lowering the activation energies and thus create more favorable reaction pathways [1-4]. However, there are very few reactions which do not follow the classical Eyring theory [5,6]. The rate of these reactions is not dependent on an activation barrier but controlled by quantum mechanical transition probabilities between two quantum states [7-10]. The majority of these quantum chemically forbidden reactions are photochemical processes or transition metal reactions including transitions between spin states or electronic states. We recently discovered a purely organic system in the ground state, whose reaction rate is accelerated from days to seconds by electronic coupling to a bulk gold surface via a conjugated linker over 11 bonds and 14 Å [11]. Thermal *cis*→*trans* isomerizations of azobenzenes are usually slow with half-lives of the *trans*-isomer within the range of hours to days at room temperature (parent azobenzene: 4–5 d at 25 °C) [12]. Rotation around the N=N bond is a symmetry-forbidden process and the slow isomerization proceeds via inversion at the

N atoms [13]. The rate of isomerization is temperature dependent and follows a classical Arrhenius type behavior [12]. However, the rate and the mechanism change dramatically if the azobenzenes are electronically coupled to bulk gold [14-17]. To investigate the *cis*→*trans* isomerizations of azobenzenes as a function of electronic coupling systematically, we used the so-called platform approach [18]. The azobenzenes are not directly adsorbed on the surface, but covalently mounted on "TATA" (triazatriangulenium) platforms which adsorb on Au(111) surfaces. A spacer, such as an ethynyl group is connected to the central carbon atom like a post and the azobenzene is mounted on top of the spacer. After preparation of an ordered self-assembled monolayer on gold, the azobenzene units are freestanding upright on the surface. The platform defines the lateral distance between next neighbors and provides the free volume for unhindered isomerization of the azobenzene units [19,20]. The length and electronic nature of the spacer units control the distance from the surface and define the electronic coupling with the metal surface [11,18]. With increasing π-conjugation from the azobenzene into the platform, and thus coupling to the gold surface, the activation barrier drops to almost zero (≈8 kJ mol^{-1}) and the frequency factors (log A) become negative [11]. Vanishing barriers and low frequency factors are typical for non-adiabatic reactions [9]. The mechanism was elucidated as a singlet–triplet–singlet spin change process, which is forbidden in solution but mediated by coupling to the conduction band of the bulk gold. We are now exploring scope and limitations of this peculiar spin catalysis. To investigate if the reverse isomerization process from the *trans* to the *cis*-configuration would also be accelerated, and to further scrutinize the coupling effects, we prepared analogous diazocine systems. Diazocines are bridged azobenzenes [21]. Imposed by the ring strain of the central eight-membered ring, the *cis*-configuration (boat conformation) is more stable than the *trans*-isomer (twist conformation). Upon irradiation with ≈400 nm the *cis*-form switches to the *trans*-isomer, and irradiation with ≈500 nm or heating leads back to the *cis*-form [22]. Hence, the diazocines are quasi reversed azobenzenes that are more stable in their *trans*-configurations [23].

To investigate the electronic coupling effects, we synthesized two diazocine derivatized TATA platforms with ethynyl spacers (diazocine-TATAs). In compound **1** the diazocine is connected to the platform with the ethynyl group in *para*-position to the azo group, providing a full π-conjugation path of the N=N unit through the ethynyl spacer into the platform. Diazocine-TATA **2** is connected in *meta*-position and thus interrupting conjugation [24,25]. Both diazocine-TATAs are equipped with methoxy groups, which serve as "reporter units" indicating the configuration of the molecules on metal surfaces [15]. In **1** the OMe group is attached *para* and in **2** the methoxy group is *meta* with respect to the azo group. Model calculations predict that the C_{phenyl}–O bonds in the *cis*-isomers thus are parallel, and in the *trans*-isomers orthogonal to the surface (Figure 1). Previous investigations have shown that IRRAS (infrared absorption reflection spectroscopy) in combination with the surface selection rules (stretching mode orthogonal to the surface→high intensity, parallel to the surface→low intensity) is a suitable method to determine the configuration and to measure kinetics on surfaces [15]. The C–O stretching frequencies proved to be ideal reporter signals to determine the configuration and to measure kinetics in monolayers of azo-TATAs on surfaces.

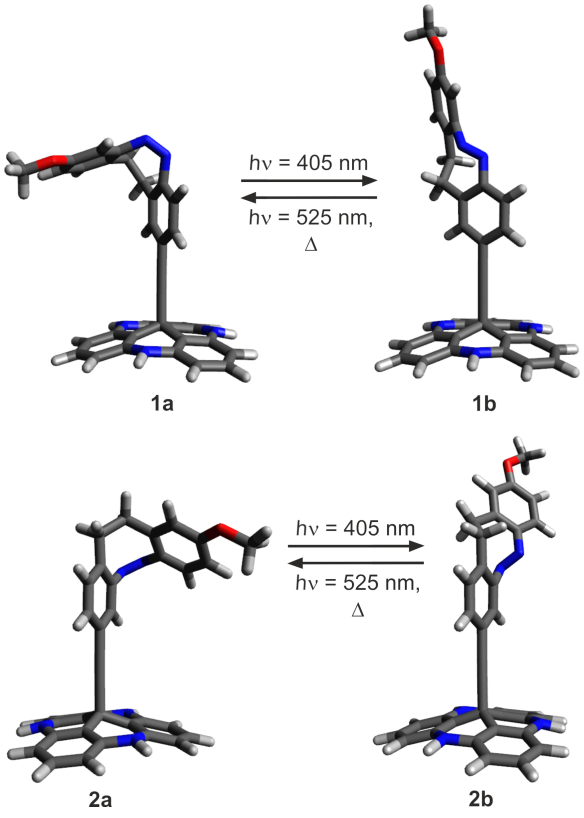


Figure 1: Structures of diazocine platform molecules (diazocine-TATAs) **1** and **2** in *cis* (**1a**, **2a**) and *trans*-configuration (**1b**, **2b**) (octyl side chains are replaced by protons for simplification). The *cis*-diazocines (**1a**, **2a**) isomerize upon irradiation with 405 nm to the metastable *trans*-diazocines (**1b**, **2b**) and with 525 nm or thermally back to the *cis*-diazocines (**1a**, **2a**).

Results and Discussion

To obtain information on preferred conformations of **1** and **2** in their *cis* and *trans*-configurations and to predict thermodynamic and kinetic stabilities, we performed DFT calculations at the M06-2X/def2-TZVP level of theory (Table 1, for details see Supporting Information File 1, chapter VI). As expected for

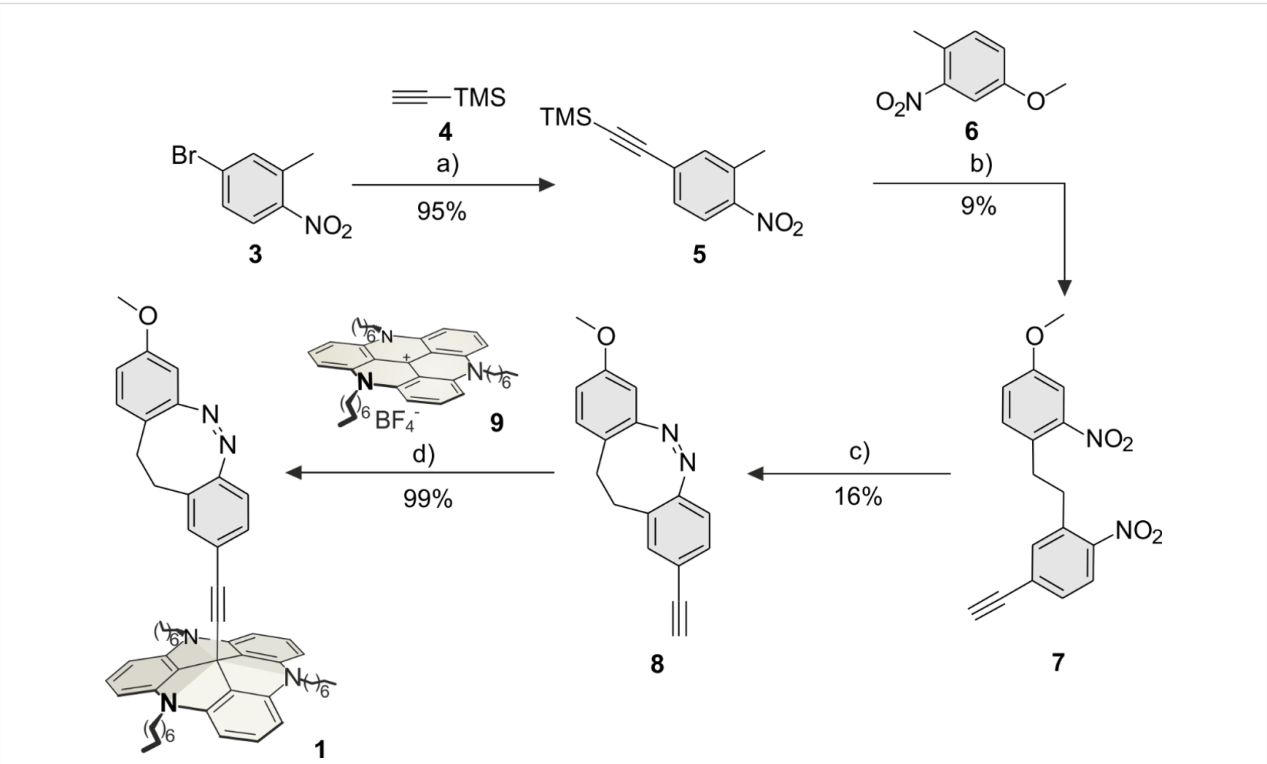
diazocine-based molecules our calculations predict the *cis* configuration for both compounds as the thermodynamically most stable isomers. For the corresponding *trans*-configuration two different conformations were found: the twist and the chair structures. The twist conformation is about 2.5 kcal mol^{-1} more stable than the chair conformation. Our calculations predict reaction barriers (*trans*-twist→*cis*-boat) for both compounds of approximately 23 kcal mol^{-1} (96 kJ mol^{-1}). Obviously, the TATA platform and the ethynyl spacer have only marginal effects on the isomerization process. Hence, the diazocines **1** and **2** are ideal candidates to investigate the effect of bulk gold as a function of electronic coupling (conjugation) of the azo unit to gold.

Table 1: Calculated quantum chemical energies E_{rel} (M06-2X/def2-TZVP) of the twist and chair conformation of the *trans*-configuration of *para*-ethynyl-substituted diazocine **1b** (*para*-diazocine), and *meta*-diazocine **2b**, relative to the boat conformation of the *cis*-isomers **1a** and **2a**. $\Delta H^{\neq}$ are the calculated reaction barriers (*trans*-twist→*cis*-boat). All energies are given in kcal mol^{-1}.

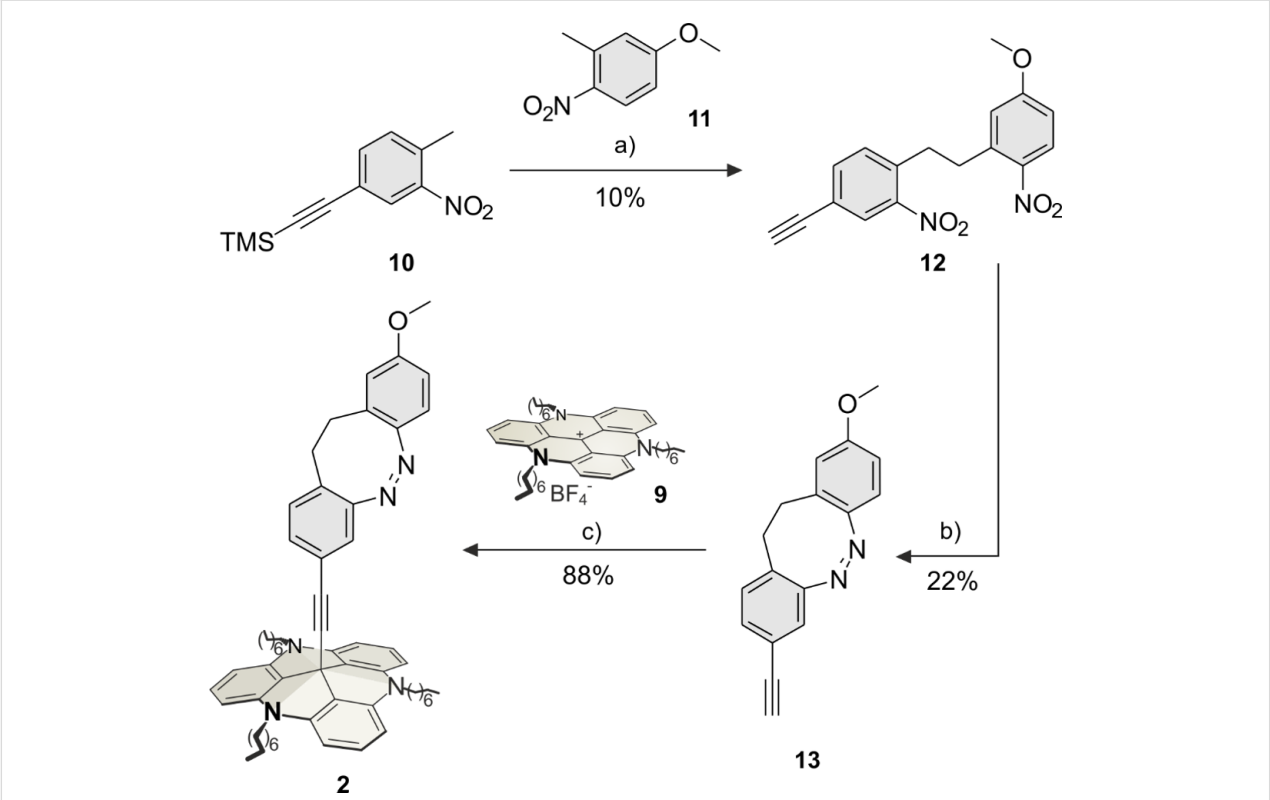
	E_{rel} *trans* twist	E_{rel} *trans* chair	$\Delta H^{\neq}$
para-diazocine **1**	7.9	10.6	22.6
meta-diazocine **2**	8.0	10.3	23.0

The *para*-diazocine-TATA **1** was synthesized in a 5-step synthesis route (Scheme 1). Bromotoluene **3** was synthesized as described [26]. In a Sonogashira cross-coupling reaction acetylene-substituted toluene **5** was prepared from bromotoluene **3** with TMS-protected acetylene **4** (95%). The C–C bond formation of **5** and **6** to give dibenzoyl **7** was achieved with potassium butoxide and elemental bromine (9%) according to a literature procedure [27]. The *para*-ethynyldiazocine **8** was obtained by reduction of both nitro groups, followed by oxidation of the formed hydrazine (16%). The unprotected ethynyldiazocine **8** was deprotonated with potassium hydroxide and connected to the central carbon atom of the TATA platform **9** (synthesized according to Laursen and Krebs [28]) to obtain target *para*-diazocine mounted on the octyl-substituted TATA platform **1** (99%).

The synthesis of the *meta*-diazocine platform molecule **2** was achieved in a 4-step synthesis route (Scheme 2). Nitrotoluene **10** was synthesized as described in literature [29]. The reaction of ethynyltoluene **10** with methoxytoluene **11** gave dibenzoyl **12** (10%) according to the same procedure as for dibenzoyl **7** (Scheme 1). Diazocine **13** was obtained by reduction and oxidation in moderate yields (22%). The reaction of diazocine **13** with the TATA ion **9** gave the target diazocine **2** (88%, Scheme 2).



Scheme 1: Synthesis route of *para*-diazocine platform molecule **1**. a) $Pd(dppf)Cl_2$, Cu(I)I, Et_3N, 1 h, 60 °C; b) 1: KO*t*-Bu, THF, 3 min, 0 °C, N_2; 2: Br_2, 5 min, 0 °C; c) 1: $Ba(OH)_2$, Zn, EtOH, H_2O, 4.75 h, reflux; 2: 0.1 M NaOH/MeOH, $Cu(II)Cl_2$, 6 h, rt; d) KOH, THF, 3.5 h, reflux, N_2.



Scheme 2: Synthesis route of *meta*-diazocine platform **2**. a) 1: KO*t*-Bu, THF, 3 min, 0 °C, N_2; 2: Br_2, 5 min, 0 °C, N_2; b) 1: $Ba(OH)_2$, Zn, EtOH, H_2O, 4.75 h, reflux; 2: 0.1 M NaOH/MeOH, $Cu(II)Cl_2$, 13 h, rt; c) KOH, THF, 2 h, reflux, N_2.

The photophysical properties and the switching behavior of **1** and **2** were determined in solution (THF). The UV–vis spectra of **1** and **2** are shown before and after irradiation with 405 nm and 525 nm. Both diazocine-TATAs **1** and **2** exhibit similar UV spectra. The $n \rightarrow \pi^*$ transition of *cis*-**1** appears at 403 nm and at 494 nm in the *trans*-isomer. The corresponding absorption maxima in diazocine-TATA **2** are 409 nm (*cis*) and 493 nm (*trans*) (Figure 2).

The photostationary states of **1** and **2** were determined in toluene-d_8 by ^{1}H NMR measurements (Table 2). Optimal wavelengths for the *cis*→*trans* isomerization are 405 nm (**1**: 53%

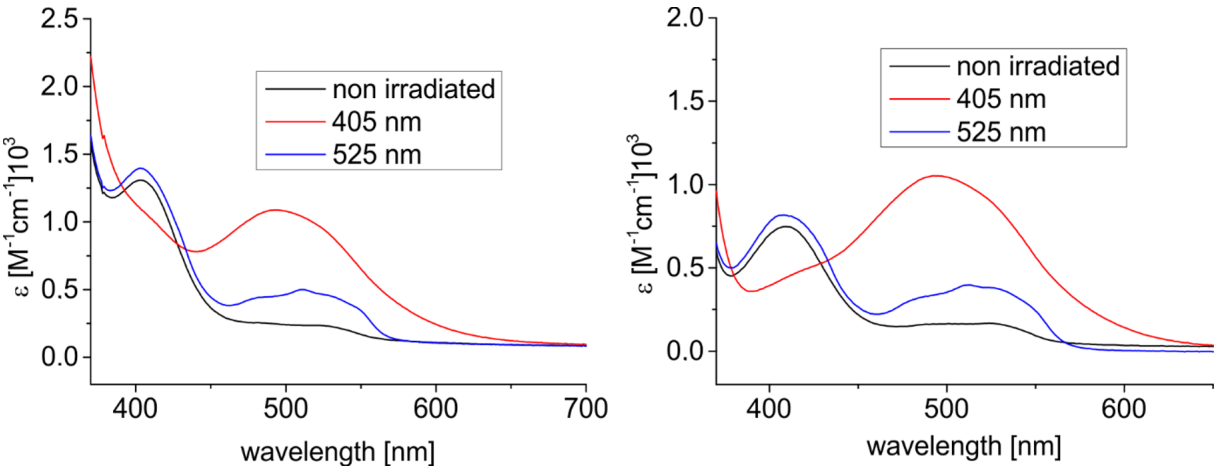


Figure 2: UV–vis spectra of **1** (left) and **2** (right) in THF at room temperature. Black: as synthesized, red: after irradiation with 405 nm, and blue: after irradiation with 525 nm.

trans, **2**: 65% *trans*). Back-isomerization to the *cis*-isomer with 525 nm is nearly quantitative. The half-lives (298 K) are similar for both systems (2.12 h for **1** and 2.32 h for **2**). The lack of conjugation between the azo function and the ethynyl spacer of **2** yields in a slightly higher half-life, which is in agreement with earlier results [11].

Table 2: Photostationary states (PSS) of *para*-diazocine-TATA **1** (2.05 mmol/L) and *meta*-diazocine-TATA **2** (2.27 mmol/L) upon irradiation with light of 405 nm, 525 nm and thermal isomerization half-life ($t_{1/2}$) determined with ^{1}H NMR spectroscopy (in deuterated toluene). The activation energies (E_a) are calculated from the linear fit of an Arrhenius plot.

	para-diazocine **1**	*meta*-diazocine **2**
PSS (405 nm)	53% (*trans*)	65% (*trans*)
PSS (525 nm)	93% (*cis*)	93% (*cis*)
$t_{1/2}$ (290.5 K)	5.27 h	5.76 h
$t_{1/2}$ (298 K)	2.12 h	2.32 h
$t_{1/2}$ (308 K)	0.69 h	0.73 h
E_A (kJ mol^{-1})	86.5	84.7

STM Measurements

The adsorption behavior of the diazocine-TATA molecules on Au(111) surfaces was studied by STM at room temperature (Figure 3). Adlayers of both compounds show a hexagonally ordered superstructure with lattice constants of **1** and **2** being (12.2 ± 0.6) Å and (12.1 ± 0.5) Å, respectively. Additionally, two rotational domains with an angle of (15 ± 4)° are observed. Altogether these parameters are in good agreement with a ($\sqrt{19} \times \sqrt{19}$) *R*23.4° superstructure which has been also observed in previous STM investigations of TATA and azobenzene-TATA molecules with octyl ligands [18,20,30].

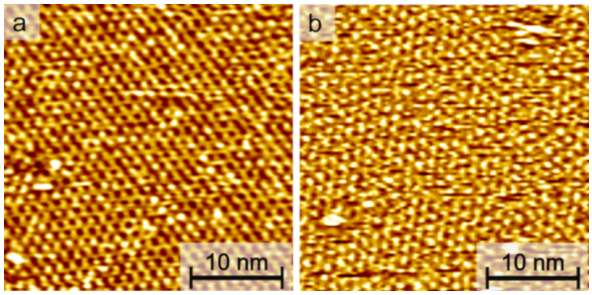


Figure 3: STM images (30 × 30 nm², U_{bias} = 0.3 V, I_t = 40 pA) of self-assembled monolayers of (a) compound **1** and (b) compound **2** on Au(111).

Conclusion

In summary, we present the syntheses of two different diazocines mounted on TATA platforms (**1**, **2**). The photochemical switching between the stable *cis* and metastable *trans*-isomers was investigated. Upon irradiation with light of 405 nm diazocine-TATAs **1** and **2** convert to their *trans*-configurations in moderate to good yields. The metastable *trans*-isomers of **1** and **2** isomerize back to the *cis*-isomer with half-lives of 2.12 h and 2.32 h at 298 K. The *trans*→*cis* activation energies with 86.5 kJ mol^{-1} for **1** and with 84.7 kJ mol^{-1} for **2** are similar to the structurally related azobenzenes [11]. Both diazocine-TATAs form highly ordered monolayers on Au(111) surfaces. Further studies will include IRRAS measurements to determine the *trans*→*cis* isomerization kinetics on Au(111) surfaces.

Experimental

For detailed experimental procedures, including NMR, UV–vis and MS spectra see Supporting Information File 1, chapters I–IV, for kinetic studies see Supporting Information File 1, chapter V.

Supporting Information

Supporting Information File 1

Analytical methods, experimental procedures, NMR and UV spectra, kinetic studies and DFT calculations.
[https://www.beilstein-journals.org/bjoc/content/supplementary/1860-5397-15-150-S1.pdf]

Acknowledgements

The authors gratefully acknowledge financial support by the Deutsche Forschungsgesellschaft within the Sonderforschungsbereich 677, “Function by Switching”.

ORCID® iDs

Roland Löw - https://orcid.org/0000-0002-3051-7831
Talina Rusch - https://orcid.org/0000-0001-8123-6792
Fynn Röhricht - https://orcid.org/0000-0001-9935-9256
Rainer Herges - https://orcid.org/0000-0002-6396-6991

Preprint

A non-peer-reviewed version of this article has been previously published as a preprint doi:10.3762/bxiv.2019.11.v1

References

1. Hauffe, K., Ed. *Katalyse;* DE GRUYTER: Berlin, New York, 1976; p 119. doi:10.1515/9783110829990
2. Ostbald, W. *Z. Phys. Chem.* **1894,** *15,* 705–706.
3. Oyama, S. T.; Somorjai, G. A. *J. Chem. Educ.* **1988,** *65,* 765–769. doi:10.1021/ed065p765
4. Shriver, D. F.; Atkins, P. W.; Langford, C. H. In *Anorganische Chemie,* 2nd ed.; Heck, J.; Kaim, W.; Weidenbruch, M., Eds.; Wiley-VCH: Weinheim, Germany, 1997; p 692.
5. Eyring, H. *J. Chem. Phys.* **1935,** *3,* 107–115. doi:10.1063/1.1749604

6. Gowenlock, B. G. *Q. Rev., Chem. Soc.* **1960,** *14,* 133–145. doi:10.1039/qr9601400133
7. Hauser, A. *Coord. Chem. Rev.* **1991,** *111,* 275–290. doi:10.1016/0010-8545(91)84034-3
8. Xie, C.-L.; Hendrickson, D. N. *J. Am. Chem. Soc.* **1987,** *109,* 6981–6988. doi:10.1021/ja00257a013
9. Harvey, J. N. *Phys. Chem. Chem. Phys.* **2007,** *9,* 331–343. doi:10.1039/b614390c
10. Schreiner, P. R.; Reisenauer, H. P.; Pickard IV, F. C.; Simmonett, A. C.; Allen, W. D.; Mátyus, E.; Császár, A. G. *Nature* **2008,** *453,* 906–909. doi:10.1038/nature07010
11. Schlimm, A.; Löw, R.; Rusch, T.; Röhricht, F.; Strunskus, T.; Tellkamp, T.; Sönnichsen, F.; Manthe, U.; Magnussen, O.; Tuczek, F.; Herges, R. *Angew. Chem., Int. Ed.* **2019,** *58,* 6574–6578. doi:10.1002/anie.201814342
12. Hartley, G. S. *J. Chem. Soc.* **1938,** 633–642. doi:10.1039/jr9380000633
13. Shinkai, S.; Kusano, Y.; Shigematsu, K.; Manabe, O. *Chem. Lett.* **1980,** *9,* 1303–1306. doi:10.1246/cl.1980.1303
14. Jung, U.; Schütt, C.; Filinova, O.; Kubitschke, J.; Herges, R.; Magnussen, O. *J. Phys. Chem. C* **2012,** *116,* 25943–25948. doi:10.1021/jp310451c
15. Jacob, H.; Ulrich, S.; Jung, U.; Lemke, S.; Rusch, T.; Schütt, C.; Petersen, F.; Strunskus, T.; Magnussen, O.; Herges, R.; Tuczek, F. *Phys. Chem. Chem. Phys.* **2014,** *16,* 22643–22650. doi:10.1039/c4cp03438d
16. Krekiehn, N. R.; Müller, M.; Jung, U.; Ulrich, S.; Herges, R.; Magnussen, O. M. *Langmuir* **2015,** *31,* 8362–8370. doi:10.1021/acs.langmuir.5b01645
17. Hagen, S.; Kate, P.; Peters, M. V.; Hecht, S.; Wolf, M.; Tegeder, P. *Appl. Phys. A: Mater. Sci. Process.* **2008,** *93,* 253–260. doi:10.1007/s00339-008-4831-5
18. Baisch, B.; Raffa, D.; Jung, U.; Magnussen, O. M.; Nicolas, C.; Lacour, J.; Kubitschke, J.; Herges, R. *J. Am. Chem. Soc.* **2009,** *131,* 442–443. doi:10.1021/ja807923f
19. Ulrich, S.; Jung, U.; Strunskus, T.; Schütt, C.; Bloedorn, A.; Lemke, S.; Ludwig, E.; Kipp, L.; Faupel, F.; Magnussen, O.; Herges, R. *Phys. Chem. Chem. Phys.* **2015,** *17,* 17053–17062. doi:10.1039/c5cp01447f
20. Kuhn, S.; Baisch, B.; Jung, U.; Johannsen, T.; Kubitschke, J.; Herges, R.; Magnussen, O. *Phys. Chem. Chem. Phys.* **2010,** *12,* 4481. doi:10.1039/b922882a
21. Duval, H. *Bull. Soc. Chim. Fr.* **1910,** *7,* 727.
22. Siewertsen, R.; Neumann, H.; Buchheim-Stehn, B.; Herges, R.; Näther, C.; Renth, F.; Temps, F. *J. Am. Chem. Soc.* **2009,** *131,* 15594–15595. doi:10.1021/ja906547d
23. Hartley, G. S. *Nature* **1937,** *140,* 281. doi:10.1038/140281a0
24. Yaliraki, S. N.; Ratner, M. A. *Ann. N. Y. Acad. Sci.* **2002,** *960,* 153–162. doi:10.1111/j.1749-6632.2002.tb03030.x
25. Mayor, M.; Büschel, M.; Fromm, K. M.; Lehn, J.-M.; Daub, J. *Ann. N. Y. Acad. Sci.* **2002,** *960,* 16–28. doi:10.1111/j.1749-6632.2002.tb03022.x
26. Wahhab, A.; Therrien, E. Small Molecule Inhibitors of Protein Arginine methyltransferases. PCT Pat. Appl. WO2008104077 A1, Feb 28, 2007.
27. Moormann, W.; Langbehn, D.; Herges, R. *Synthesis* **2017,** *49,* 3471–3475. doi:10.1055/s-0036-1590685
28. Laursen, B. W.; Krebs, F. C. *Chem. – Eur. J.* **2001,** *7,* 1773–1783. doi:10.1002/1521-3765(20010417)7:8<1773::aid-chem17730>3.0.co;2-f
29. Park, K.; Lee, B. M. Novel phenylethynyl benzamide glucokinase activator and method for preparing same. PCT Pat. Appl. WO2014112798 A1, Jan 16, 2013.
30. Lemke, S.; Ulrich, S.; Claußen, F.; Bloedorn, A.; Jung, U.; Herges, R.; Magnussen, O. M. *Surf. Sci.* **2015,** *632,* 71–76. doi:10.1016/j.susc.2014.08.028

License and Terms

This is an Open Access article under the terms of the Creative Commons Attribution License (http://creativecommons.org/licenses/by/4.0). Please note that the reuse, redistribution and reproduction in particular requires that the authors and source are credited.

The license is subject to the *Beilstein Journal of Organic Chemistry* terms and conditions: (https://www.beilstein-journals.org/bjoc)

The definitive version of this article is the electronic one which can be found at: doi:10.3762/bjoc.15.150

BEILSTEIN JOURNAL OF ORGANIC CHEMISTRY

Norbornadiene-functionalized triazatriangulenium and trioxatriangulenium platforms

Roland Löw[1], Talina Rusch[2], Tobias Moje[1], Fynn Röhricht[1], Olaf M. Magnussen[*2] and Rainer Herges[*1]

Full Research Paper

Open Access

Address:
[1]Otto Diels Institute for Organic Chemistry, University of Kiel, Otto-Hahn-Platz 4, 24118 Kiel, Germany and [2]Institute for Experimental and Applied Physics, University of Kiel, Leibnizstraße 19, 24098 Kiel, Germany

Email:
Olaf M. Magnussen[*] - magnussen@physik.uni-kiel.de;
Rainer Herges[*] - rherges@oc.uni-kiel.de

* Corresponding author

Keywords:
[2 + 2] cycloaddition; [2 + 2] cycloreversion; norbornadiene; photochemical isomerization; quadricyclane; self-assembled monolayers; TATA platform; thermal isomerization; TOTA platform

Beilstein J. Org. Chem. **2019,** *15,* 1815–1821.
doi:10.3762/bjoc.15.175

Received: 11 April 2019
Accepted: 17 July 2019
Published: 30 July 2019

This article is part of the thematic issue "Molecular switches".

Guest Editor: W. Szymanski

© 2019 Löw et al.; licensee Beilstein-Institut.
License and terms: see end of document.

Abstract

Triazatriangulenium (TATA) and trioxatriangulenium (TOTA) ions are particularly suited systems to mount functional molecules onto atomically flat surfaces such as Au(111). The TATA and TOTA units serve as platforms that absorb onto the surface and form ordered monolayers, while the functional groups are protruding upright and freestanding from the central carbon atoms. Azobenzene derivatized TATA's are known to exhibit extremely fast *cis*→*trans* isomerization on metal surfaces, via a peculiar non-adiabatic singlet→triplet→singlet mechanism. We now prepared norbornadienes (NBD) and quadricyclanes (QC) attached to TATA and TOTA platforms which can be used to check if these accelerated rates and the spin change mechanism also apply to [2 + 2] cycloreversions (QC→NBD).

Introduction

Recently, we discovered that the thermochemically forbidden *cis–trans* isomerization of azobenzenes can be efficiently catalysed by a very peculiar mechanism on bulk gold [1]. In heterogeneous catalysis, the surface is chemically involved in bond making and breaking. In contrast to this conventional surface catalysis the new mechanism does not involve direct contact with the surface. Electronic coupling via a conjugated π-system to the conducting band of a bulk metal is sufficient to accelerate the rate of isomerization by three orders of magnitude [2-4]. To keep the reacting azobenzene molecule at a distance of about 14 Å from the surface, it is not directly absorbed onto the surface but mounted on a carefully designed molecular framework. This approach was named the platform approach [5]. Three molecular units are combined in a modular way to achieve a controlled adsorption on the surface: the platform, a spacer and the functional molecule. Triazatriangulenium

(TATA) and trioxatriangulenium (TOTA) units are used as molecular platforms. They adsorb on the surface and form ordered monolayers. A linear, π-conjugated spacer (e.g., an ethynyl unit) is attached to the central carbon atom and the functional molecule is mounted on top. This architecture allows investigating molecules on surfaces under controlled conditions. The size of the platforms determines the intermolecular distances and enforces an upright orientation of the free standing functional groups [6]. The length and the nature of the spacer is used to tune the distance and electronic coupling of the functional system on top [1].

Preliminary experiments proved that the electronic coupling to the surface is the decisive parameter controlling the *cis–trans* rate acceleration of azobenzenes and not the length of the spacer [1]. A full conjugation path from the azobenzene on top through the ethynyl spacer and the platform to a bulk gold surface shortens the half-life of the metastable *cis*-isomer from days to seconds even though the azo N=N group is 11 bonds and 14 Å away from the surface. A singlet→triplet→singlet pathway was suggested to explain the dramatic rate acceleration.

To obtain further insight into this unusual mechanism and to explore the scope and limitation of the general concept, we are aiming at the extension from simple *cis*→*trans* isomerization to other thermochemically forbidden reactions such as [2 + 2] cycloreversions. Moreover, a deeper understanding of the nonadiabatic, catalytic process and successful application of the concept to the QC→NBD isomerization could contribute to the elucidation of the mechanisms of bulk metal catalysis and open new ways to design new catalytic systems.

Towards this end, and following the "platform concept", we designed a cyano-substituted norbornadiene, which is functionalized with an acetylene spacer on a TATA platform to investigate an eventual "spin-catalysed" [2 + 2] cycloreversion on bulk gold of quadricyclane **1b** to norbornadiene **1a** (Figure 1).

The cycloreversion of most quadricyclane systems proceeds smoothly in solution upon irradiation in the presence of triplet sensitizers [7]. If **1b** is adsorbed on a gold surface the bulk gold could take the role of a triplet sensitizer, mediate the spin change (which otherwise is forbidden) and accelerate the cycloreversion. Substitution in the 2 and 3 positions shifts the bathochromic absorption to 375 nm which is in agreement with similar systems [8]. Furthermore, the cyano and ethynyl groups provide a complete conjugation path across the double bond of norbornadiene to the metal. Additionally, it is known that electron-withdrawing groups in 2 or 3 position change the triplet energy hypersurface in such a way that a triplet excited quadricyclane **1b** decays into the ground state of the norbornadiene **1a** [9], which is a precondition for an efficient QC→NBD isomerization via our postulated non-adiabatic singlet→triplet→singlet mechanism.

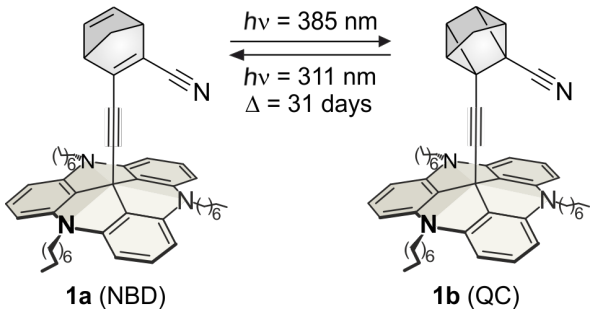


Figure 1: Structures of the norbornadiene platform **1a** and the quadricyclane platform **1b** (for geometry coordinates and further details see Supporting Information File 1). The norbornadiene isomerizes upon irradiation with 385 nm to the quadricyclane **1b**. Back-isomerization to the norbornadiene **1a** is achieved upon irradiation with 311 nm or thermochemically with a half-life of 31 days.

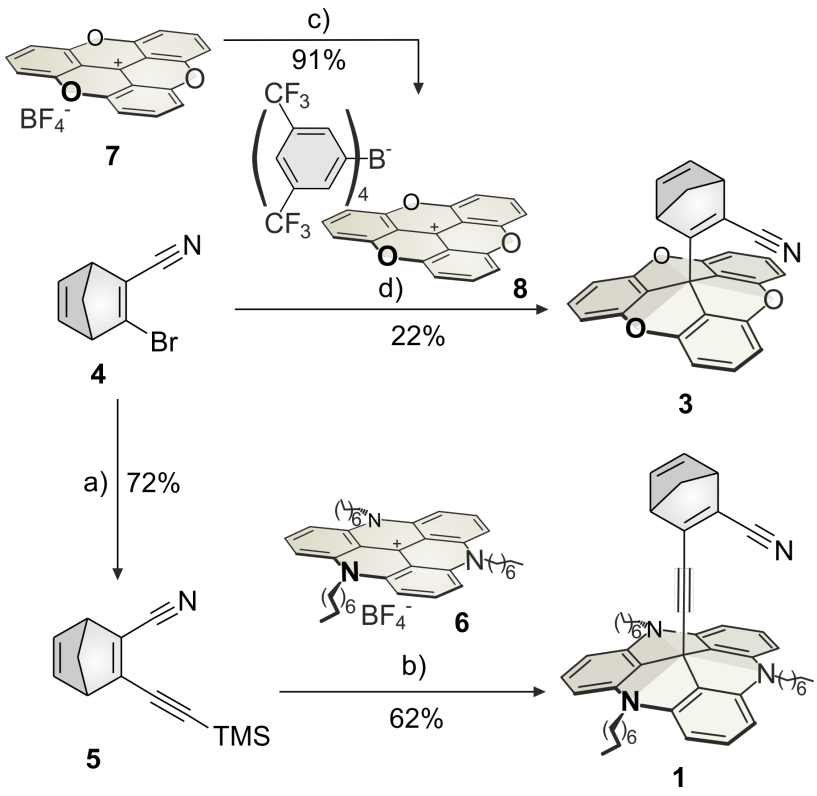
Results and Discussion

If our proposed spin change mechanism, mediated by the conducting electrons in bulk gold were correct, interruption of the conjugation path and decoupling from the surface should restore the properties of the system (half-life of the metastable quadricyclane) in solution. According to this line of thought, we synthesized molecule **2** with a 2-methylphenyl group inserted into the spacer unit (see below Scheme 2). The methyl group prevents a planar arrangement of the phenyl group and the double bond of the NBD unit and thus lowers the conjugation.

We also synthesized the corresponding system directly connected to a TOTA platform **3**. Functionalized TOTA molecules are more stable than the corresponding TATA systems and usually can be sublimed without decomposition, which is a necessary precondition for ultra-high vacuum STM investigations.

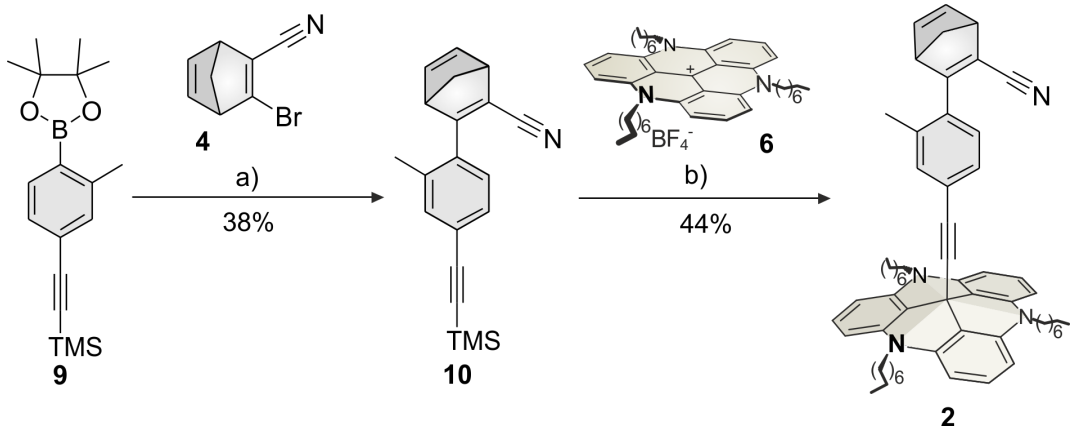
The 3-bromo-2-cyano-substituted norbornadiene **4** was synthesized as described in the literature (Scheme 1) [10-12].

4 was converted to **5** with trimethylsilylacetylene (72%) in a Sonogashira cross-coupling reaction. The triazatriangulenium ion **6** was synthesized according to a procedure of Laursen and Krebs [13]. The platform **6** was functionalized with norbornadiene **5** by deprotection of the acetylene with potassium hydroxide and in situ formation of the C–C bond between the acetylene and the central C atom of the platform **6** to yield the norbornadiene-substituted platform **1** (62%).



Scheme 1: Syntheses of the norbornadiene TATA platform **1** and TOTA platform **3**. a) TMS-acetylene, $Pd(PPh_3)_4$, Cu(I)I, Et_3N, toluene, N_2, 60 °C, 1.3 h; b) KOH, THF, N_2, reflux, 5 h; c) sodium tetrakis[3,5-bis(trifluoromethyl)phenyl]borate ($NaBAr^F_4$), DCM, rt, 2 h; d) *n*-BuLi, THF, N_2, −78 °C to rt, 20 h.

The TOTA cation with the tetrakis(3,5-bis(trifluoromethyl)phenyl)borate anion ($TOTA^+$ $[BAr^F_4]^-$, **8**) was obtained by ion exchange of the TOTA tetrafluoroborate **7** ($TOTA^+$ BF_4^-) to achieve a high solubility in organic solvents [14]. 3-Bromo-2-cyanonorbornadiene (**4**) was subjected to halogen–metal exchange with *n*-BuLi and coupled with the central atom of the TOTA platform **8** to obtain the norbornadiene-functionalized TOTA platform **3** (22%, Scheme 1). The synthesis of the corresponding TATA platform including an additional 2-methylphenyl group (**2**) was obtained in a convergent synthesis (Scheme 2). Boronic ester **9** was synthesized as described in the literature [15]. In a Suzuki cross-coupling reaction norborna-



Scheme 2: Synthesis of methylphenylnorbornadiene platform **2**. a) $Pd(PPh_3)_4$, Na_2CO_3, toluene, EtOH, H_2O, N_2, reflux, 12 h; b) KOH, THF, N_2, reflux, 1 h.

diene **4** was coupled with **9** to the extended norbornadiene **10** (38%), which was attached to the TATA platform **6** to yield the extended norbornadiene platform **2** (44%).

The photophysical properties and the switching behaviour of **1**, **2** and **3** were determined in solution (THF). The UV–vis spectra of the norbornadienes (NBD, black, **1a**, **2a**, **3a**) and quadricylanes (QC, red, **1b**, **2b**, **3b**) and the spectra of the QCs after irradiation with 311 nm for **1b** and **2b** or 254 nm for **3b** (blue) are shown in Figure 2. The bathochromic absorption maximum of norbornadiene **1a** is at 375 nm (as compared to <300 nm in parent norbornadiene) [16,17]. The absorption maximum of quadricyclane **1b** is at 336 nm (as compared to 187 nm in parent quadricyclane) [18]. The weak and broad absorption band with a maximum at 524 nm is due to the TATA cation generated by decomposition during irradiation with 311 nm.

The photostationary states were determined in deuterated oxygen containing deuterated benzene and degassed deuterated benzene by ^{1}H NMR measurements (Figure 3). Norbornadiene **1a** isomerizes quantitatively to quadricyclane **1b** by irradiation with 385 nm. Upon irradiation of **1b** under nitrogen with 311 nm, the cycloreversion yields 28% norbornadiene (Table 1).

The efficiency of the cycloreversion is higher under air (52%), however, slow decomposition was observed (cleavage of the TATA$^+$ platform). Obviously, in the presence of oxygen, the photochemical cycloreversion proceeds via a triplet radical mechanism. This agrees with observations described in the literature [16]. In degassed benzene neither **1a** nor **1b** exhibits decomposition upon repeated irradiation with 385 nm and 311 nm.

The thermal isomerization of QC **1b** back to NBD **1a** was investigated by ^{1}H NMR measurements (Figure 4).

The cycloreversion follows a first order reaction, the rate constant could be determined by logarithmic fitting of the integrals of the CH_2 signals next to the nitrogen atoms of the platform as

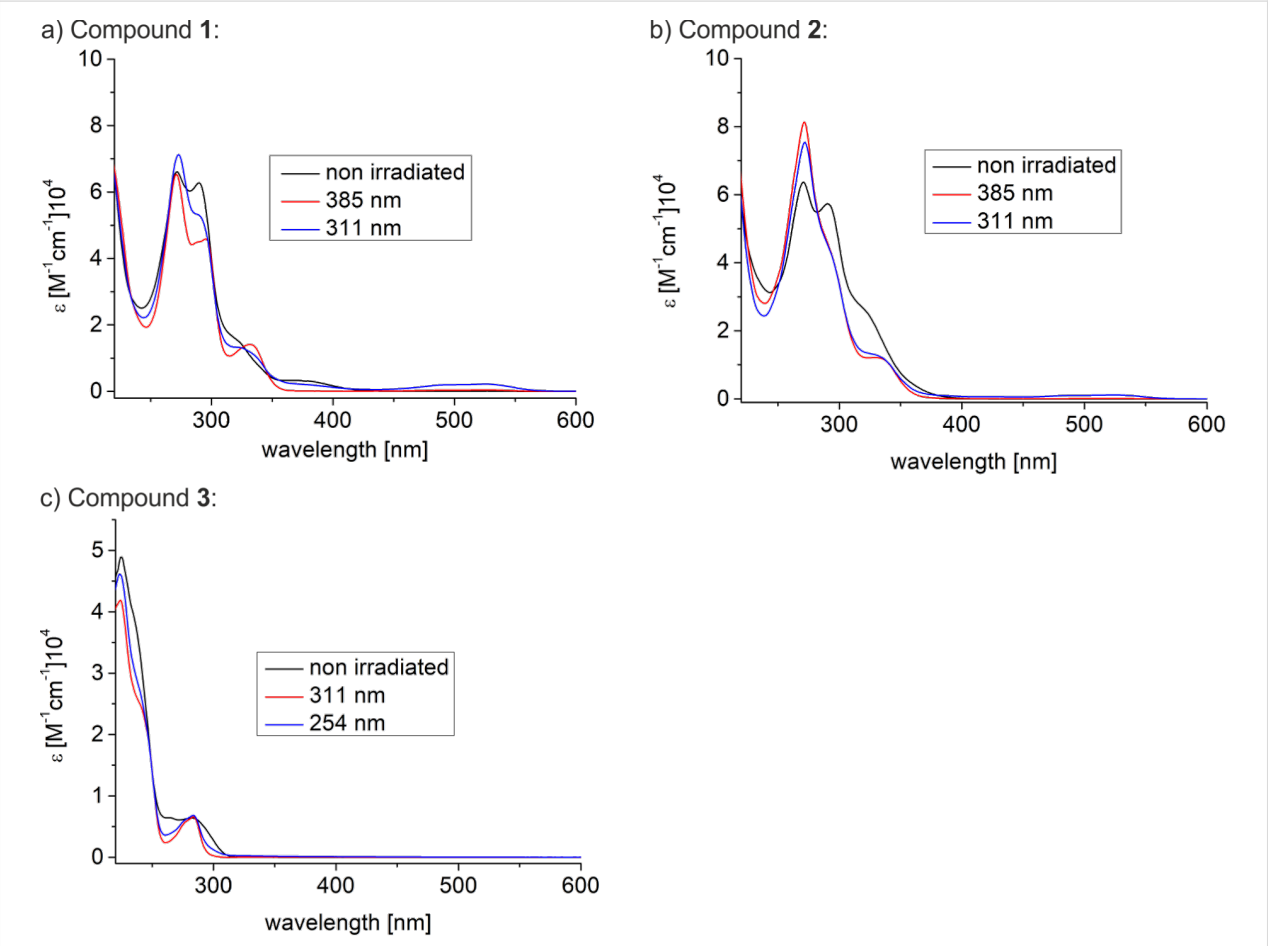


Figure 2: UV–vis spectra of platform molecules **1** (a), **2** (b) and **3** (c) (in THF at rt): Norbornadiene (black), quadricyclane (red) and after irradiation with 311 nm (compound **1b** and **2b**) or 254 nm (compound **3b**) for 2.5 min (blue).

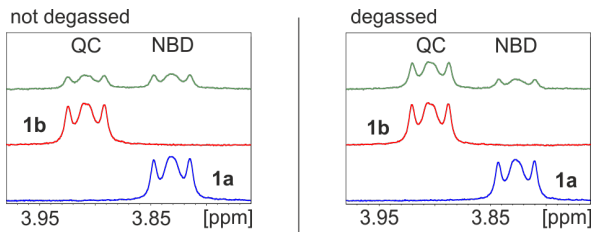


Figure 3: ^{1}H NMR spectra of **1** in deuterated oxygen containing deuterated benzene (left) and degassed deuterated benzene (right). Shown are the signals of the CH_2 groups of the alkyl side chains next to the nitrogen atoms in the TATA platforms, which are indicative of the isomerization. Left bottom (blue): non-irradiated NBD **1a**; left middle (red): pure QC **1b** obtained after irradiation of **1b** with 385 nm for one minute; and left top (green): photostationary state of **1a** and **1b** after 1 h irradiation with 311 nm under air (52% **1a**/48% **1b**). Right bottom (blue): pure NBD **1a**; right middle (red): pure QC **1b** obtained after irradiation of **1a** with 385 nm for one minute and right top (green): photostationary state of **1a** and **1b** after 2 h irradiation with 311 nm under nitrogen atmosphere (28% **1a**/72% **1b**).

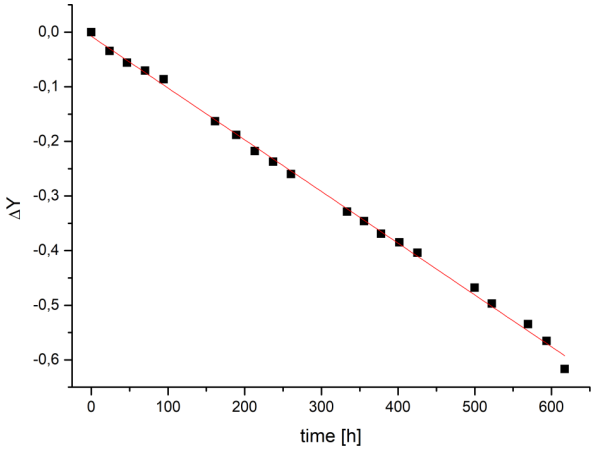


Figure 4: Determination of the thermal isomerization rate k of **1b** (QC) by ^{1}H NMR spectroscopy (toluene, 293.5 K, 800 µmol/L, under nitrogen). ΔY: ln {$[QC]_t/[QC]_0$}, $[QC]_t$: ^{1}H NMR integral of the CH_2 group neighbouring the N bridge atom of the TATA platform in QC **1b** at time t, $[QC]_0$ corresponding ^{1}H integral at t = 0. A rate constant of $k = 0.95 \cdot 10^{-3}$ s^{-1} was determined from a linear fit of the ΔY/t curve.

$k = 1.06 \cdot 10^{-3}$ s^{-1} under air and $0.95 \cdot 10^{-3}$ s^{-1} under nitrogen. Hence, the thermal reaction (in contrast to the photochemical reaction) is not largely affected by oxygen. The half-life of the metastable quadricyclane is $t_{1/2}$ = 655 h in benzene under air at 293 K (Table 1). Minor amounts of degradation products (<1%) after following the cycloreversion within a period of one month are visible in the ^{1}H NMR spectrum. Under nitrogen atmosphere the half-life of the cycloreversion is $t_{1/2}$ = 732 h (294 K).

The rate constant as a function of the temperature follows an Arrhenius-type relationship. The activation energy for the cycloreversion was determined by linear fit of ln (k) as a function of 1/T. The cycloreversion of QC **1b** to NBD **1a** has an activation energy of 111 kJ mol^{-1} (degassed deuterated benzene). The switching efficiency of NBD **2a** to QC **2b** is quantitative (≈100%) after irradiation with 385 nm, whereas the photostationary state of NBD **3a** to QC **3b** is lower with 91%.

No thermal cycloreversion of the quadricyclanes **2b** and **3b** was observed at room temperature within a period of one month. Obviously, a cyano as well as a neighbouring ethynyl substituent are necessary to induce the back-isomerisation at ambient conditions as realized in compound **1**. Consequently, future surface chemistry investigations will be performed with compound **1** including the TATA platform and an ethynyl spacer.

STM Measurements

The adsorption behaviour of the NBD **1a** on Au(111) surfaces was studied by scanning tunnelling microscopy (STM) at room temperature (Figure 5a). The molecules form a hexagonally ordered self-assembled monolayer (SAM) with an intermolecular distance of (1.23 ± 0.07) nm. This is in agreement with a (√19 × √19) R23.4° superstructure, which was observed in our previous investigations of adlayers of octyl-TATA derivatives [1,6,19-21]. Two types of molecules with a distinct difference in apparent height of ≈1 Å were observed in the STM images (Figure 5b). Both types of molecules are located at identical positions of the (√19 × √19) R23.4° lattice and seem to be distri-

Table 1: Photostationary states (PSS) of norbornadiene platforms **1**, **2** and **3** upon irradiation with light of the wavelengths λ_{irrad} = 385 nm (**1a**, **2a**) or 311 nm (**3a**) and 311 nm (**1b**, **2b**) or 254 nm (**3b**) and the thermal isomerization half-life $t_{1/2}$ determined by ^{1}H NMR spectroscopy (deuterated benzene under air/degassed deuterated benzene).

Compound	atmosphere	PSS % QC (λ_{irrad})	PSS % NBD (λ_{irrad})	$t_{1/2}$ (h)	EA kJ/mol
1	air	≈100 (385 nm)	52 (311 nm)	655 (293 K)	/
1	N_2	≈100 (385 nm)	28 (311 nm)	732 (294 K)	111
2	N_2	≈100 (385 nm)	48 (311 nm)	>1 year	/
3	N_2	91 (311 nm)	33 (254 nm)	>1 year	/

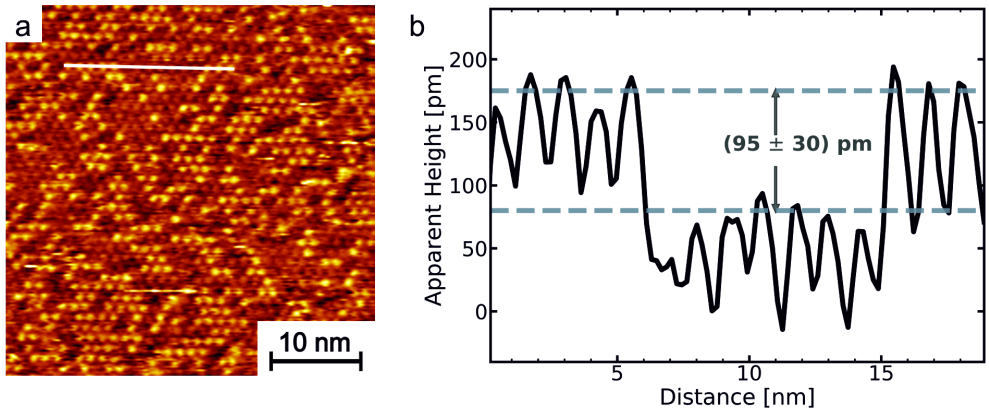


Figure 5: (a) STM image of self-assembled monolayers of compound **1** on Au(111) (40 × 40 nm^2, I_t = 0.05 nA, U_{bias} = 0.40 V) and (b) crossection along the white line in (a).

buted rather randomly on the surface. Two explanations are possible to account for the presence of these two species: Either they correspond to a mixture of adsorbed NBD-TATA **1a** and QC-TATAs **1b** or to coadsorption of **1a** and the pure octyl-TATA **6**. The first case may be possible, because the molecules are able to switch to the **1b** state at a wavelength of 385 nm and the substance was exposed to daylight during preparation and incorporation into the STM. However, since the ratio on the surface is 42% for molecules with a greater apparent height and 58% for molecules with a lower apparent height, this assumption is unlikely as at least 42% of the molecules would have to be in the switched state **1b**. The second explanation, i.e., that the mixed monolayer consists of octyl-TATA **6** and the NBD-TATA **1a**, seems to be more likely, since molecule **1** decays slowly under irradiation in contact with oxygen. Previous measurements have shown that self-assembly from solutions containing pure and vertically functionalized TATA molecules leads to the formation of stochastically mixed monolayers with a highly ordered ($\sqrt{19} \times \sqrt{19}$) R23.4° superstructure [22]. This would be also expected for self-assembly from solution containing **1a** and **6**. The composition of the adlayer on the surface does not necessarily have to be identical to the ratio of the two species in solution. In fact, in our previous study the fraction of adsorbed octyl-TATA **6** as compared to that of the functionalized TATA was found to be much higher than the ratio in solution. We attributed this to the smaller size of **6** and its correspondingly higher diffusion coefficient, which results in faster transport to the Au surface and accordingly enhanced surface coverages. Thus, even low decay rates of **1a** may lead to sufficiently high concentrations of **6** for obtaining mixed adlayers. By varying the preparation conditions, e.g., performing the preparation in a nitrogen atmosphere, decomposition might be avoided and monolayers of better quality could be achievable.

Conclusion

In summary, we present the syntheses of three different norbornadiene functionalized platform molecules **1**–**3**. The photochemical switching between the norbornadiene and quadricyclane isomers with two different wavelengths was investigated. Norbornadienes **1** and **2** are quantitatively converted to the corresponding quadricyclanes upon irradiation with light of 385 nm. Back-isomerization with 311 nm to the norbornadiene isomer **1a** is less efficient (52%). The high-energy quadricyclane isomer **1b** is thermochemically unstable at room temperature (half-life 31 d at 21 °C in benzene) only if a cyano as well as an ethynyl substituent are present. No thermal conversion under ambient conditions was observed for **2** and **3**, which are lacking ethynyl substitution. Further studies will be devoted to the surface chemistry of these compounds. Norbornadiene **1** forms highly ordered monolayers on Au(111) surfaces with two different apparent heights. It is not clear if a mixture of norbornadiene **1a** and quadricyclane **1b** or norbornadiene **1a** and octyl-TATA **6** form these mixed monolayers.

Experimental

For detailed experimental procedures, including NMR, UV–vis, MS spectra and STM measurements see Supporting Information File 1, chapters I–IV, and for kinetic studies see chapter V.

Supporting Information

Supporting Information File 1

Experimental and analytical data.
[https://www.beilstein-journals.org/bjoc/content/supplementary/1860-5397-15-175-S1.pdf]

Acknowledgements

The authors gratefully acknowledge financial support by the Deutsche Forschungsgesellschaft within the Sonderforschungsbereich 677, “Function by Switching”.

ORCID® iDs

Roland Löw - https://orcid.org/0000-0002-3051-7831
Fynn Röhricht - https://orcid.org/0000-0001-9935-9256
Rainer Herges - https://orcid.org/0000-0002-6396-6991

Preprint

A non-peer-reviewed version of this article has been previously published as a preprint doi:10.3762/bxiv.2019.5.v1

References

1. Schlimm, A.; Löw, R.; Rusch, T.; Röhricht, F.; Strunskus, T.; Tellkamp, T.; Sönnichsen, F.; Manthe, U.; Magnussen, O.; Tuczek, F.; Herges, R. *Angew. Chem., Int. Ed.* **2019,** *58,* 6574–6578. doi:10.1002/anie.201814342
2. Jung, U.; Schütt, C.; Filinova, O.; Kubitschke, J.; Herges, R.; Magnussen, O. *J. Phys. Chem. C* **2012,** *116,* 25943–25948. doi:10.1021/jp310451c
3. Jacob, H.; Ulrich, S.; Jung, U.; Lemke, S.; Rusch, T.; Schütt, C.; Petersen, F.; Strunskus, T.; Magnussen, O.; Herges, R.; Tuczek, F. *Phys. Chem. Chem. Phys.* **2014,** *16,* 22643–22650. doi:10.1039/c4cp03438d
4. Bronner, C.; Tegeder, P. *New J. Phys.* **2014,** *16,* 053004. doi:10.1088/1367-2630/16/5/053004
5. Baisch, B.; Raffa, D.; Jung, U.; Magnussen, O. M.; Nicolas, C.; Lacour, J.; Kubitschke, J.; Herges, R. *J. Am. Chem. Soc.* **2009,** *131,* 442–443. doi:10.1021/ja807923f
6. Ulrich, S.; Jung, U.; Strunskus, T.; Schütt, C.; Bloedorn, A.; Lemke, S.; Ludwig, E.; Kipp, L.; Faupel, F.; Magnussen, O.; Herges, R. *Phys. Chem. Chem. Phys.* **2015,** *17,* 17053–17062. doi:10.1039/c5cp01447f
7. Nishino, H.; Toki, S.; Takamuku, S. *J. Am. Chem. Soc.* **1986,** *108,* 5030–5032. doi:10.1021/ja00276a067
8. Quant, M.; Lennartson, A.; Dreos, A.; Kuisma, M.; Erhart, P.; Börjesson, K.; Moth-Poulsen, K. *Chem. – Eur. J.* **2016,** *22,* 13265–13274. doi:10.1002/chem.201602530
9. Ikezawa, H.; Kutal, C.; Yasufuku, K.; Yamazaki, H. *J. Am. Chem. Soc.* **1986,** *108,* 1589–1594. doi:10.1021/ja00267a032
10. Kenndoff, J.; Polborn, K.; Szeimies, G. *J. Am. Chem. Soc.* **1990,** *112,* 6117–6118. doi:10.1021/ja00172a031
11. Tranmer, G. K.; Yip, C.; Handerson, S.; Jordan, R. W.; Tam, W. *Can. J. Chem.* **2000,** *78,* 527–535. doi:10.1139/v00-047
12. Gunes, Y.; Arcelik, N.; Sahin, E.; Fleming, F. F.; Altundas, R. *Eur. J. Org. Chem.* **2015,** 6679–6686. doi:10.1002/ejoc.201500895
13. Laursen, B. W.; Krebs, F. C. *Chem. – Eur. J.* **2001,** *7,* 1773–1783. doi:10.1002/1521-3765(20010417)7:8<1773::aid-chem17730>3.0.co;2-f
14. Martin, J. C.; Smith, R. G. *J. Am. Chem. Soc.* **1964,** *86,* 2252–2256. doi:10.1021/ja01065a030
15. Browne, D. L.; Baumann, M.; Harji, B. H.; Baxendale, I. R.; Ley, S. V. *Org. Lett.* **2011,** *13,* 3312–3315. doi:10.1021/ol2010006
16. Gray, V.; Lennartson, A.; Ratanalert, P.; Börjesson, K.; Moth-Poulsen, K. *Chem. Commun.* **2014,** *50,* 5330–5332. doi:10.1039/c3cc47517d
17. Dilling, W. L. *Chem. Rev.* **1966,** *66,* 373–393. doi:10.1021/cr60242a002
18. Srinivasan, R.; Baum, T.; Epling, G. *J. Chem. Soc., Chem. Commun.* **1982,** 437–438. doi:10.1039/c39820000437
19. Hammerich, M.; Rusch, T.; Krekiehn, N. R.; Bloedorn, A.; Magnussen, O. M.; Herges, R. *ChemPhysChem* **2016,** *17,* 1870–1874. doi:10.1002/cphc.201600147
20. Schlimm, A.; Stucke, N.; Flöser, B. M.; Rusch, T.; Krahmer, J.; Näther, C.; Strunskus, T.; Magnussen, O. M.; Tuczek, F. *Chem. – Eur. J.* **2018,** *24,* 10732–10744. doi:10.1002/chem.201800911
21. Lemke, S.; Ulrich, S.; Claußen, F.; Bloedorn, A.; Jung, U.; Herges, R.; Magnussen, O. M. *Surf. Sci.* **2015,** *632,* 71–76. doi:10.1016/j.susc.2014.08.028
22. Rusch, T. R.; Hammerich, M.; Herges, R.; Magnussen, O. M. submitted for publication.

License and Terms

This is an Open Access article under the terms of the Creative Commons Attribution License (http://creativecommons.org/licenses/by/4.0). Please note that the reuse, redistribution and reproduction in particular requires that the authors and source are credited.

The license is subject to the *Beilstein Journal of Organic Chemistry* terms and conditions: (https://www.beilstein-journals.org/bjoc)

The definitive version of this article is the electronic one which can be found at: doi:10.3762/bjoc.15.175

BEILSTEIN JOURNAL OF ORGANIC CHEMISTRY

Fluorinated azobenzenes as supramolecular halogen-bonding building blocks

Esther Nieland[1], Oliver Weingart[*2] and Bernd M. Schmidt[*1]

Letter

Open Access

Address:
[1]Institut für Organische Chemie und Makromolekulare Chemie, Heinrich-Heine-Universität Düsseldorf, Universitätsstraße 1, D-40225 Düsseldorf, Germany and [2]Institut für Theoretische Chemie und Computerchemie, Heinrich-Heine-Universität Düsseldorf, Universitätsstraße 1, D-40225 Düsseldorf, Germany

Email:
Oliver Weingart[*] - Oliver.Weingart@hhu.de; Bernd M. Schmidt[*] - Bernd.Schmidt@hhu.de

* Corresponding author

Keywords:
azobenzene; DFT calculations; fluorine chemistry; halogen bonding; photochemistry

Beilstein J. Org. Chem. **2019,** *15,* 2013–2019.
doi:10.3762/bjoc.15.197

Received: 01 July 2019
Accepted: 16 August 2019
Published: 23 August 2019

This article is part of the thematic issue "Molecular switches".

Guest Editor: W. Szymanski

© 2019 Nieland et al.; licensee Beilstein-Institut.
License and terms: see end of document.

Abstract

ortho-Fluoroazobenzenes are a remarkable example of bistable photoswitches, addressable by visible light. Symmetrical, highly fluorinated azobenzenes bearing an iodine substituent in *para*-position were shown to be suitable supramolecular building blocks both in solution and in the solid state in combination with neutral halogen bonding acceptors, such as lutidines. Therefore, we investigate the photochemistry of a series of azobenzene photoswitches. Upon introduction of iodoethynyl groups, the halogen bonding donor properties are significantly strengthened in solution. However, the bathochromic shift of the $\pi\rightarrow\pi^*$ band leads to a partial overlap with the $n\rightarrow\pi^*$ band, making it slightly more difficult to address. The introduction of iodine substituents is furthermore accompanied with a diminishing thermal half-life. A series of three azobenzenes with different halogen bonding donor properties are discussed in relation to their changing photophysical properties, rationalized by DFT calculations.

Introduction

The halogen bond is an attractive noncovalent interaction between a polarized halogen atom (the halogen bond donor) and a Lewis base (the halogen bond acceptor) [1,2]. A prominent example regarding the origin of halogen bonding can be found in inorganic solid-state chemistry. The structurally diverse group of polyiodides, with its rich structural chemistry is governed by halogen bonding, where I^- and I_3^- are considered the nucleophilic (halogen bond acceptor) and I_2 the electrophilic (halogen bond donor) subcomponent [3-7]. Neutral halogen bonds on the other hand can be generally described by R–X···Y, where R–X is the halogen bond donor, R is covalently bound to X, and Y is the Lewis basic halogen bond acceptor [1]. In recent years, halogen bonding was used to assemble molecules, leading to a variety of supramolecular architectures [8-19], as well as

discrete supermolecules [20-24]. Huber and co-workers demonstrated the activation of a carbonyl group by halogen bonding, and successfully applied this concept to catalysts for Michael addition reactions [25] and also employed neutral [26], and hypervalent iodolium derivatives as activators in a halide abstraction reaction and as organocatalysts in Diels–Alder reactions [27]. The group of Metrangolo also reported halogen bonding-promoted catalysis in water by exploiting a halogen bonding amino acid, which combines excellent donor properties with good water solubility [28], in addition to their seminal contributions in the field of crystal engineering [1]. Only few supramolecular capsules were reported so far [29], including the resorcin[4]arene capsules of Diederich and co-workers [21,23], triangular macrocycles assembled by self-complemented halogen bonding [20] and halogen bond templated, polyfluorinated stilbene squares used for topochemical polymerization [22]. Additionally, halonium ions [N···I^+···N] were reported to form several charged, discrete supramolecular capsules [30-33] and helicates [34]. In the same line, we have demonstrated recently that both *E*-4,4'-di(iodo)perfluoroazobenzene (**A2**) and *E*-4,4'-di(iodoethynyl)perfluoroazobenzene (**A3**) halogen bond donors can be combined with rigid u-shaped anthracene building blocks, bearing two 3,5-lutidine acceptors in 1 and 8 positions, to form self-assembled boxes of 25–30 Å length in solution and in the solid state [35].

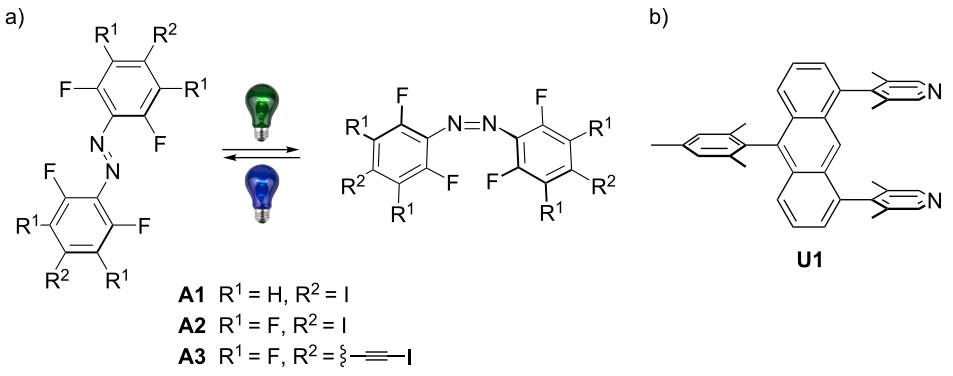
We chose azobenzene because azobenzene is one of the simplest molecules that can undergo photoinduced isomerisation of its N=N central double bond. The photoisomerisation reaction in n→π and π →π* excited states has been studied with experimental [36-38] and theoretical approaches [39-44]. By substituting azobenzenes in the *ortho*-positions to the N=N bond with electron-withdrawing fluorine substituents [45,46], the red-shifting of the n→π* transitions enables selective addressing of both the *E*- and *Z*-isomer using visible light. Stabilization of the n-orbitals in the *Z*-isomers leads to a very high thermal stability of the *Z*-isomer, now exhibiting thermal half-lives up to two years at room temperature [36]. Most important for application in supramolecular systems, it should be possible to study both states of the system on a laboratory timescale, a key aspect in the design of our halogen bonded boxes [35]. Therefore, we herein present a comprehensive investigation of the photochemistry of highly fluorinated azobenzenes. Our efforts are supported by theoretical calculations, showing that these azobenzenes are suitable for the use as building blocks in supramolecular architectures.

Results and Discussion

Three different azobenzenes **A1**–**3** were studied with regard to halogen bonding and photochemical properties (Scheme 1).

In our experiments, tetrafluorinated **A1** does not form halogen bonded boxes with acceptor **U1**, neither in solution, nor in the solid state. Octafluorinated **A2** forms [2 + 2] boxes in the solid state and possibly in solution, whereas tetrafluoroiodoethynyl **A3** is as donor strong enough to reliably permit the characterization of the boxes formed in solution and in the solid state [35]. Electrostatic interaction plays a dominant role in halogen bonding [1,12,13]. Therefore, we calculated the molecular electrostatic potentials of the halogen bond donors **A1**–**3** to visualize their capabilities to form halogen bonded architectures (Figure 1).

Looking at the electrostatic surface potentials of the halogen bond donors, one can see that **A3** shows a maximum value on the iodine atom that is most positive compared to that of **A2** and **A1**. The evolution of the iodine potential follows our experimental observation with iodoethynylazobenzene **A3** being the strongest halogen bond donor and **A1** being the weakest, within this series [48]. For potential, reversible photochemical control of supramolecular assemblies, the halogen donors need to bind both in the *E*- and *Z*-state. This is the case according to our



Scheme 1: a) Azobenzenes **A1**–**3** employed in this study. b) U-shaped anthracene halogen bond acceptor bearing two 3,5-lutidines in 1 and 8 positions.

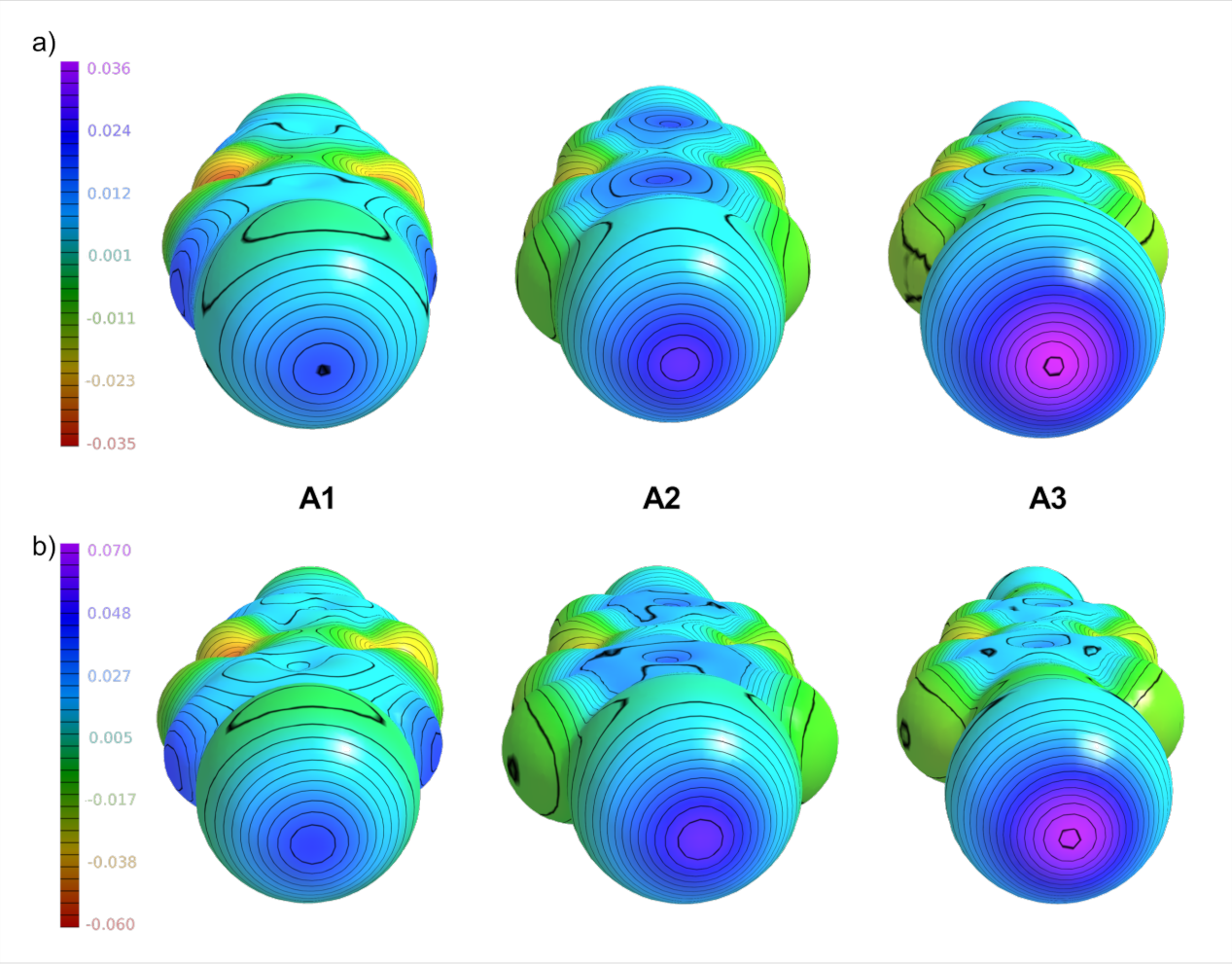


Figure 1: Electrostatic potential map at different isodensity values (B3LYP/ def2/TZVP/DGZVP optimized geometries) with a) ρ = 0.0001, and b) ρ = 0.001. For visualization, the MoleCoolQt software was used [47].

computations, as isodensity values remain almost identical upon switching (Figure S14 in Supporting Information File 1). We therefore turned our attention to elucidate the change of photochemical properties upon introducing the heavy iodine to the azobenzene building block, as well as the effect of the ethynyl group in case of **A3** (Figure 2). Vertical electronic absorption spectra of the different azobenzenes were calculated at the TD-B3LYP/def2-TZVP level of theory including Grimme D3 dispersion correction, using the Gaussian 16 program package (see Supporting Information File 1). The azobenzenes were embedded in a continuum using the polarizable continuum model (PCM) for the solvent MeCN. The DGZVP all electron basis was used for iodine. Vertical excitation energies for the $\pi\rightarrow\pi^*$ and $n\rightarrow\pi^*$ transitions of *E* and *Z*-isomers are listed in the Table S9 (Supporting Information File 1).

The computational absorption spectra are in fair agreement with the experimental ones (Table 1) and trends are reproduced accordingly (measured and calculated absorption spectra of **A1** can be found in the Supporting Information File 1, Figures S1 and S12). By introduction of fluorine atoms *ortho* to the azo bond, the two $n\rightarrow\pi^*$ of *E*- and *Z*-state become sufficiently separated to address them individually using visible light sources. Along with averting UV light for the photochemical reaction, high PSS ratios can be observed, which is very desirable for application in supramolecular systems [12,13,35]. Tetra- and octafluorinated **A1** and **A2** show clear spectral separation of the $n\rightarrow\pi^*$ bands, whereas the extended π-system of iodoethynyl **A3** lead to a bathochromic shift of the $\pi\rightarrow\pi^*$ band by 24 nm, now partially overlapping with the, also broadened, $n\rightarrow\pi^*$ band of *Z*-**A3**. Apart from the photoisomerisation using light, azobenzenes **A1**–**3** also undergo thermal back reaction, which we studied experimentally and theoretically. To gain insight into the effect of the iodine atoms on the thermal stability we investigated **A1**, **A2** and **A3** in MeCN at elevated temperature (60 °C), following the works of Hecht and co-workers [45,46]. The data is presented in Table 2. Additionally, we studied **A3** in a wide range of temperatures in MeCN.

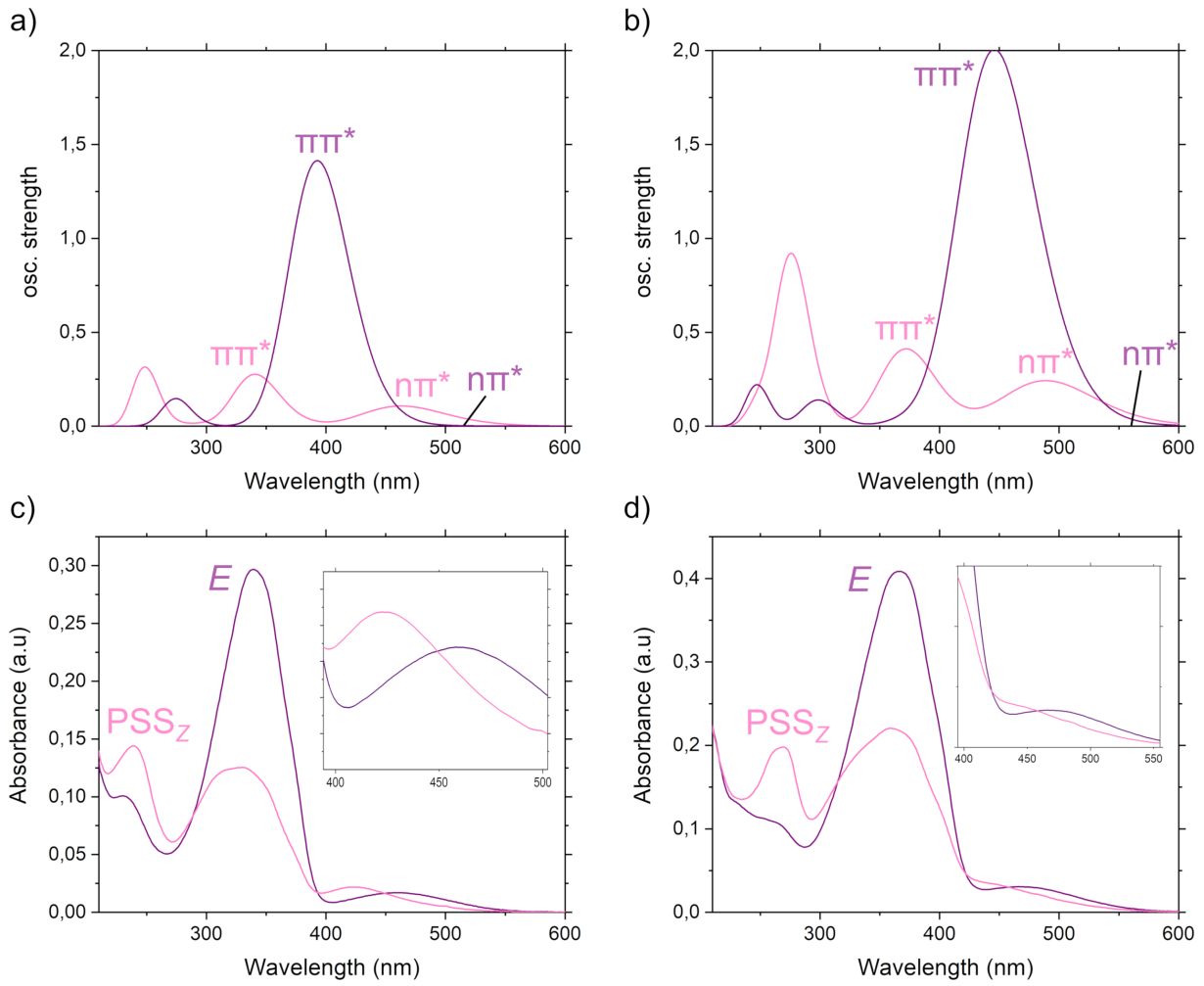


Figure 2: Top: Vertical electronic absorption spectra of a) **A2** and b) **A3**, calculated using TD-B3LYP/def2-TZVP level of theory with Grimme D3 dispersion corrections and implicit MeCN solvent. Pink line: *Z*-isomer, purple line: *E*-isomer. Bottom: *E*-state of c) **A2** and d) **A3** (from left to right, purple) and photostationary state (PSS, pink) after photoirradiation with λ_{irr} = 565 nm, monitored by UV–vis (MeCN, *c* = 10.5 and 9.3 µmol/L, respectively). The inlets of c) and d) were smoothed using the Savitzky–Golay filter implemented in OriginPro to facilitate readability.

Table 1: Spectroscopic properties in MeCN for *E*-state and PSS after photoirradiation with λ_{irr} = 565 nm. Maxima were determined using the "Peak Analyzer" implemented in OriginPro. Kinetic measurements were performed in MeCN at 60 °C (Supporting Information File 1).

	$\lambda_{max}(E)$ [nm]	$\varepsilon_{max}(E)$ [M^{-1} cm^{-1}]	$\lambda_{max}(PSS_Z)$ [nm]	$\varepsilon_{max}(PSS_Z)$ [M^{-1} cm^{-1}]	$\tau_{1/2}$ [h]
A1	335	3.48×10^4	241	1.68×10^4	44.92
A2	340	2.84×10^4	239	1.38×10^4	17.17
A3	364	4.41×10^4	359	2.38×10^4	0.92

The half-lives decrease from **A1** to **A3**, an effect that correlates with the increase in dipole moment of the transition state (TS, see Supporting Information File 1, Table S8). In the B3LYP computations this value is larger than for the corresponding *Z*-isomer and leads to a stabilization of the TS in polar solvents [46].

The bistable character is obviously weakened upon improving the halogen bonding properties. However, most importantly, the azobenzenes still can be conveniently handled at room temperature with a half-life of at least a working day, allowing for studying both states of the systems without needs for in situ irradiation (the thermal half-life of **A3** at room temperature is

Table 2: Activation process parameters for the *E*→*Z* isomerisation in MeCN at 60 °C, B3LYP, def-TZVP basis for C, H, N, F, DGZVP all electron basis for iodine. Grimme D3 dispersion correction was applied. Values were computed using the KistHelp program [49] employing classical transition state theory and including the effects of Wigner-tunnelling (Supporting Information File 1).

	ΔU [kJ mol^{-1}]	ΔG [kJ mol^{-1}]	ΔH [kJ mol^{-1}]	ΔS [J mol^{-1}]	$k_{Z\text{-}E}$ [s^{-1}]	$\tau_{1/2}$ [h]	$\tau_{1/2}$ exp. [h]
A1	124.10	114.32	119.06	14.22	9.46×10^{-6}	20.35	44.92
A2	118.86	108.73	114.49	17.28	7.06×10^{-6}	2.73	17.17
A3	113.13	99.89	108.69	26.42	1.70×10^{-6}	0.11	0.92

14.98 hours in MeCN, see the Supporting Information File 1, Figures S6–S8).

In addition to that, slow evaporation of an equimolar solution of **U1** and **A2** in benzene furnished red-orange single crystals suitable for X-ray analysis of a [2 + 2] halogen-bonded box, **U1**···**A2**, over the course of a few days in quantitative yield. Single-crystal analysis confirms the formation of a **U1**···**A2** box in the solid state (Figure 3).

The **U1**···**A2** box has a principal length of approximately 25 Å (anthracene–anthrance distance) and a height of 5 Å (distance between the *ipso*-carbons of the lutidines). The lutidine acceptor units are curved inwards (with N···I–C angles of 165 and 172°) and show N···I distances of 2.78 and 2.82 Å to the azobenzene donors. As observed for the other boxes assembled by halogen bonding reported by us [35], parts containing fluorinated azobenzenes **A2** are segregated from the perhydrogenated anthracene **U1** units, connected by C–H···F contacts. The azobenzenes **A2** interact by lamellar 2D π-stacking, anthracene **U1** interact predominantly by C–H···π interactions as both the solubilizing mesitylene group and the two perpendicular lutidine acceptors effectively prevent stacking of the anthracenes body (Supporting Information File 1, Figure S17). This was also the key to being able to lower the temperature to characterize formation in the ^{1}H NMR, where the solubility of the assemblies in benzene was improved by adding a solubilizing mesitylene group to the halogen bonding acceptor **U1** to avoid precipitation of box **A2**···**U1** during previous titration experiments [35].

Conclusion

The performed calculations show that both *E*- and *Z*-isomer are equally able to undergo halogen bonding. By improving the strength of halogen bonding going from tetrafluorinated **A1** to octafluorinated **A2** to **A3**, especially by introducing the

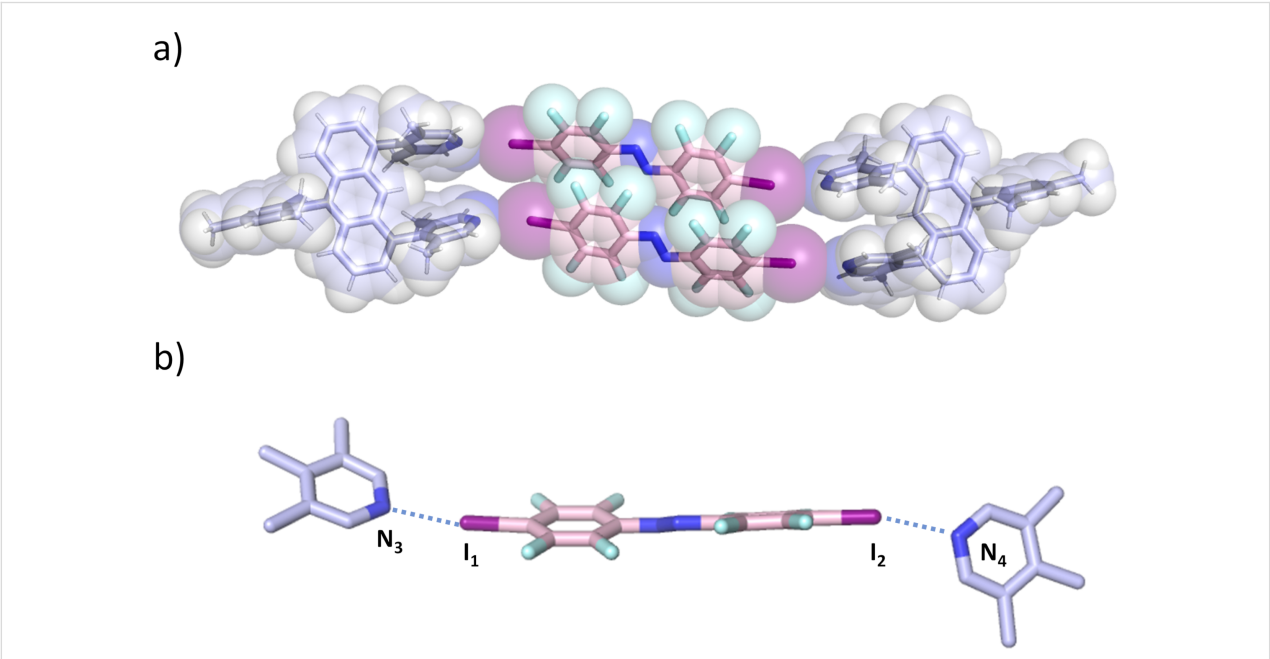


Figure 3: a) Space-filling model of **U1**···**A2**. The kinked alignment of both the lutidine units of **U1** and the azobenzenes **A2** can be seen. b) Part of the X-ray crystal structure showing the halogen bonding azobenzene **A2** in detail. Selected bond lengths: N_3–I_1 2.7810(2), I_2–N_4 2.816(2) Å.

iodoethynyl group, as trade-off, photophysical properties are changing. The bathochromic shift of the π→π* band leads to an overlap with the n→π* excitation, making it more difficult to address, together with a diminishing thermal half-life. Both effects can be qualitatively reproduced and understood with the help of quantum mechanical calculations involving a combination of low-cost implicit solvation models and hybrid density functionals when including dispersion corrections.

Supporting Information

Supporting Information File 1

General experimental information, synthetic procedures, UV–vis photochemistry and kinetic studies, computational methods, and X-ray crystallographic details.
[https://www.beilstein-journals.org/bjoc/content/supplementary/1860-5397-15-197-S1.pdf]

Acknowledgements

We acknowledge the Fonds der Chemischen Industrie for a material cost allowance grant (B.M.S) and the Strategic Research Fund of Heinrich Heine University (F-2018/1460-4). E.N. is supported by a Deutschlandstipendium. We thank Y. Garmshausen for his advices on azobenzene photochemistry and C. Czekelius for sharing analytical equipment. Computational support and infrastructure was provided by the "Centre for Information and Media Technology" (ZIM) at the Heinrich Heine University.

ORCID® iDs

Esther Nieland - https://orcid.org/0000-0001-5213-6303
Oliver Weingart - https://orcid.org/0000-0001-6033-3702
Bernd M. Schmidt - https://orcid.org/0000-0003-3622-8106

References

1. Cavallo, G.; Metrangolo, P.; Milani, R.; Pilati, T.; Priimagi, A.; Resnati, G.; Terraneo, G. *Chem. Rev.* **2016,** *116,* 2478–2601. doi:10.1021/acs.chemrev.5b00484
2. Gilday, L. C.; Robinson, S. W.; Barendt, T. A.; Langton, M. J.; Mullaney, B. R.; Beer, P. D. *Chem. Rev.* **2015,** *115,* 7118–7195. doi:10.1021/cr500674c
3. Peuronen, A.; Rinta, H.; Lahtinen, M. *CrystEngComm* **2015,** *17,* 1736–1740. doi:10.1039/c4ce01866d
4. Reiss, G. J. *Z. Kristallogr. - New Cryst. Struct.* **2019,** *234,* 737–739. doi:10.1515/ncrs-2019-0082
5. van Megen, M.; Reiss, G. J. *Inorganics* **2013,** *1,* 3–13. doi:10.3390/inorganics1010003
6. Reiss, G. J.; van Megen, M. *Z. Naturforsch., B: J. Chem. Sci.* **2012,** *67,* 5–10. doi:10.5560/znb.2012.67b0005
7. Svensson, P. H.; Kloo, L. *Chem. Rev.* **2003,** *103,* 1649–1684. doi:10.1021/cr0204101
8. Aakeröy, C. B.; Baldrighi, M.; Desper, J.; Metrangolo, P.; Resnati, G. *Chem. – Eur. J.* **2013,** *19,* 16240–16247. doi:10.1002/chem.201302162
9. Resnati, G.; Boldyreva, E.; Bombicz, P.; Kawano, M. *IUCrJ* **2015,** *2,* 675–690. doi:10.1107/s2052252515014608
10. Dichiarante, V.; Kaiho, T.; Metrangolo, P.; Pilati, T.; Resnati, G.; Terraneo, G.; Ursini, M. *Chem. Commun.* **2019,** *55,* 4234–4237. doi:10.1039/c9cc01092k
11. Szell, P. M. J.; Zablotny, S.; Bryce, D. L. *Nat. Commun.* **2019,** *10,* 916. doi:10.1038/s41467-019-08878-8
12. Saccone, M.; Spengler, M.; Pfletscher, M.; Kuntze, K.; Virkki, M.; Wölper, C.; Gehrke, R.; Jansen, G.; Metrangolo, P.; Priimagi, A.; Giese, M. *Chem. Mater.* **2019,** *31,* 462–470. doi:10.1021/acs.chemmater.8b04197
13. Saccone, M.; Kuntze, K.; Ahmed, Z.; Siiskonen, A.; Giese, M.; Priimagi, A. *J. Mater. Chem. C* **2018,** *6,* 9958–9963. doi:10.1039/c8tc02611d
14. Han, C.; Zhao, D.; Dong, S. *Chem. Commun.* **2018,** *54,* 13099–13102. doi:10.1039/c8cc07993e
15. Nikolayenko, V. I.; Castell, D. C.; van Heerden, D. P.; Barbour, L. J. *Angew. Chem., Int. Ed.* **2018,** *57,* 12086–12091. doi:10.1002/anie.201806399
16. Pfrunder, M. C.; Brock, A. J.; Brown, J. J.; Grosjean, A.; Ward, J.; McMurtrie, J. C.; Clegg, J. K. *Chem. Commun.* **2018,** *54,* 3974–3976. doi:10.1039/c8cc02178c
17. Liu, P.; Li, Z.; Shi, B.; Liu, J.; Zhu, H.; Huang, F. *Chem. – Eur. J.* **2018,** *24,* 4264–4267. doi:10.1002/chem.201800312
18. Bai, L.; Bose, P.; Gao, Q.; Li, Y.; Ganguly, R.; Zhao, Y. *J. Am. Chem. Soc.* **2017,** *139,* 436–441. doi:10.1021/jacs.6b11057
19. Priimagi, A.; Cavallo, G.; Forni, A.; Gorynsztejn-Leben, M.; Kaivola, M.; Metrangolo, P.; Milani, R.; Shishido, A.; Pilati, T.; Resnati, G.; Terraneo, G. *Adv. Funct. Mater.* **2012,** *22,* 2572–2579. doi:10.1002/adfm.201200135
20. Szell, P. M. J.; Siiskonen, A.; Catalano, L.; Cavallo, G.; Terraneo, G.; Priimagi, A.; Bryce, D. L.; Metrangolo, P. *New J. Chem.* **2018,** *42,* 10467–10471. doi:10.1039/c8nj00759d
21. Dumele, O.; Schreib, B.; Warzok, U.; Trapp, N.; Schalley, C. A.; Diederich, F. *Angew. Chem., Int. Ed.* **2017,** *56,* 1152–1157. doi:10.1002/anie.201610884
22. Sinnwell, M. A.; MacGillivray, L. R. *Angew. Chem., Int. Ed.* **2016,** *55,* 3477–3480. doi:10.1002/anie.201510912
23. Dumele, O.; Trapp, N.; Diederich, F. *Angew. Chem., Int. Ed.* **2015,** *54,* 12339–12344. doi:10.1002/anie.201502960
24. Jungbauer, S. H.; Bulfield, D.; Kniep, F.; Lehmann, C. W.; Herdtweck, E.; Huber, S. M. *J. Am. Chem. Soc.* **2014,** *136,* 16740–16743. doi:10.1021/ja509705f
25. Gliese, J.-P.; Jungbauer, S. H.; Huber, S. M. *Chem. Commun.* **2017,** *53,* 12052–12055. doi:10.1039/c7cc07175b
26. Walter, S. M.; Jungbauer, S. H.; Kniep, F.; Schindler, S.; Herdtweck, E.; Huber, S. M. *J. Fluorine Chem.* **2013,** *150,* 14–20. doi:10.1016/j.jfluchem.2013.02.027
27. Heinen, F.; Engelage, E.; Dreger, A.; Weiss, R.; Huber, S. M. *Angew. Chem., Int. Ed.* **2018,** *57,* 3830–3833. doi:10.1002/anie.201713012
28. Bergamaschi, G.; Lascialfari, L.; Pizzi, A.; Martinez Espinoza, M. I.; Demitri, N.; Milani, A.; Gori, A.; Metrangolo, P. *Chem. Commun.* **2018,** *54,* 10718–10721. doi:10.1039/c8cc06010j
29. Pan, F.; Dashti, M.; Reynolds, M. R.; Rissanen, K.; Trant, J. F.; Beyeh, N. K. *Beilstein J. Org. Chem.* **2019,** *15,* 947–954. doi:10.3762/bjoc.15.91

30. Turunen, L.; Warzok, U.; Schalley, C. A.; Rissanen, K. *Chem* **2017,** *3,* 861–869. doi:10.1016/j.chempr.2017.08.010
31. Warzok, U.; Marianski, M.; Hoffmann, W.; Turunen, L.; Rissanen, K.; Pagel, K.; Schalley, C. A. *Chem. Sci.* **2018,** *9,* 8343–8351. doi:10.1039/c8sc03040e
32. Turunen, L.; Peuronen, A.; Forsblom, S.; Kalenius, E.; Lahtinen, M.; Rissanen, K. *Chem. – Eur. J.* **2017,** *23,* 11714–11718. doi:10.1002/chem.201702655
33. Turunen, L.; Warzok, U.; Puttreddy, R.; Beyeh, N. K.; Schalley, C. A.; Rissanen, K. *Angew. Chem., Int. Ed.* **2016,** *55,* 14033–14036. doi:10.1002/anie.201607789
34. Vanderkooy, A.; Gupta, A. K.; Földes, T.; Lindblad, S.; Orthaber, A.; Pápai, I.; Erdélyi, M. *Angew. Chem., Int. Ed.* **2019,** *58,* 9012–9016. doi:10.1002/anie.201904817
35. Nieland, E.; Topornicki, T.; Kunde, T.; Schmidt, B. M. *Chem. Commun.* **2019,** *55,* 8768–8771. doi:10.1039/c9cc03061a
36. Stranius, K.; Börjesson, K. *Sci. Rep.* **2017,** *7,* 41145. doi:10.1038/srep41145
37. Siampiringue, N.; Guyot, G.; Monti, S.; Bortolus, P. *J. Photochem.* **1987,** *37,* 185–188. doi:10.1016/0047-2670(87)85039-6
38. Bortolus, P.; Monti, S. *J. Phys. Chem.* **1979,** *83,* 648–652. doi:10.1021/j100469a002
39. Granucci, G.; Persico, M. *Theor. Chem. Acc.* **2007,** *117,* 1131–1143. doi:10.1007/s00214-006-0222-1
40. Weingart, O.; Lan, Z.; Koslowski, A.; Thiel, W. *J. Phys. Chem. Lett.* **2011,** *2,* 1506–1509. doi:10.1021/jz200474g
41. Gámez, J. A.; Weingart, O.; Koslowski, A.; Thiel, W. *J. Chem. Theory Comput.* **2012,** *8,* 2352–2358. doi:10.1021/ct300303s
42. Gámez, J. A.; Weingart, O.; Koslowski, A.; Thiel, W. *Phys. Chem. Chem. Phys.* **2013,** *15,* 11814–11821. doi:10.1039/c3cp51316e
43. Böckmann, M.; Doltsinis, N. L.; Marx, D. *J. Phys. Chem. A* **2010,** *114,* 745–754. doi:10.1021/jp910103b
44. Conti, I.; Garavelli, M.; Orlandi, G. *J. Am. Chem. Soc.* **2008,** *130,* 5216–5230. doi:10.1021/ja710275e
45. Bléger, D.; Schwarz, J.; Brouwer, A. M.; Hecht, S. *J. Am. Chem. Soc.* **2012,** *134,* 20597–20600. doi:10.1021/ja310323y
46. Knie, C.; Utecht, M.; Zhao, F.; Kulla, H.; Kovalenko, S.; Brouwer, A. M.; Saalfrank, P.; Hecht, S.; Bléger, D. *Chem. – Eur. J.* **2014,** *20,* 16492–16501. doi:10.1002/chem.201404649
47. Hübschle, C. B.; Dittrich, B. *J. Appl. Crystallogr.* **2011,** *44,* 238–240. doi:10.1107/s0021889810042482
48. Dumele, O.; Wu, D.; Trapp, N.; Goroff, N.; Diederich, F. *Org. Lett.* **2014,** *16,* 4722–4725. doi:10.1021/ol502099j
49. Canneaux, S.; Bohr, F.; Henon, E. *J. Comput. Chem.* **2014,** *35,* 82–93. doi:10.1002/jcc.23470

License and Terms

This is an Open Access article under the terms of the Creative Commons Attribution License (http://creativecommons.org/licenses/by/4.0). Please note that the reuse, redistribution and reproduction in particular requires that the authors and source are credited.

The license is subject to the *Beilstein Journal of Organic Chemistry* terms and conditions: (https://www.beilstein-journals.org/bjoc)

The definitive version of this article is the electronic one which can be found at:
doi:10.3762/bjoc.15.197

BEILSTEIN JOURNAL OF ORGANIC CHEMISTRY

Click chemistry towards thermally reversible photochromic 4,5-bisthiazolyl-1,2,3-triazoles

Chenxia Zhang[1], Kaori Morinaka[1], Mahmut Kose[1,2], Takashi Ubukata[1] and Yasushi Yokoyama[*1]

Letter

Open Access

Address:
[1]Department of Chemistry and Life Science, Graduate School of Engineering Science, Yokohama National University, 79-5, Tokiwadai, Hodogaya, Yokohama 240-8501, Japan and [2]Department of Chemistry, Faculty of Arts and Science, Zonguldak Bülent Ecevit University, 67100, Zonguldak, Turkey

Email:
Yasushi Yokoyama[*] - yokoyama-yasushi-wp@ynu.ac.jp

* Corresponding author

Keywords:
aromatic stabilization energy; diarylethene; ruthenium(I) catalysed Huisgen cyclization; terarylene; thermally reversible photochromism

Beilstein J. Org. Chem. **2019,** *15,* 2161–2169.
doi:10.3762/bjoc.15.213

Received: 27 June 2019
Accepted: 28 August 2019
Published: 13 September 2019

This article is part of the thematic issue "Molecular switches".

Guest Editor: W. Szymanski

© 2019 Zhang et al.; licensee Beilstein-Institut.
License and terms: see end of document.

Abstract

Three new diarylethenes were synthesized from 1,2-bis(5-methyl-2-(4-substituted-phenyl)thiazol-4-yl)ethyne and benzyl azide through Ru(I)-catalyzed Huisgen cyclization reactions. The 4,5-bisthiazolyl-1,2,3-triazoles thus prepared, which belong to the terarylene family, showed thermally reversible photochromism. The absorption maximum wavelengths of the closed forms are longer than other terarylenes reported so far. The thermal back reactions are much faster when the substituents on the terminal phenyl groups are electron-withdrawing cyano groups than when they are electron-donating methoxy groups.

Introduction

Diarylethenes are one of the most widely investigated among the photochromic families [1-3]. They are known to show thermally irreversible photochromism. However, some of them are thermally reversible [4]: (1) when the aromatic stabilization energy of the aromatic rings is large [5]; (2) when the substituent groups on the ring-closing carbon atoms are large [6]; (3) when the substituent groups on the ring-closing carbon atoms are strongly electron-withdrawing [7]; or (4) when the dialkylamino group on the side chain [8] or a carbon atom of the conjugation system in a strained closed form [9] are protonated.

Terarylenes [10,11], one of the closely related families of diarylethenes, are largely thermally reversible [10,12] although some are irreversible when the aromatic stabilization energy of the aromatic rings is small [11]. Their syntheses are usually carried out by the sequential construction of the central aromatic ring at the final stage [10] or the introduction of two aromatic rings to the central aromatic ring [11]. If the construction of three contiguous aromatic-ring arrays can be easily achieved, a new and facile synthesis method for the photochromic family which undergoes 6π-electrocyclization can be realized [13].

Early in the 21st century, Sharpless and co-workers proposed the concept of "click chemistry" [14], which stands for the secure, quick, selective, general and facile reaction between two organic functional groups. In click chemistry, the Huisgen cyclization, which occurs between an organic azide and a terminal alkyne catalyzed by a Cu(I) ion, was regarded as the representative reaction [15,16]. This reaction occurs even in aqueous media, the chemical yield is always high, and the regiochemical structure of the product is always 1,4-disubstituted triazole.

Cu(I)-catalyzed Huisgen cyclization proceeds by the formation of copper acetylide as the intermediate [15,17], resulting in the formation of 1,4-disubstituted triazoles. In contrast, when Ru(I) complexes are employed as the catalyst, the reaction mechanism is different from the case of Cu(I), and the major products are 1,5-disubstituted triazoles. Another more important difference is that Ru(I) catalysts work on the disubstituted alkynes to give 1,4,5-trisubstituted triazoles (Scheme 1) [18,19]. When both substituents of an internal alkyne are aromatic groups, the triazoles thus formed include the hexatriene motif in the structure.

Although a number of photochromic diarylethenes containing triazole groups have been reported [20-31], all of them use the triazole ring as the linker of the second functional molecule with the diarylethene core. To the best of our knowledge, no diarylethenes or terarylenes possessing the triazole ring as one of the components of the hexatriene moiety has been reported to date.

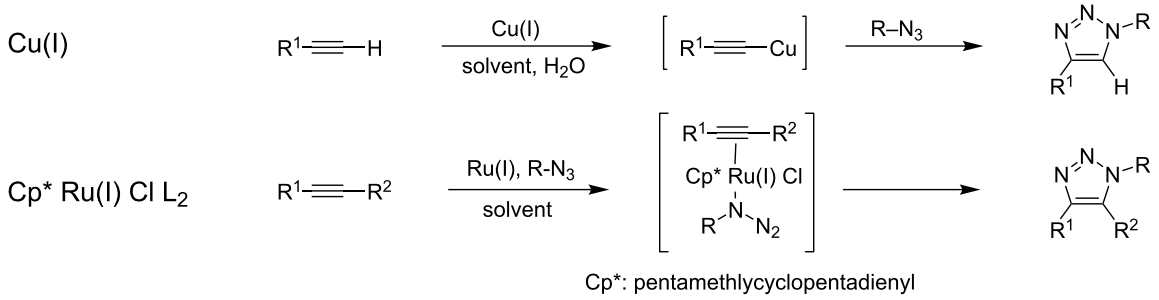
Accordingly, we decided to employ a Ru(I) catalyst to synthesize 4,5-diaryl-1-substituted-1,2,3-triazoles **1o**–**3o** as possible photochromic compounds (Scheme 2).

Results and Discussion

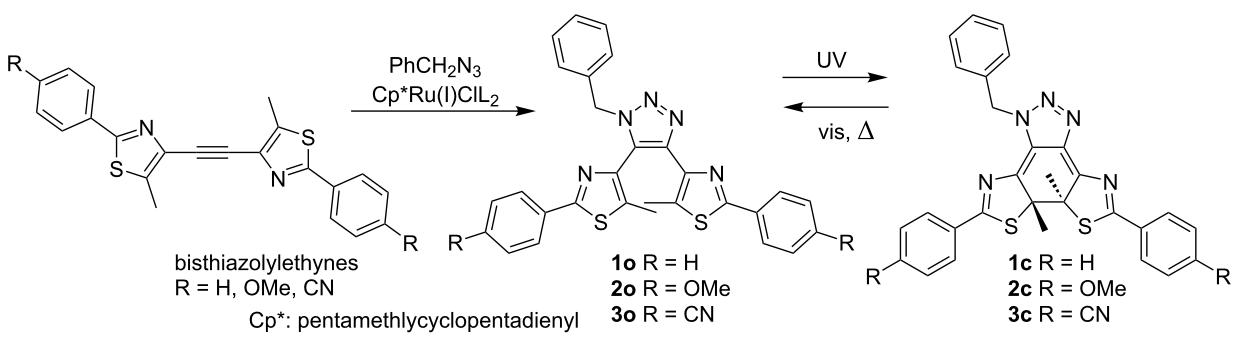
Molecular design and synthesis

As the organic azide we used commercially available benzyl azide. Since 1,2-bis(5-methyl-2-phenylthiazol-4-yl)ethyne was used in our previous research [32-34], we employed bisthiazolylethynes as the foundation for the skeleton of the target compounds. In order to examine the substituent effects of the terminal phenyl groups on the photochromic properties, compounds with methoxy groups or cyano groups at the *para*-position of the phenyl groups were also synthesized. To avoid the generation of isomers with a substitution pattern by Huisgen cyclization, the same substituents were introduced to both phenyl groups.

The Ru(I)-catalyzed Huisgen cyclization reaction proceeded rather smoothly to give **1o**, **2o** and **3o** in moderate chemical



Scheme 1: Reaction mechanisms of Huisgen cyclization catalyzed by Cu(I) and Ru(I).



Scheme 2: Synthesis and photochromism of bisthiazolyltriazoles.

yields of 36%, 53% and 20%, respectively. Since the reported chemical yield of the reaction of tolan, the simplest bisarylethyne, and 2-phenylethyl azide was 63% [19], it could be considered reasonable that the reactions of the sterically more congested ethynes and benzyl azide gave triazoles with less chemical yields. Details of the synthesis are described in Supporting Information File 1.

Photochromic reactions

Photochemical cyclizations

Triazoles were dissolved in ethanol (EtOH), acetonitrile (MeCN), ethyl acetate (AcOEt) and toluene, and each solution was irradiated with 313 nm light. The changes in the absorption spectra during UV light irradiation in MeCN are shown in Figure 1 (spectra of the compounds in the other solvents are shown in Figures S1–S9 in Supporting Information File 1). The absorption spectral properties are summarized in Table 1 together with their predicted absorption maxima obtained by TD DFT calculations in vacuum [35]. Although **1o** and **2o** showed substantial coloration, **3o** showed only a slight coloration at room temperature.

The solvent effects on the absorption maximum wavelengths of the closed forms were not remarkable. The tendency observed was of the absorption maximum wavelength being a few nanometers longer in less polar toluene than for the other solvents.

When the substituents on the terminal phenyl rings are electron-withdrawing cyano groups, the measured absorption maximum of the closed form was about 40 nm longer than the others in any solvent. The substituent effect observed here is different from the small substituent effect on the closed forms of the representative bisthienylhexafluorocyclopentenes **4c** (R = H, 562 nm), **5c** (R = OMe, 570 nm) and **6c** (R = CN, 570 nm) in hexane (Scheme 3) [36]. In triazoles, while the introduction of electron-donating methoxy groups had little effect on the absorption maximum wavelengths, the introduction of electron-withdrawing cyano groups induced a large bathochromic shift. This observation was well-reproduced by TD DFT calculations (Table 1 and chapter SI-4 in Supporting Information File 1).

When the absorption maximum wavelength of **1c**, whose central ethene moiety is triazole, is compared with those of the

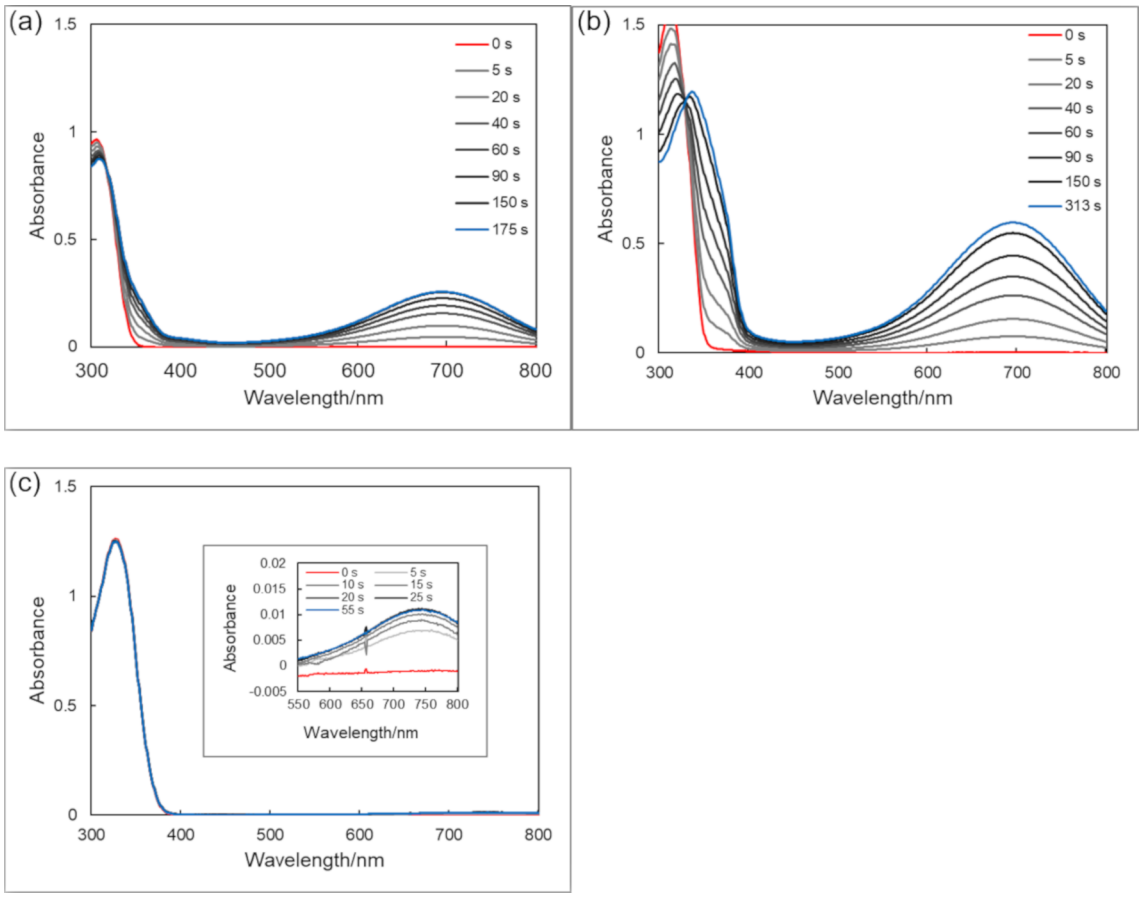
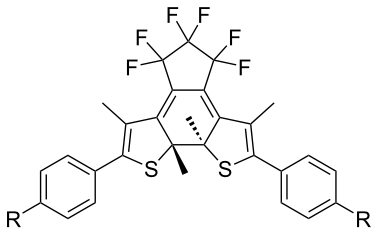


Figure 1: Absorption spectral change of triazoles **1o**–**3o** upon irradiation of 313 nm light in MeCN at 28 °C. Light intensity: 1.8 mW cm^{-2}. (a) **1o**. 4.44 × 10^{-5} mol dm^{-3}. (b) **2o**. 4.38 × 10^{-5} mol dm^{-3}. (c) **3o**. 4.73 × 10^{-5} mol dm^{-3}.

Table 1: Wavelengths of absorption maxima of the closed forms of photochromic triazoles.

Solvent and calculation method	EtOH	MeCN	AcOEt	toluene	TD DFT[a]
e_r [b]	24.55	35.94	6.02	2.38	in vacuum
E_T^N [c]	0.654	0.460	0.228	0.099	
			λ_{max}/nm		
1c (R = H)	692	695	693	698	704
2c (R = OMe)	697	696	693	699	699
3c (R = CN)	737	739	737	739	759

[a]In vacuum [35]. [b]Relative dielectric constant. [c]Normalized $E_T(30)$ value.



4c R = H 562 nm
5c R = OMe 570 nm
6c R = CN 570 nm

Scheme 3: Wavelengths of absorption maxima of the closed forms of bisthienyletenes in hexane [36].

closely related **7c** (cyclopentene) [37], **8c** (hexafluorocyclopentene) [38], **9c** (thiazole) [39], and **10c** (imidazole) [40] in nonpolar solvents, **1c** has a much longer absorption maximum in toluene (Scheme 4, Table 2). It should also be noted that the absorption maximum wavelength is longer when the central ethene moiety is part of the aromatic ring than when it is an isolated ethene in their open-form structures.

Table 2: Absorption spectral data of triazoles and other related photochromic compounds.

	λ_{max}/nm	
	In solution	TD DFT[a]
1c	698[b]	704
7c	500[c] [37]	537
8c	525[d] [38]	541
9c	587[d] [39]	636
10c	654[d] [40]	668

[a]In vacuum [35]. [b]In toluene. [c]In cyclohexane. [d]In hexane.

Thermal back reactions

As expected, all closed forms of triazoles showed thermal back reactions since the photochemical cyclization results in the loss of the aromatic stabilization energy [41] of the three contiguous aromatic rings. The changes in the absorption spectra of thermal decoloration in MeCN at room temperature are shown in Figure 2.

In order to clarify the nature of the thermal back reaction of triazoles, **1o**, **2o** and **3o** were irradiated with 313 nm light in four different solvents, and the decrease in the absorbance of the absorption maximum wavelengths in the visible region was observed at three different temperatures. The first order reaction rate constants of the thermal back reactions at different temperatures were then determined. Arrhenius plots of ln k against $1/T$ gave pre-exponential factors (A) and Arrhenius activation energy E_a of these thermally reversible photochromic triazoles (Figures S10–S13 in Supporting Information File 1). The kinetic data of the thermal back reactions of **1c**–**3c** in toluene are shown in Table 3 together with the literature data of related compounds **9c** [39] and **10c** [40] shown in Scheme 4.

As shown in Table 3, the thermal back reaction is fast when the aromatic stabilization energy of the central aromatic ring is large. Although E_a of **10** is smaller than that of **1** and **2**, the pre-exponential factors (A) of **1** and **2** are about 10^4 times and 10^3 times larger, respectively, than that of **10**.

When the thermal kinetic data of **1**, **2** and **3** are compared, the thermal back reaction rate of **3** is extremely faster than the others, although the central aromatic ring is common to these compounds.

As shown in Table 4, neither electronic charge distribution on the carbon atoms (natural charge [42]) comprising the thermally breaking C–C bond, its bond length nor its bond order, which were obtained by DFT calculations of these compounds, did not give a clear explanation for the difference in the reaction rate. Possible evidence of the fast back reaction of **3c** may be found in the bond lengths and Mulliken bond orders between the atoms constructing the conjugation system around the central cyclohexadiene moiety (Scheme 5).

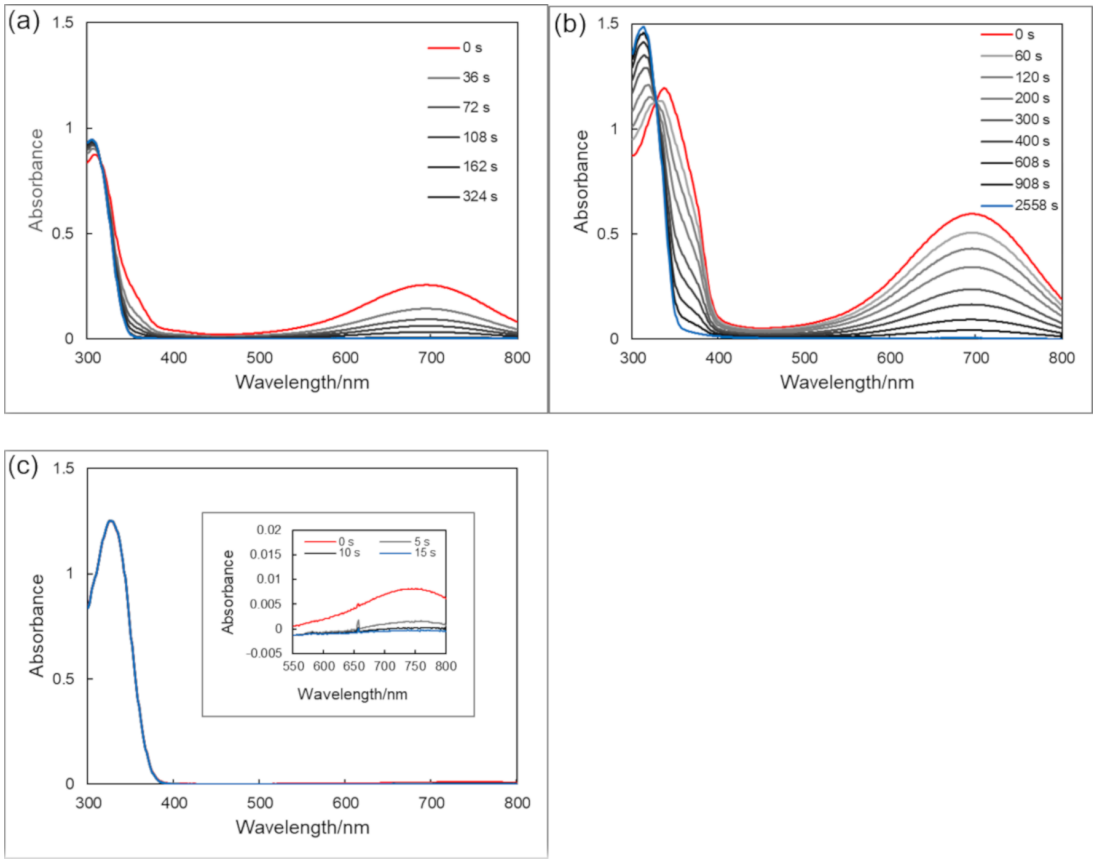
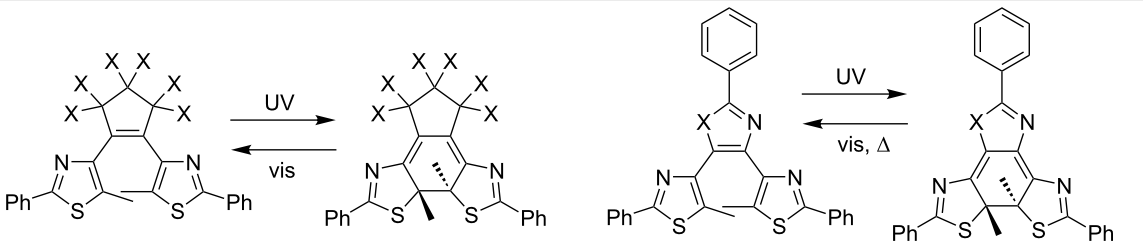


Figure 2: Absorption spectral change of triazoles **1c**–**3c** during the thermal back reaction after 313-nm light irradiation to **1o**–**3o** in MeCN at 28 °C. Concentration of compounds are the same as in Figure 1. (a) **1c**. (b) **2c**. (c) **3c**.



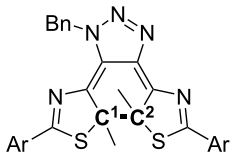
Scheme 4: Photochromism of closely related compounds.

Table 3: Kinetic data of thermal back reactions and aromatic stabilization energy of **1c**–**3c**, **9c** and **10c**.

	A/s^{-1}	E_a/kJ mol^{-1}	k (293K)/s^{-1}	$t_{1/2}$ (293 K)[a]	ASE[b]/kJ mol^{-1}
9c[c]	7.1×10^{11}	112	6.7×10^{-9}[d]	3.3 years	72.9
10c[c]	1.3×10^{9}	85	8.7×10^{-7}[d]	9.2 days	78.6
1c[e]	1.21×10^{13}	87.8	2.80×10^{-3}	248 s	102.0
2c[e]	2.79×10^{12}	87.9	6.14×10^{-4}	1130 s	102.0
3c[e]	1.26×10^{13}	81.4	3.92×10^{-2}	17.7 s	102.0

[a]$t_{1/2}$ (293 K): Half-life at 293 K. [b]ASE: Aromatic stabilization energy of the central aromatic rings when unsubstituted. Data taken from ref. [41]. [c]In toluene. Data taken from ref. [39] for **9** and ref. [40] for **10**. [d]Calculated from $t_{1/2}$ at 293 K.[e]In toluene.

Table 4: Natural charge, bond length and bond order of the bond-breaking carbon atoms of triazoles **1c** – **3c** in the thermal back reactions obtained by DFT calculations.



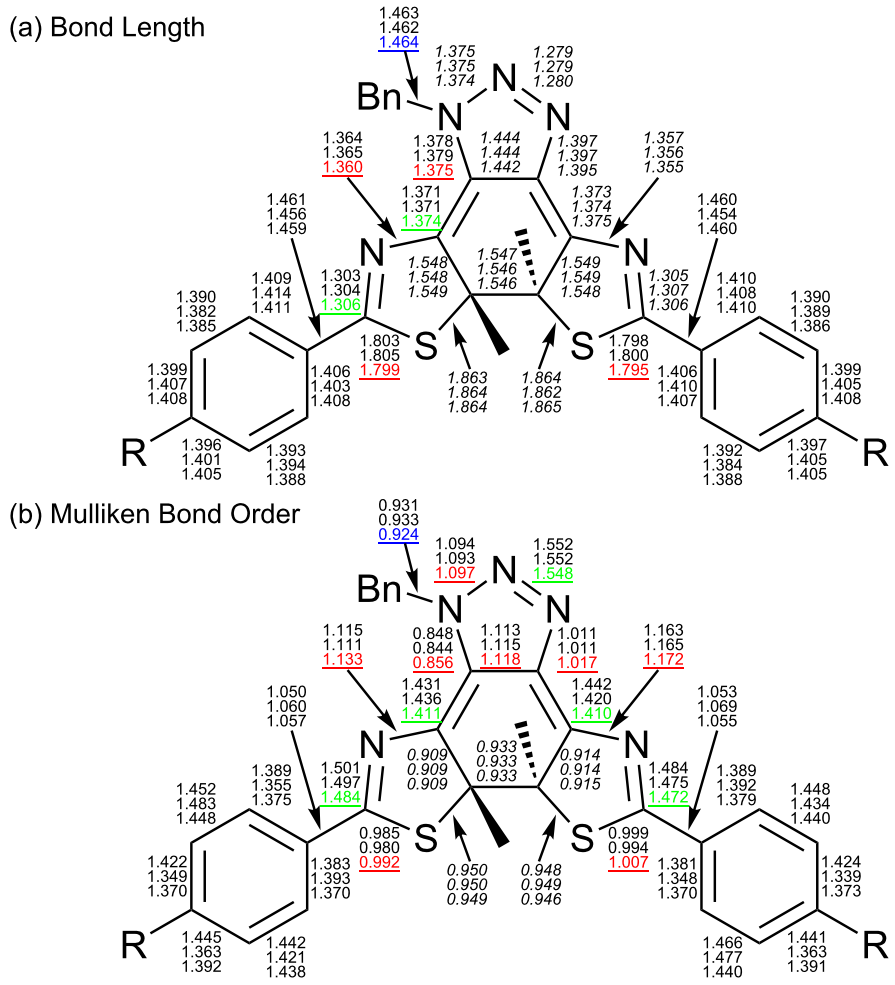
	Natural charge[a]		Bond length/Å	Mulliken bond order
	C^1	C^2	C^1–C^2	C^1–C^2
1c	−0.198	−0.204	1.547	0.933
2c	−0.195	−0.204	1.546	0.933
3c	−0.198	−0.204	1.546	0.933

[a]Calculated by DFT calculations as the number of positive charges [42].

In Scheme 5a, the single bonds of **3c** written in red are shorter than in the other two compounds, implying that they have a stronger double bond character. Similarly, the double bonds of **3c** written in green are longer, showing the stronger single bond character. This suggests a stronger bond alteration tendency in **3c** than in **1c** and **2c**, and this distinctive character of **3c** can be seen more clearly in Scheme 5b.

In addition, since the bond order of the N–Bn bond in blue of **3c** is the smallest, it can be reasonably assumed that the lone pair on this nitrogen atom participates in the conjugation in the molecular core more strongly than in **1c** and **2c**. This distinctive character of **3c** originates from the electron-withdrawing cyano groups in the molecule.

Data on the terminal phenyl rings in Scheme 5 do not give any convergent tendency of the substituents due to the electron-do-



Scheme 5: Bond length (a) (in Å) and Mulliken bond order (b) of **1c**–**3c** obtained by DFT calculations. Top number of each set: **1c**. Second number: **2c**. Bottom number: **3c**. Red numbers of **3c**: indicates stronger double bond character. Green numbers of **3c**: indicates stronger single bond character. Blue numbers of **3c**: indicates weaker bond character. Italic numbers around the central conjugation systems: no significant difference between the three compounds.

nating character of the methoxy groups in **2c** and the electron-withdrawing character of the cyano groups in **3c**. However, it is safe to say the cyano groups in **3c** are pulling the electrons and this effect reaches the nitrogen atom bearing the benzyl group through the conjugation.

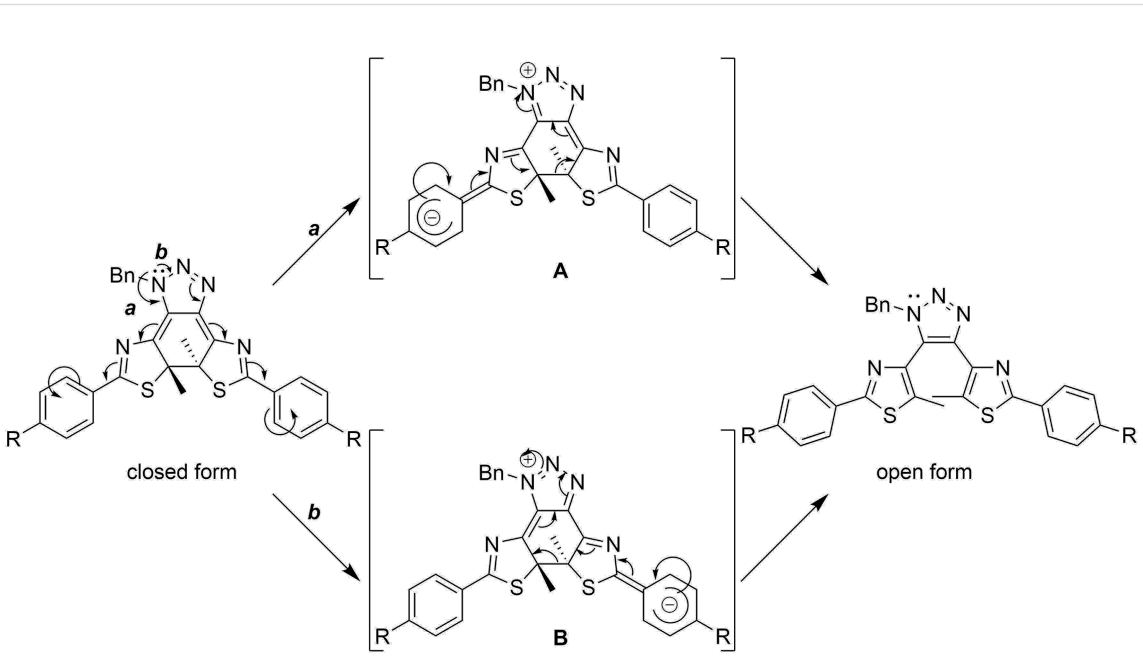
Then how does this effect accelerate the thermal back reaction in **3c**? We propose the conventional reaction mechanism shown in Scheme 6. When the delocalized lone pair on the nitrogen atom moves back from the resonance structures **A** and **B**, it may break the central C–C single bond to give the open form, as shown with the arrows. The resonance structures are stabilized more strongly when R is a cyano group so that the C–C bond scission occurs easily. Thus, it is possible to control the rate of the thermal back reaction by: (1) changing the aromatic ring at the ethene moiety, and (2) changing the substituents on the phenyl rings at the peripheral of the molecule.

Finally, we would like to discuss the solvent effects on the thermal back reactions of **1c**, **2c**, and **3c**. As can be seen in Figure S13, the solvents are classified into two categories: (1) polar solvents (EtOH and MeCN) and (2) less polar solvents (AcOEt and toluene). Although the gradient of the lines (*E*a) for the same compound in Figure S13a–c are quite similar, the intercepts (*A*) are clearly different for the two solvent groups of **1c** and **2c**. As for **3c**, although its categorization is not as clear as **1c** and **2c**, differences can still be observed. In general, the thermal back reactions are faster in the more polar solvents, and faster in MeCN than in EtOH among these two solvents. However, for **2c**, it is faster in EtOH than in MeCN. This may have originated from the hydrogen-bond formation between EtOH molecules and the methoxy groups in **2c**, which reduces the electrostatic repulsion between the methoxy groups and the negatively charged phenyl groups in the intermediate resonance structures **A** and **B** shown in Scheme 6.

In less polar solvents, the thermal back reactions of **1c** and **2c** are faster in toluene than in AcOEt. However, the reaction of **3c** is the opposite. This could be explained by the strong electron-withdrawing power of the cyano groups in **3c**, which enhanced the charge-separation character in the intermediate resonance structures **A** and **B**. These structures are stabilized more strongly in more polar AcOEt than in toluene, and the thermal back reaction rate in AcOEt was increased.

Conclusion

We have synthesized three novel thermally reversible 4,4'-(1-benzyl-1*H*-1,2,3-triazole-4,5-diyl)bis(5-methyl-2-(4-substituted-phenyl)thiazole)s **1o**–**3o** by Ru(I)-catalysed Huisgen cyclization, which is a type of "click" reaction. They showed thermally reversible photochromism in various solvents. The absorption maximum wavelengths of **1c** (with unsubstituted peripheral phenyl groups) and **2c** (with methoxy groups on the phenyl groups) are close to 700 nm, while that of **3c** (with cyano groups on the phenyl groups) was about 740 nm. The thermal back reactions of these compounds proved that **3c** with



Scheme 6: Possible reaction mechanism of thermal ring opening of the closed forms.

the electron-withdrawing cyano groups is the fastest while **2c** with electron-donating methoxy groups was the slowest. DFT and TD DFT calculations supported these experimental results.

The Cu(I)-catalyzed Huisgen reaction has been used many times to connect two functional molecules. When the Ru(I)-catalyzed Huisgen reaction is employed to connect two functional molecules, the linker itself possesses the thermally reversible photochromic property. Thus, this work can open the door to the creation of promising new materials with highly integrated functions.

Supporting Information

Experimental details including the synthesis of **1o**, **2o** and **3o**. Changes in the absorption spectra of **1o**, **2o** and **3o** in ethanol, ethyl acetate and toluene. Analysis processes of the thermal back reactions of **1o**, **2o** and **3o**. DFT and TD DFT calculation results of **1c**, **2c** and **3c** and ^{1}H NMR, IR and mass spectra of new compounds.

Supporting Information File 1

Additional experimental data and spectra.
[https://www.beilstein-journals.org/bjoc/content/supplementary/1860-5397-15-213-S1.pdf]

Acknowledgements

This work was supported by MEXT KAKENHI Grant Number JP19050004 in Grant-in-Aid for Scientific Research in Priority Areas “New Frontiers in Photochromism (No. 471)” and JSPS KAKENHI Grant Number JP26107009 in Scientific Research on Innovative Areas “Photosynergetics”. The authors are also grateful to the Instrumental Analysis Center of Yokohama National University for their support in the NMR and MS measurements.

ORCID® iDs

Mahmut Kose - https://orcid.org/0000-0003-2689-6661
Takashi Ubukata - https://orcid.org/0000-0001-5124-4986
Yasushi Yokoyama - https://orcid.org/0000-0002-8654-1320

References

1. Irie, M.; Fukaminato, T.; Matsuda, K.; Kobatake, S. *Chem. Rev.* **2014,** *114,* 12174–12277. doi:10.1021/cr500249p
2. Tian, H.; Yang, S. *Chem. Soc. Rev.* **2004,** *33,* 85–97. doi:10.1039/b302356g
3. Irie, M. *Chem. Rev.* **2000,** *100,* 1685–1716. doi:10.1021/cr980069d
4. Kitagawa, D.; Sasaki, K.; Kobatake, S. *Bull. Chem. Soc. Jpn.* **2011,** *84,* 141–147. doi:10.1246/bcsj.20100274
5. Nakamura, S.; Irie, M. *J. Org. Chem.* **1988,** *53,* 6136–6138. doi:10.1021/jo00261a035
6. Kobatake, S.; Uchida, K.; Tsuchida, E.; Irie, M. *Chem. Lett.* **2000,** *29,* 1340–1341. doi:10.1246/cl.2000.1340
7. Gilat, S. L.; Kawai, S. H.; Lehn, J.-M. *Chem. – Eur. J.* **1995,** *1,* 275–284. doi:10.1002/chem.19950010504
8. Kobatake, S.; Terakawa, Y. *Chem. Commun.* **2007,** 1698–1700. doi:10.1039/b700177k
9. Jurissek, C.; Berger, F.; Eisenreich, F.; Kathan, M.; Hecht, S. *Angew. Chem., Int. Ed.* **2019,** *58,* 1945–1949. doi:10.1002/anie.201812284
10. Krayushkin, M. M.; Ivanov, S. N.; Martynkin, A. Y.; Lichitsky, B. V.; Dudinov, A. A.; Uzhinov, B. M. *Russ. Chem. Bull.* **2001,** *50,* 116–121. doi:10.1023/a:1009541605405
11. Kawai, T.; Iseda, T.; Irie, M. *Chem. Commun.* **2004,** 72–73. doi:10.1039/b311334e
12. Kawai, S.; Nakashima, T.; Atsumi, K.; Sakai, T.; Harigai, M.; Imamoto, Y.; Kamikubo, H.; Kataoka, M.; Kawai, T. *Chem. Mater.* **2007,** *19,* 3479–3483. doi:10.1021/cm0630340
13. Kochi, J.; Ubukata, T.; Yokoyama, Y. *J. Org. Chem.* **2018,** *83,* 10695–10700. doi:10.1021/acs.joc.8b01341
14. Kolb, H. C.; Finn, M. G.; Sharpless, K. B. *Angew. Chem., Int. Ed.* **2001,** *40,* 2004–2021. doi:10.1002/1521-3773(20010601)40:11<2004::aid-anie2004>3.3.co;2-x
15. Rostovtsev, V. V.; Green, L. G.; Fokin, V. V.; Sharpless, K. B. *Angew. Chem., Int. Ed.* **2002,** *41,* 2596–2599. doi:10.1002/1521-3773(20020715)41:14<2596::aid-anie2596>3.0.co;2-4
16. Kolb, H. C.; Sharpless, K. B. *Drug Discovery Today* **2003,** *8,* 1128–1137. doi:10.1016/s1359-6446(03)02933-7
17. Worrell, B. T.; Malik, J. A.; Fokin, V. V. *Science* **2013,** *340,* 457–460. doi:10.1126/science.1229506
18. Zhang, L.; Chen, X.; Xue, P.; Sun, H. H. Y.; Williams, I. D.; Sharpless, K. B.; Fokin, V. V.; Jia, G. *J. Am. Chem. Soc.* **2005,** *127,* 15998–15999. doi:10.1021/ja054114s
19. Boren, B. C.; Narayan, S.; Rasmussen, L. K.; Zhang, L.; Zhao, H.; Lin, Z.; Jia, G.; Fokin, V. V. *J. Am. Chem. Soc.* **2008,** *130,* 8923–8930. doi:10.1021/ja0749993
20. Finden, J.; Kunz, T. K.; Branda, N. R.; Wolf, M. O. *Adv. Mater. (Weinheim, Ger.)* **2008,** *20,* 1998–2002. doi:10.1002/adma.200702455
21. Ouhenia-Ouadahi, K.; Métivier, R.; Maisonneuve, S.; Jacquart, A.; Xie, J.; Léaustic, A.; Yu, P.; Nakatani, K. *Photochem. Photobiol. Sci.* **2012,** *11,* 1705–1714. doi:10.1039/c2pp25129a
22. Ding, H.; Liu, G.; Pu, S.; Zheng, C. *Dyes Pigm.* **2014,** *103,* 82–88. doi:10.1016/j.dyepig.2013.11.022
23. Pu, S.; Ding, H.; Liu, G.; Zheng, C.; Xu, H. *J. Phys. Chem. C* **2014,** *118,* 7010–7017. doi:10.1021/jp5001495
24. Maisonneuve, S.; Métivier, R.; Yu, P.; Nakatani, K.; Xie, J. *Beilstein J. Org. Chem.* **2014,** *10,* 1471–1481. doi:10.3762/bjoc.10.151
25. Ma, L.; Liu, G.; Pu, S.; Ding, H.; Li, G. *Tetrahedron* **2016,** *72,* 985–991. doi:10.1016/j.tet.2015.12.068
26. Duan, F.; Liu, G.; Fan, C.; Pu, S. *Tetrahedron Lett.* **2016,** *57,* 1963–1966. doi:10.1016/j.tetlet.2016.03.079
27. Xue, D.; Zheng, C.; Qu, S.; Liao, G.; Fan, C.; Liu, G.; Pu, S. *Luminescence* **2017,** *32,* 652–660. doi:10.1002/bio.3234
28. Singh, R.; Wu, H.-Y.; Kumar Dwivedi, A.; Singh, A.; Lin, C.-M.; Raghunath, P.; Lin, M.-C.; Wu, T.-K.; Wei, K.-H.; Lin, H.-C. *J. Mater. Chem. C* **2017,** *5,* 9952–9962. doi:10.1039/c7tc03071a
29. Wang, N.; Wang, R.; Tu, Y.; Pu, S.; Liu, G. *Spectrochim. Acta, Part A* **2018,** *196,* 303–310. doi:10.1016/j.saa.2018.02.018

30. Guo, S.; Liu, G.; Fan, C.; Pu, S. *RSC Adv.* **2018,** *8,* 22786–22798. doi:10.1039/c8ra03443e
31. Kang, H.; Fan, C.; Xu, H.; Liu, G.; Pu, S. *Tetrahedron* **2018,** *74,* 4390–4399. doi:10.1016/j.tet.2018.07.002
32. Morinaka, K.; Ubukata, T.; Yokoyama, Y. *Org. Lett.* **2009,** *11,* 3890–3893. doi:10.1021/ol901497t
33. Ogawa, H.; Takagi, K.; Ubukata, T.; Okamoto, A.; Yonezawa, N.; Delbaere, S.; Yokoyama, Y. *Chem. Commun.* **2012,** *48,* 11838–11840. doi:10.1039/c2cc35793c
34. Nakagawa, T.; Miyasaka, Y.; Yokoyama, Y. *Chem. Commun.* **2018,** *54,* 3207–3210. doi:10.1039/c8cc00566d
35. DFT and TD DFT calculations were carried out with Spartan'18 (Wavefunction) at the B3LYP/6-31G* level.
36. Irie, M.; Sakemura, K.; Okinaka, M.; Uchida, K. *J. Org. Chem.* **1995,** *60,* 8305–8309. doi:10.1021/jo00130a035
37. Herder, M.; Schmidt, B. M.; Grubert, L.; Pätzel, M.; Schwarz, J.; Hecht, S. *J. Am. Chem. Soc.* **2015,** *137,* 2738–2747. doi:10.1021/ja513027s
38. Uchida, K.; Ishikawa, T.; Takeshita, M.; Irie, M. *Tetrahedron* **1998,** *54,* 6627–6638. doi:10.1016/s0040-4020(98)00330-5
39. Nakashima, T.; Atsumi, K.; Kawai, S.; Nakagawa, T.; Hasegawa, Y.; Kawai, T. *Eur. J. Org. Chem.* **2007,** 3212–3218. doi:10.1002/ejoc.200700074
40. Nakashima, T.; Goto, M.; Kawai, S.; Kawai, T. *J. Am. Chem. Soc.* **2008,** *130,* 14570–14575. doi:10.1021/ja802986y
41. Cyrañski, M. K.; Krygowski, T. M.; Katritzky, A. R.; Schleyer, P. v. R. *J. Org. Chem.* **2002,** *67,* 1333–1338. doi:10.1021/jo016255s
42. Reed, A. E.; Curtiss, L. A.; Weinhold, F. *Chem. Rev.* **1988,** *88,* 899–926. doi:10.1021/cr00088a005

License and Terms

This is an Open Access article under the terms of the Creative Commons Attribution License (http://creativecommons.org/licenses/by/4.0). Please note that the reuse, redistribution and reproduction in particular requires that the authors and source are credited.

The license is subject to the *Beilstein Journal of Organic Chemistry* terms and conditions: (https://www.beilstein-journals.org/bjoc)

The definitive version of this article is the electronic one which can be found at: doi:10.3762/bjoc.15.213

BEILSTEIN JOURNAL OF ORGANIC CHEMISTRY

Azologization and repurposing of a hetero-stilbene-based kinase inhibitor: towards the design of photoswitchable sirtuin inhibitors

Christoph W. Grathwol[1], Nathalie Wössner[2], Sören Swyter[2], Adam C. Smith[3], Enrico Tapavicza[3], Robert K. Hofstetter[1], Anja Bodtke[1], Manfred Jung[2] and Andreas Link[*1]

Full Research Paper

Open Access

Address:
[1]Institute of Pharmacy, University of Greifswald, Friedrich-Ludwig-Jahn-Str. 17, 17489 Greifswald, Germany, [2]Institute of Pharmaceutical Sciences, University of Freiburg, Albertstr. 25, 79104 Freiburg, Germany and [3]Department of Chemistry and Biochemistry, California State University Long Beach, 1250 Bellflower Boulevard, Long Beach, CA, 90840 USA

Email:
Andreas Link[*] - link@uni-greifswald.de

* Corresponding author

Keywords:
azo compounds; epigenetics; photoswitch; sirtuins; stilbenes

Beilstein J. Org. Chem. **2019,** *15,* 2170–2183.
doi:10.3762/bjoc.15.214

Received: 28 June 2019
Accepted: 29 August 2019
Published: 16 September 2019

This article is part of the thematic issue "Molecular switches".

Guest Editor: W. Szymanski

© 2019 Grathwol et al.; licensee Beilstein-Institut.
License and terms: see end of document.

Abstract

The use of light as an external trigger to change ligand shape and as a result its bioactivity, allows the probing of pharmacologically relevant systems with spatiotemporal resolution. A hetero-stilbene lead resulting from the screening of a compound that was originally designed as kinase inhibitor served as a starting point for the design of photoswitchable sirtuin inhibitors. Because the original stilbenoid structure exerted unfavourable photochemical characteristics it was remodelled to its heteroarylic diazeno analogue. By this intramolecular azologization, the shape of the molecule was left unaltered, whereas the photoswitching ability was improved. As anticipated, the highly analogous compound showed similar activity in its thermodynamically stable stretched-out (*E*)-form. Irradiation of this isomer triggers isomerisation to the long-lived (*Z*)-configuration with a bent geometry causing a considerably shorter end-to-end distance. The resulting affinity shifts are intended to enable real-time photomodulation of sirtuins in vitro.

Introduction

Sirtuins are protein deacylases that cleave off not only acetyl, but also other acyl groups from the ε-amino group of lysines in histones and many other substrate proteins. This class of lysine deacetylases (KDACs) is distinguished from others by their dependence on the cosubstrate NAD^+. In mammals, seven sirtuin isoforms have been identified to date [1]. These can be grouped into five classes (I, II, III, IV and V) according to their phylogenetic relationship [2]. The isoforms Sirt1, Sirt2 and Sirt3 originate from the same phylogenetic branch (class I), but differ in their subcellular localization. Although Sirt1 and Sirt2 were

shown to shuttle between nucleus and cytoplasm in a cell-type and cell-cycle dependent manner, Sirt1 is mainly found in the nucleoplasm and Sirt2 in the cytoplasm [3-7]. Sirt3 primarily resides in the mitochondrion [8]. Facing the multitude of diseases that are associated with a dysregulation of sirtuin activity, they represent a promising target for pharmaceutical intervention. For example, selisistat (EX-527, **1**), a nanomolar and selective Sirt1 inhibitor, passed phase II clinical trials as a disease-modifying therapeutic for Huntington's disease (HD) and was acquainted by AOP Orphan Pharmaceuticals AG for phase III trials in 2017 [9,10]. Its structure comprises a carboxamide moiety, which mimics the amide group of the endogenous pan-sirtuin inhibitor nicotinamide (Figure 1). Likewise Sirt2 inhibition was shown to have beneficial effects in animal and cell models of neurodegenerative diseases like HD and Parkinson's disease [11,12]. Sirt3 activity recently was found to play an important role in cardiovascular diseases and extended ageing in humans [13-16]. Regarding tumorigenesis, the knowledge on the influence of sirtuins is inconsistent. Sirt1, Sirt2 and Sirt3 all have been reported to act either as tumor suppressors or promotors, depending on the particular cell type [1,17].

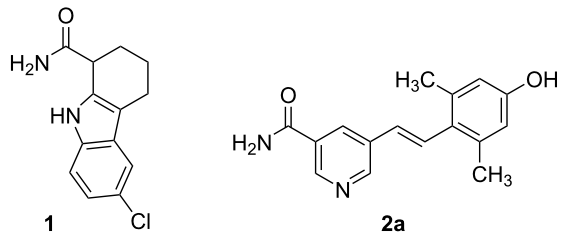


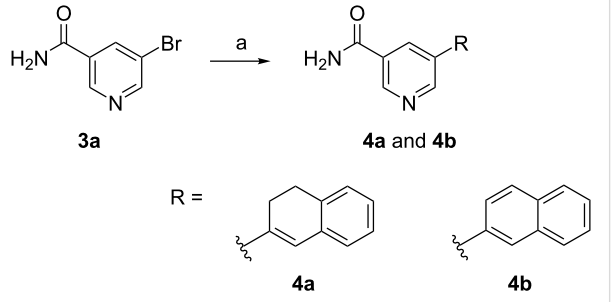
Figure 1: Selisistat (**1**) and hit compound GW435821X (**2a**).

The ability to externally control the biological activity of small molecules in vitro or in vivo comprises numerous opportunities for example in the elucidation of biochemical pathways or the reduction of systemic side effects in drug therapy. Molecular photoswitches, i.e., compounds that undergo changes in their geometry and physicochemical properties upon irradiation with light, represent one major approach to this. One of the most common light-driven transformations exploited in molecular photoswitches is the *E–Z* isomerization of double bonds [18]. In this context, the photochemistry of stilbenes and the closely related azobenzenes has been studied intensely in the past [19-23]. Due to the multifaceted photoreactivity of unsubstituted stilbenes, an appropriate modification of the stilbene core is necessary to prevent unwanted irreversible side reactions [24,25]. On the contrary, the photochemical properties of azobenzenes are more convenient as already proven by their use as photoswitches in countless biological applications [26-30]. However, their heteroaromatic counterparts still seem underrepresented [31]. The approach to new chemotypes for sirtuin inhibition via known adenosine mimicking kinase inhibitors has already been fruitful in the past [32,33]. Therefore, a focused kinase inhibitor library from GlaxoSmithKline was screened for biological activity on human sirtuin isoforms Sirt1–Sirt3. Azastilbene derivative GW435821X (**2a,** Figure 1), initially published as c-RAF kinase inhibitor, was identified as a moderately active Sirt2 inhibitor with low selectivity [34,35]. In this work, the photoresponsiveness of the hetero-stilbene core structure is examined. Furthermore, an intramolecular azologization approach is performed in order to obtain photoswitchable sirtuin inhibitors, which could be useful tools in the further investigation of the biochemistry and pharmacology of sirtuins.

Results

Chemistry of azastilbenes

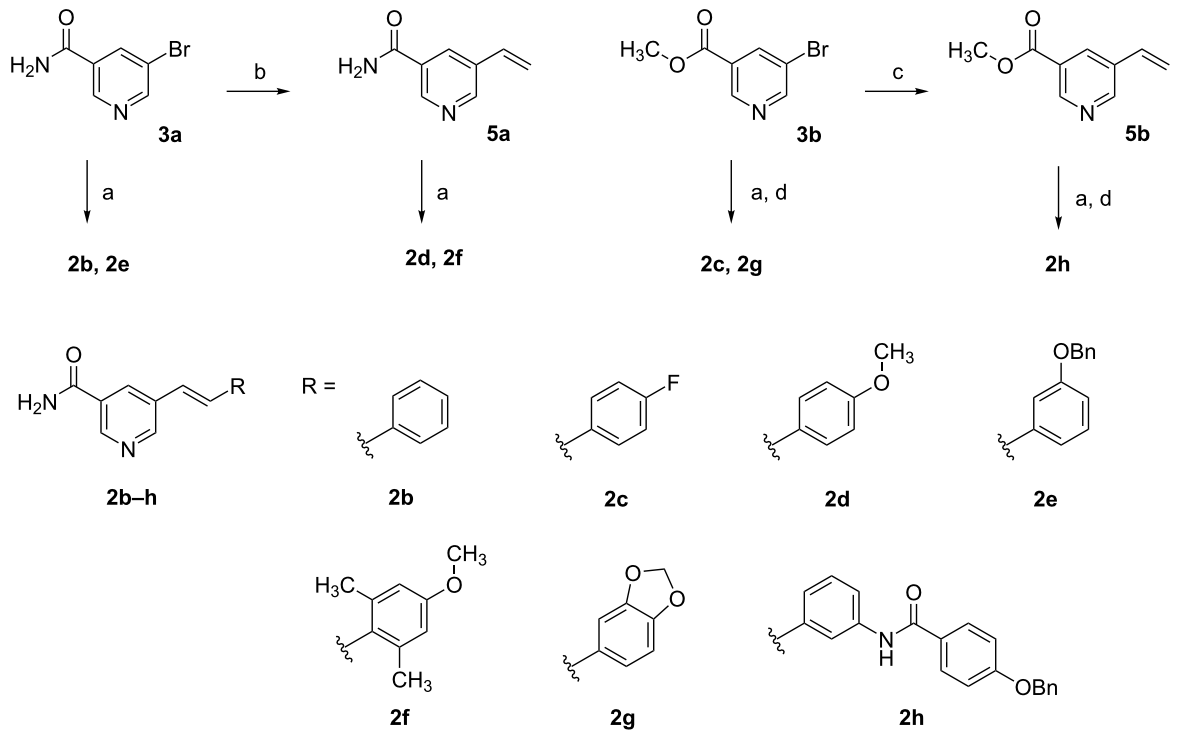
All azastilbene derivatives were synthesised by palladium-catalysed cross-coupling reactions using either commercially available 5-bromonicotinamide (**3a**) or methyl 5-bromonicotinate (**3b**). If **3b** was used, transformation to the nicotinamide was accomplished almost quantitatively by addition of a saturated solution of ammonia in anhydrous methanol and stirring in a closed vessel at 40 °C. Compounds **4a** and **b** could easily be obtained through Suzuki coupling with commercially available naphthalene-2-ylboronic acid or (3,4-dihydronaphthalen-2-yl)boronic acid (Scheme 1). The latter was synthesized according to a literature procedure [36].



Scheme 1: Reagents and conditions: a) appropriate boronic acid, $Pd(PPh_3)_4$, Na_2CO_3, DMF, H_2O, microwave, 15 min, 150 °C, 43–64%.

Formation of compounds **2b–h** was accomplished through Heck coupling of aryl bromides with the appropriate styrenes (Scheme 2) [37].

Compounds **2b** and **2e** were obtained in moderate yield using **3a** as the aryl halide in the Heck reaction. The use of **3b** in the Heck reaction resulted in a substantial improvement of yield in the synthesis of **2g** but not for **2c**. Interchanging the roles by using 5-vinylnicotinamide (**5a**) or methyl 5-vinylnicotinate (**5b**) as alkene component had detrimental effects on the yields in the



Scheme 2: Reagents and conditions: a) $Pd_2(dba)_3$ or $Pd(OAc)_2$, P(*o*-tol)$_3$, TEA, DMF, 120–140 °C, 0.7–24 h, 11–75%; b) potassium vinyltrifluoroborate, Cs_2CO_3, $PdCl_2(PPh_3)_2$, ACN, H_2O, 1.5 h, 120 °C, 78% c) tributylvinyltin, $Pd(PPh_3)_4$; toluene, reflux, 3 h, 76%; d) NH_3, MeOH, 40 °C, 3 d, 87–95%.

synthesis of **2d**, **2f** and **2h**. Intermediates **5a** and **5b** were accessible from **3a** and **3b** via Suzuki–Miyaura or Stille coupling [34].

Biology

The influence on deacetylase activity of three human sirtuin isoforms (Sirt1–3) was determined in a fluorescence-based assay, using *Z*-Lys(acetyl)-AMC (ZMAL) as a substrate [38]. Compared to the lead structure **2a**, all compounds except **2e**–**h** show increased inhibitory activity against Sirt2 (Table 1). Compound **2c** represents the most potent inhibitior with an IC_{50} value of about 7 μM. Moreover, a slight increase in selectivity for Sirt2 and Sirt3 over Sirt1 could be observed for **2c**, **4a** and **4b**. While none of the modifications provided complete isoenzyme specificity, **2c** preferentially inhibited Sirt2 (IC_{50} 6.6 ± 0.5) and Sirt3 (IC_{50} 7.5 ± 0.9 μM) compared to

Table 1: Sirt1–3 inhibition for compounds **2a–h**, **4a**/**4b** and **8a**.

Compound	Sirt1 inhibition[a]	Sirt2 inhibition[a]	Sirt3 inhibition[a]
2a	27% @ 50 μM	24.6 ± 2.8 μM[b]	41.7 ± 2.0 μM[b]
2b	71% @ 10 μM	8.7 ± 0.2 μM[b]	89% @ 50 μM
2c	51% @ 100 μM	6.6 ± 0.5 μM[b]	7.5 ± 0.9 μM[b]
2d	51% @ 10 μM	64% @ 10 μM	90% @ 50 μM
2e	61% @ 50 μM	69% @ 50 μM	60% @ 50 μM
2f	26% @ 10 μM	21% @ 10 μM	79% @ 50 μM
2g	52% @ 50 μM	62% @ 50 μM	87% @ 50 μM
2h	n.i.	9% @ 10 μM	n.i.
4a	n.i.	48% @ 10 μM	38% @ 10 μM
4b	n.i.	45% @ 10 μM	38% @ 10 μM
8a	n.i.	n.i.	n.i.

[a]Percent inhibition relative to controls at the indicated concentration, n.i. = no inhibition detected. [b]IC_{50} values (μM) with statistical limits; values are the mean ± SD of duplicate experiments.

Sirt1 (51% inhibition at 100 μM). Though not photoswitchable, compounds **4a** and **4b** were synthesized to test the influence of a rigid conformation around the C=C double bond on sirtuin inhibition. Interestingly, this increased rigidity provokes a complete loss of activity against Sirt1. Despite the fact, that all mammalian sirtuins possess profound similarity in their catalytic core domains, many isotype selective inhibitors have been developed in recent years [39-45]. In the case of Sirt2 it was shown that appropriate ligand binding can induce conformational changes of the enzyme, revealing a so-called selectivity pocket, which allows for isotype-specific interactions [46]. A recently developed fluorescence polarization (FP)-based assay enables mapping of ligand binding to this specific binding site [35]. For **2a** an interaction with the selectivity pocket was already implied in the same work. Additionally performed docking studies proposed a binding mode in which **2a** mimics the nicotinamide residue of NAD^+, whereas aromatic amino acid residues of the selectivity pocket stabilize the dimethylphenol ring [35]. As photoisomerization in stilbenes and azo dyes is accompanied by a perpendicular twist of the phenyl ring towards the former molecular plane, we assumed that this conformational change should provoke a differential binding situation at least for the dimethylphenol residue in **2a**. Unfortunately, binding of **2b** and **c** could not be localised in the vicinity of the selectivity pocket of Sirt2, so that the binding pose remains unclear.

Photochemistry of azastilbenes

The photochemical behaviour of stilbenes has been subject to intense investigation in the past. It is reported that unsubstituted stilbene undergoes $E \rightarrow Z$ photoisomerization [47], as well as photocyclization to dihydrophenanthrene upon UV irradiation, which is oxidized to phenantrene in the presence of oxygen [48]. In high concentrations, (*E*)-stilbene furthermore undergoes photocyclodimerization to cyclobutane derivatives [49]. Photoisomerization and photocyclization are also reported for 3-styrylpyridines, forming two regioisomeric dihydroazaphenanthrenes that are oxidized to 2- and 4-azaphenantrene (not shown), respectively [50].

Photochemistry of compounds **2b** and **2f** was investigated via UV–vis spectroscopy, LC–HRMS and NMR spectroscopy. Compound **2b** represents the core structure of the azastilbenes investigated, whereas in **2f** the influence of *ortho* methylation was intended to be examined. For UV–vis spectroscopy 50 μM solutions in 5% DMSO (v/v) in enzyme assay buffer were used, as this reflects the enzyme assay conditions. However, for LC-HRMS and NMR analysis, a higher concentration of 10 mM in methanol was necessary to receive reliable chromatograms and spectra.

Upon exposure of **2b** to radiation of 365 nm, changes in the UV–vis spectra proceeded slowly, due to the low absorbance of **2b** in this wavelength region. However, shorter wavelengths, i.e. 254 nm, revealed fast and dramatic changes (Figure 2). After an initial decline and blue shift of the absorption maximum, the UV–vis spectrum of **2b** developed a more complex structure with further illumination. The initial spectrum did not restore, neither thermally by standing in the dark nor photochemically when exposed to daylight. Regarding **2f**, 254 nm radiation was obligatory to obtain changes in the UV–vis spectrum. However even long-term radiation did not lead to a complex spectrum as with **2b**, yet no stationary state was reached in the examined time. As in the case of **2b**, the spectrum of **2f** was not altered by daylight, nor by standing several days in the dark at room temperature.

LC–HRMS analysis provided deeper insights and clarified the differential behaviour observed in the UV–vis spectra of **2b** and **2f** after UV irradiation. As anticipated, UV irradiation lead to $E \rightarrow Z$ isomerization of the C=C double bond in both compounds. The (*Z*)-isomers were found to be slightly more polar

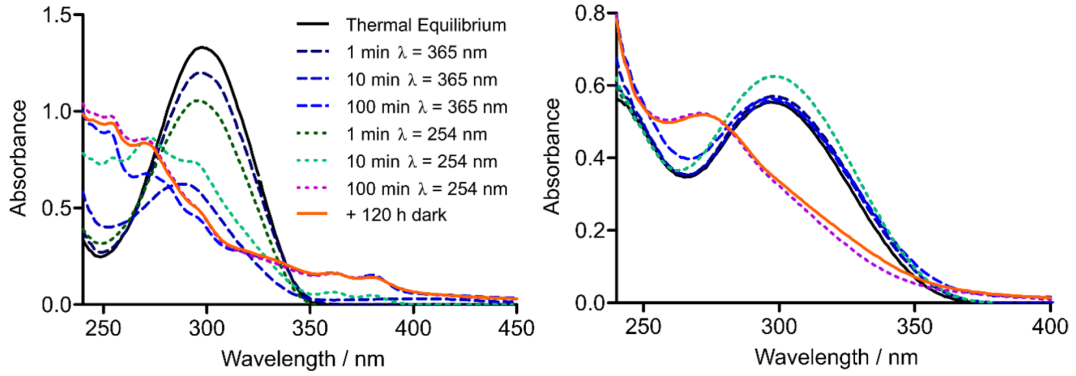


Figure 2: (Left) UV–vis spectrum of **2b** 50 μM in 5% DMSO (v/v) in assay buffer after varying durations of irradiation with 254 nm and 365 nm, respectively. (Right) UV–vis spectrum of **2f** 50 μM in 5% DMSO (v/v) in assay buffer after varying durations of UV radiation.

than the respective (*E*)-isomers and their absorption maxima appeared blue shifted as demonstrated by the UV–vis spectra extracted from the LC runs. Unfortunately, the amount of photoisomerization was only moderate, since after 100 minutes of continuous irradiation still substantial amounts of the (*E*)-isomers were present in the mixtures (Figure 3). Proton NMR analysis implied photostationary states comprising a relative percentage of 45% (*Z*)-**2b** and 57% (*Z*)-**2f**, respectively after 100 minutes of 254 nm irradiation. The NMR spectra can be found in Supporting Information File 1.

The degree of photoisomerization could not be enhanced by extended illumination. Instead, for **2b** prolonged irradiation resulted in the formation of several side products, so that after 10 hours the fractions containing (*E*)-**2b** and (*Z*)-**2b** had declined significantly. This decrease was primarily accompanied by an increase of the fractions containing the benzoquinoline carboxamide isomers **8a** and **b** formed by photocyclization and successive oxidation (Scheme 3). Furthermore, small amounts of cycloaddition products in two fractions were found, probably due to the high concentration of **2b** in the irradiated

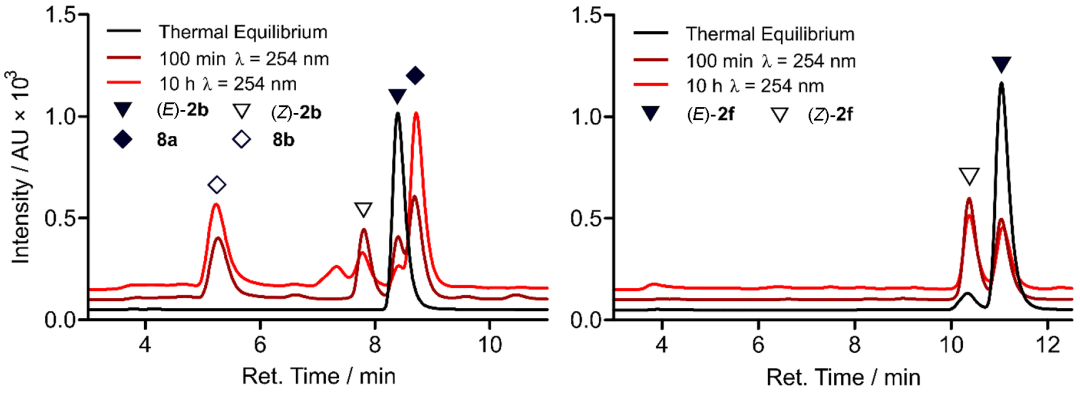
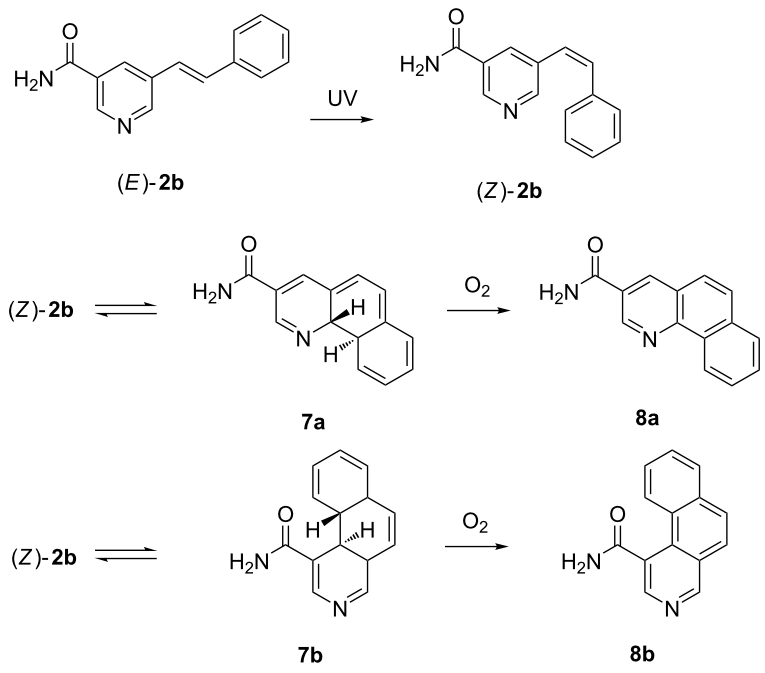


Figure 3: (Left) LC chromatogram of the LC–HRMS analysis of **2b** after varying durations of irradiation with 254 nm. Identity of **8a** was assigned by the reference compound synthesized and allowed differentiation of the two fractions containing photocyclized compounds, as indicated by mass spectra. (Right) LC chromatogram of the LC–HRMS analysis of **2f** after varying durations of irradiation with 254 nm.



Scheme 3: Photocyclization and oxidation reaction of **2b** upon UV irradiation.

solution. In contrast, **2f** was remarkably stable to long-term UV radiation. Even though the ratio of the double bond isomers was left unaffected, only small traces of the cycloaddition product and some unidentified compounds were registered. No formation of benzoquinoline carboxamides was registered as in the case of **2b**. Hence, due to the sterically blocking *ortho* methyl groups in **2f**, intramolecular photocyclization could be prevented.

To verify the hypothetical structures derived from irradiation of **2b**, we carried out quantum chemical calculations of the double bond isomers (*E*)-**2b** and (*Z*)-**2b** as well as the oxidized compounds **8a** and **8b**. We used density functional theory (DFT) to optimize the ground state equilibrium structures of (*E*)-**2b**, (*Z*)-**2b**, **8a** and **8b**, and used time-dependent DFT (TDDFT) and high-level correlated methods to obtain UV–vis absorption energies and oscillator strengths. To obtain the simulated absorption spectrum and λ_{max} values, oscillator strengths were converted into molar decadic extinction coefficients using a Gaussian line shape with a full-width-at-half-maximum of 0.3 eV. The correlated methods used were second-order approximated coupled cluster singles and doubles (CC2) and its approximation, algebraic diagrammatic construction to second-order (ADC(2)) [51-53]. ADC2 calculations have also been carried out with the implicit solvent continuum model COSMO using a dielectricity constant and refractive index of a methanol/water mixture, which was used as solvent in the experimental UV–vis measurements of the LC-HRMS fractions [54,55]. Geometries for reactants (*E*)-**2b** and (*Z*)-**2b** were optimized for two different rotational isomers ((*E*)-**2b-A** and (*E*)-**2b-B**; (*Z*)-**2b-A** and (*Z*)-**2b-B**), defined in Supporting Information File 1. In the following, we report only the results for (*E*)-**2b-B** and (*Z*)-**2b-A**, since they possess lower ground state energies and therefore are expected to be the dominant species at room temperature. Energy differences of the ground state structures of two pairs of isomers, however, are less than 0.6 kcal/mol, and computed spectra differ only slightly. Extensive results of all structures and all applied computational methods are summarized in the Supporting Information. While TDDFT systematically underestimates the λ_{max} values of the lowest absorption of all compounds by 0.1–0.75 eV, CC2 and ADC(2) agree with the λ_{max} values of the lowest absorption bands with a maximum deviation of 0.15 eV, similar to the previously determined accuracy [56]. We notice a good agreement between ADC(2) gas phase calculations with CC2 gas phase calculations, which justifies the usage of the approximate ADC(2) method.

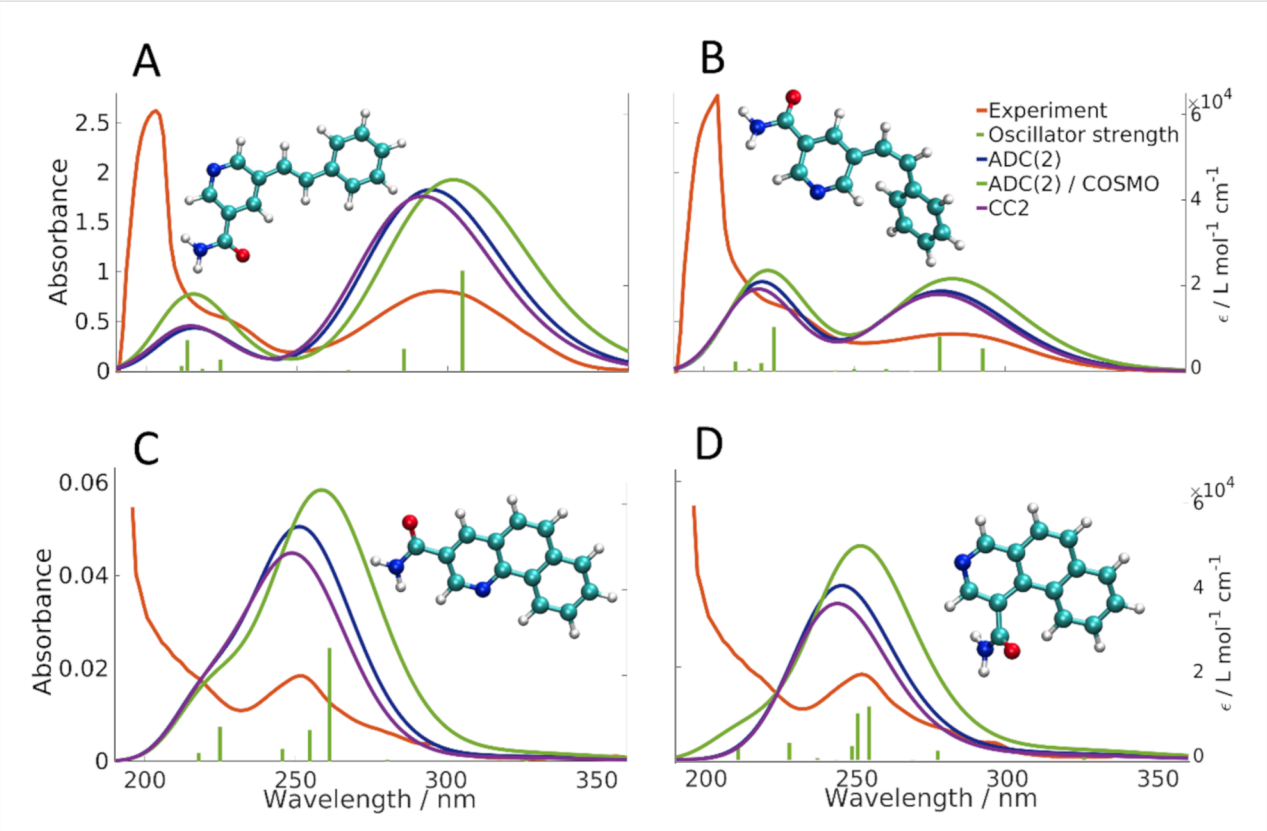


Figure 4: Calculated and experimental absorption spectra of compounds (*E*)-**2b-B** (A), (*Z*)-**2b-A** (B), and products **8a** (C) and **8b** (D). Oscillator strengths (green sticks) correspond to the ADC(2)/COSMO calculation.

Comparing the calculated absorption spectra for (*E*)-**2b-B** and (*Z*)-**2b-A** to the experimental spectra obtained from LC-HRMS (Figure 4A,B), we see that all calculations consistently confirm the experimentally found blue shift of about 15 nm (0.22 eV) for the λ_{max} value of the lowest absorption band. Blue shifts predicted by CC2, ADC(2), ADC(2)/COSMO are 14, 16, and 20 nm, respectively. Consistent with the experimental spectra, all theoretical methods predict the maximum extinction of the lowest absorption band of (*Z*)-**2b** to approximately one half of the one of (*E*)-**2b**. Since the maximum error of the methods (0.15 eV) is smaller than the observed blue shift (0.22 eV), we conclude that the computed λ_{max} values are meaningful and clearly support the successful formation of the *Z*-isomer. Regarding the spectra of the photocyclization and oxidation products **8a** and **8b** (Figure 4C,D), theoretical methods predict the λ_{max} value of the lowest absorption bands within 8 nm (≈0.15 eV) of the value of the experimental spectrum of the LC–HRMS, clearly confirming the experimentally found blue shift of 0.75 eV and 0.54 eV compared to compounds (*E*)-**2b** and (*Z*)-**2b**, respectively. Also here, we conclude that the calculations clearly support the formation of compounds **8a** and/or **8b**. However, due to the similarity of the spectra of **8a** and **8b**, calculations do not allow to predict which of the two isomers was present in the respective fraction analysed.

Regarding the high similarity between **8a**/**8b** and selisistat, it was likely that these cyclized compounds could possess biological activity against sirtuins, too. On the other hand they resemble a fixed (*Z*)-configuration of the stilbene double bond. Therefore, comparison with **2b** could provide information concerning differential biological activity of the two photoisomers. By applying Mallory reaction conditions to a solution of **2b** in methanol utilizing oxygen and iodine as oxidants we were able to isolate a preparative amount of **8a** and tested it for its biological activity against Sirt1, Sirt2 and Sirt3. Surprisingly, **8a** showed complete inactivity towards all sirtuins tested (Table 1). Hence it can be assumed that *E*→*Z* photoisomerization in similar compounds lowers inhibitory strength accordingly.

Synthesis and photochemistry of photoswitchable diazeno analogue

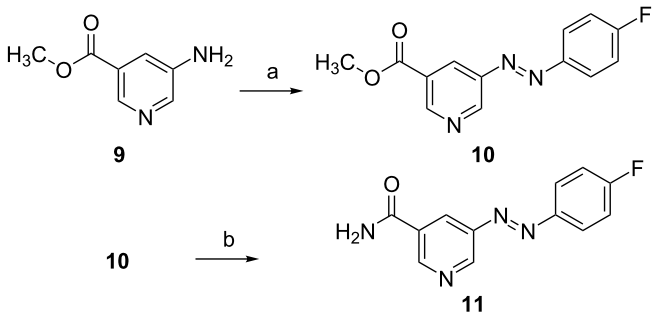
Even though the photochemical properties of *ortho* methylated azastilbenes like **2f** could be improved by preventing photocyclization, they were still unsuitable for the use as photoswitchable sirtuin inhibitors in the enzyme assay. The long irradiation periods that were necessary to obtain significant amounts of the (*Z*)-isomers did not permit switching of the inhibitors in the enzyme assay mixture, as the fluorescent substrate and the enzyme would be harmed by long-term UV radiation. We envisioned to replace the stilbene motive of selected stilbene **2c** by a diazeno group, because photoisomerization of azo dyes was anticipated to proceed fast and reversible by application of UV irradiation and visible light, respectively in this analogue.

5-Diazenylnicotinamide **11** was synthetically accessible in two steps through conversion of commercially available methyl 5-aminonicotinate (**9**) and 4-fluoroaniline to **10** under Mill's reaction conditions and subsequent ammonolysis of the methyl ester **10** to amide **11** (Scheme 4).

Photoswitching of (*E*)-**11** to a long-lived PSS ($t_{½}$ = 300 h) containing 84% of (*Z*)-**11** was possible by short term UV irradiation of 365 nm. The photoisomerization could be reversed by exposure to visible light, i.e. 452 nm, albeit the PSS at 452 nm still comprised about 25% of (*Z*)-**11** as determined by HPLC analysis using UV–vis detection at the isosbestic points (Table 2). Light of 500 nm could also reverse photoisomerization, but was not as effective as 452 nm radiation. 630 nm irradiation, in contrast, did not lead to an altered PSS composition

Table 2: Percentage of *E*/*Z*-isomers of **11** at the thermal equilibrium (Δ), and photostationary states (PSS) after 365 nm and 452 nm irradiation.

	Δ	PSS 5 min 365 nm	PSS 1 min 452 nm
(*E*)-**11**/(*Z*)-**11**	99:1	16:84	75:25



Scheme 4: Reagents and conditions: a) 4-fluoroaniline, oxone, HAc, 60 °C, 14 d, 42%; b) NH_3, MeOH, rt, 3 d, 98%.

obtained by UV irradiation of 365 nm. Switching between the two PSS could be repeated several times without any observable fatigue of the compound (Figure 5).

The photoswitchable diazeno compound **11** was subjected to biological evaluation to test the effect of photoisomerization on the inhibitory activity. The enzyme assay mixture containing **11** was exposed to 5 minutes of 365 nm radiation and compared with the results of a non-irradiated measurement. The applied radiation did not perturb the proper enzyme functioning as proved by an unaltered enzyme activity in the blank tests. Unfortunately, 365 nm radiation turned out to have only minor effects on the IC_{50} values of **11** (Table 3).

Table 3: Sirt1-3 inhibition for compound **11** at the thermal equilibrium (Δ) and the photostationary state (PSS) after 5 minutes of 365 nm irradiation.

Entry	Sirt1 inhibition[a]	Sirt2 inhibition[a]	Sirt3 inhibition[a]
Δ	35% @ 100 μM	18.9 ± 1.38 μM	27.5 ± 3.42 μM
PSS	19% @ 100 μM	24.1 ± 1.69 μM	29.9 ± 2.11 μM

[a]Percent inhibition relative to controls at the indicated concentration, n.i. = no inhibition detected.

Discussion

In recent years, photopharmacology has become a reputable strategy to optically control biochemical processes in the field of enzyme and ion channel modulation and recently 7TM-receptors also called GPCRs. Whereas in most approaches towards photoswitchable ligands the structure of the lead has to be changed considerable in order to incorporate a photoswitchable structural element, this was not the case with azastilbene-based lead structure **2a**. Unfortunately, due to several disadvantages the azastilbene moiety itself was unsuitable as photoswitchable element in this application. Even though competing azaphenantrene formation could be prevented by implementation of blocking *ortho* methyl groups in **2f**, the degree of photoisomerization in the two compounds observed was only moderate and required UV radiation over an extended period of time. Furthermore, the irreversibility of photoisomerization remained a major drawback and made an exchange with a diazeno group mandatory. Typically, it is not clear from the beginning, if the remodelling of the bioactive compounds will lead to an active diazeno derivative or not. The so-called azologization approach, moulded by Trauner et al., features a rational strategy for the design of photoswitchable compounds from established drug molecules through replacing certain core motives with an bioisosteric azobenzene moiety [57-59]. Recent examples have proven successful for receptor ligands by exchange of a linear alkinyl spacer for the zigzag shaped (*E*)-diazeno group [60,61]. In that instance, the geometry of the lead had to be changed considerably but careful design led to useful photoswitches. In the case of lead **2a** no such alteration of geometry was necessary and thus it seemed highly likely, that biological activity could be maintained. Indeed, this hypothesis could be proven. Exchange of the azastilbene double-bond with a diazeno bridge caused only a slight decrease in inhibitory potency against Sirt2 and Sirt3, and the selectivity profile of diazeno compound **11** equals the profile of its direct stilbene analogue **2c**. Concerning photoswitchability, **11** was superior to the stilbenoid structures, as it could be toggled reversibly between two states comprising high amounts of (*E*)-**11** and (*Z*)-**11**, respectively. The other part of the hypothesis was, that by this photoinduced isomerization a considerable drop of activity would occur due to the conformational change and the resulting changed geometry and polarity. However, this part of our hypothesis turned out to be wrong. The over-all conformational changes upon photoisomerization were too small or did not lead to a hindered binding, as antici-

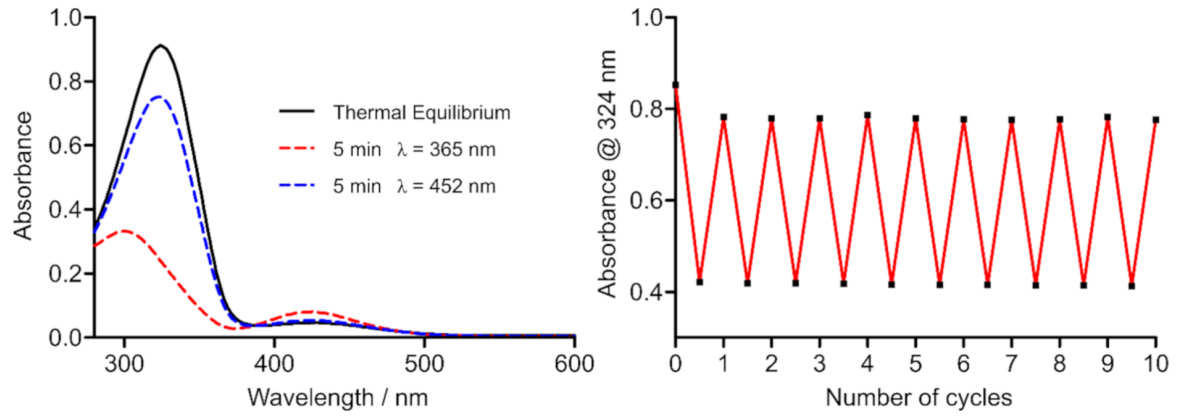


Figure 5: (Left) UV–vis spectrum of **11**, 50 μM in 5% DMSO (v/v), in assay buffer at the thermal equilibrium and the photostationary states (PSS) after 365 nm or 452 nm radiation. (Right) Fatigue resistance of **11**, 50 μM in 5% DMSO (v/v), in assay buffer over 10 cycles of alternating 365 nm and 452 nm radiation.

pated. This result is disappointing, because the photoswitchable sirtuin inhibitor **11** cannot be switched between active and inactive state, as envisioned. Possible reasons could be assigned to substituent effects as demonstrated by Simeth et al. [62]. As recently reported by Schehr et al., reducing agents like DTT, used to prevent enzyme oxidation in crystallization mixtures or in vitro assays, can reduce azo dyes to hydrazine derivatives very fast and thus disable photoisomerization [63]. However, in our enzyme assay no such reducing agents were present, which is why we assume that the photoswitchable diazeno group should still be intact in the enzyme assay mixture. Even if the change in space orientation does not alter binding after irradiation, we would have predicted, that at least the significant difference in polarity of (*E*)-**11** and (*Z*)-**11** should lead to marked differences of sirtuin engagement in vitro. However, recent results from a carefully designed azologization study performed by Rustler et al. led to comparable difficulties [64].

Conclusion

Based on lead structure GW435821X (**2a**) a small library of analogous azastilbene compounds was designed, synthesized and tested for their inhibitory activity against the human sirtuin isoforms Sirt1, Sirt2 and Sirt3. Compared to the lead structure the inhibitory potency could be increased to single digit μM potency for some compounds, while isoenzyme selectivity still remains an issue. The photochemistry of azastilbene compounds **2b** and **2f** was studied. For **2b**, besides photoisomerization, formation of benzoquinoline carboxamides by photocyclization and oxidation was indicated by high accuracy mass spectroscopy. Formation of 4-azaphenantrene derivative **8a** could be proven by isolation and characterization of a preparative sample. Theoretical UV–vis spectra for (*E*)-**2b**, (*Z*)-**2b** and two isomeric benzoquinoline carboxamides reproduced the experimental data. Compound **2f** was unsusceptible to photocyclization due to sterically blocking *ortho* methyl groups but could not be toggled between (*E*)- and (*Z*)-configuration. This lead to the synthesis of a first diazenyl derivative of the lead structure **2a** with promising photochemical characteristics for a new class of photoswitchable sirtuin inhibitors, but the activity difference for the (*E*)- and (*Z*)-isomers needs dramatic improvement before a useful molecular probe can be obtained by this approach.

Experimental

General remarks

All solvents and reagents were obtained from commercial suppliers and were used without purification. Anhydrous solvents were purchased from Acros Organics. Thin-layer chromatography (TLC) was executed on silica gel 60 F_{254} aluminium plates purchased from Merck. Visualization of the compounds was accomplished by UV-light (254 nm and 366 nm) and by staining with iodine, DNPH/H_2SO_4 (2 g 2,4-dinitrophenylhydrazine and 5 mL H_2SO_4 in 50 mL EtOH and 16 mL water) or vanillin/sulfuric acid (3.0 g vanillin and 0.5 mL H_2SO_4 in 100 mL EtOH) reagent. Synthesis was additionally monitored using high speed SFC/MS runs performed by a Nexera SFE-SFC/UHPLC switching system (Shimadzu Corporation, Kyoto, Japan) consisting of a pumping system (one LC-30ADSF for liquid CO_2 and two LC-20ADXR for modifier and make-up delivery), an on-line supercritical fluid extraction module (SFE-30A auto extractor equipped with 0.2 mL extraction vessels) for reaction monitoring, an autosampler (SIL-30AC) for purified compounds, a column thermostat (CTO-20AC) equipped with a Torus DIOL (Waters) or Phenomenex CSP (Lux Amylose-2, i-Amylose-3, i-Cellulose-5), a degasser (DGU-20A5R), a communications module (CBM-20A), and two back pressure regulators BPR A and B (SFC-30A). UV and MS spectra were recorded via photodiode array detection (SPD-M20A) and electrospray ionization single quadrupole MS (LCMS-2020) controlled by Shimadzu LabSolution software (Version 5.91). Chromatographic purification of products was performed by flash chromatography on silica gel (20–45 μm, Carl Roth) applying pressured air up to 0.8 bar. NMR spectra were recorded on a Bruker Avance III instrument (^{1}H NMR: 400 MHz, ^{13}C NMR: 100.6 MHz). Chemical shifts were referenced to tetramethylsilane (TMS) as internal standard in deuterated solvents and reported in parts per million (ppm). Coupling constants (*J*) are reported in Hz using the abbreviations: s = singlet, d = doublet, t = triplet, q = quartet, m = multiplet and combinations thereof, br = broad. Infrared (IR) spectra were recorded on a Bruker Alpha FT-IR spectrometer equipped with a diamond ATR unit and are indicated in terms of absorbance frequency [cm^{-1}]. Microwave synthesis was conducted in a Monowave 300 microwave synthesis reactor from Anton Paar equipped with appropriate sealed reaction vessels G10 (6 mL) or G30 (20 mL), applying a maximum initial power of 850 W to reach a given temperature (IR sensor) for a given time with stirring at 600 rpm. Melting points were measured in open capillary tubes using a Melting Point M-565 apparatus from Büchi and are uncorrected. High accuracy mass spectra were recorded on a Shimadzu LCMS-IT-TOF using ESI ionization. Purity of final compounds was determined by HPLC with DAD (applying the 100% method at 220 nm). Preparative and analytical HPLC were performed using Shimadzu devices CBM-20A, LC-20A P, SIL-20A, FRC-10A with SPD 20A UV–vis detector and an ELSD-LTII. In analytical mode a LiChroCART® (250 × 4 mm) and in preparative mode a Hibar® RT (250 × 25 mm) column, both containing LiChrospher® 100 RP-18e (5 μm), were used. An Elementar Vario MICRO cube was used for the experimental determination of elemental configurations of final pure products. UV–vis spectra were obtained using a Thermo Scientific Genesys 10S UV–vis spectrophotometer.

Synthesis

General procedure for synthesis of nicotinamides from methyl nicotinates: The respective methyl nicotinate was treated with a saturated solution of ammonia in anhydrous MeOH (30 mL) and stirred in a sealed vessel at 40 °C until thin layer chromatography indicated complete conversion of the starting material. The solvent was evaporated under reduced pressure and the residue washed sparingly with cold MeOH.

(*E*)-5-Styrylnicotinamide (2b): In a microwave reaction vessel **3a** (1.01 g, 5.00 mmol, 1.00 equiv) was mixed with styrene (651 mg, 6.25 mmol, 1.25 equiv), tris(*o*-tolyl)phosphine (61 mg, 0.20 mmol, 0.04 equiv), $Pd_2(dba)_3$ (92 mg, 0.10 mmol, 0.02 equiv) and NEt_3 (863 ML, 0.63 g, 6.25 mmol, 1.25 equiv) and suspended in anhydrous DMF (6 mL). The reaction was conducted at 120 °C for 40 min in a microwave reactor. After cooling to room temperature the mixture was taken up in EtOAc and filtered through a pad of Celite®. The filtrate was washed with water (3 × 30 mL) and sat. aq. NaCl solution (30 mL), dried over $MgSO_4$ and concentrated under reduced pressure. The formed precipitate was collected by filtration and recrystallized from EtOAc. The product was obtained as colourless crystals (0.55 g, 2.45 mmol, 49%): R_f = 0.25 (cyclohexane/THF 1:1); mp: 196.4 °C; ^{1}H NMR (400 MHz, DMSO-d_6) δ (ppm) 8.93 (d, *J* = 2.0 Hz, 1H), 8.90 (d, *J* = 2.1 Hz, 1H), 8.50 (pseudo-t, *J* = 2.0 Hz, 1H), 8.24 (s, br, 1H), 7.71–7.62 (m, 3H), 7.54–7.28 (m, 5H); ^{13}C NMR, DEPT135, HSQC, HMBC (75.5 MHz, DMSO-d_6) δ (ppm) 166.4, 150.4, 147.3, 136.4, 132.4, 131.4, 131.3, 129.6, 128.7, 128.2, 126.7, 124.2; IR (ATR) ν (cm^{-1}): 3372, 3168, 1649, 1619, 1492, 1394, 961, 746, 691, 568; HRESIMS: calcd for $[C_{14}H_{12}N_2O + H]^+$ 224.0950, found 224.0939; comp. purity (220 nm): 100 %; anal. calcd for $C_{14}H_{12}N_2O$: N, 12.49; C, 74.98; H, 5.39; found: N, 12.38; C, 74.81; H, 5.15.

Methyl (*E*)-5-(4-fluorostyryl)nicotinate: Synthesis was conducted according to the procedure of **2b** using **3b** (648 mg, 3.00 mmol, 1.00 equiv), 1-fluoro-4-vinylbenzene (550 mg, 4.50 mmol, 1.50 equiv), tris(*o*-tolyl)phosphine (183 mg, 0.60 mmol, 0.20 equiv), $Pd_2(dba)_3$ (67 mg, 0.30 mmol, 0.10 equiv) and NEt_3 (1.25 mL, 9.00 mmol, 3.00 equiv) in anhydrous DMF (4 mL). The reaction was conducted at 140 °C for 1.5 h. The raw product was purified by silica gel column chromatography (*n*-hexane/EtOAc 2:1) yielding a colourless solid (97 mg, 0.38 mmol, 13%): R_f = 0.50 (*n*-hexane/EtOAc 2:1); mp: 108.2 °C; ^{1}H NMR, H,H-COSY (400 MHz, $CDCl_3$) δ (ppm) 9.09 (d, *J* = 1.8 Hz, 1H), 8.90 (d, *J* = 2.1 Hz, 1H), 8.52 (pseudo-t, *J* = 2.0 Hz, 1H), 7.57–7.49 (m, 2H), 7.26 (d, *J* = 16.4 Hz, 1H), 7.13–7.06 (m, 2H), 7.03 (d, *J* = 16.4 Hz, 1H); 4.00 (s, 3H, H-8); ^{13}C NMR, DEPT135, HSQC, HMBC (75.5 MHz, $CDCl_3$) δ (ppm) 165.3, 163.2 (d, *J* = 249.4 Hz), 150.1, 147.7, 135.0, 134.0, 135.7, 132.4 (d, *J* = 3.4 Hz), 132.2, 128.8 (d, *J* = 8.2 Hz), 126.9, 122.9 (d, *J* = 2.3 Hz), 116.2 (d, *J* = 21.8 Hz), 52.9; IR (ATR) ν (cm^{-1}): 2957, 1718, 1508, 1433, 1299, 1230, 986, 821, 763; HRESIMS: calcd for $[C_{15}H_{12}NO_2F + H]^+$ 257.0852, found 257.0850.

(*E*)-5-(4-Fluorostyryl)nicotinamide (2c): Synthesis was conducted following the general procedure of nicotinamides from methyl nicotinates, using methyl (*E*)-5-(4-fluorostyryl)nicotinate (75 mg, 0.31 mmol, 1.00 equiv). The product was obtained as colourless solid (65 mg, 0.27 mmol, 87%): R_f = 0.48 (EtOAc/MeOH 95:5); mp: 205.6 °C; ^{1}H NMR, H,H-COSY (400 MHz, DMSO-d_6) δ (ppm) 8.91 (d, *J* = 1.9 Hz, 1H), 8.88 (d, *J* = 2.0 Hz, 1H), 8.47 (pseudo-t, *J* = 2.0 Hz, 1H), 8.22 (s, 1H), 7.76–7.68 (m, 2H), 7.49 (d, *J* = 16.6 Hz, 1H), 7.31 (d, *J* = 16.6 Hz, 1H), 7.29–7.22 (m, 2H); ^{13}C NMR, DEPT135, HSQC, HMBC (75.5 MHz, DMSO-d_6) δ (ppm) 166.4, 161.9, 150.3, 147.3, 133.1 (d, *J* = 3.2 Hz), 132.3, 131.4, 130.1, 129.7, 128.6 (d, *J* = 8.2 Hz), 124.1 (d, *J* = 2.2 Hz), 115.7 (d, *J* = 21.6 Hz); IR (ATR) ν (cm^{-1}): 3364, 3172, 1650, 1620, 1507, 1397, 1212, 968, 857, 601; HRESIMS: calcd for $[C_{14}H_{11}N_2OF + H]^+$ 242.0855, found 242.0844; comp. purity (220 nm): 100%; anal. calcd for $C_{14}H_{11}N_2OF$: N, 11.56; C, 69.41; H, 4.58; found: N, 11.53; C, 69.89; H, 4.51.

Methyl 5-[(4-fluorophenyl)diazenyl]nicotinate (10): 4-Fluoroaniline (444 mg, 4.00 mmol, 1.00 equiv) was dissolved in DCM (15 mL) and treated with a solution of oxone (4.92 g, 8.00 mmol, 2.00 equiv) in water (50 mL). The biphasic mixture was vigorously stirred until thin layer chromatography indicated complete consumption of the starting material. The watery phase was discarded and the organic phase washed with an aq. HCl-solution (1 M, 3 × 10 mL) and water (3 × 10 mL), then dried over $MgSO_4$. The solution was concentrated to a volume of 5 mL under reduced pressure and added to a solution of **9** (609 mg, 4.00 mmol, 1.00 equiv) in acetic acid (20 mL). The reaction mixture was stirred at 60 °C for two weeks, cooled to room temperature, poured onto ice cooled sat. aq. $NaHCO_3$-solution and extracted with EtOAc (3 × 50 mL). The combined organic extracts were washed with water (3 × 50 mL), sat. aq. NaCl solution (30 mL) and dired over $MgSO_4$. The solvent was evaporated under reduced pressure and the residue purified by silica gel column chromatography (cyclohexane/EtOAc 3:1). The product was obtained as orange solid (431 mg, 1.67 mmol, 42%): R_f = 0.52 (cyclohexane/EtOAc 3:1); mp: 103.6 °C; ^{1}H NMR, H,H-COSY (400 MHz, DMSO-d_6) δ (ppm) 9.34 (d, *J* = 2.3 Hz, 1H), 9.22 (d, *J* = 2.0 Hz, 1H), 8.50 (pseudo-t, *J* = 2.2 Hz, 1H), 8.09–8.01 (m, 2H), 7.52–7.44 (m, 2H), 3.95 (s, 3H); ^{13}C NMR, DEPT135, HSQC, HMBC (75.5 MHz, DMSO-d_6) δ (ppm) 164.5, 164.4 (d, *J* = 251.8 Hz), 151.8, 150.3, 148.5 (d, J = 2.8 Hz), 146.7, 126.4

(d, J = 6.7 Hz), 125.4 (d, J = 9.5 Hz), 116.6 (d, J = 23.2 Hz), 52.7; IR (ATR) ν (cm^{-1}): 3081, 1713, 1583, 1496, 1286, 1222, 1092, 1000, 843, 498.

5-[(4-Fluorophenyl)diazenyl]nicotinamide (11): Synthesis was conducted following the general procedure of nicotinamides from methyl nicotinates, using **10** (160 mg, 0.62 mmol, 1.00 equiv). The product was obtained as orange solid (149 mg, 0.61 mmol, 98%): R_f = 0.65 (EtOAc/MeOH 95:5); mp: 212.3 °C; ^{1}H NMR, H,H-COSY (400 MHz, DMSO-d_6) δ (ppm) 9.24 (d, J = 2.3 Hz, 1H), 9.20 (d, J = 2.0 Hz, 1H), 8.58 (pseudo-t, J = 2.2 Hz, 1H), 8.38 (s, br, 1H), 8.08–8.02 (m, 2H), 7.80 (s, br, 1H), 7.53–7.45 (m, 2H); ^{13}C NMR, DEPT135, HSQC, HMBC (75.5 MHz, DMSO-d_6) δ (ppm) 165.6, 164.3 (d, J = 251.4 Hz), 150.7, 148.6 (d, J = 2.8 Hz), 148.2, 146.7, 130.5, 125.7, 125.3 (d, J = 9.4 Hz), 116.6 (d, J = 23.2 Hz); IR (ATR) ν (cm^{-1}): 3359, 3125, 1669, 1628, 1496, 1398, 1136, 838, 808, 692; HRESIMS: calcd for $[C_{12}H_9N_4OF + H]^+$ 224.0760, found 224.0753; comp. purity (220 nm): 100%; anal. calcd for $C_{12}H_9N_4OF$: N, 22.94; C, 59.02; H, 3.71; found: N, 22.95; C, 59.46; H, 3.92.

Cloning, expression and purification of recombinant proteins: Expression and purification of $Sirt1_{133-747}$, $Sirt2_{56-356}$, and $Sirt3_{118-395}$ was carried out as described previously. Identity and purity were verified by SDS-PAGE [65]. Protein concentration was determined by the Bradford assay [66]. Deacylase activity of sirtuin isotypes could be inhibited with nicotinamide and was shown to be NAD^+-dependent.

Bioassay: The inhibitory effect of compounds **2a**–**h**, **4a**/**b**, **8a** and **11** on Sirt1–3 was detected via a previously reported fluorescence based assay [38]. The synthetic substrate *Z*-Lys(acetyl)-AMC (ZMAL) is deacetylated by sirtuins, followed by tryptic digestion and thereby release of 7-amino-methylcoumarin, leading to a fluorescent readout. Inhibition was determined by comparing percentage substrate conversion to a DMSO control after subtraction of the blank fluorescence signal. All compounds were tested at 100 μM, 50 μM and 10 μM, respectively. For compounds that showed more than 50% inhibition at 10 μM an IC_{50} value was determined. IC_{50} values were calculated with OriginPro 9.0 G using a non-linear regression to fit the dose response curve. An enzyme-free blank control and a 100% conversion control using AMC instead of ZMAL were measured as well. Inhibition measurements were performed in biological duplicates for all compounds.

Photochemistry: All photoisomerization experiments were conducted under ruby light of 630 nm. Illumination was executed using a Bio-Link 254 Crosslinker from Vilber-Lourmat equipped with six Vilber-Lourmat T8-C lamps (8 W, 254 nm) or six Vilber-Lourmat T8-L lamps (8W, 365 nm), respectively. Visible light radiation of 630 nm (red), 500 nm (green) and 452 nm (blue) was derived from a Paulmann FlexLED 3D strip. All compounds were irradiated in solution, using spectrophotometric grade solvents. Photoisomerization and UV–vis spectra measurement was conducted in quartz cuvettes at room temperature.

Computational details: All calculations were carried out using the TURBOMOLE version 7.2 quantum chemistry package [67]. Geometry optimizations of all compounds in different conformers were carried out using DFT with PBE approximation to the exchange-correlation (XC) functional and employing the SV(P) basis set [68,69]. The 10 lowest excitation energies and their oscillator strengths were computed using the SV(P) basis and the larger def2-TZVP basis set [69]. This was done using TDDFT with the hybrid approximation to the XC functional PBE0, CC2, and ADC(2) [51-53,70-72]. ADC(2) and CC2 calculations make use of the resolution-of-identity approximation [73]. ADC(2) calculations were also done using the continuum solvent model COSMO as previously described [54,55,74-76]. A dielectric constant of 62.14 and a refractive index of 1.3379 were used, which corresponds to a solvent of a 6/4-mixture of methanol/water, as experimentally determined [77,78]. Broadened absorption spectra were simulated by converting oscillator strengths to decadic extinction coefficients using a Gaussian line shape with a full-width-at-half-maximum of 0.3 eV [79-82].

Supporting Information

The Supporting Information features experimental and analytical data for the synthesis of intermediates and compounds **4a**, **4b**, **2c–2h** and **8a** and ^{1}H and ^{13}C NMR spectra for all synthesized compounds. Procedures of photochemical experiments and their analysis are described. Detailed summaries of electronic structure calculations for two conformers (A and B) of each double bond isomer ((*E*)-**2b** and (*Z*)-**2b**), photocyclization and oxidation products **8a** and **8b** are given.

Supporting Information File 1

Experimental procedures, analytical data and quantum chemical calulations.
[https://www.beilstein-journals.org/bjoc/content/supplementary/1860-5397-15-214-S1.pdf]

Acknowledgements

The Jung group thanks the Deutsche Forschungsgemeinschaft (DFG, Ju295/14-1 and RTG1976) for funding.

ORCID® iDs

Christoph W. Grathwol - https://orcid.org/0000-0003-0232-3279
Enrico Tapavicza - https://orcid.org/0000-0002-0640-0297
Robert K. Hofstetter - https://orcid.org/0000-0002-1077-9703
Manfred Jung - https://orcid.org/0000-0002-6361-7716
Andreas Link - https://orcid.org/0000-0003-1262-6636

Preprint

A non-peer-reviewed version of this article has been previously published as a preprint doi:10.3762/bxiv.2019.53.v1

References

1. Schiedel, M.; Robaa, D.; Rumpf, T.; Sippl, W.; Jung, M. *Med. Res. Rev.* **2018,** *38,* 147–200. doi:10.1002/med.21436
2. Frye, R. A. *Biochem. Biophys. Res. Commun.* **2000,** *273,* 793–798. doi:10.1006/bbrc.2000.3000
3. Vaziri, H.; Dessain, S. K.; Eaton, E. N.; Imai, S.-I.; Frye, R. A.; Pandita, T. K.; Guarente, L.; Weinberg, R. A. *Cell* **2001,** *107,* 149–159. doi:10.1016/s0092-8674(01)00527-x
4. Perrod, S.; Cockell, M. M.; Laroche, T.; Renauld, H.; Ducrest, A.-L.; Bonnard, C.; Gasser, S. M. *EMBO J.* **2001,** *20,* 197–209. doi:10.1093/emboj/20.1.197
5. Tanno, M.; Sakamoto, J.; Miura, T.; Shimamoto, K.; Horio, Y. *J. Biol. Chem.* **2007,** *282,* 6823–6832. doi:10.1074/jbc.m609554200
6. Rumpf, T.; Schiedel, M.; Karaman, B.; Roessler, C.; North, B. J.; Lehotzky, A.; Oláh, J.; Ladwein, K. I.; Schmidtkunz, K.; Gajer, M.; Pannek, M.; Steegborn, C.; Sinclair, D. A.; Gerhardt, S.; Ovádi, J.; Schutkowski, M.; Sippl, W.; Einsle, O.; Jung, M. *Nat. Commun.* **2015,** *6,* 6263. doi:10.1038/ncomms7263
7. North, B. J.; Verdin, E. *PLoS One* **2007,** *2,* e784. doi:10.1371/journal.pone.0000784
8. Schwer, B.; North, B. J.; Frye, R. A.; Ott, M.; Verdin, E. *J. Cell Biol.* **2002,** *158,* 647–657. doi:10.1083/jcb.200205057
9. AOP Orphan Pharmaceuticals AG. 2017; https://www.aoporphan.com/global_en/our-company/newsroom/aop-orphan-pharmaceuticals-ag-to-acquire-selisistat-a-clinical-stage-drug-candidate-for-the-treatment-of-huntingtons-disease-hd (accessed June 17, 2019).
10. Süssmuth, S. D.; Haider, S.; Landwehrmeyer, G. B.; Farmer, R.; Frost, C.; Tripepi, G.; Andersen, C. A.; Di Bacco, M.; Lamanna, C.; Diodato, E.; Massai, L.; Diamanti, D.; Mori, E.; Magnoni, L.; Dreyhaupt, J.; Schiefele, K.; Craufurd, D.; Saft, C.; Rudzinska, M.; Ryglewicz, D.; Orth, M.; Brzozy, S.; Baran, A.; Pollio, G.; Andre, R.; Tabrizi, S. J.; Darpo, B.; Westerberg, G.; the PADDINGTON Consortium. *Br. J. Clin. Pharmacol.* **2015,** *79,* 465–476. doi:10.1111/bcp.12512
11. Chopra, V.; Quinti, L.; Kim, J.; Vollor, L.; Narayanan, K. L.; Edgerly, C.; Cipicchio, P. M.; Lauver, M. A.; Choi, S. H.; Silverman, R. B.; Ferrante, R. J.; Hersch, S.; Kazantsev, A. G. *Cell Rep.* **2012,** *2,* 1492–1497. doi:10.1016/j.celrep.2012.11.001
12. Outeiro, T. F.; Kontopoulos, E.; Altmann, S. M.; Kufareva, I.; Strathearn, K. E.; Amore, A. M.; Volk, C. B.; Maxwell, M. M.; Rochet, J.-C.; McLean, P. J.; Young, A. B.; Abagyan, R.; Feany, M. B.; Hyman, B. T.; Kazantsev, A. G. *Science* **2007,** *317,* 516–519. doi:10.1126/science.1143780
13. Pillai, V. B.; Bindu, S.; Sharp, W.; Fang, Y. H.; Kim, G.; Gupta, M.; Samant, S.; Gupta, M. P. *Am. J. Physiol.: Heart Circ. Physiol.* **2016,** *310,* H962–H972. doi:10.1152/ajpheart.00832.2015
14. Lu, Y.; Wang, Y.-d.; Wang, X.-y.; Chen, H.; Cai, Z.-j.; Xiang, M.-x. *Int. J. Cardiol.* **2016,** *220,* 700–705. doi:10.1016/j.ijcard.2016.06.236
15. He, X.; Zeng, H.; Chen, J.-X. *Int. J. Cardiol.* **2016,** *215,* 349–357. doi:10.1016/j.ijcard.2016.04.092
16. Bellizzi, D.; Rose, G.; Cavalcante, P.; Covello, G.; Dato, S.; De Rango, F.; Greco, V.; Maggiolini, M.; Feraco, E.; Mari, V.; Franceschi, C.; Passarino, G.; De Benedictis, G. *Genomics* **2005,** *85,* 258–263. doi:10.1016/j.ygeno.2004.11.003
17. Serrano, L.; Martínez-Redondo, P.; Marazuela-Duque, A.; Vazquez, B. N.; Dooley, S. J.; Voigt, P.; Beck, D. B.; Kane-Goldsmith, N.; Tong, Q.; Rabanal, R. M.; Fondevila, D.; Muñoz, P.; Krüger, M.; Tischfield, J. A.; Vaquero, A. *Genes Dev.* **2013,** *27,* 639–653. doi:10.1101/gad.211342.112
18. Cameron, D.; Eisler, S. *J. Phys. Org. Chem.* **2018,** *31,* e3858. doi:10.1002/poc.3858
19. Suzuki, H. *Bull. Chem. Soc. Jpn.* **1952,** *25,* 145–150. doi:10.1246/bcsj.25.145
20. Bandara, H. M. D.; Burdette, S. C. *Chem. Soc. Rev.* **2012,** *41,* 1809–1825. doi:10.1039/c1cs15179g
21. Cammenga, H. K.; Emel'yanenko, V. N.; Verevkin, S. P. *Ind. Eng. Chem. Res.* **2009,** *48,* 10120–10128. doi:10.1021/ie900800q
22. Meier, H. *Angew. Chem., Int. Ed. Engl.* **1992,** *31,* 1399–1420. doi:10.1002/anie.199213993
23. Han, W.-G.; Lovell, T.; Liu, T.; Noodleman, L. *ChemPhysChem* **2002,** *3,* 167–178. doi:10.1002/1439-7641(20020215)3:2<167::aid-cphc167>3.0.co;2-g
24. Irie, M. *Chem. Rev.* **2000,** *100,* 1685–1716. doi:10.1021/cr980069d
25. Chung, J. W.; Yoon, S.-J.; An, B.-K.; Park, S. Y. *J. Phys. Chem. C* **2013,** *117,* 11285–11291. doi:10.1021/jp401440s
26. Lerch, M. M.; Hansen, M. J.; van Dam, G. M.; Szymanski, W.; Feringa, B. L. *Angew. Chem., Int. Ed.* **2016,** *55,* 10978–10999. doi:10.1002/anie.201601931
27. Hüll, K.; Morstein, J.; Trauner, D. *Chem. Rev.* **2018,** *118,* 10710–10747. doi:10.1021/acs.chemrev.8b00037
28. Hoorens, M. W. H.; Szymanski, W. *Trends Biochem. Sci.* **2018,** *43,* 567–575. doi:10.1016/j.tibs.2018.05.004
29. Tochitsky, I.; Kienzler, M. A.; Isacoff, E.; Kramer, R. H. *Chem. Rev.* **2018,** *118,* 10748–10773. doi:10.1021/acs.chemrev.7b00723
30. Szymański, W.; Beierle, J. M.; Kistemaker, H. A. V.; Velema, W. A.; Feringa, B. L. *Chem. Rev.* **2013,** *113,* 6114–6178. doi:10.1021/cr300179f
31. Crespi, S.; Simeth, N. A.; König, B. *Nat. Rev. Chem.* **2019,** *3,* 133–146. doi:10.1038/s41570-019-0074-6
32. Trapp, J.; Jochum, A.; Meier, R.; Saunders, L.; Marshall, B.; Kunick, C.; Verdin, E.; Goekjian, P.; Sippl, W.; Jung, M. *J. Med. Chem.* **2006,** *49,* 7307–7316. doi:10.1021/jm060118b
33. Falenczyk, C.; Schiedel, M.; Karaman, B.; Rumpf, T.; Kuzmanovic, N.; Grøtli, M.; Sippl, W.; Jung, M.; König, B. *Chem. Sci.* **2014,** *5,* 4794–4799. doi:10.1039/c4sc01346h
34. McDonald, O.; Lackey, K.; Davis-Ward, R.; Wood, E.; Samano, V.; Maloney, P.; Deanda, F.; Hunter, R. *Bioorg. Med. Chem. Lett.* **2006,** *16,* 5378–5383. doi:10.1016/j.bmcl.2006.07.063
35. Swyter, S.; Schiedel, M.; Monaldi, D.; Szunyogh, S.; Lehotzky, A.; Rumpf, T.; Ovádi, J.; Sippl, W.; Jung, M. *Philos. Trans. R. Soc., B* **2018,** *373,* 20170083. doi:10.1098/rstb.2017.0083
36. Buettelmann, B.; Alanine, A.; Bourson, A.; Gill, R.; Heitz, M.-P.; Mutel, V.; Pinard, E.; Trube, G.; Wyler, R. *Chimia* **2004,** *58,* 630–633. doi:10.2533/000942904777677579
37. Heck, R. F. *Palladium reagents in organic syntheses;* Academic Press: London, United Kingdom, 1990.

38. Heltweg, B.; Trapp, J.; Jung, M. *Methods* **2005,** *36,* 332–337. doi:10.1016/j.ymeth.2005.03.003
39. Cui, H.; Kamal, Z.; Ai, T.; Xu, Y.; More, S. S.; Wilson, D. J.; Chen, L. *J. Med. Chem.* **2014,** *57,* 8340–8357. doi:10.1021/jm500777s
40. Ai, T.; Wilson, D. J.; More, S. S.; Xie, J.; Chen, L. *J. Med. Chem.* **2016,** *59,* 2928–2941. doi:10.1021/acs.jmedchem.5b01376
41. Schiedel, M.; Rumpf, T.; Karaman, B.; Lehotzky, A.; Oláh, J.; Gerhardt, S.; Ovádi, J.; Sippl, W.; Einsle, O.; Jung, M. *J. Med. Chem.* **2016,** *59,* 1599–1612. doi:10.1021/acs.jmedchem.5b01517
42. Rumpf, T.; Schiedel, M.; Karaman, B.; Roessler, C.; North, B. J.; Lehotzky, A.; Oláh, J.; Ladwein, K. I.; Schmidtkunz, K.; Gajer, M.; Pannek, M.; Steegborn, C.; Sinclair, D. A.; Gerhardt, S.; Ovádi, J.; Schutkowski, M.; Sippl, W.; Einsle, O.; Jung, M. *Nat. Commun.* **2015,** *6,* 6263. doi:10.1038/ncomms7263
43. Suzuki, T.; Khan, M. N. A.; Sawada, H.; Imai, E.; Itoh, Y.; Yamatsuta, K.; Tokuda, N.; Takeuchi, J.; Seko, T.; Nakagawa, H.; Miyata, N. *J. Med. Chem.* **2012,** *55,* 5760–5773. doi:10.1021/jm3002108
44. Sundriyal, S.; Moniot, S.; Mahmud, Z.; Yao, S.; Di Fruscia, P.; Reynolds, C. R.; Dexter, D. T.; Sternberg, M. J. E.; Lam, E. W.-F.; Steegborn, C.; Fuchter, M. J. *J. Med. Chem.* **2017,** *60,* 1928–1945. doi:10.1021/acs.jmedchem.6b01690
45. Huang, S.; Song, C.; Wang, X.; Zhang, G.; Wang, Y.; Jiang, X.; Sun, Q.; Huang, L.; Xiang, R.; Hu, Y.; Li, L.; Yang, S. *J. Chem. Inf. Model.* **2017,** *57,* 669–679. doi:10.1021/acs.jcim.6b00714
46. Robaa, D.; Monaldi, D.; Wössner, N.; Kudo, N.; Rumpf, T.; Schiedel, M.; Yoshida, M.; Jung, M. *Chem. Rec.* **2018,** *18,* 1701–1707. doi:10.1002/tcr.201800044
47. Smakula, A. *Z. Phys. Chem.* **1934,** *25B,* 90–98. doi:10.1515/zpch-1934-2508
48. Buckles, R. E. *J. Am. Chem. Soc.* **1955,** *77,* 1040–1041. doi:10.1021/ja01609a073
49. Ciamician, G.; Silber, P. *Ber. Dtsch. Chem. Ges.* **1902,** *35,* 4128–4131. doi:10.1002/cber.19020350450
50. Lewis, F. D.; Kalgutkar, R. S.; Yang, J.-S. *J. Am. Chem. Soc.* **2001,** *123,* 3878–3884. doi:10.1021/ja0042027
51. Christiansen, O.; Koch, H.; Jørgensen, P. *Chem. Phys. Lett.* **1995,** *243,* 409–418. doi:10.1016/0009-2614(95)00841-q
52. Hättig, C.; Köhn, A. *J. Chem. Phys.* **2002,** *117,* 6939–6951. doi:10.1063/1.1506918
53. Hättig, C. *Adv. Quantum Chem.* **2005,** *50,* 37–60. doi:10.1016/s0065-3276(05)50003-0
54. Klamt, A.; Schüürmann, G. *J. Chem. Soc., Perkin Trans. 2* **1993,** 799–805. doi:10.1039/p29930000799
55. Lunkenheimer, B.; Köhn, A. *J. Chem. Theory Comput.* **2013,** *9,* 977–994. doi:10.1021/ct300763v
56. Send, R.; Kühn, M.; Furche, F. *J. Chem. Theory Comput.* **2011,** *7,* 2376–2386. doi:10.1021/ct200272b
57. Broichhagen, J.; Frank, J. A.; Trauner, D. *Acc. Chem. Res.* **2015,** *48,* 1947–1960. doi:10.1021/acs.accounts.5b00129
58. Schoenberger, M.; Damijonaitis, A.; Zhang, Z.; Nagel, D.; Trauner, D. *ACS Chem. Neurosci.* **2014,** *5,* 514–518. doi:10.1021/cn500070w
59. Morstein, J.; Awale, M.; Reymond, J.-L.; Trauner, D. *ACS Cent. Sci.* **2019,** *5,* 607–618. doi:10.1021/acscentsci.8b00881
60. Hauwert, N. J.; Mocking, T. A. M.; Da Costa Pereira, D.; Lion, K.; Huppelschoten, Y.; Vischer, H. F.; De Esch, I. J. P.; Wijtmans, M.; Leurs, R. *Angew. Chem., Int. Ed.* **2019,** *58,* 4531–4535. doi:10.1002/anie.201813110
61. Hauwert, N. J.; Mocking, T. A. M.; Da Costa Pereira, D.; Lion, K.; Huppelschoten, Y.; Vischer, H. F.; De Esch, I. J. P.; Wijtmans, M.; Leurs, R. *Angew. Chem.* **2019,** *131,* 4579–4583. doi:10.1002/ange.201813110
62. Simeth, N. A.; Bellisario, A.; Crespi, S.; Fagnoni, M.; König, B. *J. Org. Chem.* **2019,** *84,* 6565–6575. doi:10.1021/acs.joc.8b02973
63. Schehr, M.; Ianes, C.; Weisner, J.; Heintze, L.; Müller, M. P.; Pichlo, C.; Charl, J.; Brunstein, E.; Ewert, J.; Lehr, M.; Baumann, U.; Rauh, D.; Knippschild, U.; Peifer, C.; Herges, R. *Photochem. Photobiol. Sci.* **2019,** *18,* 1398–1407. doi:10.1039/c9pp00010k
64. Rustler, K.; Maleeva, G.; Bregestovski, P.; König, B. *Beilstein J. Org. Chem.* **2019,** *15,* 780–788. doi:10.3762/bjoc.15.74
65. Schiedel, M.; Herp, D.; Hammelmann, S.; Swyter, S.; Lehotzky, A.; Robaa, D.; Oláh, J.; Ovádi, J.; Sippl, W.; Jung, M. *J. Med. Chem.* **2018,** *61,* 482–491. doi:10.1021/acs.jmedchem.6b01872
66. Laemmli, U. K. *Nature* **1970,** *227,* 680–685. doi:10.1038/227680a0
67. *TURBOMOLE,* V7.2 2017; University of Karlsruhe and Forschungszentrum Karlsruhe GmbH, TURBOMOLE GmbH: Karlsruhe, Germany, 2007, http://www.turbomole.com.
68. Perdew, J. P.; Burke, K.; Ernzerhof, M. *Phys. Rev. Lett.* **1996,** *77,* 3865–3868. doi:10.1103/physrevlett.77.3865
69. Schäfer, A.; Horn, H.; Ahlrichs, R. *J. Chem. Phys.* **1992,** *97,* 2571–2577. doi:10.1063/1.463096
70. Perdew, J. P.; Ernzerhof, M.; Burke, K. *J. Chem. Phys.* **1996,** *105,* 9982–9985. doi:10.1063/1.472933
71. Bauernschmitt, R.; Ahlrichs, R. *Chem. Phys. Lett.* **1996,** *256,* 454–464. doi:10.1016/0009-2614(96)00440-x
72. Furche, F.; Ahlrichs, R. *J. Chem. Phys.* **2002,** *117,* 7433–7447. doi:10.1063/1.1508368
73. Eichkorn, K.; Weigend, F.; Treutler, O.; Ahlrichs, R. *Theor. Chem. Acc.* **1997,** *97,* 119–124. doi:10.1007/s002140050244
74. De Haan, D. O.; Tapavicza, E.; Riva, M.; Cui, T.; Surratt, J. D.; Smith, A. C.; Jordan, M.-C.; Nilakantan, S.; Almodovar, M.; Stewart, T. N.; de Loera, A.; De Haan, A. C.; Cazaunau, M.; Gratien, A.; Pangui, E.; Doussin, J.-F. *Environ. Sci. Technol.* **2018,** *52,* 4061–4071. doi:10.1021/acs.est.7b06105
75. Thompson, T.; Tapavicza, E. *J. Phys. Chem. Lett.* **2018,** *9,* 4758–4764. doi:10.1021/acs.jpclett.8b02048
76. Tapavicza, E.; Thompson, T.; Redd, K.; Kim, D. *Phys. Chem. Chem. Phys.* **2018,** *20,* 24807–24820. doi:10.1039/c8cp05181j
77. Mashimo, S.; Kuwabara, S.; Yagihara, S.; Higasi, K. *J. Chem. Phys.* **1989,** *90,* 3292–3294. doi:10.1063/1.455883
78. Herráez, J. V.; Belda, R. *J. Solution Chem.* **2006,** *35,* 1315–1328. doi:10.1007/s10953-006-9059-4
79. Epstein, S. A.; Tapavicza, E.; Furche, F.; Nizkorodov, S. A. *Atmos. Chem. Phys.* **2013,** *13,* 9461–9477. doi:10.5194/acp-13-9461-2013
80. Schalk, O.; Geng, T.; Thompson, T.; Baluyot, N.; Thomas, R. D.; Tapavicza, E.; Hansson, T. *J. Phys. Chem. A* **2016,** *120,* 2320–2329. doi:10.1021/acs.jpca.5b10928
81. Cisneros, C.; Thompson, T.; Baluyot, N.; Smith, A. C.; Tapavicza, E. *Phys. Chem. Chem. Phys.* **2017,** *19,* 5763–5777. doi:10.1039/c6cp08064b
82. Tapavicza, E.; Furche, F.; Sundholm, D. *J. Chem. Theory Comput.* **2016,** *12,* 5058–5066. doi:10.1021/acs.jctc.6b00720

License and Terms

This is an Open Access article under the terms of the Creative Commons Attribution License (http://creativecommons.org/licenses/by/4.0). Please note that the reuse, redistribution and reproduction in particular requires that the authors and source are credited.

The license is subject to the *Beilstein Journal of Organic Chemistry* terms and conditions: (https://www.beilstein-journals.org/bjoc)

The definitive version of this article is the electronic one which can be found at: doi:10.3762/bjoc.15.214

BEILSTEIN JOURNAL OF ORGANIC CHEMISTRY

Aggregation-induced emission effect on turn-off fluorescent switching of a photochromic diarylethene

Luna Kono[1], Yuma Nakagawa[1], Ayako Fujimoto[1], Ryo Nishimura[1], Yohei Hattori[1], Toshiki Mutai[2], Nobuhiro Yasuda[3], Kenichi Koizumi[4], Satoshi Yokojima[4,5], Shinichiro Nakamura[4] and Kingo Uchida[*1,4]

Full Research Paper

Open Access

Address:
[1]Department of Materials Chemistry, Ryukoku University, Seta, Otsu, Shiga 520-2194, Japan, [2]Department of Materials and Environmental Science, the University of Tokyo, 4-6-1, Komaba, Meguro-ku, Tokyo 153-8505, Japan, [3]Japan Synchrotron Radiation Research Institute, 1-1-1 Kouto, Sayo-cho, Sayo-gun, Hyogo 679-5198 Japan, [4]Nakamura Laboratory, RIKEN Cluster for Science, Technology and Innovation Hub, 2-1 Hirosawa, Wako, Saitama 351-0198, Japan and [5]Tokyo University of Pharmacy and Life Sciences, 1432-1 Horinouchi, Hachioji, Tokyo 192-0392, Japan

Email:
Kingo Uchida* - uchida@rins.ryukoku.ac.jp

* Corresponding author

Keywords:
AIE; diarylethene; ESIPT fluorescent switching; turn-off fluorescence

Beilstein J. Org. Chem. **2019,** *15,* 2204–2212.
doi:10.3762/bjoc.15.217

Received: 10 July 2019
Accepted: 02 September 2019
Published: 20 September 2019

This article is part of the thematic issue "Molecular switches".

Guest Editor: W. Szymanski

© 2019 Kono et al.; licensee Beilstein-Institut.
License and terms: see end of document.

Abstract

Background: Diarylethenes are well-known photochromic compounds, which undergo cyclization and cycloreversion reactions between open- and closed-ring isomers. Recently, diarylethene derivatives with photoswitchable fluorescent properties were prepared. They are applicable for fluorescence imaging including bio-imaging. On the other hand, a new system called “excited state intramolecular proton transfer (ESIPT)” is reported. In the system, absorption and emission bands are largely separated due to the proton transfer, hence it showed strong fluorescence even in the crystalline state. We aimed to construct the photochromic system incorporating the ESIPT mechanism.

Results: A diarylethene incorporating a fluorescent moiety that exhibit ESIPT behavior was prepared. The ESIPT is one of the examples which express the mechanisms of aggregation-induced emission (AIE). This compound emits orange fluorescence with a large Stokes shift derived from ESIPT in aprotic solvents such as THF or hexane, while it exhibits only a photochromic reaction in protic solvents such as methanol. In addition, it shows turn-off type fluorescence switching in an aprotic solvent and in crystals. The fluorescence is quenched as the content of closed-ring isomers increases upon UV light irradiation.

Conclusions: A diarylethene containing an ESIPT functional group was prepared. It showed fluorescent turn-off behavior during photochromism in aprotic solvents as well as in crystalline state upon UV light irradiation. Furthermore, it showed AIE in THF/water mixtures with blue-shift of the emission.

Introduction

Diarylethenes are well-known photochromic molecules and are widely applied to molecular switches and systems [1,2]. Recently, the photo-switching of fluorescence signals by using diarylethene switches has attracted much attention because of the potential in various optoelectronic applications [3]. For example, fluorescence switching for molecular level recording [4], multiple-fluorescence for logic circuits [5] as well as biological applications [6] and super-resolution microscopy for bioimaging [7,8]. The fluorescence switching in solid state is attracting much attention from both scientific and technological points of view, such as sensors, electroluminescent displays, memory devices [9].

On the other hand, molecular aggregation also affects the intensity of fluorescence [10,11]. Some material shows fluorescence by aggregation (aggregation-induced emission (AIE)), while the others decay the fluorescence by aggregation (aggregation-caused quenching (ACQ)). The luminogenic materials with AIE have attracted much interest since Tang et al. reported the AIE concept [12]. The introduction of photo-switching ability in the system will be interesting for creating new AIE systems. In addition, organic photochromic crystals are inherently capable of photo-reversible luminescence switching because the electronic structures of photochromic molecules reversibly change upon photoisomerization [13,14]. However, such a fluorescent system in condensed phase emits fluorescence often absorbed in adjacent molecules, therefore a large Stokes shift is indispensable for such a system.

One of the possible choices to achieve such a large Stokes shift is to introduce the excited-state intramolecular proton transfer (ESIPT). The process of ESIPT is a fast process even comparable to the internal conversion [15,16]. This is because the proton transfer occurs through an intramolecular hydrogen bond. This is also an origin of a large Stokes shift (8,000–11,000 cm^{-1}) in the emission from the ESIPT state. Consequently, yellow luminescence was observed by UV-excitation [17,18]. Mutai et al. reported an ESIPT luminescence of an imidazo[1,2-*a*]pyridine derivative, in which remarkable fluorescence was observed and no overlapping from the absorption band due to the large Stokes shift of the fluorescence [19,20]. Photochromic diarylethene systems with ESIPT moieties are already reported in some research groups [21-23].

Herein, we prepared a diarylethene incorporating the imidazo[1,2-*a*]pyridine moiety with ESIPT ability and reported the fluorescence switching of the system.

Results and Discussion

The diarylethene **1o** having an ESIPT moiety was prepared by a coupling reaction of asymmetric diarylethene **3** [24] and 6-bromo-2-(2'-methoxyphenyl)imidazo[1,2-*a*]pyridine **4** [25] followed by ether cleavage according to Figure 1.

The photochromic reaction and spectral changes are shown in Figure 2 and Figure 3. The photochromic absorption spectral changes in THF are shown in Figure 3. Upon UV light irradia-

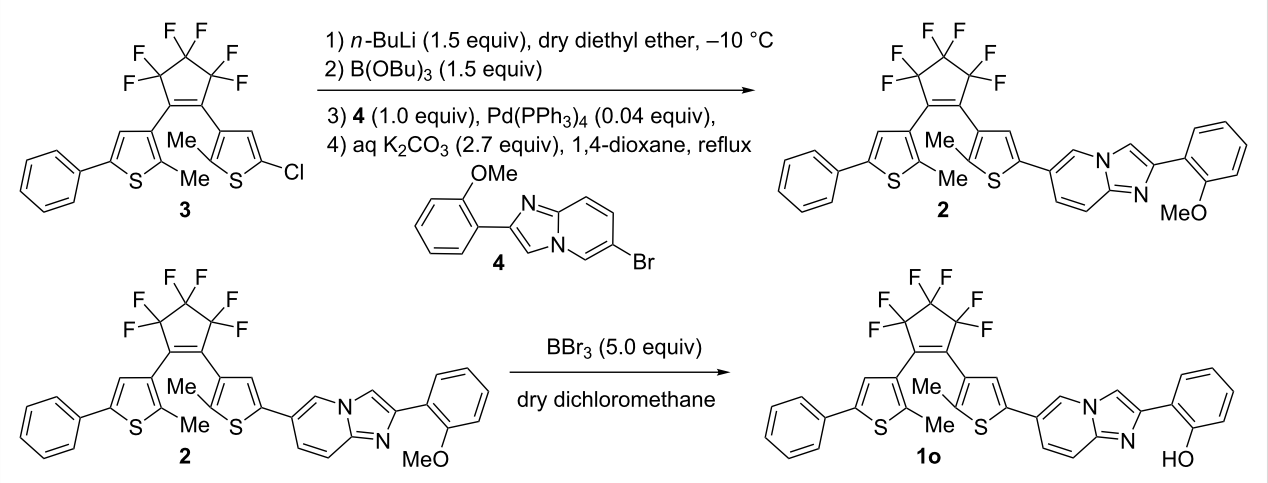


Figure 1: Synthetic procedure for a diarylethene (**1o**).

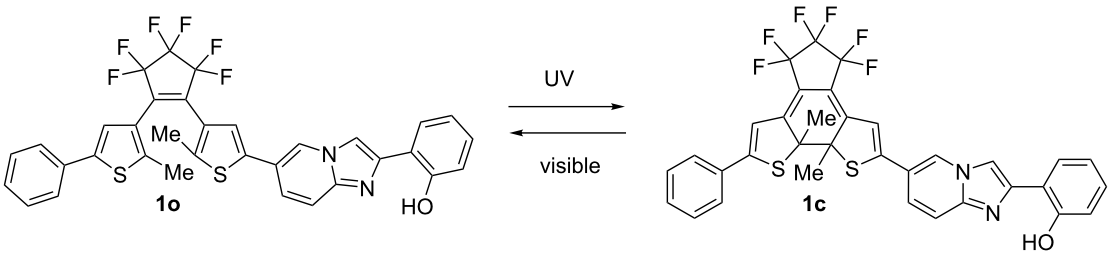


Figure 2: Photochromic reaction of diarylethene **1o** having an ESIPT moiety.

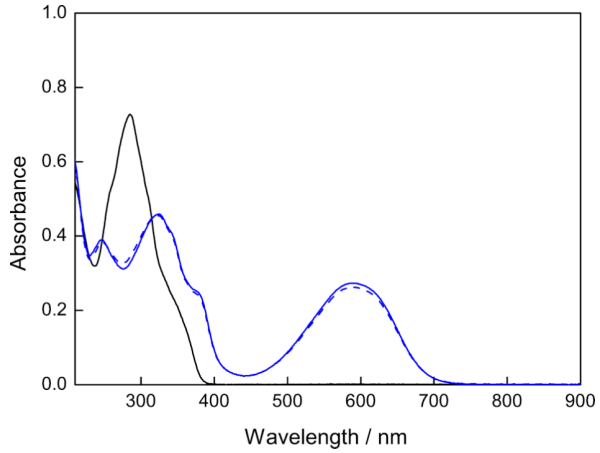


Figure 3: Absorption spectral changes of diarylethene **1o** having an ESIPT moiety in THF (c = 1.3×10^{-5} M). Black solid line: **1o**, blue solid line: **1c**, blue broken line: photostationary state under irradiation with 313 nm light (**1o**/**1c** = 4.2: 95.8) (irradiation. for 30 s).

tion of the solution of **1o**, the color changed to blue with increasing the absorption band at 587 nm of the closed-ring isomer **1c**, then by visible light irradiation the color disappeared and reproducing the absorption spectra at 285 nm of **1o**. The cyclization and cycloreversion reactions of **1** were measured in THF and methanol. The results were summarized in Table 1.

The quantum yields of cyclization and cycloreversion reactions of **1o** in THF are obtained to be 0.31 and 6.2 × 10^{-3}, respectively. They are a little bit smaller than those of simple diarylethene switches having thiophene rings as aryl groups [26]. It may be due to the connection with an ESIPT moiety. Only slight changes were observed in absorption spectra as well as photochromic quantum yields in two solvents.

In the protic solvents including methanol, **1o** and **1c** did not emit fluorescence, while only **1o** emitted in aprotic solvent, i.e., in hexane, orange fluorescence with a fluorescence quantum yield (Φ_f) of 0.027. The fluorescent emission spectra of **1o** in several solvents were shown in Figure 4, and λ_{max} of the emission spectra and the fluorescence quantum yields in the solvents are summarized in Table 2. These emission spectra of **1o** were largely red-shifted, indicating the ESIPT property. Generally, the fluorescence quantum yields decreased with increasing

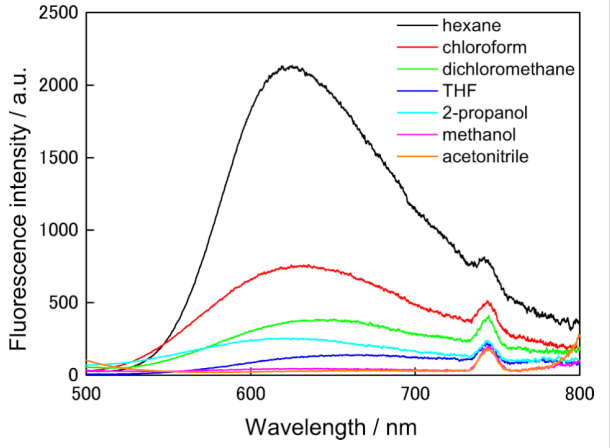


Figure 4: Fluorescent spectra of **1o** in several solvents (λ_{ex} = 370 nm). Hexane (black line), chloroform (red line), dichloromethane (green line), THF (blue line), 2-propanol (pale blue line), methanol (pink line), acetonitrile (orange line). The absorption at the excited wavelength of each solution was adjusted to 0.05. (emission peaks at 740 nm is attributed to the 2nd order diffracted excitation light.)

Table 1: Photochromic properties of a diarylethene **1** in methanol and THF.

compounds	λ_{max}/nm (ε/10^4 M^{-1} cm^{-1})		$\Phi_{o\rightarrow c}$ (313 nm)	$\Phi_{c\rightarrow o}$ (577 nm)
	open-ring isomer	closed-ring isomer		
1 (in THF)	285 (5.7)	587 (2.1)	0.31	0.0062
1 (in methanol)	283 (5.5)	584 (2.0)	0.34	0.0073

Table 2: Emission maxima of the fluorescence spectra and the relative fluorescence quantum yields Φ_f in several solvents.

solution	λ_{max}[a] / nm	Φ_f[a]	permittivity / F m^{-1}	refractive index [27]
hexane	625	0.027	2.0	1.3727
chloroform	635	0.013	4.8	1.4459
THF	670	0.002	7.5	1.4050
dichloromethane	650	0.006	9.1	1.4242
2-propanol	623	0.004	18	1.3776
methanol	–	–	33	1.3288
acetonitrile	–	–	37	1.3442

[a]λ_{ex} = 370 nm.

the permittivity of the solvents. No fluorescence was observed for methanol and acetonitrile solutions, indicating the suppression of ESIPT, because the solvents were used without dehydration.

The intensity of the fluorescence decreased gradually upon UV light irradiation accompanied with the formation of **1c**, because of excitation energy transfer from the ESIPT moiety to the closed-ring isomer (Figure 5) [4].

The wavelengths of absorption (Table 3) and fluorescence (Table 4) were obtained computationally by using density functional theory (DFT) and time-dependent DFT (TDDFT). The excitation wavelengths as well as the emission wavelength

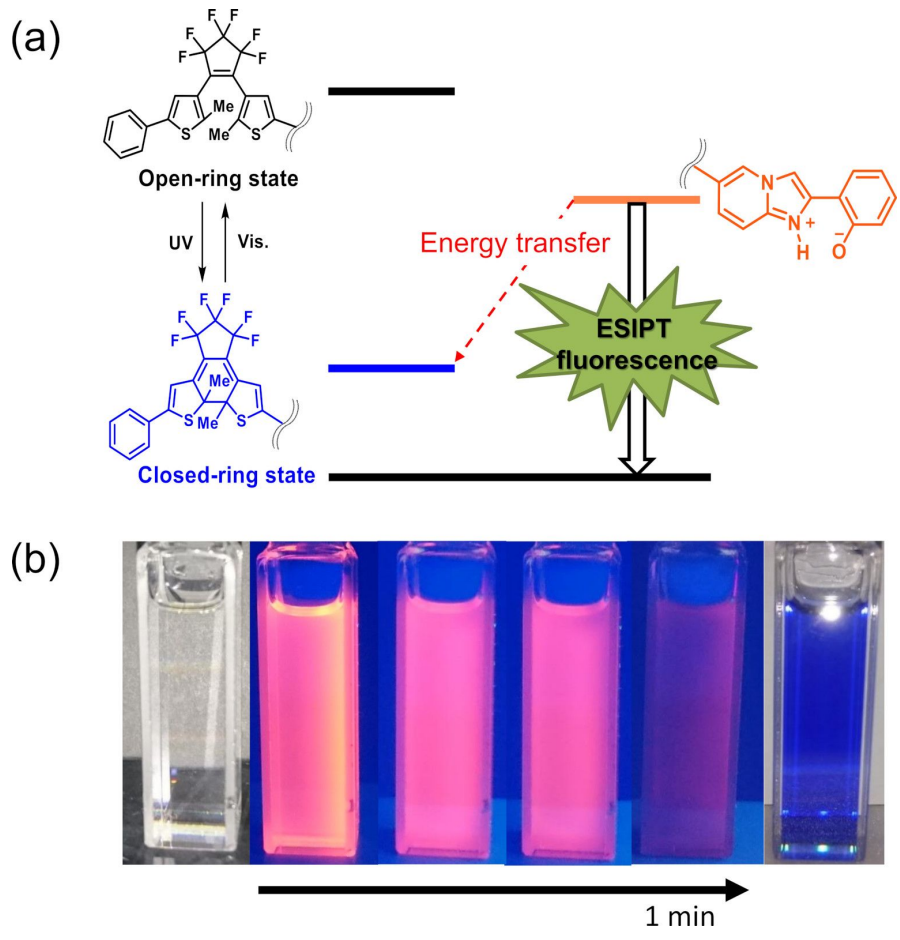


Figure 5: (a) The energy diagram of the ESIPT process of **1**. (b) ESIPT fluorescence quenching upon UV light (λ = 313 nm) irradiation of **1o** in THF solution. The fluorescence is quenched by photo-generated closed-ring isomer **1c**.

Table 3: Excitation energies for **1o** and **1c** in THF.

	excited state	excitation energies (λ)	oscillator strength
1o	1	3.38 eV (366 nm)	0.2108
	2	3.48 eV (356 nm)	0.2089
1c	1	1.97 eV (630 nm)	0.6744
	2	2.53 eV (490 nm)	0.0308

Table 4: Emission energies for **1o** and **1c** in THF.

	excited state	emission energies (λ)	oscillator strength
1o	1	1.69 eV (735 nm)	0.0027
	2	2.31 eV (538 nm)	0.3004
1c	1	1.40 eV (887 nm)	0.5519
	2	2.23 eV (555 nm)	0.0471

qualitatively agrees with the experimental results. Since compound **1** consists of a diarylethene moiety and an imidazo[1,2-*a*]pyridine moiety, the characteristic of **1** has the combination of these two moieties. As it is expected, the stable structure of the ESIPT is found computationally only in the excited state. (Hereafter, we denote **1o-NH** (**1c-NH**) as the ESIPT state of **1o** (**1c**) and **1o-OH** (**1c-OH**) as the original structure shown in Figure 2 to emphasize the structural difference.) Unexpectedly, however, the optimized structure at the first excited state, **1o-NH** is stable, but **1c-NH** is not (the energy difference between **1c-OH** and **1c-NH** is 11.1 kcal/mol). This is because the first excited state of **1c** is mainly localized on the diarylethene moiety. The HOMO orbital of **1o** is localized on the imidazo-[1,2-*a*]pyridine moiety whereas the LUMO orbital is manly localized on the diarylethene moiety. Thus, the proton-transfer in the excited state is favorable at the first excited state of **1o**.

To the THF solution of **1o**, water was gradually added, and the intensities and color changes of the fluorescence were moni-

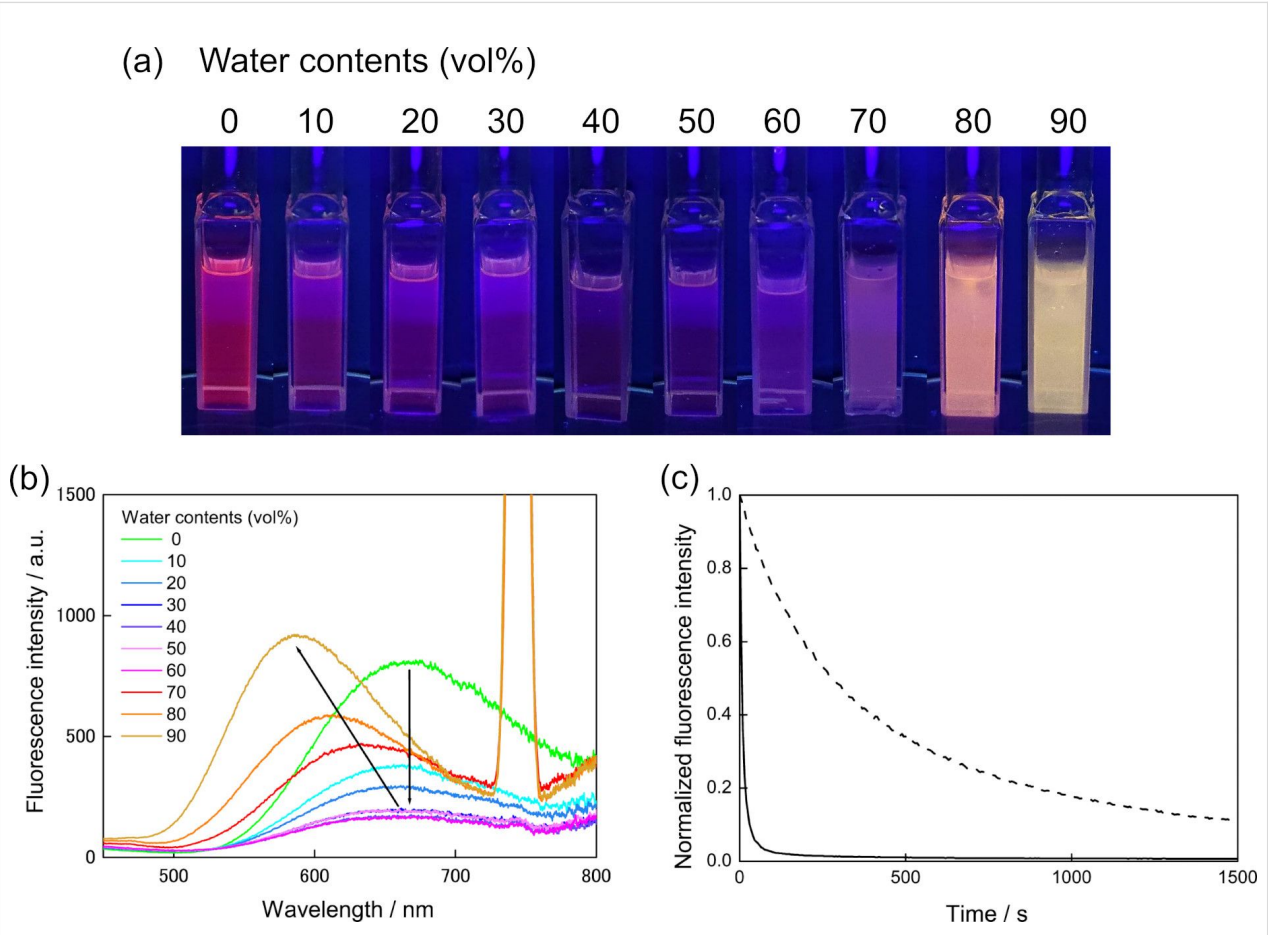


Figure 6: (a) Fluorescence photographs of solutions/suspensions of **1o** (1.2×10^{-4} M) in THF/water mixtures with different water contents under UV light (λ = 365 nm) irradiation. (b) The fluorescence spectra of **1o** solutions (λ_{ex} = 370 nm). (c) The fluorescence quenching of THF 100 vol % (water 0 vol %) solution at 670 nm (broken line) and that of THF/water = 10:90 (v/v) at 585 nm (solid line) upon UV irradiation.

tored. By adding 10 vol % water the fluorescence was dramatically reduced. However, by the addition of 80 vol %, color of fluorescence changed to orange and the intensity increased (Figure 6a). In the mixture of 90 vol % water and 10 vol % THF the fluorescence band was blue-shifted, and the color changed to yellow, and the intensity was enhanced (Figure 6b). Such a blue shift of ESIPT fluorescence was already reported and it is ascribed to suppression of the stabilization of the excited zwitterionic species through solvent rearrangement and/or further conformational changes of the substrate [19].

The X-ray analysis data of a single crystal of **1o** is shown in Figure S1 and Table S1 in Supporting Information File 1. The distance between two reactive carbon atoms in the thiophene rings was obtained to be 3.534 Å, which is less than 4.2 Å. It indicates the molecule is photoreactive in the crystalline state [28].

In the crystalline state, **1o** emitted green fluorescence (Φ_f = 0.031) as shown in Figure 7b. The color is more blue-shifted color compared with the mixed solution (THF/water = 10:90 (v/v)). The fluorescence is also quenched with the formation of **1c** upon UV light irradiation, indicating turn-off type fluorescent switch (Figure 6c and Figure 7e) [29,30]. The emission from the aggregates quenched much faster than the solution (Figure 6c) (Supporting Information File 2, Movie 1). This is due to a "giant amplification of fluorescence photoswitching" ascribed by a very efficient intermolecular Förster Resonance Energy Transfer (FRET) process between the fluorescent units and the photochromic moieties in their closed form within the aggregated state [29]. The crystal did not show any vapochromism, while a dramatic fluorescent color change from green to pink was observed when chloroform was dropped to the UV light irradiated crystal **1o** (Supporting Information File 3, Movie 2).

The rate of fluorescence quenching ($\tau_{1/2}$ is less than 0.2 s) in the crystalline state is much faster than those observed in solutions. This is attributed to the degree of condensation which is much higher in the crystalline state. The mechanism of the fast quenching is expected to be related to the amplification of photo-switching of a photochromic organic nanoparticle system as well as the crystalline system reported by Fukaminato and co-workers [29,30]. A detailed study of the amplification will be carried out in the future.

Conclusion

In summary, we prepared a new diarylethene derivative having an ESIPT functional moiety. It shows the pink fluorescence upon UV light irradiation. Prolonged irradiation with UV light,

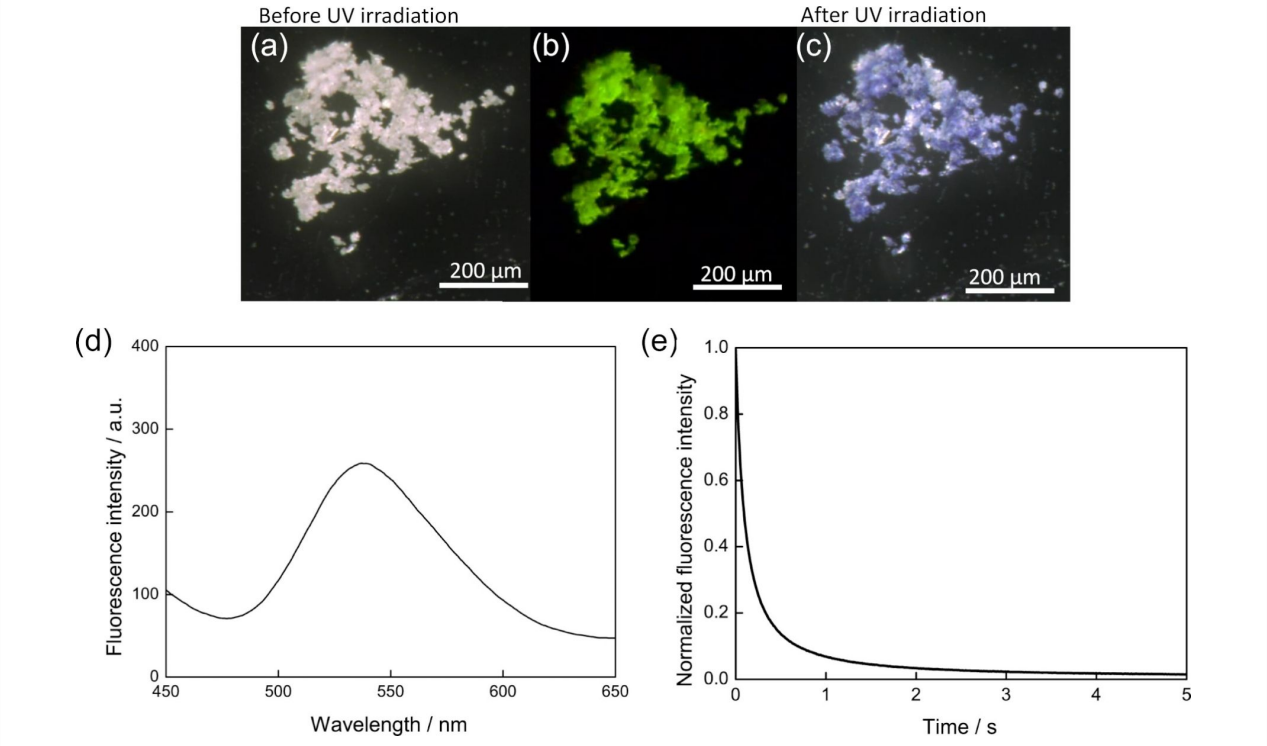


Figure 7: (a) Crystals of **1o** before UV light irradiation, (b) Green fluorescence of **1o** observed under UV light (λ = 365 nm) irradiation, (c) Cyclization proceeded to form **1c** with suppression of the fluorescence, (d) Fluorescence spectra of **1o** in the crystalline state (λ_{ex} = 370 nm, λ_{max} = 537 nm), (e) The fluorescence quenching of **1o** in the crystalline state (λ_{ex} = 370 nm, λ_{em} = 537 nm) upon UV irradiation.

resulted in the suppressed emission accompanied with a proceeding photocyclization reaction. This is turn-off type fluorescence. The fluorescence was also suppressed in protic and polar solvents because of prohibition of the ESIPT. In the THF/water mixed solvents, when the content of water was increased to 10–60 vol %, the fluorescence was quenched; however, strong fluorescence and blue-shift of emission band was observed above 80 vol % of water content. This is attributable to the AIE effect. The effect was much more remarkable in crystalline state. The emission can be switchable by diarylethene moiety. The effect was also observed in the crystal. The crystal of **1o** emits green fluorescence, and the emission was also suppressed by forming the closed-ring isomer. The crystal shows pink fluorescence once chloroform droplets were dropped on the crystal. The system will be useful for sensors and color indicators.

Experimental

General: Starting materials were commercially available and were used without further purification. Melting points were determined on a Yanaco MP-500D melting point apparatus and are uncorrected. ^{1}H (400 MHz), ^{13}C (100 MHz) and ^{19}F NMR (376 MHz) spectra were recorded on a JEOL JNM-400 spectrometer at ambient temperature. The splitting patterns are designated as follows: s (singlet); d (doublet); dd (double doublet); t (triplet); q (quartet); m (multiplet) and br (broad). Chemical shifts are denoted in δ (ppm) referenced to the residual protic solvent peaks. Coupling constants *J* are denoted in Hz. Mass spectra were recorded on a MALDI-Spiral-TOF-MS mass spectrometer with DCTB (10 mg/mL in $CHCl_3$) as a matrix. Absorption and emission spectra were monitored on Hitachi U-4150 spectrophotometer and Hitachi F-7100 fluorescence spectrophotometer, respectively. Fluorescence quantum yields in several solvents were obtained as comparison with that of 9,10-bis(phenylethynyl)anthracene in hexane (Φ_f = 1.0) [31]. The luminescence quantum yields of crystalline solids were measured using a JASCO ILF-533 integral sphere attached to a JASCO FP-6600 spectrofluorophotometer. The mixture of microcrystalline compounds (2 mg) and powdered sodium chloride (1 g) were put into a 5 mm quartz cell, which was then placed in the integral sphere. The quantum yield was calculated using an installed software. The solid-state absorption spectrum was obtained by Kubelka–Munk conversion of a diffractive reflectance spectrum of the above mixture measured on a JASCO FP-6600 spectrofluorophotometer equipped with ILF-533 integral sphere. KEYENCE VHX-500, VH-S30, VH-Z20 were used to monitor the crystals. For the UV light irradiation, KEYENCE UV-400, UV-50H (λ = 365 nm), Spectronics Corporation Westbury, New York, USA Spectro Line Highest Ultraviolet Intensity Guaranteed (100 V, 40 A, λ = 313 nm) and AS ONE Handy UV Lamp SLUV-4 (λ = 365 nm) were used. For visible light irradiation, a 500W USHIO SX-UI501XQ Xenon lamp attached with Toshiba color filters (Y-48, Y-44, and UV-29) was used.

The Gaussian09 program package [32] was used for geometry optimizations with DFT for ground states and subsequent TDDFT calculations. For the calculation of the fluorescence, the geometry optimizations were performed for the first excited state obtained by TDDFT. The hybrid B3LYP functional [33-35] was adopted to exchange-correlation term of DFT. The gaussian 6-31G(d,p) basis set was adopted to all calculations. As for the solvent effect, polarizable continuum model (PCM) [36] was employed for THF.

X-ray crystallographic analysis for crystal of **1o** was carried out at BL40XU beamline of SPring-8. Si(111) channel cut monochromator was used and the wavelength and the size of X-ray beam were 0.81106 Å and 150 × 150 μm (square), respectively. The diffraction data was collected by oscillation method using EIGER detector at 173 K. The data were corrected for absorption effects by multi-scan method with ABSCOR [37]. The structure was solved by the direct method and refined by the full-matrix least-squares method using the SHELX-2014/7 program. The positions of all hydrogen atoms were calculated geometrically and refined by the riding model. The crystallographic data can be obtained free of charge from The Cambridge Crystallographic Data Center via http://www.ccdc.cam.ac.uk/data_request/cif (CCDC 1920569).

Synthesis

Diarylethene (**2**)

To a 50 mL three neck flask containing 1.15 g (2.40 mmol, 1.0 equiv) of 1-(2-methyl-5-phenylthien-3-yl)-2-(5-chloro-2-methylthien-3-yl)perfluorocyclopentene (**3**) [24] and 15 mL of anhydrous diethyl ether, 2.20 mL (3.52 mmol, 1.5 equiv) of 1.6 N *n*-BuLi in hexane solution was added followed by stirring for 1 h at −10 °C on ice-salt bath under argon gas atmosphere. Then, 0.96 mL (3.58 mmol, 1.5 equiv) of $B(OBu)_3$ was added and the temperature of the mixture was allowed to warm to room temperature and stirred for 1 h. After ascertaining the formation of boronic acid by TLC, 5 mL of H_2O was added, and solvent was removed in vacuo. To a 200 mL three necked flask, the boronic acid, 0.90 g (6.51 mmol, 2.7 equiv) of K_2CO_3, 0.72 g (2.37 mmol, 1.0 equiv) of 6-bromo-2-(2'-methoxyphenyl)imidazo[1,2-a]pyridine (**4**) [25], 0.11 g (0.09 mmol, 0.04 equiv) of $Pd(PPh_3)_4(0)$, and 80 mL of mixture of 1,4-dioxane/H_2O (3:1) were added, and refluxed for 16 h. After the reaction was finished, the mixture was cooled down to room temperature. Then the mixture was extracted with 40 mL of diethyl ether for four times. The combined

organic layer was washed with 400 mL of water twice and dried over anhydrous sodium sulfate. After filtration, the solvents were removed in vacuo. The residue was purified by silica gel chromatography (eluent: hexane and followed by a mixture of hexane and ethyl acetate (98:2)) to obtain 0.42 g of **2** as a pale-blue oil in 26% yield. The oil was purified with GPC followed by silica gel chromatography (eluent: hexane and followed by a mixture of hexane/diethyl ether (7:3) to obtain 0.31 g (0.47 mmol) of **2** as bluish viscous solid in 19% yield. ^{1}H NMR (400 MHz, $CDCl_3$, ppm) δ 8.40 (dd, *J* = 7.7, 1.7 Hz, 1H), 8.32 (s, 1H), 8.23 (s, 1H), 7.64 (d, *J* = 9.3 Hz, 1H), 7.54 (d, *J* = 7.8 Hz, 2H), 7.41–7.28 (m, 6H), 7.24 (s, 1H), 7.11 (ddd, *J* = 7.6, 7.4, 1.0 Hz, 1H), 7.02 (d, *J* = 8.2 Hz, 1H), 4.01 (s, 3H), 2.00 (s, 6H); ^{13}C NMR (100 MHz, $CDCl_3$, ppm) δ 156.9, 143.7, 142.6, 142.2, 141.5, 141.4, 138.4, 133.4, 129.2, 129.2, 129.2, 129.1, 129.0, 128.9, 128.1, 126.1, 125.9, 125.7, 125.6, 123.9, 123.0, 122.5, 122.2, 121.7, 121.2, 119.4, 117.5, 113.2, 111.0, 55.5, 14.7, 14.77; ^{19}F NMR (376 MHz, $CDCl_3$, ppm) δ −113.1 (s, 2F), −113.3 (s, 2F), −135.0 (s, 2F); HRMS (MALDI–TOF) *m*/*z*: calcd for $C_{35}H_{24}F_6N_2OS_2$, 666.1234; found, 666.1229.

Diarylethene (**1o**)

To 5 mL of dichloromethane anhydrous solution containing 0.21 g (0.31 mmol, 1.0 equiv) of diarylethene **2**, 1.5 mL (1.5 mmol, 5.0 equiv) of 1.0 M BBr_3 dichloromethane solution was added on dry-ice/methanol bath (−78 °C) under argon gas atmosphere, and stirred overnight at room temperature. After the reaction was finished, saturated sodium bicarbonate aqueous solution was added to stop the reaction. To the mixture, 70 mL of water was added and the mixture was extracted with 30 mL of chloroform for four times. The combined organic layer was washed with saturated sodium bicarbonate aqueous solution and water, successively, then dried over sodium sulfate anhydrous. After the filtration, solvents were removed in vacuo. The residue was purified by silica gel chromatography (eluent: chloroform) to obtain 0.08 g (0.12 mmol) of **1** as colorless prism shaped crystals in 41% yield. mp 215.0–215.8 °C; ^{1}H NMR (400 MHz, $CDCl_3$, ppm) δ 12.5 (s, 1H), 8.33 (s, 1H), 7.89 (s, 1H), 7.62 (d, *J* = 9.3 Hz, 1H), 7.59 (dd, *J* = 7.7, 1.5, Hz, 1H), 7.55 (d, *J* = 7.4 Hz, 2H), 7.42 (dd, *J* = 9.3, 1.7, Hz, 1H), 7.40 (t, *J* = 7.4 Hz, 2H), 7.33-7.23 (m, 4H), 7.05 (d, *J* = 7.7 Hz, 1H), 6.90 (t, *J* = 7.7 Hz, 1H), 2.02 (s, 3H), 2.00 (s, 3H); ^{13}C NMR (100 MHz, $CDCl_3$, ppm) δ 157.4, 146.3, 142.8, 142.6, 142.1, 141.4, 137.7, 133.4, 1 30.1, 129.2, 129.2, 128.2, 126.3, 125.9, 125.9, 125.8, 125.8, 124.6, 123.7, 122.5, 121.5, 120.7, 119.2, 117.9, 117.0, 116.1, 107.3, 14.7, 14.7; ^{19}F NMR (376 MHz, $CDCl_3$, ppm) δ −113.1 (s, 2F), −113.3 (s, 2F), −135.0 (s, 2F); HRMS (MALDI–TOF) *m*/*z*: calcd for $C_{34}H_{22}F_6N_2OS_2$, 652.1078; found, 652.1072.

Supporting Information

Supporting Information File 1

X-ray analysis data of a single crystal of **1o**.
[https://www.beilstein-journals.org/bjoc/content/supplementary/1860-5397-15-217-S1.pdf]

Supporting Information File 2

Movie 1, quenching rate dependence on the environmental conditions.
[https://www.beilstein-journals.org/bjoc/content/supplementary/1860-5397-15-217-S2.mp4]

Supporting Information File 3

Movie 2, fluorescent color change of **1o**.
[https://www.beilstein-journals.org/bjoc/content/supplementary/1860-5397-15-217-S3.mp4]

Acknowledgements

This work was supported by JSPS KAKENHI Grant Number JP26107012 in Scientific Research on Innovative Areas “Photo-synergetics”, the CREST program (JPMJCR17N2) of the Japan Science and Technology Agency. We thank Ms Y. Nishikawa (NAIST) for conducting the mass-spectroscopic measurement. The synchrotron radiation experiments were performed using the BL40XU beamlines of SPring-8 with the approval of the Japan Synchrotron Radiation Research Institute (JASRI) (Proposal No. 2019A1110).

ORCID® iDs

Luna Kono - https://orcid.org/0000-0002-9053-123X
Yuma Nakagawa - https://orcid.org/0000-0002-5636-1396
Ayako Fujimoto - https://orcid.org/0000-0002-6854-4739
Ryo Nishimura - https://orcid.org/0000-0002-6341-6447
Toshiki Mutai - https://orcid.org/0000-0002-5562-7121
Nobuhiro Yasuda - https://orcid.org/0000-0003-4286-4344
Kenichi Koizumi - https://orcid.org/0000-0003-4006-1791
Satoshi Yokojima - https://orcid.org/0000-0002-6555-0877
Shinichiro Nakamura - https://orcid.org/0000-0002-6437-6993
Kingo Uchida - https://orcid.org/0000-0001-5937-0397

Preprint

A non-peer-reviewed version of this article has been previously published as a preprint doi:10.3762/bxiv.2019.66.v1

References

1. Feringa, B. L.; Browne, W. R., Eds. *Molecular Switches;* Wiley-VCH Verlag GmbH: Weinheim, Germany, 2011. doi:10.1002/9783527634408
2. Irie, M.; Fukaminato, T.; Matsuda, K.; Kobatake, S. *Chem. Rev.* **2014,** *114,* 12174–12277. doi:10.1021/cr500249p

3. Fukaminato, T.; Ishida, S.; Métivier, R. *NPG Asia Mater.* **2018,** *10,* 859–881. doi:10.1038/s41427-018-0075-9
4. Irie, M.; Fukaminato, T.; Sasaki, T.; Tamai, N.; Kawai, T. *Nature* **2002,** *420,* 759–760. doi:10.1038/420759a
5. Pu, S.; Ding, H.; Liu, G.; Zheng, C.; Xu, H. *J. Phys. Chem. C* **2014,** *118,* 7010–7017. doi:10.1021/jp5001495
6. Chen, Y.; Xie, N. *J. Mater. Chem.* **2005,** *15,* 3229–3232. doi:10.1039/b506381g
7. Arai, Y.; Ito, S.; Fujita, H.; Yoneda, Y.; Kaji, T.; Takei, S.; Kashihara, R.; Morimoto, M.; Irie, M.; Miyasaka, H. *Chem. Commun.* **2017,** *53,* 4066–4069. doi:10.1039/c6cc10073b
8. Kashihara, R.; Morimoto, M.; Ito, S.; Miyasaka, H.; Irie, M. *J. Am. Chem. Soc.* **2017,** *139,* 16498–16501. doi:10.1021/jacs.7b10697
9. Morimoto, M.; Kashihara, R.; Mutoh, K.; Kobayashi, Y.; Abe, J.; Sotome, H.; Ito, S.; Miyasaka, H.; Irie, M. *CrystEngComm* **2016,** *18,* 7241–7248. doi:10.1039/c6ce00725b
10. Mei, J.; Leung, N. L. C.; Kwok, R. T. K.; Lam, J. W. Y.; Tang, B. Z. *Chem. Rev.* **2015,** *115,* 11718–11940. doi:10.1021/acs.chemrev.5b00263
11. Hong, Y.; Lam, J. W. Y.; Tang, B. Z. *Chem. Soc. Rev.* **2011,** *40,* 5361–5388. doi:10.1039/c1cs15113d
12. Luo, J.; Xie, Z.; Lam, J. W. Y.; Cheng, L.; Tang, B. Z.; Chen, H.; Qiu, C.; Kwok, H. S.; Zhan, X.; Liu, Y.; Zhu, D. *Chem. Commun.* **2001,** 1740–1741. doi:10.1039/b105159h
13. Fukaminato, T.; Kobatake, S.; Kawai, T.; Irie, M. *Proc. Jpn. Acad., Ser. B* **2001,** *77,* 30–35. doi:10.2183/pjab.77.30
14. Williams, D. E.; Rietman, J. A.; Maier, J. M.; Tan, R.; Greytak, A. B.; Smith, M. D.; Krause, J. A.; Shustova, N. B. *J. Am. Chem. Soc.* **2014,** *136,* 11886–11889. doi:10.1021/ja505589d
15. Barbatti, M.; Aquino, A. J. A.; Lischka, H.; Schriever, C.; Lochbrunner, S.; Riedle, E. *Phys. Chem. Chem. Phys.* **2009,** *11,* 1406–1415. doi:10.1039/b814255f
16. Lochbrunner, S.; Schultz, T.; Schmitt, M.; Shaffer, J. P.; Zgierski, M. Z.; Stolow, A. *J. Chem. Phys.* **2001,** *114,* 2519–2522. doi:10.1063/1.1345876
17. Ormson, S. M.; Brown, R. G. *Prog. React. Kinet.* **1994,** *19,* 45–91.
18. Khan, A. U.; Kasha, M. *Proc. Natl. Acad. Sci. U. S. A.* **1983,** *80,* 1767–1770. doi:10.1073/pnas.80.6.1767
19. Mutai, T.; Tomoda, H.; Ohkawa, T.; Yabe, Y.; Araki, K. *Angew. Chem., Int. Ed.* **2008,** *47,* 9522–9524. doi:10.1002/anie.200803975
20. Shono, H.; Ohkawa, T.; Tomoda, H.; Mutai, T.; Araki, K. *ACS Appl. Mater. Interfaces* **2011,** *3,* 654–657. doi:10.1021/am200022z
21. Kim, D.; Kwon, J. E.; Park, S. Y. *Adv. Opt. Mater.* **2016,** *4,* 790–797. doi:10.1002/adom.201500699
22. Nakahama, T.; Mukaiyama, T.; Kitagawa, D.; Kobatake, S. *Res. Chem. Intermed.* **2017,** *43,* 5321–5336. doi:10.1007/s11164-017-2928-1
23. Lim, S.-J.; Seo, J.; Park, S. Y. *J. Am. Chem. Soc.* **2006,** *128,* 14542–14547. doi:10.1021/ja0637604
24. Browne, W. R.; de Jong, J. J. D.; Kudernac, T.; Walko, M.; Lucas, L. N.; Uchida, K.; van Esch, J. H.; Feringa, B. L. *Chem. – Eur. J.* **2005,** *11,* 6430–6441. doi:10.1002/chem.200500163
25. Mutai, T.; Ohkawa, T.; Shono, H.; Araki, K. *J. Mater. Chem. C* **2016,** *4,* 3599–3606. doi:10.1039/c6tc00376a
26. Sumi, T.; Takagi, Y.; Yagi, A.; Morimoto, M.; Irie, M. *Chem. Commun.* **2014,** *50,* 3928–3930. doi:10.1039/c4cc00396a
27. Lide, D. R. *CRC Handbook of Chemistry and Physics,* 95th ed.; CRC Press: New York, NY, U.S.A., 2015; 3-1.
28. Kobatake, S.; Uchida, K.; Tsuchida, E.; Irie, M. *Chem. Commun.* **2002,** 2804–2805. doi:10.1039/b208419h
29. Su, J.; Fukaminato, T.; Placial, J.-P.; Onodera, T.; Suzuki, R.; Oikawa, H.; Brosseau, A.; Brisset, F.; Pansu, R.; Nakatani, K.; Métivier, R. *Angew. Chem., Int. Ed.* **2016,** *55,* 3662–3666. doi:10.1002/anie.201510600
30. Ishida, S.; Kitagawa, D.; Kobatake, S.; Kim, S.; Kurihara, S.; Fukaminato, T. *Chem. Commun.* **2019,** *55,* 5681–5684. doi:10.1039/c9cc02441g
31. Demeter, A. *J. Phys. Chem. A* **2014,** *118,* 9985–9993. doi:10.1021/jp507626h
32. *Gaussian 09,* Revision C.01; J. Gaussian, Inc.: Wallingford, CT, U.S.A., 2010.
33. Becke, A. D. *J. Chem. Phys.* **1993,** *98,* 5648–5652. doi:10.1063/1.464913
34. Becke, A. D. *Phys. Rev. A* **1988,** *38,* 3098–3100. doi:10.1103/physreva.38.3098
35. Lee, C.; Yang, W.; Parr, R. G. *Phys. Rev. B* **1988,** *37,* 785–789. doi:10.1103/physrevb.37.785
36. Tomasi, J.; Mennucci, B.; Cammi, R. *Chem. Rev.* **2005,** *105,* 2999–3094. doi:10.1021/cr9904009
37. *Higashi, T. ABSCOR;* Rigaku Corporation: Tokyo, Japan, 1995.

License and Terms

This is an Open Access article under the terms of the Creative Commons Attribution License (http://creativecommons.org/licenses/by/4.0). Please note that the reuse, redistribution and reproduction in particular requires that the authors and source are credited.

The license is subject to the *Beilstein Journal of Organic Chemistry* terms and conditions: (https://www.beilstein-journals.org/bjoc)

The definitive version of this article is the electronic one which can be found at: doi:10.3762/bjoc.15.217

BEILSTEIN JOURNAL OF ORGANIC CHEMISTRY

Excited state dynamics for visible-light sensitization of a photochromic benzil-subsituted phenoxyl-imidazolyl radical complex

Yoichi Kobayashi[1], Yukie Mamiya[2], Katsuya Mutoh[2], Hikaru Sotome[3], Masafumi Koga[3], Hiroshi Miyasaka[3] and Jiro Abe[*2]

Full Research Paper

Open Access

Address:
[1]Department of Applied Chemistry, College of Life Sciences, Ritsumeikan University, 1-1-1 Nojihigashi, Kusatsu, Shiga 525-8577, Japan, [2]Department of Chemistry, School of Science and Engineering, Aoyama Gakuin University, 5-10-1 Fuchinobe, Chuo-ku, Sagamihara, Kanagawa 252-5258, Japan and [3]Division of Frontier Materials Science and Center for Promotion of Advanced Interdisciplinary Research, Graduate School of Engineering Science, Osaka University, Toyonaka, Osaka 560-8531, Japan

Email:
Jiro Abe[*] - jiro_abe@chem.aoyama.ac.jp

* Corresponding author

Keywords:
biradical; energy transfer; photochromism; sensitizer; transient absorption spectroscopy

Beilstein J. Org. Chem. **2019,** *15,* 2369–2379.
doi:10.3762/bjoc.15.229

Received: 22 June 2019
Accepted: 27 September 2019
Published: 04 October 2019

This article is part of the thematic issue "Molecular switches".

Guest Editor: W. Szymanski

© 2019 Kobayashi et al.; licensee Beilstein-Institut.
License and terms: see end of document.

Abstract

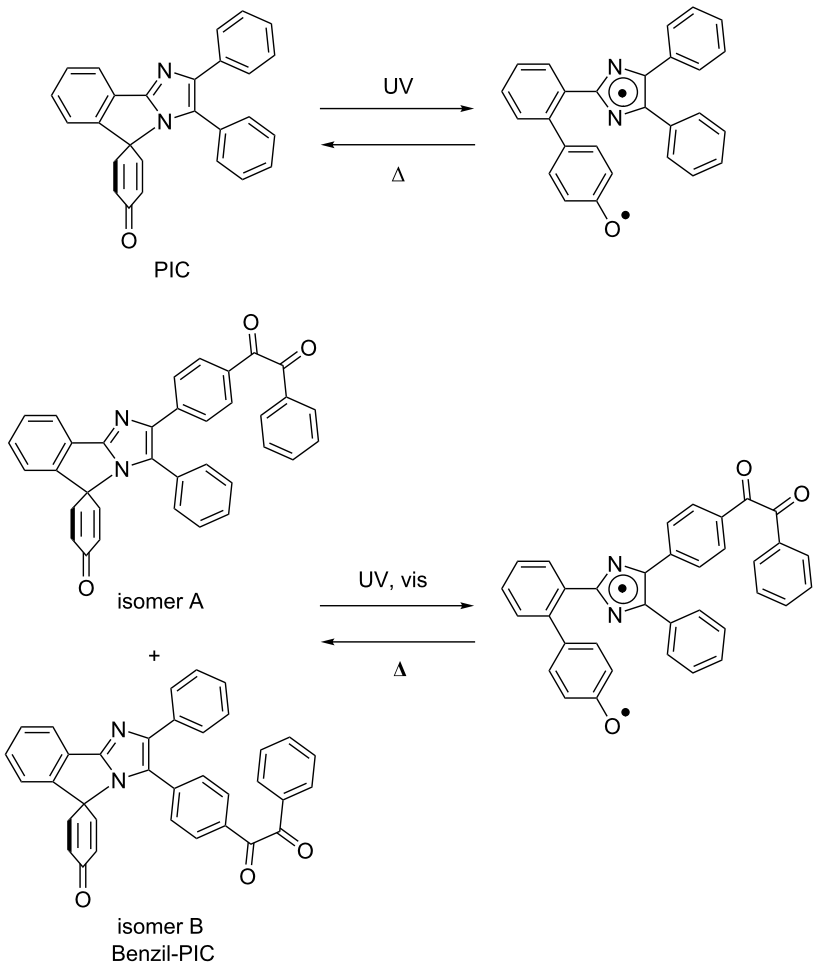
Visible-light sensitized photoswitches have been paid particular attention in the fields of life sciences and materials science because long-wavelength light reduces photodegradation, transmits deep inside of matters, and achieves the selective excitation in condensed systems. Among various photoswitch molecules, the phenoxyl-imidazolyl radical complex (PIC) is a recently developed thermally reversible photochromic molecule whose thermal back reaction can be tuned from tens of nanoseconds to tens of seconds by rational design of the molecular structure. While the wide range of tunability of the switching speed of PIC opened up various potential applications, no photosensitivity to visible light limits its applications. In this study, we synthesized a visible-light sensitized PIC derivative conjugated with a benzil unit. Femtosecond transient absorption spectroscopy revealed that the benzil unit acts as a singlet photosensitizer for PIC by the Dexter-type energy transfer. Visible-light sensitized photochromic reactions of PIC are important for expanding the versatility of potential applications to life sciences and materials science.

Introduction

Photochromism, which is defined as the reversible transformation of a chemical species between two structural isomers by light, has been extensively studied over decades [1-4]. Recently, visible-light sensitized photochromic materials have been paid particular attention in the fields of life sciences and materials science because long-wavelength light reduces photodegradation, transmits deep inside of matters, and achieves the selective excitation in condensed systems [5-12]. General strategies

for the sensitization of the photochromic reactions to visible light are to extend the π-conjugation and to utilize photosensitizers. Especially, triplet photosensitizers, which form the triplet state of a molecule by the triplet–triplet energy transfer, have been frequently used in photoresists, photodynamic therapy, and photocatalysts because the lowest triplet excited (T_1) state can be formed by light whose energy is smaller than that of the optically active transition [13-16]. However, photochromic reactions of some systems do not proceed via the T_1 state. For example, it was reported that the photochromic reaction of hexaarylbiimidazole (HABI), which is a well-known radical-dissociation-type photochromic molecule [17-20], is not sensitized by triplet photosensitizers [21-23]. On the other hand, it was reported that singlet photosensitizers effectively sensitize the photochromic reaction of HABI to the visible light [21,23]. While the S_0–S_1 transition of HABI is located at the visible-light region, the transition is optically forbidden. Therefore, the photochromic reaction of HABI without singlet photosensitizers occurs via the S_0–S_n transition, which is located at the UV region. On the other hand, singlet photosensitizers efficiently transfer the visible-light energy to the optically inactive S_1 state of HABI, and thus the photochromic reaction of HABI proceeds with visible light.

The phenoxyl-imidazolyl radical complex (PIC, Scheme 1) is one of the recently developed rate-tunable T-type photochromic compounds which reversibly generate an imidazolyl radical and a phenoxyl radical (biradical form) in a molecule upon UV light irradiation [24]. The great advantage of PIC is the tunability of the thermal back reaction from tens of nanoseconds to tens of seconds by simple and rational molecular design [25]. The wide ranges of thermal back reactions of photoswitches expand the potential applications of photochromic materials such as to dynamic holographic display [26-28], switchable fluorescent markers [29-31], and anticounterfeit inks. However, PIC is photosensitive only in the UV region, which limits the application fields. It was reported that the S_0–S_1 transition of PIC is optically forbidden and is located at the visible-



Scheme 1: Photochromic reaction schemes of (a) PIC and (b) Benzil-PIC.

light region as similar to that of HABI [32]. It is expected that the photochromic reaction of PIC occurs via the optically forbidden S_1 state as similar to other radical dissociation-type photochromic molecules such as HABI and pentaarylbiimidazole (PABI) [33-35]. Therefore, if we could substitute a singlet photosensitizer unit to PIC, the visible-light sensitivity could be achieved by singlet–singlet energy transfer. The visible-light sensitization of PIC expands the versatility of the rate-tunable photoswitches of PIC systems.

In this study, we synthesized a novel PIC derivative conjugated with a visible-light photosensitizer (Benzil-PIC, Scheme 1) and investigated the excited state dynamics. We used a benzil framework as a photosensitizer unit because aryl ketones have been widely used as visible-light photosensitizers [36]. While most of aryl ketones were used as triplet photosensitizers, the benzil unit in the present study acts as a singlet photosensitizer. The detail of the sensitization processes was investigated by wide ranges of time-resolved spectroscopies.

Results and Discussion

Steady-state absorption spectra

The synthetic procedure of Benzil-PIC is described in the Experimental part. Benzil-PIC has two structural isomers (isomer A and isomer B) as shown in Scheme 1. These isomers were separated by high-performance liquid chromatography (HPLC), and each isomer was characterized by steady-state absorption spectra and time-dependent density functional theory (TDDFT) calculations as shown below. Figure 1 shows the steady-state absorption spectra of the two isomers of Benzil-PIC and PIC in benzene at 298 K.

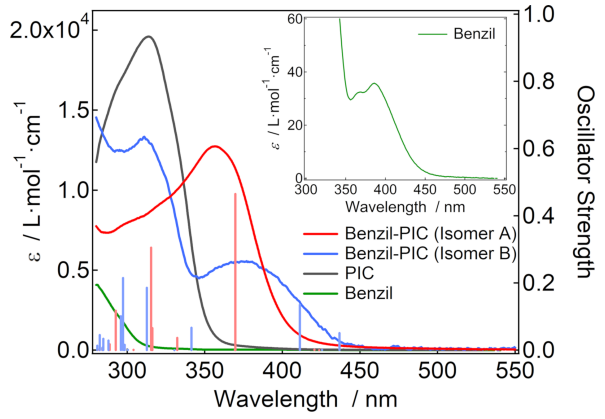


Figure 1: Absorption spectra of PIC, benzil, and the two isomers of Benzil-PIC in benzene at 298 K. The inset shows the magnified absorption spectrum of benzil in benzene. The calculated spectra (MPW1PW91/6-31+G(d,p)//M05-2X/6-31+G(d,p) level of the theory) of two isomers of Benzil-PIC are shown as the vertical lines.

While the absorption of PIC appears only at wavelength shorter than 350 nm, those of the two isomers of Benzil-PIC are extended to the visible-light region. The simulated absorption spectra by TDDFT calculations (MPW1PW91/6-31+G(d,p)//M05-2X/6-31+G(d,p) level of the theory) are also shown as the vertical lines in Figure 1. The simulated absorption spectra well explain the experimental absorption spectra of the two isomers. Therefore, the absorption spectra of isomers A and B were assigned as shown in Figure 1. The absorption band at 357 nm of isomer A is assigned to the electronic transition from the molecular orbital distributed around the triphenylimidazole unit (highest occupied molecular orbital: HOMO) to that around the benzil unit (the second lowest unoccupied molecular orbital: LUMO+1) (Figure S14, Supporting Information File 1). On the other hand, the absorption band at 375 nm of isomer B is assigned to the electronic transition from the molecular orbital distributed around the triphenylimidazole unit (HOMO) to that around the benzil unit and the phenoxyl unit (mainly the lowest unoccupied molecular orbital: LUMO and LUMO+1, Figure S15, Supporting Information File 1). While the HOMOs of isomer A and isomer B are very similar, the LUMO and LUMO+1 of isomer B are more delocalized than the LUMO+1 of isomer A, suggesting that the LUMO and LUMO+1 levels of isomer B are lower than those of isomer A. This would be the most plausible reason why isomer B has an absorption band at the longer wavelength than isomer A.

PIC generates the biradical species upon UV-light irradiation and shows the broad transient absorption spectrum over the visible- to near infrared-light regions. The half-life of the thermal back reaction of the biradical in benzene is 250 ns (the lifetime is 360 ns) at 298 K. To investigate the difference in the photochromic properties between two isomers of Benzil-PIC, we measured the absorption spectra and nanosecond-to-microsecond transient absorption dynamics of isomer A in benzene upon repeated irradiation of 355 nm nanosecond laser pulses (355 nm, 7 mJ pulse^{-1}, Figure S8a, Supporting Information File 1). The absorption band at 357 nm of isomer A gradually decreases upon irradiation of the nanosecond laser pulses and the absorption edge alternatively shifts to the longer wavelength. It indicates that the irradiation of the UV pulse induces the photochromic reactions (breaking of the C–N bond) and interconverts between isomer A and isomer B. The system reaches the photostationary state (PPS) within 696 shots of the laser pulses. The ratio of isomer A and isomer B is estimated to be 22:78 by the curve fitting of the absorption spectrum at the PPS with those of pure isomer A and isomer B (Figure S9, Supporting Information File 1). Figure S8b (Supporting Information File 1) shows the nanosecond-to-microsecond transient absorption dynamics of isomer A probed at 650 nm under repeated irradiation with the 355 nm nanosecond laser pulses at

298 K. While the transient absorption dynamics of isomer A accumulated by 8 shots are slightly fluctuated most probably because of the low signal-to-noise ratio, the decay kinetics do not change by repeated irradiation with UV-light pulses. It shows that both isomers generate the same biradical form by UV-light irradiation as shown in Scheme 1, indicating that the excited state dynamics of the two isomers of Benzil-PIC after the bond breaking are identical. Therefore, the mixture solution of the two isomers was used for further time-resolved spectroscopic measurements.

Nanosecond-to-microsecond transient absorption spectra

To investigate the photochromic properties of Benzil-PIC, the nanosecond-to-microsecond transient absorption measurements were conducted by the randomly interleaved pulse train (RIPT) method [37]. Figure 2a shows the transient absorption spectra of Benzil-PIC in benzene (2.9×10^{-4} M) under argon atmosphere at room temperature excited with a 355 nm picosecond laser pulse (pulse duration = 25 ps, intensity = 30 μJ pulse^{-1}). At 0.5 ns after the excitation, two broad transient absorption bands are observed at 660 and <450 nm. The spectral shape is more or less similar to that of the biradical form of PIC [24], indicating Benzil-PIC generates the biradical by 355 nm light irradiation. The transient absorption spectra gradually decay with a time scale of hundreds of nanoseconds and another absorption band at 580 nm remains after 900 ns. The transient absorption dynamics at 590 nm was fitted with a biexponential decay function and the lifetimes are estimated to be 260 and 820 ns (Figure 2c). On the other hand, while the transient absorption spectra of Benzil-PIC in benzene under air show the same transient absorption spectrum as under argon at 0.5 ns, the transient absorption band at 580 nm is not observed in the time scale of microseconds. The transient absorption dynamics at 590 nm can be fitted with a single exponential decay function and the lifetime is 220 ns (Figure 2d), which is almost identical to that of the fast decay component under argon atmosphere. Because the transient absorption spectrum at 0.5 ns is similar to that of PIC and because the fast decay component does not depend on the molecular oxygen, the fast and slow decay components can be

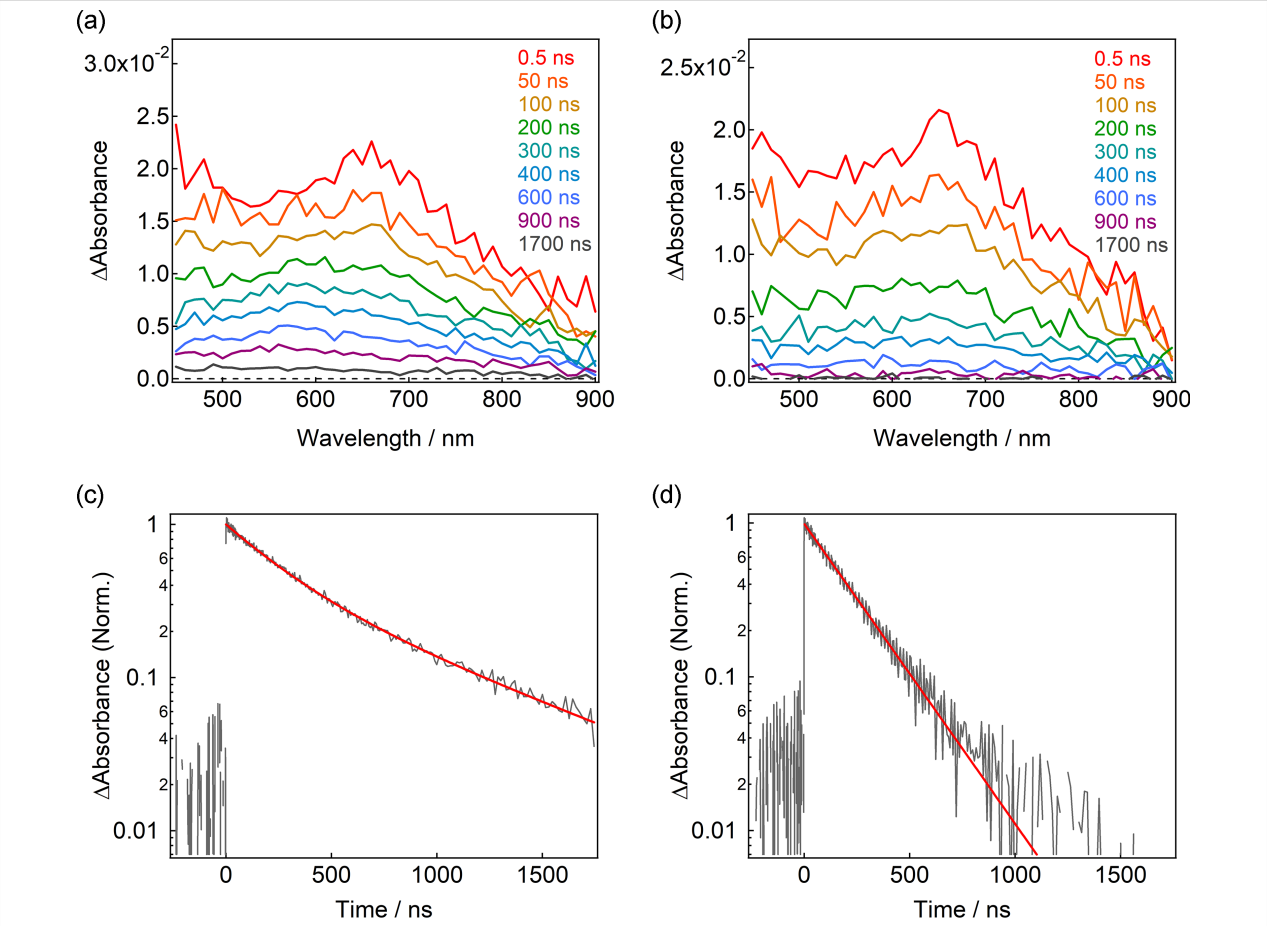


Figure 2: Nanosecond-to-microsecond transient absorption spectra of Benzil-PIC in benzene under (a) argon and (b) air at room temperature excited with a 355 nm picosecond laser pulse (30 μJ pulse^{-1}). Decay profiles of the transient species of Benzil-PIC in benzene probed at 590 nm under (c) argon and (d) air at the same conditions.

assigned to the biradical form generated by the C–N bond breaking and the T_1 state of Benzil-PIC, respectively. It is worth mentioning that the T_1 state of Benzil-PIC would be formed by some portions of the S_1 of the benzil unit where the energy transfer did not occur to the PIC unit (discussed below).

Femtosecond-to-nanosecond transient absorption spectra

To investigate the sensitization process by the benzil unit of Benzil-PIC in detail, we performed femtosecond transient absorption measurements using a 400 nm excitation pulse. The instrumental response function is ≈170 fs. It is noted that the excitation wavelength for femtosecond transient absorption spectroscopy (400 nm) is slightly different from that for nanosecond transient absorption spectroscopy (355 nm). The difference may affect the ratio of isomer A and isomer B at the photostationary state (PSS) and initial relaxation kinetics at sub-picosecond time scales. Benzil was used for a reference sample. Figure 3a shows the time evolution of the transient absorption spectra of benzil in benzene (6.8×10^{-2} M).

At 0.3 ps after the excitation, a transient absorption band is observed at 546 nm. The transient absorption band continuously shifts to 531 nm and a shoulder is observed at 500 nm. It was reported that the spectral shift of the transient absorption spectra of benzil at the sub-picosecond time scale was assigned to the structural change from the skewed structure to the planar structure [38]. Solvent and vibrational relaxations would also take place in this time scale. After the rapid spectral shift, the transient absorption spectra are preserved until 100 ps. This

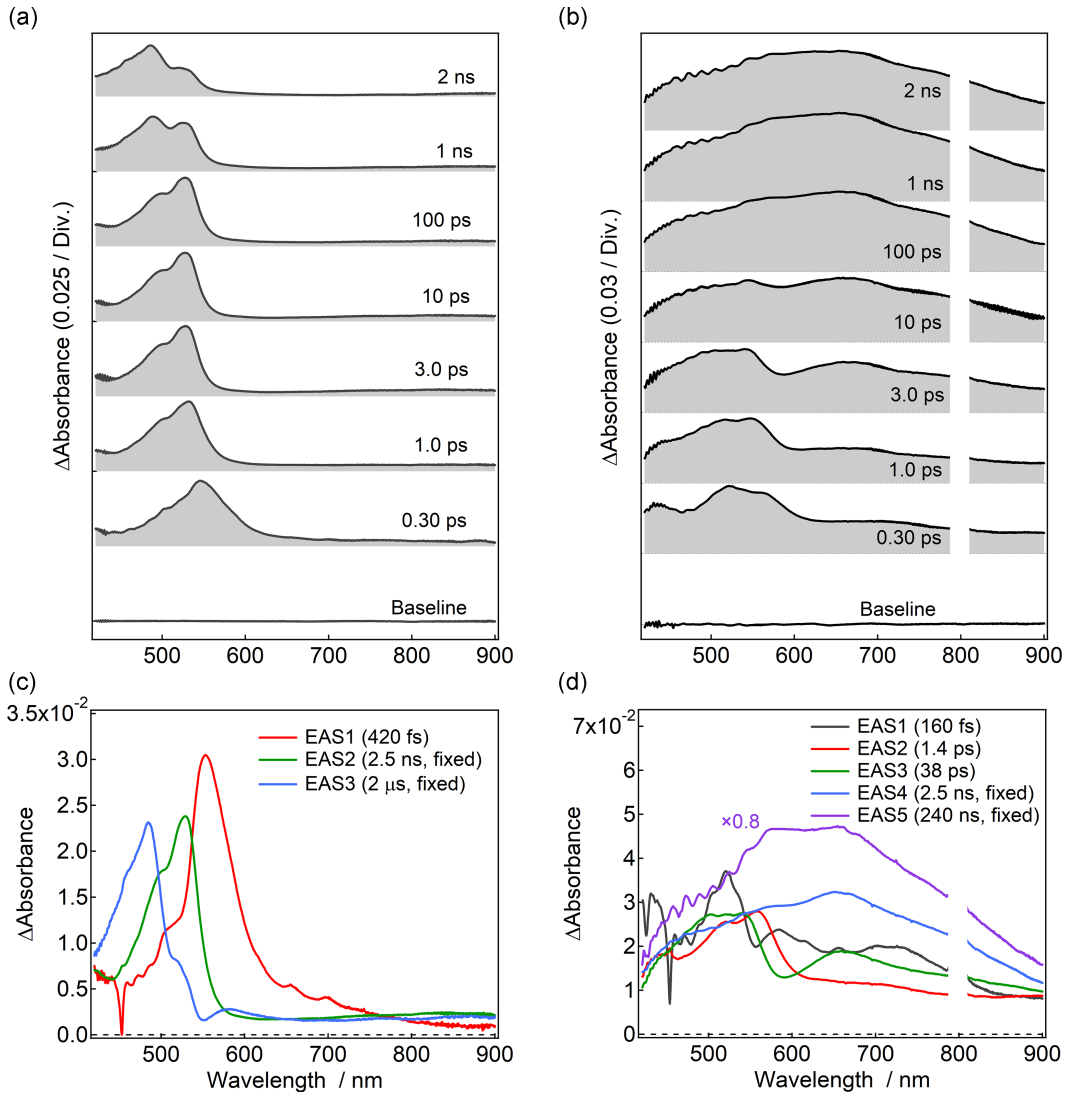


Figure 3: Femtosecond-to-nanosecond transient absorption spectra of (a) benzil and (b) Benzil-PIC (right) in benzene at room temperature excited at 400 nm (100 nJ pulse^{-1}, ≈100 fs laser pulse). The evolution associated spectra (EAS) of (c) benzil and (d) Benzil-PIC in benzene at the same experimental conditions. The signal around 800 nm of Benzil-PIC was omitted because of the second-order diffraction of the excitation pulse.

signal can be assigned to the excited state absorption from the lowest vibrational level of the S_1 state. The transient absorption band at 531 nm gradually decreases with a time scale of nanoseconds and another transient absorption band appears at 485 nm. The transient absorption band at 485 nm was assigned to the T_1 state according to previous studies [39-41]. The quantum yield of the formation of the triplet excited state was reported as 92% [42], indicating that most of the S_1 state is converted to the T_1 state in benzil.

Figure 3b shows the transient absorption spectra of Benzil-PIC in benzene (2.2×10^{-3} M) excited at 400 nm with a femtosecond laser pulse. The signal around 800 nm was omitted because it was perturbed by the second order diffraction of the excitation pulse around 400 nm. At 0.3 ps after the excitation, two transient absorption bands are observed at 520 and 563 nm, which are most probably assigned to the transient absorption of the benzil unit of Benzil-PIC. The absorption is slightly shifted to the red as compared to those of benzil probably due to the extended π-conjugation of the benzil unit connected to the PIC unit. The two peaks continuously shift to the shorter wavelength (503 and 543 nm, respectively) with a time scale of picoseconds as similar to that of benzil, which supports that these bands are originated from the benzil unit. In addition to the two bands, a broad absorption band over the visible-light region is also observed at 0.3 ps. Because the spectral band shape of this absorption band is similar to that observed in Figure 2, this absorption band is ascribable to the biradical form of PIC, which was directly excited at 400 nm and underwent the rapid radical formation in the sub-picosecond time range. The instantaneous formation of the biradical form under these excitation conditions suggests that a peak at ≈430 nm at 0.3 ps would be most probably assigned to the S_1 state of the PIC unit. In addition to this rapid appearance of the biradical form, the gradual increase of the absorption due to the biradical is observed in picoseconds to tens of picoseconds region, together with the decay of the S_1 state of the benzil unit. This slow process of the biradical formation indicates the energy transfer from the benzil unit to the PIC unit. The amplitude of the increased biradical form with a time scale of tens of picoseconds is larger than the instantaneously generated biradical form at the early time scale, indicating that the energy transfer process is dominant for the photochromic reaction of Benzil-PIC under the excitation with 400 nm. In the nanoseconds time region, the absorption around 580 nm slightly increases with a time scale of nanoseconds.

To elucidate the details of the reaction dynamics, we performed global analyses with singular value decomposition (SVD) with the Glotaran program (http://glotaran.org) [43]. We tentatively used the three-state sequential kinetic model for benzil (Equation 1) and the five-state sequential kinetic model for Benzil-PIC (Equation 2) convolved with Gaussian pulse. The detail of the SVD analyses are shown in Supporting Information File 1.

$$[\mathrm{A}] \rightarrow [\mathrm{B}] \rightarrow [\mathrm{C}] \rightarrow \text{ground state} \quad (1)$$

$$[\mathrm{A}] \rightarrow [\mathrm{B}] \rightarrow [\mathrm{C}] \rightarrow [\mathrm{D}] \rightarrow [\mathrm{E}] \rightarrow \text{ground state} \quad (2)$$

The evolution associated spectra (EAS) thus obtained indicate the resolved transient absorption spectra into each component of the kinetic models. Because the time window of our measurements was limited to 2 ns, it was difficult to determine the time constant of nanosecond time scale exactly. Therefore, the lifetimes of the intersystem crossing (ISC) of benzil and the benzil unit of Benzil-PIC were fixed to a reported value of benzil (2.5 ns) [44]. The lifetime of the T_1 state of benzil was fixed to 2.0 μs according to the nanosecond-to-microsecond transient absorption spectroscopy. In the benzil system, time constants of three EAS are revealed to be 420 fs, 2.5 ns (fixed), and 2.0 μs (fixed), respectively (Figure 3c). Each EAS species (A to E in the Equation 1 and Equation 2) is denoted as EAS1 to EAS5 in the order of the time constants as shown in Figure 3c and Figure 3d. The fastest time constant of benzil reflects the structural change from the skewed structure to the planar structure and solvent and vibrational relaxations. However, it should be noted that the lifetime of 420 fs is the apparent lifetime because the conformational change from the skewed to the planar structure at sub-picosecond time scale induces the continuous spectral shift. Because the present SVD global analyses do not consider the continuous spectral shift, it is difficult to extract the exact time constant at the early stage of the transient absorption spectra. The EAS with time constants of 2.5 ns and 2.0 μs are safely assigned to the absorption spectra of the S_1 and the T_1 states, respectively, because of the similarity of the spectra to those reported previously [39,40].

In the Benzil-PIC system, the time constants of five EAS were obtained to be 160 fs, 1.4 ps, 38 ps, 2.5 ns (fixed), and 240 ns (fixed), respectively (Figure 3d). EAS1 has 4 peaks located at 430, 520, 582, ≈710 nm, respectively. The absorption bands at 430 and ≈710 nm are ascribable to the S_1 state of the PIC unit and the biradical generated instantaneously, respectively. It indicates that the biradical was also formed by the direct excitation of the PIC unit with 400 nm light. The spectral evolution from EAS1 (160 fs, grey line in Figure 3d) to EAS2 (1.4 ps, red line in Figure 3d) shows the C–N bond cleavage of the PIC unit and the spectral shift due to the benzil unit (from 582 nm to 556 nm). In PABI, which is a similar photochromic molecule to PIC, it was reported that the C–N bond fission occurs with the time constant of 140 fs and the broad absorption assigned to the

biradical form was formed with a time constant of ≈2 ps [45]. The similarity of the time constant of the bond breaking to that of EAS1 supports that the C–N bond is cleaved by the direct excitation of the PIC unit. The spectral evolution from EAS2 (1.4 ps) to EAS3 (38 ps, green in Figure 3d) shows the continuous spectral shift due to the benzil unit and the increase in the absorption due to the biradical form (660 nm). Because the continuous spectral shift due to the benzil unit is still observed in EAS2 (1.4 ps), it is suggested that the structural change of the benzil unit of Benzil-PIC is somehow slightly decelerated as compared to that of benzil (420 fs). However, it should be mentioned that it was difficult to resolve the structural change of the benzil unit and the formation process of the PIC unit by the present SVD analysis.

The spectral evolution from EAS3 (38 ps) to EAS4 (2.5 ns, fixed, blue line in Figure 3d) shows the decay of the S_1 state of the benzil unit and the alternative increase in the biradical form of the PIC unit. This result clearly shows that the energy of the S_1 state of the benzil unit is used for the photochromic reaction of the PIC unit. It is important to note that the S_0–S_1 transition energy of PIC, which is optically forbidden, was reported to be 2.8 eV (≈440 nm) [32]. These results suggest that the energy transfer occurs from the S_1 state of the benzil unit to the ground state of the PIC unit with the time constant of 38 ps. Since the bond-breaking process from the S_1 state of the PIC unit would be much faster than this time scale (hundreds of femtoseconds), the time constant of 38 ps reflects the singlet–singlet energy transfer process from the benzil unit to the PIC unit. It should be noted that the fluorescence quantum yield of benzil was quite low (<0.001) [43] and the PIC unit has no absorption in the emission wavelength of the benzil. Accordingly, the effective energy transfer by the Förster mechanism is not plausible. The energy transfer of the 38 ps time constant is probably due to the Dexter mechanism at weak or very weak coupling regimes owing to the overlap of the wave functions of the benzil and the PIC units in the excited state.

The spectral evolution from EAS4 (2.5 ns, fixed) to EAS5 (240 ns, fixed, purple line in Figure 3d) shows the increase in the absorption around 580 nm. Although both lifetimes of EAS4 and EAS5 are longer than the measured time window (≈2 ns), the spectral difference around 580 nm at 10–100 ps and that at nanosecond time scales enable to resolve these spectra. The increased absorption band is similar to the transient absorption band assigned to the T_1 state of Benzil-PIC (Figure 2a). It indicates that the spectral evolution over nanosecond time scale is ascribable to ISC of the benzil unit. It should be noted, however, that this slow rise of the T_1 state of the benzil unit by ISC indicates that some portions of the benzil unit do not undergo the effective energy transfer to the PIC unit because the S_1 state of the benzil was deactivated with the time constant of 38 ps. Although the clear mechanism is not yet elucidated at the present stage of the investigation, the reason for the two relaxation pathways (energy transfer and ISC) from the S_1 state of the benzil unit of Benzil-PIC might be due to the difference in the mutual orientation of benzil and PIC units including the structural isomers (isomer A and isomer B). As was discussed above, the energy transfer is due to the overlap of the wave function of the both units, of which mechanism might be sensitive to the difference in the mutual orientation.

Effect of triplet–triplet energy transfer

Ultrafast spectroscopy revealed that the benzil unit acts as a singlet photosensitizer for Benzil-PIC by the Dexter-type energy transfer. It was reported that benzil was often used as a triplet photosensitizer because the quantum yield for the T_1 state formation is 92% [42]. To investigate the possibility for the triplet–triplet energy transfer process in Benzil-PIC, we performed two experiments. Firstly, we measured the phosphorescence spectra of benzil and PIC in EPA (diethyl ether/isopentane/ethanol 5:5:2) at low temperature to estimate the energy levels of the T_1 states of benzil and PIC. In the conventional emission measurement setups at low temperature, both fluorescence and phosphorescence are observed upon irradiation of excitation light. To extract the phosphorescence spectra, the excitation light (continuous wave laser, 355 nm, 1 mW) was chopped at 1 Hz and the afterglow emission under blocking the beam was accumulated as the phosphorescence spectra. Figure 4 shows the phosphorescence spectra of benzil in EPA at 77 and 100 K.

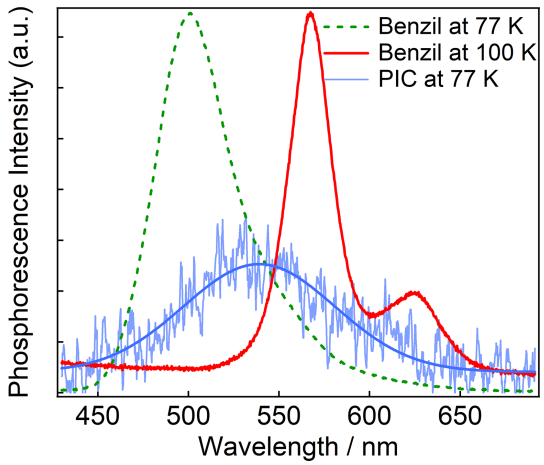


Figure 4: Phosphorescence spectra of benzil at 77 K and 100 K and that of PIC at 77 K in EPA. A blue solid line on the phosphorescence spectra of PIC is the Gaussian fitting line.

While the phosphorescence spectrum of benzil at 77 K is broad and observed at 500 nm, that at 100 K becomes sharper and the

peak is shifted to 567 nm with a vibrational fine structure at 625 nm. The spectral shift with the increase in temperature is most probably due to the rigidity of the environment of molecules. At 77 K, it is expected that the solvent is too rigid for benzil to change the conformation in the excited state, namely, the conformation of benzil is fixed to the skewed conformation. On the other hand, it is expected that the increase in the temperature to 100 K softens the rigid matrix and allows the benzil to form the planar conformation at the T_1 state. The energy level of the T_1 state of benzil was estimated from the phosphorescence at 100 K because the T_1 state of benzil in solution forms the planar conformation. The energy level of the T_1 state was determined by an edge of the high energy side of the phosphorescence, where a tangent line crosses the *x*-axis. The energy level of the T_1 state of benzil is estimated to be 53 kcal mol^{-1}, which is consistent with a reported value (53.7 kcal mol^{-1}) [38]. On the other hand, the phosphorescence of PIC was only observed at 77 K and the signal is very weak. Because the conformation of PIC is relatively rigid, we tentatively estimated the T_1 state energy level from the phosphorescence at 77 K. The T_1 state energy level of PIC is estimated to be 63 kcal mol^{-1}. It suggests that the T_1 state energy level of benzil is slightly lower than that of PIC.

Moreover, the triplet photosensitization was examined by the microsecond transient absorption measurements of the mixture solution of benzil and PIC in benzene (3.7×10^{-3} M and 2.8×10^{-5} M for benzil and PIC, respectively). A 450 nm excitation pulse was used to selectively excite benzil. The transient absorption dynamics of the mixture solution of benzil and PIC probed at 500 nm is identical to that of benzil, which is assigned to the T_1 state (Figure S13, Supporting Information File 1). It indicates that the triplet–triplet energy transfer is negligible between the benzil and PIC units. The plausible reason for the negligible triplet–triplet energy transfer is the lower energy level of the T_1 state of the benzil unit than that of the PIC unit.

Conclusion

Figure 5 describes the energy diagram for the photochromic reaction of Benzil-PIC.

While PIC absorbs light of wavelength only shorter than 350 nm, the introduction of the benzil unit extends the photosensitivity of the photochromic reaction to the visible-light region. When Benzil-PIC absorbs visible light, the conformation of the benzil unit, which is the skewed structure in the ground state, quickly changes to the planar structure with a time scale of picoseconds and the S_1 state of the benzil is formed. While the photochromic reaction partly proceeds via the direct excitation of the PIC unit, most of the photochromic reaction is induced via the Dexter-type singlet–singlet energy transfer from

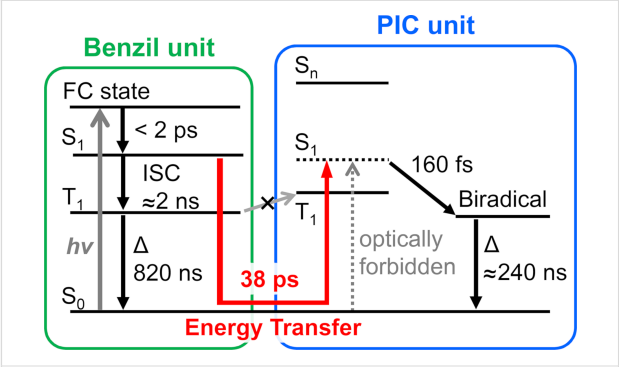


Figure 5: Energy diagram of the visible-light sensitized photochromic reaction of Benzil-PIC.

the benzil to the PIC units with the time constant of 38 ps. The triplet photosensitization does not occur in Benzil-PIC most probably because the triplet energy level of the PIC unit is higher than that of the benzil unit. The clarification of the visible-light sensitization mechanism of PIC is important for expanding the versatility of potential applications of PIC in life and materials sciences.

Experimental

Synthetic procedures

All reactions were monitored by thin-layer chromatography carried out on 0.2 mm E. Merck silica gel plates (60F-254). Column chromatography was performed on silica gel (Silica Gel 60N (spherical, neutral), 40–50 μm, Kanto Chemical Co., Inc.). ^{1}H NMR spectra were recorded at 400 MHz on a Bruker AVANCE III 400 NanoBay. DMSO-d_6 and $CDCl_3$ were used as deuterated solvents. Mass spectra (ESI-TOF-MS) were measured by using a Bruker micrOTOFII-AGA1. All reagents were purchased from TCI, Wako Co. Ltd., Aldrich Chemical Company, Inc. and Kanto Chemical Co., Inc., and were used without further purification.

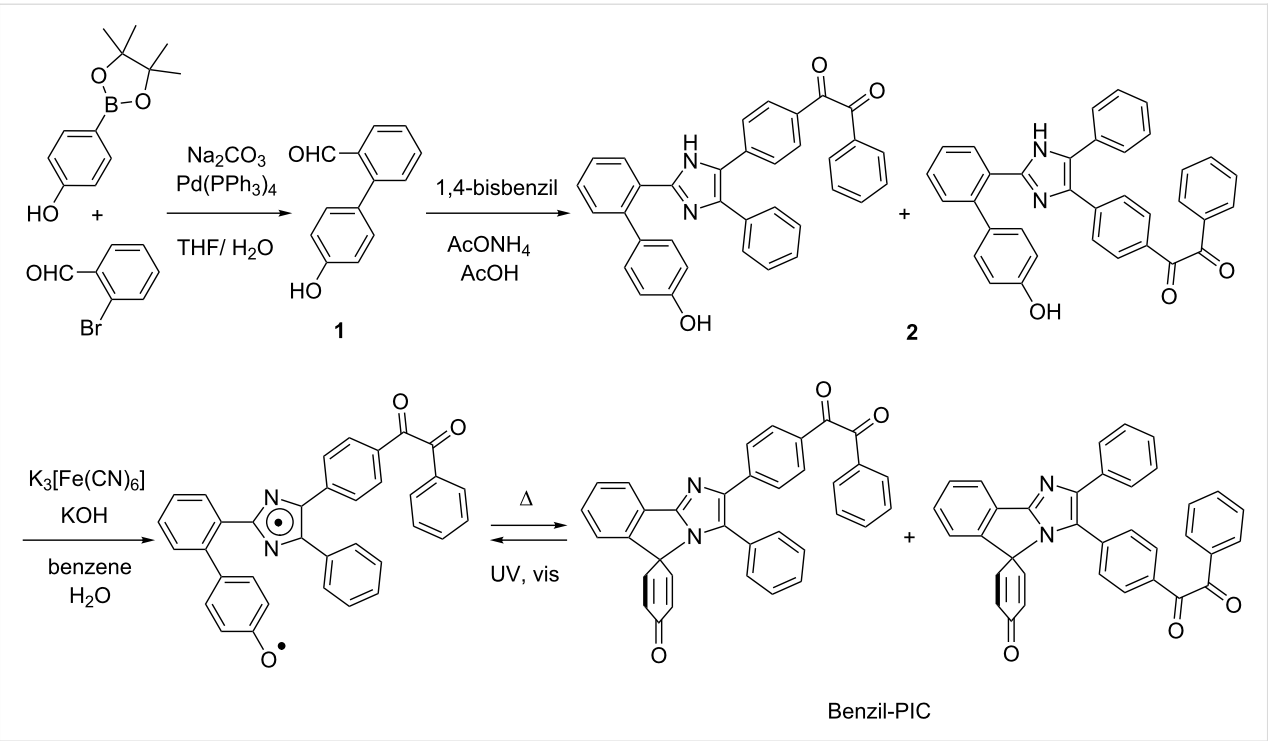
The synthetic procedure of Benzil-PIC is shown in Scheme 2. The synthetic procedure is analogous to that of PIC [24].

4'-Hydroxy-[1,1'-biphenyl]-2-carbaldehyde (**1**)

Compound **1** was prepared according to a literature procedure [24].

1-(4-(2-(4'-Hydroxy-[1,1'-biphenyl]-2-yl)-4-phenyl-1*H*-imidazol-5-yl)phenyl)-2-phenylethane-1,2-dione (**2**)

4'-Hydroxy-[1,1'-biphenyl]-2-carbaldehyde (**1**, 0.088 g, 0.44 mmol), 1,4-bisbenzil (0.176 g, 0.51 mmol) and ammonium acetate (0.240 g, 3.12 mmol) were stirred at 110 °C in acetic acid (2.7 mL) for 6 h. The reaction mixture was cooled and neutralized by aqueous NH_3. The precipitate was filtered and



Scheme 2: Synthetic procedure of Benzil-PIC (analogous to synthesis of PIC in [24]).

washed with water. The crude product was purified by silica gel column chromatography (CH_2Cl_2/AcOEt 20:1 to 3:1), to give the desired product as a mixture of two structural isomers as a yellow solid, 0.0674 g (0.130 mmol, 29%). ^{1}H NMR (DMSO-d_6, 400 MHz) δ 12.21 (s, 1H, one structural isomer), 12.11 (s, 1H, one structural isomer), 9.42 (s, 1H, one structural isomer), 9.40 (s, 1H, one structural isomer), 7.92–7.90 (m, 4H, two structural isomers), 7.81–7.79 (m, 6H, two structural isomers), 7.72–7.69 (m, 5H, two structural isomers), 7.65–7.61 (m, 4H, two structural isomers), 7.53–7.50 (m, 3H, two structural isomers), 7.45–7.37 (m, 10H, two structural isomers), 7.33–7.30 (m, 4H, two structural isomers), 7.07–7.04 (m, 4H, two structural isomers), 6.73–6.69 (m, 4H, two structural isomers); ESI-TOF MS *m*/*z*: $[M + H]^+$ calcd for $C_{35}H_{24}N_2O_3$: 521.1859691; found, 521.1836034.

Benzil-PIC

A solution of potassium ferricyanide (0.968 g, 2.94 mmol) and KOH (0.741 g, 13.2 mmol) in water (3.3 mL) was added to a suspension of **2** (70 mg, 0.14 mmol) in benzene (7.3 mL). After stirring for 3 h at room temperature, the resultant mixture was then extracted with benzene and the organic extract was washed with water and brine. After removal of solvents, the crude product was purified by silica gel column chromatography (AcOEt/hexane 2:3) to give the desired product as a yellow powder, 42 mg (0.081 mmol, 58%). Two structural isomers were separated by HPLC (eluent: CH_3CN/H_2O 7:3). ^{1}H NMR ($CDCl_3$, 400 MHz) (isomer A) δ 8.01 (d, *J* = 7.5 Hz, 1H), 7.97–7.94 (m, 2H), 7.84 (d, *J* = 8.6 Hz, 2H), 7.72 (d, *J* = 8.7 Hz, 2H), 7.66–7.48 (m, 5H), 7.39 (t, *J* = 7.0 Hz, 2H), 7.35–7.29 (m, 3H), 7.16 (d, *J* = 7.7 Hz, 1H), 6.57 (d, *J* = 10.0 Hz, 2H), 6.27 (d, *J* = 10.0 Hz, 2H), (isomer B) δ 7.98–8.02 (m, 3H), 7.89 (d, *J* = 8.4 Hz, 2H), 7.69 (t, *J* = 6.2 Hz, 1H), 7.57–7.48 (m, 8H), 7.40 (t, *J* = 7.6 Hz, 1H), 7.31–7.29 (m, 2H), 7.16 (d, *J* = 7.7 Hz, 1H), 6.64 (d, *J* = 10.0 Hz, 2H), 6.36 (d, *J* = 10.0 Hz, 2H); ESI-TOF MS *m*/*z*: $[M + H]^+$ calcd for $C_{35}H_{22}N_2O_3$, 519.1703190; found, 519.1696883.

Experimental setups

Steady-state measurements

Steady-state absorption spectra were measured with an UV-3600 Plus (SHIMADZU) at room temperature with 1 cm quartz cuvette. Phosphorescence spectra were measured by home-build millisecond time-resolved emission spectrometer at 77 K with nitrogen cryostat (OptistatDN2, Oxford instruments). Briefly, the cooled samples in EPA (diethyl ether/isopentane/ethanol 5:5:2) under argon atmosphere were excited with a 355-nm continuous wave (CW) laser (Genesis CX355 100SLM AO, Coherent) and the emission was detected by EMCCD (Newton DU920P-OE, Andor Technology). The excitation light was blocked with 1 Hz by an optical shutter (76992 and 6995, ORIEL) and the time evolution of the emission spectra was measured to separate the fluorescence and phosphorescence. The shutter was controlled by LabVIEW.

Nanosecond transient absorption measurements

The laser flash photolysis experiments were carried out with a TSP-2000 time resolved spectrophotometer system (Unisoku Co., Ltd.). A 10 Hz Q-switched Nd:YAG laser (Continuum Minilite II) with the third harmonic at 355 nm (pulse width, 5 ns) was employed for the excitation light and the photodiode array was used for a detector. Transient absorption measurements on the nanosecond to microsecond time scale were conducted by the randomly interleaved pulse train (RIPT) method [37]. A picosecond laser, PL2210A (EKSPLA, 1 kHz, 25 ps, 30 μJ pulse^{-1} for 355 nm), and a supercontinuum (SC) radiation source (SC-450, Fianium, 20 MHz, pulse width: 50–100 ps depending on the wavelength, 450–2000 nm) were employed as the pump–pulse and probe sources, respectively. A 355 nm laser pulse was used to excite the samples. The measurements were performed in a benzene solution placed in a 2 mm quartz cell under stirring at room temperature. We used the mixture solution of isomer A and isomer B as was obtained by the synthesis and irradiated a 355 nm pulse laser during the measurements. By considering the duration of the measurements (usually it takes one hour) and the total photon numbers, the system probably reaches the PSS. The ratio of isomer A and isomer B at the PSS upon excitation with the 355 nm pulse is 22:78.

Femtosecond transient absorption measurements

Transient absorption spectra in the visible-light region were measured using a home-built setup. The overall setup was driven by a Ti:Sapphire regenerative amplifier (Spitfire, Spectra-Physics, 802 nm, 1 W, 1 kHz, 100 fs) seeded by a Ti:Sapphire oscillator (Tsunami, Spectra-Physics, 802 nm, 820 mW, 80 MHz, 100 fs). The output of the amplifier was equally divided into two portions. The first one was frequency-doubled with a 50 μm β-barium borate (BBO) crystal, and the generated second harmonics was used for excitation of the sample. The second portion was introduced into a collinear optical parametric amplifier (OPA, TOPAS-Prime, Light Conversion) and converted into the infrared pulse at 1180 nm. This 1180 nm pulse was focused into a 2 mm CaF_2 plate after passing through a delay stage, so as to generate femtosecond white light continuum for the probe pulse. The probe pulse was divided into signal and reference pulses. The signal pulse was guided into the sample and then the both pulses were detected using a pair of multichannel photodiode array (PMA-10, Hamamatsu). The chirping of the white light continuum was evaluated by an optical Kerr effect of carbon tetrachloride and used for the corrections of the spectra. The FWHM of the cross correlation between the excitation and probe pulses was ca. 170 fs. The polarization of the excitation pulse was set to the magic angle with respect to that of the probe pulse. The typical excitation power was 100 nJ pulse^{-1} at the sample position. During the measurement, the sample solution was circulated with a home-made rotation cell with 1 mm optical length. Steady-state absorption spectra were recorded before and after the transient absorption measurement to examine photodegradation of the sample and no permanent change in absorbance was observed. We used the mixture solution of isomer A and isomer B as was obtained by the synthesis and irradiated a 400 nm pulse laser during the measurements. By considering the duration of the measurements (usually takes several hours), the system probably reaches the PSS. Under the irradiation of the 400 nm laser, the ratio of isomer A and isomer B at the PSS depends on each absorption coefficients and the efficiency for the bond cleavage. The absorption coefficients of isomer A and isomer B at 400 nm are 2.1×10^3 M^{-1} cm^{-1} and 4.1×10^3 M^{-1} cm^{-1}, respectively.

Supporting Information

Supporting Information File 1

Details of materials characterizations and analyses.
[https://www.beilstein-journals.org/bjoc/content/supplementary/1860-5397-15-229-S1.pdf]

Acknowledgements

This work was supported partly by JSPS KAKENHI Grant Numbers, JP18H05263, JP26107010 in Scientific Research on Innovative Areas “photosynergetics”. The authors acknowledge Dr. Tatsuo Nakagawa and Mr. Hiroaki Hanada, UNISOKU Co., Ltd., for nanosecond to microsecond time-resolved transient absorption measurements.

ORCID® iDs

Yoichi Kobayashi - https://orcid.org/0000-0003-3339-3755
Katsuya Mutoh - https://orcid.org/0000-0002-9778-8329
Hikaru Sotome - https://orcid.org/0000-0002-6391-1851
Masafumi Koga - https://orcid.org/0000-0001-7587-6742
Hiroshi Miyasaka - https://orcid.org/0000-0002-6020-6591
Jiro Abe - https://orcid.org/0000-0002-0237-815X

Preprint

A non-peer-reviewed version of this article has been previously published as a preprint doi:10.3762/bxiv.2019.46.v1

References

1. Irie, M.; Fukaminato, T.; Matsuda, K.; Kobatake, S. *Chem. Rev.* **2014,** *114,* 12174–12277. doi:10.1021/cr500249p
2. Yokohama, Y.; Nakatani, K., Eds. *Photon-Working Switches;* Springer Japan: Tokyo, Japan, 2017. doi:10.1007/978-4-431-56544-4
3. Crano, J. C.; Guglielmetti, R. J., Eds. *Organic Photochromic and Thermochromic Compounds;* Springer US: Boston, MA, U.S.A., 2002. doi:10.1007/b114211

4. Dürr, H.; Bouas-Laurent, H. *Photochromism: Molecules and Systems;* Elsevier: Amsterdam, Netherlands, 2003.
5. Hatano, S.; Horino, T.; Tokita, A.; Oshima, T.; Abe, J. *J. Am. Chem. Soc.* **2013,** *135,* 3164–3172. doi:10.1021/ja311344u
6. Bléger, D.; Hecht, S. *Angew. Chem., Int. Ed.* **2015,** *54,* 11338–11349. doi:10.1002/anie.201500628
7. Guo, X.; Zhou, J.; Siegler, M. A.; Bragg, A. E.; Katz, H. E. *Angew. Chem., Int. Ed.* **2015,** *54,* 4782–4786. doi:10.1002/anie.201410945
8. Tsivgoulis, G. M.; Lehn, J.-M. *Chem. – Eur. J.* **1996,** *2,* 1399–1406. doi:10.1002/chem.19960021112
9. Bléger, D.; Schwarz, J.; Brouwer, A. M.; Hecht, S. *J. Am. Chem. Soc.* **2012,** *134,* 20597–20600. doi:10.1021/ja310323y
10. Dong, M.; Babalhavaeji, A.; Samanta, S.; Beharry, A. A.; Woolley, G. A. *Acc. Chem. Res.* **2015,** *48,* 2662–2670. doi:10.1021/acs.accounts.5b00270
11. Yamaguchi, T.; Kobayashi, Y.; Abe, J. *J. Am. Chem. Soc.* **2016,** *138,* 906–913. doi:10.1021/jacs.5b10924
12. Helmy, S.; Leibfarth, F. A.; Oh, S.; Poelma, J. E.; Hawker, C. J.; Read de Alaniz, J. *J. Am. Chem. Soc.* **2014,** *136,* 8169–8172. doi:10.1021/ja503016b
13. Indelli, M. T.; Carli, S.; Ghirotti, M.; Chiorboli, C.; Ravaglia, M.; Garavelli, M.; Scandola, F. *J. Am. Chem. Soc.* **2008,** *130,* 7286–7299. doi:10.1021/ja711173z
14. Ko, C.-C.; Wing-Wah Yam, V. *J. Mater. Chem.* **2010,** *20,* 2063–2070. doi:10.1039/b919418e
15. Zhao, J.; Wu, W.; Sun, J.; Guo, S. *Chem. Soc. Rev.* **2013,** *42,* 5323–5351. doi:10.1039/c3cs35531d
16. Majumdar, P.; Nomula, R.; Zhao, J. *J. Mater. Chem. C* **2014,** *2,* 5982–5997. doi:10.1039/c4tc00659c
17. Hayashi, T.; Maeda, K. *Bull. Chem. Soc. Jpn.* **1960,** *33,* 565–566. doi:10.1246/bcsj.33.565
18. Hayashi, T.; Maeda, K.; Morinaga, M. *Bull. Chem. Soc. Jpn.* **1964,** *37,* 1563–1564. doi:10.1246/bcsj.37.1563
19. Hayashi, T.; Maeda, K.; Takeuchi, M. *Bull. Chem. Soc. Jpn.* **1964,** *37,* 1717–1718. doi:10.1246/bcsj.37.1717
20. Dessauer, R. *Photochemistry, History and Commercial Applications of Hexaarylbiimidazoles;* Elsevier: Amsterdam, Netherlands, 2006.
21. Liu, A. D.; Trifunac, A. D.; Krongauz, V. V. *J. Phys. Chem.* **1992,** *96,* 207–211. doi:10.1021/j100180a040
22. Lin, Y.; Liu, A.; Trifunac, A. D.; Krongauz, V. V. *Chem. Phys. Lett.* **1992,** *198,* 200–206. doi:10.1016/0009-2614(92)90072-u
23. Monroe, B. M.; Weed, G. C. *Chem. Rev.* **1993,** *93,* 435–448. doi:10.1021/cr00017a019
24. Yamashita, H.; Ikezawa, T.; Kobayashi, Y.; Abe, J. *J. Am. Chem. Soc.* **2015,** *137,* 4952–4955. doi:10.1021/jacs.5b02353
25. Kobayashi, Y.; Mutoh, K.; Abe, J. *J. Photochem. Photobiol., C* **2018,** *34,* 2–28. doi:10.1016/j.jphotochemrev.2017.12.006
26. Ishii, N.; Kato, T.; Abe, J. *Sci. Rep.* **2012,** *2,* 819. doi:10.1038/srep00819
27. Ishii, N.; Abe, J. *Appl. Phys. Lett.* **2013,** *102,* 163301. doi:10.1063/1.4803025
28. Kobayashi, Y.; Abe, J. *Adv. Opt. Mater.* **2016,** *4,* 1354–1357. doi:10.1002/adom.201600218
29. Mutoh, K.; Sliwa, M.; Abe, J. *J. Phys. Chem. C* **2013,** *117,* 4808–4814. doi:10.1021/jp309917s
30. Mutoh, K.; Sliwa, M.; Fron, E.; Hofkens, J.; Abe, J. *J. Mater. Chem. C* **2018,** *6,* 9523–9531. doi:10.1039/c8tc02713g
31. Mutoh, K.; Miyashita, N.; Arai, K.; Abe, J. *J. Am. Chem. Soc.* **2019,** *141,* 5650–5654. doi:10.1021/jacs.9b01870
32. Yamamoto, K.; Mutoh, K.; Abe, J. *J. Phys. Chem. A* **2019,** *123,* 1945–1952. doi:10.1021/acs.jpca.8b12384
33. Satoh, Y.; Ishibashi, Y.; Ito, S.; Nagasawa, Y.; Miyasaka, H.; Chosrowjan, H.; Taniguchi, S.; Mataga, N.; Kato, D.; Kikuchi, A.; Abe, J. *Chem. Phys. Lett.* **2007,** *448,* 228–231. doi:10.1016/j.cplett.2007.09.081
34. Miyasaka, H.; Satoh, Y.; Ishibashi, Y.; Ito, S.; Nagasawa, Y.; Taniguchi, S.; Chosrowjan, H.; Mataga, N.; Kato, D.; Kikuchi, A.; Abe, J. *J. Am. Chem. Soc.* **2009,** *131,* 7256–7263. doi:10.1021/ja809195s
35. Yamashita, H.; Abe, J. *Chem. Commun.* **2014,** *50,* 8468–8471. doi:10.1039/c4cc03137g
36. Crivello, J. V.; Sangermano, M. *J. Polym. Sci., Part A: Polym. Chem.* **2001,** *39,* 343–356. doi:10.1002/1099-0518(20010201)39:3<343::aid-pola1001>3.0.co;2-j
37. Nakagawa, T.; Okamoto, K.; Hanada, H.; Katoh, R. *Opt. Lett.* **2016,** *41,* 1498. doi:10.1364/ol.41.001498
38. Morantz, D. J.; Wright, A. J. C. *J. Chem. Phys.* **1971,** *54,* 692–697. doi:10.1063/1.1674897
39. Encinas, M. V.; Scaiano, J. C. *J. Am. Chem. Soc.* **1979,** *101,* 7740–7741. doi:10.1021/ja00520a031
40. Mohapatra, G. K. D.; Bhattacharya, J.; Bandopadhyay, J.; Bera, S. C. *J. Photochem. Photobiol., A* **1987,** *40,* 47–58. doi:10.1016/0047-2670(87)87043-0
41. Vieira Ferreira, L. F.; Ferreira Machado, I.; Da Silva, J. P.; Oliveira, A. S. *Photochem. Photobiol. Sci.* **2004,** *3,* 174–181. doi:10.1039/b307956b
42. Bhattacharya, B.; Jana, B.; Bose, D.; Chattopadhyay, N. *J. Chem. Phys.* **2011,** *134,* 044535. doi:10.1063/1.3533797
43. Snellenburg, J.; Laptenok, S.; Seger, R.; Mullen, K.; van Stokkum, J. *J. Stat. Software* **2012,** *49,* 1–22. doi:10.18637/jss.v049.i03
44. Flamigni, L.; Barigelletti, F.; Dellonte, S.; Orlandi, G. *J. Photochem.* **1983,** *21,* 237–244. doi:10.1016/0047-2670(83)80027-6
45. Kobayashi, Y.; Okajima, H.; Sotome, H.; Yanai, T.; Mutoh, K.; Yoneda, Y.; Shigeta, Y.; Sakamoto, A.; Miyasaka, H.; Abe, J. *J. Am. Chem. Soc.* **2017,** *139,* 6382–6389. doi:10.1021/jacs.7b01598

License and Terms

This is an Open Access article under the terms of the Creative Commons Attribution License (http://creativecommons.org/licenses/by/4.0). Please note that the reuse, redistribution and reproduction in particular requires that the authors and source are credited.

The license is subject to the *Beilstein Journal of Organic Chemistry* terms and conditions: (https://www.beilstein-journals.org/bjoc)

The definitive version of this article is the electronic one which can be found at: doi:10.3762/bjoc.15.229

BEILSTEIN JOURNAL OF ORGANIC CHEMISTRY

Targeted photoswitchable imaging of intracellular glutathione by a photochromic glycosheet sensor

Xianzhi Chai[1], Hai-Hao Han[1,2], Yi Zang[*2], Jia Li[2], Xiao-Peng He[1], Junji Zhang[*1] and He Tian[1]

Full Research Paper

Open Access

Address:
[1]Key Laboratory for Advanced Materials and Joint International Research Laboratory of Precision Chemistry and Molecular Engineering, Feringa Nobel Prize Scientist Joint Research Center, School of Chemistry and Molecular Engineering, East China University of Science and Technology, 130 Meilong Road, Shanghai 200237, People's Republic of China and [2]National Center for Drug Screening, State Key Laboratory of Drug Research, Shanghai Institute of Materia Medica, Chinese Academy of Sciences, 189 Guo Shoujing Rd., Shanghai 201203, People's Republic of China

Email:
Yi Zang[*] - yzang@simm.ac.cn; Junji Zhang[*] - zhangjunji@ecust.edu.cn

* Corresponding author

Keywords:
intracellular GSH; molecular switches; photochromic glycosheet; photoswitchable imaging; 2D MnO_2 nanosheets

Beilstein J. Org. Chem. **2019,** *15,* 2380–2389.
doi:10.3762/bjoc.15.230

Received: 12 July 2019
Accepted: 24 September 2019
Published: 07 October 2019

This article is part of the thematic issue "Molecular switches".

Guest Editor: W. Szymanski

© 2019 Chai et al.; licensee Beilstein-Institut.
License and terms: see end of document.

Abstract

The development of photochromic fluorescence sensors with dynamic and multiple-signaling is beneficial to the improvement of biosensing/imaging precision. However, elaborate designs with complicated molecular structures are always required to integrate these functions into one molecule. By taking advantages of both redox-active/high loading features of two-dimensional (2D) manganese dioxide (MnO_2) and dynamic fluorescence photoswitching of photochromic sensors, we here design a hybrid photochromic MnO_2 glycosheet (**Glyco-DTE@MnO_2**) to achieve the photoswitchable imaging of intracellular glutathione (GSH). The photochromic glycosheet manifests significantly turn-on fluorescence and dynamic ON/OFF fluorescence signals in response to GSH, which makes it favorable for intracellular GSH double-check in targeted human hepatoma cell line (HepG2) through the recognition between β-D-galactoside and asialoglycoprotein receptor (ASGPr) on cell membranes. The dynamic fluorescence signals and excellent selectivity for detection and imaging of GSH ensure the precise determination of cell states, promoting its potential applications in future disease diagnosis and therapy.

Introduction

Cells are the basic structure and functional unit of biological organisms. Human diseases and aging are closely related to the states of cells. Thorough understanding of intracellular signal transduction and metabolic processes may provide great opportunities for early disease diagnosis and treatment. To achieve this goal, cell-imaging with fluorescence sensors becomes a booming research field since it enables the high-resolution visualization of intracellular activities [1,2]. Nonetheless, conventional fluorescence sensors always encounter background signal interferences during cell imaging, which are usually generated from bioluminescence and light scattering in the intracellular environment [3]. This may lead to the deviation in judging the morphology and state of the cells, e.g., causing false-positive/negative results. Generally, strategies like designing ratiometric [4,5] or near-infrared [6-8] fluorescence sensors are applied to overcome this obstacle. Recently, a novel category of photochromic probes with light-controlled dynamic fluorescence signals has been developed, aiming at reducing interferences and improving sensing precision in complex physiological environments [9-17]. This photoresponsive design presents several advantages over conventional probes: 1) The light-activation mode endows the probe with light-controllable "ON/OFF" working states. The OFF-state (one of the photoisomer or photocaged structure) "masks" the probe before reaching the target analyte, avoiding unwanted interactions with other abundant species in the "working zone", or unnecessary consumption with analyte in nontargeted locations during in vivo/intracellular transport [18-20]. 2) A dynamic ON/OFF fluorescence signal is generated for reversible imaging of a targeted analyte (termed as "double-check"), which can facilitate a better discrimination of the analyte signal from the background interferences [9-11]. As a result, more precise outputs can be obtained for targeted analytes even at low concentrations.

Though promising, common "photochromophore–fluorophore"-type sensors require elaborate designs to integrate multifunctionality (e.g., photoswitching, fluorescence sensing, targetability, water solubility, etc.) into one molecule that could be accessible to various biosensing scenarios and ensure the imaging precision. This might cause limitations in further applications as complicated structures may lead to unpredictable performances and high cost that are not suitable for future commercialization. To simplify the sensor design and further broaden the availability of photoswitchable biosensing, herein we report a glycosheet hybrid sensor (**Glyco-DTE@MnO_2**) fabricated by 2D MnO_2 nanosheets and dithienylethene fluorescence reporter (**Glyco-DTE**) to achieve cell-targeted photoswitchable imaging of intracellular GSH. As shown in Scheme 1, **Glyco-DTE@MnO_2** glycosheets were formed by assembling **Glyco-DTE** onto the surface of 2D MnO_2 nanosheets, which quench the fluorescence from **Glyco-DTE** reporter. Recent studies discovered that 2D MnO_2 nanosheets tend to undergo a facile reduction with GSH, $MnO_2 + 2GSH + 2H^+ \rightarrow Mn^{2+} + GSSG + 2H_2O$ [21], and be degraded into Mn^{2+} that revives initial fluorescence signals. Furthermore, the generated Mn^{2+} can also perform as potential trigger for sequential functions, e.g., DNAzymes [22]. These interesting performances promote MnO_2 nanosheets as promising candidate for various physiological applications as biosensing/imaging, bioactivity modulation, drug delivery, etc [23,24].

In our system, the **Glyco-DTE@MnO_2** hybrid sensor undergoes decomposition when encountering the overexpressed intracellular GSH in HepG2 cell lines, following the recovery of the photoswitchable fluorescence signal regulated by **Glyco-DTE**. More importantly, the β-D-galactoside cell-targeting moiety linked with **Glyco-DTE** forms a glyco-array on the MnO_2 nanosheets that not only enhances the water solubility but also the cell targetability of the hybrid system towards HepG2 cell lines [25,26]. Therefore, by simply incorporating the photochromic fluorescence reporter into GSH-responsive MnO_2 nanosheets, a highly efficient photoswitchable hybrid biosensor is successfully presented with the demanded functionality for precise cell imaging.

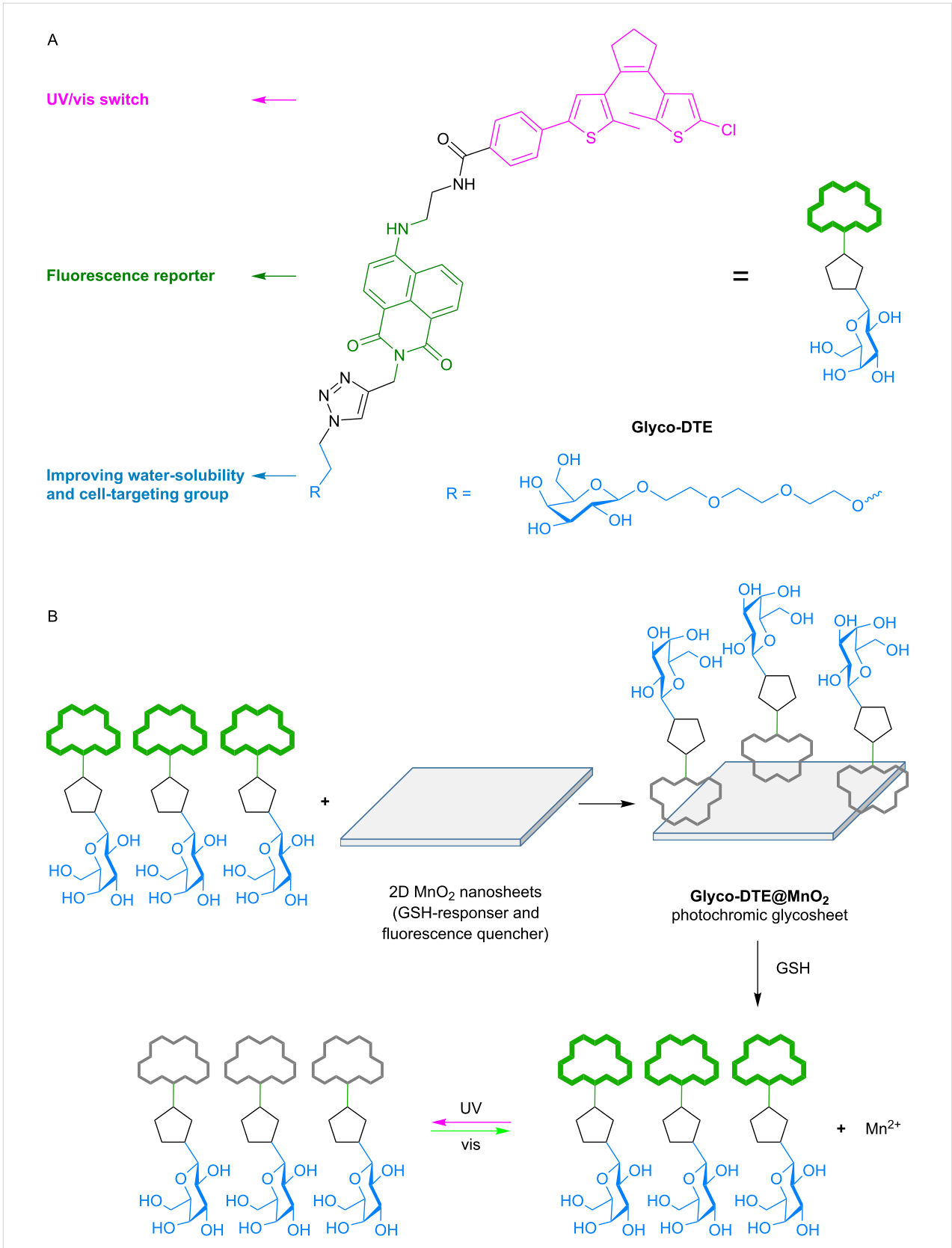
Results and Discussion

Synthesis of dithienylethene fluorescence reporter (Glyco-DTE)

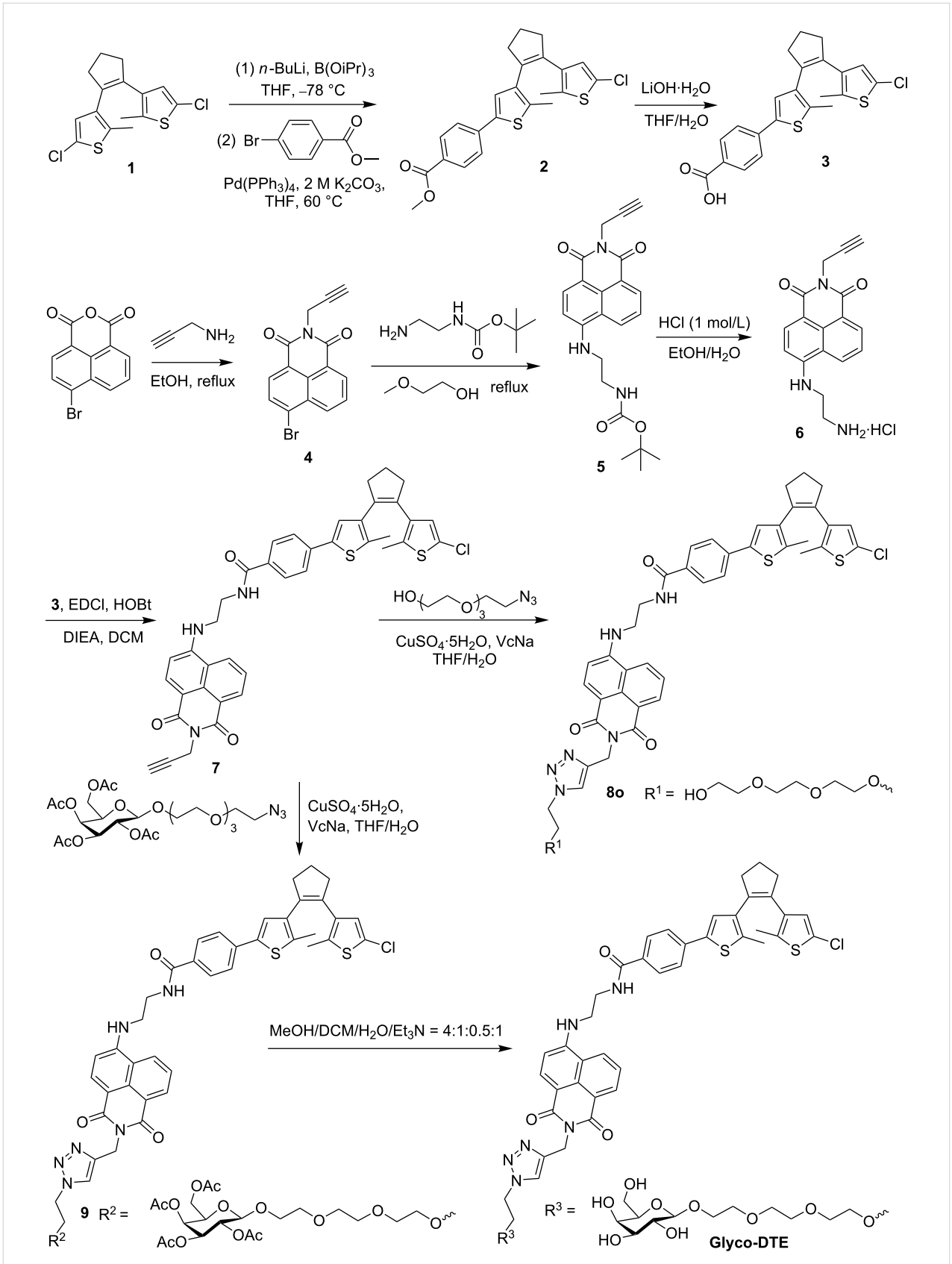
The synthesis of dithienylethene fluorescence reporter **Glyco-DTE** is shown in Scheme 2. The dithienylethene derivative **3** was prepared by Suzuki coupling of dithienylethene **1** with methyl 4-bromobenzoate followed by hydrolysis with lithium hydroxide. The naphthalimide fluorophore **6** was synthesized through bromide **4** according to reported methods [27]. Then, the photochromic fluorophore intermediate **7** was synthesized by coupling compounds **3** and **6** through amidation. The **Glyco-DTE** reporter was prepared by click reaction between compound **7** and acetylated β-D-galactoside, followed by deacetylation. Similarly, a control reporter **8o** with a PEG chain instead of the galactoside targeting group was also prepared. The detailed synthetic procedures and characterizations are given in Supporting Information File 1.

Photochromic performances of Glyco-DTE

The photoswitching performances of **Glyco-DTE** (1×10^{-5} mol/L) were first measured in PBS buffer at room temperature. As shown in Figure 1A, a decreased absorption band at 327 nm and a subsequent appearance of a new band centered at 550 nm were observed upon irradiation of **Glyco-DTE** with UV light, which indicated a photocyclization or ring-



Scheme 1: The structure (A) of reporter **Glyco-DTE** and working principle (B) of photochromic glycosheet **Glyco-DTE@MnO_2** for targeted detection and imaging of GSH in HepG2 cells.



Scheme 2: Synthetic route to dithienylethene fluorescence reporters **Glyco-DTE** and **8o**. VcNa: sodium ascorbate.

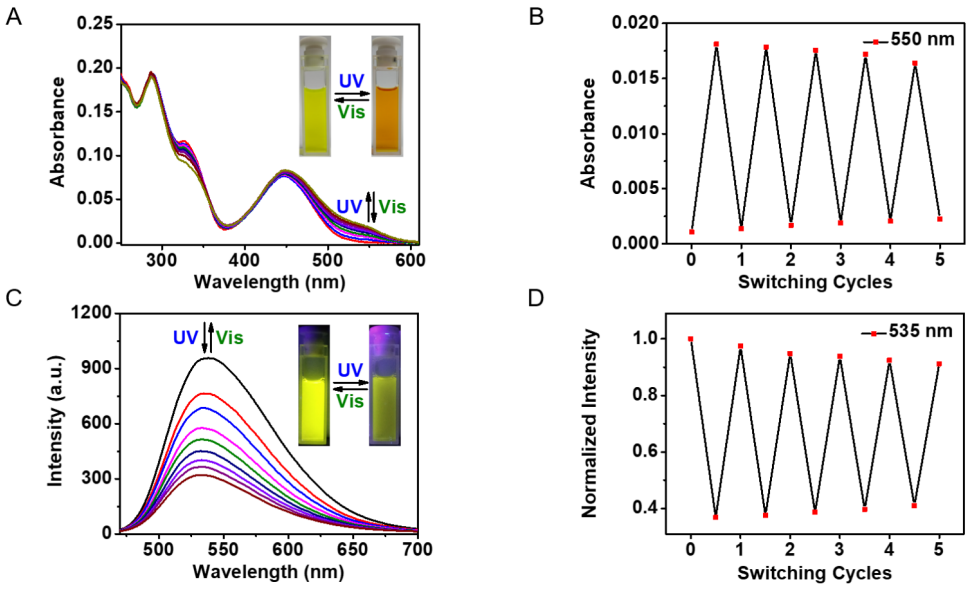


Figure 1: Absorption spectral changes (A), absorption fatigue resistance (B), emission spectral changes (C) and emission fatigue resistance (D) of reporter **Glyco-DTE** (1×10^{-5} mol/L) in PBS buffer (pH 7.4, 0.25‰ Triton X-100) upon alternating irradiation with UV (254 nm) and visible light (>500 nm). Emission spectra were produced upon excitation at 448 nm.

closing process to form the ring-closed photoisomer [28]. The absorption band at 550 nm remained unchanged after 3 min of irradiation as the photostationary state (PSS) was reached. The absorption spectra of the ring-opened isomer could be fully recovered upon visible light irradiation (4 min), suggesting a photocycloreversion or ring-opening process from the ring-closed photoisomer to the original ring-opened photoisomer. The photo fatigue resistance of **Glyco-DTE** was then examined at 550 nm via an alternate irradiation with UV and visible light at room temperature. The ring-closing/opening cycles of **Glyco-DTE** could be repeated several times in buffer solution without obvious degradation (Figure 1B), demonstrating the robustness of **Glyco-DTE**.

Figure 1C shows the photoswitching of emission spectra of **Glyco-DTE** (1×10^{-5} mol/L) in PBS buffer upon alternating UV and visible light irradiation at room temperature. Upon excitation with 448 nm light, the fluorescence emission peak of **Glyco-DTE** was observed at 535 nm ($\Phi_F = 0.263$, Table S1 in Supporting Information File 1). Owing to the good overlap between the emission band of the naphthalimide fluorophore and the absorption band of DTE closed isomer, the fluorescence was remarkably quenched to ca. 30% ($\Phi_F = 0.085$, Table S1 in Supporting Information File 1) through an efficient intramolecular fluorescence resonance energy transfer (FRET) mechanism [29,30] after the photocyclization of **Glyco-DTE**. The fluorescence was fully recovered by irradiation with visible light and the emission fatigue resistance was also examined and found to tolerate more than five switching cycles in PBS buffer (Figure 1D). Similar performances were also observed for control reporter **8o** (Supporting Information File 1, Figure S1). The characteristic photoswitchable ON/OFF fluorescence signals as well as the robust fatigue resistance suggest the reporter designed here has great potential for photoswitchable fluorescence imaging in biological systems.

Fabrication of Glyco-DTE@MnO_2 glycosheets

The fast and simple synthesis of 2D MnO_2 nanosheets was performed according to reported procedures [31,32], in which the freshly prepared MnO_2 from $MnCl_2{\cdot}4H_2O$ was washed and sonicated in ultrapure water. As shown in Figure 2A, the obtained MnO_2 solution exhibited a wide band in the range of 300–1000 nm with a peak located at 375 nm, which is the characteristic absorption of 2D MnO_2 nanosheets [21,33]. The broad and strong absorption makes the 2D MnO_2 nanosheets a potential energy acceptor for the fluorophores which are stacked on the nanosheets plane, leading to the fluorescence quenching through FRET mechanism [32,34]. The transmission electron microscopy (TEM) image of the prepared product revealed obvious morphology of nanosheets which presented a large 2D and ultrathin plane with a diameter of ca. 200 nm (Figure 2B) [33,34].

By virtue of the expansive surface, 2D MnO_2 nanosheets possess the ability to load dozens of fluorophores. An array of fluorescent reporters thus formed, which facilitate endocytosis and significantly lower the background signal for intracellular fluo-

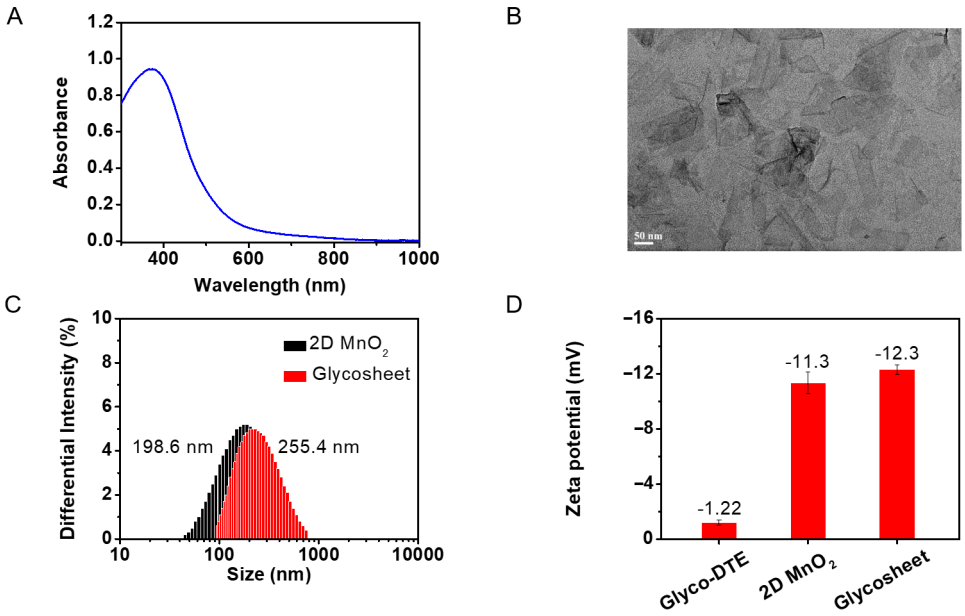


Figure 2: (A) The absorbance spectrum and (B) high resolution TEM image of 2D MnO_2 nanosheets (1×10^{-5} g/mL) in ultrapure water; (C) DLS and Zeta potential characterizations of 2D MnO_2 photochromic glycosheet.

rescence imaging [25,26]. Upon the incubation of the dithienylethene fluorescence reporter **Glyco-DTE** with 2D MnO_2 nanosheets, the reporter was adsorbed on the surface of the nanosheets, forming the **Glyco-DTE@MnO_2** photochromic glycosheet which β-D-galactosides pointing away from the surface. Dynamic light scattering (DLS) exhibited a size of 198.6 nm for the 2D MnO_2 nanosheets (Figure 2C), which was in accordance with the TEM characterization. The size of the photochromic **Glyco-DTE@MnO_2** glycosheet was determined as 255.4 nm, indicating the successful coating of MnO_2 nanosheets with the **Glyco-DTE** reporter [25]. An increasing Zeta potential was also observed after the assembly, confirming again the successful fabrication of **Glyco-DTE@MnO_2** glycosheet (Figure 2D) [26].

GSH sensing and fluorescence photoswitching of Glyco-DTE@MnO_2 glycosheet

The fluorescence emission of **Glyco-DTE@MnO_2** was efficiently quenched to ca. 15% (Φ_F = 0.023, Table S1 in Supporting Information File 1) when increasing concentrations of 2D MnO_2 nanosheets were added, and reached saturation around 25 μg/mL (Figure 3A). The quenched fluorescence indicated the effective FRET between the attached **Glyco-DTE** and 2D MnO_2, which again suggested the close stacking of **Glyco-DTE** to the nanosheet surface. Aggregation-caused quenching might be another reason for the fluorescence quenching because of the close distance between fluorescence molecules when absorbed on the surface of nanosheets. Apart from the quenched fluorescence, the photoswitchable emission was also prohibited (Figure S2, Supporting Information File 1), probably due to the significantly reduced emission operation window of **Glyco-DTE**.

We then investigated the GSH-responsive performance of **Glyco-DTE@MnO_2** in PBS buffer. As shown in Figure 3B, the emission of **Glyco-DTE** was restored to ca. 90% (Φ_F = 0.256, Table S1 in Supporting Information File 1) with the addition of 1.5 mM GSH. The recovery of emission can be attributed to the reduction of MnO_2 to Mn^{2+} [21], leading to the decomposition of MnO_2 nanosheets. This result reveals that the photochromic glycosheet is capable of recognizing GSH, leading to a significant turn-on of the quenched fluorescence. The photoswitchable fluorescence signal was also activated alongside the recovery of naphthalimide emission. As shown in Figure 3C, the fluorescence intensity at 535 nm performed an ON/OFF switching cycle upon irradiation of UV–vis light with a decent fatigue resistance (Figure 3D), which is in good accordance with the results of **Glyco-DTE** in buffer solution.

The selectivity of **Glyco-DTE@MnO_2** towards other intracellular species was next tested by fluorescence spectroscopy. As shown in Figure S3A (Supporting Information File 1), GSH showed a distinct selectivity over other analytes, suggesting a specific GSH detection performance of **Glyco-DTE@MnO_2**. A linear response of the normalized fluorescent intensity I/I_{max} at 535 nm within 0–0.4 mM GSH concentration range was deter-

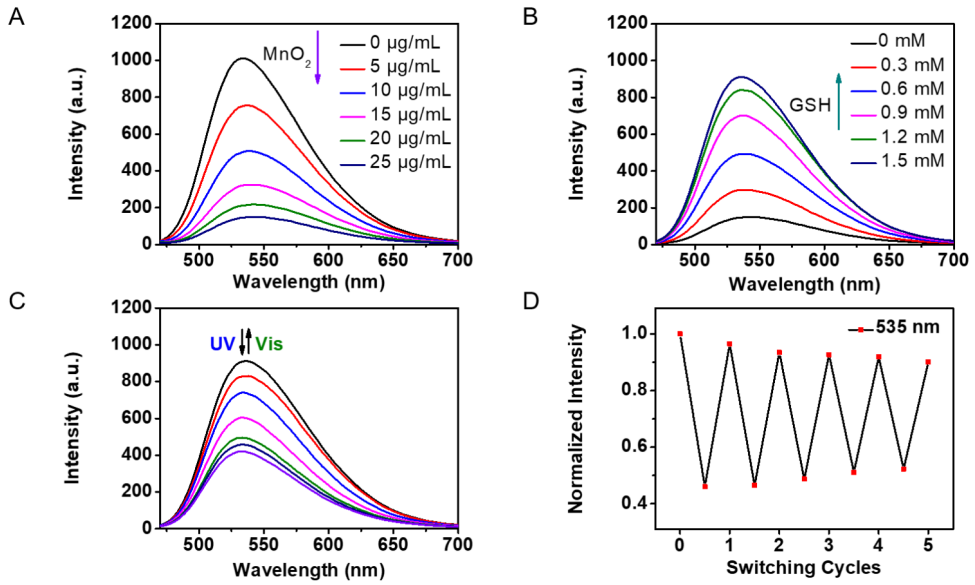


Figure 3: (A) Emission spectral changes of reporter **Glyco-DTE** (1×10^{-5} mol/L in PBS buffer, 0.25‰ Triton X-100) upon addition of 0–25 μg/mL MnO_2, (B) emission spectral changes of glycosheet upon addition of 0–1.5 mM GSH, (C) emission spectral changes and (D) fatigue resistance of reporter **Glyco-DTE** (after the degradation of MnO_2 with GSH) upon irradiation with UV (254 nm) and visible light (>500 nm). Emission spectra were produced upon excitation at 448 nm.

mined (Supporting Information File 1, Figure S3B), where I_{max} represents the emission intensity before the addition of MnO_2 and I is the emission intensity after the addition of GSH, through which the limit of detection (LOD) was calculated to be 0.99 μM. These results demonstrate the high sensitivity of **Glyco-DTE@MnO_2** hybrid sensor towards GSH, which allows the detection of intracellular GSH in the complex physiological environment of cells. The kinetic analysis of **Glyco-DTE@MnO_2** in the presence of GSH (Supporting Information File 1, Figure S3C) suggests a short response time (3 min) with a reaction constant of $k = 2.39 \times 10^{-2}$ s^{-1} (Supporting Information File 1, Figure S3D), demonstrating a fast response of the hybrid sensor on GSH sensing.

The investigation above verifies that the photochromic glycosheet we designed can perform as an "activation and photoswitching" sensor towards GSH, which is illustrated as fluorescence turn-on and sequential on-off cycles. Besides, the quenching of the reporter fluorescence by MnO_2 contributes to a significantly lowered background signal, which makes it an excellent material for intracellular precision imaging.

Cell-targeted photoswitchable imaging of intracellular GSH

With the photochromic glycosheet in hand, we then investigated its applications as a biosensor for targeted intracellular GSH imaging. The presence of the β-D-galactoside residue offers a selective recognition site for ASGPr receptor which is overexpressed in HepG2 cell lines, endowing our hybrid sensor with specific cell target ability [35]. The cytoselectivity of the **Glyco-DTE** reporter was firstly checked in PBS buffer through lectin binding experiments. The lectin used here, peanut agglutinin (PNA), can selectively bind with β-D-galactoside that mimics the role of ASGPr on HepG2 cell membranes [36,37]. As shown in Figure S4 (Supporting Information File 1), the addition of PNA to the solution of **Glyco-DTE** resulted in a fluorescence enhancement with an obvious spectral blue-shift, while the addition of another lectin, conconavalin A (Con A), did not cause a substantial variation of the fluorescence spectra. For control reporter **8o**, either the addition of PNA or Con A led to minute changes in the emission spectra. The phenomena described above solidly proved the cell target ability of the β-D-galactoside moiety of the **Glyco-DTE** reporter.

In the next step, HepG2 and HeLa cells were simultaneously incubated with **Glyco-DTE** and then imaged with an Operetta high content imaging system. As shown in Figure 4A, a bright fluorescence signal was detected in HepG2 cells but almost no fluorescence signal was observed in HeLa cells. This suggested a good selectivity of **Glyco-DTE** towards HepG2 cell lines. The specific interaction between β-D-galactoside and cell transmembrane receptor ASGPr facilitates the selective cell internalization [38,39]. On the contrary, HepG2 and HeLa cells incubated with the control reporter **8o** lacking a β-D-galactoside moiety presented undiscernible fluorescence signals, confirming again the selective targeting ability of **Glyco-DTE**. Next, the intracel-

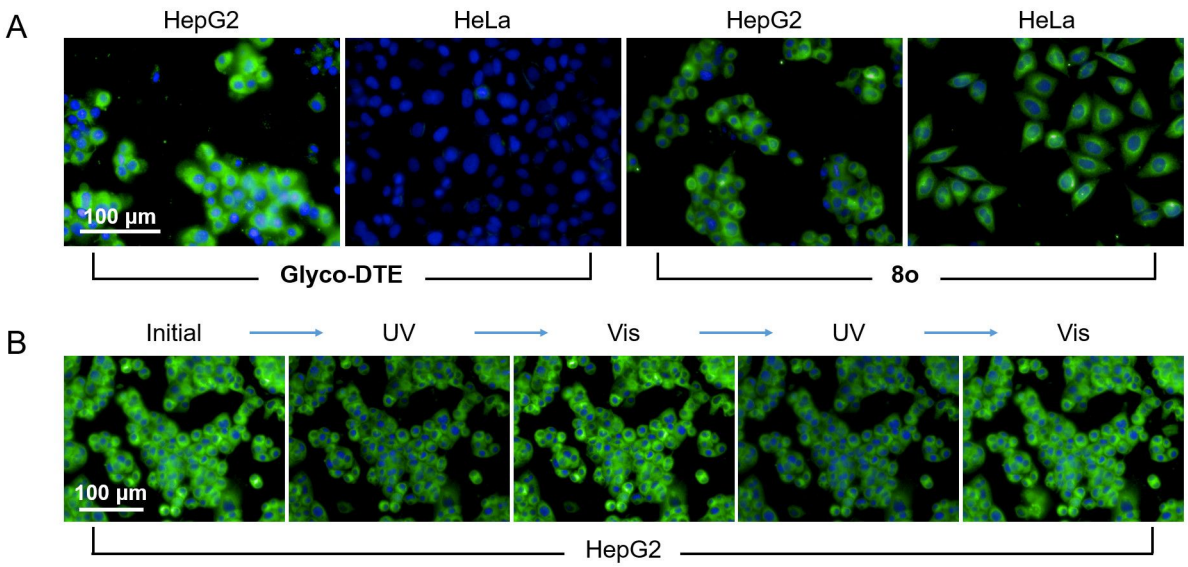


Figure 4: (A) Fluorescence imaging of HepG2 cells and HeLa cells after incubated with reporters **Glyco-DTE** (20 μM) and **8o** (20 μM) for 30 min. (B) The photochromic fluorescence imaging of HepG2 cells after incubated with reporter **Glyco-DTE** (20 μM) upon alternating irradiation with UV (254 nm) and visible light (>500 nm). The excitation wavelength is 440 nm and the emission channel is 450–550 nm.

lular photoswitchable imaging experiment of **Glyco-DTE** in HepG2 cells was operated. Upon irradiation of alternate UV–vis light, an evident fluorescence ON/OFF cycle of HepG2 cells was observed (Figure 4B). In addition to the selective internalization, **Glyco-DTE** is capable of taking remote light orders for intracellular photoswitchable imaging. The dynamic ON/OFF cycle, or photoblinking, of fluorescence from the photochromic probe guarantees the source of the signal [9]. Compared to the conventional sensor, which is vulnerable towards the inherent background signals from the intracellular environment, the photochromic probe provides a smart strategy of well-discrimination from physiological interferences.

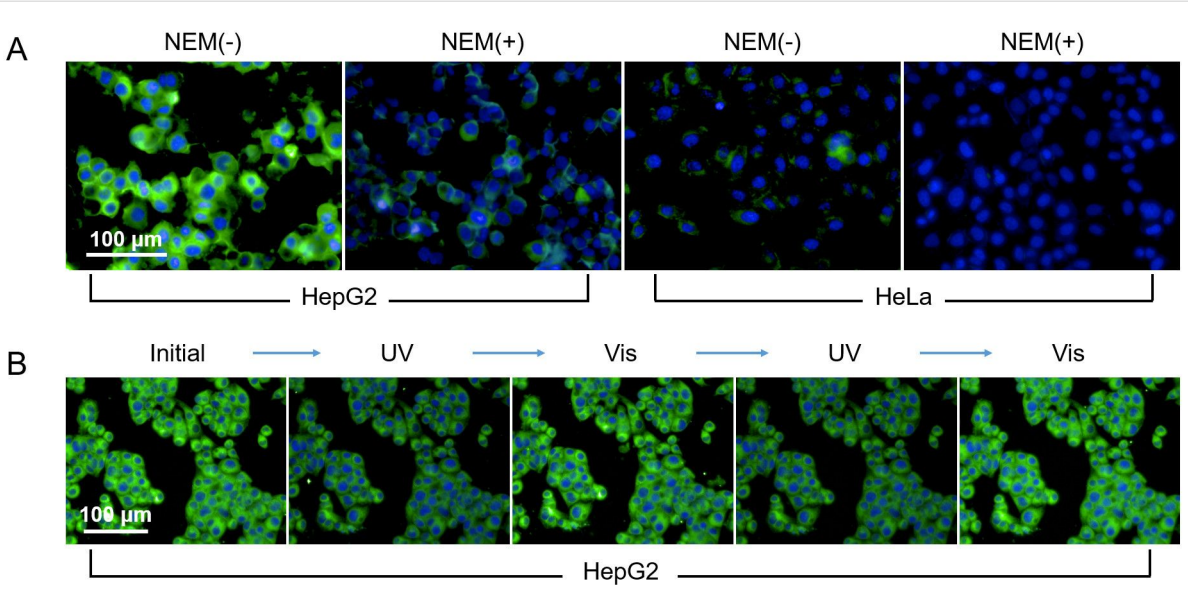


Figure 5: (A) Fluorescence imaging of HepG2 cells and HeLa cells after incubated with **Glyco-DTE@MnO_2** photochromic glycosheet in the absence and presence of NEM. (B) The photochromic fluorescence imaging of HepG2 cells after incubated with glycosheet upon irradiation with UV (254 nm) and visible light (>500 nm). The excitation wavelength is 440 nm and the emission channel is 450–550 nm.

Apart from the over-expressed ASGPr receptors on cell membranes, the high intracellular concentration of GSH is another feature for HepG2 cells. Therefore, amounts of work on HepG2 cell imaging have targeted GSH as the characteristic biomarker [40,41]. Strategies like reduction of disulfide [42-44] and Michael addition [45-47] have been utilized to design fluorescent sensors for detecting intracellular GSH or discriminative sensing of GSH with other common biothiols (e.g., Cys and Hcy) [45,46]. In this work, the highly accessible 2D MnO_2 nanosheet is used as the GSH responsive site instead of traditional functional groups that require elaborate design for high selectivity and reactivity. Besides, the incorporation of **Glyco-DTE** with MnO_2 nanosheets quenches the fluorescence and further suppresses the background signal for intracellular imaging. To investigate the capability of our **Glyco-DTE@MnO_2** hybrid sensor (glycosheet) for targeted photoswitchable imaging of intracellular GSH, HepG2 and HeLa cells were incubated with the glycosheet and subsequently imaged under an optical microscope. As shown in Figure 5A, HepG2 cells incubated with the glycosheet exhibited a strong fluorescence signal, indicating a high level of GSH expressed in HepG2 cells. The addition of NEM (*N*-ethylmaleimide, a GSH scavenger) resulted in a significant decrease of fluorescence intensity [40,41,46], suggesting the efficient quenching effect of MnO_2 nanosheets towards **Glyco-DTE** reporter. In HeLa cells, as a control experiment, a fluorescence signal is hardly observed no matter treated with NEM or not. These results strongly support the feasibility of targeted intracellular GSH imaging with our **Glyco-DTE@MnO_2** hybrid sensor. Consequently, the intracellular GSH photoswitchable imaging with the liberated **Glyco-DTE** in HepG2 cells was operated. Similar to the above results, an efficient fluorescence ON/OFF cycling upon UV–vis irradiation of HepG2 cells was performed, which provides the dynamic fluorescence signal for "double-check" of intracellular GSH. The "first check" was the recovery of the silenced fluorescence in the presence of GSH. The following "second check" was the blinking ON/OFF fluorescence signal which ensures the origin of fluorescence signal from the photochromic probe. Hence, the intracellular sensing precision is significantly improved.

Conclusion

In summary, photochromic glycosheet **Glyco-DTE@MnO_2** was developed for cell-targeted and photoswitchable intracellular GSH imaging in human hepatoma cell lines. The hybrid sensing system presented here provides the MnO_2 nanosheets for GSH detection and **Glyco-DTE** reporter for dynamic fluorescence signal modulation. Besides, the high affinity of β-D-galactoside towards ASGPr receptors on the membrane of HepG2 cells enables the specific cell-targetability of **Glyco-DTE@MnO_2** hybrid sensor. Compared to conventional GSH biosensors, our strategy offers a simple yet smart design that circumvents the elaborate molecular design and laborious synthesis for multifunctional sensors, further broadening the availability of photochromic sensors in various physiological scenarios. These findings not only enable promising applications in targeted-cell imaging but also provide a new sensor platform useful for multiple fluorescence signaling and improving the detection precision.

Supporting Information

Supporting Information File 1

Experimental procedures and spectral data.
[https://www.beilstein-journals.org/bjoc/content/supplementary/1860-5397-15-230-S1.pdf]

Acknowledgements

The authors thank the NSFC (21878086, 21420102004), Shanghai Municipal Science and Technology Major Project (2018SHZDZX03), the international cooperation program of Shanghai Science and Technology Committee (17520750100) and the Shanghai Rising-Star Program (19QA1402500 to J. Z.).

ORCID® iDs

Junji Zhang - https://orcid.org/0000-0003-2823-4637
He Tian - https://orcid.org/0000-0003-3547-7485

References

1. Gao, M.; Yu, F.; Lv, C.; Choo, J.; Chen, L. *Chem. Soc. Rev.* **2017,** *46,* 2237–2271. doi:10.1039/c6cs00908e
2. Zhang, J.; Chai, X.; He, X.-P.; Kim, H.-J.; Yoon, J.; Tian, H. *Chem. Soc. Rev.* **2019,** *48,* 683–722. doi:10.1039/c7cs00907k
3. Huang, X.; Song, J.; Yung, B. C.; Huang, X.; Xiong, Y.; Chen, X. *Chem. Soc. Rev.* **2018,** *47,* 2873–2920. doi:10.1039/c7cs00612h
4. Ma, T.; Hou, Y.; Zeng, J.; Liu, C.; Zhang, P.; Jing, L.; Shangguan, D.; Gao, M. *J. Am. Chem. Soc.* **2018,** *140,* 211–218. doi:10.1021/jacs.7b08900
5. Reinhardt, C. J.; Zhou, E. Y.; Jorgensen, M. D.; Partipilo, G.; Chan, J. *J. Am. Chem. Soc.* **2018,** *140,* 1011–1018. doi:10.1021/jacs.7b10783
6. Verwilst, P.; Kim, H.-R.; Seo, J.; Sohn, N.-W.; Cha, S.-Y.; Kim, Y.; Maeng, S.; Shin, J.-W.; Kwak, J. H.; Kang, C.; Kim, J. S. *J. Am. Chem. Soc.* **2017,** *139,* 13393–13403. doi:10.1021/jacs.7b05878
7. Miao, Q.; Yeo, D. C.; Wiraja, C.; Zhang, J.; Ning, X.; Xu, C.; Pu, K. *Angew. Chem., Int. Ed.* **2018,** *57,* 1256–1260. doi:10.1002/anie.201710727
8. Xu, G.; Yan, Q.; Lv, X.; Zhu, Y.; Xin, K.; Shi, B.; Wang, R.; Chen, J.; Gao, W.; Shi, P.; Fan, C.; Zhao, C.; Tian, H. *Angew. Chem., Int. Ed.* **2018,** *57,* 3626–3630. doi:10.1002/anie.201712528
9. Zhang, J.; Fu, Y.; Han, H.-H.; Zang, Y.; Li, J.; He, X.-P.; Feringa, B. L.; Tian, H. *Nat. Commun.* **2017,** *8,* 987. doi:10.1038/s41467-017-01137-8
10. Fu, Y.; Han, H.-H.; Zhang, J.; He, X.-P.; Feringa, B. L.; Tian, H. *J. Am. Chem. Soc.* **2018,** *140,* 8671–8674. doi:10.1021/jacs.8b05425

11. Fu, Y.; Zhang, X.; Cao, F.; Wang, W.; Qian, G.; Zhang, J. *Sci. China: Chem.* **2019,** *62,* 1204–1212. doi:10.1007/s11426-019-9490-x
12. Xiong, Y.; Vargas Jentzsch, A.; Osterrieth, J. W. M.; Sezgin, E.; Sazanovich, I. V.; Reglinski, K.; Galiani, S.; Parker, A. W.; Eggeling, C.; Anderson, H. L. *Chem. Sci.* **2018,** *9,* 3029–3040. doi:10.1039/c8sc00130h
13. Roubinet, B.; Weber, M.; Shojaei, H.; Bates, M.; Bossi, M. L.; Belov, V. N.; Irie, M.; Hell, S. W. *J. Am. Chem. Soc.* **2017,** *139,* 6611–6620. doi:10.1021/jacs.7b00274
14. Zhang, W.; Huo, F.; Yin, C. *Org. Lett.* **2019,** *21,* 5277–5280. doi:10.1021/acs.orglett.9b01879
15. Roubinet, B.; Bossi, M. L.; Alt, P.; Leutenegger, M.; Shojaei, H.; Schnorrenberg, S.; Nizamov, S.; Irie, M.; Belov, V. N.; Hell, S. W. *Angew. Chem., Int. Ed.* **2016,** *55,* 15429–15433. doi:10.1002/anie.201607940
16. Zhou, Y.; Zhuang, Y.; Li, X.; Ågren, H.; Yu, L.; Ding, J.; Zhu, L. *Chem. – Eur. J.* **2017,** *23,* 7642–7647. doi:10.1002/chem.201700947
17. Jia, X.; Shao, C.; Bai, X.; Zhou, Q.; Wu, B.; Wang, L.; Yue, B.; Zhu, H.; Zhu, L. *Proc. Natl. Acad. Sci. U. S. A.* **2019,** *116,* 4816–4821. doi:10.1073/pnas.1821991116
18. Zhang, Y.; Song, K.-H.; Tang, S.; Ravelo, L.; Cusido, J.; Sun, C.; Zhang, H. F.; Raymo, F. M. *J. Am. Chem. Soc.* **2018,** *140,* 12741–12745. doi:10.1021/jacs.8b09099
19. Thiel, Z.; Rivera-Fuentes, P. *Angew. Chem., Int. Ed.* **2019,** *58,* 11474–11478. doi:10.1002/anie.201904700
20. Goldberg, J. M.; Wang, F.; Sessler, C. D.; Vogler, N. W.; Zhang, D. Y.; Loucks, W. H.; Tzounopoulos, T.; Lippard, S. J. *J. Am. Chem. Soc.* **2018,** *140,* 2020–2023. doi:10.1021/jacs.7b12766
21. Deng, R.; Xie, X.; Vendrell, M.; Chang, Y.-T.; Liu, X. *J. Am. Chem. Soc.* **2011,** *133,* 20168–20171. doi:10.1021/ja2100774
22. Chen, F.; Bai, M.; Cao, K.; Zhao, Y.; Wei, J.; Zhao, Y. *Adv. Funct. Mater.* **2017,** *27,* 1702748. doi:10.1002/adfm.201702748
23. Chen, Y.; Ye, D.; Wu, M.; Chen, H.; Zhang, L.; Shi, J.; Wang, L. *Adv. Mater. (Weinheim, Ger.)* **2014,** *26,* 7019–7026. doi:10.1002/adma.201402572
24. Yang, G.; Xu, L.; Chao, Y.; Xu, J.; Sun, X.; Wu, Y.; Peng, R.; Liu, Z. *Nat. Commun.* **2017,** *8,* 902. doi:10.1038/s41467-017-01050-0
25. Zhang, H.-L.; Wei, X.-L.; Zang, Y.; Cao, J.-Y.; Liu, S.; He, X.-P.; Chen, Q.; Long, Y.-T.; Li, J.; Chen, G.-R.; Chen, K. *Adv. Mater. (Weinheim, Ger.)* **2013,** *25,* 4097–4101. doi:10.1002/adma.201300187
26. Ji, D.-K.; Zhang, Y.; Zang, Y.; Li, J.; Chen, G.-R.; He, X.-P.; Tian, H. *Adv. Mater. (Weinheim, Ger.)* **2016,** *28,* 9356–9363. doi:10.1002/adma.201602748
27. Ma, Z.; Zhang, P.; Yu, X.; Lan, H.; Li, Y.; Xie, D.; Li, J.; Yi, T. *J. Mater. Chem. B* **2015,** *3,* 7366–7371. doi:10.1039/c5tb01191d
28. Chai, X.; Fu, Y.-X.; James, T. D.; Zhang, J.; He, X.-P.; Tian, H. *Chem. Commun.* **2017,** *53,* 9494–9497. doi:10.1039/c7cc04427e
29. Wu, H.; Chen, Y.; Liu, Y. *Adv. Mater. (Weinheim, Ger.)* **2017,** *29,* 1605271. doi:10.1002/adma.201605271
30. Shi, Z.; Tu, Y.; Wang, R.; Liu, G.; Pu, S. *Dyes Pigm.* **2018,** *149,* 764–773. doi:10.1016/j.dyepig.2017.11.051
31. Kai, K.; Yoshida, Y.; Kageyama, H.; Saito, G.; Ishigaki, T.; Furukawa, Y.; Kawamata, J. *J. Am. Chem. Soc.* **2008,** *130,* 15938–15943. doi:10.1021/ja804503f
32. Yuan, Y.; Wu, S.; Shu, F.; Liu, Z. *Chem. Commun.* **2014,** *50,* 1095–1097. doi:10.1039/c3cc47755j
33. Fan, D.; Shang, C.; Gu, W.; Wang, E.; Dong, S. *ACS Appl. Mater. Interfaces* **2017,** *9,* 25870–25877. doi:10.1021/acsami.7b07369
34. Fan, H.; Yan, G.; Zhao, Z.; Hu, X.; Zhang, W.; Liu, H.; Fu, X.; Fu, T.; Zhang, X.-B.; Tan, W. *Angew. Chem., Int. Ed.* **2016,** *55,* 5477–5482. doi:10.1002/anie.201510748
35. He, X.-P.; Tian, H. *Chem* **2018,** *4,* 246–268. doi:10.1016/j.chempr.2017.11.006
36. Wu, X.; Tan, Y. J.; Toh, H. T.; Nguyen, L. H.; Kho, S. H.; Chew, S. Y.; Yoon, H. S.; Liu, X.-W. *Chem. Sci.* **2017,** *8,* 3980–3988. doi:10.1039/c6sc05251g
37. Hang, Y.; Cai, X.; Wang, J.; Jiang, T.; Hua, J.; Liu, B. *Sci. China: Chem.* **2018,** *61,* 898–908. doi:10.1007/s11426-018-9259-3
38. Su, T. A.; Shihadih, D. S.; Cao, W.; Detomasi, T. C.; Heffern, M. C.; Jia, S.; Stahl, A.; Chang, C. J. *J. Am. Chem. Soc.* **2018,** *140,* 13764–13774. doi:10.1021/jacs.8b08014
39. Ye, Z.; Wu, W.-R.; Qin, Y.-F.; Hu, J.; Liu, C.; Seeberger, P. H.; Yin, J. *Adv. Funct. Mater.* **2018,** *28,* 1706600. doi:10.1002/adfm.201706600
40. Han, X.; Song, X.; Yu, F.; Chen, L. *Chem. Sci.* **2017,** *8,* 6991–7002. doi:10.1039/c7sc02888a
41. Jiang, Y.; Cheng, J.; Yang, C.; Hu, Y.; Li, J.; Han, Y.; Zang, Y.; Li, X. *Chem. Sci.* **2017,** *8,* 8012–8018. doi:10.1039/c7sc03338a
42. Wu, X.; Sun, X.; Guo, Z.; Tang, J.; Shen, Y.; James, T. D.; Tian, H.; Zhu, W. *J. Am. Chem. Soc.* **2014,** *136,* 3579–3588. doi:10.1021/ja412380j
43. Li, Q.; Cao, J.; Wang, Q.; Zhang, J.; Zhu, S.; Guo, Z.; Zhu, W.-H. *J. Mater. Chem. B* **2019,** *7,* 1503–1509. doi:10.1039/c8tb03188f
44. Yu, F.; Zhang, F.; Tang, L.; Ma, J.; Ling, D.; Chen, X.; Sun, X. *J. Mater. Chem. B* **2018,** *6,* 5362–5367. doi:10.1039/c8tb01360h
45. Liu, J.; Sun, Y.-Q.; Huo, Y.; Zhang, H.; Wang, L.; Zhang, P.; Song, D.; Shi, Y.; Guo, W. *J. Am. Chem. Soc.* **2014,** *136,* 574–577. doi:10.1021/ja409578w
46. Yang, X.; Qian, Y. *J. Mater. Chem. B* **2018,** *6,* 7486–7494. doi:10.1039/c8tb02309c
47. Jiang, X.; Yu, Y.; Chen, J.; Zhao, M.; Chen, H.; Song, X.; Matzuk, A. J.; Carroll, S. L.; Tan, X.; Sizovs, A.; Cheng, N.; Wang, M. C.; Wang, J. *ACS Chem. Biol.* **2015,** *10,* 864–874. doi:10.1021/cb500986w

License and Terms

This is an Open Access article under the terms of the Creative Commons Attribution License (http://creativecommons.org/licenses/by/4.0). Please note that the reuse, redistribution and reproduction in particular requires that the authors and source are credited.

The license is subject to the *Beilstein Journal of Organic Chemistry* terms and conditions: (https://www.beilstein-journals.org/bjoc)

The definitive version of this article is the electronic one which can be found at: doi:10.3762/bjoc.15.230

BEILSTEIN JOURNAL OF ORGANIC CHEMISTRY

Reversible switching of arylazopyrazole within a metal–organic cage

Anton I. Hanopolskyi[1,§], Soumen De[1], Michał J. Białek[1], Yael Diskin-Posner[2], Liat Avram[2], Moran Feller[1] and Rafal Klajn[*1]

Full Research Paper

Open Access

Address:
[1]Department of Organic Chemistry, Weizmann Institute of Science, Rehovot 76100, Israel and [2]Chemical Research Support, Weizmann Institute of Science, Rehovot 76100, Israel

Email:
Rafal Klajn[*] - rafal.klajn@weizmann.ac.il

* Corresponding author
§ On leave from: Institute of High Technologies, Taras Shevchenko National University of Kyiv, Kyiv 01033, Ukraine

Keywords:
arylazopyrazoles; coordination cages; inclusion complexes; molecular switches; photochromism

Beilstein J. Org. Chem. **2019,** *15,* 2398–2407.
doi:10.3762/bjoc.15.232

Received: 19 July 2019
Accepted: 26 September 2019
Published: 10 October 2019

This article is part of the thematic issue "Molecular switches".

Guest Editor: W. Szymanski

© 2019 Hanopolskyi et al.; licensee Beilstein-Institut.
License and terms: see end of document.

Abstract

Arylazopyrazoles represent a new family of molecular photoswitches characterized by a near-quantitative conversion between two states and long thermal half-lives of the metastable state. Here, we investigated the behavior of a model arylazopyrazole in the presence of a self-assembled cage based on Pd–imidazole coordination. Owing to its high water solubility, the cage can solubilize the *E* isomer of arylazopyrazole, which, by itself, is not soluble in water. NMR spectroscopy and X-ray crystallography have independently demonstrated that each cage can encapsulate two molecules of *E*-arylazopyrazole. UV-induced switching to the *Z* isomer was accompanied by the release of one of the two guests from the cage and the formation of a 1:1 cage/*Z*-arylazopyrazole inclusion complex. DFT calculations suggest that this process involves a dramatic change in the conformation of the cage. Back-isomerization was induced with green light and resulted in the initial 1:2 cage/*E*-arylazopyrazole complex. This back-isomerization reaction also proceeded in the dark, with a rate significantly higher than in the absence of the cage.

Introduction

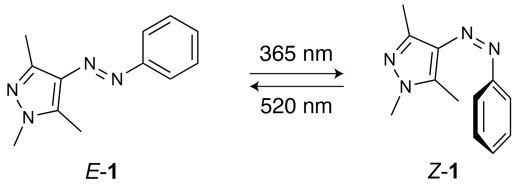
The importance of confinement for chemical reactivity is becoming increasingly appreciated. Confining reactive species to small volumes can greatly increase their effective molarity and consequently, promote chemical reactions. Such reaction acceleration has been demonstrated at interfaces [1-3], in self-assembled cages [4-7], on DNA chains [8], and on the surfaces of inorganic nanoparticles [9,10]. Additionally, nanosized cages can induce preorganization of the encapsulated species, thus inducing unusual regioselectivities in various chemical reactions [11-13]. The limited dimensions of cage cavities can also be used for arresting the growth of polycondensates at an early stage, thereby making it possible to isolate labile species. For example, Fujita and co-workers demonstrated the stabilization of cyclic trimers of siloxanes inside small self-assembled

cages [14] and, using larger cages, the synthesis of 4 nm silica nanoparticles, which would be difficult to obtain otherwise [15].

One class of organic compounds that exhibit various intriguing properties under confinement is photochromic molecules. In a seminal contribution, unusual switching patterns have been revealed within densely packed monolayers of azobenzene on planar gold [16]. In contrast, placing azobenzene inside the cavity of an octahedral cage renders it photochemically inert, stabilizing the typically metastable *Z* isomer [17]. Similarly, a related cage has recently been shown to induce negative photochromism in the spiropyran switch [18]. Other recent studies of photochromic systems within macrocyclic and supramolecular hosts [19] include dihydroazulene switches [20] and red-shifted azobenzenes [21,22] inside cucurbiturils and cyclodextrins. The behavior of light-responsive compounds can also be affected by their confinement to the surfaces of inorganic nanoparticles. Among other examples, the isomerization kinetics of azobenzene could be tuned by a factor of >5000 by the molecules with which it was co-adsorbed on gold nanoparticles [23], and donor–acceptor Stenhouse adduct (DASA) switches were found to be stabilized in their zwitterionic form when confined to iron oxide nanoparticles [24]. Similarly, the ability of anthracenes to photodimerize greatly depends on the curvature of their "host" nanoparticle [25]. Despite these advances, we are still far from achieving the ease and elegance, with which natural systems employ confinement effects to control photoisomerization reactions [26].

Recently, much effort has been devoted to developing new families of heterocyclic azo switches [27-31], largely driven by the rapid growth of the emerging field of photopharmacology [32-34]. Among them, arylazopyrazoles have attracted considerable interest because of their synthetic availability and desirable photochemical properties, such as the high thermal stability of the *Z* isomer and a large band separation between the *E* and *Z* isomers, allowing each to be addressed with a high selectivity [35-40]. Consequently, arylazopyrazoles have been employed as photoresponsive gelators [41] and adhesives [42] and for controlling antimicrobial response [43,44], cell adhesion to surfaces [45], as well as DNA [46] and microtubule [47] self-assembly using light.

Here, we focused on the prototypical arylazopyrazole **1** [35] (Scheme 1) and a previously reported [48] metal–organic cage **2** (see Figure 1). We have recently demonstrated that various azobenzenes formed 2:1 inclusion complexes with **2** [49] and hypothesized, based on the structural similarity between azobenzenes and arylazopyrazoles, that **2** would similarly encapsulate *E*-**1**.



Scheme 1: Reversible photoisomerization of phenylazotrimethylpyrazole **1**.

Results and Discussion

Arylazopyrazole *E*-**1** has a very low solubility in water and its encapsulation in cage **2** was attempted from the solid state. Encouragingly, when a colorless aqueous solution of **2** was stirred with an excess of solid *E*-**1**, it turned to intense yellow within several hours. Figure 1 shows a ^{1}H NMR spectrum of the resulting solution, where the identity of all the proton resonances was assigned using a combination of two-dimensional NMR techniques, including ^{1}H-^{1}H homonuclear correlation spectroscopy (COSY), ^{1}H-^{1}H nuclear Overhauser effect spectroscopy (NOESY), ^{1}H-^{13}C heteronuclear single quantum correlation spectroscopy (HSQC), and ^{1}H-^{13}C heteronuclear multiple bond correlation spectroscopy (HMBC) (see the Supporting Information File 1, Figures S5–S13). The spectrum showed the presence of all of *E*-**1**'s protons, with the resonances associated with the *ortho* protons of **1**'s phenyl ring, as well as the protons of all three methyl groups markedly upfield-shifted compared to free *E*-**1** in $CDCl_3$ (see Figure S14 in Supporting Information File 1). These shifts (by ~1.0–2.2 ppm) cannot be accounted for by replacing the solvent from $CDCl_3$ to D_2O; rather, they suggest that **1** resides in the hydrophobic cavity of **2**, interacting with its aromatic walls. Integration of the signals due to **1** and **2** confirmed that each molecule of the host encapsulates two molecules of the guest.

The presence of a complex is also evident from the NOE spectrum, which shows multiple host–guest correlations (see Figure S6 in Supporting Information File 1 for a full-range spectrum). For example, *E*-**1**'s protons $H_{\mathbf{d}}$ at 6.22 ppm correlate both with the resonances at 7.78 ppm and at 7.57 ppm, which all originate from **2**'s protons ($H_{\mathbf{2}}$ + $H_{\mathbf{3}}$ and $H_{\mathbf{5}}$ + $H_{\mathbf{7}}$, respectively). Similarly, the $H_{\mathbf{a}}$ protons are correlated with $H_{\mathbf{1}}$, $H_{\mathbf{3}}$, and $H_{\mathbf{7}}$, whereas the $H_{\mathbf{c}}$ protons are correlated with $H_{\mathbf{4}}$, $H_{\mathbf{8}}$, and $H_{\mathbf{5}}$ (see the partial NOE spectrum in Figure 2; see below for further analysis of this spectrum).

Single crystals of (*E*-**1**)$_2$⊂**2** suitable for X-ray diffraction were obtained by slow water evaporation from an aqueous solution of the complex. The data were collected immediately after dipping the crystal in Paratone oil and flash-cooling. We found that

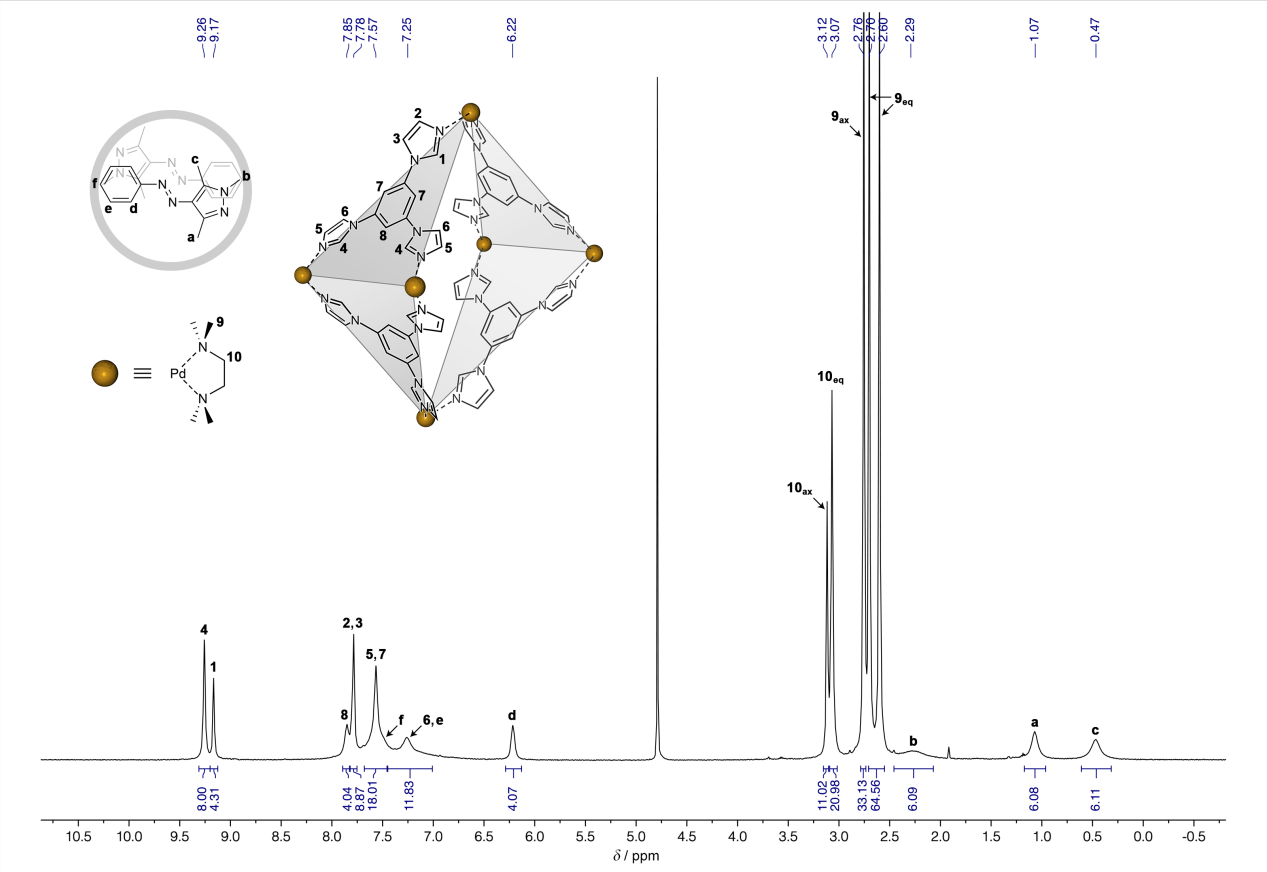


Figure 1: ^{1}H NMR spectrum of (*E*-**1**)$_2$⊂**2** (500 MHz, D_2O, 298 K).

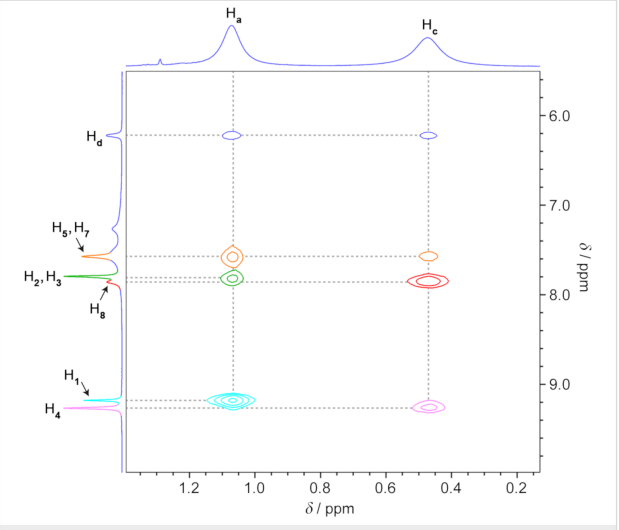


Figure 2: Partial ^{1}H-^{1}H NOESY NMR spectrum of (*E*-**1**)$_2$⊂**2** showing NOE correlations between host **2** and guest **1** (500 MHz, D_2O, 298 K) (the corresponding full-range spectrum is shown in Figure S6, Supporting Information File 1).

(*E*-**1**)$_2$⊂**2** crystallizes in the monoclinic space group $P2_1/c$, with one molecule of **1** and a half-molecule of **2** in the asymmetric unit. In other words, each cage encapsulated two molecules of *E*-**1** (in agreement with the NMR spectra), arranged in an antiparallel fashion (Figure 3). The binding of *E*-**1** within **2** is driven by a combination of π–π stacking, van der Waals forces, and C–H···π interactions (vide infra); in addition, the encapsulation is likely facilitated by the release of "high-energy" water molecules from the cavity of **2** [50,51].

Determining the X-ray structure was challenging; the difficulty lies in the fact that both the cage and the encapsulated guest dimer exist in the form of two different conformations. Figure 3 shows (*E*-**1**)$_2$⊂**2** that features the main conformations of both (*E*-**1**)$_2$ and **2**, amounting to 59% and 93% of the total population of the guest and the host component, respectively. The remaining 41% of (*E*-**1**)$_2$ features the same separation distance between the two guest molecules (d = 3.503 Å vs 3.497 Å in the major isomer; a distance typical of π–π-stacked moieties), but a significantly larger offset in the horizontal direction (the distance between *para* carbon atoms of the two guests, d = 11.154 Å vs 10.638 Å for the major isomer; see Figure S15, Supporting Information File 1). The difference between the major (93%) and the minor (7%) conformation of the host is small and is mostly related to the positions of the Pd centers (Figure S16, Supporting Information File 1).

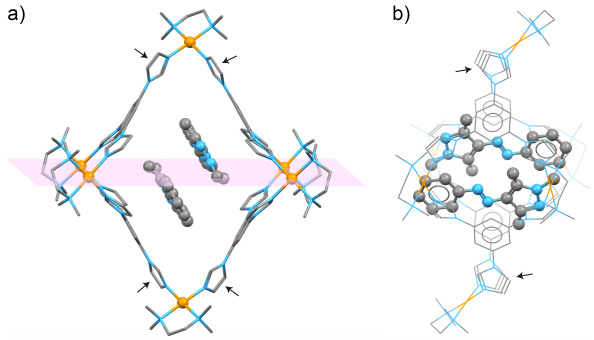


Figure 3: Front view (a) and side view (b) of the X-ray crystal structure of $(E\text{-}\mathbf{1})_2\subset\mathbf{2}$ (major conformations of **1** and **2**; see also Supporting Information File 1, Figures S15 and S16). The horizontal plane (pink) denotes the positions of eight equatorial imidazole groups; four axial imidazoles are denoted by black arrows. Color codes: C, gray; N, blue; Pd, orange. Hydrogens, counterions, and solvent molecules are not shown for clarity.

We were pleased to find that the structural features of $(E\text{-}\mathbf{1})_2\subset\mathbf{2}$ resolved by X-ray crystallography were in full agreement with a detailed analysis of the complex's NOE spectra (see Figure 2 above). For example, *E*-**1**'s $H_\mathbf{a}$ protons at 1.07 ppm correlate with **2**'s axial – but not equatorial – acidic imidazole $H_\mathbf{1}$ protons (cyan in Figure 2), which is in agreement with the close proximity of these two protons in the X-ray structure ($d_{\mathbf{a}-\mathbf{1}}$ = 3.68 Å). Conversely, $H_\mathbf{c}$ protons only correlate with the equatorial $H_\mathbf{4}$ protons (pink in Figure 2; $d_{\mathbf{c}-\mathbf{4}}$ = 3.32 Å). Interestingly, the NOE correlations we found can only be explained by taking into account the coexistence of both configurations of $(E\text{-}\mathbf{1})_2$, which suggests that they coexist not only in the crystalline state, but also in solution. For example, $H_\mathbf{c}$'s correlation with the resonance at 7.57 ppm (due to cage's $H_\mathbf{5}$ + $H_\mathbf{7}$) can be explained by the close distance between $H_\mathbf{c}$ and $H_\mathbf{5}$ in the complex's minor (41%) isomer, $d_{\mathbf{c}-\mathbf{5}}$ = 2.88 Å (for the major isomer, $d_{\mathbf{c}-\mathbf{5}}$ = 4.10 Å and $d_{\mathbf{c}-\mathbf{7}}$ = 4.13 Å). On the other hand, only the major isomer is expected to show a correlation between $H_\mathbf{a}$ and $H_\mathbf{d}$ ($d_{\mathbf{a}-\mathbf{d}}$ = 3.38 Å; for the minor isomer, $d_{\mathbf{a}-\mathbf{d}}$ = 4.28 Å). Furthermore, the presence of NOE correlations between $H_\mathbf{d}$ and both $H_\mathbf{a}$ and $H_\mathbf{c}$ not only confirm the presence of two molecules of guest *E*-**1** inside host **2**, but also their antiparallel arrangement.

We also note that the mutual arrangement of the two guest molecules within the X-ray structure is such that the *N*-bound methyl group (i.e., $H_\mathbf{b}$ protons) of one guest lies directly above the phenyl ring of the other guest (see Figure S15, Supporting Information File 1). Specifically, the distance between $H_\mathbf{b}$ and the plane of the phenyl ring was determined as 2.42 Å, which corresponds to a fairly strong C–H···π interaction. Interestingly, a signature of this interaction can be found in the ^{1}H NMR spectrum of $(E\text{-}\mathbf{1})_2\subset\mathbf{2}$, where the signal due to $H_\mathbf{b}$ was significantly broader than those due to $H_\mathbf{a}$ and $H_\mathbf{c}$ (Figure 1).

Next, we investigated the photoisomerization of encapsulated *E*-**1**. UV irradiation (365 nm light-emitting diode, LED) of the transparent yellow solution of $(E\text{-}\mathbf{1})_2\subset\mathbf{2}$ in water did not result in any pronounced visual changes. However, UV–vis absorption spectroscopy showed (Figure 4) a dramatic decrease in the intensity of *E*-**1**'s absorption at 336 nm, along with the concomitant appearance of a broader peak at ~430 nm, which can be attributed to the n–π* transition in *Z*-**1**. Subsequent exposure to a 520 nm LED (a region with negligible absorption of *E*-**1**; see Figure 4) regenerated the initial spectrum, indicating the nearly complete reversibility of the process. The presence of a well-defined isosbestic point (at 391 nm) suggests a clean $E \rightleftharpoons Z$ transformation in both directions. This process appears to be fully reversible for many cycles (Figure 4, inset).

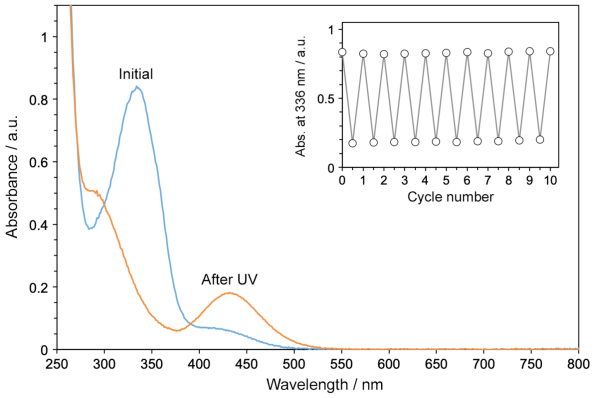


Figure 4: UV–vis absorption spectrum of an aqueous solution of $(E\text{-}\mathbf{1})_2\subset\mathbf{2}$ (blue) and following exposure of this solution to UV light for 5 min (orange). Inset: Ten cycles of reversible $E\text{-}\mathbf{1} \rightleftharpoons Z\text{-}\mathbf{1}$ photoisomerization. In each cycle, 5 min of UV was applied, followed by 2 min of green light.

Figure S17 (Supporting Information File 1) shows the ^{1}H NMR spectrum of $(E\text{-}\mathbf{1})_2\subset\mathbf{2}$ exposed to UV light. Notably, all six resonances of **1**'s protons have shifted, indicating a highly efficient photoisomerization to *Z*-**1**. The corresponding NOE spectra (Figures S18–S20, Supporting Information File 1) feature multiple correlations between the host's and the guest's protons. For example, the set of signals at 7.88–7.60 (all of which could be attributed to **2**) correlate strongly with the protons of all three methyl groups of *Z*-**1** ($H_\mathbf{a}$, $H_\mathbf{b}$, and $H_\mathbf{c}$), in addition to exhibiting weaker NOE correlations with $H_\mathbf{d}$, $H_\mathbf{e}$, and $H_\mathbf{f}$. Furthermore, the acidic imidazole protons correlate with most of *Z*-**1**'s protons; the strongest correlations were found between $H_\mathbf{a}$ and $H_\mathbf{1}$ and between $H_\mathbf{c}$ and $H_\mathbf{4}$ (Figure S20, Supporting Information File 1; note that the opposite was found for the *E* isomer, cf. Figure 2).

Despite repeated efforts, we did not succeed in preparing crystals of the (*Z*-**1**)⊂**2** inclusion complex suitable for X-ray diffraction. To obtain hints about the packing of *Z*-**1** within **2**, we therefore performed density functional theory (DFT) calculations. Compared with the complex before photoisomerization, the cage in (*Z*-**1**)⊂**2** is severely distorted (Figure 5; see also Supporting Information File 3), assuming a bowl-like shape (in contrast, the conformation of the bound guest is very similar to that of free *Z*-**1**). The optimized model of (*Z*-**1**)⊂**2** features strong interactions between the host and the guest. In particular, *Z*-**1**'s methyl groups H_a and H_c reside in close proximity to **2**'s acidic imidazole protons (H_1 and H_4, respectively), in agreement with the NMR findings (see Section 4 in the Supporting Information File 1). The apparent desymmetrization of **2** is not manifested by multiplication of signals due to H_1 and H_4, which can be attributed to the dynamic fluctuations of the cage in solution.

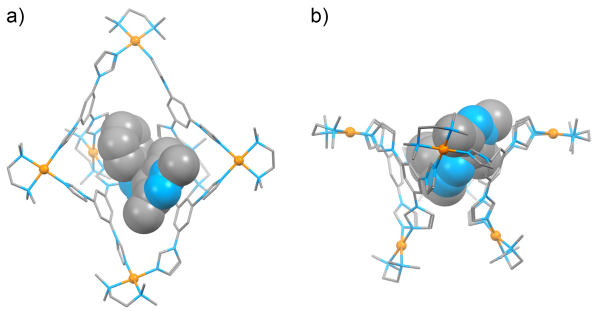


Figure 5: Top view (a) and side view (b) of the energy-optimized structure of (*Z*-**1**)⊂**2**. Color codes: C, gray; N, blue; Pd, orange. Hydrogens and counterions are not shown for clarity.

We have previously noted that 1:1 complexes of **2** with the *Z* isomers of various azobenzenes are notoriously difficult to crystallize [18]. We believe that the insights by DFT calculations reported here for (*Z*-**1**)⊂**2** can be extended to the complexes of **2** with other *Z*-azo guests as well.

To gain further insight into the photoisomerization reaction, we investigated it by NMR spectroscopy under in-situ irradiation (with an optical fiber inserted into the NMR spectrometer). Figure 6 shows a series of spectra recorded after increasing UV irradiation times. We found that whereas the position of **2**'s H_4 signal did not change (9.26 ppm), the signal due to H_1 shifted upfield by 0.20 ppm. This behavior is analogous to our previous findings, which showed that shifts of H_1 protons are indicative of switching of the bound guest and/or (de)encapsulation [18,49]. Integrating the signals due to *E*-**1**'s H_c protons (cyan in Figure 6) allowed us to estimate the yield of photoisomerization as >98%. This result, combined with the UV–vis absorption data in Figure 4, inset, indicates that the switching between *E*- and *Z*-**1** is near-quantitative in both directions.

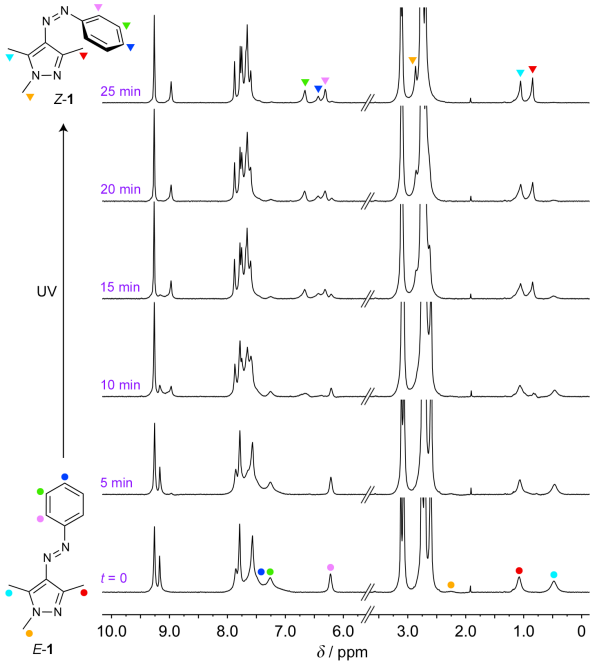


Figure 6: A series of ^{1}H NMR spectra of (*E*-**1**)$_2$⊂**2** (500 MHz, D_2O, 298 K) before (bottom) and after exposure to UV light (λ = 365 nm) inside the NMR spectrometer (using an optical fiber) for different periods of time (indicated in purple font) for up to 25 min.

To complete the cycle, we first allowed the system to relax thermally while recording NMR spectra (Figure S21, Supporting Information File 1). However, only 25% of *Z*-**1** back-isomerized to the *E* isomer within 3 h in the dark. Subsequent irradiation with green light (20 min) re-generated the initial solution of (*E*-**1**)$_2$⊂**2**. Interestingly, the final spectrum, although virtually free of *Z*-**1**, exhibited a residual (≈7%) peak of **2** with a conformation that binds *Z*-**1** (see Figure S22, Supporting Information File 1, red arrow at 8.97 ppm). This result suggests that the *Z*-**1** → *E*-**1** back-isomerization is faster than the conformational change of **2**, and that the cage gradually adapts its shape to that of the bound guest.

Further analysis of the NOE spectra of UV-irradiated solutions revealed correlations between *Z*-**1**'s i) H_a and H_d, ii) H_a and H_e, iii) H_c and H_d, and iv) H_c and H_e (all expected from the *Z* isomer alone), but no correlations between i) H_b with any of the three aromatic protons and ii) H_f with any of the three methyl groups. Furthermore, we note that the resonance due to H_b – very broad in complex (*E*-**1**)$_2$⊂**2** as a consequence of dimer formation – becomes as sharp as those of the other protons after UV irradiation (compare spectra **i** and **ii** in Figure

S23, Supporting Information File 1). Taken together, these observations indicate the absence of *Z*-**1**–*Z*-**1** interactions, thereby confirming that only one molecule of *Z*-**1** occupies the cavity of the cage. This conclusion is not surprising given the more bulky nature of the *Z* isomer – in fact, we have previously reported that photoirradiation of the 1:2 complex of **2** and tetra-*o*-fluoroazobenzene yields a 1:1 mixture of *Z*⊂**2** and free *Z*-azobenzene, which is insoluble in water and precipitates from the solution [49]. The *Z* isomer of **1**, however, has much higher water solubility and, following expulsion from the cage, can remain stable in solution. To verify this notion, we prepared pure *Z*-**1** (by evaporating the solvent from a solution of *E*-**1** in acetonitrile under continuous UV irradiation) and i) confirmed its high solubility in water (see Figure S24 in Supporting Information File 1 for an NMR spectrum of *Z*-**1** in D_2O) and ii) demonstrated light-controlled precipitation and re-solubilization of **1** (Figure S25, Supporting Information File 1).

Overall, the reaction taking place in the system can be written down as $(E\text{-}\mathbf{1})_2{\subset}\mathbf{2} \rightarrow (Z\text{-}\mathbf{1}){\subset}\mathbf{2} + Z\text{-}\mathbf{1}$. Interestingly, however, despite the existence of *Z*-**1** as two distinct species (encapsulated and non-encapsulated), the NMR spectrum of the UV-adapted solution showed the presence of only one set of guest peaks. This can be attributed to the rapid (on the NMR time scale) exchange between the free and encapsulated *Z*-**1**, resulting in a single peak for each proton, located in between the two expected peaks. To confirm this hypothesis, we recorded ^{1}H NMR spectra of i) *Z*-**1** in D_2O (spectrum **i** in Figure S27) and ii) (*Z*-**1**)⊂**2** without free *Z*-**1** (**ii** in Figure S27, Supporting Information File 1) (the latter was prepared by treating a UV-irradiated solution of $(E\text{-}\mathbf{1})_2{\subset}\mathbf{2}$ (i.e., a mixture of (*Z*-**1**)⊂**2** and *Z*-**1**) with an extra ~2.5 equivalents of **2**). Indeed, the resonances due to all **1**'s protons in (*E*-**1**)2⊂**2** exposed to UV light (Figure S26, Supporting Information File 1, spectrum **iii**) appeared at chemical shifts that constituted the averages of those found in spectra **i** and **ii**. As a control experiment, we added the same excess of **2** to a solution of $(E\text{-}\mathbf{1})_2{\subset}\mathbf{2}$ prior to UV irradiation and, as expected, did not observe any shifts of **1**'s signals.

To further confirm the photoswitching-induced guest expulsion, we performed detailed diffusion-ordered spectroscopy (DOSY) measurements. A representative DOSY spectrum of $(E\text{-}\mathbf{1})_2{\subset}\mathbf{2}$ is shown in Figure 7, left. The spectrum indicates the presence of a single species (the diffusion coefficient for **1**, D_1 = 1.91 (±0.01) · 10^{-10} $m^2{\cdot}s^{-1}$ (based on averaging H_a and H_d); the diffusion coefficient for **2**, D_2 = 1.85 (±0.01) · 10^{-10} $m^2{\cdot}s^{-1}$ (based on H_4); each diffusion measurement was repeated three times). In contrast, DOSY spectra recorded after UV irradiation exhibited two distinct sets of diffusion coefficients, associated with resonances of **1** and **2** (red and green shades in Figure 7, center). The average diffusion coefficients were determined as D_1 = 3.44 (±0.04) · 10^{-10} $m^2{\cdot}s^{-1}$ and D_2 = 1.86 (±0.01) · 10^{-10} $m^2{\cdot}s^{-1}$. The greatly increased D_1 value confirms that i) **1** was partially expelled from the cages, which can only accommodate one molecule of *Z*-**1** each, and ii) the free and bound *Z*-**1** are in rapid exchange

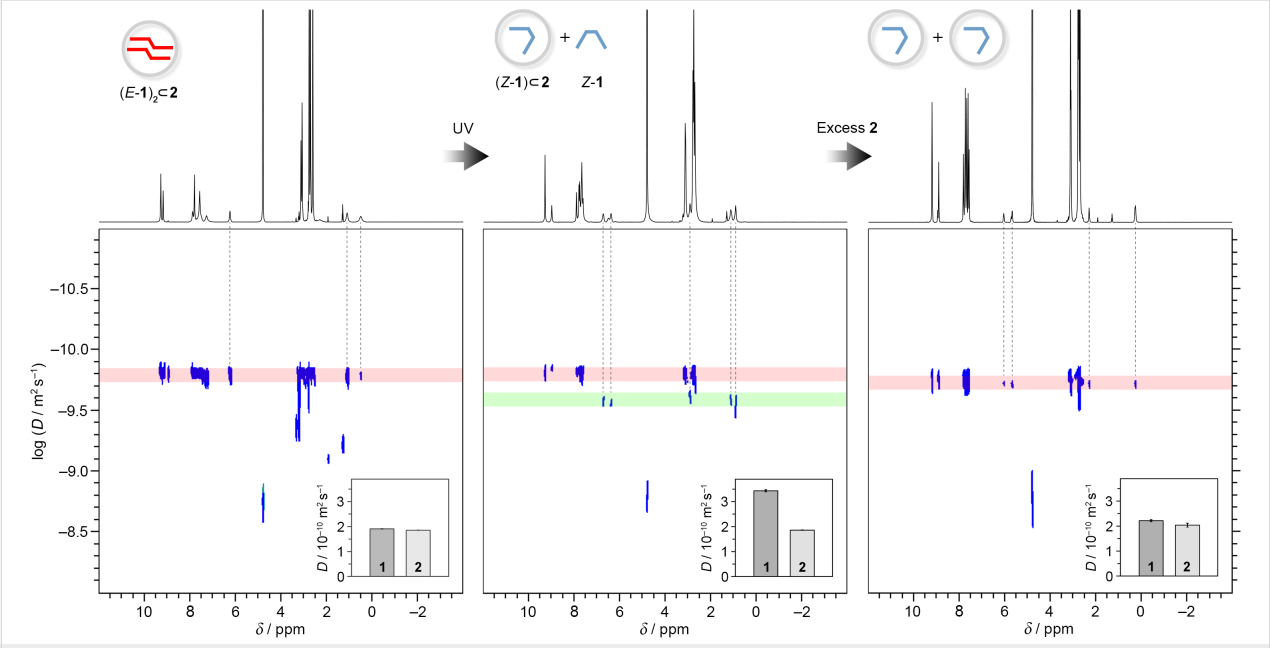


Figure 7: ^{1}H NMR and ^{1}H DOSY spectra of $(E\text{-}\mathbf{1})_2{\subset}\mathbf{2}$ (500 MHz, D_2O, 298 K) before (left) and after (center) UV irradiation and after the addition of ~2.5 equiv of **2** (right). The vertical dashed lines denote the resonances of **1**'s protons.

with each other. Finally, the addition of enough cages to re-encapsulate all the expelled *Z*-**1** results in a spectrum once again featuring a single set of diffusion coefficients (Figure 7, right; $D_{\mathbf{1}}$ = 2.22 (±0.04) · 10^{-10} $m^2 \cdot s^{-1}$ and $D_{\mathbf{2}}$ = 2.04 (±0.08) · 10^{-10} $m^2 \cdot s^{-1}$).

Finally, we were interested in how the presence of cage **2** affects the kinetics of the thermal back-isomerization of **1** (i.e., *Z*-**1** → *E*-**1** in the dark). This reaction was followed by monitoring the recovery of absorbance at 336 nm, which corresponds to the maximal absorbance (λ_{max}) of the *E* isomer. The orange circles in Figure 8a show the recovery profile of *E*-**1** in the presence of 0.5 equiv of **2**, following the reaction equation, (*Z*-**1**)⊂**2** + *Z*-**1** → (*E*-**1**)$_2$⊂**2**. The linear profile of the recovery suggests that the reaction obeys first-order kinetics, with a rate constant of 0.0975 h^{-1}, corresponding to a thermal half-life of *Z*-**1**, $\tau_{1/2}$ ≈ 7.1 hours. This value of $\tau_{1/2}$ is surprisingly small vis-à-vis the previously reported [35] $\tau_{1/2}$ ≈ 10 days in acetonitrile. To verify that this dramatic destabilization of *Z*-**1** does not reflect the effect of the solvent, we independently studied back-isomerization in an aqueous solution (Figure 8a, empty circles) and found that the presence of water does promote the *Z*→*E* reaction ($\tau_{1/2}$ ≈ 27.9 hours), although to a much lesser extent than does aqueous **2**.

These results suggest that cage **2** can catalyze the thermal back-isomerization of *Z*-**1** to *E*-**1**, whose kinetics can be written down as:

$$-\frac{\partial c_{Z\text{-}\mathbf{1}}}{\partial t} = k c_{Z\text{-}\mathbf{1}} c_{\mathbf{2}} = k_{obs} c_{Z\text{-}\mathbf{1}}, \qquad (1)$$

where the pseudo-first-order rate constant k_{obs} is the product of k and the concentration of the cage, $c_{\mathbf{2}}$, which remains constant over time. To validate this model, we studied the kinetics of *Z*→*E* back-isomerization in the presence of various concentrations of the cage (blue, purple, red, and yellow circles in Figure 8a) and found that k_{obs} indeed scales roughly linearly with $c_{\mathbf{2}}$ (Figure 8b).

We hypothesized that the acceleration effect may be due to Pd^{2+} ions residing at the corners of **2**. Although all Pd^{2+}s within the cage are coordinately saturated, **2** may exist in equilibrium with a small amount of a species, in which one of three imidazole groups of a triimidazole panel is temporarily dissociated from Pd^{2+}, enabling its interaction with *Z*-**1** (Figure 8c, step **i**). Coordination of Pd^{2+} to the azo moiety, combined with the strongly electron-donating pyrazole moiety, affords (Figure 8c, step **ii**) a system akin to push–pull azobenzenes, whose *Z* isomers can back-isomerize rapidly due to a reduced order of the N=N bond [52-54] (Figure 8c, step **iii**). The resulting *E*-**1** can be liberated and the Pd^{2+} center is available to carry out the cycle on another molecule of *Z*-**1** (Figure 8c, step **iv**). This reasoning is supported by the observation that Pd^{2+} intentionally added to a solution of *Z*-**1** (in the form of [$Pd(NO_3)_2$(tmeda)]; 0.944 mM) also induces a fast back-isomerization reaction, with k_{obs} ≈ 0.255 h^{-1}. The fast acceleration in the presence of **2** – despite low concentrations of the active Pd species – is likely due to the fast encapsulation of *Z*-**1** in **2**, which greatly increases the local concentration of Pd^{2+}. Indeed, when *Z*-**1** was mixed with a premade complex of **2** with a tightly bound guest, tetra-*o*-fluoroazobenzene [49], no acceleration effect was observed.

Conclusion

In summary, we investigated the encapsulation and switching of a prototypical arylazopyrazole in the hydrophobic cavity of a water-soluble metal–organic cage. A host–guest inclusion complex incorporating two molecules of arylazopyrazole was obtained in a quantitative yield. The complex was characterized

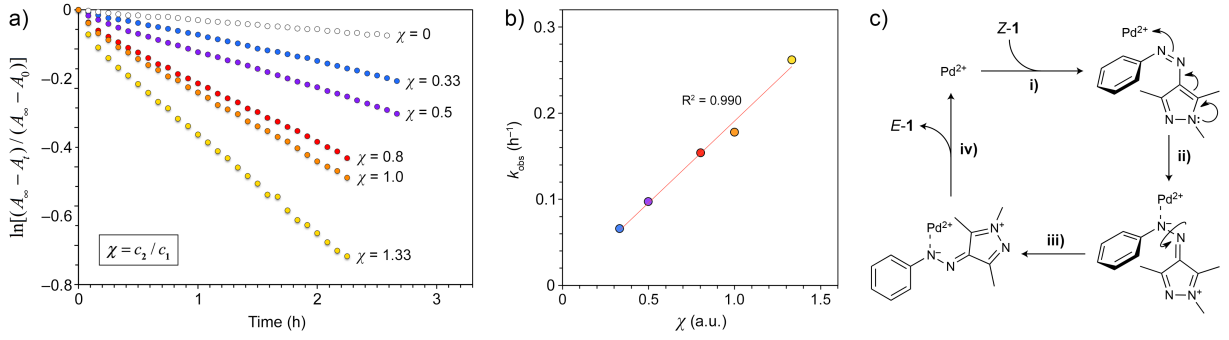


Figure 8: Palladium-accelerated back-isomerization of *Z*-**1**. a) Kinetics of the thermal back-isomerization of *Z*-**1** (*c* = 0.187 mM) in the presence of increasing concentrations of **2** (A_∞ denotes the absorbance at λ_{max} before irradiation; A_0 – immediately after exposure to UV light; A_t – after thermal relaxation for time *t*). b) Cage concentration dependence of the pseudo-first-order rate constant k_{obs}. c) The proposed mechanism underlying the Pd^{2+}-accelerated back-isomerization of *Z*-**1**.

by a series of NMR techniques, which showed that the resonances of the guest protons were upfield-shifted by up to 2.2 ppm. An antiparallel configuration of the guest molecules inside the cage was demonstrated independently by NMR spectroscopy and single-crystal X-ray diffraction. Exposure to UV light resulted in an $E \rightarrow Z$ isomerization of the guest, which was accompanied by the expulsion of one of two guest molecules from the cage. Different from the previously reported azobenzene complex, the photoisomerization was not accompanied by precipitation of the released *Z*-arylazopyrazole, which has good water solubility. The expulsion of the *Z* isomer was confirmed by diffusion-ordered NMR spectroscopy, which also showed that the released and the encapsulated *Z*-arylazopyrazole were in rapid exchange with each other. The back-isomerization reaction was achieved by irradiation with green light and it was accompanied by regeneration of the initial 2:1 complex; the $E \rightleftharpoons Z$ transformation proceeded in a near-quantitative fashion in both directions. The back-isomerization also proceeded thermally in a reaction that was accelerated by the cage. The acceleration could be attributed to the coordination of Pd^{2+} to the N=N moiety, as reported previously for azobenzene back-isomerization in the presence of Cu^{2+} [55] and for *Z*-arylazopyrazoles in the presence of an acid [56]. Overall, the results reported here strengthen our understanding of the behavior of molecular switches in confined spaces.

Experimental

Synthesis of cage 2: Cage **2** was prepared based on a modified literature known procedure [18]. Briefly, a solution of $[Pd(NO_3)_2(tmeda)]$ (200 mg, 0.577 mmol) in 25 mL of water was slowly added to 1,3,5-tri(1*H*-imidazol-1-yl)benzene (106 mg, 0.384 mmol) and the resulting mixture was stirred for 24 h at room temperature. Then, all the insoluble materials were removed by centrifugation and the supernatant was concentrated in vacuo. Crystalline **2** was obtained by acetone vapor diffusion to an aqueous solution of **1** (290 mg; yield = 95%). Cage **2** has an excellent solubility in water and is stable in the pH range of 4–9. It also exhibits high thermal stability, remaining stable for prolonged periods at 80 °C.

Synthesis of inclusion complex (E-1)$_2$⊂2: *E*-**1** was encapsulated by stirring excess solid *E*-**1** with a solution of **2** in water (H_2O/D_2O). Encapsulation of *E*-**1** by **2** was followed by UV–vis absorption spectroscopy; stirring was discontinued when no further coloration of the solution was observed. Excess *E*-**1** was removed by filtration. ^{1}H NMR (500 MHz, D_2O) δ 9.26 (s, 8H), 9.17 (s, 4H), 7.85 (s, 4H), 7.78 (br, 8H), 7.57 (br, 18H), 7.25 (br, 12H), 6.22 (br, 4H), 3.12 (s, 8H), 3.07 (s, 16H), 2.76 (s, 24H), 2.70 (s, 24H), 2.60 (s, 24H), 2.29 (s, 6H), 1.07 (s, 6H), 0.47 (s, 6H); ^{13}C{^{1}H} NMR (125 MHz, D_2O) δ 152.0, 138.8, 138.3, 138.1, 137.1, 133.2, 131.7, 130.5, 130.4, 129.8, 121.6, 120.9, 120.5, 112.9, 111.8, 63.3, 63.2, 51.0, 50.9, 50.7, 34.6, 12.5, 7.3 (the signal assignment is based on COSY, NOESY, HSQC, and HMBC spectra of the complex, as well as COSY, NOESY, and HSQC spectra of free *E*-**1** recorded in $CDCl_3$).

Thermal back-isomerization studies: The *Z* isomer of **1** was first prepared by UV irradiation of a solution of *E*-**1** in acetonitrile, followed by solvent evaporation under UV light. *Z*-**1** was dissolved in pure water and a desired amount of an aqueous solution of cage **2** was added (final concentration of *Z*-**1** = 0.187 mM; $c_{\mathbf{2}}$ = 0.0623 mM (0.33 equiv); 0.0935 mM (0.5 equiv); 0.150 mM (0.8 equiv), 0.187 mM (1.0 equiv); 0.249 mM (1.33 equiv)). The rate of back-isomerization was followed by monitoring the increase in absorbance at λ_{max} (336 nm). In control experiments, we followed the back-isomerization of *Z*-**1** (0.187 mM) in the absence of **2** and in the presence of $[Pd(NO_3)_2(tmeda)]$ (0.944 mM) and a 1:2 complex of **2** and tetra-*o*-fluoroazobenzene [49].

Supporting Information

The Supporting Information features further experimental details, including synthesis and characterization of arylazopyrazole **1**, characterization of inclusion complexes (E-**1**)$_2$⊂**2** and (Z-**1**)⊂**2**, photoisomerization and thermal relaxation studies, and details on X-ray data collection and refinement. In addition, X-ray data for inclusion complex (E-**1**)$_2$⊂**2** and the energy-optimized structure for inclusion complex (Z-**1**)⊂**2** are given.

Supporting Information File 1

Further experimental details.
[https://www.beilstein-journals.org/bjoc/content/supplementary/1860-5397-15-232-S1.pdf]

Supporting Information File 2

X-ray data for inclusion complex (E-**1**)$_2$⊂**2**.
[https://www.beilstein-journals.org/bjoc/content/supplementary/1860-5397-15-232-S2.cif]

Supporting Information File 3

Energy-optimized structure for inclusion complex (Z-**1**)⊂**2**.
[https://www.beilstein-journals.org/bjoc/content/supplementary/1860-5397-15-232-S3.mol2]

Acknowledgements

This work was supported by the European Research Council (grant #820008) and the Minerva Foundation with funding from the Federal German Ministry for Education and Research. DFT

calculations were carried out using resources provided by the Wroclaw Centre for Networking and Supercomputing (grant #329).

ORCID® iDs

Soumen De - https://orcid.org/0000-0003-4674-9183
Michał J. Białek - https://orcid.org/0000-0002-4890-2156
Yael Diskin-Posner - https://orcid.org/0000-0002-9008-8477
Liat Avram - https://orcid.org/0000-0001-6535-3470
Rafal Klajn - https://orcid.org/0000-0002-6320-8875

References

1. Narayan, S.; Muldoon, J.; Finn, M. G.; Fokin, V. V.; Kolb, H. C.; Sharpless, K. B. *Angew. Chem., Int. Ed.* **2005,** *44,* 3275–3279. doi:10.1002/anie.200462883
2. Bain, R. M.; Sathyamoorthi, S.; Zare, R. N. *Angew. Chem., Int. Ed.* **2017,** *56,* 15083–15087. doi:10.1002/anie.201708413
3. Fallah-Araghi, A.; Meguellati, K.; Baret, J.-C.; El Harrak, A.; Mangeat, T.; Karplus, M.; Ladame, S.; Marques, C. M.; Griffiths, A. D. *Phys. Rev. Lett.* **2014,** *112,* 028301. doi:10.1103/physrevlett.112.028301
4. Kang, J.; Rebek, J., Jr. *Nature* **1997,** *385,* 50–52. doi:10.1038/385050a0
5. Hastings, C. J.; Pluth, M. D.; Bergman, R. G.; Raymond, K. N. *J. Am. Chem. Soc.* **2010,** *132,* 6938–6940. doi:10.1021/ja102633e
6. Zhang, Q.; Tiefenbacher, K. *Nat. Chem.* **2015,** *7,* 197–202. doi:10.1038/nchem.2181
7. Wang, K.; Cai, X.; Yao, W.; Tang, D.; Kataria, R.; Ashbaugh, H. S.; Byers, L. D.; Gibb, B. C. *J. Am. Chem. Soc.* **2019,** *141,* 6740–6747. doi:10.1021/jacs.9b02287
8. Li, X.; Liu, D. R. *Angew. Chem., Int. Ed.* **2004,** *43,* 4848–4870. doi:10.1002/anie.200400656
9. Xu, P.; Kang, L.; Mack, N. H.; Schanze, K. S.; Han, X.; Wang, H.-L. *Sci. Rep.* **2013,** *3,* 2997. doi:10.1038/srep02997
10. Jenkins, S. V.; Chen, S.; Chen, J. *Tetrahedron Lett.* **2015,** *56,* 3368–3372. doi:10.1016/j.tetlet.2015.03.041
11. Chen, J.; Rebek, J. *Org. Lett.* **2002,** *4,* 327–329. doi:10.1021/ol0168115
12. Yoshizawa, M.; Tamura, M.; Fujita, M. *Science* **2006,** *312,* 251–254. doi:10.1126/science.1124985
13. Zhao, H.; Sen, S.; Udayabhaskararao, T.; Sawczyk, M.; Kučanda, K.; Manna, D.; Kundu, P. K.; Lee, J.-W.; Král, P.; Klajn, R. *Nat. Nanotechnol.* **2016,** *11,* 82–88. doi:10.1038/nnano.2015.256
14. Yoshizawa, M.; Kusukawa, T.; Fujita, M.; Sakamoto, S.; Yamaguchi, K. *J. Am. Chem. Soc.* **2001,** *123,* 10454–10459. doi:10.1021/ja010875t
15. Suzuki, K.; Sato, S.; Fujita, M. *Nat. Chem.* **2010,** *2,* 25–29. doi:10.1038/nchem.446
16. Dri, C.; Peters, M. V.; Schwarz, J.; Hecht, S.; Grill, L. *Nat. Nanotechnol.* **2008,** *3,* 649–653. doi:10.1038/nnano.2008.269
17. Kusukawa, T.; Fujita, M. *J. Am. Chem. Soc.* **1999,** *121,* 1397–1398. doi:10.1021/ja9837295
18. Samanta, D.; Galaktionova, D.; Gemen, J.; Shimon, L. J. W.; Diskin-Posner, Y.; Avram, L.; Král, P.; Klajn, R. *Nat. Commun.* **2018,** *9,* 641. doi:10.1038/s41467-017-02715-6
19. Qu, D.-H.; Wang, Q.-C.; Zhang, Q.-W.; Ma, X.; Tian, H. *Chem. Rev.* **2015,** *115,* 7543–7588. doi:10.1021/cr5006342
20. Petersen, M. Å.; Rasmussen, B.; Andersen, N. N.; Sauer, S. P. A.; Nielsen, M. B.; Beeren, S. R.; Pittelkow, M. *Chem. – Eur. J.* **2017,** *23,* 17010–17016. doi:10.1002/chem.201703196
21. Wei, J.; Jin, T.-T.; Yin, Y.-F.; Jiang, X.-M.; Zheng, S.-T.; Zhan, T.-G.; Cui, J.; Liu, L.-J.; Kong, L.-C.; Zhang, K.-D. *Org. Chem. Front.* **2019,** *6,* 498–505. doi:10.1039/c8qo01157e
22. Huang, H.; Juan, A.; Katsonis, N.; Huskens, J. *Tetrahedron* **2017,** *73,* 4913–4917. doi:10.1016/j.tet.2017.05.026
23. Chu, Z.; Han, Y.; Bian, T.; De, S.; Král, P.; Klajn, R. *J. Am. Chem. Soc.* **2019,** *141,* 1949–1960. doi:10.1021/jacs.8b09638
24. Ahrens, J.; Bian, T.; Vexler, T.; Klajn, R. *ChemPhotoChem* **2017,** *1,* 230–236. doi:10.1002/cptc.201700009
25. Zdobinsky, T.; Maiti, P. S.; Klajn, R. *J. Am. Chem. Soc.* **2014,** *136,* 2711–2714. doi:10.1021/ja411573a
26. Shichida, Y.; Matsuyama, T. *Philos. Trans. R. Soc., B* **2009,** *364,* 2881–2895. doi:10.1098/rstb.2009.0051
27. Simeth, N. A.; Crespi, S.; Fagnoni, M.; König, B. *J. Am. Chem. Soc.* **2018,** *140,* 2940–2946. doi:10.1021/jacs.7b12871
28. Calbo, J.; Weston, C. E.; White, A. J. P.; Rzepa, H. S.; Contreras-García, J.; Fuchter, M. J. *J. Am. Chem. Soc.* **2017,** *139,* 1261–1274. doi:10.1021/jacs.6b11626
29. Xu, Y.; Gao, C.; Andréasson, J.; Grøtli, M. *Org. Lett.* **2018,** *20,* 4875–4879. doi:10.1021/acs.orglett.8b02014
30. Weston, C. E.; Richardson, R. D.; Fuchter, M. J. *Chem. Commun.* **2016,** *52,* 4521–4524. doi:10.1039/c5cc10380k
31. Travieso-Puente, R.; Budzak, S.; Chen, J.; Stacko, P.; Jastrzebski, J. T. B. H.; Jacquemin, D.; Otten, E. *J. Am. Chem. Soc.* **2017,** *139,* 3328–3331. doi:10.1021/jacs.6b12585
32. Broichhagen, J.; Frank, J. A.; Trauner, D. *Acc. Chem. Res.* **2015,** *48,* 1947–1960. doi:10.1021/acs.accounts.5b00129
33. Velema, W. A.; Szymanski, W.; Feringa, B. L. *J. Am. Chem. Soc.* **2014,** *136,* 2178–2191. doi:10.1021/ja413063e
34. Pianowski, Z. L. *Chem. – Eur. J.* **2019,** *25,* 5128–5144. doi:10.1002/chem.201805814
35. Weston, C. E.; Richardson, R. D.; Haycock, P. R.; White, A. J. P.; Fuchter, M. J. *J. Am. Chem. Soc.* **2014,** *136,* 11878–11881. doi:10.1021/ja505444d
36. Stricker, L.; Fritz, E.-C.; Peterlechner, M.; Doltsinis, N. L.; Ravoo, B. J. *J. Am. Chem. Soc.* **2016,** *138,* 4547–4554. doi:10.1021/jacs.6b00484
37. Wang, Y.-T.; Liu, X.-Y.; Cui, G.; Fang, W.-H.; Thiel, W. *Angew. Chem., Int. Ed.* **2016,** *55,* 14009–14013. doi:10.1002/anie.201607373
38. Pandit, R. P.; Kim, S. H.; Lee, Y. R. *Org. Biomol. Chem.* **2016,** *14,* 6996–7000. doi:10.1039/c6ob01158f
39. Stricker, L.; Böckmann, M.; Kirse, T. M.; Doltsinis, N. L.; Ravoo, B. J. *Chem. – Eur. J.* **2018,** *24,* 8639–8647. doi:10.1002/chem.201800587
40. Niehues, M.; Tegeder, P.; Ravoo, B. J. *Beilstein J. Org. Chem.* **2019,** *15,* 1407–1415. doi:10.3762/bjoc.15.140
41. Chu, C.-W.; Stricker, L.; Kirse, T. M.; Hayduk, M.; Ravoo, B. J. *Chem. – Eur. J.* **2019,** *25,* 6131–6140. doi:10.1002/chem.201806042
42. Lamping, S.; Stricker, L.; Ravoo, B. J. *Polym. Chem.* **2019,** *10,* 683–690. doi:10.1039/c8py01496e
43. Weston, C. E.; Krämer, A.; Colin, F.; Yildiz, Ö.; Baud, M. G. J.; Meyer-Almes, F.-J.; Fuchter, M. J. *ACS Infect. Dis.* **2017,** *3,* 152–161. doi:10.1021/acsinfecdis.6b00148
44. Bian, Q.; Chen, S.; Xing, Y.; Yuan, D.; Lv, L.; Wang, G. *Acta Biomater.* **2018,** *76,* 39–45. doi:10.1016/j.actbio.2018.06.039
45. Wiemann, M.; Niebuhr, R.; Juan, A.; Cavatorta, E.; Ravoo, B. J.; Jonkheijm, P. *Chem. – Eur. J.* **2018,** *24,* 813–817. doi:10.1002/chem.201705426

46. Adam, V.; Prusty, D. K.; Centola, M.; Škugor, M.; Hannam, J. S.; Valero, J.; Klöckner, B.; Famulok, M. *Chem. – Eur. J.* **2018,** *24,* 1062–1066. doi:10.1002/chem.201705500
47. Zhang, Y.-M.; Zhang, N.-Y.; Xiao, K.; Yu, Q.; Liu, Y. *Angew. Chem., Int. Ed.* **2018,** *57,* 8649–8653. doi:10.1002/anie.201804620
48. Samanta, D.; Mukherjee, S.; Patil, Y. P.; Mukherjee, P. S. *Chem. – Eur. J.* **2012,** *18,* 12322–12329. doi:10.1002/chem.201201679
49. Samanta, D.; Gemen, J.; Chu, Z.; Diskin-Posner, Y.; Shimon, L. J. W.; Klajn, R. *Proc. Natl. Acad. Sci. U. S. A.* **2018,** *115,* 9379–9384. doi:10.1073/pnas.1712787115
50. Biedermann, F.; Nau, W. M.; Schneider, H.-J. *Angew. Chem., Int. Ed.* **2014,** *53,* 11158–11171. doi:10.1002/anie.201310958
51. Biedermann, F.; Uzunova, V. D.; Scherman, O. A.; Nau, W. M.; De Simone, A. *J. Am. Chem. Soc.* **2012,** *134,* 15318–15323. doi:10.1021/ja303309e
52. Nishimura, N.; Kosako, S.; Sueishi, Y. *Bull. Chem. Soc. Jpn.* **1984,** *57,* 1617–1625. doi:10.1246/bcsj.57.1617
53. Bushuyev, O. S.; Singleton, T. A.; Barrett, C. J. *Adv. Mater. (Weinheim, Ger.)* **2013,** *25,* 1796–1800. doi:10.1002/adma.201204831
54. Poprawa-Smoluch, M.; Baggerman, J.; Zhang, H.; Maas, H. P. A.; De Cola, L.; Brouwer, A. M. *J. Phys. Chem. A* **2006,** *110,* 11926–11937. doi:10.1021/jp054982b
55. Ciccone, S.; Halpern, J. *Can. J. Chem.* **1959,** *37,* 1903–1910. doi:10.1139/v59-278
56. Gibson, R. S. L.; Calbo, J.; Fuchter, M. J. *ChemPhotoChem* **2019,** *3,* 372–377. doi:10.1002/cptc.201900065

License and Terms

This is an Open Access article under the terms of the Creative Commons Attribution License (http://creativecommons.org/licenses/by/4.0). Please note that the reuse, redistribution and reproduction in particular requires that the authors and source are credited.

The license is subject to the *Beilstein Journal of Organic Chemistry* terms and conditions: (https://www.beilstein-journals.org/bjoc)

The definitive version of this article is the electronic one which can be found at: doi:10.3762/bjoc.15.232

BEILSTEIN JOURNAL OF ORGANIC CHEMISTRY

Effect of ring size on photoisomerization properties of stiff stilbene macrocycles

Sandra Olsson[1], Óscar Benito Pérez[2], Magnus Blom[1] and Adolf Gogoll[*1]

Full Research Paper

Open Access

Address:
[1]Department of Chemistry-BMC, Uppsala University, S-751 23 Uppsala, Sweden and [2]Faculty of Chemistry, Universitat de Barcelona, C/ Martí i Franquès 1, 08028 Barcelona, Spain

Email:
Adolf Gogoll[*] - adolf.gogoll@kemi.uu.se

* Corresponding author

Keywords:
DFT; molecular mechanics; photostability; photo-switch; ring-strain; stiff stilbene

Beilstein J. Org. Chem. **2019,** *15,* 2408–2418.
doi:10.3762/bjoc.15.233

Received: 27 May 2019
Accepted: 27 September 2019
Published: 11 October 2019

This article is part of the thematic issue "Molecular switches".

Guest Editor: W. Szymanski

© 2019 Olsson et al.; licensee Beilstein-Institut.
License and terms: see end of document.

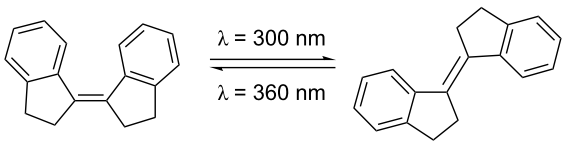
Abstract

A series of stiff stilbene macrocycles have been studied to investigate the possible impact of the macrocycle ring size on their photodynamic properties. The results show that reducing the ring size counteracts the photoisomerization ability of the macrocycles. However, even the smallest macrocycle studied (stiff stilbene subunits linked by a six carbon chain) showed some degree of isomerization when irradiated. DFT calculations of the energy differences between the *E*- and *Z*-isomers show the same trend as the experimental results. Interestingly the DFT study highlights that the energy difference between the *E*- and *Z*-isomers of even the largest macrocycle (linked by a twelve carbon chain) is significantly higher than that of the stiff stilbene unit itself. In general, it is indicated that addition of even a flexible chain to the stiff stilbene unit may significantly affect its photochemical properties and increase the photostability of the resulting macrocycle.

Introduction

The stiff stilbene (SS) molecule has drawn a lot of interest due to its photodynamic properties [1]. Stiff stilbenes typically undergo light triggered isomerization from *Z* to *E* at 300 nm and from *E* to *Z* at 360 nm (Scheme 1) [2]. The photochemical mechanism of this reaction is thoroughly described by Quick et al. [2]. The stiff stilbenes ability to photoisomerize has made it a useful building block of photodynamic triggers, switches and machines [3-11]. The interplay between the forces involved in the switching action and the pull from groups attached to the stiff stilbene has been investigated, e.g., as molecular force probes [12-18]. While these do incorporate other isomerizable units in addition to stiff stilbene, we were interested in the effect that the length of an *n*-alkane chain connecting the two halves of stiff stilbene might have. Similar studies, with stilbene and pyrene as the modulating units, have recently been published [19,20]. Our group has reported a SS-based bis-metalloporphyrin molecular tweezer that binds ditopically to guest molecules [21,22]. This kind of complex would behave like a macrocycle upon photoisomerization, arising the question whether it might be possible to predict such photoisomeriz-

ability and to relate it to the length of a ditopically bound guest molecule connecting the two metalloporphyrin units.



Scheme 1: The stiff stilbene photoisomerization from *Z* to *E* and vice versa by irradiation at 300 nm and 360 nm, respectively.

To investigate the photoisomerization ability of the stiff stilbene as a macrocycle segment a series of model compounds were chosen (Figure 1). To keep the system as simple as possible the SS was attached to an aliphatic carbon chain via ether groups. Four different lengths of carbon chains were used, with distances between the terminal carbons of 6.4 Å (C6), 8.9 Å (C8), 11.4 Å (C10) and 13.9 Å (C12). The SS-macrocycles have been studied both experimentally and by computational techniques.

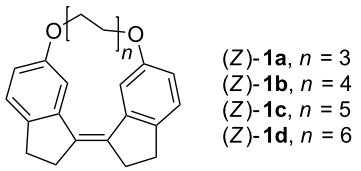


Figure 1: The investigated SS-macrocycles (*Z*)-**1a–d**.

Results and Discussion

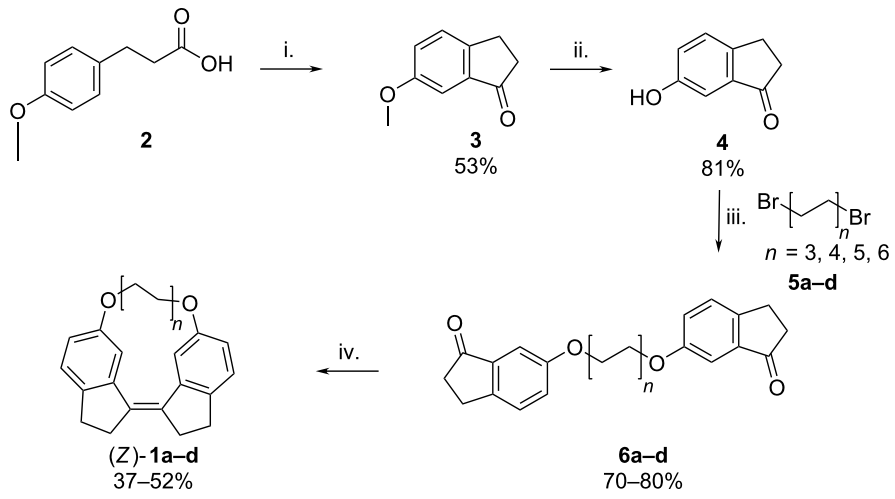
Synthesis

The synthesis of the macrocycles was based on well-established reactions (Scheme 2). The indanone is formed by intramolecular Friedel–Crafts acylation of **2** under microwave radiation as reported by Oliverio et al. [23]. The second step is the demethylation of indanone methyl ether **3** by aluminium trichloride in toluene at reflux [24]. Two indanone units are then attached to an *n*-alkanediyl linker using a Williamson ether synthesis to yield the diethers **6a–d**. Finally, the stiff stilbene unit is formed by an intramolecular McMurry reaction resulting in **1a–d** [25,26]. The *Z*-isomer is formed in huge excess in these reactions and any trace amounts of *E*-isomer are removed during purification.

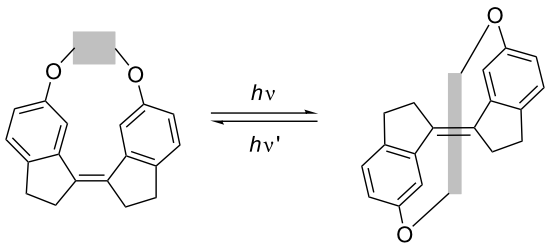
Compared to syntheses of other stiff stilbene macrocycles that typically start from indanone derivatives [15,16], our approach yields the target compounds in fewer steps from a simpler starting material, i.e., 3-(4'-methoxyphenyl)propionic acid (Scheme 2).

Photoisomerization

Photoisomerizing the (*Z*)-**1a–d** to the (*E*)-**1a–d** isomers requires to stretch the linker. The isomerization was achieved by irradiation of a degassed solution of (*Z*)-**1a–d** in chloroform or deuterated chloroform using either a 280 or 300 nm filter (Scheme 3). The conversion was followed by UV–vis or ^{1}H NMR spectroscopy. Compounds were irradiated until an increase in isomerization yield could no longer be observed (see Supporting Information File 1 for details).

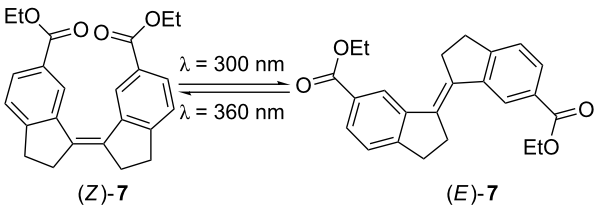


Scheme 2: Synthetic route to SS-macrocycles. i. (1) Triflic acid (3 equiv), DCM (dry), Ar atmosphere, MW (110 °C, 1 h), (2) H_2O (0 °C). ii. (1) $AlCl_3$ (3 equiv), toluene (dry), Δ 1.5 h, (2) H_2O. iii. (1) K_2CO_3 (4 equiv), TBAB (0.2 equiv), DMF (dry), Ar atmosphere, MW (150 °C, 15 min). iv. (1) $TiCl_4$ (3 equiv), Zn powder (6 equiv), THF, Δ, 12 h.



Scheme 3: The photoisomerization of the stiff stilbene macrocycles, showing the stretching of the linker (grey box).

To set the results of this photoisomerization into perspective a noncyclic stiff stilbene was used as a reference (Scheme 4). The photodynamic properties of this compound have been reported previously [27].



Scheme 4: Noncyclic stiff stilbene diester **7** used as reference in the photoisomerization study.

The *E*- and *Z*-isomers give distinctively separated chemical shifts for the CH_2 protons next to the double bond. This makes the determination of the *Z*/*E* ratio straightforward. The composition of the photostable mixtures as compared to the noncyclic reference is presented in Figure 2. As the linker chain gets shorter the *E*-isomer becomes less favored. What is particularly interesting is that even with the longest chain of twelve carbons a significantly lower amount of *E*-isomer as compared to the reference is obtained. Clearly even a loose linking chain has a considerable effect on the system.

Computations

Relative energies of *E*- and *Z*-isomers

The Gibbs free energies of (*Z*)-**1a–d** and (*E*)-**1a–d** were calculated at the DFT level using the B3LYP functional with the 6-31G(d,p) basis set and SCRF-SMD solvent model (chloroform) [28-37]. The photoisomerization of stiff stilbenes involves a complex potential energy surface with several excited species in equilibria, eventually reaching the *cis* or *trans* ground state [2]. Macroscopic parameters such as extinction coefficients and quantum yields also affect the composition of the photostationary state. Ground state energies might therefore not be directly related to the isomerization reaction without investigation of the exited state potential energy surface. However, the difference in Gibbs free energy (Δ*G*, Figure 3) between the *E*- and *Z*-isomers shows a trend reminiscent of the experimental photoisomerization results (Figure 2), i.e., shorter chain lengths result in larger Δ*G* as well as in larger *Z*:*E* ratios.

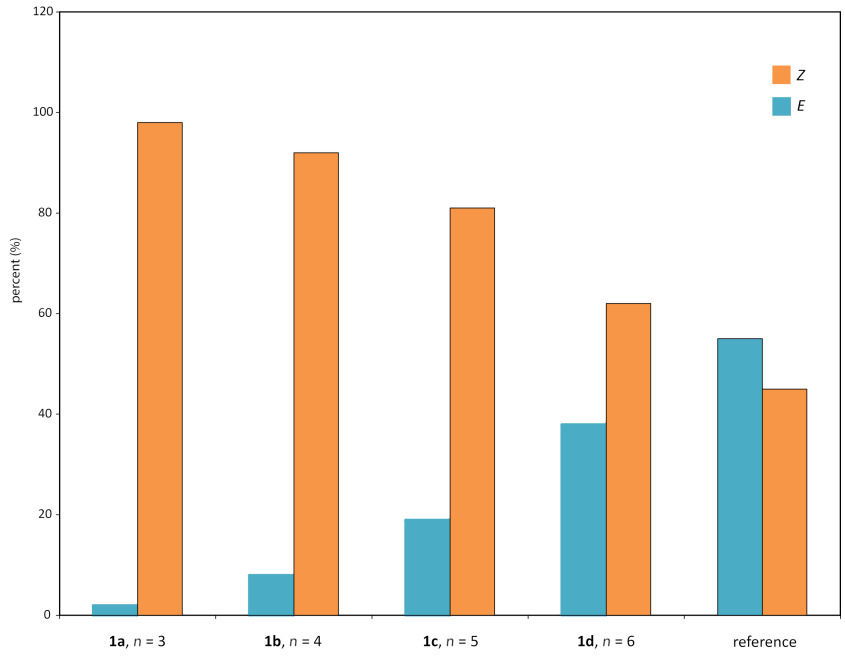


Figure 2: The photoisomerization of the SS-macrocycles shows a clear correlation between the *Z*/*E* ratio in the photostable mixture and the linker length. The non-cyclic SS-diester **7** is included as a reference.

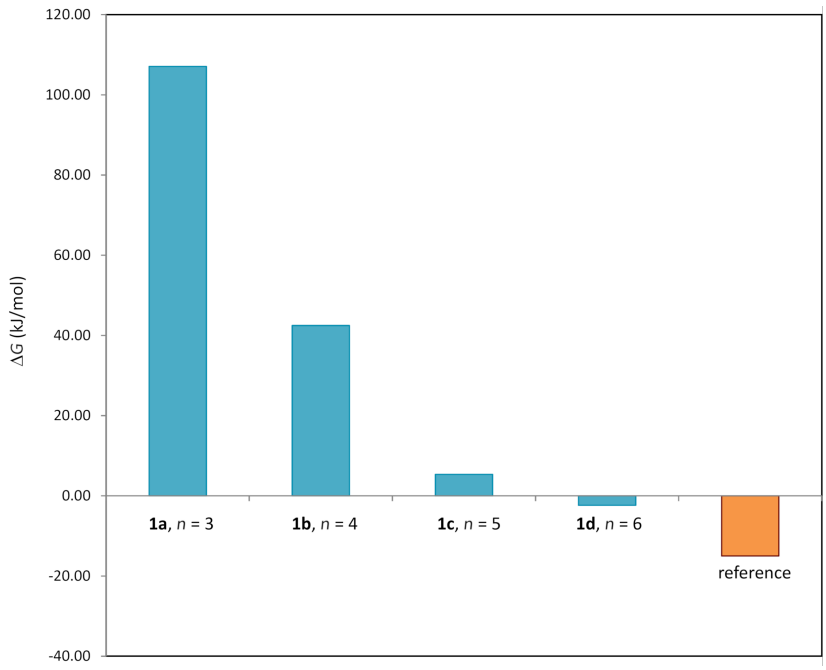


Figure 3: Gibbs free energy differences (Δ*G*) between *Z*- and *E*-isomers of **1a–d** and of the reference compound **7** calculated using B3LYP. The results show a pronounced effect of linker length on the energy difference between *Z*- and *E*-isomers.

Ring strain

The ring strain energies of compounds (*Z*)-**1a–d** and (*E*)-**1a–d** were calculated for an isodesmic reaction [38] transforming the cyclic diethers into noncyclic diethers (Supporting Information File 1) and the results are visualized in Figure 4.

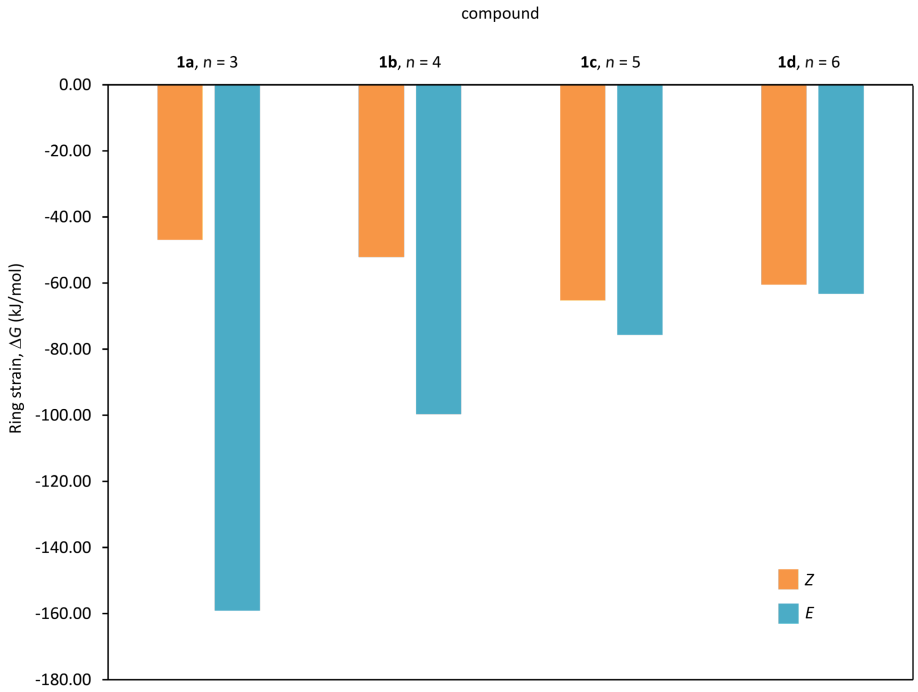


Figure 4: Ring strain for *E* and *Z*-isomers of **1a–d** expressed as the Gibbs free energy difference to an acyclic analogue, using an isodesmic reaction (Figure S47, Supporting Information File 1).

For (*E*)-**1a–d** the ring strain decreases with increased linker length. For the less strained (*Z*)-**1a–d** the ring strain increases slightly with increased linker length and for the longer linkers (**1c**,**d**) the ring strains of the *E*- and *Z*-isomers are similar. The differences in ring strain between the *E*- and *Z*-isomers show an exponential correlation to the linker length (Figure 5).

Conformational analysis

To obtain further information regarding the reason for the observed photoisomerization properties of the macrocyclic stiff stilbene diethers, a conformational analysis was undertaken (Figure 6).

According to X-ray crystallography, in compound (*E*)-**7** (Scheme 4) the aromatic rings of the two indane units are in the same plane (dihedral angle 180°), whereas in (*Z*)-**7** this angle is 9.1° [21]. In the macrocyclic diethers **1a–d**, all *Z*-isomers have a dihedral angle of 12–14°, roughly similar to the one in the crystal structure of (*Z*)-**7**. The deviation of this angle from 0° is due to steric interaction between two aromatic protons in position 4 (Figure 9). In the *E*-isomers, an increasing distortion of the stiff stilbene segment with decreasing ring size is indicated by the substantial deviation of the dihedral angle from 180°. Furthermore, the alkyl chains adopt more similar conformations in the *E*-isomers with stretched alkyl chains. In the *Z*-isomers, the alkyl chains adopt a larger variety of conformations. This will add an entropy penalty for the *E*-isomers.

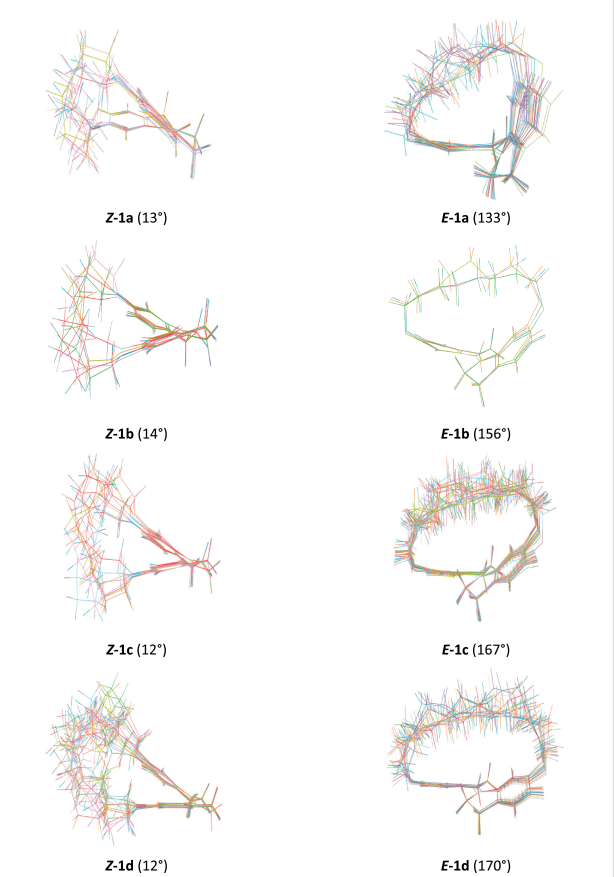


Figure 6: Conformer ensembles for the macrocyclic stiff stilbene diethers **1a–d**. Dihedral angles between the two aromatic rings are given in parentheses.

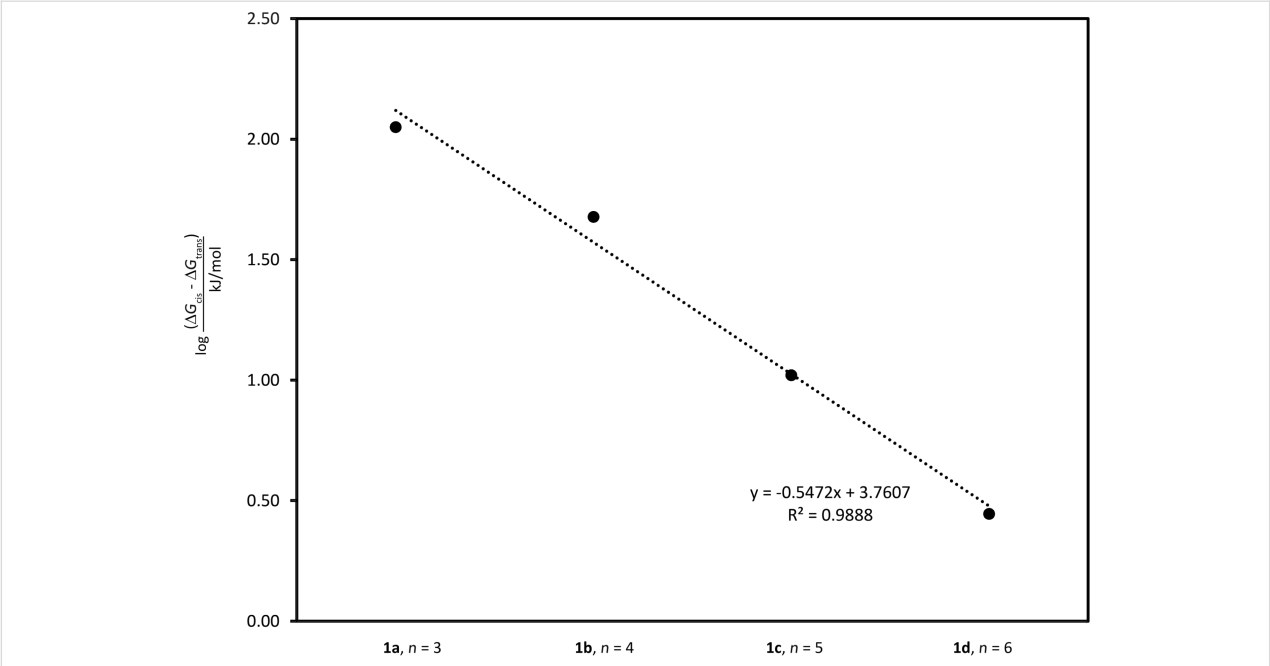


Figure 5: The differences in ring strain between the *E*- and *Z*-isomers show an exponential correlation to the linker length.

Interatomic distances from NOE buildup rates

Interatomic distances, derived from NOE buildup rates, are summarized in Figure 7. Signal overlap prevented an analysis accounting for the presence of an ensemble of conformers such as NAMFIS [39,40]. For example, each CH_2 signal is generated by four CH_2 protons which are chemically equivalent in the averaged chemical structure (≈ the 2D molecular structure) but not in individual conformers. They cannot be distinguished on the NMR timescale. Therefore, the calculated distances r_{ave}, being averages with contributions from all conformers, are biased for shorter distances, i.e., $r_{ave} = \langle 1/r^6 \rangle$ instead of $r_{ave} = 1/\langle r^6 \rangle$ [41]. However, they still should allow a comparison between the different compounds (*Z*)-**1a–d**. Thus, increased conformational flexibility is indicated by increasing distances from (*Z*)-**1a** to **1d** for methylene protons further along the chain, such as distance 4 and distance 5 (Figure 7). An exception is the slight decrease of distance 7 when comparing (*Z*)-**1c** to (*Z*)-**1d**. This might be due to larger mobility of the alkyl chain.

Conclusion

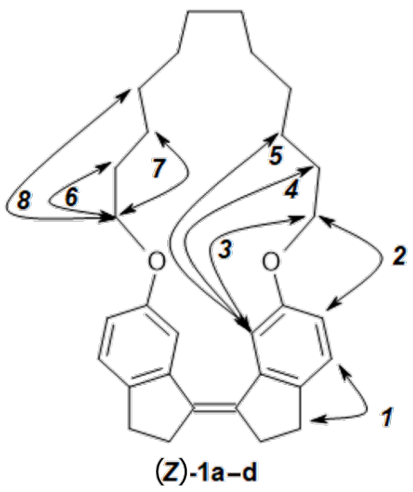
A series of novel stiff stilbene macrocycles has been synthesised and used to investigate the effect of the ring size on the photoisomerization of the stiff stilbene unit. Both experimental photoisomerization and DFT calculations show that the strain of the linking chain affects the isomerization even for the longest chains. As stiff stilbene is gaining popularity as a unit in molecular machines and photodynamic systems a clear understanding of the effect of cyclisation on the photoisomerization is of general interest.

Experimental

Starting materials, solvents and reagents were commercially available and used without further purification except dichloromethane (DCM), ethyl acetate, pentane, tetrahydrofuran (THF) and toluene that were distilled before use. *N*,*N*-Dimethylformamide (DMF) was used as supplied (biotech. grade, ≥99.9%). Unless stated differently, all reactions were carried out under atmospheric pressure and with argon atmosphere.

Microwave (MW) heating was carried out in a Biotage+ Initiator microwave using 10–20 mL Biotech MW vials, applying MW irradiation at 2.45 GHz, with a power setting up to 40 W and an average pressure of 4–5 bar when DCM was the solvent and 90 W/1 bar when the solvent was DMF. Analytical TLC was performed using Merck precoated silica gel 60 F254 plates, visualized with UV light and Hannessian's stain (5% ammonium molybdate, 1% cerium sulfate and 10% sulfuric acid in water). Flash chromatography (CC) was performed over Matrex silica gel (60 Å, 35–70 μm) on a regular column or on a Grace Reveleris X2 Flash chromatography system.

^{1}H and ^{13}C NMR spectra were recorded on Varian Mercury Plus (^{1}H at 300.03 MHz), Agilent 400-MR DD2 (^{1}H at 399.98 MHz, ^{13}C at 100.58 MHz), Varian Unity Inova (^{1}H at 499.94 MHz) and Bruker Avance Neo (^{1}H at 500.15 MHz, ^{13}C at 125.78 MHz) spectrometers at 25 °C. Chemical shifts (δ) are reported in ppm referenced indirectly to tetramethylsilane via the residual solvent signal ($CDCl_3$, ^{1}H at 7.26 and ^{13}C at 77.0 ppm). Coupling constants are given in Hz. Signal assignments were derived from ^{1}H-gCOSY [42,43],



Distance 1	**a**: 2.68 **b**: 2.79 **c**: 2.77 **d**: 2.78	Distance 5	**a**: 2.94 **b**: 4.10 **c**: 4.61 **d**: n. d.
Distance 2	**a**: 2.51 **b**: 2.41 **c**: 2.46 **d**: 2.53	Distance 6	**a**: 2.23 **b**: 2.38 **c**: 2.37 **d**: 2.40
Distance 3	**a**: 2.31 **b**: 2.41 **c**: 2.42 **d**: 2.40	Distance 7	**a**: 2.36 **b**: 2.80 **c**: 2.80 **d**: 2.70
Distance 4	**a**: 3.02 **b**: 3.72 **c**: 4.48 **d**: 4.55	Distance 8	**a**: – **b**: 2.66 **c**: n. d. **d**: 3.20

Figure 7: Distances derived from NOE buildup experiments. Distances between pairs of protons or groups of protons attached to the indicated carbons are designated as distance 1 through 8. n.d.: NOE cross peak not detectable. – : distance does not exist.

gTOCSY [44], gHSQC [45], gHMBC [46], and gNOESY [47] spectra.

Experimental conditions for NOE buildup experiments: gradient enhanced NOESY spectra were obtained for non-degassed solutions (16–46 mM) in $CDCl_3$ at 25 °C, 400 MHz, mixing times = 0.1, 0.2, 0.3, 0.5, 0.7 s. The distance between aromatic ortho protons (H-6 and H-7 in Figure 9) was used as reference distance r_{ref} at 2.51 Å. Volume integrals for NOESY diagonal and cross peaks were measured for mixing times during the linear NOE buildup phase. For each signal pair A/B with a NOESY cross peak an average cross peak volume was calculated from measured volume integrals as:

$$\text{average volume} = \sqrt{\frac{(\text{cross peak}_{AB} \times \text{cross peak}_{BA})}{(\text{diagonal peak A} \times \text{diagonal peak B})}} \quad (1)$$

The slope σ from the plot of average volume vs mixing time was determined and from it the distance r_{AB} calculated assuming $r_{AB} = r_{ref}(\sigma_{ref}/\sigma_{AB})^{1/6}$.

Mass spectra were obtained on an Advion Expression-L CMS with APCI+ interface. High-resolution mass spectra were obtained on a Thermo Scientific Q-Exactive instrument in APCI positive mode. UV–vis spectra were recorded on a Shimadzu UV-1650PC spectrophotometer using 10 mm quartz cuvettes. Photoisomerizations were performed using an Oriel 1000 W Xe ARC light source equipped with a band pass filter 10BPF10-300 or 10BPF10-280 (Newport).

Computational details

The DFT calculations on the stiff stilbene macrocycles were performed with the B3LYP functional as implemented in the Gaussian 16 program package [28-32]. The SCRF solvent model with the SMD variation was used with chloroform as solvent [33-36]. Geometries were optimized using the 6-31G(d,p) basis set [37]. Frequency calculations were performed at the same level to confirm that a minimum had been reached and to extract free energy corrections, which were evaluated at 298.15 K. A stability analysis was performed to ensure that a stable wave-function was attained for all species.

Conformational analyses of the stiff stilbene macrocycles were calculated in MacroModel 9.9 with the OPLS3e force field, $CHCl_3$ as solvent and dielectric constant 9.1 [48,49]. Redundant conformer elimination in MacroModel was used to reduce the number of conformations to 10–20 structures [50].

Synthesis

Synthesis of 6-methoxyindan-1-one (**3**)

Compound **2** (2.523 g, 14.0 mmol) was dissolved in dry DCM (10 mL) in a flame-dried MW vial and cooled in ice-bath. TfOH (3.7 mL, 41.9 mmol) was added dropwise. The vial was sealed, the air was replaced by argon gas, and the reaction mixture was heated in the MW to 110 °C, 5 bar, for 1 h. The reaction mixture was poured on ice. The water phase was extracted three times with DCM (3 × 100 ml). The combined organic phases were dried over $MgSO_4$ and the solvent was removed by rotary evaporation. The crude product was purified by CC (pentane/EtOAc 1:0 to 1:4). The solvent was evaporated, giving a light yellow solid, 1.204 g, 53% yield. ^{1}H NMR ($CDCl_3$, 500 MHz) δ 7.37 (m, 1H, Ar-H), 7.20 (m, 1H, Ar-H), 7.18 (m, 1H, Ar-H), 3.84 (s, 3H, OCH_3), 3.07 (m, 2H, CH_2CH_2CO), 2.72 (m, 2H, CH_2CO); ^{13}C NMR ($CDCl_3$, 100.6 MHz) δ 207.0 (CO), 159.4 (C-OCH_3), 148.0 (C, Ar), 138.2 (C, Ar), 127.3 (CH, Ar), 124.0 (CH, Ar), 104.9 (CH, Ar), 55.6 (OCH_3), 37.0 (CH_2CO), 25.1 (CH_2CH_2CO); APCI–MS *m/z*: $[M + H]^+$ calcd for $C_{10}H_{10}O_2$, 163; found, 163. Data in agreement with the literature [51].

Synthesis of 6-hydroxyindan-1-one (**4**)

Compound **3** (1.367 g, 8.4 mmol) and $AlCl_3$ (3.483 g, 26.1 mmol) were dissolved in dry toluene (50 mL) and refluxed for 1.5 h. The reaction mixture was cooled to rt. H_2O (70 mL) was added and the organic phase collected. The water phase was extracted three times with EtOAc (3 × 50 mL). The combined organic phases were washed with brine two times (2 × 75 mL) and dried over $MgSO_4$. The solvent was removed by rotary evaporation. The orange crude product was purified by CC (pentane/EtOAc 1:0 to 1:4). The solvent was evaporated, giving a light orange solid, 1.103 g, 81% yield. ^{1}H NMR ($CDCl_3$, 500 MHz) δ 7.36 (d, *J* = 8.3 Hz, 1H, Ar-H), 7.22 (d, *J* = 2.4 Hz, 1H, Ar-H), 7.16 (dd, *J* = 2.4, 8.3 Hz, 1H, Ar-H), 5.67 (s, 1H, OH), 3.08 (m, 2H, CH_2CH_2CO), 2.73 (m, 2H, CH_2CO); ^{13}C NMR ($CDCl_3$, 100.6 MHz) δ 207.4 (CO), 155.4 (C-OH), 147.8 (C, Ar), 138.3 (C, Ar), 127.6 (CH, Ar), 123.4 (CH, Ar), 108.7 (CH, Ar), 37.0 (CH_2CO), 25.1 (CH_2CH_2CO); APCI–MS *m/z*: $[M + H]^+$ calcd for $C_9H_8O_2$, 149; found, 149. Data in agreement with the literature [52].

General procedure A: Williamson ether synthesis (assisted by MW)

Compound **4** (2 equiv), dibromoalkane **5** (1 equiv), TBAB (0.2 equiv) and K_2CO_3 (4 equiv) were dissolved in dry DMF (15 mL) in a flame-dried MW vial. The vial was sealed, put under argon and heated in the MW to 150 °C for 15 min (the reaction was followed by NMR). The reaction mixture was cooled to rt and poured on DCM (40 mL), filtered and washed with water four times (4 × 50 mL) and brine three times

(3 × 50 mL). The organic phase was dried over $MgSO_4$ and the solvent removed by rotary evaporation. The product was dried under high vacuum overnight.

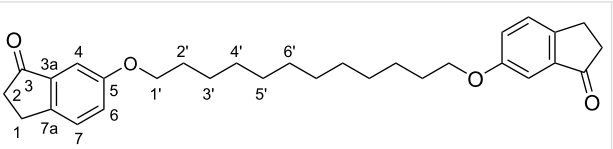


Figure 8: Numbering of carbons in compounds **6a–d**, showing **6d** as an example.

Synthesis of 6-[2-(3-oxoindan-5-yl)oxyhexyloxy]indan-1-one (**6a**)

The synthesis followed general procedure A with compound **4** (0.201 g, 1.4 mmol) and 1,6-dibromohexane (**5a**, 0.11 mL, 0.7 mmol) as starting materials, giving a brown solid which was sufficiently pure for subsequent steps, 0.176 g, 69% yield. ^{1}H NMR ($CDCl_3$, 500 MHz) δ 7.36 (m, 2H, H-7), 7.20–7.16 (m, 4H, H-4 H-6), 4.00 (t, *J* = 6.6 Hz, 4H, CH_2-1'), 3.07 (m, 4H, CH_2-1), 2.72 (m, 4H, CH_2-2), 1.84 (m, 4H, CH_2-2'), 1.54 (m, 4H, CH_2-3'); ^{13}C NMR ($CDCl_3$, 100.6 MHz) δ 207.1 (C, C-3), 158.8 (C, C-5), 147.8 (C, C-3a), 138.2 (C, C-7a), 127.3 (CH, C-7), 124.4 (CH, C-6), 105.6 (CH, C-4), 68.2 (CH_2, C-1'), 37.0 (CH_2, C-2), 29.0 (CH_2, C-2'), 25.8 (CH_2, C-3'), 25.1 (CH_2, C-1); APCI–MS *m*/*z*: $[M + H]^+$ calcd for $C_{24}H_{26}O_4$, 379; found, 379; UV–vis (CH_2Cl_2) λ_{max}: 320, 249 nm.

Synthesis of 6-[2-(3-oxoindan-5-yl)oxyoctyloxy]indan-1-one (**6b**)

The synthesis followed general procedure A with compound **4** (0.115 g, 0.8 mmol) and 1,8-dibromooctane (**5b**, 0.07 mL, 0.4 mmol) as starting materials, giving an orange solid which was sufficiently pure for subsequent steps, 0.121 g, 78% yield. ^{1}H NMR ($CDCl_3$, 500 MHz) δ 7.36 (m, 2H, H-7), 7.20–7.16 (m, 4H, H-4 H-6), 3.98 (t, *J* = 6.6 Hz, 4H, CH_2-1'), 3.06 (m, 4H, CH_2-1), 2.71 (m, 4H, CH_2-2), 1.80 (dt, *J* = 6.6, 14.8 Hz, 4H, CH_2-2'), 1.47 (m, 4H, CH_2-3'), 1.40 (m, 4H, CH_2-4'); ^{13}C NMR ($CDCl_3$, 100.6 MHz) δ 207.1 (C, C-3), 158.8 (C, C-5), 147.8 (C, C-3a), 138.2 (C, C-7a), 127.3 (CH, C-7), 124.4 (CH, C-6), 105.6 (CH, C-4), 68.3 (CH_2, C-1'), 37.0 (CH_2, C-2), 29.2 (CH_2, C-4'), 29.1 (CH_2, C-2'), 25.9 (CH_2, C-3'), 25.1 (CH_2, C-1); APCI–MS *m*/*z*: $[M + H]^+$ calcd for $C_{26}H_{30}O_4$, 407; found, 407; HRMS (CI) *m*/*z*: $[M + H]^+$ calcd for $C_{26}H_{30}O_4$, 407.2217; found, 407.2217; UV–vis (CH_2Cl_2) λ_{max}: 320, 249 nm.

Synthesis of 6-[2-(3-oxoindan-5-yl)oxydecyloxy]indan-1-one (**6c**)

The synthesis followed general procedure A with compound **4** (0.397 g, 2.7 mmol) and 1,10-dibromodecane **5c** (0.405 g, 1.3 mmol) as starting materials, giving a light brown solid which was sufficiently pure for subsequent steps, 0.471 g, 80% yield. ^{1}H NMR ($CDCl_3$, 500 MHz) δ 7.34 (m, 2H, H-7), 7.20–7.16 (m, 4H, H-4 H-6), 3.98 (t, *J* = 6.8 Hz, 4H, CH_2-1'), 3.07 (m, 4H, CH_2-1), 2.71 (m, 4H, CH_2-2), 1.79 (dt, *J* = 6.8, 15.0 Hz, 4H, CH_2-2'), 1.46 (m, 4H, CH_2-3'), 1.40–1.30 (m, 8H, CH_2-4' CH_2-5'); ^{13}C NMR ($CDCl_3$, 100.6 MHz) δ 207.1 (C, C-3), 158.9 (C, *C*-5), 147.8 (C, C-3a), 138.2 (C, C-7a), 127.3 (CH, C-7), 124.4 (CH, C-6), 105.6 (CH, C-4), 68.4 (CH_2, C-1'), 37.0 (CH_2, C-2), 29.4 (CH_2, C-5'), 29.2 (CH_2, C-4'), 29.1 (CH_2, C-2'), 26.0 (CH_2, C-3'), 25.1 (CH_2, C-1); APCI–MS *m*/*z*: $[M + H]^+$ calcd for $C_{28}H_{34}O_4$, 435; found, 435. HRMS (CI) *m*/*z*: $[M + H]^+$ calcd for $C_{28}H_{34}O_4$, 435.2530; found: 435.2527; UV–vis (CH_2Cl_2) λ_{max}: 320, 248 nm.

Synthesis of 6-[2-(3-oxoindan-5-yl)oxydodecyloxy]indan-1-one (**6d**)

The synthesis followed General procedure A with compound **4** (0.102 g, 0.7 mmol) and 1,12-dibromododecane **5d** (0.112 g, 3.5×10^{-2} mmol) as starting materials, giving a light brown solid which was sufficiently pure for subsequent steps, 0.112 g, 71% yield. ^{1}H NMR ($CDCl_3$, 500 MHz) δ 7.36 (m, 2H, H-7), 7.20–7.17 (m, 4H, H-4 H-6), 3.98 (t, *J* = 6.8 Hz, 4H, CH_2-1'), 3.07 (m, 4H, CH_2-1), 2.71 (m, 4H, CH_2-2), 1.79 (dt, *J* = 6.8, 14.8 Hz, 4H, CH_2-2'), 1.45 (m, 4H, CH_2-3'), 1.39–1.27 (m, 12H, CH_2-4' CH_2-5' CH_2-6'); ^{13}C NMR ($CDCl_3$, 100.6 MHz) δ 207.1 (C, C-3), 158.9 (C, C-5), 147.7 (C, C-3a), 138.2 (C, C-7a), 127.3 (CH, C-7), 124.4 (CH, C-6), 105.6 (CH, C-4), 68.4 (CH_2, C-1'), 37.0 (CH_2, C-2), 29.5 (CH_2, 4C, C-5' C-6'), 29.3 (CH_2, C-4'), 29.1 (CH_2, C-2'), 26.0 (CH_2, C-3'), 25.1 (CH_2, C-1); APCI–MS: *m*/*z*: $[M + H]^+$ calcd for $C_{30}H_{38}O_4$, 463; found, 463; HRMS (CI) *m*/*z*: $[M + H]^+$ calcd for $C_{30}H_{38}O_4$, 463.2843; found, 463.2836; UV–vis (CH_2Cl_2) λ_{max}: 320, 248 nm.

General procedure B: McMurry coupling

Zinc powder previously grinded (12 equiv) was suspended in dry THF (30 mL). The suspension was cooled to 0 °C in an ice bath and $TiCl_4$ (6 equiv) added over 10 minutes. The resulting slurry was refluxed for 1.5 h. A solution of compound **6** in dry THF (50–100 mL) was added over a 5–7 h period to the refluxing reaction mixture by syringe pump. The refluxing was continued for 40 min after the addition was complete. The reaction mixture was cooled to rt and poured on a saturated aqueous solution of NH_4Cl. The water phase was extracted three times with DCM (3 × 100 mL). The combined organic phases were washed two times with brine (2 × 100 mL) then dried over $MgSO_4$ and the solvent was removed by rotary evaporation. Unless stated differently, the obtained yellow oil was purified by CC (pentane/DCM 1:0 to 1:1). The obtained product was dried under high vacuum overnight.

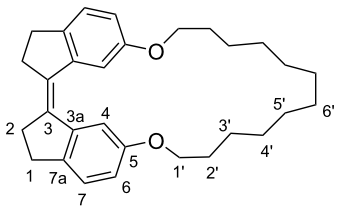


Figure 9: Numbering of carbons in compounds (*Z*)-**1a**–**d**, showing (*Z*)-**1d** as an example.

Synthesis of macrocyclic stiff stilbene diether (*Z*)-**1a**

The synthesis followed general procedure B with compound **6a** (0.279 g, 0.7 mmol) as starting material and gave the pure product as a light yellow solid, 0.093 g, 37% yield. ^{1}H NMR ($CDCl_3$, 500 MHz) δ 7.75 (d, *J* = 2.3 Hz, 2H, H-4), 7.19 (d, *J* = 8.0 Hz, 2H, H-7), 6.80 (dd, *J* = 2.3, 8.0 Hz, 2H, H-6), 4.07 (t, *J* = 6.5 Hz, 4H, CH_2-1'), 2.94 (m, 4H, CH_2-1), 2.82 (m, 4H, CH_2-2), 1.80 (m, 4H, CH_2-2'), 1.59 (m, 4H, CH_2-3'); ^{13}C NMR ($CDCl_3$, 100.6 MHz) δ 157.6 (C, C-5), 141.6 (C, C-7a), 141.1 (C, C-3a), 135.2 (C, C-3), 125.5 (CH, C-7), 116.2 (CH, C-6), 111.9 (CH, C-4), 69.7 (CH_2, C-1'), 35.0 (CH_2, C-2), 30.0 (CH_2, C-1), 28.8 (CH_2, C-2'), 24.4 (CH_2, C-3'); APCI–MS *m*/*z*: $[M + H]^+$ calcd for $C_{24}H_{26}O_2$, 347; found, 347; HRMS (CI) *m*/*z*: $[M + H]^+$ calcd for $C_{24}H_{26}O_2$, 347.2006; found, 347.1996; UV–vis (CH_2Cl_2) λ_{max}: 350, 298, 253 nm.

Synthesis of macrocyclic stiff stilbene diether (*Z*)-**1b**

The synthesis followed general procedure B with compound **6b** (0.105 g, 0.3 mmol) as starting material and gave the pure product as a light yellow solid, 0.038 g, 39% yield. ^{1}H NMR ($CDCl_3$, 500 MHz) δ 7.69 (d, *J* = 2.5 Hz, 2H, H-4), 7.18 (d, *J* = 8.2 Hz, 2H, H-7), 6.74 (dd, *J* = 2.5, 8.2 Hz, 2H, H-6), 3.97 (t, *J* = 6.1 Hz, 4H, CH_2-1'), 2.93 (m, 4H, CH_2-1), 2.82 (m, 4H, CH_2-2), 1.82 (dt, *J* = 6.1, 12.8 Hz, 4H, CH_2-2'), 1.56 (m, 4H, CH_2-3'), 1.45 (m, 4H, CH_2-4'); ^{13}C NMR ($CDCl_3$, 100.6 MHz) δ 157.6 (C, C-5), 141.6 (C, C-7a), 140.5 (C, C-3a), 135.4 (C, C-3), 125.4 (CH, C-7), 113.9 (CH, C-6), 110.0 (CH, C-4), 68.1 (CH_2, C-1'), 35.4 (CH_2, C-2), 29.8 (CH_2, C-1), 28.1 (CH_2, C-2'), 27.6 (CH_2, C-4'), 25.3 (CH_2, C-3'); APCI–MS *m*/*z*: $[M + H]^+$ calcd for $C_{26}H_{30}O_2$, 375; found, 375; HRMS (CI) *m*/*z*: $[M + H]^+$ calcd for $C_{26}H_{30}O_2$, 375.2319; found, 375.2311; UV–vis (CH_2Cl_2) λ_{max}: 361, 349, 300, 253 nm.

Synthesis of macrocyclic stiff stilbene diether (*Z*)-**1c**

The synthesis followed general procedure B with compound **6c** (0.350 g, 0.8 mmol) as starting material and gave the pure product as a light yellow solid, 0.171g, 53% yield. ^{1}H NMR ($CDCl_3$, 500 MHz) δ 7.66 (d, *J* = 2.4 Hz, 2H, H-4), 7.19 (d, *J* = 8.3 Hz, 2H, H-7), 6.75 (dd, *J* = 2.4, 8.3 Hz, 2H, H-6), 3.92 (t, *J* = 5.9 Hz, 4H, C*H*$_2$-1'), 2.93 (m, 4H, CH_2-1), 2.82 (m, 4H, CH_2-2), 1.79 (dt, *J* = 5.9, 12.6 Hz, 4H, CH_2-2'), 1.55 (dt, *J* = 5.9, 12.6 Hz, 4H, CH_2-3'), 1.45–1.37 (m, 8H, C*H*$_2$-4' C*H*$_2$-5'); ^{13}C NMR ($CDCl_3$, 100.6 MHz) δ 157.7 (C, C-5), 141.7 (C, C-7a), 140.4 (C, C-3a), 135.5 (C, C-3), 125.4 (CH, C-7), 113.6 (CH, C-6), 109.5 (CH, C-4), 67.1 (CH_2, C-1'), 35.6 (CH_2, C-2), 29.8 (CH_2, C-1), 28.4 (CH_2, C-2'), 26.9 (CH_2, C-4'), 26.4 (CH_2, C-5'), 24.8 (CH_2, C-3'); APCI–MS *m*/*z*: $[M + H]^+$ calcd for $C_{28}H_{34}O_2$, 403; found, 403; HRMS (CI) *m*/*z*: $[M + H]^+$ calcd for $C_{28}H_{34}O_2$, 403.2632; found: 403.2624; UV–vis (CH_2Cl_2) λ_{max}: 361, 349, 301, 252 nm.

Synthesis of macrocyclic stiff stilbene diether (*Z*)-**1d**

The synthesis followed general procedure B with compound **6d** (0.312 g, 0.7 mmol) as starting material and gave the pure product as a light yellow solid, 0.152 g, 52% yield. ^{1}H NMR ($CDCl_3$, 500 MHz) δ 7.64 (d, *J* = 2.4 Hz, 2H, H-4), 7.19 (d, *J* = 8.3 Hz, 2H, H-7), 6.76 (dd, *J* = 2.4, 8.3 Hz, 2H, H-6), 3.91 (t, *J* = 6.3 Hz, 4H, CH_2-1'), 2.93 (m, 4H, CH_2-1), 2.82 (m, 4H, CH_2-2), 1.76 (dt, *J* = 6.3, 15.0 Hz, 4H, CH_2-2'), 1.49 (m, 4H, CH_2-3'), 1.44–1.26 (m, 12H, CH_2-4' CH_2-5' CH_2-6'); ^{13}C NMR ($CDCl_3$, 100.6 MHz) δ 157.8 (C, C-5), 141.6 (C, C-7a), 140.5 (C, C-3a), 135.4 (C, C-3), 125.4 (CH, C-7), 114.1 (CH, C-6), 109.3 (CH, C-4), 68.4 (CH_2, C-1'), 35.5 (CH_2, C-2), 29.8 (CH_2, C-1), 29.6 (CH_2, C-2'), 27.4 (CH_2, C-4'), 27.1 (CH_2, C-5'), 26.2 (CH_2, C-6'), 25.1 (CH_2, C-3'); APCI–MS *m*/*z*: $[M + H]^+$ calcd for $C_{30}H_{38}O_2$, 431; found, 431; HRMS (CI) *m*/*z*: $[M + H]^+$ calcd for $C_{30}H_{38}O_2$, 431.2945; found, 431.2928; UV–vis (CH_2Cl_2) λ_{max}: 359, 349, 298, 252 nm.

Photoisomerizations (followed by NMR spectroscopy)

$CDCl_3$ solutions of products (*Z*)-**1d** and stiff stilbene were irradiated after degassing by argon bubbling for 15 min. As reaction vessels, 5 mm NMR tubes, type 5Hp, 178 mm were used. The course of isomerization was assessed by ^{1}H NMR spectroscopy.

Photoisomerizations (followed by UV–vis spectroscopy)

$CHCl_3$ solutions of products (*Z*)-**1d** and stiff stilbene were irradiated after degassing by argon bubbling for 15 min. As reaction vessels, 10 mm quartz UV–vis cuvettes were used. The course of isomerization was assessed by UV–vis spectroscopy.

Supporting Information

Supporting Information File 1

Experimental and theoretical data.
[https://www.beilstein-journals.org/bjoc/content/supplementary/1860-5397-15-233-S1.pdf]

Acknowledgements

This study made use of the NMR Uppsala infrastructure, which is funded by the Department of Chemistry - BMC and the Disciplinary Domain of Medicine and Pharmacy. Financial support by the Swedish Research Council (grant nr. 621-2012-3379) and by the Carl Tryggers Foundation (CTS 16:156) is gratefully acknowledged. The computations were performed on resources provided by the Swedish National Infrastructure for Computing (SNIC) at National Supercomputer Centre (NSC), Linköping University. We are indebted to Dr. Lisa Haigh, Imperial College London, Department of Chemistry, Mass spectrometry service, for the HRMS analyses.

ORCID® iDs

Sandra Olsson - https://orcid.org/0000-0002-4871-0613
Óscar Benito Pérez - https://orcid.org/0000-0002-2536-2943
Adolf Gogoll - https://orcid.org/0000-0002-9092-261X

Preprint

A non-peer-reviewed version of this article has been previously published as a preprint doi:10.3762/bxiv.2019.30.v1

References

1. Waldeck, D. H. *Chem. Rev.* **1991,** *91,* 415–436. doi:10.1021/cr00003a007
2. Quick, M.; Berndt, F.; Dobryakov, A. L.; Ioffe, I. N.; Granovsky, A. A.; Knie, C.; Mahrwald, R.; Lenoir, D.; Ernsting, N. P.; Kovalenko, S. A. *J. Phys. Chem. B* **2014,** *118,* 1389–1402. doi:10.1021/jp411656x
3. Wang, Y.; Tian, Y.; Chen, Y.-Z.; Niu, L.-Y.; Wu, L.-Z.; Tung, C.-H.; Yang, Q.-Z.; Boulatov, R. *Chem. Commun.* **2018,** *54,* 7991–7994. doi:10.1039/c8cc04542a
4. Zhu, N.; Li, X.; Wang, Y.; Ma, X. *Dyes Pigm.* **2016,** *125,* 259–265. doi:10.1016/j.dyepig.2015.10.033
5. Shimasaki, T.; Kato, S.-i.; Ideta, K.; Goto, K.; Shinmyozu, T. *J. Org. Chem.* **2007,** *72,* 1073–1087. doi:10.1021/jo061127v
6. Wezenberg, S. J.; Feringa, B. L. *Org. Lett.* **2017,** *19,* 324–327. doi:10.1021/acs.orglett.6b03423
7. Zhu, H.; Shangguan, L.; Xia, D.; Mondal, J. H.; Shi, B. *Nanoscale* **2017,** *9,* 8913–8917. doi:10.1039/c7nr03160b
8. O'Hagan, M. P.; Haldar, S.; Duchi, M.; Oliver, T. A. A.; Mulholland, A. J.; Morales, J. C.; Galan, M. C. *Angew. Chem., Int. Ed.* **2019,** *58,* 4334–4338. doi:10.1002/anie.201900740
9. Wang, Y.; Xu, J.-F.; Chen, Y.-Z.; Niu, L.-Y.; Wu, L.-Z.; Tung, C.-H.; Yang, Q.-Z. *Chem. Commun.* **2014,** *50,* 7001–7003. doi:10.1039/c4cc02760d
10. Yan, X.; Xu, J.-F.; Cook, T. R.; Huang, F.; Yang, Q.-Z.; Tung, C.-H.; Stang, P. J. *Proc. Natl. Acad. Sci. U. S. A.* **2014,** *111,* 8717–8722. doi:10.1073/pnas.1408620111
11. Wang, Y.; Sun, C.-L.; Niu, L.-Y.; Wu, L.-Z.; Tung, C.-H.; Chen, Y.-Z.; Yang, Q.-Z. *Polym. Chem.* **2017,** *8,* 3596–3602. doi:10.1039/c7py00326a
12. Huang, Z.; Yang, Q.-Z.; Khvostichenko, D.; Kucharski, T. J.; Chen, J.; Boulatov, R. *J. Am. Chem. Soc.* **2009,** *131,* 1407–1409. doi:10.1021/ja807113m
13. Yang, Q.-Z.; Huang, Z.; Kucharski, T. J.; Khvostichenko, D.; Chen, J.; Boulatov, R. *Nat. Nanotechnol.* **2009,** *4,* 302–306. doi:10.1038/nnano.2009.55
14. Huang, Z.; Yang, Q.-Z.; Kucharski, T. J.; Khvostichenko, D.; Wakeman, S. M.; Boulatov, R. *Chem. – Eur. J.* **2009,** *15,* 5212–5214. doi:10.1002/chem.200900521
15. Kucharski, T. J.; Huang, Z.; Yang, Q.-Z.; Tian, Y.; Rubin, N. C.; Concepcion, C. D.; Boulatov, R. *Angew. Chem., Int. Ed.* **2009,** *48,* 7040–7043. doi:10.1002/anie.200901511
16. Tian, Y.; Kucharski, T. J.; Yang, Q.-Z.; Boulatov, R. *Nat. Commun.* **2013,** *4,* 2538. doi:10.1038/ncomms3538
17. Li, W.; Edwards, S. A.; Lu, L.; Kubar, T.; Patil, S. P.; Grubmüller, H.; Groenhof, G.; Gräter, F. *ChemPhysChem* **2013,** *14,* 2687–2697. doi:10.1002/cphc.201300252
18. Stauch, T.; Dreuw, A. *Phys. Chem. Chem. Phys.* **2016,** *18,* 15848–15853. doi:10.1039/c6cp02395a
19. García-Iriepa, C.; Sampedro, D.; Mendicuti, F.; Léonard, J.; Frutos, L. M. *J. Phys. Chem. Lett.* **2019,** *10,* 1063–1067. doi:10.1021/acs.jpclett.8b03802
20. Fernández-González, M. Á.; Rivero, D.; García-Iriepa, C.; Sampedro, D.; Frutos, L. M. *J. Chem. Theory Comput.* **2017,** *13,* 727–736. doi:10.1021/acs.jctc.6b01020
21. Blom, M.; Norrehed, S.; Andersson, C.-H.; Huang, H.; Light, M.; Bergquist, J.; Grennberg, H.; Gogoll, A. *Molecules* **2015,** *21,* 16. doi:10.3390/molecules21010016
22. Olsson, S.; Schäfer, C.; Blom, M.; Gogoll, A. *ChemPlusChem* **2018,** *83,* 1169–1178. doi:10.1002/cplu.201800564
23. Oliverio, M.; Nardi, M.; Costanzo, P.; Cariati, L.; Cravotto, G.; Giofrè, S.; Procopio, A. *Molecules* **2014,** *19,* 5599–5610. doi:10.3390/molecules19055599
24. Wang, B.; Zhang, L.; Fu, K.; Luo, Y.; Lu, W.; Tang, J. *Org. Prep. Proced. Int.* **2009,** *41,* 309–314. doi:10.1080/00304940903078053
25. Williamson, A. *London, Edinburgh Dublin Philos. Mag. J. Sci.* **1850,** *37,* 350–356. doi:10.1080/14786445008646627
26. McMurry, J. E. *Chem. Rev.* **1989,** *89,* 1513–1524. doi:10.1021/cr00097a007
27. Blom, M. Light-Triggered Conformational Switches for Modulation of Molecular Recognition: Applications for Peptidomimetics and Supramolecular Systems. Ph.D. Thesis, Uppsala, Sweden, 2015.
28. Becke, A. D. *J. Chem. Phys.* **1993,** *98,* 1372–1377. doi:10.1063/1.464304
29. Lee, C.; Yang, W.; Parr, R. G. *Phys. Rev. B* **1988,** *37,* 785–789. doi:10.1103/physrevb.37.785
30. Vosko, S. H.; Wilk, L.; Nusair, M. *Can. J. Phys.* **1980,** *58,* 1200–1211. doi:10.1139/p80-159
31. Stephens, P. J.; Devlin, F. J.; Chabalowski, C. F.; Frisch, M. J. *J. Phys. Chem.* **1994,** *98,* 11623–11627. doi:10.1021/j100096a001
32. *Gaussian 16,* Revision B.01; Gaussian, Inc.: Wallingford, CT, U.S.A., 2016.
33. Miertuš, S.; Scrocco, E.; Tomasi, J. *Chem. Phys.* **1981,** *55,* 117–129. doi:10.1016/0301-0104(81)85090-2
34. Miertuš, S.; Tomasi, J. *Chem. Phys.* **1982,** *65,* 239–245. doi:10.1016/0301-0104(82)85072-6
35. Pascual-ahuir, J. L.; Silla, E.; Tuñon, I. *J. Comput. Chem.* **1994,** *15,* 1127–1138. doi:10.1002/jcc.540151009
36. Marenich, A. V.; Cramer, C. J.; Truhlar, D. G. *J. Phys. Chem. B* **2009,** *113,* 6378–6396. doi:10.1021/jp810292n
37. Hariharan, P. C.; Pople, J. A. *Theor. Chim. Acta* **1973,** *28,* 213–222. doi:10.1007/bf00533485

38. Slavov, C.; Yang, C.; Heindl, A. H.; Stauch, T.; Wegner, H. A.; Dreuw, A.; Wachtveitl, J. *J. Phys. Chem. Lett.* **2018,** *9,* 4776–4781. doi:10.1021/acs.jpclett.8b02159
39. Cicero, D. O.; Barbato, G.; Bazzo, R. *J. Am. Chem. Soc.* **1995,** *117,* 1027–1033. doi:10.1021/ja00108a019
40. Norrehed, S.; Johansson, H.; Grennberg, H.; Gogoll, A. *Chem. – Eur. J.* **2013,** *19,* 14631–14638. doi:10.1002/chem.201300533
41. Claridge, T. D. W. *High-Resolution NMR Techniques in Organic Chemistry,* 2nd ed.; Tetrahedron Organic Chemistry, Vol. 27; Elsevier: Amsterdam, Netherlands, 2009. doi:10.1016/s1460-1567(08)x0001-7
42. Wokaun, A.; Ernst, R. R. *Chem. Phys. Lett.* **1977,** *52,* 407–412. doi:10.1016/0009-2614(77)80476-4
43. Shaka, A. J.; Freeman, R. *J. Magn. Reson. (1969-1992)* **1983,** *51,* 169–173. doi:10.1016/0022-2364(83)90117-8
44. Braunschweiler, L.; Ernst, R. R. *J. Magn. Reson. (1969-1992)* **1983,** *53,* 521–528. doi:10.1016/0022-2364(83)90226-3
45. Davis, A. L.; Keeler, J.; Laue, E. D.; Moskau, D. *J. Magn. Reson. (1969-1992)* **1992,** *98,* 207–216. doi:10.1016/0022-2364(92)90126-r
46. Hurd, R. E.; John, B. K. *J. Magn. Reson. (1969-1992)* **1991,** *91,* 648–653. doi:10.1016/0022-2364(91)90395-a
47. Wagner, R.; Berger, S. *J. Magn. Reson., Ser. A* **1996,** *123,* 119–121. doi:10.1006/jmra.1996.0222
48. Mohamadi, F.; Richards, N. G. J.; Guida, W. C.; Liskamp, R.; Lipton, M.; Caufield, C.; Chang, G.; Hendrickson, T.; Still, W. C. *J. Comput. Chem.* **1990,** *11,* 440–467. doi:10.1002/jcc.540110405
49. Harder, E.; Damm, W.; Maple, J.; Wu, C.; Reboul, M.; Xiang, J. Y.; Wang, L.; Lupyan, D.; Dahlgren, M. K.; Knight, J. L.; Kaus, J. W.; Cerutti, D. S.; Krilov, G.; Jorgensen, W. L.; Abel, R.; Friesner, R. A. *J. Chem. Theory Comput.* **2016,** *12,* 281–296. doi:10.1021/acs.jctc.5b00864
50. Watts, K. S.; Dalal, P.; Murphy, R. B.; Sherman, W.; Friesner, R. A.; Shelley, J. C. *J. Chem. Inf. Model.* **2010,** *50,* 534–546. doi:10.1021/ci100015j
51. Zhao, K.-Q.; Chen, C.; Monobe, H.; Hu, P.; Wang, B.-Q.; Shimizu, Y. *Chem. Commun.* **2011,** *47,* 6290–6292. doi:10.1039/c1cc10299k
52. Vautravers, N. R.; Regent, D. D.; Breit, B. *Chem. Commun.* **2011,** *47,* 6635–6637. doi:10.1039/c1cc10683j

License and Terms

This is an Open Access article under the terms of the Creative Commons Attribution License (http://creativecommons.org/licenses/by/4.0). Please note that the reuse, redistribution and reproduction in particular requires that the authors and source are credited.

The license is subject to the *Beilstein Journal of Organic Chemistry* terms and conditions: (https://www.beilstein-journals.org/bjoc)

The definitive version of this article is the electronic one which can be found at: doi:10.3762/bjoc.15.233

BEILSTEIN JOURNAL OF ORGANIC CHEMISTRY

Photochromic diarylethene ligands featuring 2-(imidazol-2-yl)pyridine coordination site and their iron(II) complexes

Andrey G. Lvov*[1], Max Mörtel[2], Anton V. Yadykov[1], Frank W. Heinemann[2], Valerii Z. Shirinian[1] and Marat M. Khusniyarov*[2]

Letter

Open Access

Address:
[1]N. D. Zelinsky Institute of Organic Chemistry, Russian Academy of Sciences, 47, Leninsky prosp., 119991 Moscow, Russian Federation and [2]Department of Chemistry and Pharmacy, Friedrich-Alexander University Erlangen-Nürnberg (FAU), Egerlandstraße 1, 91058 Erlangen, Germany

Email:
Andrey G. Lvov* - lvov-andre@yandex.ru; Marat M. Khusniyarov* - marat.khusniyarov@fau.de

* Corresponding author

Keywords:
diarylethene; 2-(imidazol-2-yl)pyridine; iron(II) complex; photochromism

Beilstein J. Org. Chem. **2019,** *15,* 2428–2437.
doi:10.3762/bjoc.15.235

Received: 25 June 2019
Accepted: 27 September 2019
Published: 15 October 2019

This article is part of the thematic issue "Molecular switches".

Guest Editor: W. Szymanski

© 2019 Lvov et al.; licensee Beilstein-Institut.
License and terms: see end of document.

Abstract

A new family of photochromic diarylethene-based ligands bearing a 2-(imidazol-2-yl)pyridine coordination unit has been developed. Four members of the new family have been synthesized. The photoactive ligands feature non-aromatic ethene bridges (cyclopentene, cyclopentenone, and cyclohexenone), as well as closely spaced photoactive and metal coordination sites aiming a strong impact of photocyclization on the electronic structure of the coordinated metal ion. The ligands with cyclopentenone and cyclohexenone bridges show good cycloreversion quantum yields of 0.20–0.32. The thermal stability of closed-ring isomers reveals half-lives of up to 20 days in solution at room temperature. The ligands were used to explore coordination chemistry with iron(II) targeting photoswitchable spin-crossover complexes. Unexpectedly, dinuclear and tetranuclear iron(II) complexes were obtained, which were thoroughly characterized by X-ray crystallography, magnetic measurements, and Mössbauer spectroscopy. The formation of multinuclear complexes is facilitated by two coordination sites of the diarylethene, acting as a bridging ligand. The bridging nature of the diarylethene in the complexes prevents photocyclization.

Introduction

Transition metal complexes with photoactive ligands are of great interest for advanced photonic applications [1-7]. Reversible change of the electronic structure of diarylethene photochromes [8-10] upon photocyclization is a promising tool to control the electronic structure of coordinated metal ions and, consequently, associated properties. Thus, diarylethenes were

integrated into well-known ligand systems, including 1,10-phenanthroline, 2-(azol-2-yl)pyridine, and related frameworks to yield photochromic ligands. The latter can be divided into two groups based on the position of the metal coordination site relative to the photoactive hexatriene unit of a diarylethene. Some diarylethene-based ligands with *pendant* coordination sites were synthesized, which allowed the remote control of luminescent, nonlinear optical and magnetic properties of transition metal complexes to some extent [11-16]. However, a *close* arrangement of hexatriene and coordination sites is the preferred approach for achieving a strong impact of the photochromic reaction on the electronic structure of a coordinated metal ion.

Previously reported examples of the second group ligands are collected in Figure 1. Yam et al. developed diarylethenes **I** [17] and **II** [18] and synthesized their rhenium(I) complexes, which possess prominent luminescent and spectral properties, including photocyclization with visible and NIR light. Using the photochromic ligand **I**, a spin-crossover (SCO) Fe(II) complex was developed, which allowed a reversible paramagnetic (high-spin, $S = 2$) → diamagnetic (low-spin, $S = 0$) transition at the iron(II) ion at room temperature (rt) in solution via ligand photocyclization [19]. More recently, the remarkable photoswitching between high-spin and low-spin states at rt in the solid state and thin films was demonstrated [20-22]. Kawai et al. obtained a luminescent complex of europium(III) with terarylene **III** showing the photomodulation of emission intensity [23]. A number of diarylethene ligands with a perfluorocyclopentene bridge were designed. Yu and co-workers reported a series of 2-(thiazol-2-yl)pyridine derivatives [24-26]. Reversible photoinduced release and trapping of copper(II) ions was achieved with **IV**. Diarylethene **V** and its analogs were used as chemical sensors for a number of metal ions [27].

Despite of recent advances in this area, the scarcity of reported examples requires the search and design of novel photoswitchable ligands with advanced properties. In this context, it is important to specify some design principles for such ligands. Firstly, novel ligands should feature a non-aromatic ethene bridge to increase the life-time of a photoinduced closed-ring isomer [28]. Secondly, photoactive hexatriene and metal coordination sites should be close to each other.

To meet these requirements, a new family of ligands **VI** based on the 2-(imidazol-2-yl)pyridine unit as a heteroaryl moiety and various ethene bridges is presented in this work. Diarylethenes with the 2-(imidazol-2-yl)pyridine being a part of the ethene bridge were previously developed [18,29] and their complexes with rhodium(I) [18], platinum(II) [30], and iridium(III) [31] were reported. In contrast, in our work, the 2-(imidazol-2-yl)pyridine unit is used as a heterocyclic moiety of diarylethenes with cyclopentenone, cyclopentene, and cyclohexenone ethene bridges. The novel ligands have been tested in the coordination chemistry with iron(II) aiming photoswitchable SCO systems.

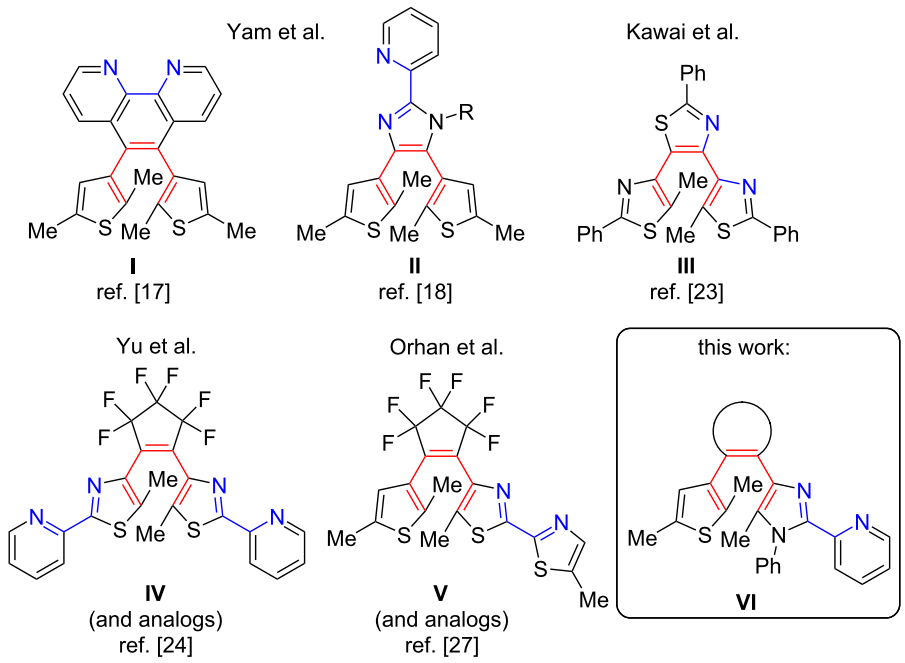
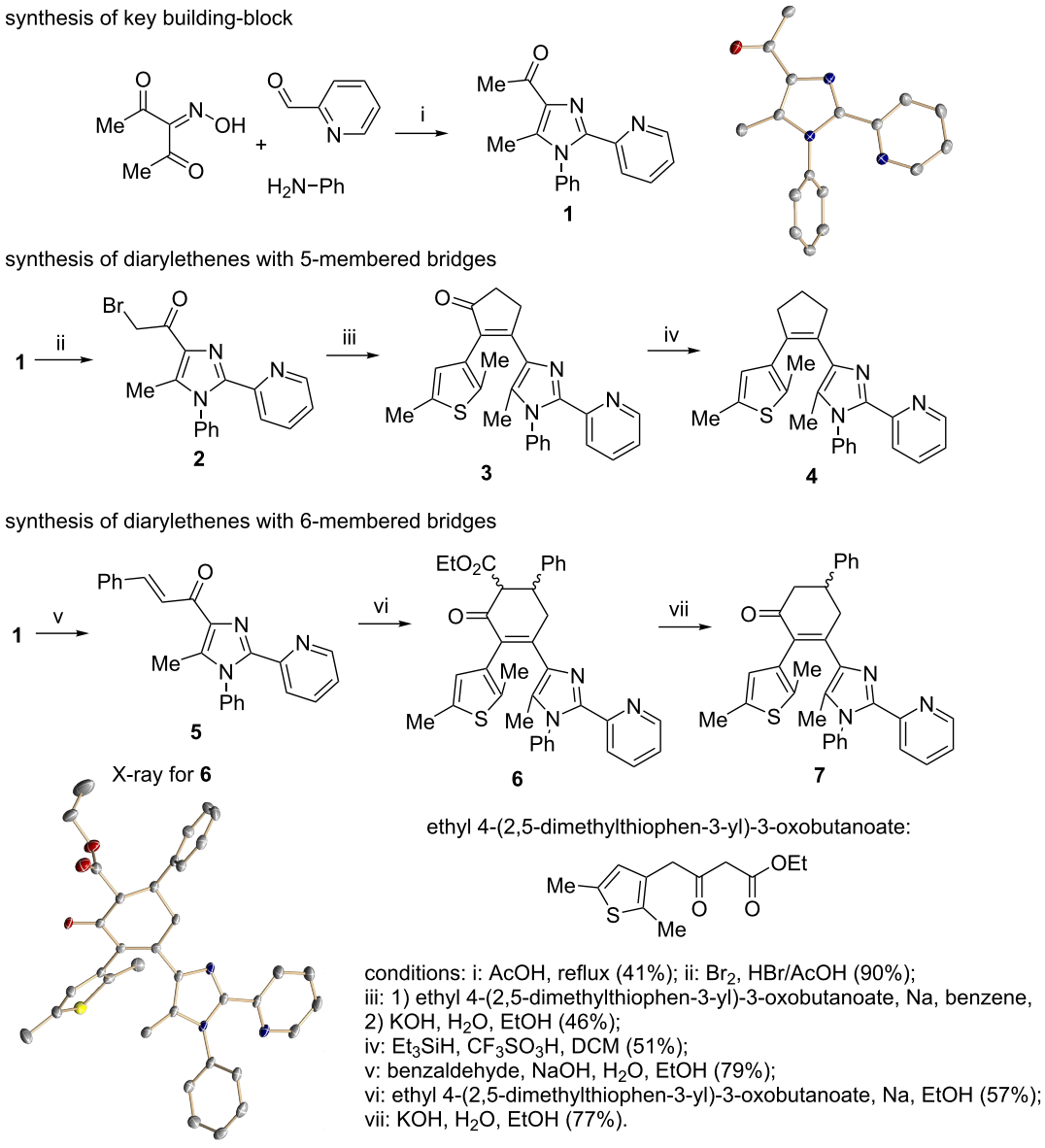


Figure 1: Families of diarylethene-bases ligands with spatial proximity of coordination site (blue) and photoactive framework (red).

Results and Discussion

Synthesis and structure of photochromic ligands

Recently, some of us have developed original methods for the synthesis of various diarylethenes with cyclopentenone, cyclopentene, and cyclohexenone bridges [32]. These methods utilize ethyl 4-(2,5-dimethylthiophen-3-yl)-3-oxobutanoate (Scheme 1) or its analogs as starting materials. To obtain novel diarylethenes with 2-(imidazol-2-yl)pyridine moiety, here we have synthesized a previously unknown imidazole derivative **1** by a one-pot condensation [33] of 3-(hydroxyimino)pentane-2,4-dione, aniline, and 2-pyridinecarboxaldehyde (Scheme 1). The structure of **1** was confirmed by X-ray crystallography [34]. The ketone **1** was subsequently used for the synthesis of desired photochromic ligands with cyclopentenone (**3**), cyclopentene (**4**), and cyclohexenone (**6** and **7**) bridges via intermediate bromoketone **2** and chalkone **5**. Cyclopentenone **3** was synthesized by adapting a previously reported two-step protocol [35] starting from ethyl 4-(2,5-dimethylthiophen-3-yl)-3-oxobutanoate and bromoketone **2**. Ionic hydrogenation [36] of **3** provided diarylethene **4** with a cyclopentene bridge with 51% yield. Robinson-type reaction [37] of ethyl 4-(2,5-dimethylthiophen-3-yl)-3-oxobutanoate and chalkone **5** resulted in cyclohexenone derivative **6** (57% yield). The saponification/



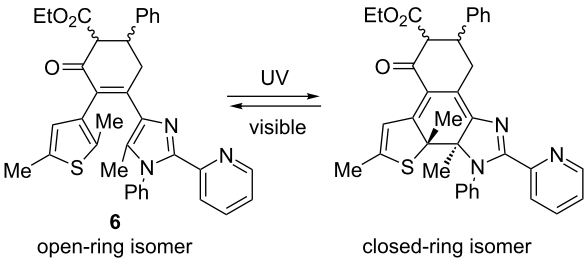
Scheme 1: Synthesis of photochromic ligands.

decarboxylation of **6** gave cyclohexenone **7**. Thus, the previously developed methodology was successfully applied for the synthesis of a new family of photochromic ligands.

The structures of the synthesized diarylethene-based ligands **3**, **4**, **6**, and **7** were confirmed by ^{1}H and ^{13}C NMR spectroscopy and mass spectrometry. The molecular structure of **6** was additionally confirmed by X-ray crystallography. In good accordance with previous DFT calculations [37], the molecule shows exclusively antiparallel conformation [8] of the thiophene and imidazole groups of the photoactive diarylethene moiety, with the respective α-methyl groups pointing in different directions. The thiophene and imidazole rings are rotated out of the cyclohexenone plane by 47.7° and 44.1°, respectively. The distance between the reactive carbon atoms is 3.6 Å. This value is shorter than 4.2 Å, which is favorable for photocyclization [38]. The cyclohexenone moiety adopts a distorted half-chair (sofa) conformation, with the phenyl substituted carbon atom forming an out-of-plane corner.

Photochemical studies

We have studied spectroscopic and photochemical properties of the ligands **3**, **4**, **6**, and **7** in nonpolar toluene and polar acetonitrile solvents. All ligands show typical for diarylethenes photochromic properties: colorless open-ring isomer and the emergence of a new band in visible upon UV light irradiation (Figure 2) [8]. This color change is due to the reversible photocyclization and formation of a closed-ring isomer (Scheme 2).



Scheme 2: Reversible photocyclization of ligand **6**.

The results of photochemical studies are listed in Table 1. Absorption maxima of the open-ring ligands are in the 310–323 nm range. Interestingly, the carbocycle size and the presence/absence of carbonyl group are weakly reflected in the position of absorption maxima of open-ring isomers. For example, the reduction of carbonyl group in **3** (compared to **4**) leads to insignificant bathochromic shift of the absorption maximum from 322 nm to 323 nm in toluene, which is, however, accompanied by a large hypochromic shift from 31100 to 20000 $M^{-1}cm^{-1}$. The expansion from cyclopentenone to cyclohexenone bridge gives a similar effect.

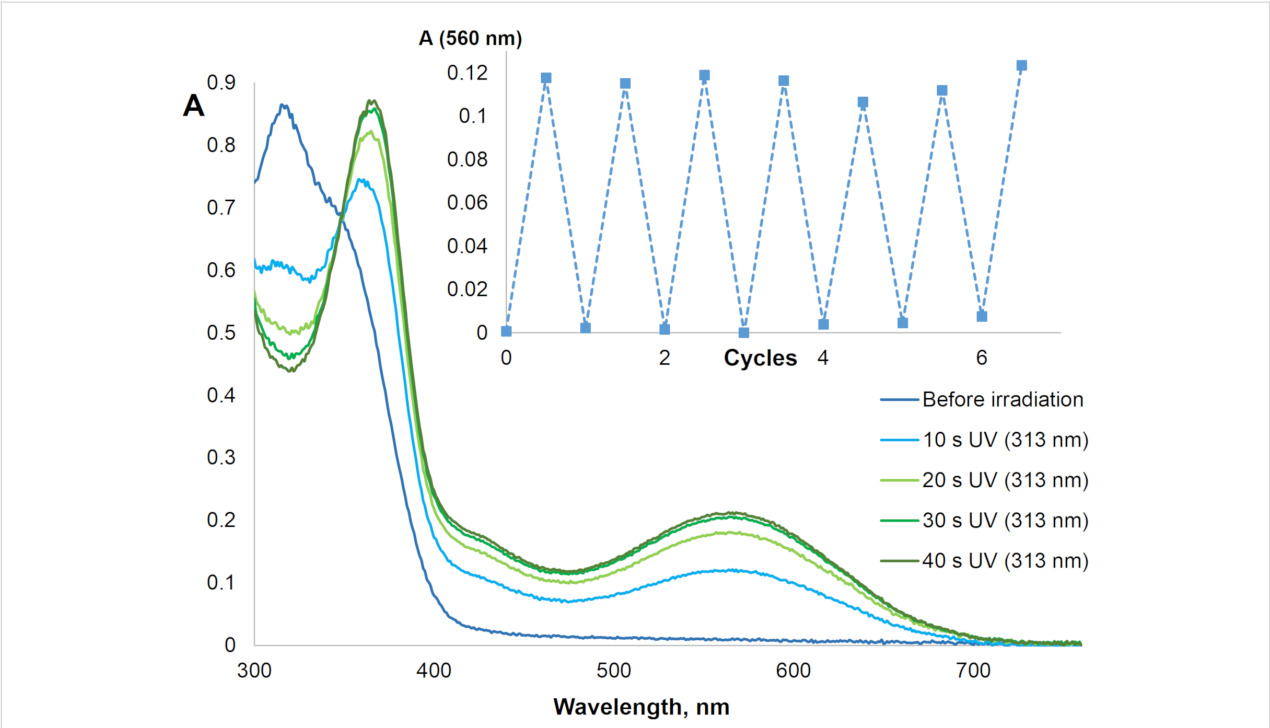
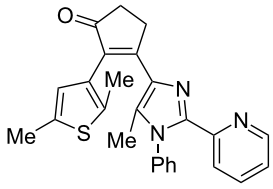
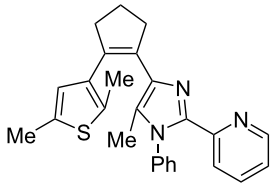
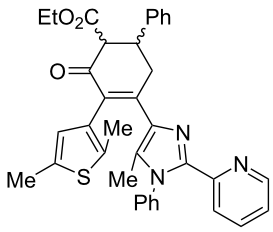
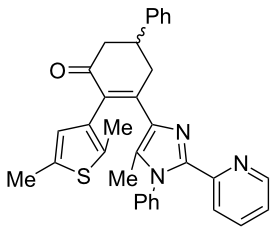


Figure 2: Electronic spectra of diarylethene **6** upon UV irradiation (313 nm, toluene, $c = 3.4 \times 10^{-5}$ M). Inset: fatigue resistance upon multiple subsequent irradiation with UV (365 nm) and visible light (green LED) in acetonitrile.

Table 1: Spectroscopic and photochemical properties of photochromic ligands.

Diarylethene	Solvent	λ_{max}^{A}, nm (ε, $M^{-1}\cdot cm^{-1}$)[a]	λ_{max}^{B}, nm (ε, $M^{-1}\cdot cm^{-1}$)[b]	Φ_{AB}[c]	Φ_{BA}[d]	Conv at PSS[e]	$\tau^{BA}_{1/2}$ (days)[f]
 **3**	toluene	322 (31100)	572 (7000)	0.40	0.32	0.93	19.4
	MeCN	319 (31900)	563 (6700)	0.35	0.22	0.91	8.6
 **4**	toluene	323 (20000)	504 (8400)	0.42	0.04	0.89	19.6
	MeCN	317 (19900)	490 (7300)	0.39	0.06	0.85	17.0
 **6**	toluene	315 (22200), 346 (sh)	567 (6900)	0.25	0.29	0.89	
	MeCN	309 (18300), 341 (15500)	560 (5200)	0.26	0.20	0.91	–[g]
 **7**	toluene	310 (24200)	560 (5600)	0.22	0.28	0.83	14.2
	MeCN	310 (18600)	549 (4800)	0.27	0.21	0.70	13.0

[a]Absorption maxima (extinction coefficients) of open-ring isomers. [b]Absorption maxima (extinction coefficients) of closed-ring isomers. [c]Quantum yields of photocyclization under irradiation with 313 nm. [d]Quantum yields of cycloreversion under irradiation with 480 nm. [e]Conversion at PSS under irradiation with 313 nm. [f]Thermal stability of the closed-ring isomer – half-life at 25 ºC (days). [g]Additional thermal process of photoinduced form was detected.

Cyclopentene derivative **4** shows an absorption maximum of the closed-ring isomer at 504 nm in toluene, while a hypsochromic shift of 14 nm was observed in acetonitrile. This influence of solvent polarity was detected for all ligands [39]. The carbonyl group in the ethene bridge of **3** causes a significant bathochromic shift (68 nm in toluene) of the closed-ring isomer maximum in comparison with **4**. The expansion of the five-membered carbocyclic bridge to a six-membered ring in **7** leads to a slight hypsochromic shift. The presence of a CO_2Et group in the cyclohexenone bridge in **6** results in further minor hypsochromic shift. Thus, the absorption maxima of the closed-ring ligands are located in the wide range 490–563 nm. Photocyclization/cycloreversion of all ligands can be repeated several times without notable fatigue (see inset of Figure 2).

Extinction coefficients of closed-ring isomers were determined using ^{1}H NMR and electronic absorption spectroscopy (for representative NMR spectra, see section VI in Supporting Information File 1). This allowed us to determine the quantum yields of photochemical reactions. Cyclopentene (**4**) and cyclopentenone (**3**) derivatives show the highest photocyclization quantum yields up to 0.42 in toluene. In polar acetonitrile the cyclization quantum yield is lower [40]. The quantum yields for cyclohexenone derivatives **6** and **7** are in the 0.22–0.27 range.

Similar to some other cyclopentene derivatives [41], diarylethene **4** possesses low cycloreversion quantum yields at 4–6%. However, in accordance with previous results on imidazole derivatives [42], **3** with a cyclopentenone bridge shows much high quantum yields of 0.32 and 0.22 in toluene and acetonitrile, respectively. Cyclohexenone derivatives **6** and **7** show high cycloreversion quantum yields 0.20–0.29, too. Note, that in comparison with common cyclopentene and perfluorocyclopentene derivatives [8], ligands **3**, **6**, and **7** possess high cycloreversion quantum yields. Note, that the photostationary state for the cyclization with λ = 313 nm is characterized by a high conversion to the close-ring isomers at 0.70–0.93.

Finally, thermal stability of closed-ring isomers was determined. Previously, it was demonstrated that imidazole as a heteroaryl moiety decreases thermal stability [42]. In particular, a close analogue of **3** with a phenyl instead of a pyridyl group showed a half-live of the ring-closed isomer as low as 7.3 days. In accordance to this data, diarylethene **3** showed a half-life of 8.6 days. However, in nonpolar toluene the half-life was much higher (19.4 days). Cyclopentene and cyclohexenone derivatives **4** and **7** show similar values of thermal stability (19.6 h and 14.2 h in toluene). Interestingly, we have detected an unexpected thermal process for the closed-ring isomer of **6** in the dark, resulted in the hypsochromic shift of long-wavelength absorption band, which could be due to keto–enol tautomerization in the ethene bridge [43]. Overall, the thermal stabilities of the new ligands are comparable to those of phenanthroline-based photochromic ligand **I** [19].

Synthesis and structure of iron complexes

Previously, ligand **I** (Figure 1) and its analogs were successfully used in the synthesis of SCO $[Fe^{II}(H_2B(pz)_2)_2\mathbf{I}]$ complexes (pz = 1-pyrazolyl) [19-22,44]. We tested the ligands **3**, **4**, **6**, and **7** for the synthesis of analogous complexes aiming at efficient light-induced SCO at rt. In all cases, the mixing of in situ-prepared "$Fe(H_2B(pz)_2)_2$" with the ligands in MeOH resulted in the formation of red solutions. For ligand **6** bearing a CO_2Et group, almost instant precipitation was observed. In contrast to **6**, our attempts to obtain crystalline solids using **3**, **4**, and **7** were unsuccessful.

Crystals suitable for X-ray structure were obtained in a fritted U-shape tube by the slow diffusion of methanol solutions of in situ-prepared "$Fe(H_2B(pz)_2)_2$" and diarylethene **6**. Unexpectedly, we have found that the structure of the product depends on the reaction time. Reproducible crystals isolated after growing for 1 month and less – a dinuclear complex **8**, and unique crystals after 2-year storage – a tetranuclear complex **9**, have different molecular structures (Figure 3). Both complexes represent unusual cyclic complexes, comprising two diarylethene ligands and two or four iron(II) ions in **8** and **9**, respectively. The β-keto ester fragment in the bridge of **6** serves as a second coordination site, which eliminates a proton under the action of $H_2B(pz)_2^{1-}$ as base in both complexes [45].

The complex **8** ($[Fe_2(H_2B(pz)_2)_2(\mathbf{6}\text{-H})_2]\cdot 4CH_3OH$) crystallizes as red blocks in the monoclinic *C*2/*c* space group with four molecules of **8** and 16 molecules of co-crystallized CH_3OH in the unit cell. The compound reveals a crystallographically symmetrical dimeric structure with two iron centers linked by two ligands **6**. Each iron ion is coordinated equatorially by the β-keto ester moiety of one molecule **6** and chelated via the imidazole and pyridine groups of another moelcule **6**. The distorted octahedral coordination sphere is completed by a $H_2B(pz)_2^{1-}$ anion. Fe–N bond distances of 2.1602(15)–2.1615(15) Å for the pyrazoles and 2.2489(14)–2.2462(14) Å for the imidazole and pyridine moieties are typical for high-spin (HS) iron(II) complexes [46,47]. Similarly, Fe–O bond distances of 1.9912(11) and 2.1238(12) Å also provide evidence for HS iron(II) [46,48,49]. The two Fe–O bonds are not equivalent as the ligand appears in its deprotonated enolate form. Furthermore, a *trans*-effect due to the $H_2B(pz)_2^{1-}$ anion can further elongate that bond. Two iron(II) centers are 8.057 Å apart in the dimer. The ligand **6** appears in the open-ring form and the parallel conformation [8], with the α-methyl groups pointing in similar directions. While still appearing in a distorted half-chair conformation, the phenyl substituent of the cyclohexenone moiety no longer forms the out-of-plane corner. Instead, the unsubstituted CH_2 position twists out of the plane towards the thiophene moiety of another ligand **6**.

Long time precipitation of crystalline material resulted in a tetranuclear species $[Fe_2(H_2B(pz)_2)_2Fe_2(B(OMe)_3(pz))_2(\mathbf{6}\text{-H})_2]$ (complex **9**). Apparently, this product is the result of destruction of bis(pyrazolyl)borate moieties of complex **8** by methanol. Species **9** crystallizes as red, block-shaped crystals in the triclinic *P*−1 space group with one molecule in the unit cell. The crystal structure reveals two pairs of differently substituted iron ions connected by a so far unprecedented trimethoxypyrazolylborate bridging group. The periphery Fe ions reveal an octahedral coordination environment with two $H_2B(pz)_2^{1-}$ anions and two methoxy groups of the bridging moiety. The Fe–N bond distances ranging from 2.1361(19) to 2.1631(19) Å in **9** appear similar to those in **8**, which confirms a HS-Fe(II) ion. The Fe–O bond lengths vary between 2.1333(15) Å and 2.3110(16) Å. Curiously, the O–B bond distances to the tetrahedral boron ion do not differ in length with 1.453(3) and 1.449(3) Å, respectively.

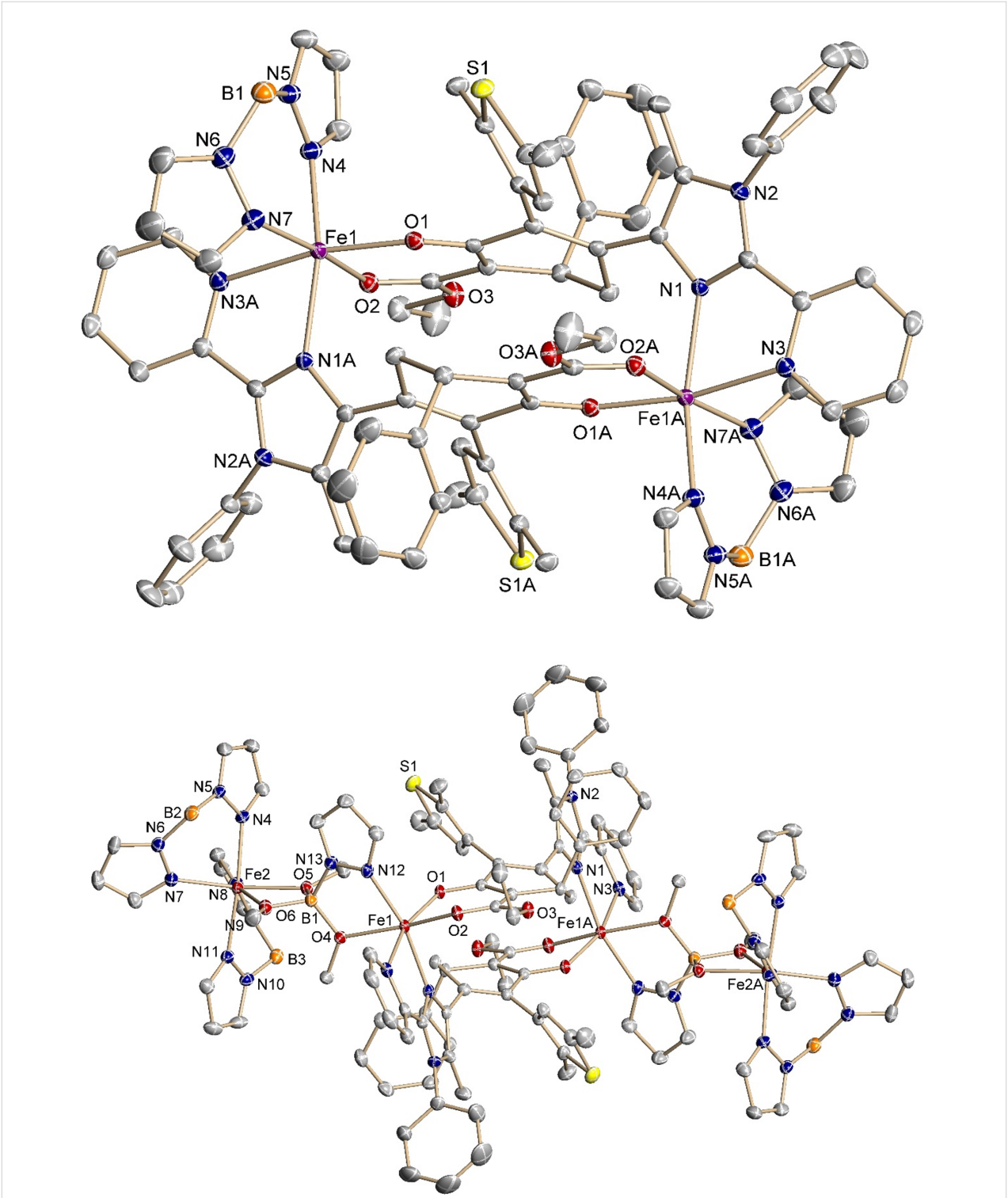


Figure 3: Molecular structure of complexes **8** (top) and **9** (bottom) at 100 K. The H atoms are omitted for clarity; the thermal ellipsoids are drawn at the 50% probability level.

Each of the two interior Fe ions is linked to the bridging unit via its remaining methoxy group and the pyrazole moiety. The octahedral coordination environment is completed with the β-keto ester moiety of one ligand **6** and by the imidazole and pyridine groups of the second ligand **6**. The Fe–O and Fe–N bond lengths to the bridging unit are 2.1687(15) Å and 2.1190(19) Å.

The pyridine and imidazole Fe–N bond distances are 2.2467(19) Å and 2.1793(18) Å, which are very similar to those found for the dimer **8**. On the contrary, the Fe–O bond distances to the β-keto ester moiety differ much less with 2.0812(15) Å and 2.0098(15) Å. The iron–donor bond distances are in good agreement with an iron(II) HS state. The two iron(II) ions linked by the trimethoxypyrazolylborate group are 5.945 Å apart. The distance between the iron(II) ions connected by ligand **6** in **9** is elongated by 0.244 Å to 8.301 Å compared to **8**. The ligand **6** appears also in its open-ring form and parallel conformation.

Electronic structure of complexes **8** and **9**

Microcrystalline samples of **8** and **9** were used for magnetic susceptibility measurements. Complex **8** shows a nearly constant χT product of 7.63 $cm^3 \cdot mol^{-1} \cdot K$ above 125 K (Figure 4). It increases gradually upon lowering the temperature, reaching a maximum of 8.80 $cm^3 \cdot mol^{-1} \cdot K$ at 13 K, which is indicative of ferromagnetic coupling between the two iron(II) ions. By lowering the temperature further, the χT product decreases sharply due to zero-field splitting (ZFS). The rt value of the χT product of 7.63 $cm^3 \cdot mol^{-1} \cdot K$ is slightly higher than expected spin-only value for two non-interacting HS-Fe(II) ions ($\chi_{so}T$ = 6.00 $cm^3 \cdot mol^{-1} \cdot K$) due to orbital contribution. The fit for $S_1 = S_2 = 2$ spin system (see section VII in Supporting Information File 1) affords a ferromagnetic coupling constant J = +0.5 cm^{-1}, axial ZFS D = 5.0 cm^{-1}, and $g_1 = g_2$ = 2.24. To get further insight, field dependent measurements up to 7 T were conducted. At fields >4 T the (reduced) magnetization saturates, reaching a plateau at 8 $N_A\mu_B$, which corresponds to two ferromagnetically coupled HS-Fe(II) ions in the ground state. Zero-field ^{57}Fe Mössbauer spectrometry confirm HS-Fe(II) state at 77 K and 297 K.

The χT product of **9** increases to almost constant value of 14.61 $cm^3 \cdot mol^{-1} \cdot K$ at rt, which is in good agreement with four uncoupled HS-Fe(II) ions ($\chi_{so}T$ = 12.00 $cm^3 \cdot mol^{-1} \cdot K$) (Figure 1). A significant drop of χT observed at temperatures below 40 K is due to ZFS. The fit for $S_1 = S_2 = S_3 = S_4 = 2$ spin system yields g = 2.20 and D = 5.9 cm^{-1}. Field-dependent magnetic measurements show a more gradual increase of magnetization compared to **8**. Although the magnetization does not saturate even at 7 T, the maximum of 14.17 $N_A\mu_B$ points to four S_{Fe} = 2 ions (16 $N_A\mu_B$ is expected).

The complex **8** shows a single major absorption band in the low energy UV region at 346 nm ($\varepsilon = 6.22 \times 10^4$ $M^{-1} \cdot cm^{-1}$), which appears bathochromically shifted compared to the free ligand. No charge transfer (CT) bands are visible in the spectrum. The low intensity broad shoulder, which spans almost the entire visible region up to 750 nm, can be attributed to *d*–*d* transitions (for details, see Supporting Information File 1). The electronic absorption spectrum of **9** shows no CT bands in the visible region. The absorption maximum at 346 nm ($\varepsilon = 2.28 \times 10^4$ $M^{-1} \cdot cm^{-1}$) appears sharper compared to **8**. The broad shoulder presumably due to *d*–*d* transitions also appears contracted, as it disappears at lower wavelengths (<650 nm).

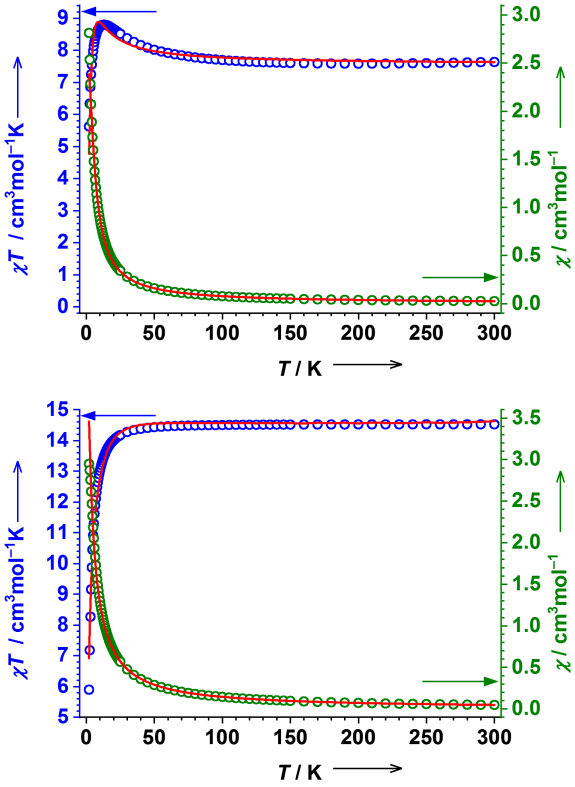


Figure 4: Variable temperature χT product (blue) and χ (green) of **8** (top) and **9** (bottom) measured at an external magnetic field of 1 T in the heating mode (see Supporting Information File 1 for fitting parameters).

Attempts to induce photocyclization of diarylethenes in complexes **8** and **9** with UV light (λ = 365 nm) in dichloromethane show no appearance of new bands. Prolonged irradiation results in slow photodecomposition. Both **8** and **9** share a common structural motif that prevents photocyclization. Coordination of the β-keto ester moiety and the imidazole/pyrazole moiety to two different iron(II) ions puts the ligand under severe strain. Thus, the structural reorganization necessary to accommodate a new planar structure formed by the photocyclization reaction is impossible without breaking Fe–N or Fe–O bonds.

Note, that the obtained complexes **8** and **9** represent cyclic complexes of diarylethenes with Fe(II) ions. In recent years, related derivatives of photochromic diarylethenes [50,51] became of great interest for realization of light-triggered guest uptake/

release [52] and light-controlled interconversion between distinct supramolecular assemblies [53]. Ligand **6** featuring two coordination sites in the heteroaryl moiety and bridge provides unique opportunities to construct novel macrocyclic systems. Our future efforts will be concentrated on the synthesis of photoactive complexes based on ligand **6**.

Conclusion

A new class of photochromic diarylethene-based ligands featuring a 2-(imidazol-2-yl)pyridine coordination unit as a heteroaryl moiety has been developed. Four members of the new family have been synthesized. All ligands show good combinations of cyclization/cycloreversion quantum yields, whereas the thermal stability of closed-ring isomers is comparable with those reported for a diarylethene-based ligand with a phenanthroline bridge. Cyclohexenone ligand **6** readily forms a dimeric complex **8** with "$Fe^{II}(H_2B(pz)_2)_2$", with its β-keto ester moiety acting as a second coordination site. Slow crystallization yielded a tetranuclear Fe(II) complex **9**, where the base dimeric unit is expanded by an unprecedented trimethoxypyrazolylborate bridging group. The photocyclization of iron complexes is inhibited due to the rigid coordination of the imidazole group to the metal ion, which prevents the rotation of the group needed for cyclization.

Supporting Information

Supporting Information File 1

Experimental details and peripheral discussion.
[https://www.beilstein-journals.org/bjoc/content/supplementary/1860-5397-15-235-S1.pdf]

Supporting Information File 2

X-ray data for compounds **1**, **6**, **8**, and **9**.
[https://www.beilstein-journals.org/bjoc/content/supplementary/1860-5397-15-235-S2.zip]

Acknowledgements

Synthesis and studies of diarylethenes were supported by the Russian Science Foundation (RSF Grant 18-73-00290). Synthesis and investigation of complexes were supported by the Deutsche Forschungsgemeinschaft (DFG Research Grant KH 279/3). MMK is grateful to Prof. Karsten Meyer (FAU Erlangen-Nürnberg) for providing access to spectroscopic facilities and his general support. Dr. Jörg Sutter (FAU Erlangen-Nürnberg) is acknowledged for measuring Mössbauer spectra. Prof. Yulia V. Nelyubina (INEOS RAS) is acknowledged for X-ray crystallography of compound **1**. AGL thanks Deutscher Akademischer Austauschdienst for research fellowship (Forschungsstipendien – Kurzstipendien program). AGL is grateful to Felix Ruf for his invaluable support at the first stage of the project.

ORCID® iDs

Andrey G. Lvov - https://orcid.org/0000-0003-2951-2651
Frank W. Heinemann - https://orcid.org/0000-0002-9007-8404
Marat M. Khusniyarov - https://orcid.org/0000-0002-2034-421X

References

1. Ko, C.-C.; Yam, V. W.-W. *Acc. Chem. Res.* **2018,** *51,* 149–159. doi:10.1021/acs.accounts.7b00426
2. Hasegawa, Y.; Nakagawa, T.; Kawai, T. *Coord. Chem. Rev.* **2010,** *254,* 2643–2651. doi:10.1016/j.ccr.2009.12.036
3. Harvey, E. C.; Feringa, B. L.; Vos, J. G.; Browne, W. R.; Pryce, M. T. *Coord. Chem. Rev.* **2015,** *282–283,* 77–86. doi:10.1016/j.ccr.2014.06.008
4. Guerchais, V.; Ordronneau, L.; Le Bozec, H. *Coord. Chem. Rev.* **2010,** *254,* 2533–2545. doi:10.1016/j.ccr.2010.01.013
5. Bianchi, A.; Delgado-Pinar, E.; García-España, E.; Giorgi, C.; Pina, F. *Coord. Chem. Rev.* **2014,** *260,* 156–215. doi:10.1016/j.ccr.2013.09.023
6. Boillot, M.-L.; Zarembowitch, J.; Sour, A. *Top. Curr. Chem.* **2004,** *234,* 261–276. doi:10.1007/b95419
7. Kume, S.; Nishihara, H. *Dalton Trans.* **2008,** 3260–3271. doi:10.1039/b716947g
8. Irie, M.; Fukaminato, T.; Matsuda, K.; Kobatake, S. *Chem. Rev.* **2014,** *114,* 12174–12277. doi:10.1021/cr500249p
9. Zhang, J.; Tian, H. *Adv. Opt. Mater.* **2018,** *6,* 1701278. doi:10.1002/adom.201701278
10. Lvov, A. G.; Khusniyarov, M. M.; Shirinian, V. Z. *J. Photochem. Photobiol., C* **2018,** *36,* 1–23. doi:10.1016/j.jphotochemrev.2018.04.002
11. Li, Z.-Y.; Dai, J.-W.; Damjanović, M.; Shiga, T.; Wang, J.-H.; Zhao, J.; Oshio, H.; Yamashita, M.; Bu, X.-H. *Angew. Chem., Int. Ed.* **2019,** *58,* 4339–4344. doi:10.1002/anie.201900789
12. Jukes, R. T. F.; Adamo, V.; Hartl, F.; Belser, P.; De Cola, L. *Inorg. Chem.* **2004,** *43,* 2779–2792. doi:10.1021/ic035334e
13. Ordronneau, L.; Nitadori, H.; Ledoux, I.; Singh, A.; Williams, J. A. G.; Akita, M.; Guerchais, V.; Le Bozec, H. *Inorg. Chem.* **2012,** *51,* 5627–5636. doi:10.1021/ic2025457
14. Zhong, Y.-W.; Vila, N.; Henderson, J. C.; Abruña, H. D. *Inorg. Chem.* **2009,** *48,* 7080–7085. doi:10.1021/ic802272q
15. Zhong, Y.-W.; Vila, N.; Henderson, J. C.; Abruña, H. D. *Inorg. Chem.* **2009,** *48,* 991–999. doi:10.1021/ic801588y
16. Aubert, V.; Guerchais, V.; Ishow, E.; Hoang-Thi, K.; Ledoux, I.; Nakatani, K.; Le Bozec, H. *Angew. Chem., Int. Ed.* **2008,** *47,* 577–580. doi:10.1002/anie.200704138
17. Yam, V. W.-W.; Ko, C.-C.; Zhu, N. *J. Am. Chem. Soc.* **2004,** *126,* 12734–12735. doi:10.1021/ja047446q
18. Lee, P. H.-M.; Ko, C.-C.; Zhu, N.; Yam, V. W.-W. *J. Am. Chem. Soc.* **2007,** *129,* 6058–6059. doi:10.1021/ja067425r
19. Milek, M.; Heinemann, F. W.; Khusniyarov, M. M. *Inorg. Chem.* **2013,** *52,* 11585–11592. doi:10.1021/ic401960x
20. Rösner, B.; Milek, M.; Witt, A.; Gobaut, B.; Torelli, P.; Fink, R. H.; Khusniyarov, M. M. *Angew. Chem., Int. Ed.* **2015,** *54,* 12976–12980. doi:10.1002/anie.201504192
21. Poggini, L.; Milek, M.; Londi, G.; Naim, A.; Poneti, G.; Squillantini, L.; Magnani, A.; Totti, F.; Rosa, P.; Khusniyarov, M. M.; Mannini, M. *Mater. Horiz.* **2018,** *5,* 506–513. doi:10.1039/c7mh01042g

22. Mörtel, M.; Witt, A.; Heinemann, F. W.; Bochmann, S.; Bachmann, J.; Khusniyarov, M. M. *Inorg. Chem.* **2017,** *56,* 13174–13186. doi:10.1021/acs.inorgchem.7b01952
23. Nakagawa, T.; Hasegawa, Y.; Kawai, T. *J. Phys. Chem. A* **2008,** *112,* 5096–5103. doi:10.1021/jp712079n
24. Giraud, M.; Léaustic, A.; Charlot, M.-F.; Yu, P.; Césario, M.; Philouze, C.; Pansu, R.; Nakatani, K.; Ishow, E. *New J. Chem.* **2005,** *29,* 439–446. doi:10.1039/b409274k
25. Giraud, M.; Leaustic, A.; Guillot, R.; Yu, P.; Lacroix, P. G.; Nakatani, K.; Pansu, R.; Maurel, F. *J. Mater. Chem.* **2007,** *17,* 4414–4425. doi:10.1039/b704806h
26. Giraud, M.; Léaustic, A.; Guillot, R.; Yu, P.; Dorlet, P.; Métivier, R.; Nakatani, K. *New J. Chem.* **2009,** *33,* 1380–1385. doi:10.1039/b901201j
27. Gundogdu, L.; Kose, M.; Takeuchi, S.; Yokoyama, Y.; Orhan, E. *J. Lumin.* **2018,** *203,* 568–575. doi:10.1016/j.jlumin.2018.06.014
28. Milić, J. V.; Schaack, C.; Hellou, N.; Isenrich, F.; Gershoni-Poranne, R.; Neshchadin, D.; Egloff, S.; Trapp, N.; Ruhlmann, L.; Boudon, C.; Gescheidt, G.; Crassous, J.; Diederich, F. *J. Phys. Chem. C* **2018,** *122,* 19100–19109. doi:10.1021/acs.jpcc.8b05019
29. Peng, X.; Deng, J.-G.; Xu, H.-B. *RSC Adv.* **2013,** *3,* 24146–24153. doi:10.1039/c3ra43110j
30. Wong, H.-L.; Zhu, N.; Yam, V. W.-W. *J. Organomet. Chem.* **2014,** *751,* 430–437. doi:10.1016/j.jorganchem.2013.07.048
31. Cao, D.-K.; Hu, J.-S.; Li, M.-Q.; Gong, D.-P.; Li, X.-X.; Ward, M. D. *Dalton Trans.* **2015,** *44,* 21008–21015. doi:10.1039/c5dt03809j
32. Lvov, A. G.; Yokoyama, Y.; Shirinian, V. Z. *Chem. Rec.* **2019**. doi:10.1002/tcr.201900015
See for review.
33. Lettau, H. *Z. Chem.* **1971,** *11,* 10–11.
34. Crystallographic data were deposited with the Cambridge Crystallographic Data Centre (CCDC No. 1935238 (**1**), 1934792 (**6**), 1934793 (**8**), 1934794 (**9**)).
35. Shirinian, V. Z.; Shimkin, A. A.; Lonshakov, D. V.; Lvov, A. G.; Krayushkin, M. M. *J. Photochem. Photobiol., A* **2012,** *233,* 1–14. doi:10.1016/j.jphotochem.2012.02.011
36. Lvov, A. G.; Bulich, E. Y.; Metelitsa, A. V.; Shirinian, V. Z. *RSC Adv.* **2016,** *6,* 59016–59020. doi:10.1039/c6ra11791k
37. Lvov, A. G.; Kavun, A. M.; Kachala, V. V.; Nelyubina, Y. V.; Metelitsa, A. V.; Shirinian, V. Z. *J. Org. Chem.* **2017,** *82,* 1477–1486. doi:10.1021/acs.joc.6b02665
38. Kobatake, S.; Uchida, K.; Tsuchida, E.; Irie, M. *Chem. Commun.* **2002,** 2804–2805. doi:10.1039/b208419h
39. Meng, S.; Ma, J. *J. Phys. Chem. A* **2012,** *116,* 913–923. doi:10.1021/jp210846b
40. Irie, M.; Sayo, K. *J. Phys. Chem.* **1992,** *96,* 7671–7674. doi:10.1021/j100198a035
41. Herder, M.; Schmidt, B. M.; Grubert, L.; Pätzel, M.; Schwarz, J.; Hecht, S. *J. Am. Chem. Soc.* **2015,** *137,* 2738–2747. doi:10.1021/ja513027s
42. Shirinian, V. Z.; Lvov, A. G.; Bulich, E. Y.; Zakharov, A. V.; Krayushkin, M. M. *Tetrahedron Lett.* **2015,** *56,* 5477–5481. doi:10.1016/j.tetlet.2015.08.028
43. This phenomenon was found for related dithienylethene: Lvov, A. G.; Yadykov, A. V.; Lyssenko, K. A.; Khusniyarov, M. M.; Shirinian, V. Z. *Manuscript in preparation.*
44. Nihei, M.; Suzuki, Y.; Kimura, N.; Kera, Y.; Oshio, H. *Chem. – Eur. J.* **2013,** *19,* 6946–6949. doi:10.1002/chem.201300767
45. Jung, O. S.; Jeong, J. H.; Sohn, Y. S. *Organometallics* **1991,** *10,* 2217–2221. doi:10.1021/om00053a026
46. Min, K. S.; Swierczek, K.; DiPasquale, A. G.; Rheingold, A. L.; Reiff, W. M.; Arif, A. M.; Miller, J. S. *Chem. Commun.* **2008,** 317–319. doi:10.1039/b715271j
47. Naggert, H.; Rudnik, J.; Kipgen, L.; Bernien, M.; Nickel, F.; Arruda, L. M.; Kuch, W.; Näther, C.; Tuczek, F. *J. Mater. Chem. C* **2015,** *3,* 7870–7877. doi:10.1039/c5tc00930h
48. Min, K. S.; DiPasquale, A. G.; Golen, J. A.; Rheingold, A. L.; Miller, J. S. *J. Am. Chem. Soc.* **2007,** *129,* 2360–2368. doi:10.1021/ja067208q
49. Chiou, Y.-M.; Que, L. *J. Am. Chem. Soc.* **1995,** *117,* 3999–4013. doi:10.1021/ja00119a015
50. Chen, S.; Chen, L.-J.; Yang, H.-B.; Tian, H.; Zhu, W. *J. Am. Chem. Soc.* **2012,** *134,* 13596–13599. doi:10.1021/ja306748k
51. Li, M.; Chen, L.-J.; Cai, Y.; Luo, Q.; Li, W.; Yang, H.-B.; Tian, H.; Zhu, W.-H. *Chem* **2019,** *5,* 634–648. doi:10.1016/j.chempr.2018.12.006
52. Han, M.; Michel, R.; He, B.; Chen, Y.-S.; Stalke, D.; John, M.; Clever, G. H. *Angew. Chem., Int. Ed.* **2013,** *52,* 1319–1323. doi:10.1002/anie.201207373
53. Han, M.; Luo, Y.; Damaschke, B.; Gómez, L.; Ribas, X.; Jose, A.; Peretzki, P.; Seibt, M.; Clever, G. H. *Angew. Chem., Int. Ed.* **2016,** *55,* 445–449. doi:10.1002/anie.201508307

License and Terms

This is an Open Access article under the terms of the Creative Commons Attribution License (http://creativecommons.org/licenses/by/4.0). Please note that the reuse, redistribution and reproduction in particular requires that the authors and source are credited.

The license is subject to the *Beilstein Journal of Organic Chemistry* terms and conditions: (https://www.beilstein-journals.org/bjoc)

The definitive version of this article is the electronic one which can be found at:
doi:10.3762/bjoc.15.235

BEILSTEIN JOURNAL OF ORGANIC CHEMISTRY

Ultrafast processes triggered by one- and two-photon excitation of a photochromic and luminescent hydrazone

Alessandro Iagatti[1], Baihao Shao[2], Alberto Credi[3,4], Barbara Ventura[*4], Ivan Aprahamian[*2] and Mariangela Di Donato[*1,5]

Full Research Paper

Open Access

Address:
[1]LENS – European Laboratory for Non-linear Spectroscopy, via N. Carrara 1, 50019 Sesto Fiorentino (FI), Italy, [2]Department of Chemistry, Dartmouth College, Hanover, New Hampshire 03755, United States, [3]CLAN – Center for Light Activated Nanostructures, Dipartimento di Scienze e Tecnologie Agro-alimentari, Università di Bologna, viale Fanin 50, 40127 Bologna, Italy, [4]Istituto per la Sintesi Organica e la Fotoreattività, Consiglio Nazionale delle Ricerche, via Gobetti 101, 40129 Bologna, Italy and [5]INO – Istituto Nazionale di Ottica, Largo Enrico Fermi 6, 50125 Firenze, Italy

Email:
Barbara Ventura[*] - barbara.ventura@isof.cnr.it; Ivan Aprahamian[*] - ivan.aprahamian@dartmouth.edu; Mariangela Di Donato[*] - didonato@lens.unifi.it

* Corresponding author

Keywords:
hydrazone; molecular switch; pump-probe spectroscopy; time-resolved fluorescence

Beilstein J. Org. Chem. **2019,** *15,* 2438–2446.
doi:10.3762/bjoc.15.236

Received: 26 June 2019
Accepted: 30 September 2019
Published: 15 October 2019

This article is part of the thematic issue "Molecular switches".

Guest Editor: W. Szymanski

© 2019 Iagatti et al.; licensee Beilstein-Institut.
License and terms: see end of document.

Abstract

In this work we apply a combination of steady state and time resolved luminescence and absorption spectroscopies to investigate the excited-state dynamics of a recently developed molecular photoswitch, belonging to the hydrazone family. The outstanding properties of this molecule, involving fluorescence toggling, bistability, high isomerization quantum yield and non-negligible two-photon absorption cross section, make it very promising for numerous applications. Here we show that the light induced *Z*/*E* isomerization occurs on a fast <1 ps timescale in both toluene and acetonitrile, while the excited state lifetime of the *Z*-form depends on solvent polarity, suggesting a partial charge transfer nature of its low lying excited state. Time-resolved luminescence measurements evidence the presence of a main emission component in the 500–520 nm spectral range, attributed to the *Z*-isomer, and a very short living blue-shifted emission, attributed to the *E*-isomer. Finally, transient absorption measurements performed upon far-red excitation are employed as an alternative method to determine the two-photon absorption cross-section of the molecule.

Introduction

Molecular switches are systems that are able to rapidly respond to an external stimulus, which can be of chemical or physical nature, through a variation of their conformational, chemical or physical properties [1]. The possibility to control their operation in a direct and specific manner paves the way for applications in many different fields, involving the production of

responsive materials and surfaces [2,3], energy conversion [4-6], catalysis [7], drug delivery [8,9], design of molecular machines [10-13], super resolution microscopy [14,15], together with biological applications, among which photopharmacology is currently gaining increasing attention [16-19].

Photochromic molecules, which respond to light as an external stimulus, raise particular interest among the different classes of switches which have been developed to date. Light enables very specific spatial and temporal control of the switching event, allowing for selective response and bidirectional operation. It is thus not surprising that different classes of photoswitches have been developed and successfully employed in many technological fields [20-23]. Among others, azobenzenes [24], spiropyranes [25], diarylethenes [26] and their derivatives have been intensively applied. Despite the numerous successful applications of several synthetized switches, some drawbacks still remain, calling for the development of new systems with improved behavior. Although the properties of a successful photoswitch have to be tailored on the application for which it is designed, there are several aspects whose improvement can be of benefit on a general basis. Major concerns on a widespread use of the most commonly employed systems have indeed often be related to low quantum yields or poor photochemical stability, low fatigue resistance, or difficult synthesis. Furthermore, in the specific case of biological applications, inappropriate absorption wavelength is often an issue, considering that most of the commonly used switches absorb in the UV spectral window, as well as low solubility in water.

Among the variety of newly developed systems, a promising class of switches is based on the hydrazone molecular motif [27]. These systems present a variety of interesting properties: they can be chemically or photochemically controlled, can undergo a configurational change by acid or base addition and have interconversion timescales which can span over several orders of magnitude. Furthermore, a substantial shift of their absorption profile can be enabled through substitution patterns, yielding systems that absorb in the red part of the visible spectrum [28].

Recently, a new hydrazone-based photochromic compound, exhibiting outstanding properties, has been synthetized and characterized [29]. This molecule presents fluorescence ON/OFF switching under both one-photon and two-photon excitation (i.e., near infrared (NIR) light), which is also maintained in serum and solid state, has a very high photochemical stability and excellent fatigue resistance. Although the main photochemical properties of this molecule have been recently reported [29], a detailed analysis of its photoswitching mechanism, aimed at characterizing the timescale of the photoinduced structure variation and the solvent dependence of its fluorescence properties, is still lacking. Here we present a spectroscopic characterization of this hydrazone species, using both steady state and time resolved absorption and fluorescence techniques with the aim of better characterizing the actinic step of its operation. Furthermore, we employ time resolved spectroscopy to evaluate the two-photon absorption cross section of the molecule and, by comparing the results with those previously obtained using a fluorescence method, we show that this can be a successful alternative to evaluate two-photon properties, particularly useful in case of non-fluorescent molecules.

Results and Discussion

Spectroscopic properties

The UV–vis absorption spectrum of hydrazone **1** shows an intense absorption band peaked at 395 nm in toluene, as shown in Figure 1. Irradiation of a solution of **1** using 442 nm light induces a *Z/E* isomerization resulting in a color change, evidenced by the decrease of the absorption at 395 nm and the appearance of a new band with a maximum at 343 nm.

The *E*-form is extremely stable (half-life of 75 years in toluene at room temperature) and can be reverted to the *Z*-form by irradiation at 340 nm or heat. The molecule also presents peculiar fluorescence properties. Indeed, while the *Z*-form has an intense emission band peaked at 525 nm in toluene, fluorescence is suppressed for the *E*-form (Figure 1). The maximum of the fluorescence band and the emission quantum yield depend on the solvent, with the emission strongly quenched in protic media [29].

Time-resolved fluorescence

Detailed analysis of the fluorescence features of the two forms in toluene has been performed by time-resolved luminescence measurements in the picosecond time regime (see Materials and Methods for details).

Upon excitation of **1** in the *Z* form at 400 nm, the fluorescence is characterized by a mono-exponential decay on the whole emission spectral range, with an average lifetime of 173 ps (Figure 2, bottom). It can be pointed out that the fluorescence intensity gradually decreases during the measurement, because of the photoisomerisation process, but the use of a low laser power (0.8 μJ/pulse) and the acquisition of a large number of frames (10000) in photon counting mode allowed the characterization of the emission properties of this form. The obtained lifetime value is in accordance with the excited state lifetime previously measured for the *Z*-isomer [29].

After complete *Z/E* isomerization, obtained by irradiating the solution at 440 nm, the time-resolved luminescence of the

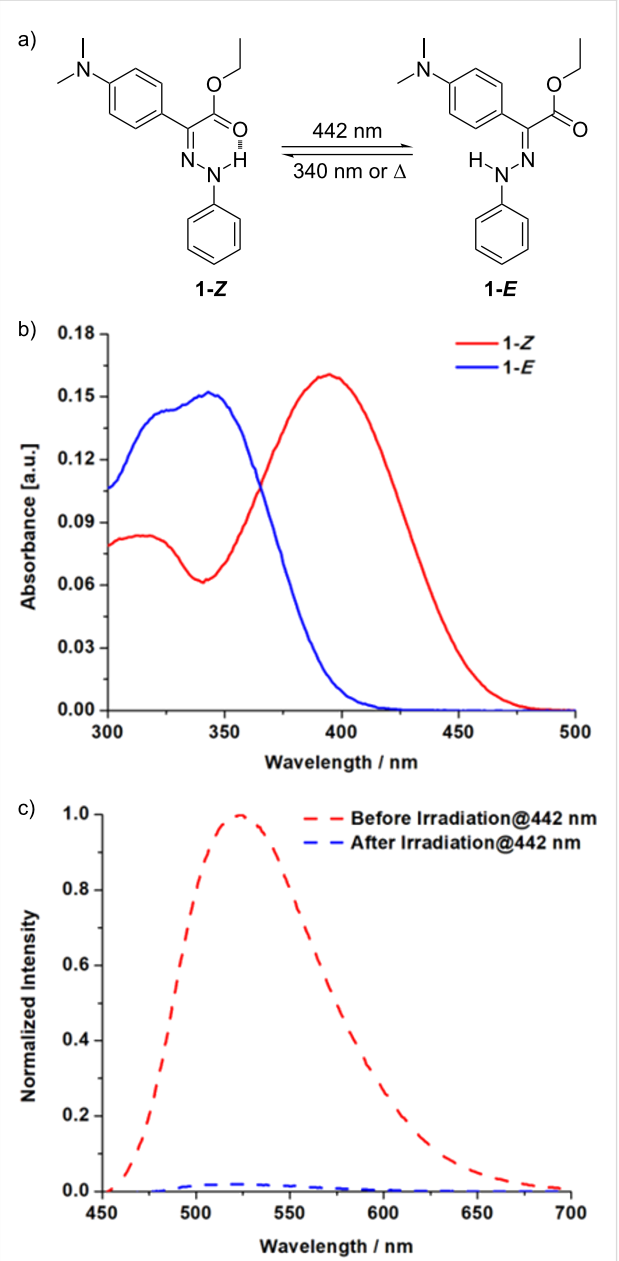


Figure 1: a) The photoinduced *Z*/*E* isomerization of hydrazone **1**, and accompanied changes in b) UV–vis absorption (1×10^{-5} M; toluene) and c) fluorescence emission spectra (1×10^{-6} M; toluene) before (red) and after (blue) irradiation at 442 nm.

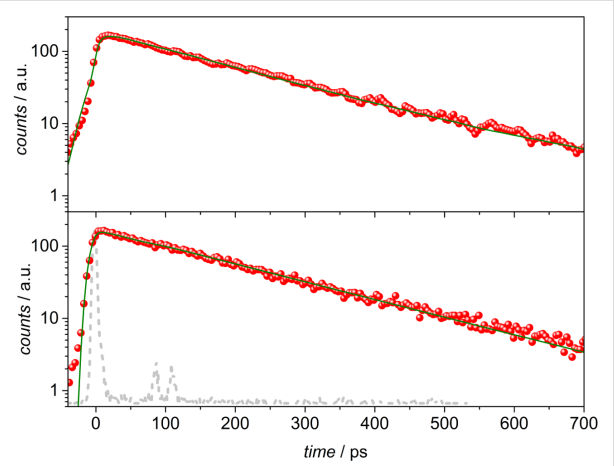


Figure 2: Fluorescence decays (dots) in the 500–520 nm spectral region (emission range of the *Z*-isomer) for **1** in toluene upon excitation of the *E*-form at 350 nm (top; induced *Z*-emission), and upon excitation of the *Z*-form at 400 nm (bottom). The mono-exponential fittings are reported as full lines. The excitation profile is shown in dashed light grey.

E-form was analyzed upon excitation at 350 nm. The spectral distribution of the excited-state decays reveals the presence of a short component in the blue region of the spectrum (440–460 nm) which is not present in the remaining emission region (500–600 nm). A weak emission in this region is also observed in the steady-state fluorescence spectra obtained upon excitation, below 390 nm, of an *E*-rich acetonitrile solution of **1**, which might be attributed to the emission of this isomer as the more intense band at 570 nm originates from the *Z*-form (Figure S1, Supporting Information File 1). Figure 3 shows the comparison between the luminescence decays collected in the 440–460 nm range (blue dots) and in the 500–520 nm range (red dots) of the same streak camera image. A double exponential fitting of the profile in the blue region results in a main component with a lifetime of 1.3 ps (at the limit of the detection of the system: 1.0 ps) accounting for 97% of the decay, and a second component with a longer lifetime of ca. 160 ps. The decay in the 500–520 nm region can be fitted by a mono-exponential function yielding a lifetime of 160 ps, close to the value obtained for the fluorescence of the Z-form upon excitation at 400 nm (the comparison on a longer time scale is shown in Figure 2). The short lifetime of 1.3 ps can be ascribed to the fluorescence of the *E*-form, mainly centered in the 440–460 nm region, which accounts for the very low emission quantum yield of this form observed in the steady-state experiment. The emission from the *Z*-form is detected even upon excitation at 350 nm, because of the induced *E*/*Z* photoisomerization process occurring within the experiment.

Finally, the kinetics of the fluorescence decay of the *Z*-isomer has also been determined in acetonitrile, upon excitation at 400 nm, resulting in a lifetime of 479 ps (Figure S2, Supporting Information File 1).

Transient absorption spectroscopy

To get more insights into the isomerization and fluorescence mechanism of **1**, we measured transient absorption spectra of the molecule in different solvents. A fresh solution of the *Z*-form was excited using 400 nm light, and spectra were recorded in a time interval spanning from a few hundred femto-

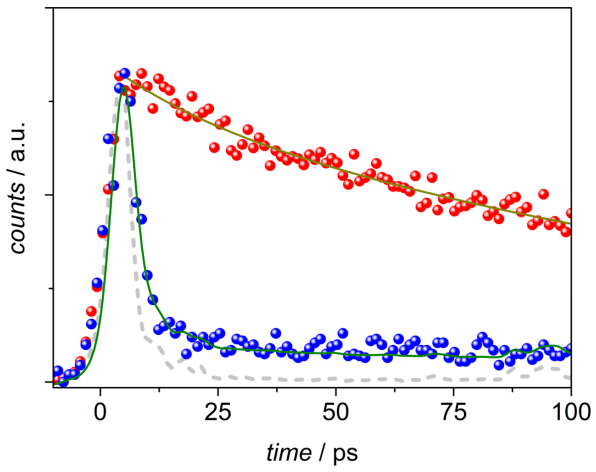


Figure 3: Fluorescence decays (dots) in the 500–520 nm spectral region (red; induced *Z*-emission), and in the 440–460 nm spectral region (blue) for **1** in toluene upon excitation of the *E*-form at 350 nm. The fittings are reported as full lines. The excitation profile is shown in dashed light grey.

seconds up to 1.5 ns. The transient signal recorded for a solution of **1** dissolved in toluene shows the appearance of a negative band peaking at about 400 nm, corresponding to the bleaching of the ground state absorption, an intense very broad positive excited state absorption band peaking at about 600 nm and a less intense positive band in the low wavelength region. A pronounced dip is furthermore observed at ca. 500 nm, most probably because of the superposition of a stimulated emission signal with the broad excited state absorption band, see Figure 4a. The excited state absorption signal increases in intensity and broadens towards the red on a fast timescale. At the same time the stimulated emission band partially recovers, shifting towards the red and a positive band in the lower wavelength region increases in intensity. The rise of a positive signal at <380 nm, where absorption of the *E*-isomer is expected, signals the occurrence of isomerization. This event is also associated to the aforementioned evolution in the visible region, clearly indicating a variation of the excited state electronic distribution. No further band-shape changes are observable at a later timescale, the transient signal almost completely recovers on a ca. 140 ps timescale, which is similar to the fluorescence lifetime of the *Z*-isomer measured in this solvent.

To extract a quantitative kinetic information from the transient absorption data, they have been fitted using a global analysis procedure, which consists in the simultaneous fit of the kinetic traces in the entire probed spectral window with a combination of exponential decay functions [30]. The number of exponential components is determined by performing a preliminary SVD (singular value decomposition) analysis of the kinetic traces matrix [31]. In this case, although three exponential functions could be sufficient to satisfactory fit the data, the addition of a fourth long living component, associated to a small spectral offset remaining on the long timescale, substantially improved the fit. The output of the global analysis retrieves the kinetic constants describing the evolution of the system and the associated spectral components, the so-called EADS (evolution associated difference spectra) which are shown in Figure 4b. As it can be noticed, the evolution occurring on the 0.6 ps timescale, corresponding to the transition from the black to the red EADS, mainly consists in the rise of the positive band at short wavelengths and in a red-shift of both the excited state absorption band and of the stimulated emission band, which also partially recovers on this same timescale. The rise of an absorption band in the region where the *E*-isomer absorbs is indicative of the photoinduced *Z*/*E* isomerization event, which

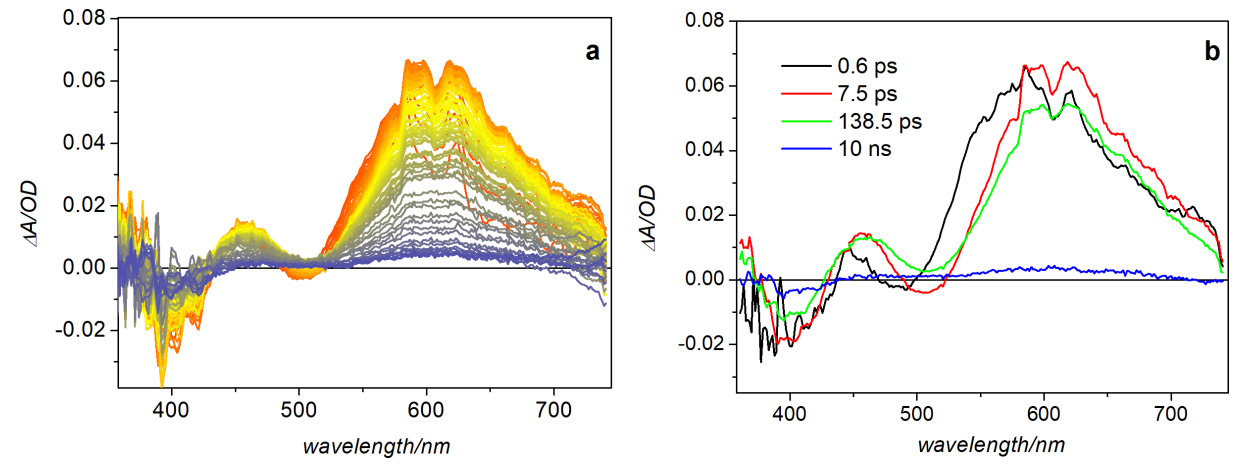


Figure 4: a) Transient absorption data recorded for hydrazone **1** in toluene upon excitation at 400 nm; b) EADS (evolution associated difference spectra) obtained by global fit of the data.

thus results to be an ultrafast process, as observed for other photoswitches – azobenzene in particular [32]. Upon this initial ultrafast evolution, the transient absorption signal intensity slightly decreases on the 7.5 ps timescale, as the result of vibrational relaxation, and mostly recovers on a ca. 140 ps timescale.

Transient absorption measurements upon 400 nm excitation were also performed in acetonitrile and methanol. While the *Z*-form is fluorescent in acetonitrile, the emission is strongly reduced in methanol [29]. The data were analyzed with the same global analysis procedure used for toluene, yielding the EADS shown in Figure 5.

The spectral evolution is very similar in these two solvents, although the time constants obtained by fitting the data are different. Due to lower solubility of the sample in the polar solvents, and increased scattering, data at short wavelengths are quite noisy in these measurements, especially in methanol, where a cutoff filter at 405 nm has been used during the measurement. Similarly, to what observed in toluene, at the short timescale the transient signal is characterized by a negative band peaked at about 400 nm, corresponding to ground state bleaching of the *Z*-form, an intense excited state absorption centered at about 600 nm, and a dip peaked at about 500 nm, as a result of stimulated emission; the latter is also observed in methanol. In acetonitrile, substantial spectral evolution is observed on a 0.5 ps timescale, mainly corresponding to the disappearance of the dip at about 500 nm and an overall blue shift of the positive signal (evolution from black to red EADS in Figure 5a). As previously observed in toluene, such an evolution, also associated to the rise of a positive band at <380 nm, whose observation is precluded due to scattering in polar solvents, reveals the occurrence of *Z*/*E* isomerization, whose kinetics is thus similar in toluene and acetonitrile. In the latter solvent, the signal intensity then decreases on a 50 ps timescale and recovers almost completely in about 500 ps. In methanol, although the spectral evolution is qualitatively similar to that observed in acetonitrile, the kinetics associated with the detected spectral changes differ substantially. The initial evolution, corresponding to the recovery of the dip at 500 nm and the decrease in intensity of the excited state absorption band centered around 600 nm, occurs on a longer timescale – about 1.8 ps, as compared to the sub-ps timescale observed both in acetonitrile and toluene. A blue shift of the excited state absorption band is then observed on a 10 ps timescale, and the almost complete recovery of the transient signal occurs in 34 ps. The very short excited state lifetime observed in methanol agrees with the low fluorescence in this solvent. Possibly, in the protic solvent the molecule adopts a less planar conformation, because of the competition between the intramolecular hydrogen bond between the N–H and C=O groups in the *Z*-form and hydrogen bonds formed by these functional groups with solvent molecules. The conformational distortion and the increased conformational disorder arising from hydrogen bonding with the solvent can be responsible for the fluorescence quenching in the *Z*-form. A comparison of the kinetic traces recorded on the maximum of the excited state absorption band in the three analyzed solvents (Figure 6) demonstrates that the excited state decay time decreases on going from acetonitrile to toluene, and further decreases in methanol. As shown in Supporting Information File 1 (Figure S3) the bleaching recovery of the not isomerized population fraction follows the same kinetics. The observed solvent dependence of the ESA decay could indicate that the excited state of the *Z*-form has a partial charge transfer nature, so that it can be stabilized in polar media where its lifetime slightly increases. In the protic solvent, however, where the molecule can adopt a partially twisted conformation, the increased conformational disorder most probably activates differ-

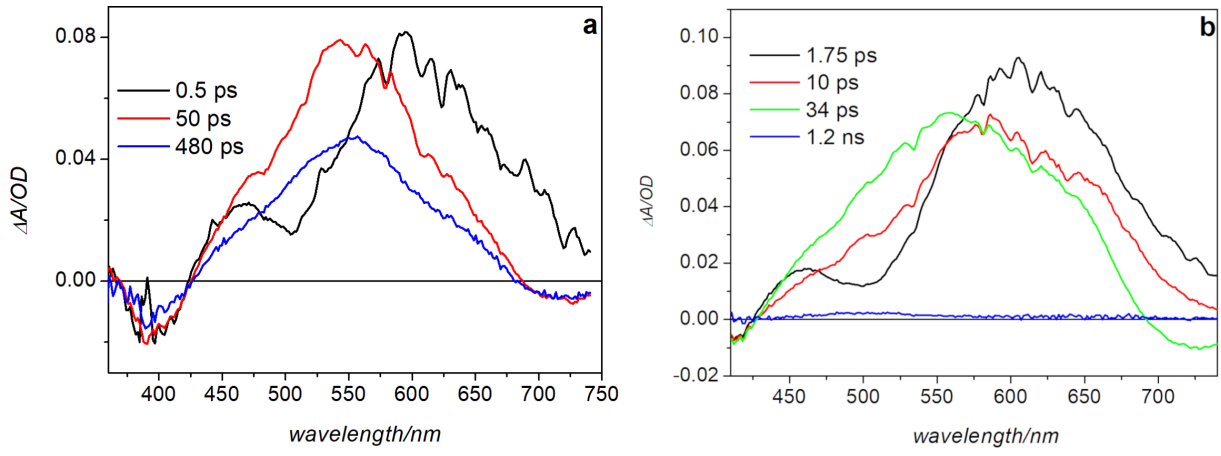


Figure 5: EADS obtained by global fit of the transient data recorded in a) acetonitrile and b) methanol upon excitation at 400 nm.

ent non-radiative decay channels, shortening the excited state lifetime.

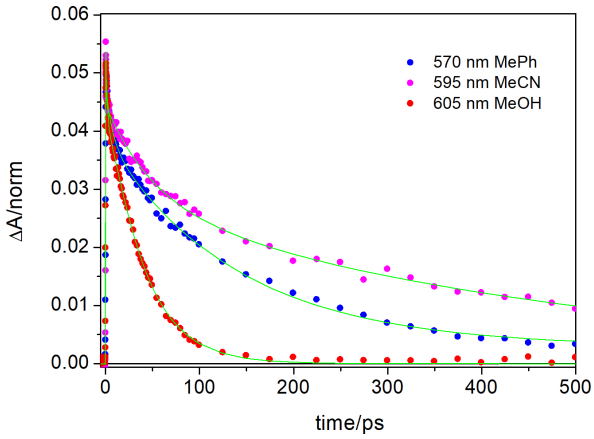


Figure 6: Kinetic traces recorded at the maximum of the excited state absorption band in toluene, acetonitrile and methanol.

Two-photon excitation

Earlier experiments revealed that hydrazone **1** is able to isomerize also upon two-photon excitation [29]. In the present study we used transient absorption spectroscopy as an alternative method to determine the two-photon absorption cross section of the molecule, and compared the results with those previously obtained by exploiting the two-photon fluorescence of the system [29]. The transient spectra registered in toluene upon two-photon excitation, using a pump pulse at a 785 nm (Figure 7a), are qualitatively similar to those obtained upon 400 nm excitation (Figure 4), although the spectral region accessible to the probe is narrower than in the latter case. The bleaching signal is in fact covered as a consequence of the higher sample concentration needed to obtain a transient signal of sufficiently high intensity in order to get a good signal-to-noise ratio. Furthermore, the long wavelength region is strongly affected by the scattering of the excitation light, because of the quite intense pump pulse used for the experiment.

The comparison of the kinetic traces recorded at the maximum of the excited state absorption band upon one-photon and two-photon excitation, reported in Figure 7b, shows that the excited state evolution is similar in the two excitation conditions. A noticeable difference, however, is observed at short delay times after excitation, with a fast decay phase taking place for excitation at 785 nm. Nevertheless, the overall similarity of the successive evolution and of the transient spectra detected in the two cases indicates that a similar reactivity is induced upon one-photon and two-photon excitation, further confirming the two-photon photoswitching ability of hydrazone **1** already inferred by previous measurements [29].

Using a suitable standard, the transient absorption data recorded upon excitation at 785 nm allow for the determination of the two-photon absorption cross section, using the following expression [33]:

$$\delta_2 = \delta_1 \left(\frac{\Delta A_2}{\Delta A_1} \right) \frac{(\sigma_1^{ex} - \sigma_1^{gr})}{(\sigma_2^{ex} - \sigma_2^{gr})} \frac{c_1}{c_2} \qquad (1)$$

In this equation, index 1 and 2 refer respectively to the standard and the sample; ΔA is the absorbance at the maximum of the transient signal measured upon two-photon excitation, $(\sigma_1^{ex} - \sigma_1^{gr})$ is the difference in the absorption coefficient between the excited and ground state, which is retrieved by the one-photon transient absorption measurement, and c is the concentration of the sample. Taking a solution of coumarin 153

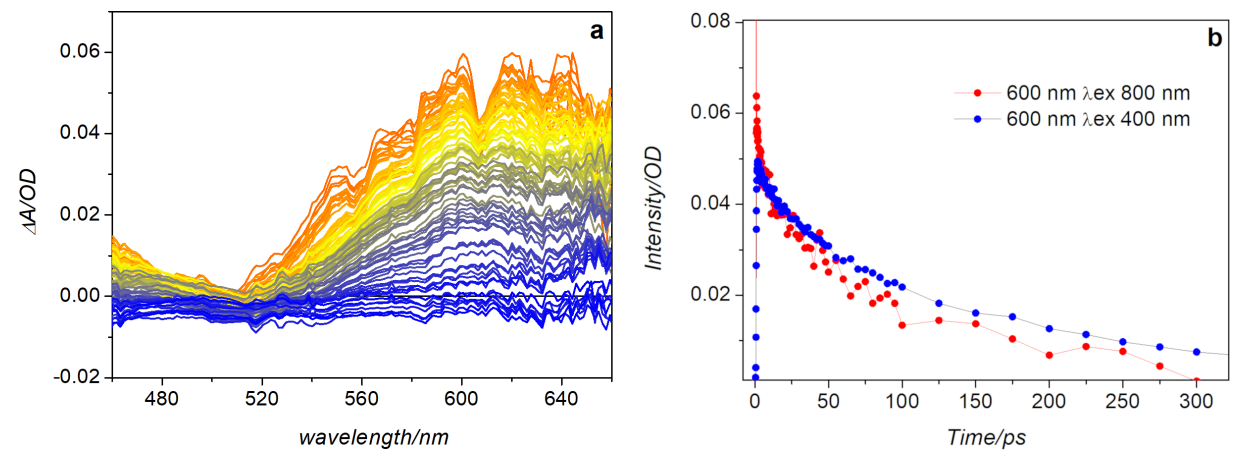


Figure 7: a) Transient absorption spectra measured for hydrazone **1** in toluene upon excitation at 785 nm. b) Comparison of the kinetic traces registered at 600 nm upon excitation at 400 nm and 785 nm.

(δ_1 = 47.4 GM [34]) as a reference, for which transient absorption spectra have been measured upon excitation at both 400 nm and 785 nm (see Figure S4, Supporting Information File 1), the estimated value for **1** in toluene is 12.6 GM, a value in good agreement with that previously determined through two-photon fluorescence measurements [29].

Conclusion

Hydrazones are a promising new class of molecular photoswitches. In this work we investigated the spectroscopic properties of hydrazone **1**, a member of this family showing very interesting properties, such as high-isomerization quantum yield, fluorescence toggling and two-photon induced switching. Using a combination of time-resolved fluorescence and transient absorption spectroscopies we were able to gain new insights into the isomerization process of this molecule. Time-resolved luminescence measurements allowed us to determine the excited state lifetime of the *Z*-form, which strongly emits in the 500–520 nm spectral range. A fast component (1.3 ps in toluene) was also observed at shorter wavelengths and attributed to the *E*-isomer. The very short lifetime of this component accounts for the low emission quantum yield or even the absence of steady-state fluorescence of the *E*-isomers in most solvents. Transient absorption spectroscopy measurements, repeated in different solvents, allowed us to estimate the timescale of the *Z/E* isomerization process, which is about 0.5 ps in both toluene and acetonitrile, thus showing a negligible dependence on the solvent polarity. On the contrary, the excited state lifetime of the *Z*-isomer depends on the solvent properties and is especially short in MeOH, suggesting that the excited state of the molecule could have a partial charge transfer nature. Finally, transient absorption spectroscopy was employed as an alternative method to estimate the two-photon absorption cross section of hydrazone **1**, resulting in a value that is in very good agreement with the previous determination of this property, performed on the basis of fluorescence measurements [29].

Materials and Methods

Hydrazone **1** was synthesized by following a previously reported procedure [29]. Its UV–vis spectra were recorded on a Shimadzu UV-1800 UV–vis spectrophotometer. A Photon Technology International QuantaMaster 4 spectrofluorometer outfitted with a LPS-100 lamp power supply and Xenon arc lamp housing, ASOC-10 electronics interface, MD-4 motor driver control, and a model 914D photomultiplier detector system were used to collect the fluorescence spectra of **1**.

Time-resolved luminescence

Spectroscopic grade toluene from Merck was used as received. Solutions of **1** (4×10^{-5} M) in toluene were freshly prepared. Time-resolved and spectral analysis of the fluorescence of the compound in the picosecond time regime were performed by means of a Hamamatsu synchroscan streak-camera apparatus (C10910-05 main unit and M10911-01 synchroscan unit) equipped with an ORCA-Flash 4.0 V2 charge-coupled device (CCD) and an Acton spectrograph SP2358. As excitation source a Newport Spectra Physics Solstice-F-1K-230 V laser system, combined with a TOPAS Prime (TPR-TOPAS-F) optical parametric amplifier (pulse width: 100 fs, 1 kHz repetition rate) [35] was used, tuned at 400 nm and 350 nm for predominant excitation of the *Z* and *E*-forms of **1**, respectively. To reduce photodegradation and limit the photoisomerization processes, the pump energy on the sample was reduced to 0.8 μJ/pulse at 400 nm and 4 μJ/pulse at 350 nm. Emission from the sample, collected at right angle with a 1 mm slit, was focused by means of a system of lenses into the spectrograph slit. Streak images were taken both in analog integration (200 exposures, 100 ms exposure time) and in photon counting (1000–10000 exposures, 20–30 ms exposure time). The decays were collected over emission spectral ranges of 20 nm. HPD-TA 9.3 software from Hamamatsu was used for data acquisition and analysis. The overall time resolution of the system after deconvolution procedure is 1 ps.

For fluorescence lifetime measurements in acetonitrile, solutions of **1** (1×10^{-5} M) were used. Fluorescence lifetime was determined by time-correlated single photon-counting (TCSPC) using a Photon Technology International QuantaMaster 4 spectrofluorometer integrated with Deltadiode-375L diode laser (λ_{ex} = 373 nm, <70 ps pulse width) as the excitation source. The fluorescence decays were detected using a fast PPD-850 detector. In all cases, decays were recorded until peak counts reached 10,000. The decay traces were analyzed by the one-exponential fitting method using Felix data analysis from Horiba Scientific Ltd.

Transient absorption spectroscopy

The apparatus used for the transient absorption spectroscopy (TAS) measurements is based on a Ti:sapphire regenerative amplifier (BMI Alpha 1000) system pumped by a Ti:sapphire oscillator (Spectra Physics Tsunami). The system produces 100 fs pulses at 785 nm, 1 kHz repetition rate and average power of 450–500 mW. Excitation pulses at 400 nm have been obtained by second harmonic generation of the fundamental laser output. In case of two-photon excitation the fundamental beam at 785 nm has been directly employed as the pump. The pump beam polarization has been set to magic angle with respect to the probe beam by rotating a λ/2 plate. Excitation powers were on the order of 50–100 nJ for one-photon excitation and 1.7 μJ in case of two-photon excitation. The probe pulse was generated by focusing a small portion of the funda-

mental laser output radiation on a 2 mm thick calcium fluoride window. Pump-probe delays were introduced by sending the probe beam through a motorized stage. Multichannel detection was achieved by sending the white light continuum after passing through the sample to a flat field monochromator coupled to a home-made CCD detector. TAS measurements were carried out in a quartz cell (2 mm thick) mounted on a movable stage to avoid sample photodegradation and multiple photon excitation. The recorded kinetic traces and transient spectra have been analyzed by using a global analysis [30]. The number of kinetic components has been estimated by performing a preliminary singular values decomposition (SVD) analysis [31], global analysis was performed using the GLOTARAN package (http://glotaran.org) [36], and employing a linear unidirectional "sequential" model.

Supporting Information

Supporting Information File 1

Additional spectra.
[https://www.beilstein-journals.org/bjoc/content/supplementary/1860-5397-15-236-S1.pdf]

Acknowledgements

This work was supported by the European Union, through the Horizon 2020 Research and Innovation Program (RIA "Laserlab-Europe", n. 654148 and ERC AdG "Leaps" n. 692981 to A. C.). I. A. acknowledges the generous support of the National Science Foundation (DMR-1506170). Support from Italian CNR (Project 'PHEEL') is also acknowledged.

ORCID® iDs

Alessandro Iagatti - https://orcid.org/0000-0003-3600-0849
Baihao Shao - https://orcid.org/0000-0003-0072-2946
Alberto Credi - https://orcid.org/0000-0003-2546-9801
Barbara Ventura - https://orcid.org/0000-0002-8207-1659
Ivan Aprahamian - https://orcid.org/0000-0003-2399-8208
Mariangela Di Donato - https://orcid.org/0000-0002-6596-7031

Preprint

A non-peer-reviewed version of this article has been previously published as a preprint doi:10.3762/bxiv.2019.48.v1

References

1. Feringa, B. L.; Browne, W. R., Eds. *Molecular Switches;* Wiley-VCH: Weinheim, Germany, 2011. doi:10.1002/9783527634408
2. Klajn, R.; Stoddart, J. F.; Grzybowski, B. A. *Chem. Soc. Rev.* **2010,** *39,* 2203–2237. doi:10.1039/b920377j
3. Pathem, B. K.; Claridge, S. A.; Zheng, Y. B.; Weiss, P. S. *Annu. Rev. Phys. Chem.* **2013,** *64,* 605–630. doi:10.1146/annurev-physchem-040412-110045
4. Gust, D.; Moore, T. A.; Moore, A. L. *Chem. Commun.* **2006,** 1169–1178. doi:10.1039/b514736k
5. Lennartson, A.; Roffey, A.; Moth-Poulsen, K. *Tetrahedron Lett.* **2015,** *56,* 1457–1465. doi:10.1016/j.tetlet.2015.01.187
6. Otsuki, J.; Tsujino, M.; Iizaki, T.; Araki, K.; Seno, M.; Takatera, K.; Watanabe, T. *J. Am. Chem. Soc.* **1997,** *119,* 7895–7896. doi:10.1021/ja970386m
7. Blanco, V.; Leigh, D. A.; Marcos, V. *Chem. Soc. Rev.* **2015,** *44,* 5341–5370. doi:10.1039/c5cs00096c
8. Senthilkumar, T.; Zhou, L.; Gu, Q.; Liu, L.; Lv, F.; Wang, S. *Angew. Chem., Int. Ed.* **2018,** *57,* 13114–13119. doi:10.1002/anie.201807158
9. Yu, J.-J.; Cao, Z.-Q.; Zhang, Q.; Yang, S.; Qu, D.-H.; Tian, H. *Chem. Commun.* **2016,** *52,* 12056–12059. doi:10.1039/c6cc06458b
10. Feringa, B. L. *Angew. Chem., Int. Ed.* **2017,** *56,* 11060–11078. doi:10.1002/anie.201702979
11. Kassem, S.; van Leeuwen, T.; Lubbe, A. S.; Wilson, M. R.; Feringa, B. L.; Leigh, D. A. *Chem. Soc. Rev.* **2017,** *46,* 2592–2621. doi:10.1039/c7cs00245a
12. Sauvage, J.-P. *Angew. Chem., Int. Ed.* **2017,** *56,* 11080–11093. doi:10.1002/anie.201702992
13. Stoddart, J. F. *Angew. Chem., Int. Ed.* **2017,** *56,* 11094–11125. doi:10.1002/anie.201703216
14. Laptenok, S. P.; Gil, A. A.; Hall, C. R.; Lukacs, A.; Iuliano, J. N.; Jones, G. A.; Greetham, G. M.; Donaldson, P.; Miyawaki, A.; Tonge, P. J.; Meech, S. R. *Nat. Chem.* **2018,** *10,* 845–852. doi:10.1038/s41557-018-0073-0
15. Zhang, X.; Zhang, M.; Li, D.; He, W.; Peng, J.; Betzig, E.; Xu, P. *Proc. Natl. Acad. Sci. U. S. A.* **2016,** *113,* 10364–10369. doi:10.1073/pnas.1611038113
16. Hüll, K.; Morstein, J.; Trauner, D. *Chem. Rev.* **2018,** *118,* 10710–10747. doi:10.1021/acs.chemrev.8b00037
17. Broichhagen, J.; Frank, J. A.; Trauner, D. *Acc. Chem. Res.* **2015,** *48,* 1947–1960. doi:10.1021/acs.accounts.5b00129
18. Lerch, M. M.; Hansen, M. J.; van Dam, G. M.; Szymanski, W.; Feringa, B. L. *Angew. Chem., Int. Ed.* **2016,** *55,* 10978–10999. doi:10.1002/anie.201601931
19. Velema, W. A.; Szymanski, W.; Feringa, B. L. *J. Am. Chem. Soc.* **2014,** *136,* 2178–2191. doi:10.1021/ja413063e
20. Bléger, D.; Hecht, S. *Angew. Chem., Int. Ed.* **2015,** *54,* 11338–11349. doi:10.1002/anie.201500628
21. Fihey, A.; Perrier, A.; Browne, W. R.; Jacquemin, D. *Chem. Soc. Rev.* **2015,** *44,* 3719–3759. doi:10.1039/c5cs00137d
22. Szymański, W.; Beierle, J. M.; Kistemaker, H. A. V.; Velema, W. A.; Feringa, B. L. *Chem. Rev.* **2013,** *113,* 6114–6178. doi:10.1021/cr300179f
23. Baroncini, M.; Groppi, J.; Corra, S.; Silvi, S.; Credi, A. *Adv. Opt. Mater.* **2019,** *7,* 1900392. doi:10.1002/adom.201900392
24. Bandara, H. M. D.; Burdette, S. C. *Chem. Soc. Rev.* **2012,** *41,* 1809–1825. doi:10.1039/c1cs15179g
25. Irie, M.; Fukaminato, T.; Matsuda, K.; Kobatake, S. *Chem. Rev.* **2014,** *114,* 12174–12277. doi:10.1021/cr500249p
26. Klajn, R. *Chem. Soc. Rev.* **2014,** *43,* 148–184. doi:10.1039/c3cs60181a
27. Aprahamian, I. *Chem. Commun.* **2017,** *53,* 6674–6684. doi:10.1039/c7cc02879b
28. Yang, Y.; Hughes, R. P.; Aprahamian, I. *J. Am. Chem. Soc.* **2012,** *134,* 15221–15224. doi:10.1021/ja306030d

29. Shao, B.; Baroncini, M.; Qian, H.; Bussotti, L.; Di Donato, M.; Credi, A.; Aprahamian, I. *J. Am. Chem. Soc.* **2018,** *140,* 12323–12327. doi:10.1021/jacs.8b07108
30. van Stokkum, I. H. M.; Larsen, D. S.; van Grondelle, R. *Biochim. Biophys. Acta, Bioenerg.* **2004,** *1657,* 82–104. doi:10.1016/j.bbabio.2004.04.011
31. Henry, E. R.; Hofrichter, J. Singular value decomposition: Application to analysis of experimental data. In *Methods in Enzymology;* Brand, L.; Johnson, M. L., Eds.; Academic Press, 1992; Vol. 210, pp 129–192. doi:10.1016/0076-6879(92)10010-b
32. Schultz, T.; Quenneville, J.; Levine, B.; Toniolo, A.; Martínez, T. J.; Lochbrunner, S.; Schmitt, M.; Shaffer, J. P.; Zgierski, M. Z.; Stolow, A. *J. Am. Chem. Soc.* **2003,** *125,* 8098–8099. doi:10.1021/ja021363x
33. Oulianov, D. A.; Tomov, I. V.; Dvornikov, A. S.; Rentzepis, P. M. *Opt. Commun.* **2001,** *191,* 235–243. doi:10.1016/s0030-4018(01)01121-x
34. Niesner, R.; Roth, W.; Gericke, K.-H. *ChemPhysChem* **2004,** *5,* 678–687. doi:10.1002/cphc.200300881
35. Briš, A.; Trošelj, P.; Margetić, D.; Flamigni, L.; Ventura, B. *ChemPlusChem* **2016,** *81,* 985–994. doi:10.1002/cplu.201600231
36. Snellenburg, J. J.; Laptenok, S. P.; Seger, R.; Mullen, K. M.; van Stokkum, I. H. M. *J. Stat. Software* **2012,** *49*. doi:10.18637/jss.v049.i03

License and Terms

This is an Open Access article under the terms of the Creative Commons Attribution License (http://creativecommons.org/licenses/by/4.0). Please note that the reuse, redistribution and reproduction in particular requires that the authors and source are credited.

The license is subject to the *Beilstein Journal of Organic Chemistry* terms and conditions: (https://www.beilstein-journals.org/bjoc)

The definitive version of this article is the electronic one which can be found at: doi:10.3762/bjoc.15.236

BEILSTEIN JOURNAL OF ORGANIC CHEMISTRY

Experimental and computational electrochemistry of quinazolinespirohexadienone molecular switches – differential electrochromic vs photochromic behavior

Eric W. Webb, Jonathan P. Moerdyk, Kyndra B. Sluiter, Benjamin J. Pollock, Amy L. Speelman, Eugene J. Lynch, William F. Polik and Jason G. Gillmore*

Full Research Paper

Open Access

Address:
Department of Chemistry, Hope College, 35 East 12th Street, Holland, MI 49422-9000, USA

Email:
Jason G. Gillmore* - gillmore@hope.edu

* Corresponding author

Keywords:
cyclic voltammetry; density functional theory; heterocycles; molecular switches; photochromic photooxidants; spirocycles

Beilstein J. Org. Chem. **2019,** *15,* 2473–2485.
doi:10.3762/bjoc.15.240

Received: 03 July 2019
Accepted: 10 October 2019
Published: 18 October 2019

This article is part of the thematic issue "Molecular switches".

Guest Editor: W. Szymanski

© 2019 Webb et al.; licensee Beilstein-Institut.
License and terms: see end of document.

Abstract

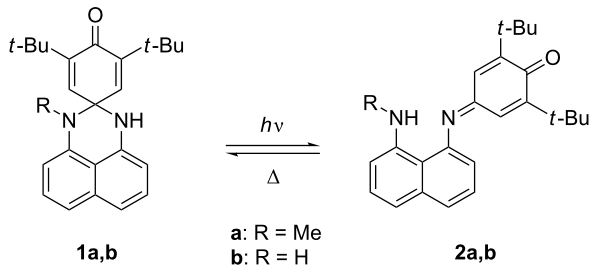
Our undergraduate research group has long focused on the preparation and investigation of electron-deficient analogs of the perimidinespirohexadienone (PSHD) family of photochromic molecular switches for potential application as "photochromic photooxidants" for gating sensitivity to photoinduced charge transfer. We previously reported the photochemistry of two closely related and more reducible quinazolinespirohexadienones (QSHDs), wherein the naphthalene of the PSHD is replaced with a quinoline. In the present work, we report our investigation of the electrochemistry of these asymmetric QSHDs. In addition to the short wavelength and photochromic long-wavelength isomers, we have found that a second, distinct long-wavelength isomer is produced electrochemically. This different long-wavelength isomer arises from a difference in the regiochemistry of spirocyclic ring-opening. The structures of both long-wavelength isomers were ascertained by cyclic voltammetry and ^{1}H NMR analyses, in concert with computational modeling. These results are compared to those for the symmetric parent PSHD, which due to symmetry possesses only a single possible regioisomer upon either electrochemical or photochemical ring-opening. Density functional theory calculations of bond lengths, bond orders, and molecular orbitals allow the rationalization of this differential photochromic vs electrochromic behavior of the QSHDs.

Introduction

Photochromic molecular switches, in which light initiates reversible coloration of a short-wavelength isomer (SW) to a long-wavelength isomer (LW), which fades back to SW either thermally or photochemically, have become ubiquitous in a wide range of applications [1-5]. Typically, organic photochromism results from a spirocyclic ring-opening or other isomeri-

zation which results in increased conjugation. Electrochromism is also of increasing materials relevance, e.g., for self-dimming automotive mirror and aircraft window darkening applications [6-8]. In electrochromic applications, the color change is generally due to a change in the oxidation state of a conjugated system. This change in the oxidation state is most often concomitant with conformational and orbital occupancy changes, rather than any σ-bond-forming or breaking processes. The viologens are perhaps the most ubiquitous example of small molecule organic electrochromism [6,7,9].

One example that combines photochromic and electrochromic behavior (the latter of an unusual sort) is the class of perimidinespirohexadienones **1** (PSHDs) whose synthesis, electrochemistry and UV–vis spectroscopy were reported by Minkin and co-workers [10] for **1a** (Scheme 1). Electrochemically, they report observing a single, two-electron reduction peak and two distinct one-electron oxidation peaks upon scanning using cyclic voltammetry. They therefore proposed [10] that the electrolysis of **1a** proceeds by an "ECE" (electrochemical-chemical-electrochemical) mechanism (**1a** → $\mathbf{1a}^{\bullet-}$ → $\mathbf{2a}^{\bullet-}$ → $\mathbf{2a}^{2-}$ → $\mathbf{2a}^{\bullet-}$ → **2a**) in which the dienone portion of the molecule accepted the first electron, followed by a radical anion rearrangement to the long-wavelength isomer, whose radical anion is so much easier to reduce that it immediately accepts a second electron at this potential; on the oxidative return wave the subsequent oxidations of the LW dianion to its radical anion and then its neutral state are observed. Thus, in this unusual system, electrochromism proceeds by the same sort of spirocyclic ring-opening as the photochromic rearrangement but occurs from the radical anion rather than a photoexcited state. The reduction of the molecular switch necessary for electrochromism is in a sense catalytic: the rearranged product is reoxidized to a neutral LW isomer, which reverts thermally to SW upon standing, just as it does when the LW is generated photochemically.



Scheme 1: PSHD photochromism [10].

The PSHD system was of interest to us as a potential photochromic photooxidant that would add an additional level of gating to photoinduced charge transfer (PICT) initiated processes (Figure 1). PSHDs were promising for this, as their photochromic reversion of LW back to SW proceeds purely thermally, leaving the long-wavelength absorption available for bimolecular PICT. Moreover, the LW is sufficiently more reducible that, even accounting for its lower excitation energy, the LW excited state, LW*, is more reducible than SW*, making LW the more potent photooxidant of the two. However, for practical use as photooxidants, the difference in the reduction potential between LW and SW would need to be increased further, and LW would need to be more reducible to be of use in photooxidation of relevant substrates (e.g., Dewar benzenes, quadricyclanes, or bishomocubanes as quantum amplified isomerization substrates [11-15], or vinylcarbazole or alkoxystyrene derivatives for radical cation cylcloaddition and polymerization reactions [16-20]). We thus proposed the replacement of the naphthalene in **1a** with a more electron-deficient quinoline ring. Due to the saturated spirocyclic carbon insulating the dienone electrophore from the quinoline moiety in the SW form, we expected minimal change in the SW reduction potential relative to the PSHDs, but a significant difference for the completely conjugated LW isomer(s). Previously we reported the detailed synthesis of two novel quinazolinespirohexadienone (QSHD) photochromes **3a**,**b** (Scheme 2) and their photochemical properties as well as a proof of structure for the photochemically generated long-wavelength isomer (pLW) **4a**,**b** (not **5a**,**b**) [21]. Herein, we report the electrochemistry of these QSHDs.

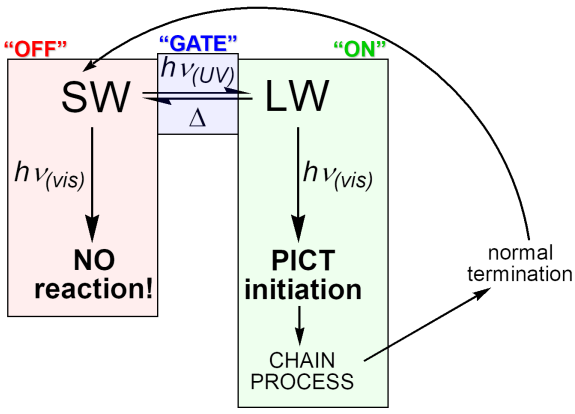
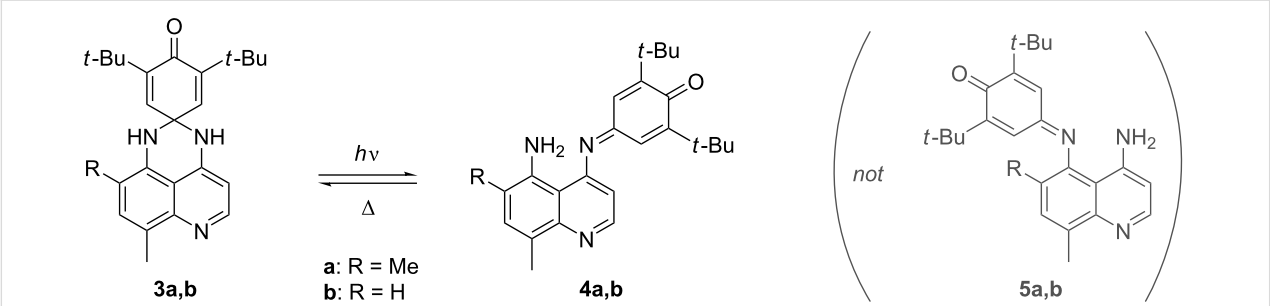


Figure 1: Proposed gating of sensitivity to photoinduced charge transfer by a photochromic photooxidant in which only LW is a competent photooxidant of the donor of interest.

Results and Discussion

Electrochemical analysis

When we replicated cyclic voltammetry (CV) experiments on PSHDs, we observed similar voltammograms for both **1a** and **1b** (Figure 2), consistent with the two-electron reduction and two one-electron oxidation processes reported by Minkin for **1a**



Scheme 2: QSHD photochromism [21].

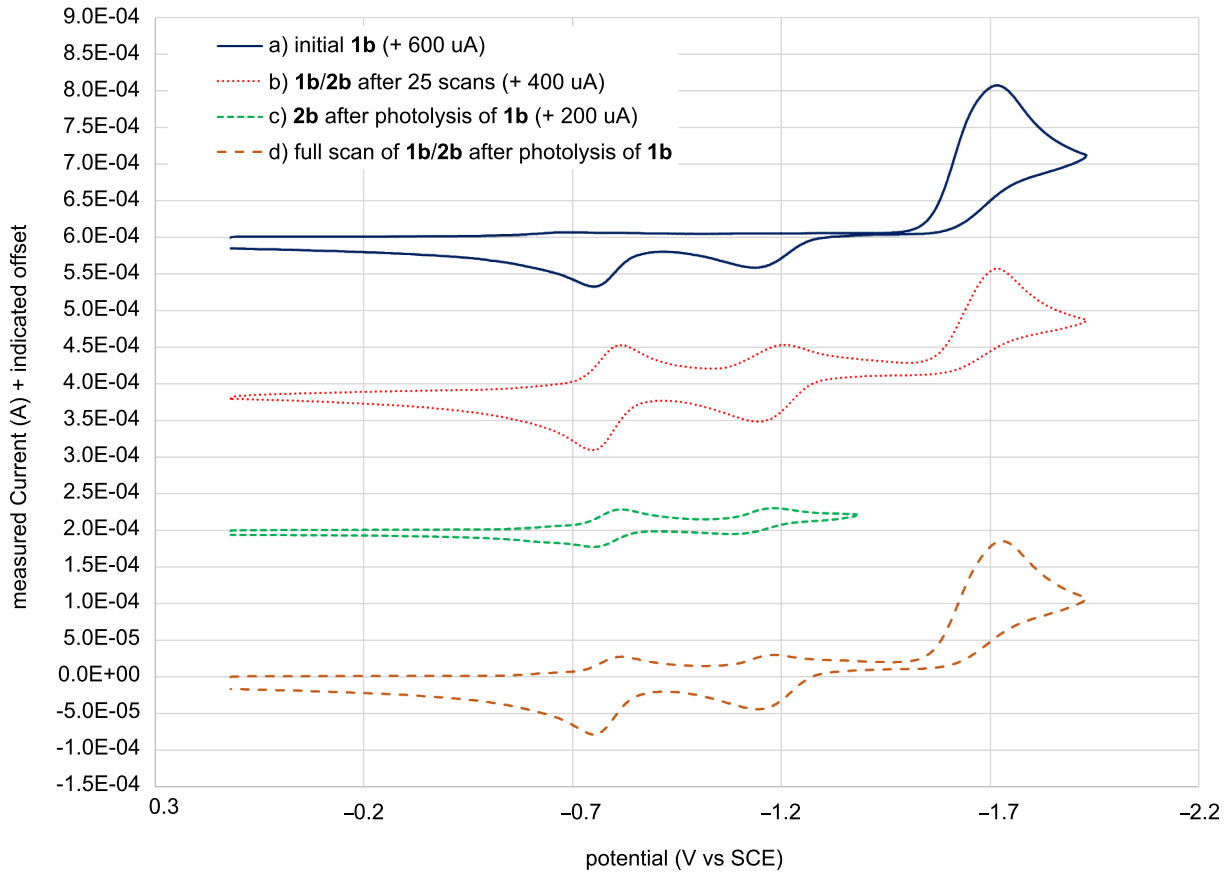


Figure 2: Cyclic voltammograms of a) **1b** before irradiation or electrolysis (solid blue), b) **1b**/**2b** after 25 scans (dotted red), c) **1b**/**2b** upon photolysis of **1b** (dashed green) scanned over a narrower potential window so as not to reduce **1b**, and d) **1b**/**2b** scanning the full potential window after photolysis of **1b** (dashed orange).

[10]. As expected, a growth of two reversible one-electron reduction–oxidation peaks was observed upon multiple scans, representing the reduction and oxidation of the electrogenerated long-wavelength form **1b** generated in situ. As expected, either photolysis or multiple CV scans led to the same LW reduction and oxidation peaks (within the error bars indicated in Table 1). We also report an identical E^{o}_{red} of **2a** as Minkin [10], though a 140 mV difference was found in the E^{o}_{red} of **1a**, which can be attributed at least in part to our use of half-peak potentials for all irreversible peaks, while Minkin reported peak potentials (our peak potentials were within 60 mV of Minkin's value). We found the parent compound **1b**, whose electrochemistry was not previously reported by Minkin, to be 50 mV less reducible than **1a** (−1.68 V vs −1.63 V for **1a**), in qualitative agreement with our computational predictions [22]. Similarly, **2b** differed from **2a** by only 20 mV (Table 1) where computa-

Table 1: Experimental and computational E^{o}_{red} of **1a**,**b** and **3a**,**b** and their LW isomers, reported in V vs SCE.

		Electrochemical			Photochemical	
Compd.	Type	E^{o}_{red} (SW)[a]	E^{o}_{red} (eLW$^{\cdot-}$)	E^{o}_{red} (eLW)	E^{o}_{red} (pLW$^{\cdot-}$)	E^{o}_{red} (pLW)
1a	literature[b]	−1.77	−1.325	−0.85		
	exptl.[c]	−1.628 ± 0.031	−1.220 ± 0.049	−0.857 ± 0.010		
	predicted[d]	*−1.56*		*−0.89*		*−0.89*
1b	exptl[c]	−1.681 ± 0.013	−1.202 ± 0.032	−0.871 ± 0.013	−1.170 ± 0.060	−0.865 ± 0.005
	predicted[d]	*−1.70*		*−0.90*		*−0.90*
3a	exptl[c]	−1.632 ± 0.030	−1.26 ± 0.11	−0.866 ± 0.009	−1.029 ± 0.035	−0.730 ± 0.005
	predicted[d]	*−1.61*		*−0.88*		*−0.72*
3b	exptl[c]	−1.631 ± 0.017	−1.069[ad] ± 0.029	−0.843 ± 0.012	−1.008 ± 0.024	−0.729 ± 0.004
	predicted[d]	*−1.63*		*−0.86*		*−0.72*

[a]Irreversible peak. E^{o}_{red} is reported as the half-peak potential $E^{p/2}_{red}$ (except in literature value for **1a**). [b]Reference [10]. Irreversible SW peak reported as peak potential (E^{p}_{red}), not half-peak potential ($E^{p/2}_{red}$). [c]Experimental values in CH_3CN containing 0.1 M Bu_4NPF_6, standardized vs ferrocene/ferrocenium and corrected to vs SCE as in reference [23]; error bars = one standard deviation from the mean of at least 7 replicates. [d]Computational E^{o}_{red} predicted using correlation 6 in reference [22] based on the energies of the corresponding ground-state and one-electron-reduced species computed using B3LYP/6-31G(d) with implicit acetonitrile solvent using the CPCM solvent model with UAKS radii, on geometries optimized in the gas-phase; predictions of second reduction potentials are not possible by this method.

tions predicted a minimal difference. The electrogeneration of **2b** through repeated potential step bulk electrolysis of **1b** in acetonitrile-d_3 yielded a sufficient quantity of LW to obtain a ^{1}H NMR spectrum, which revealed identical chemical shifts as those for the photogenerated **2b**. First and second reduction potentials were also the same, within error limits, for photogenerated and electrogenerated **2b**, as would be expected. This is consistent with the excellent overlap of all four voltammograms in Figure 2.

The ECE mechanism reported by Minkin for the electrochromism was further supported by bulk electrochemical experiments. With repetitive conditioning and scanning under argon-deaerated conditions, the initially yellow **1b** solution turned to an orange-red color, which we hypothesized to be the LW dianion, **2b**$^{2-}$. Upon exposure to air this solution immediately turned green, the known color of the LW isomer **2b**. The addition of benzoquinone (a chemical oxidant) to the electrochemically reduced solution under argon gave similar results, consistent with our hypothesis. When the yellow solution remained open to the atmosphere during electrolysis, the initially yellow solution turned green at first (presumably while air oxidation of **2b**$^{2-}$ to **2b** could keep up with electrochemical reduction). With further electrolysis even these solutions turned to the orange-red color observed for the deaerated solutions. The solutions did become green upon prolonged exposure to air. This behavior seems indicative of insufficient transport of air into the cell through the small vents in the cell cap to replace the oxygen being consumed during repeated electrolytic scans. Similar results were observed for solutions of **3b** suggesting a similar ECE mechanism to that of **1a** is likely also occurring for **3b**.

Cyclic voltammetric analysis of quinazolinespirohexadienone (QSHD) **3b** (Figure 3) was qualitatively similar to the parent PSHDs **1a**,**b** as expected based on structural similarity and computationally calculated molecular orbital diagrams (Figure 6 and Supporting Information File 1). Surprisingly, the E^{o}_{red} of the electrochemically generated LW form of **3a** was more negative by 10 mV than that of **2a**, even with the more electron-deficient quinoline ring. Presumably this is because the 5-position on the benzene ring of the quinoline, is the least withdrawing point of attachment, and the inductive withdrawing properties of the quinoline nitrogen are far enough removed from the electrophore to not cause any appreciable change in reduction potential. The other qualitative difference for **3b** was the presence of two LW reduction peaks (LW → LW$^{\bullet-}$ → LW^{2-}) on the first scan (Figure 3a, dotted red). However, the observation of the two LW reduction peaks was consistent with UV–vis spectroscopy that indicated a significant amount of a LW isomer upon solvation, and repetitive electrochemical scans exhibited the anticipated growth of the LW reduction–oxidation peaks as more of the LW isomer was generated electrochemically (Figure 3b, solid blue).

Most surprisingly, when **3b** was photolyzed to form **4b** in solution under similar conditions to our previous report [21] and then analyzed electrochemically (Figure 3c and d, dashed green and orange), four reduction (and oxidation) peaks in the region of the LW isomer were observed. Two reduction–oxidation

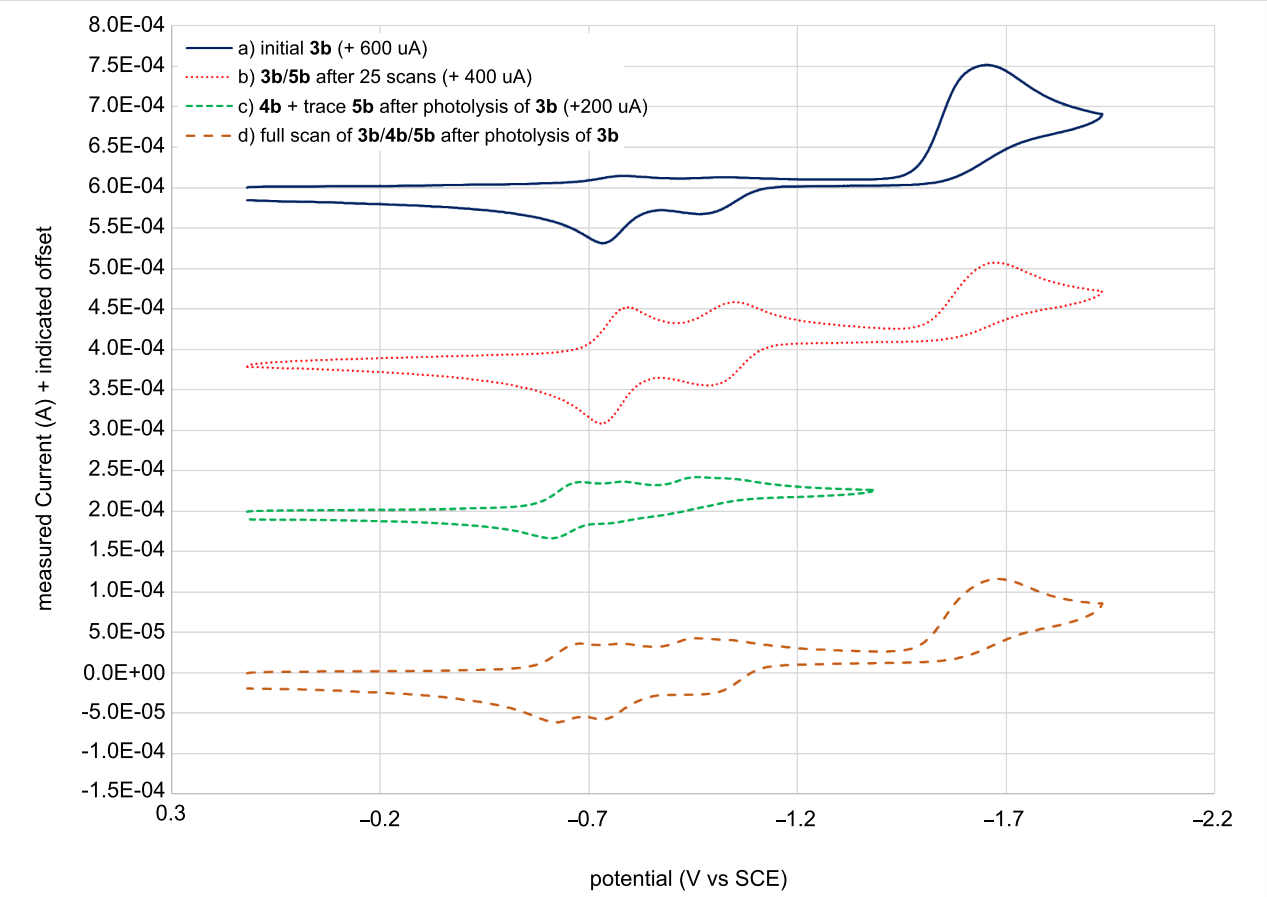


Figure 3: Cyclic voltammograms of a) **3b** (with trace **5b**) before irradiation or electrolysis (solid blue), b) **3b** + **5b** after 25 scans (dotted red) showing the growth of the two **5b** reduction peaks, c) **3b** (with trace **5b**) after photolyzing but without reducing **3b** in the electrolysis (dashed green) which shows the two initial eLW **5b** and two new pLW **4b** reversible redox waves observed, and d) **3b** + **4b** + **5b** observed by scanning the full potential window after the photolysis of **3b** (dashed orange).

couples matched the potential of the electrogenerated LW form observed earlier while the other two peaks were shifted more positive by 60–110 mV indicating the presence of a third electroactive species in addition to **3b** and photogenerated **4b**. Given the asymmetric nature of **3b**, two distinct options for spirocyclic ring-opening exist, leading to **4b** or **5b**. Thus, we postulated that the electrogenerated LW form was in fact **5b**.

Having found two distinct LW forms depending on generation by photolysis or electrolysis of SW **3b**, we turned our attention to whether a similar phenomenon was observed for **3a**. Indeed, different redox peaks were observed in the same general LW region for the CV of photolyzed versus electrogenerated LW forms of **3a**, consistent with the electrogenerated formation of **5a** compared against the known formation of **4a** via photolysis. The voltammograms of **3a** (Figure 4) did however differ from both **3b** and **1b**. A (presumably two-electron) reduction peak was observed for **3a** but only one return oxidation wave was observed. Upon repeated scanning the two one-electron reductions of **5a** → $\mathbf{5a}^{\bullet-}$ → $\mathbf{5a}^{2-}$ were observed, but still only a single (likely two-electron) return oxidation peak was observed, possibly indicating a large overpotential for the oxidation of $\mathbf{5a}^{2-}$. It is possible that **3a** undergoes only a one-electron reduction and rearrangement of **3a** → $\mathbf{3a}^{\bullet-}$→ $\mathbf{5a}^{\bullet-}$ (without further reduction to $\mathbf{5a}^{2-}$) and subsequently only one oxidation to **5a**. But this would make the second one-electron reduction (thought to be $\mathbf{5a}^{\bullet-}$ → $\mathbf{5a}^{2-}$) observed on repeated cycling unexplainable. A more likely explanation is that the two-electron ECE reduction of **3a** still occurs to give $\mathbf{5a}^{2-}$ but that the slight electron-donating nature of the additional methyl group destabilizes $\mathbf{5a}^{\bullet-}$ enough to require a substantial overpotential for reoxidation of $\mathbf{5a}^{2-}$ to $\mathbf{5a}^{\bullet-}$, such that it occurs at the same potential as oxidation of $\mathbf{5a}^{\bullet-}$ back to neutral **5a**. This could occur either sequentially at the same potential or in a single two-electron process. The latter explanation seems qualitatively in better agreement with the observed voltammogram in Figure 4.

In terms of achieving more potent photooxidants through the exchange of the naphthalene ring of the PSHDs for the more electron-deficient quinoline in the QSHDs, we had expected the

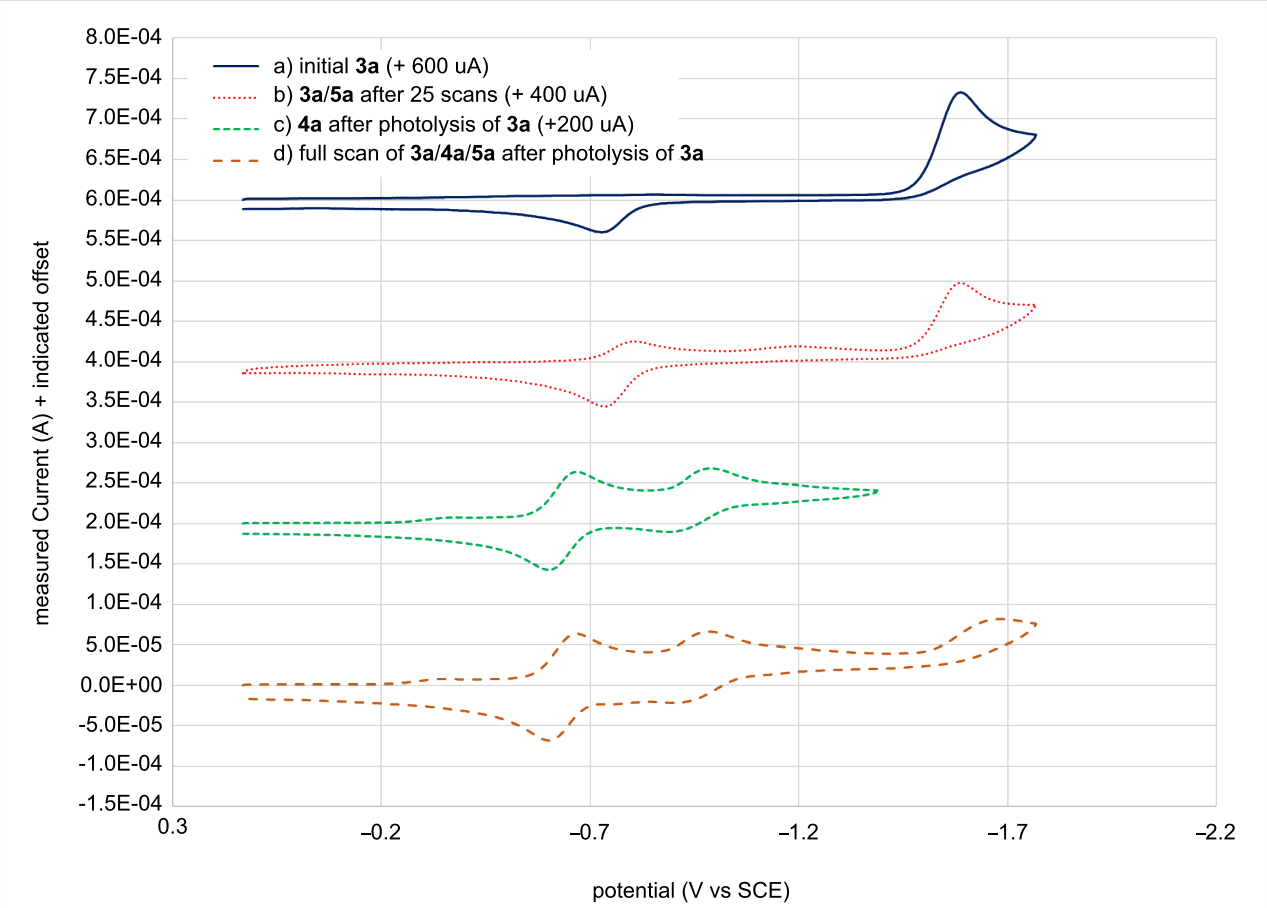


Figure 4: Cyclic voltammograms of a) **3a** before irradiation or electrolysis (solid blue), b) **3a** + **5a** after 25 scans (dotted red) showing the growth of the two eLW **5a** reduction peaks, c) **3a** after photolyzing but without reducing **3a** in the electrolysis (dashed green) which shows the two different reversible redox waves observed for pLW **4a**, and d) **3a** + **4a** + **5a** scanning the full potential window after the photolysis (dashed orange).

LW isomers to become more easily reducible, with minimal change in reduction potential for the SW isomers. Indeed E^{o}_{red} of the SW isomers **1b**, **3a**, and **3b** were the same within the error, and only 50 mV more reducible than **1a**. Comparing the E^{o}_{red} of pLW isomers (**4a**,**b** relative to **2a**,**b**), a roughly 140 mV difference is observed, with **4** being more reducible than **2** as expected. However, the difference in reduction potential between PSHD and QSHD for eLW was much less. For **5b** E^{o}_{red} was 28 mV more positive than **2b** indicating that **5b** is a slightly better oxidant than the parent PSHD. But E^{o}_{red} of eLW **5a** was surprisingly shifted 10 mV more negative than PSHD LW **2a**, meaning it was actually harder to oxidize. Ultimately E^{o}_{red} of **2a**, **2b**, **5a**, and **5b** are essentially the same within error limits. Apparently, the quinoline is not nearly as electron withdrawing when linked through the benzo ring as when it is linked through the heteroaromatic ring.

Spectroscopic analysis

The potential for two distinct products from electrolysis or photolysis as indicated through electrochemical analysis was further supported through NMR. Previous work [21] had conclusively shown through ^{1}H NOE NMR spectroscopy that the LW isomers resulting from photolysis of **3a** and **3b** were **4a** and **4b**, which open toward the more electron-deficient heteroaromatic ring of the quinoline and away from the R group. Unfortunately, efforts to obtain a sufficient quantity of the electrogenerated LW form of **3a** (i.e., **4a** or **5a**) for definitive ^{1}H NMR spectra or NOE experiments were not successful However, both UV–vis and electrochemical measurements indicated small amounts of a long wavelength form present in the dark immediately upon solvation (i.e., a thermal or solvatochromic LW form), particularly in **3a**. The presence of a LW isomer prior to irradiation or electrolysis was also consistent with the ^{1}H NMR spectrum of a sample of **3a** which, while known to be pure in the solid state [21]), in solution showed the expected **3a** chemical shifts but also smaller peaks (ca. 20% relative to **3a**) with similar splitting and chemical shifts as those for photogenerated **4a** (to which we initially erroneously attributed them [21]). However, the frequencies for this solvatochromic LW were slightly but distinctly different from either

3a or photogenerated **4a** (Figure 5a, e.g., consider protons **n**, **g**, and **v**). Signals for **4a** began to grow in with even very brief photolysis (Figure 5b), intentionally taken to low conversion (ca. 8% relative to **3a**) to enable comparison to the solvatachromic LW (ca. 20% relative to **3a**). Moreover, as the oxidation and reduction peaks associated with eLW **5a** (Figure 3b, dotted red) grow with increasing numbers of CV scans and match those present initially in solution in small amounts thermally (Figure 3a, solid blue), we conclude the electrogenerated and thermal LW forms are the same isomer **5a**, while it is the pLW isomer **4a** that grows in upon photolysis (Figure 3c, dashed green; Figure 5b). Furthermore, modest NOE enhancements can be observed even on the small amounts of **5a** present in these solutions. These NOEs, while weak, did aid in assigning the peaks as labelled in Figure 5b and demonstrate that the blue-labelled eLW peaks in Figure 5 are indeed on the same molecule, and that this is distinct from pLW **4a** as studied previously by NOE [21]. Thus, NMR, while not conclusive on its own, was able to provide additional support for our structural assignment.

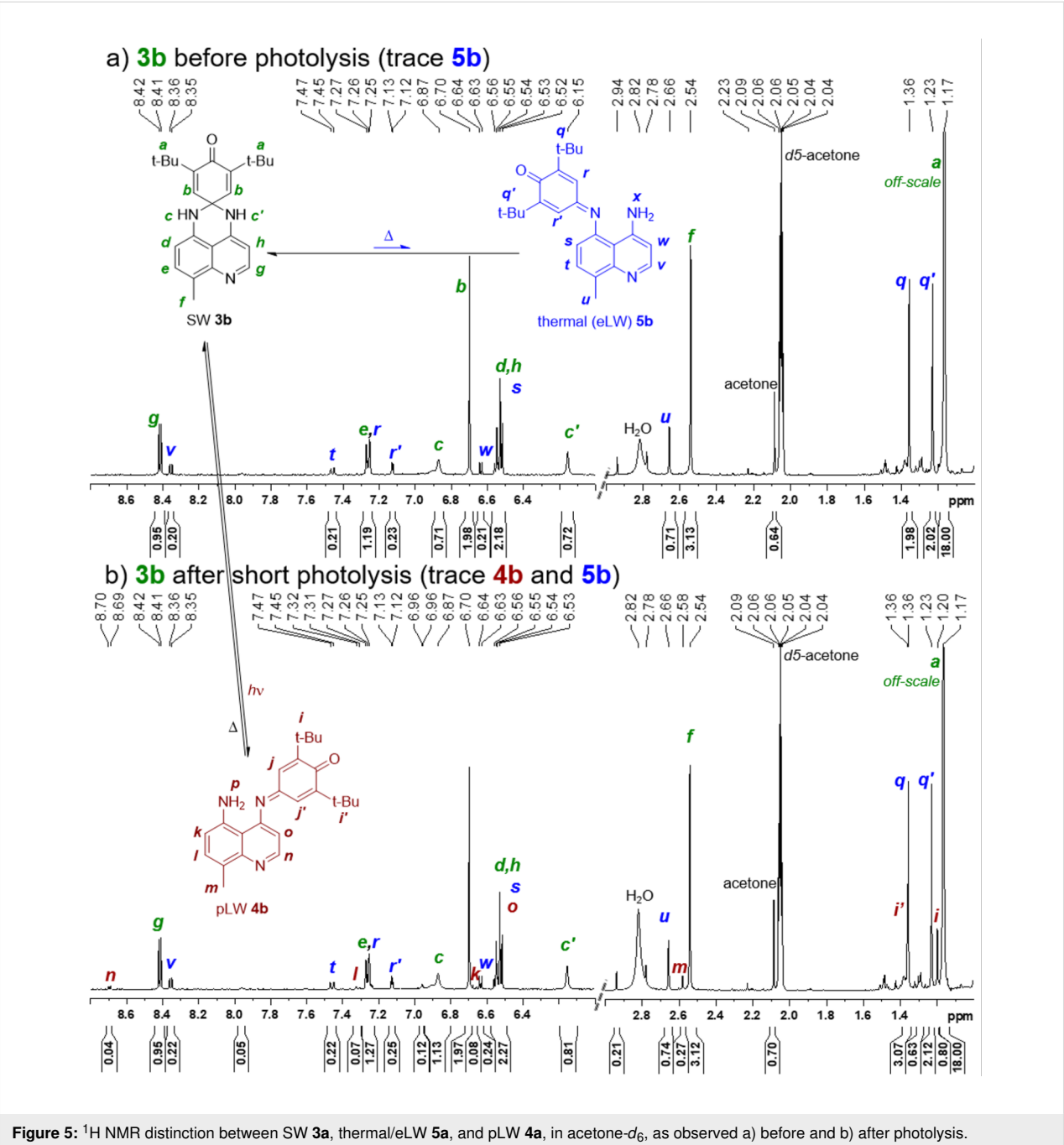


Figure 5: ^{1}H NMR distinction between SW **3a**, thermal/eLW **5a**, and pLW **4a**, in acetone-d_6, as observed a) before and b) after photolysis.

UV–vis spectra taken of eLW solutions generated by bulk electrolysis in acetonitrile and acetonitrile-d_3 were compared against photoirradiated (pLW) solutions. No difference was observed in the UV–vis spectrum of the LW isomer prepared from either photolysis or electrolysis of solutions of **1b** (as expected due to symmetry). The λ_{max} for the **2b** photogenerated solution was at 574 nm in acetonitrile and acetonitrile-d_3. The electrogenerated **2b** λ_{max} at 573 nm in both solvents differed by only 1 nm, within error limits of our instrumentation. For **4a**/**5a** the λ_{max} in acetonitrile-d_3 was 539 nm for the photolyzed solution (**4a**) versus 529 nm for the electrolyzed (**5a**). Similarly, for **4b** and **5b**, the photolyzed λ_{max} in acetonitrile was 558 nm versus 549 nm for the electrogenerated and was 564 nm versus the electrogenerated 550 nm in acetonitrile-d_3. The differences in the UV–vis spectrum of about 10 nm between eLW and pLW isomers of QSHDs **3** indicated a similar length for the conjugated system but a significant enough difference to indicate different species. This is consistent with the formation of two constitutional LW isomers that are structurally similar yet distinct, as the difference in absorbance would be expected to be noticeable but not large. Observation of no difference in the UV–vis spectrum of the LW isomer prepared from either photolysis or electrolysis of solutions of **1b** (able to only form one LW isomer, **2b**) supports the formation of two different LW isomers for **3a**,**b** rather than attributing the small spectral changes to the presence of electrolyte in the electrolyzed solutions, to an interaction with air, or to a side reaction in solution. The shorter wavelength for electrogenerated **5a**,**b** may result from slightly less planarity and decreased conjugation versus the photogenerated **4a**,**b**. The additional *ortho*-methyl group in **5b** may exacerbate this sterically, and/or could contribute an inductively donating effect.

Finally, the thermal reversion of eLW **5a**,**b** was visually and spectroscopically obvious to have begun within a few minutes, and to be complete within 12–18 hours. This is similar to what we previously reported for pLW **4a**,**b** [21]. This comparatively slow and purely thermal reversion is consistent with the need for a thermodynamically unfavorable intramolecular (or solvent or adventitious acid/base-mediated) proton transfer to begin the reversion mechanism, as Minkin has described [10]. Interestingly, reversion of either LW species to SW is observed immediately upon removal of solvent, which played a role in complicating our analysis, as the LW species cannot be isolated as solids.

Computational analysis

As shown above, computationally predicted reduction potentials [7] were in very good agreement with those determined experimentally (Table 1). The mean absolute deviation between computational prediction and experimental measurement of E^{o}_{red} for all SW and LW structures in Table 1 is just 21 mV (27 mV root mean squared deviation), not far from the 14 mV mean standard deviation in the experimental measurements. This demonstrates that the computational correlation employed is useful in structural assignment and accurate within a standard of error of the experimental reduction potentials of these spirohexadienones' different constitutional SW and LW isomers.

Density functional theory (DFT) calculated molecular orbitals (MOs, e.g., Figure 6 and Supporting Information File 1) indicate that the LUMO (MO 106 for **3a**) lies exclusively on the dienone moiety both in **1b** and in the quinazolinespirohexadienone photochromes **3a**,**b**. Thus, the dienone moiety is likely the electrophore in the SW in all PSHD and QSHD switches, just as Minkin [10] specifically asserted for **1a**. These diagrams also suggested to us that QSHDs **3** might also undergo an ECE mechanism similar to PSHDs **1**, as we have now confirmed experimentally.

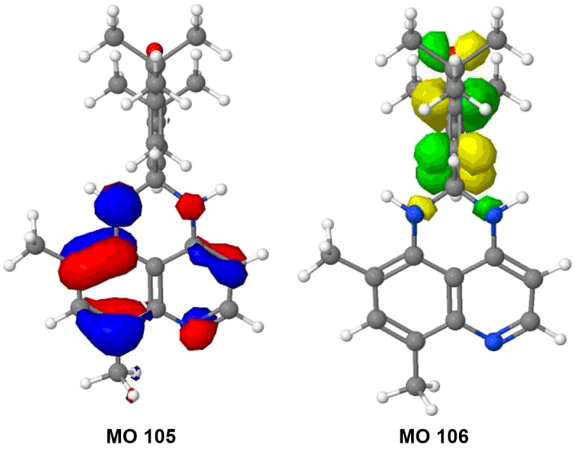
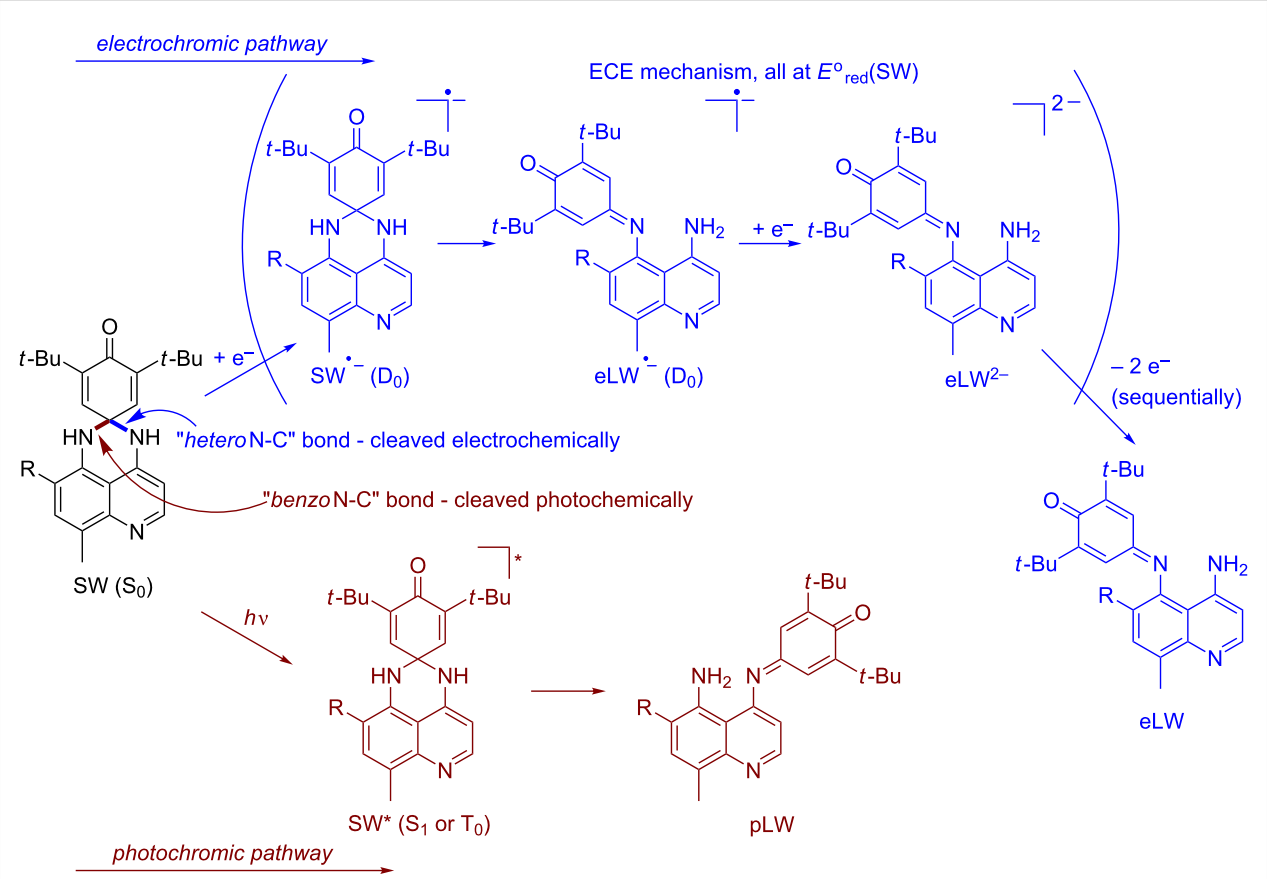


Figure 6: HOMO (MO 105, red and blue) and LUMO (MO 106, green and yellow) computed for **3a** in its ground (S_0) state. Similar results were observed for the frontier orbitals of **1b** and **3b** (see Supporting Information File 1).

Having conclusively demonstrated the differential regiospecificity of photochromic vs electrochromic ring-opening of the QSHDs (Scheme 3) by experiment, we next sought to understand *why* SW would open differently upon excitation to SW* vs reduction to $SW^{\bullet-}$. We turned to computation (of **3a**, **4a**, and **5a**) for an explanation. Due to large differences in the methods for calculating excited and ground-states, the triplet T_0 state was used instead of the singlet S_1 state as the photochemical intermediate (SW*) for computational purposes. Since T_0 is the lowest energy triplet state, it is amenable to a ground-state computation. While the real SW* photochemical intermediate may likely be the first singlet excited state (S_1), T_0 and S_1 possess



Scheme 3: Proposed mechanism for differential formation of pLW (**4**) and eLW (**5**) from SW (**3**).

equivalent orbital occupancy and differ only in their spin state. Our rationale for using T_0 rather than S_1 is that ignoring electron-exchange interaction introduces substantially less error than using different computational methods when comparing orbitals of SW* to those of SW and $SW^{\bullet-}$. Using S_1 for SW* would require unbalanced ground and excited-state calculations, e.g., time-independent and time-dependent density functional theories, or single-reference and multi-reference methods. However, using T_0 for SW* is a straightforward ground-state calculation, as are the calculations of D_0 (the radical anion) and S_0.

Clearly, as shown in Figure 7, the difference in reduction vs excitation is the occupancy in what was formerly the HOMO of SW. Because S_0 is the common precursor to both T_0 and D_0, analysis of the S_0 MOs was used to explain differences in the electron distributions that lead to two different products upon either excitation to form SW* (yielding pLW **4**) or reduction to form $SW^{\bullet-}$ (yielding eLW **5**). This approach of using the S_0 MOs was validated computationally, as we found there is little change in the character and relative energies of the MOs among S_0, T_0, and D_0. The calculated isosurface generated for the S_0 highest occupied molecular orbital (HOMO), MO 105, and lowest unoccupied molecular orbital (LUMO), MO 106, of **3a** are displayed in Figure 6. MO 105 allows for a direct comparison of the T_0 and D_0 electron distributions, as these two states differ only in the population of this orbital. There is more contribution from this MO to the N–C bond (hereafter designated the *benzo*N–C bond, cf. Scheme 3) of the nitrogen on the benzo ring of the quinoline moiety than the N–C bond of the nitrogen off the heterocyclic ring of the quinoline moiety (here-

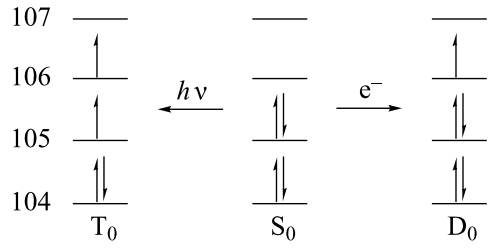


Figure 7: Frontier orbital occupancies of relevant electronic states of **3a**. Note: the photochemical excited state may be T_0 (as pictured) or perhaps more likely S_1 (inverted spin in molecular orbital 106 relative to T_0), but T_0 is more computationally tractable and is equivalent to S_1 for orbital occupancy arguments.

after referred to as the *hetero*N–C bond, cf. Scheme 3). This asymmetrical MO contribution is consistent with experimental observations. The absence of an electron from this orbital 105 in the case of T_0 results in the preferential weakening of the *benzo*N–C bond over the *hetero*N–C bond. The formation of pLW from SW (T_0) results from the breaking of this weaker bond. More electron density in the *benzo*N–C bond in orbital 105 might possibly suggest a stronger bond when the orbital is fully filled (as in D_0), and could suggest that the *hetero*N–C bond might be the more likely to rupture upon reduction to $SW^{\bullet-}$.

It is common to think of thermal ring-opening as looking more like that of the biradical (T_0 or S_1) than of the radical anion (D_0), so we might have presumed the structure of any thermal or solvatochromic LW isomer that occurred to have been that of pLW (**4**). However, the same rationalization that more electron density in the *benzo*N–C bond in orbital 105 might possibly suggest a stronger bond relative to the *hetero*N–C bond when the orbital is fully filled in S_0 is how we rationalize our observation that it is eLW (**5b**) that occurs in the only case where we see a purely thermal or solvatochromic cleavage. In turn we can then rationalize on the basis of sterics (R = Me vs H) that it is logical that this thermal or solvatochromic rupture might only be observable in **3b** (R = H) but not **3a** (R = Me). This is in good agreement with our experimental observations.

Our rationalization based on molecular orbitals was confirmed by looking at both bond lengths and bond orders of the two relevant N–C bonds in $SW^{\bullet-}$ and SW*. Bond order calculations provide a more quantitative explanation for the experimental observation. Because bond stability correlates to bond order, it is expected that the N–C bond which breaks upon forming the LW product would possess a smaller bond order. The BO calculations for intermediate states T_0 and D_0 indeed support this prediction. Table 2 summarizes the results of BO calculations for both bonds in these states. Since geometry plays a critical role in the stability of bonds, only BO calculations done from optimized geometries for each state are displayed. As shown in Table 2, *hetero*N–C has a greater bond order than *benzo*N–C in T_0, while the relative magnitude of these bond orders is reversed in D_0. This is consistent with the formation of eLW **5a** from $\mathbf{3a}^{\bullet-}$ D_0 (breaking the *hetero*N–C bond) and pLW **4a** from SW* **3a***, modelled as T_0 (breaking the *benzo*N–C bond) as shown in the proposed mechanism in Scheme 3. Finally, bond lengths were derived from geometry optimizations for D_0 and T_0 with and without solvent and are also included in Table 2. There is an obvious inverse relationship between calculated bond orders and bond lengths. For D_0, a longer bond length is observed for *hetero*N–C while a longer bond length is observed for *benzo*N–C in T_0. These results, regardless of solvent or gas-phase considerations, are consistent with the discussion above. In the cases of both D_0 and T_0, the longer bond is the one broken in the isomerization of SW **3a** to eLW **5a** and pLW **4a**, respectively. Similar results are also observed for S_0. Though the differences are much more modest in S_0, the *hetero*N–C bond is computed to be both longer and weaker, as in D_0, and thus it makes sense that any thermal or solvatochromic LW is the eLW isomer.

Conclusion

While moving from PSHD (**7**) to QSHD (**3**) increased ΔE^{o}_{red} between SW and pLW isomers, and therefore capacity to gate photoinduced charge transfer, by about 130 mV, the excited state reduction potential E^{*}_{red} of pLW **4** remains < +1.0 V vs SCE, insufficient to oxidize most donor molecules of relevance to materials applications. If our photochromic photooxidants are to be effective in real systems, the pLW will need to be made more electron deficient. Our computational predictions of the reduction potential [22], unfortunately not completed until after preparing the present system, were our first insight into the fact that electrochemical ring-opening was not yielding the structure we had previously proven for the photochromic pLW. We have thus demonstrated these computation's practical utility in a real-world experimental situation, as well as their suitably high degree of accuracy. We are therefore hopeful they can help guide our search for practical photochromic photooxidants, with a more reducible pLW*.

Table 2: Computed bond lengths and bond orders of the relevant N–C bonds for photochromic (T_0) and electrochromic (D_0) ring-opening of **3a**. Bolded (longer and weaker) bond is the one that is cleaved in each case.

State	Bond	Bond order	Bond length (Å)	Consider for
S_0	*benzo*N–C	0.9425	1.478	thermal LW/ solvatochromism
S_0	***hetero*N–C**	**0.9346**	1.478	
D_0	*benzo*N–C	0.8879	1.508	electrochromism
D_0	***hetero*N–C**	**0.8738**	**1.513**	
T_0	***benzo*N–C**	**0.8143**	**1.546**	photochromism
T_0	*hetero*N–C	0.8834	1.503	

For now, our team of undergraduate researchers has conclusively demonstrated differential regiospecificity in the photochromic vs electrochromic spirocyclic ring-opening of these QSHD molecular switches to two different LW isomers. This may provide an interesting structural framework for molecular logic or other applications that complements the recently reviewed photoelectrochromic properties observed in a range of photochromic families upon the electrochemical oxidation of either their SW or pLW isomers [24]. We have also demonstrated that any modest amount of thermal (or solvatochromic) coloration of the QSHDs is due to small amounts of the electrochromic eLW isomer **5**, rather than the photochromic pLW (**4**) as we had previously surmised [21]. Finally, we have been able to rationalize these results computationally on the basis of bond lengths, bond orders, and molecular orbital occupancy.

Experimental

Materials

Acetonitrile was of the highest HPLC grade (used as received or dispensed through a nitrogen-purged MBraun MBS-SPS 07-299 solvent purification system) or highest anhydrous grade (used as received). Acetonitrile-d_3 and acetone-d_6 were used as received in 1 g ampules (Cambridge Isotope Labs). Ferrocene, tetrabutylammonioum hexafluorophosphate (TBAH), and silver nitrate were of electrochemical grade and used as received. Photochromes **1a**,**b** were prepared according to the literature [10]. Photochromes **3a**,**b** were prepared as we previously reported [21].

Instrumentation

Photochemical irradiations and UV–vis spectroscopy were performed as previously described [21] on 3 mL or 4 mL argon-purged acetonitrile solutions of 0.1 M TBAH supporting electrolyte and 1–5 mM analyte, sufficient to attain signals much greater than background over the full potential window considered.

Cyclic voltammetry was performed on a CHI Model 604a electrochemical analyzer or a BAS epsilon e2 electrochemical analyzer. (The equivalent BAS or CHI cells and electrodes could be used on either potentiostat interchangeably, with or without the BAS C3 cell stand.) Solutions were placed in a glass cell and bubbled with argon to deaerate for 3–5 minutes. Scans were taken under an argon blanket using a glassy carbon working electrode, a platinum wire counter electrode, and a separately sparged $Ag/AgNO_3$ (10 mM) nonaqueous reference electrode isolated from the working compartment with a Vycor frit. In some cases, a bare Ag wire was used as a pseudo-reference instead. The working, reference, and counter-electrodes were arranged in a triangle through a Teflon cell cap. Rather than relying on either the $Ag/AgNO_3$ reference or Ag wire pseudo-reference, the voltammetry was corrected to a ferrocene external reference. Ferrocene solutions were cyclically scanned before and after each analyte experiment, beginning in the positive (oxidative) direction over an 800 mV window roughly centered on the reduction of Fc/Fc^+ redox couple at a scan rate of 0.1–0.5 V/s, 10^{-4} A sensitivity, and 1 mV sample interval. Internal resistance (iR) compensation was manually set to 95–99.5% of the measured resistance so that the peak separation for the reversible oxidation–reduction of ferrocene had a peak separation of ca. 60 mV and good peak shape without entering oscillation. Typical iR compensation in acetonitrile ranged from 150–230 Ω. Photochromic solutions were cyclically scanned beginning in the negative (reductive) direction at 0.1–0.5 V/s with 1 mV sample interval over an appropriate range of potentials and current sensitivity to observe the redox couples of either SW and LW or just LW isomers as desired, without reaching the solvent breakdown limit. Reduction potentials were taken as the half-peak potential of irreversible peaks or the midpoint of reversible peaks, standardized versus ferrocene (measured before and after each analyte sample), and corrected to versus SCE by adding 0.38 V [23]. At least seven replicates of each data point were obtained, with the mean value reported with error bars indicating the standard deviation from the mean among all replicates.

Potential step bulk electrolyses were performed on 3 mL argon-purged acetonitrile or acetonitrile-d_3 solutions of 2 mM analyte and 0.1 M TBAH. The solution was placed in a glass cell prepared by cutting the top off a 7 mL scintillation vial and fireglazing the edges. The outer rubber of a 19/22 septum was removed with a razor blade and used to cap the vial. The rubber had holes drilled for a reference and auxiliary electrode and a slit cut for a 7 × 70 mm platinum mesh working electrode so that the surface of the mesh faced the working and auxiliary electrodes. Teflon tubing was inserted through a pinhole in the septum for an argon purge and vent. The setup used a CHI112 nonaqueous $Ag/AgNO_3$ reference electrode. The auxiliary electrode was formed by removing the silver wire from a CHI112 nonaqueous reference electrode and replacing it with a rolled 7 × 70 mm piece of platinum mesh. The tube was filled with supporting electrolyte. Electrolyses were run on 2 to 3 mL samples, placing the platinum mesh electrode ca. 20 mm into the solution. To avoid the buildup of charge while maximizing current and efficiency, solutions were set to precondition before scanning the potential window with multiple repetitions run. Solutions of **1b** were preconditioned at −2.5 V for 5 seconds and 0 V for 6 seconds and 16–20 repetitions run. Solutions of **3a**,**b** were preconditioned at −2.2 V for 5 seconds and 0 V for 6 seconds with 16 repetitions. The electrolyzed solutions were opened to air or had a chemical oxidant (benzoquinone) added to complete the reduction of the dianion to the LW isomer.

NMR spectroscopy was performed on samples 5 mm NMR tubes (Wilmad) made of clear quartz (photolyzed samples) or amber pyrex (dark samples) on a Varian Mercury or Bruker AvanceIII 400 MHz NMR. ^{1}H NMR experiments on **5a** were performed on an argon-purged, ca. 24 mM solution in acetone-d_6. 1D NOE spectra were collected using 400 manually interleaved scans with a 4 s relaxation delay, targeting a single peak per experiment, in a manner similar to that previously reported [21] for photogenerated **4a**,**b**.

Computational modeling

Predicted ground-state reduction potentials were computed based on the energy difference of the ground-state molecule (S_0) and its one electron-reduced (D_0) radical anion and our published correlation of this energy difference with experimental reduction potentials (vs SCE in acetonitrile) [22]. Gas-phase geometries were optimized at the B3LYP/6-31G(d) level of theory. Single point energies were computed at the same level of theory with implicit acetonitrile solvent implemented using the Conductor-like Polarizable Continuum Model with UAKS radii. These computations were performed using the Gaussian 03 software package [25], implemented through the WebMO [26] graphical user interface on the Curie cluster [27] in the Hope College Computational Science & Modeling Laboratory on a single node (a single 2.60 GHz AMD Opteron-252 processor with 8 GB RAM and 250 GB HD).

Calculations of bond length, bond order, and molecular orbitals to rationalize the observed differential photochromic and electrochromic ring-opening of **1** to **2** and **3**, respectively, were performed on the Midwest Undergraduate Computation Chemistry Consortium (MU3C) cluster [28,29]. Computations were performed on a single node (dual Intel X5650 CPU, with 6 cores running at 2.66 GHz) using the Gaussian 09 [30] software package implemented through the WebMO [26] graphical user interface. Restricted open-shell Hartree-Fock (ROHF) theory [31] with the Becke 3, Lee, Yang, and Parr (B3LYP) hybrid functional [32-34] was used for geometry optimizations, molecular orbitals, and bond orders calculations with the 6-31G(d) basis set [35] for open-shell species (T_0 and D_0), while conventional B3LYP (with standard Hartree-Fock theory) was used for closed-shell S_0 calculations. The concerted use of ROHF and B3LYP provides a restricted open-shell B3LYP (DFT) method, which was particularly important to obtaining good bond orders for open-shell (T_0 and D_0) species. Bond orders were calculated using the Natural Bond Order (NBO) 3.1 package [36] contained within Gaussian 09. The geometry was first optimized for the S_0 state in the gas phase. Based on this starting point, geometries for S_0, T_0, and the one-electron reduced D_0 states were then (re)optimized with an implemented acetonitrile conductor-like polarizable continuum model (CPCM) as the self-consistent reaction field (SCRF) [37]. It is from these implicit solvent-optimized geometries that reported bond lengths were derived. Molecular orbital and bond order calculations were subsequently performed on these geometries.

Supporting Information

Supporting Information File 1

Additional figures and Z-matrices.
[https://www.beilstein-journals.org/bjoc/content/supplementary/1860-5397-15-240-S1.pdf]

Supporting Information File 2

Complete data sets for experimental and computational reduction potentials of all compounds.
[https://www.beilstein-journals.org/bjoc/content/supplementary/1860-5397-15-240-S2.xlsx]

Acknowledgements

This work was funded by a Camille & Henry Dreyfus Foundation Start-up Award (SU-04-040), a Cottrell College Science Award from Research Corporation (CC6653), and a Faculty Early Career Development Grant (CHE-0952768) from the US National Science Foundation (NSF). This work was also funded in part by a grant to Hope College from the Howard Hughes Medical Institute through the Undergraduate Science Education Program, which provided support for the Curie cluster [27] in the Hope College Computational Science & Modeling (CSM) Laboratory and to ALS (Computational Science & Modeling Scholars Program) and JPM (HHMI Research Scholars Program). Additional computations were conducted on the MU3C [28,29] cluster, supported by Major Research Instrumentation grants (CHE-0520704 and CHE-1039925) from the NSF, also housed in the Hope College CSM Laboratory. Support from CSM Laboratory director Prof. Brent P. Krueger and former staff member Mr. Paul Van Allsburg is also gratefully acknowledged. ALS acknowledges additional support from a Jean Dreyfus Boissevain Scholarship awarded to the Hope College Chemistry Department by the Camille & Henry Dreyfus Foundation. EJL (home institution College of the Canyons, Santa Clarita, CA) acknowledges support by a Research Experiences for Undergraduates Site award (CHE-0851194) to the Hope College Chemistry Department from the NSF.

ORCID® iDs

William F. Polik - https://orcid.org/0000-0003-0419-5135
Jason G. Gillmore - https://orcid.org/0000-0001-7506-3645

References

1. Crano, J. C.; Guglielmetti, R. J., Eds. *Organic Photochromic and Thermochromic Compounds;* Plenum Press: New York, NY, USA, 1999; Vol. 1. doi:10.1007/b114211
2. Duerr, H.; Bouas-Laurent, H., Eds. *Photochromism: Molecules and Systems, revised ed.;* Elsevier: Amsterdam, 2003.
3. Desvergne, J.-P.; Pozzo, J.-L., Eds. Proceedings of the fourth International Symposium on Photochromism Photoswitchable Molecular Systems and Devices. *Mol. Cryst. Liq. Cryst.* **2005,** *430–431,* 1–586. doi:10.1080/15421400590946073
4. Branda, N.; Tian, H., Eds. *Organic Photoswitchable Multifunctional Molecules and Materials*. *Dyes Pigm.* **2011,** *89,* 193–336. doi:10.1016/j.dyepig.2010.12.002
5. Favaro, G.; Irie, M., Eds. Special issue on Photochromism 1 and 2. *J. Photochem. Photobiol., C* **2011,** *12,* 71–236. doi:10.1016/j.jphotochemrev.2011.08.004
6. Monk, P. M. S.; Mortimer, R. J.; Rosseinsky, D. R. *Electrochromism and Electrochromic Devices;* Cambridge University Press: Cambridge, UK, 2007. doi:10.1017/cbo9780511550959 and references therein.
7. Baumann, K. L.; Lin, R.; Giri, P.; Franz, S. Protic-Soluble Organic Electrochromic Compounds. U.S. Pat. Appl. US2017/0146880 A1, May 25, 2017.
8. Jarosz, T.; Gebka, K.; Stolarczyk, A.; Domagala, W. *Polymers (Basel, Switz.)* **2019,** *11,* 273. doi:10.3390/polym11020273 and references therein.
9. Madasamy, K.; Velayutham, D.; Suryanarayanan, V.; Kathiresan, M.; Ho, K.-C. *J. Mater. Chem. C* **2019,** *7,* 4622–4637. doi:10.1039/c9tc00416e
10. Minkin, V. I.; Komissarov, V. N.; Kharlanov, V. A. Perimidinespirocyclohexadienones. In *Organic Photochromic and Thermochromic Compounds;* Crano, J. C.; Guglielmetti, R. J., Eds.; Plenum Press: New York, NY, USA, 1999; Vol. 1, pp 315–340. doi:10.1007/0-306-46911-1_9 and references therein.
11. Gillmore, J. G.; Neiser, J. D.; McManus, K. A.; Roh, Y.; Dombrowski, G. W.; Brown, T. G.; Dinnocenzo, J. P.; Farid, S.; Robello, D. R. *Macromolecules* **2005,** *38,* 7684–7694. doi:10.1021/ma050348k
12. Kavarnos, G. J.; Turro, N. J. *Chem. Rev.* **1986,** *86,* 401–449. doi:10.1021/cr00072a005 and references therein.
13. Borsub, N.; Kutal, C. *J. Am. Chem. Soc.* **1984,** *106,* 4826–4828. doi:10.1021/ja00329a030
14. Evans, T. R.; Wake, R. W.; Sifain, M. M. *Tetrahedron Lett.* **1973,** *14,* 701–704. doi:10.1016/s0040-4039(00)72438-5
15. Hasegawa, E.; Okada, K.; Ikeda, H.; Yamashita, Y.; Mukai, T. *J. Org. Chem.* **1991,** *56,* 2170–2178. doi:10.1021/jo00006a039
16. Bauld, N. L. Hole and electron transfer catalyzed pericyclic reactions. In *Advances in Electron Transfer Chemistry;* Mariano, P. S., Ed.; JAI Press: Greenwich, CT, 1992; pp 1–66. and references therein.
17. Bauld, N. L.; Gao, D.; Aplin, J. T. *J. Phys. Org. Chem.* **1999,** *12,* 808–818. doi:10.1002/(sici)1099-1395(199911)12:11<808::aid-poc207>3.0.co;2-m
18. Bauld, N. L.; Gao, D. *Polym. Int.* **2000,** *49,* 253–259. doi:10.1002/(sici)1097-0126(200003)49:3<253::aid-pi352>3.0.co;2-p
19. Bauld, N. L.; Roh, Y. *Tetrahedron Lett.* **2001,** *42,* 1437–1439. doi:10.1016/s0040-4039(00)02301-7
20. Roh, Y.; Gao, D.; Bauld, N. L. *Adv. Synth. Catal.* **2001,** *343,* 481–489. doi:10.1002/1615-4169(200107)343:5<481::aid-adsc481>3.0.co;2-s
21. Moerdyk, J. P.; Speelman, A. L.; Kuper, K. E., III; Heiberger, B. R.; Ter Louw, R. P.; Zeller, D. J.; Radler, A. J.; Gillmore, J. G. *J. Photochem. Photobiol., A* **2009,** *205,* 84–92. doi:10.1016/j.jphotochem.2009.04.011
22. Lynch, E. J.; Speelman, A. L.; Curry, B. A.; Murillo, C. S.; Gillmore, J. G. *J. Org. Chem.* **2012,** *77,* 6423–6430. doi:10.1021/jo300853k
23. Pavlishchuk, V. V.; Addison, A. W. *Inorg. Chim. Acta* **2000,** *298,* 97–102. doi:10.1016/s0020-1693(99)00407-7
24. Barachevsky, V. A.; Butenko, V. G. *Russ. J. Gen. Chem.* **2018,** *88,* 2747–2772. doi:10.1134/s1070363218120459
25. *Gaussian 03,* Revision D.01; Gaussian, Inc.: Wallingford, CT, 2004.
26. Schmidt, J. R.; Polik, W. F. *WebMO Pro* version 9.1, *WebMO Enterprise* versions 10.1, 12.1, 14.0; WebMO LLC: Holland, MI, 2014; available from http://www.webmo.net (accessed June 2019).
27. *Curie Cluster*. http://curie.chem.hope.edu/ (accessed June 30, 2019).
28. MU3C – *Midwest Undergraduate Computational Chemistry Consortium*. http://mu3c.chem.hope.edu/ (accessed June 30, 2019).
29. Kuwata, K. T.; Kohen, D.; Krueger, B. P.; Polik, W. F. *Counc. Undergrad. Res. Quart.* **2012,** *32* (4), 9–14.
30. *Gaussian 09,* Revision A.1; Gaussian, Inc.: Wallingford, CT, 2009.
31. Roothaan, C. C. J. *Rev. Mod. Phys.* **1960,** *32,* 179–185. doi:10.1103/revmodphys.32.179
32. Becke, A. D. *J. Chem. Phys.* **1996,** *104,* 1040–1046. doi:10.1063/1.470829
33. Becke, A. D. *Phys. Rev. A* **1988,** *38,* 3098–3100. doi:10.1103/physreva.38.3098
34. Lee, C.; Yang, W.; Parr, R. G. *Phys. Rev. B* **1988,** *37,* 785–789. doi:10.1103/physrevb.37.785
35. Hariharan, P. C.; Pople, J. A. *Theor. Chim. Acta* **1973,** *28,* 213–222. doi:10.1007/bf00533485
36. Glendening, E. D.; Reed, A. E.; Carpenter, J. E.; Weinhold, F. NBO, *Version 3.1.*
37. Tomasi, J.; Mennucci, B.; Cammi, R. *Chem. Rev.* **2005,** *105,* 2999–3094. doi:10.1021/cr9904009

License and Terms

This is an Open Access article under the terms of the Creative Commons Attribution License (http://creativecommons.org/licenses/by/4.0). Please note that the reuse, redistribution and reproduction in particular requires that the authors and source are credited.

The license is subject to the *Beilstein Journal of Organic Chemistry* terms and conditions: (https://www.beilstein-journals.org/bjoc)

The definitive version of this article is the electronic one which can be found at: doi:10.3762/bjoc.15.240

BEILSTEIN JOURNAL OF ORGANIC CHEMISTRY

In search of visible-light photoresponsive peptide nucleic acids (PNAs) for reversible control of DNA hybridization

Lei Zhang, Greta Linden and Olalla Vázquez*

Letter

Open Access

Address:
Fachbereich Chemie, Philipps-Universität Marburg, Hans-Meerwein Straße 4, 35043 Marburg, Germany

Email:
Olalla Vázquez* - olalla.vazquez@staff.uni-marburg.de

* Corresponding author

Keywords:
azobenzene; hemithioindigo; peptide nucleic acid (PNA); photoswitch; visible-light irradiation

Beilstein J. Org. Chem. **2019,** *15,* 2500–2508.
doi:10.3762/bjoc.15.243

Received: 26 July 2019
Accepted: 01 October 2019
Published: 22 October 2019

This article is part of the thematic issue "Molecular switches".

Guest Editor: W. Szymanski

© 2019 Zhang et al.; licensee Beilstein-Institut.
License and terms: see end of document.

Abstract

Photoswitchable oligonucleotides can determine specific biological outcomes by light-induced conformational changes. In particular, artificial probes activated by visible-light irradiation are highly desired in biological applications. Here, we report two novel types of visible-light photoswitchable peptide nucleic acids (PNAs) based on the molecular transducers: hemithioindigo and tetra-*ortho*-fluoroazobenzene. Our study reveals that the tetra-*ortho*-fluoroazobenzene–PNA conjugates have promising properties (fast reversible isomerization, exceptional thermal stability, high isomer conversions and sensitivity to visible-light irradiation) as reversible modulators to control oligonucleotide hybridization in biological contexts. Furthermore, we verified that this switchable modification delivers a slightly different hybridization behavior in the PNA. Thus, both melting experiments and strand-displacement assays showed that in all the cases the *trans*-isomer is the one with superior binding affinities. Alternative versions, inspired by our first compounds here reported, may find applications in different fields such as chemical biology, nanotechnology and materials science.

Introduction

Light-driven control of oligonucleotide hybridization has demonstrated an enormous potential to regulate on-demand biological responses such as gene expression [1]. There are indeed a number of successful examples based on photocaged strategies [2-5], in which modified nucleic acids interfere irreversibly with gene expression in vitro [6,7] and in vivo [8-12]. Manipulation of gene expression demonstrated therapeutic application – antisense chemistry [13]. Along these lines, photopharmacology [14,15] is an emerging field that highlights the importance of reversible photocontrollable drugs in tomorrow's medicine, but photoswitchable antisense research in the context of photopharmacology is entirely unexplored. Furthermore, reversible approaches with photoswitches will contribute to a better understanding of biological pathways as they would allow precise reversible spatio-temporal activation/deactivation of the desired targets without causing a permanent

knockout. During the last years, the pioneering structural studies of reversible photoregulation of DNA/RNA duplex stability of Asanuma and Komiyama [16,17] have become functional ones, affecting DNA/RNA cleavage [18-20], transcription [21-23], and translation [24,25]. Except a handful of current examples [22,24,26], most of these photoresponsive oligonucleotides are canonical ones where the classical azobenzene is the prominently used photoswitch; although spiropyrans [27], stilbenes [28], diarylethanes [29] and overcrowded alkenes [30] have also been employed. In vivo application demands the development of a new generation of artificial agents to target DNA/RNA-associated processes. These compounds must be able to maintain their specificity and effectivity while still being nuclease resistant, nontoxic and susceptible to light of tissue-penetrating wavelengths. Peptide nucleic acids (PNAs) [31] are synthetic nucleic acid analogues, in which nucleobases are linked to a repeating *N*-(2-aminoethyl)glycine polyamide backbone. The lack of phosphate groups provides them with both higher binding affinities to complementary DNA or RNA sequences and improved mismatch discrimination under physiological conditions than natural ones. Furthermore, PNAs have a straightforward chemical synthesis by Fmoc-based PNA solid-phase synthesis and remarkable stability against nuclease- and protease-mediated degradation [32,33]. In regard to all these beneficial properties of PNA, they may become a promising alternative to overcome the current limitations of the available photoswitchable DNA- and RNA-based systems with potential for in vivo applications too.

Only very few is known about the reversible hybridization of PNAs upon irradiation [34-36]. Besides these precedents use azobenzene-containing PNA to mainly regulate PNA/DNA triplex helix formation by illumination at low wavelengths (360 nm/425 nm) [35,36]. This effect was successfully exploited for the photocontrol of transcription by T7 RNA polymerase in vitro [36]. In fact, such a result opens new avenues for the investigation of other photoswitchable PNAs and pursuing visible-light modulation. Herein, we report the design of a versatile synthetic platform to derivatize PNAs with different photoswitches (Figure 1), which has never been studied in the context of PNA. After incorporation, their switching capacities and duplex formation were analyzed.

Our group has recently demonstrated that photoresponsive peptides can affect the transcription of genes via inhibition of histone-modifying enzymes [37]. Repression of enzymes is achievable at nucleic acid level too. Therefore, in this project we envision a minimal model based on the previously reported accessible mRNA region of the class I histone deacetylase HDAC-1: 5'-GUGAGCCAAGAAACACUGCCU-3' to investigate our photoswitchable PNAs [38]. Importantly, HDAC-1 is

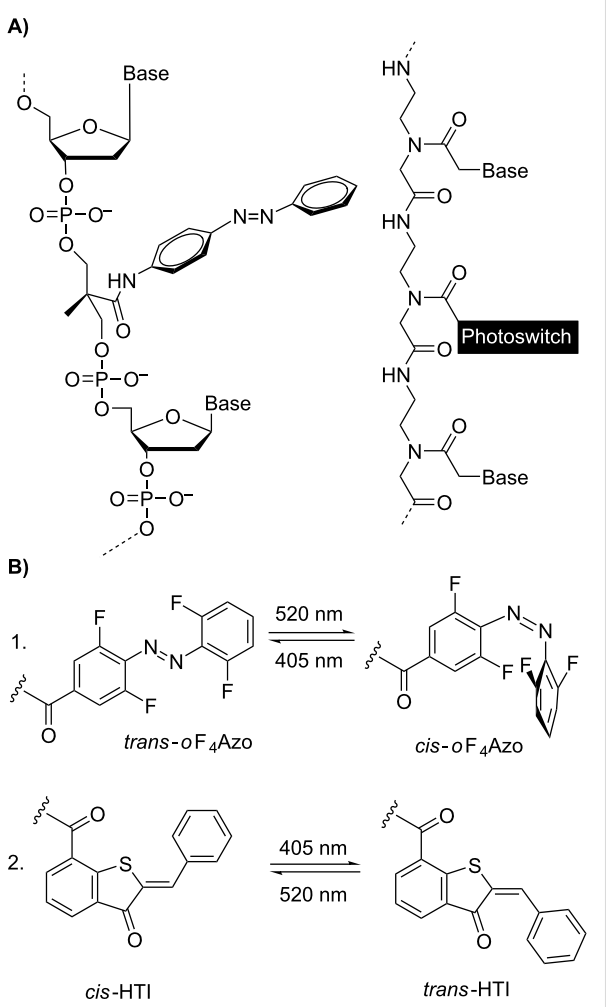


Figure 1: A) Structure of the pioneering azobenzene-modified DNA [16] compared with the photoswitchable PNA structure based on a monomer surrogate. B) Isomerization of the molecular transducers incorporated and studied in this project: 1.: tetra-*ortho*-fluoroazobenze (oF_4Azo) and 2.: hemithioindigo (HTI).

frequently overexpressed in tumors and particularly, in prostate cancer [39].

Results and Discussion

Initially, short 12-mer PNA probes (Table 1) complementary to the HDAC-1 mRNA sequence were synthesized since, in general, PNAs are active with shorter sequences than the canonical analogues due to the superior binding abilities [40]. Despite that target specificity may be compromised, 12-mer long sequences are a suitable starting point for our preliminary tests. An overview of all the sequences of this study can be found in Table 1 and Table 2.

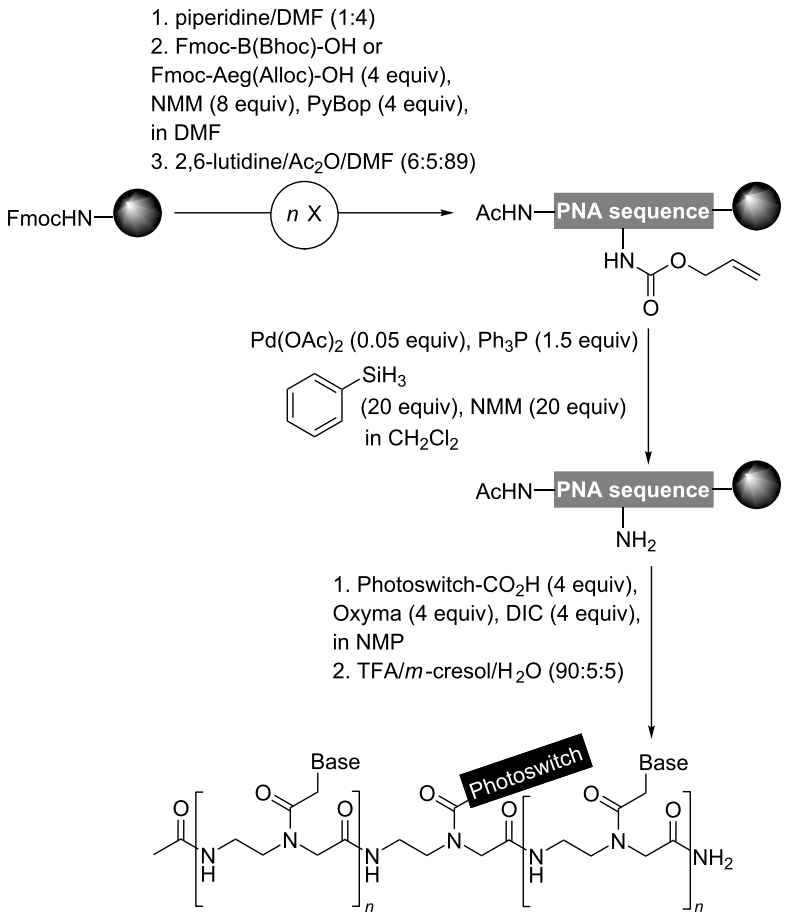
Contrary to the previous synthetic approach of azobenzene-containing PNAs [35,36,41], in which the preformed monomer building block was used, we gained versatility using the diver-

gent linear approach introduced by Seitz (Scheme 1) [42]. This strategy enabled the straightforward access to functionalized PNA via on-resin coupling of the corresponding photoswitch in good yields. Of note, this post-synthetic modification is compatible with base sensitive compounds, which undergo degradation under standard Fmoc deprotection conditions. As it is common for PNAs, our oligomers have an acetylated N-terminus and a C-terminal carboxamide group. After completion of the PNA sequences, the orthogonally protected backbone module [2-(*N*-Alloc)aminoethyl]glycine residue –Aeg(Alloc)– was selectively deprotected in the presence of $Pd(OAc)_2$, Ph_3P, NMM, $PhSiH_3$ in CH_2Cl_2 for 2 h. Subsequently, carboxy photoswitches were introduced using Oxyma and *N*,*N*'-diisopropylcarbodiimide (DIC) as coupling agent.

We explored two different types of photoswitches (Figure 1B): 1) second generation azobenzenes based on the tetra-*ortho*-fluoroazobenze (oF_4Azo) developed by Hecht [43] and 2) hemithioindigos (HTI) rediscovered by Rück-Braun [44] and Dube [45], which have not been studied in the context of DNA/RNA as molecular transducer yet. Both compounds were compatible with the standard TFA/*m*-cresol/H_2O (90:5:5) acidolysis yielding the photoswitchable PNA conjugates. These and all further studied PNAs in this work (Table 2) were purified by reversed-phase (RP) HPLC and fully characterized. Analogous compounds lacking the photoswitch were used as controls.

First, the photochromic behavior of the newly synthesized modified PNAs (Table 1, compound **3** and **4**) was investigated and compared with the corresponding photoswitchable PNA monomers (Table 1, compound **1** and **2**).

Apart from the expected increase of the band at 260 nm due to the aromatic base moieties within the PNAs, UV–vis spectroscopy of 20 µM solutions in phosphate buffer (10 mM NaH_2PO_4, 150 mM NaCl, pH 7.4) confirmed that PNA incorporation did not significantly affect the photochromism (Figures S24, S20, S30 and S33, Supporting Information File 1). This verifies the integrity of the chromophores after the cleavage from the solid support. Among the initial studied photoswitchable PNAs, the PNA_{12}(oF_4Azo) (**3**) displayed the most promising properties as reversible modulator of oligonucleotide



Scheme 1: Solid-phase synthesis of photoswitchable PNAs; Aeg = *N*-(2-aminoethyl)glycine, Bhoc = benzhydryloxycarbonyl.

Table 1: Isomerization conversions at the photostationary state (PSS).

Compound	Isomer ratio[a] [%]	
Ac-Aeg(oF$_4$Azo)CONH$_2$ (**1**)	*trans*	91
	cis	90
Ac-Aeg(HTI)CONH$_2$ (**2**)	*trans*	50
	cis	99
PNA$_{12}$(oF$_4$Azo) (**3**): Ac-ggcagAeg(oF$_4$Azo)gtttct-CONH$_2$	*trans*	95
	cis	82
PNA$_{12}$(HTI) (**4**): Ac-ggcagAeg(HTI)gtttct-CONH$_2$	*trans*	47
	cis	93

[a]Isomer ratios of a 20 µM solution of the corresponding compound in phosphate buffer (10 mM NaH_2PO_4, 150 mM NaCl, pH 7.4) were determined at the isosbestic point (275 nm, for oF$_4$Azo and HTI) by RP-HPLC; irradiation to obtain the *cis*-isomer at PSS: 520 nm for 10 min and the *trans*-isomer at PSS: 405 nm for 2 min. Mean values derived from two independent experiments; Aeg = *N*-(2-aminoethyl)glycine.

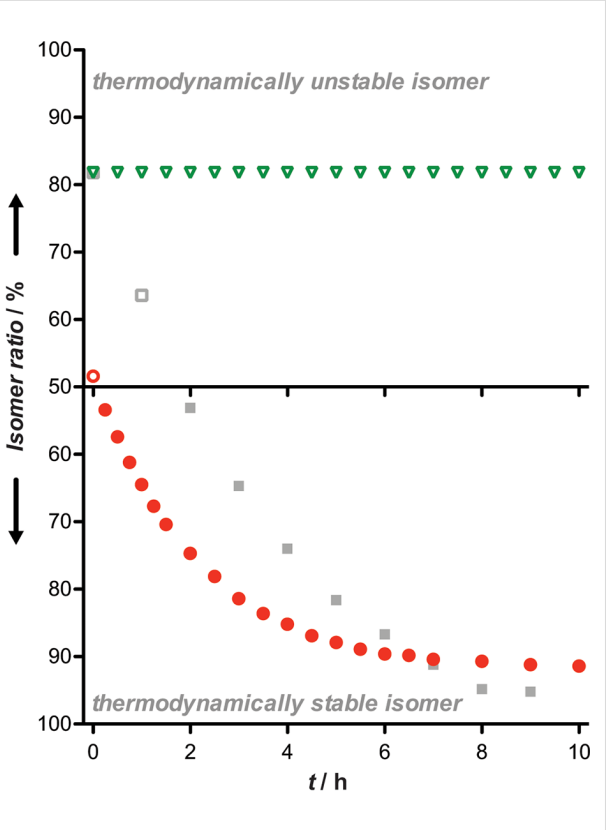


Figure 2: Time-dependent conversion to the thermodynamically stable isomer of PNA$_{12}$(oF$_4$Azo) (**3**; green triangles) and PNA$_{12}$(HTI) (**4**; red circles). 20 µM solutions of the corresponding compound in phosphate buffer (10 mM NaH_2PO_4, 150 mM NaCl, pH 7.4) were irradiated to obtain maximal *cis* (oF$_4$Azo, 520 nm, 10 min) or *trans* (HTI, 405 nm, 2 min) and stored in the dark. PNA$_{12}$(oF$_4$Azo) (**3**) was also measured with continuous heating at 90 °C (gray squares). UV–vis spectra were collected at different time points during 10 h. Curves derived were calculate from two independent experiments where the value of the absorbance at 304 nm (for **3**) or at 442 nm (for **4**) was measured.

hybridization. Thus, it displayed the fastest reversible isomerization (≈2 s for *cis* → *trans* and ≈120 s for *trans* → *cis* at these conditions, Figure S24C, Supporting Information File 1) without any signs of photodegradation and photochemical fatigue up to 20 cycles under visible-light irradiation. Regarding the photoconversion ratios between isomers (Table 1), PNA$_{12}$(oF$_4$Azo) (**3**) had the best ratios. However, the large separation between the n → π* bands of the *trans* and the *cis*-forms (Δλ = 69 nm; Figure S24, Supporting Information File 1) did not lead to the quasi-quantitative conversion for the *cis*-isomer, as for the photoswitchable PNA monomer **1** and the molecular transducer [43,46]. This slightly lower *cis* ratio was also reported in photoswitchable peptides and DNA binders equipped with oF$_4$Azo [47,48].

Regarding stability, the *cis*-PNA$_{12}$(oF$_4$Azo) (**3**) was stable at least for 24 h at 37 °C, while under the same conditions the thermodynamically unstable isomer of PNA$_{12}$(HTI) (**4**) reverted after 6 h at room temperature in the dark according to UV–vis measurements (Figure 2 and Figure S32, Supporting Information File 1). The thermal relaxation of the *cis*-PNA$_{12}$(oF$_4$Azo) (**3**) was slow even at high temperatures (Figures S27 and S28, Supporting Information File 1). Furthermore, RP-HPLC chromatograms of its *cis*-form did not show any decomposition under these conditions (Figure S27C, Supporting Information File 1), unlike when the oF$_4$Azo was grafted onto a pyrrole scaffold [48].

Next, we explored if the inclusion of oF$_4$Azo as monomer surrogate within the PNA sequence could affect its hybridization to a complementary DNA. For this purpose, we decided to measure thermal melting curves. Beforehand we verified the photostability of *cis*-PNA$_{12}$(oF$_4$Azo) (**3**) in the temperature ramp from 20 °C to 90 °C by UV–vis spectroscopy. We observed that the *cis*-isomer was always stable during the whole temperature range (Figure S27B, Supporting Information File 1). Remarkably, its time-dependent conversion to the *trans*-PNA$_{12}$(oF$_4$Azo) (**3**) at 90 °C was surprisingly slow (Figure 2 and Figure S28, Supporting Information File 1) in contrast to the reported *cis*-azobenzene tethered oligonucleotides [49]. Therefore, such unique characteristic allowed the irradiation of the photoswitchable PNA before hybridization (see Supporting Information File 1 for the detailed procedure). Thermal melting profiles showed single sigmoidal transitions (Figure 3 and Figures S37–S45, Supporting Information File 1), which enables the calculation of the melting temperatures (T_M) by the analysis of the first derivative [50]. T_M values are summarized in Table 2.

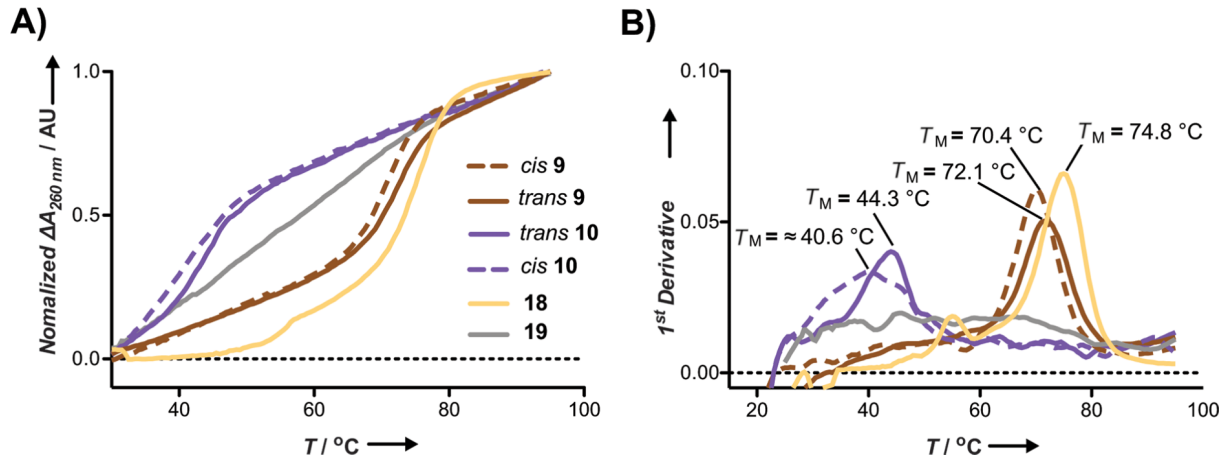


Figure 3: A) Melting curves of a 1 µM duplex solution in phosphate buffer (10 mM NaH_2PO_4, 150 mM NaCl, pH 7.4) of the PNA (**18** = yellow solid line; **19** = grey solid line; **9** = brown, *cis* dashed line, *trans* solid line; **10** = purple, *cis* dashed line, *trans* solid line and the complementary ssDNA (5'-GTG AGC CAA GAA ACA CTG CCT-3')). The melting curves were duplicates from two independent experiments combining 3 cycles of measurements from 20 °C to 95 °C at 260 nm without pre-hybridization. B) Melting temperatures (T_M) obtained by the first derivative of the data in A.

Table 2: Melting temperatures (T_M) of the duplex between the PNAs and the complementary ssDNA (5'-GTG AGC CAA GAA ACA CTG CCT-3').

	Sequence	T_M [°C]	
		cis	*trans*
3	Ac-ggcag**Aeg(*o*F$_4$Azo)**gtttct-$CONH_2$	50.5 ± 0.04	50.5 ± 0.02
5	Ac-ggcag**Aeg(Ac)**gtttct-$CONH_2$	44.3 ± 0.4	
6	Ac-*Lys*-**Aeg(*o*F$_4$Azo)**gcagtgtttcttgg-*Lys*-$CONH_2$	70.8 ± 0.3	70.6 ± 0.2
7	Ac-*Lys*-gg**Aeg(*o*F$_4$Azo)**agtgtttcttgg-*Lys*-$CONH_2$	61.4 ± 0.5	62.4 ± 0.4
8	Ac-*Lys*-ggcagt**Aeg(*o*F$_4$Azo)**tttcttgg-*Lys*-$CONH_2$	56.8 ± 0.5	57.1 ± 0.4
9	Ac-*Lys*-ggcagtgtttcttg**Aeg(*o*F$_4$Azo)**-*Lys*-$CONH_2$	70.4 ± 0.8	72.1 ± 0.4
10	Ac-*Lys*-ggc**Aeg(*o*F$_4$Azo)**gtgtttc**Aeg(*o*F$_4$Azo)**tgg-*Lys*-$CONH_2$	≈40.6[a] ± 1.0	44.3 ± 0.8
11	Ac-*Lys*-gg**Aeg(*o*F$_4$Azo)**agtg**Aeg(*o*F$_4$Azo)**ttct**Aeg(*o*F$_4$Azo)**gg-*Lys*-$CONH_2$	n.c.	n.c.
12	Ac-*Lys*-**Aeg(Azo)**-gcagtgtttcttgg-*Lys*-$CONH_2$	71.5[b] ± 0.7	71.5 ± 0.4
13	Ac-*Lys*-gg**Aeg(Azo)**agtgtttcttgg-*Lys*-$CONH_2$	62.7[b] ± 0.3	63.0 ± 0.3
14	Ac-*Lys*-ggcagt**Aeg(Azo)**tttcttgg-*Lys*-$CONH_2$	57.3[b] ± 0.3	58.0 ± 0.3
15	Ac-*Lys*-ggcagtgtttcttg**Aeg(Azo)**-*Lys*-$CONH_2$	70.0[b] ± 0.8	73.2 ± 0.3
16	Ac-*Lys*-ggc**Aeg(Azo)**gtgtttc**Aeg(Azo)**tgg-*Lys*-$CONH_2$	42.1[b] ± 0.6	44.5 ± 0.6
17	Ac-*Lys*-gg**Aeg(Azo)**agtg**Aeg(Azo)**ttct**Aeg(Azo)**gg-*Lys*-$CONH_2$	n.c.	n.c.
18	Ac-*Lys*-ggcagtgtttcttgg-*Lys*-$CONH_2$	74.8 ± 0.3	
19	Ac-*Lys*-tgagtgcgtctgttg-*Lys*-$CONH_2$	n.c.	
20	Ac-ggcagtgtttct-$CONH_2$	64.5[c]	

[a]This value might be approximate according to its 1st derivative (Figure 3B); [b]PNA and ssDNA (5'-GTG AGC CAA GAA ACA CTG CCT-3') were isomerized to the *cis*-form after hybridization, following reported procedures [36]; [c]theoretical value calculated by PNA Bio Tools (http://www.pnabio.com); n.c. = not calculated. Mean values derived from two independent experiments; Aeg = *N*-(2-aminoethyl)glycine.

The incorporation of the visible-light responsive azobenzene (PNA **3**) stabilized the duplex in comparison with the Aeg(Ac)-modified analogue **5**. However, the T_M of **3** is 14 °C lower than the one calculated for the unmodified PNA analogue (**20**). Unfortunately, no difference between isomers was observed. The potential of the functionality of our compounds could be enhanced by both changing the localization and the number of incorporated photoswitches. To try to maintain the cooperative base pairing, we synthesized longer PNA conjugates (**6**–**11**, **18** and **19**) with flanking lysines, which improved the solubility of

the probes. In addition, we compared our probes with the ones that contained the classical unmodified azobenzene moiety (Azo) (PNA **12**–**17**). The lower stability of the unmodified *cis*-Azo forced us to perform the isomerization after duplex hybridization, which resulted in only a constant 36% *cis*-isomer rate. The obtained T_M values suggested that the localization of the oF$_4$Azo affects both the duplex stability and isomer differences. Thus, the incorporation of oF$_4$Azo near the center of the PNA (**7** and **8**) sequence dramatically destabilized the PNA/DNA duplex (ΔT_M = 18 °C), which agrees with excellent capacity of PNAs for effectively discriminate between single base mismatches. However, when the exchanged base is at either the N- or C-terminus of the PNA (**6** and **9**) the effect is not that dramatic. As reported in the precedent of azobenzene-PNA [51], the C-terminus modification displayed the highest isomer difference but modest, in our case. Furthermore, always when a clear difference between isomers was detected, the duplexes containing the *trans*-oF$_4$Azo were more stable than those with the *cis*-form. In addition, we tested PNAs with the photoswitch at two (**10**) and three positions (**11**). The T_M uniformly decreased with the number of oF$_4$Azo to the point that the probe **11** with three oF$_4$Azo behaved as the scramble PNA control **19**; this means, it did not form a stable duplex. More interestingly, we could observe an improved T_M difference between the *trans*- and *cis*-PNA$_{15}$(oF$_4$Azo)$_2$ **10** (up to ≈3.7 °C), which was the best for our system.

Azobenzene (Azo)-containing PNAs behaved similarly to PNA(oF$_4$Azo) (Table 2), which verified that the fluorine substitution did not affected the binding properties. The differences between isomers were also qualitatively consistent with a slight improvement for the case of the dual-labelled PNA(oF$_4$Azo) **10**.

To corroborate our results, we developed a strand-displacement assay using fluorescence as readout. We designed a system based on three molecules (Figure 4): a black hole quencher (BHQ)-labelled single-strand (ss) DNA template, a complementary fluorescein (FAM)-labelled ssDNA and the PNA of interest. In this framework, the PNA could bind the BHQ-ssDNA; thus, its addition to the quenched BHQ/FAM-DNA duplex would trigger an exchange reaction and the release of the FAM-ssDNA. The FAM probe and the PNAs shared the same 15 base-pair sequence (Table S2, Supporting Information File 1). Fluorescence spectroscopy determined the hybridization degree and, in turn, the effect of the photoswitch.

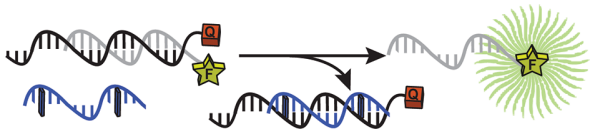


Figure 4: Outline of the displacement assay principle, in which a photoswitchable PNA probe (blue) hybridizes to a complementary quencher-labelled single-stranded (ss) DNA (black) and replaces a fluorescent-labelled ssDNA (grey); F = fluorescein; Q = black hole quencher; blue rectangle = tetra-*ortho*-fluoroazobenzene moiety.

After optimization, we found the following conditions: 0.75 μM quenched double-stranded (ds) DNA, 2 equiv PNA for 8 hours at 37 °C, as the best ones for our assay performance. As expected, the formed FAM/BHQ-dsDNA quenched effectively the

Table 3: Normalized increase of fluorescence signal derived from the strand-displacement assays.[a]

Compound	Fluorescence increase at 37 °C [%]		Fluorescence increase at 30 °C [%]	
	15-mer FAM-ssDNA		11-mer FAM-ssDNA	
	cis	*trans*	*cis*	*trans*
6	36.8 ± 1.2	36.3 ± 1.3	69.9 ± 3.4	75.8 ± 2.6
7	43.1 ± 1.7	45.9 ± 1.0	78.1 ± 4.3	82.1 ± 1.2
8	44.0 ± 2.0	45.0 ± 1.3	67.0 ± 0.9	72.7 ± 1.9
9	46.1 ± 1.3	49.0 ± 1.5	84.7 ± 2.1	82.7 ± 3.5
10	n.d.	n.d.	37.8 ± 2.2	46.3 ± 2.2
11	n.d.	n.d.	n.d.	n.d.
18	98.8 ± 1.4		94.5 ± 3.1	
19	17.0 ± 0.4		27.9 ± 3.2	
FAM-ssDNA	100		100	
background[b]	0		0	
BHQ/FAM-dsDNA	24.5 ± 0.3		36.6 ± 0.3	

[a]Percentages calculated according to the measured endpoint (8 h) fluorescence intensity values and considering the FAM-ssDNA intensity as 100%; [b]it represents the measurement of the PBS buffer: 140 mM NaCl, 10 mM Na_2HPO_4, 2.7 mM KCl, 1.8 mM KH_2PO_4, pH 8.0. Mean values derived from two independent experiments; n.d. = no displacement observed.

fluorescence of FAM-ssDNA (Figure S46, Supporting Information File 1), which was quantitatively restored in the presence of the unmodified PNA **18**. The effect of the scrambled PNA **19** is the opposite, i.e., signal decrease. We determined a slightly lower fluorescence value than in the case of BHQ-ssDNA; this can be probably attributed to the quenching ability of both PNA probes [52]. Along these lines, the quenching ability of oF$_4$Azo-containing PNA was evaluated (Figure S46, Supporting Information File 1; Table 3) and neglected because of the low impact.

Regarding the photoswitchable PNAs, we observed a correlation between the T_M and the increase of fluorescence in the displacement-strand assays. Thus, the general trend is: the higher the T_M is, the better is their strand-exchange ability (higher exchange and faster) (Table S3, Supporting Information File 1). PNAs **10** and **11** bearing two and three oF$_4$Azo moieties, respectively, did not cause an increase of fluorescence. While such result was expected for **11**, according to the melting experiments, the unfortunate outcome of **10** could be probably attributed to its low T_M in comparison with the quenched dsDNA one (≈40 °C versus 61.5 °C; Table 2, Figure S37, Supporting Information File 1). This would also explain the incomplete displacement (<50%, Table 3, left) for all modified PNAs. In order to improve our method, we tested a shorter 11-mer FAM-ssDNA provided with a toehold under lower temperatures (30 °C). This overhang together with the length of the labelled oligonucleotide must accelerate the strand exchange [53]. Indeed, the displacement was facilitated, reaching almost quantitative exchanged (70–85%; Table 3, right) with faster kinetics (Figure 5B) without compromising the specificity of the system. More importantly, this new set up led to slightly higher differences between isomers and pointed out the dual-labelled probe **10** as the best one, which is consistent with the melting experiments (Table 2 and Figure 3). Among the single mutated PNAs, those with lower T_M, displayed the best performance in our kinetics studies (Figure 5B).

Finally, in an attempt of gaining insight into the general low photoresponsivity, we performed CD (Figure S53, Supporting Information File 1) and UV–vis (Figures S54 and S55, Supporting Information File 1) experiments. The joint-evaluation of these results suggested that the photoswitch is located inside of the PNA–DNA duplex (Figure S53, Supporting Information File 1) but it may not effectively intercalate since pre-hybridization did not affect the isomerization efficiency (Figure S55, Supporting Information File 1). This would explain the low observed photoresponsivity.

Conclusion

We have successfully synthesized two novel types of visible-light photoresponsive PNAs by coupling on-resin the corresponding molecular transducer. In particular, we focused on the tetra-*ortho*-fluoroazobenzene (oF$_4$Azo) and the hemithioindigo (HTI) photoswitches; the latter has not been studied in the context of photoregulation of oligonucleotides before. The UV–vis measurements of these probes suggested that the PNA(oF$_4$Azo) displayed superior photochemical properties to control oligonucleotide hybridization by irradiation. Thus, for the case of the PNA(HTI) just 47% of *trans*-isomer was

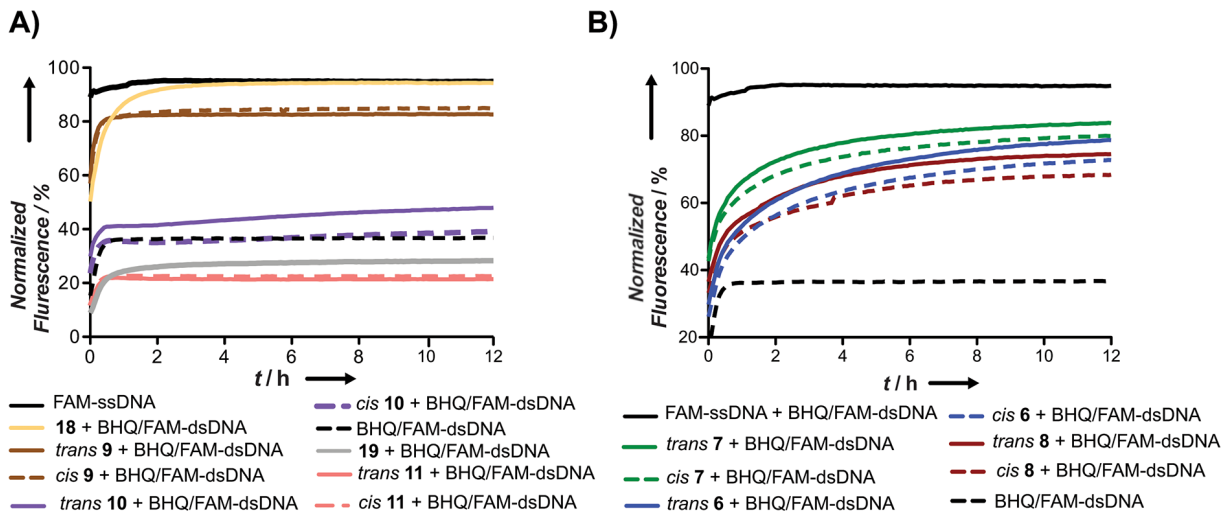


Figure 5: Time-dependent fluorescence signals from two independent experiments at 520 nm of 0.75 μM FAM/BHQ-dsDNA solutions in PBS buffer (140 mM NaCl, 10 mM Na_2HPO_4, 2.7 mM KCl, 1.8 mM KH_2PO_4, pH 8.0) with 2 equiv of the corresponding PNAs **6**–**11**, **18** and **19** placed in 96-well plates and covered with paraffin oil; fluorescence intensities were measured every 5 min during 12 h at 30 °C; PNA code: **6**: blue, **7**: green, **8**: maroon, **9**: brown, **10**: purple, **11**: coral, **18**: yellow and **19**: gray; solid line for *trans*-isomers and dashed line for *cis*-isomers. Black lines controls: solid: FAM-ssDNA without PNA and under the same conditions; dashed: BHQ/FAM-dsDNA.

detected upon irradiation at 405 nm. In addition, the stability of this isomer is compromised. On the contrary, PNA(oF$_4$Azo) had better conversions and high stability of the non-thermodynamically isomer, even at 90 °C. Both melting experiments and strand displacement assays demonstrated that mismatches had a dramatic effect on the binding affinity of the PNA, which was slightly compensated by the incorporation of oF$_4$Azo. We observed modest, yet clear, differences in the formation of PNA/DNA duplexes depending on the number and the localization of the oF$_4$Azo. Further work on increasing the photoresponsivity by exploring different connectors and approaches beyond the base-surrogate approaches is necessary. However, we first demonstrated the great potential oF$_4$Azo in the context of both PNA and oligonucleotide hybridization. Thus, we believe that the excellent photochemical properties of the oF$_4$Azo together with the use of the visible-light irradiation may overcome some of the current limitations for in vivo photoregulation of gene expression and related enzymatic reactions in the near future. Besides, having at our disposal such antisense probes, whose activation is reversibly controlled, will contribute to the deciphering of biological pathways. Furthermore, the exceptional stability of the *cis*-isomer may open new venues of this artificial photoswitchable oligonucleotide in other fields different from life science such as nanotechnology and materials science.

Supporting Information

Supporting Information File 1

Detailed experimental procedures, synthesis, characterization data.
[https://www.beilstein-journals.org/bjoc/content/supplementary/1860-5397-15-243-S1.pdf]

Acknowledgements

The authors gratefully acknowledge: Benedikt Heinrich for initial synthesis assistance, Prof. Alexander Brehm for accessibility to the Mx3000P QPCR system (Agilent Technologies, USA), N. Frommknecht for construction of custom-made LED lamps and the DFG for co-financing the AccuTOF GCv 4G (JEOL) Time of Flight (TOF) mass spectrometer (grant: INST 160/622-1 FUGG to Dr. U. Linne). This work was financially supported by German Fulbright Commission and the DFG program SPP1926 'Next Generation Optogenetics'. O.V. thanks German Fulbright Commission for the Fulbright-Cottrell Award 2016.

ORCID® iDs

Lei Zhang - https://orcid.org/0000-0002-7573-3191
Greta Linden - https://orcid.org/0000-0002-7384-084X
Olalla Vázquez - https://orcid.org/0000-0002-7555-1865

References

1. Lubbe, A. S.; Szymanski, W.; Feringa, B. L. *Chem. Soc. Rev.* **2017,** *46,* 1052–1079. doi:10.1039/c6cs00461j
2. Ando, H.; Furuta, T.; Tsien, R. Y.; Okamoto, H. *Nat. Genet.* **2001,** *28,* 317–325. doi:10.1038/ng583
3. Monroe, W. T.; McQuain, M. M.; Chang, M. S.; Alexander, J. S.; Haselton, F. R. *J. Biol. Chem.* **1999,** *274,* 20895–20900. doi:10.1074/jbc.274.30.20895
4. Shi, Y.; Koh, J. T. *ChemBioChem* **2004,** *5,* 788–796. doi:10.1002/cbic.200300823
5. Shimizu-Sato, S.; Huq, E.; Tepperman, J. M.; Quail, P. H. *Nat. Biotechnol.* **2002,** *20,* 1041–1044. doi:10.1038/nbt734
6. Tang, X.; Dmochowski, I. J. *Mol. BioSyst.* **2007,** *3,* 100–110. doi:10.1039/b614349k
7. Mayer, G.; Heckel, A. *Angew. Chem., Int. Ed.* **2006,** *45,* 4900–4921. doi:10.1002/anie.200600387
8. Li, L.; Tong, R.; Chu, H.; Wang, W.; Langer, R.; Kohane, D. S. *Proc. Natl. Acad. Sci. U. S. A.* **2014,** *111,* 17099–17103. doi:10.1073/pnas.1420105111
9. Wang, Y.; Wu, L.; Wang, P.; Lv, C.; Yang, Z.; Tang, X. *Nucleic Acids Res.* **2012,** *40,* 11155–11162. doi:10.1093/nar/gks840
10. Lucas, T.; Schäfer, F.; Müller, P.; Eming, S. A.; Heckel, A.; Dimmeler, S. *Nat. Commun.* **2017,** *8,* 15162. doi:10.1038/ncomms15162
11. Deiters, A.; Garner, R. A.; Lusic, H.; Govan, J. M.; Dush, M.; Nascone-Yoder, N. M.; Yoder, J. A. *J. Am. Chem. Soc.* **2010,** *132,* 15644–15650. doi:10.1021/ja1053863
12. Yamazoe, S.; Liu, Q.; McQuade, L. E.; Deiters, A.; Chen, J. K. *Angew. Chem., Int. Ed.* **2014,** *53,* 10114–10118. doi:10.1002/anie.201405355
13. Shen, X.; Corey, D. R. *Nucleic Acids Res.* **2018,** *46,* 1584–1600. doi:10.1093/nar/gkx1239
14. Lerch, M. M.; Hansen, M. J.; van Dam, G. M.; Szymanski, W.; Feringa, B. L. *Angew. Chem., Int. Ed.* **2016,** *55,* 10978–10999. doi:10.1002/anie.201601931
15. Hüll, K.; Morstein, J.; Trauner, D. *Chem. Rev.* **2018,** *118,* 10710–10747. doi:10.1021/acs.chemrev.8b00037
16. Asanuma, H.; Ito, T.; Yoshida, T.; Liang, X.; Komiyama, M. *Angew. Chem., Int. Ed.* **1999,** *38,* 2393–2395. doi:10.1002/(sici)1521-3773(19990816)38:16<2393::aid-anie2393>3.0.co;2-7
17. Ito, H.; Liang, X.; Nishioka, H.; Asanuma, H. *Org. Biomol. Chem.* **2010,** *8,* 5519–5524. doi:10.1039/c0ob00432d
18. Schierling, B.; Noel, A.-J.; Wende, W.; Hien, L. T.; Volkov, E.; Kubareva, E.; Oretskaya, T.; Kokkinidis, M.; Rompp, A.; Spengler, B.; Pingoud, A. *Proc. Natl. Acad. Sci. U. S. A.* **2010,** *107,* 1361–1366. doi:10.1073/pnas.0909444107
19. Zou, Y.; Chen, J.; Zhu, Z.; Lu, L.; Huang, Y.; Song, Y.; Zhang, H.; Kang, H.; Yang, C. J. *Chem. Commun.* **2013,** *49,* 8716–8718. doi:10.1039/c3cc44188a
20. Zhou, M.; Liang, X.; Mochizuki, T.; Asanuma, H. *Angew. Chem., Int. Ed.* **2010,** *49,* 2167–2170. doi:10.1002/anie.200907082
21. Liu, M.; Asanuma, H.; Komiyama, M. *J. Am. Chem. Soc.* **2006,** *128,* 1009–1015. doi:10.1021/ja055983k
22. Asanuma, H.; Liang, X.; Nishioka, H.; Matsunaga, D.; Liu, M.; Komiyama, M. *Nat. Protoc.* **2007,** *2,* 203–212. doi:10.1038/nprot.2006.465
23. Liang, X.; Wakuda, R.; Fujioka, K.; Asanuma, H. *FEBS J.* **2010,** *277,* 1551–1561. doi:10.1111/j.1742-4658.2010.07583.x

24. Kamiya, Y.; Takagi, T.; Ooi, H.; Ito, H.; Liang, X.; Asanuma, H. *ACS Synth. Biol.* **2015,** *4,* 365–370. doi:10.1021/sb5001092
25. Ogasawara, S.; Maeda, M. *Bioorg. Med. Chem. Lett.* **2011,** *21,* 5457–5459. doi:10.1016/j.bmcl.2011.06.119
26. Asanuma, H.; Ishikawa, T.; Yamano, Y.; Murayama, K.; Liang, X. *ChemPhotoChem* **2019,** *3,* 418–424. doi:10.1002/cptc.201900060
27. Brieke, C.; Heckel, A. *Chem. – Eur. J.* **2013,** *19,* 15726–15734. doi:10.1002/chem.201302640
28. Lewis, F. D.; Wu, Y.; Liu, X. *J. Am. Chem. Soc.* **2002,** *124,* 12165–12173. doi:10.1021/ja026941o
29. Cahová, H.; Jäschke, A. *Angew. Chem., Int. Ed.* **2013,** *52,* 3186–3190. doi:10.1002/anie.201209943
30. Lubbe, A. S.; Liu, Q.; Smith, S. J.; de Vries, J. W.; Kistemaker, J. C. M.; de Vries, A. H.; Faustino, I.; Meng, Z.; Szymanski, W.; Herrmann, A.; Feringa, B. L. *J. Am. Chem. Soc.* **2018,** *140,* 5069–5076. doi:10.1021/jacs.7b09476
31. Nielsen, P. E.; Egholm, M.; Berg, R. H.; Buchardt, O. *Science* **1991,** *254,* 1497–1500. doi:10.1126/science.1962210
32. Janowski, B. A.; Kaihatsu, K.; Huffman, K. E.; Schwartz, J. C.; Ram, R.; Hardy, D.; Mendelson, C. R.; Corey, D. R. *Nat. Chem. Biol.* **2005,** *1,* 210–215. doi:10.1038/nchembio724
33. Mollegaard, N. E.; Buchardt, O.; Egholm, M.; Nielsen, P. E. *Proc. Natl. Acad. Sci. U. S. A.* **1994,** *91,* 3892–3895. doi:10.1073/pnas.91.9.3892
34. Li, J.; Chen, M.; Zhang, H.; Liu, S.; Liu, J. *Chin. Sci. Bull.* **2008,** *53,* 3077–3080. doi:10.1007/s11434-008-0432-0
35. Sawada, S.; Takao, T.; Kato, N.; Kaihatsu, K. *Molecules* **2017,** *22,* 1840. doi:10.3390/molecules22111840
36. Stafforst, T.; Hilvert, D. *Angew. Chem., Int. Ed.* **2010,** *49,* 9998–10001. doi:10.1002/anie.201004548
37. Albert, L.; Xu, J.; Wan, R.; Srinivasan, V.; Dou, Y.; Vázquez, O. *Chem. Sci.* **2017,** *8,* 4612–4618. doi:10.1039/c7sc00137a
38. Noonan, E. J.; Place, R. F.; Pookot, D.; Basak, S.; Whitson, J. M.; Hirata, H.; Giardina, C.; Dahiya, R. *Oncogene* **2009,** *28,* 1714–1724. doi:10.1038/onc.2009.19
39. Ropero, S.; Esteller, M. *Mol. Oncol.* **2007,** *1,* 19–25. doi:10.1016/j.molonc.2007.01.001
40. Ratilainen, T.; Holmén, A.; Tuite, E.; Haaima, G.; Christensen, L.; Nielsen, P. E.; Nordén, B. *Biochemistry* **1998,** *37,* 12331–12342. doi:10.1021/bi9808722
41. Yue, S.; Li, J.; Zhang, J.; Lu, J.; Chen, M. *Chin. Sci. Bull.* **2009,** *54,* 4753–4755. doi:10.1007/s11434-009-0554-z
42. Jarikote, D. V.; Köhler, O.; Socher, E.; Seitz, O. *Eur. J. Org. Chem.* **2005,** 3187–3195. doi:10.1002/ejoc.200500201
43. Bléger, D.; Schwarz, J.; Brouwer, A. M.; Hecht, S. *J. Am. Chem. Soc.* **2012,** *134,* 20597–20600. doi:10.1021/ja310323y
44. Cordes, T.; Elsner, C.; Herzog, T. T.; Hoppmann, C.; Schadendorf, T.; Summerer, W.; Rück-Braun, K.; Zinth, W. *Chem. Phys.* **2009,** *358,* 103–110. doi:10.1016/j.chemphys.2008.12.027
45. Wiedbrauk, S.; Dube, H. *Tetrahedron Lett.* **2015,** *56,* 4266–4274. doi:10.1016/j.tetlet.2015.05.022
46. Knie, C.; Utecht, M.; Zhao, F.; Kulla, H.; Kovalenko, S.; Brouwer, A. M.; Saalfrank, P.; Hecht, S.; Bléger, D. *Chem. – Eur. J.* **2014,** *20,* 16492–16501. doi:10.1002/chem.201404649
47. Albert, L.; Peñalver, A.; Djokovic, N.; Werel, L.; Hoffarth, M.; Ruzic, D.; Xu, J.; Essen, L.-O.; Nikolic, K.; Dou, Y.; Vázquez, O. *ChemBioChem* **2019,** *20,* 1417–1429. doi:10.1002/cbic.201800737
48. Heinrich, B.; Bouazoune, K.; Wojcik, M.; Bakowsky, U.; Vázquez, O. *Org. Biomol. Chem.* **2019,** *17,* 1827–1833. doi:10.1039/c8ob02343c
49. Asanuma, H.; Liang, X.; Yoshida, T.; Komiyama, M. *ChemBioChem* **2001,** *2,* 39–44. doi:10.1002/1439-7633(20010105)2:1<39::aid-cbic39>3.0.co;2-e
50. Borer, P. N.; Dengler, B.; Tinoco, I., Jr.; Uhlenbeck, O. C. *J. Mol. Biol.* **1974,** *86,* 843–853. doi:10.1016/0022-2836(74)90357-x
51. Wickstrom, E.; Choob, M.; Urtishak, K. A.; Tian, X.; Sternheim, N.; Talbot, S.; Archdeacon, J.; Efimov, V. A.; Farber, S. A. *J. Drug Targeting* **2004,** *12,* 363–372. doi:10.1080/10611860412331285242
52. Nazarenko, I.; Pires, R.; Lowe, B.; Obaidy, M.; Rashtchian, A. *Nucleic Acids Res.* **2002,** *30,* 2089–2195. doi:10.1093/nar/30.9.2089
53. Zhang, D. Y.; Turberfield, A. J.; Yurke, B.; Winfree, E. *Science* **2007,** *318,* 1121–1125. doi:10.1126/science.1148532

License and Terms

This is an Open Access article under the terms of the Creative Commons Attribution License (http://creativecommons.org/licenses/by/4.0). Please note that the reuse, redistribution and reproduction in particular requires that the authors and source are credited.

The license is subject to the *Beilstein Journal of Organic Chemistry* terms and conditions: (https://www.beilstein-journals.org/bjoc)

The definitive version of this article is the electronic one which can be found at: doi:10.3762/bjoc.15.243

BEILSTEIN JOURNAL OF ORGANIC CHEMISTRY

A toolbox of molecular photoswitches to modulate the CXCR3 chemokine receptor with light

Xavier Gómez-Santacana[1,2], Sabrina M. de Munnik[1], Tamara A. M. Mocking[1], Niels J. Hauwert[1], Shanliang Sun[1], Prashanna Vijayachandran[1], Iwan J. P. de Esch[1], Henry F. Vischer[1], Maikel Wijtmans[*1] and Rob Leurs[*1]

Full Research Paper

Open Access

Address:
[1]Division of Medicinal Chemistry, Amsterdam Institute for Molecules Medicines and Systems (AIMMS), Vrije Universiteit Amsterdam, 1081 HZ, Amsterdam, The Netherlands and [2]present address: Institute of Functional Genomics, Université de Montpellier, Unité 5302 CNRS and Unité U1191, INSERM, 34090 Montpellier, France

Email:
Maikel Wijtmans[*] - m.wijtmans@vu.nl; Rob Leurs[*] - r.leurs@vu.nl

* Corresponding author

Keywords:
azo compounds; chemokine receptor; efficacy photoswitching; G protein-coupled receptors; photopharmacology

Beilstein J. Org. Chem. **2019,** *15,* 2509–2523.
doi:10.3762/bjoc.15.244

Received: 14 July 2019
Accepted: 27 September 2019
Published: 23 October 2019

This article is part of the thematic issue "Molecular switches".

Guest Editor: W. Szymanski

© 2019 Gómez-Santacana et al.; licensee Beilstein-Institut.
License and terms: see end of document.

Abstract

We report a detailed structure–activity relationship for the scaffold of VUF16216, a compound we have previously communicated as a small-molecule efficacy photoswitch for the peptidergic chemokine GPCR CXCR3. A series of photoswitchable azobenzene ligands was prepared through various synthetic strategies and multistep syntheses. Photochemical and pharmacological properties were used to guide the design iterations. Investigations of positional and substituent effects reveal that halogen substituents on the *ortho*-position of the outer ring are preferred for conferring partial agonism on the *cis* form of the ligands. This effect could be expanded by an electron-donating group on the *para*-position of the central ring. A variety of efficacy differences between the *trans* and *cis* forms emerges from these compounds. Tool compounds VUF15888 (**4d**) and VUF16620 (**6e**) represent more subtle efficacy switches, while VUF16216 (**6f**) displays the largest efficacy switch, from antagonism to full agonism. The compound class disclosed here can aid in new photopharmacology studies of CXCR3 signaling.

Introduction

Photopharmacology is an emerging discipline at the interface of medicinal chemistry and photochemistry. Classical medicinal chemistry approaches make use of small-molecule ligands binding a target protein, thereby modifying its activity. Photopharmacological approaches use light-sensitive photochromic ligands that provide an advantageous and more precise pharmacological alternative, especially with respect to spatial and temporal precision [1,2]. Photochromic ligands usually

contain a molecular photoswitch (photoswitchable moiety) that under certain wavelengths of illumination undergoes an isomerization event, thereby changing the properties of the molecule and the binding affinity for the target protein [3-5] or the intrinsic functional activity (efficacy) [6,7]. Despite the considerable number of photoswitches reported to date, such as spiropyrans, diarylethenes, fulgides or azobenzenes, the most widely used moiety in the photopharmacology is the latter one. One of the main reasons is that an azobenzene has a relatively simple structure that can resemble various biaryl moieties of bioactive compounds: two aromatic rings linked with a bridge (e.g., amide, ether, alkane or alkyne) [8]. In the case of azobenzene the bridge is a diazene group (also called azo group) and depending on the wavelength of illumination, a linear *trans*-isomer or a bent *cis*-isomer can be obtained [9]. If certain biaryl moieties are replaced by an azobenzene (i.e., azologization approach), there is a relatively good chance that one of the resulting photoisomers will have a spatial disposition similar to the original biaryl unit and, therefore, a similar biological activity that might change upon isomerization of the azobenzene [8]. The second reason for the success of azobenzene in the photopharmacology field is the robust photoisomerization. It provides typically high yields of photoisomerization with relatively low intensity of light and minimal photobleaching even over hundreds of cycles. A third reason is the relatively high synthetic accessibility to azobenzenes. All these properties make azobenzene compounds ideal molecular photoswitches to control protein activity and physiological events with light.

A number of protein targets have been explored with photochromic small-molecule ligands, such as ion channels, microtubules, enzymes and GPCRs (G protein-coupled receptors) [1,10]. We focus our photopharmacology research on GPCRs [3,7,11], which constitute a superfamily of membrane proteins that regulate many physiological processes [12]. Despite the high relevance of GPCRs both functionally and as a drug target [12], the first synthetic GPCR photochromic small-molecule ligands appeared only five years ago [13-15]. Since then, photopharmacology has been explored on GPCRs targeted endogenously by small molecules [3,4,11,16-20], small peptides [5,13] and larger peptides [7,21,22]. Most of the targeted GPCRs belong to the three rhodopsin-, secretin- and glutamate-like subfamilies and involve GPCRs that endogenously bind small-molecule ligands [10]. The ensuing photochromic GPCR ligands are usually orthosteric and the photoswitching generally affects the functional potency [4,11,23] and/or the binding affinity [3-5,11] of the ligand (Figure 1A). However, as mentioned, GPCRs that endogenously bind large molecules (large peptides or proteins) can be also targeted by allosteric photochromic ligands. In an initial communication [7], we recently reported a photochromic ligand class that is based on azologization of a biaryl ligand class [24] and that activates the chemokine CXCR3 receptor (CXCR3), a GPCR endogenously activated by large peptides CXCL9, CXCL10 and CXCL10 and involved in inflammatory responses. In fact, the six compounds reported in that study represent the first photochromic small-molecule class that harbors a dynamic efficacy photoswitch (from antagonism to agonism) on a peptidergic GPCR (Figure 1B). Here, we report the rationale and synthetic strategies behind this series of compounds, a detailed analysis of the molecular determinants that control the efficacy of the ligands (SAR, structure-activity relationship) and a toolbox of pharmacologically useful photoswitchable small-molecule CXCR3 agonists.

Results and Discussion

Azologization design

The chemokine receptor CXCR3 is endogenously activated by the chemotactic peptides CXCL11, CXCL10 and CXCL9. Synthetic small-molecule ligands can also bind to CXCR3 [25]. Multiple small-molecule CXCR3 antagonist scaffolds have been disclosed but small-molecule CXCR3 agonists are scarce and are mostly limited to peptidomimetics [25], which makes our published biaryl series a notable exception [24]. The general scaffold of these biaryl ligands consists of a polycycloaliphatic anchor and a biaryl moiety both linked to an ammonium ion. Depending on the substitution pattern of this biaryl moiety, a broad spectrum of efficacies for CXCR3 can be obtained, i.e., from antagonists to partial agonists and full agonists (Figure 1C) [24]. *Meta* and *para*-substitution yields antagonists (exemplified by **1a**,**b**), while o*rtho*-substitution with halogen atoms provides agonists, exemplified by partial agonist **1c** and equal full agonists **1d** and **1e** (VUF11418, Figure 2A). A tentative explanation for this efficacy switch includes a variation of the dihedral angle of the biaryl moiety, an increase of the electron density in the biaryl unit and/or a postulated halogen bond of the halogen substituent to the binding site of the receptor [24].

In order to obtain an efficacy photoswitching, we opted for replacing the biaryl moiety for an azobenzene in an azologization approach (Figure 1D) with the expectation that the isomerization of the azobenzene would provide changes in 3D shape that are similar to those observed in the biaryl series. To reinforce this hypothesis, molecular alignments were performed with Molecular Operating Environment (MOE) software [26] in which **1e** was used as a model for full agonism (Figure 2). Its 3D structure was superposed with both the *trans* and *cis*-isomers of parent azobenzene compound **2a** allowing flexibility of the molecules except for the conformation of the *trans* and *cis*-azobenzene moieties, which were fixed in the lowest energy conformation to ensure a shape that has also been vali-

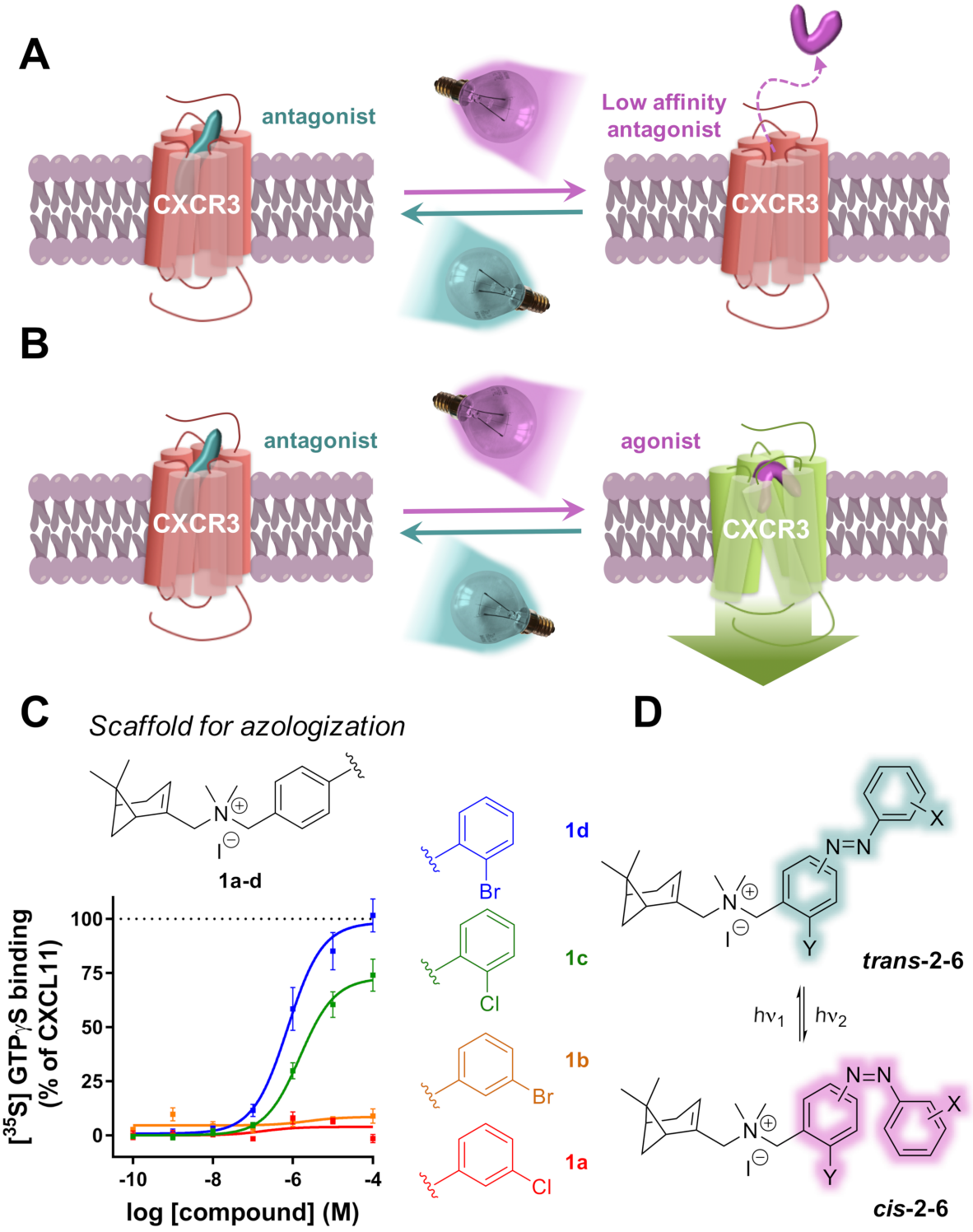


Figure 1: Design of the CXCR3 efficacy photowitchable ligands. A,B) Schematic representation of a GPCR photochromic ligand that photoisomerizes and thereby photoswitches (A) binding affinity and/or (B) functional efficacy. Red represents the inactive GPCR, while green represents the active GPCR. C) General structure and exemplary functional dose-response curves of the parent biaryl family of CXCR3 ligands disclosed in Wijtmans et al. [24], in which *ortho* substitution on the outer aromatic ring gives partial or full agonists, while *meta* substitution provides antagonists. D) Azologization of the biaryl moiety provides a family of photowitchable CXCR3 small-molecule ligands.

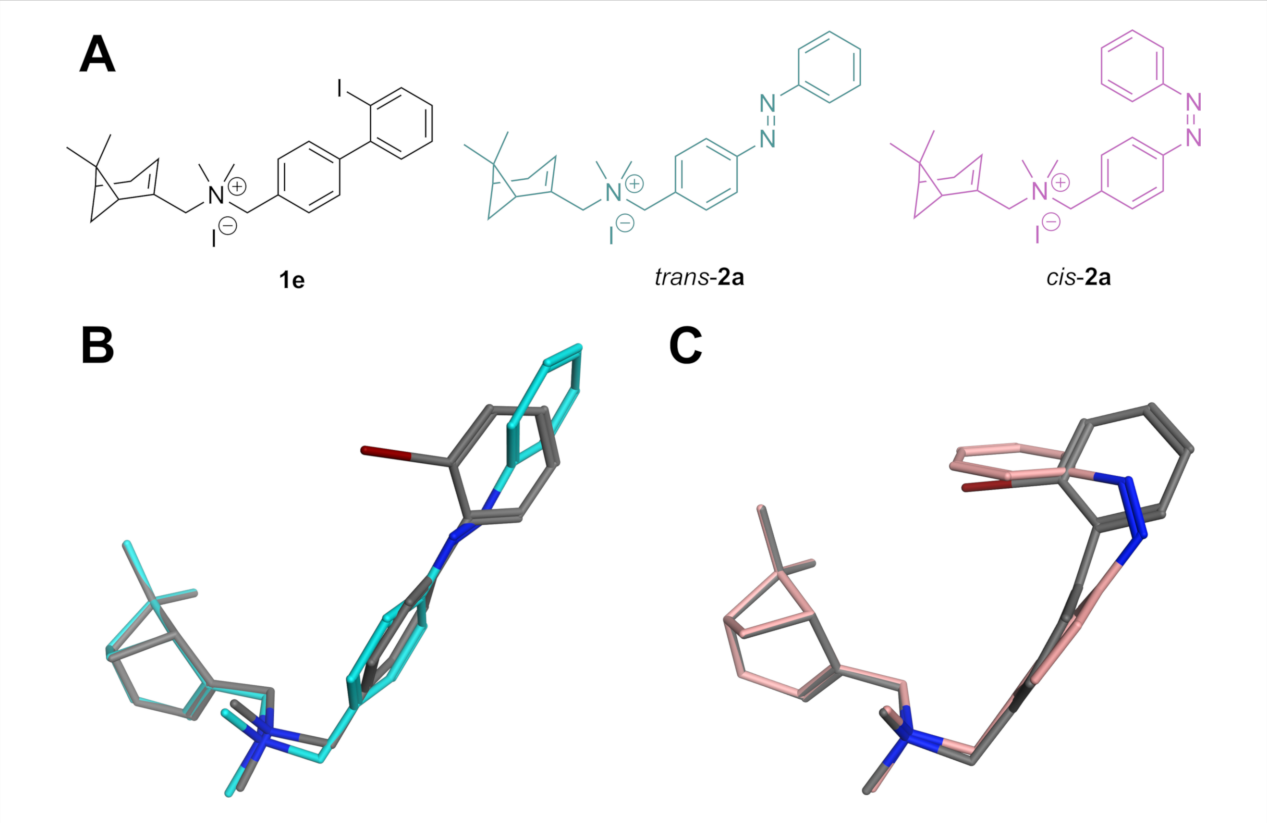


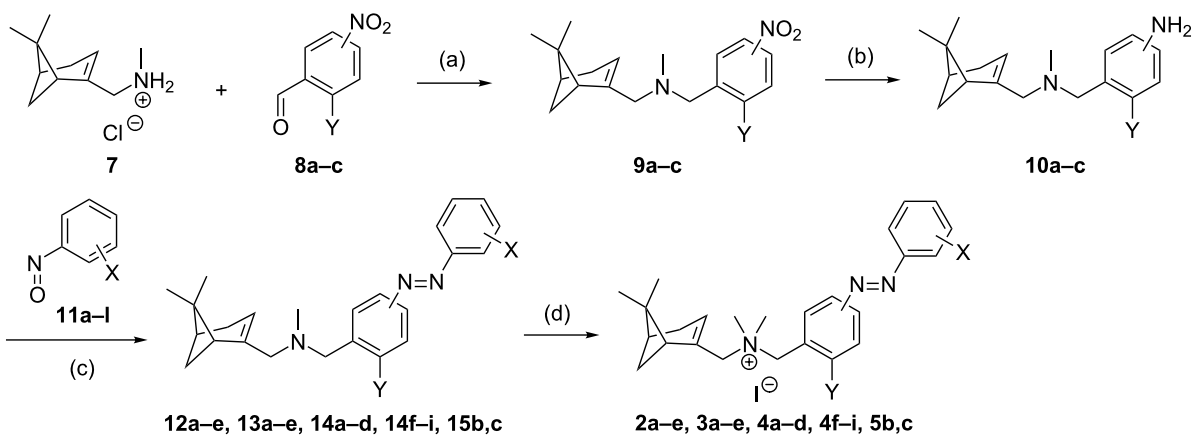
Figure 2: Conformational alignment of a biaryl CXCR3 agonist with a designed azobenzene analogue. A) 2D structure of biaryl CXCR3 agonist **1e** and designed ligand *trans*-**2a** and *cis*-**2a**. B,C) Alignments of **1e** (grey carbon atoms) and **2a**, in which the *trans* and *cis*-isomers are shown in (B) turquoise and (C) light magenta carbon atoms, respectively. The iodine atom is shown in red for clarity.

dated by crystallographic data [27]. The results show a reasonable overall alignment between *trans*-**2a** and the agonist **1e** (Figure 2B), since the planar azobenzene is partially overlapping with the biaryl moiety. However, the two aromatic rings of both compounds can evidently not be in exactly the same plane because the azobenzene moiety is planar while the tilting of the dihedral angle of the biaryl moiety of **1e** was speculated to be associated with its agonist activity (vide supra) [24]. The alignment of the *cis*-isomer of **2a** with agonist **1e** is very different. The outer aromatic ring of *cis*-**2a** goes out of plane and is now occupying the space that is also occupied by the iodine atom of **1e**. These calculations indicate that CXCR3 agonism is more likely to be associated with the *cis*-isomer than with the *trans*-isomer in our designed azobenzenes.

Synthesis of azobenzene analogues and exploration of substitution pattern on the outer aromatic ring

In addition to unsubstituted azobenzene analogue **2a,** we explored the substitution pattern of the outer aromatic ring with chlorine atoms in the *ortho*, *meta* and *para*-position (compounds **2b–d**, respectively) to also assess the possibility of agonism provided by a halogen bond. Compound **2e**, which contains a bromine atom in the *ortho*-position, was also tested since this atom type provides full agonist activity of parent **1d**. The synthesis of the compounds **2a–e** was performed according to the strategies depicted in Scheme 1. The intermediate **7** was prepared as described previously by us [28] and was used in a reductive amination with 4-nitrobenzaldehyde (**8a**) to give the corresponding tertiary amine **9a** in high yield. The nitro group of **9a** was subsequently reduced by $SnCl_2$ in high yield. The resulting aniline **10a** was used to obtain the azo compounds **12a–e** in varying yields through a Mills reaction with the corresponding nitroso compounds **11a–e**, which were commercially available or prepared as described in our previous communication [7]. A final methylation of the tertiary amine **12a–e** with MeI in DCM and subsequent precipitation with MTBE (methyl *tert*-butyl ether) gave **2a–e** as orange powders with ≥99% *trans*-isomer in moderate to high yield.

Next, we characterized the photochemical properties of **2a–e**, including absorption maxima, wavelengths of illumination and percentage of conversion from *trans* to *cis* in the photostationary state (PSS *cis*). First, UV–vis absorption spectra were measured in the dark and after illumination with a wavelength of 360 nm. In all cases the spectrum measured in the dark



Scheme 1: Synthetic strategies for compounds **2a–e**, **3a–e**, **4a–d**, **4f–i** and **5b,c** (Y = H, Cl). Reagents and conditions: (a) i) Et_3N (1.1–1.6 equiv), DCM, rt, 10–30 min; ii) $NaBH(OAc)_3$ (1.6 equiv), rt, 6–16 h, 91–97%; (b) $SnCl_2$ (5.0 equiv), EtOH, 75 °C, 2 h, 87%–quant; (c) AcOH/DCM, rt, 1–5 d, 23–73%, (d) MeI (20 equiv), DCM, rt, 6–72 h, 41–97%.

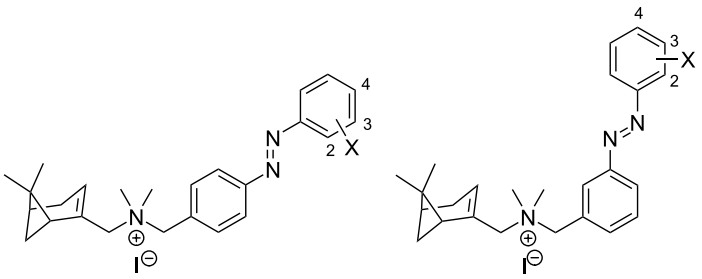
shows a large band between 320 and 330 nm that corresponds to the π–π* transition of the *trans*-isomer (Figure S1A, Supporting Information File 1). After irradiating with different wavelengths, the proportion of *trans* and *cis*-isomer varies to reach the PPS. For example, after irradiating with 360 nm the π–π* transition band of the *trans*-isomer can barely be observed, but a less intense wide band around 420 nm appears, which corresponds to the n–π* transition of the *cis*-isomer (Figure S1A, Supporting Information File 1). This indicates that, using 360 nm light, a PPS of high percentage of *cis*-isomer (PPS_{360}) can be reached. Literature evidence [7,29,30] suggests that this scaffold would have sufficiently long half-lives of the PSS state, i.e., the *cis*-isomer only slowly reverts to *trans* in the dark, which was confirmed by early-stage analyses on key compounds (data not shown). In fact, due to this bistable nature, the percentage of each photoisomer can be quantified by analytical chromatography (LC–MS). The integration wavelength (265 nm) was selected closely to the observed isosbestic point for most compounds to get an indication of mole ratios from the UV area ratios. For **2a–e** after illumination at 360 nm, PPS_{360} values of 79–90% of *cis*-isomer were obtained. We also tested 434, 460 nm and/or 494 nm to revert the isomerization process to PSS *trans* (Figure S1A, Supporting Information File 1). After re-illuminating the samples at 434 nm or 460 nm, the π–π* transition band of the *trans*-isomer re-appears, indicating a high percentage of *trans*-isomer at that PSS. The use of 494 nm affords less *trans* compound and is less efficient in achieving PSS *trans*.

Next, the CXCR3 binding properties of **2a–e** were measured (Table 1) in a competition binding assay versus displacement of a radiolabeled small-molecule CXCR3 antagonist ([^{3}H]-VUF11211 [31]). Values reported are mean ± SEM (Standard Error of the Mean). These experiments were performed with samples under dark conditions to ensure ≥99% *trans*-isomer and with samples previously illuminated with 360 nm light to obtain a high percentage of *cis* compound in the PSS_{360}. This assay setup is enabled by the bistable nature of the photoswitch (vide supra), maintaining integrity of both the *trans* and *cis*-isomer for the duration of the assay. Compounds **2a–e** under dark conditions (*trans*-isomers) bind CXCR3 with K_i values in the high nanomolar range. In contrast, compounds **2a–e** after 360 nm illumination bind CXCR3 with K_i values in the low micromolar range, although the observed photoinduced affinity shifts (PAS) are not large (<4.0-fold). To assess if the compounds have agonist or antagonist activity on CXCR3-mediated signaling, a single-dose functional [^{35}S]-GTPγS accumulation assay was performed with the compounds **2a–e** at 10 μM (Table 1). In this assay, we observed that most of the compounds are not activating the CXCR3 receptor in either *cis* or *trans* configuration, which indicates that the compounds bind to the receptor as antagonists. However, *cis*-**2b** and, more notably, *cis*-**2e** show a small partial agonist activity (11% and 23%, respectively) that gives a hint of a slight photoswitching of their efficacy. Both compounds have a halogen atom on the *ortho*-position of the outer ring, which seems to reaffirm the importance of the *ortho*-halogen atoms effect observed in the biaryl series [24]. However, the difference in efficacy between *cis* and *trans*-isomers (defined as PDE - photoinduced difference of efficacy) needed to be improved.

Optimization of positioning of azobenzene unit

Aiming to improve the position and directionality of the halogen atom, we next designed a subseries with the azo group at the *meta*-position of the central ring (scaffold **3**) instead of at

Table 1: Structures and results of photochemical, binding and functional characterization of compounds **2a–e** and **3a–h**.



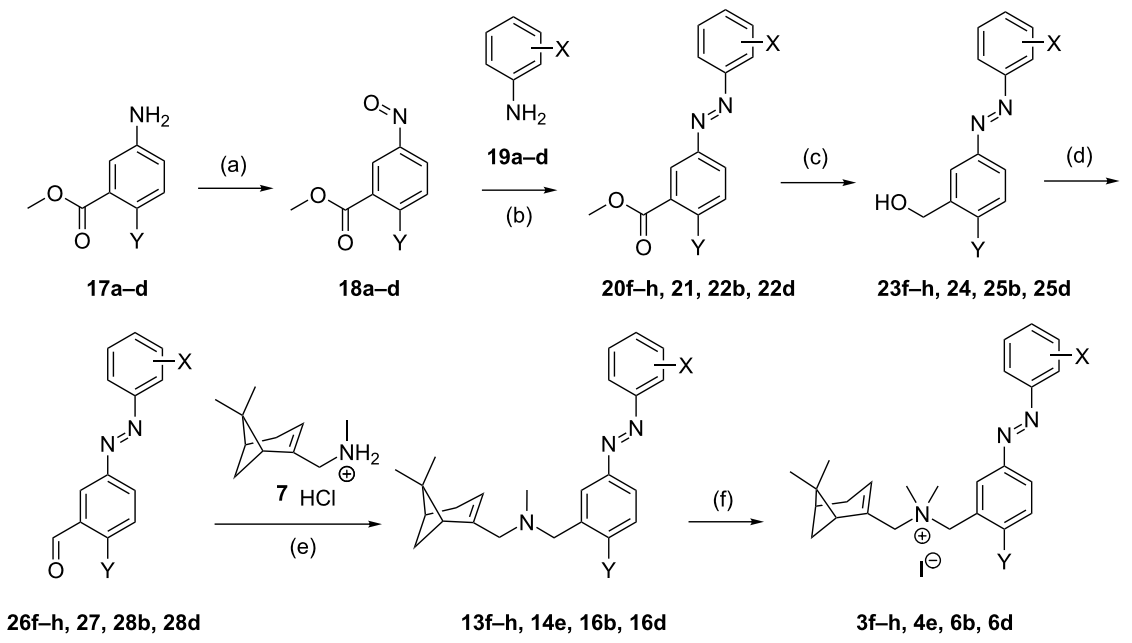
2a–e **3a–h**

		Photochemistry				*CXCR3 binding affinity*					*Functional CXCR3 activity*				
Cmpd	X	λ_{max} *trans* π–π* [a]	λ_{max} *cis* n–π* [a]	PSS_{360} (area % *cis*)[b]	SEM	pK_i *trans*[c]	SEM	pK_i PSS_{360}[c]	SEM	PAS[d]	E (%) *trans*[e]	SEM	E (%) PSS_{360}[f]	SEM	PDE (%)[g]
2a	H	321	422	88.3	0.8	6.3	0.0	5.7	0.1	4.0	−11.0	2.3	−8.3	0.7	2.7
2b	2-Cl	323	416	84.9	0.5	6.3	0.0	5.8	0.1	3.2	2.4	4.3	11.1	2.0	8.7
2c	3-Cl	320	421	79.2	0.9	6.5	0.0	6.3	0.0	1.6	−10.3	3.5	−9.6	2.7	0.7
2d	4-Cl	330	423	89.7	0.5	6.6	0.0	6.0	0.0	4.0	−9.8	3.5	−2.7	3.6	7.1
2e	2-Br	324	421	87.2	0.5	6.4	0.0	5.9	0.1	3.2	7.0	1.6	22.7	1.5	15.7
3a	H	320	423	82.0	1.5	6.0	0.1	5.4	0.1	4.0	−11.6	2.2	−4.7	1.7	6.9
3b	2-Cl	323	419	85.0	0.5	6.3	0.0	5.6	0.0	5.0	−4.7	1.7	17.4	3.7	22.1
3c	3-Cl	317	421	83.4	0.4	6.3	0.0	5.8	0.0	3.2	−8.4	2.2	−0.4	1.6	8.0
3d	4-Cl	325	424	92.0	0.3	6.4	0.0	5.7	0.0	5.0	−8.1	2.6	1.7	2.3	9.8
3e[h]	2-Br	323	421	88.9	0.4	6.3	0.0	5.7	0.1	4.0	−5.8	1.7	25.1	2.0	30.9
3f	2-I	323	422	80.9	0.2	6.2	0.0	5.8	0.1	2.5	−4.0	1.2	15.8	1.3	19.8
3g	3-I	318	422	82.5	1.5	6.1	0.1	6.1	0.0	1.0	−11.1	0.6	−7.6	2.3	3.5
3h	4-I	337	422	91.1	1.1	6.0	0.0	5.7	0.0	2.0	−15.3	1.1	5.4	1.5	20.7

[a]The absorbance maxima were extracted from UV–vis spectra at 25 μM in PBS buffer with 1% DMSO. [b]% of *cis*-isomer at the photostationary state (PSS_{360}) measured in 68% TRIS buffer and 32% DMSO (1 mM) after being pre-irradiated at 360 nm as obtained by LC–MS integration of the *cis* and *trans*-isomer signals at 265 nm. The mean and SEM of at least two experiments are shown. [c]Binding affinity of *trans*-isomer or PSS_{360} as measured using [^{3}H]-VUF11211 displacement. The mean and SEM of at least three experiments are shown. [d]The photoinduced affinity shift (PAS) is calculated as the ratio of the K_i PSS_{360} and K_i *trans*. [e]Normalized CXCR3 functional activity of *trans*-isomer (10 μM) in the dark (efficacy of **1d** set at 100% activity). The mean and SEM of at least three experiments are shown. [f]Normalized CXCR3 functional activity of a sample (10 μM) pre-irradiated at 360 nm to reach the photostationary state (efficacy of **1d** set at 100% activity). The mean and SEM of at least three experiments are shown. [g]The photoinduced difference of efficacy (PDE) is obtained by subtracting *E trans* from *E* PSS_{360}. [h]Compound was previously described by us [7].

the *para*-position as in **2a–e**. The analogue without halogen substitution (**3a**) as well as Cl/Br analogues comparable to the first series (**3b–e**) were prepared. Moreover, since the importance of the presence of a halogen in the outer ring was suggested in **2**, compounds **3f–h**, which include an iodine atom on the *ortho*, *meta* and *para*-positions, respectively, were synthesized.

The synthesis of compounds **3a–e** was performed following the strategies shown in Scheme 1 as disclosed for compounds **2a–e**. Briefly, a reductive amination of **7** and **8b** gave nitro compound **9b**, which after reduction to **10b**, coupling with nitroso compounds **11a–e** to **13a–e** and methylation gave iodide salts **3a–e** with purities of *trans*-isomers ≥99% and overall yields similar to the ones obtained for **2a–e**. However, 2-iodonitrosobenzene cannot be accessed through oxidation of the corresponding aniline owing to oxidation sensitivity of the iodine atom. Therefore, an alternative route had to be used to synthesize **3f–h** (Scheme 2). The route began with the oxidation of methyl 3-aminobenzoate (**17a**) using Oxone® to obtain a crude nitroso product **18a**, which was used in a Mills reaction with an iodoaniline (**19a–c**) at 100 °C to obtain azobenzenes **20g,h** in high yields and *ortho*-analogue **20f** in a decreased yield presumably due to steric hindrance. The methyl ester was selectively reduced with DIBAL-H to benzyl alcohols **23f–h**, which were oxidized with Dess–Martin periodinane to the corresponding benzaldehyde **26f–h**. Reductive amination of **26f–h** with **7** gave the tertiary amines **13f–h**. Methylation with iodomethane and subsequent precipitation gave **3f–h** as orange powders with ≥99% *trans*-isomer in high yields.



Scheme 2: Synthetic strategies for compounds **3f–h**, **4e**, **6b**, and **6d** (Y = H, F, Cl, Br). Reagents and conditions: (a) Oxone® (2.0 equiv), DCM/H_2O 1:4, rt, 2 h, 91–98%; (b) AcOH, 100 °C, 16–20 h, 61–96%; (c) i) DIBAL-H (3.0–4.0 equiv), THF, 0–5 °C to rt, 2–4 h; ii) NH_4Cl (aq), Rochelle salt (10% aq), EtOAc, 1–2 h, 76–99%; or for **23h** i) DIBAL-H (1.2 equiv) , DCM, −78 °C, 1 h; ii) MeOH, −78 °C to rt, 0.5 h, iii) Rochelle salt (10% aq), 3 h, 45%; (d) Dess–Martin periodinane (1.0 equiv), DCM, rt, 1–2 h, 68–97%; (e) i) Et_3N (1.1–1.6 equiv), DCM, rt, 10–30 min; ii) $NaBH(OAc)_3$ (1.6 equiv), rt, 6–16 h, 69–96%; (f) MeI (20 equiv), DCM, rt, 6–72 h, 79–95%.

The photochemical properties of **3a–h** are very similar to those of **2a–e**. For the *trans*-isomers, the maximum of the π–π* band is located around 317–325 nm, with the exception of **3h** which has an iodine atom on the *para*-position and arguably confers a larger electron delocalization of π-electrons that is translated to a bathochromic shifting of the band to lower energy wavelength (337 nm). PSS values of 81–92% are obtained when illuminating with 360 nm light. The binding properties of **3a–h** also result in outcomes similar to those of **2a–e**. That is, K_i values are in the high nanomolar range for the *trans*-isomers with no or low PAS values (1.0–5.0-fold) after isomerization. In single-dose functional assays, all *trans*-isomers do not substantially activate CXCR3, whereas three of the *cis*-isomers weakly to substantially activate CXCR3 (**3b:** 17%, **3e**: 25% and **3f:** 16%). Interestingly, these three compounds are the only ones to include a halogen atom on the *ortho*-position of the outer azobenzene ring, as is the case with *para*-compounds **2b** (11%) and **2e** (23%). However, compared to the latter, *meta*-compounds **3b**,**e**,**f** display an agonist effect that is slightly higher. Increasing the size of the *ortho*-halogen does not guarantee a maximal agonist effect, as the absolute activity of **3f** is lower than that of its Br analogue **3e**. Nevertheless, evidence emerged that the *ortho*-position of the outer aromatic ring in scaffold **3** is important to achieve agonist activity of the *cis*-isomer, but it should be complemented with other strategies to further increase intrinsic activity.

Substituent effects on the outer ring

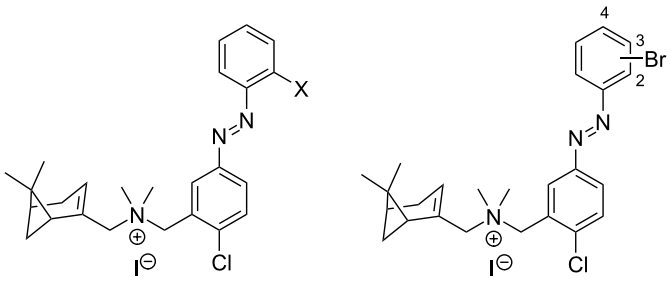
One of the postulated contributors to the CXCR3 agonism effect of parent biaryls such as **1d** and **1e** is the increased π-electron density of the aromatic rings [24]. A way to translate this effect to the azobenzene system is by including a π-donating substituent on the aromatic system. For synthetic access and thus rapid exploration, we chose a Cl atom as mildly π-EDG (electron-donating group) even though it is σ-EWG (electron-withdrawing group) on the *para*-position of the inner ring with respect to the azo bond (i.e., the *ortho*-position with respect to the benzylic position) to afford subseries **4.** This π-electron delocalization would increase the electron density of the azobenzene unit, and was also expected to have an effect on the *trans–cis* azobenzene isomerization and PSS value. In terms of the outer ring, and given that *ortho* halogen atoms in subseries **2** and **3** play an important role in conferring the *cis*-isomer with partial agonism, in subseries **4** we explored halogen atoms and groups differing in, e.g., steric and electronic properties (Me, CF_3, OMe, OCF_3). The electron-donating groups in this series (Me and OMe) also increase the electron density of the azobenzene system.

The synthesis of **4a–d** and **4f–i** was performed following the route shown in Scheme 1. Briefly, **7** was used in a reductive amination with 2-chloro-3-nitrobenzaldehyde (**8c**) to give nitro compound **9c** which was reduced to aniline **10c** and used to

obtain the azo compounds **14a–d,f–i** in variable yields through a Mills reaction with the corresponding nitroso compounds **11a-b,e–j**. Methylation of **14a–d,f–i** with MeI yielded compounds **4a–d,f–g,i** as orange powders with ≥99% *trans*-isomer in moderate to high yields. Salt **4h** did not precipitate after treatment with MTBE and was isolated as an oil, which retained substantial amounts of MTBE solvate even after extensive drying. For **4e**, we used the strategy as explained for iodo compounds **3f–h** (vide supra). Briefly, the route (Scheme 2) consists of the oxidation of methyl 5-amino-2-chlorobenzoate (**17c**) with Oxone® to **18c**, which was used in a Mills reaction with 2-iodoaniline (**19a**) to yield azobenzene **21**. The methyl ester was selectively reduced with DIBAL-H and the resulting alcohol **24** oxidized with Dess–Martin periodinane to benzaldehyde **27**. Reductive amination of **27** with **7** to **14e** and subsequent methylation gave **4e** as an orange powder with ≥99% *trans*-isomer.

Photochemical characterization of **4a–i** (Table 2) gives similar results as observed for subseries **2** and **3** (Figure S2 (Supporting Information File 1) shows an exemplary time-resolved NMR and LC–MS analysis). That is, *trans* π–π* bands have a maximum between 326 and 332 nm and PSS values generally amount to over 90% of *cis*-isomer after illuminating with 360 nm light, as predicted from the electron localization provided by the chlorine atom in the central aromatic ring. Compounds **4e**, **4i** and most notably **4g** deviate from this trend, since the percentage of *cis*-isomer in the PSS is significantly lower (58–80%). *Trans*-**4a–i** show a slight decrease in binding affinity

Table 2: Structure and results of photochemical, binding and functional characterization of compounds **4a–i** and **5b**,**c**.



4a–i **4d, 5b,c**

		Photochemistry				*CXCR3 binding affinity*					*Functional CXCR3 activity*				
Cmpd	X	λ_{max} *trans* π–π* [a]	λ_{max} *cis* n–π* [a]	PSS_{360} (area % *cis*)[b]	SEM	pK_i *trans*[c]	SEM	pK_i PSS_{360}[c]	SEM	PAS[d]	E (%) *trans*[e]	SEM	E (%) PSS_{360}[f]	SEM	PDE (%)[g]
4a	H	326	424	91.8	1.2	5.8	0.0	5.2	0.0	4.0	−2.9	1.0	12.1	0.7	15.0
4b	2-F	330	420	93.0	0.2	5.6	0.0	5.0	0.0	4.0	−4.9	0.5	14.6	0.8	19.5
4c	2-Cl	330	419	92.8	0.1	5.8	0.0	5.3	0.1	3.2	2.3	1.6	36.9	2.0	34.6
4d[h]	2-Br	328	422	92.6	0.2	5.9	0.0	5.6	0.0	2.0	13.6	2.4	49.6	2.6	36.0
4e	2-I	330	424	79.9	1.2	5.7	0.0	5.7	0.0	1.0	16.0	1.4	37.1	0.5	21.1
4f	2-Me	332	428	94.9	0.1	5.9	0.0	5.3	0.0	4.0	6.9	3.1	32.2	1.1	25.3
4g	2-CF_3	326	424	58.0	1.1	5.9	0.0	5.7	0.0	1.6	10.5	1.6	8.3	1.5	−2.2
4h	2-OMe	328	427	92.6	0.2	5.4	0.0	5.0	0.0	2.5	4.9	1.2	18.7	1.1	13.8
4i	2-OCF_3	326	422	78.8	1.2	5.9	0.0	5.6	0.0	2.0	−3.0	2.0	-2.4	3.1	0.6
4d[h]	2-Br	328	422	92.6	0.2	5.9	0.0	5.6	0.0	2.0	13.6	2.4	49.6	2.6	36.0
5b	3-Br	324	420	87.4	1.2	5.7	0.1	5.6	0.0	1.3	−1.7	1.9	10.5	0.5	12.2
5c	4-Br	335	427	93.8	0.5	6.2	0.0	5.6	0.0	4.0	−7.2	1.8	1.8	2.5	9.0

[a]The absorbance maxima were extracted from UV–vis spectra at 25 μM in PBS buffer with 1% DMSO. [b]% of *cis*-isomer at the photostationary state (PSS_{360}) measured in 68% TRIS buffer and 32% DMSO (1 mM) after being pre-irradiated at 360 nm as obtained by LC–MS integration of the *cis* and *trans*-isomer signals at 265 nm. The mean and SEM of at least two experiments are shown. [c]Binding affinity of *trans*-isomer or PSS_{360} in PBS (25 μM) as measured using [^{3}H]-VUF11211 displacement. The mean and SEM of at least three experiments are shown. [d]The photoinduced affinity shift (PAS) is calculated as the ratio of the K_i PSS_{360} and K_i *trans*. [e]Normalized CXCR3 functional activity of *trans*-isomer 10 μM in the dark (efficacy of **1d** set at 100% activity). The mean and SEM of at least three experiments are shown. [f]Normalized CXCR3 functional activity of a sample (10 μM) pre-irradiated at 360 nm to reach the photostationary state (efficacy of **1d** set at 100% activity). The mean and SEM of at least three experiments are shown. [g]The photoinduced difference of efficacy (PDE) is obtained by subtracting E *trans* from E PSS_{360}. [h]Compound was previously described by us [7].

compared to the subseries **2** and **3**, amounting to low micromolar values (Table 2). Moreover, PSS affinity values are also modest, with only four compounds that have a PAS > 2.5 (**4a–c**,**f**). However, functional data from [^{35}S]-GTPγS assays provide encouraging results. While all *trans*-isomers of **4a–i** do not or only weakly activate the receptor, some of the *cis*-isomers clearly behave as partial agonists. The highest efficacy is exerted by *cis*-**4c–f** with E values between 30–50% at 10 µM. Interestingly, one of these compounds (**4f**) includes a methyl group as *ortho*-substituent on the outer ring and its agonist effect at PSS amounts to 32%, possibly questioning one of our hypotheses that a halogen bond is involved in inducing CXCR3 agonism.

Similar to subseries **3**, the substituent on the *ortho*-position of the outer aromatic ring appears to be a driver for the agonist activity of the corresponding *cis*-isomer. Starting from weak partial agonist **4a** (X = H), the agonist response of the *cis* increases with increasing halogen atom (**4b–d**) to a maximal response with **4d** (X = Br) having an agonist effect of 50%. However, when X = I (**4e**) the agonist activity is reduced, as also observed in the **3** subseries (compare **3d** to **3e**). In general, the agonist effects and PDE values exerted by subseries **4** are larger than those of **3** (Figure 3). This could be explained by the effect of the Cl atom present in the **4** subseries, that may give a rise in electron density to the azobenzene necessary to increase the efficacy of the *cis*-isomer.

In both subseries **3** and **4**, a bromine atom on the *ortho*-position of the outer ring gives optimal results in providing CXCR3 efficacy photoswitching (Figure 3). To confirm this for subseries **4**, the analogues of **4d** with the bromine on the *meta* and *para* position (**5b** and **5c**, respectively) were also synthesized. The synthetic route (Scheme 1) utilized **10c** and 3- and 4-bromonitrosobenzene (**11k,l**) to form azobenzenes **15b**,**c**, which were methylated to obtain **5b**,**c**. The binding affinities (Table 2) obtained for the *trans* and *cis*-isomers are all in the micromolar range. More importantly, when comparing functional results of **4d**, **5b** and **5d**, the preference for a Br atom on the *ortho*-position can also be reaffirmed for subseries **4**, because *cis*-**5c** is an antagonist, while *cis*-**5b** shows only a weak activity (Table 2).

Substituent effects on the central ring

As shown, substitution of the outer ring with an *ortho*-bromine in conjunction with a Cl substituent on the central ring appeared to pave the way for efficacy photoswitching but there was still room for improvement. Our strategy in the final optimization round was to replace the mildly π-EDG Cl atom with other groups. Thus, to aim for a full-agonist *cis* compound, the subseries **6** was synthesized. In this subseries, different groups at the *para*-position of the central ring (Y) in combination with the *ortho*-Br atom on the outer aromatic ring are used to to explore optimal electron densities in the azobenzene system. Besides the H and Cl already explored (**3e** and **4d**, respectively), other groups including an EWG halogen atom (F, **6b**), EDG halogen atoms (Br, **6d** and I, **6e**) and stronger EDG moieties such as OMe (**6f**), OiPr (**6g**), SMe (**6h**) and NMe_2 (**6i**) were introduced.

Compounds **6b** and **6d** were synthesized by the route shown in Scheme 2, using in this case halogenated methyl aminobenzoates **17b**,**c** and 2-bromoaniline **19d**. The synthetic route for compound **6e** proved more challenging. The route of Scheme 1 could not be readily used because the corresponding iodinated nitro precursor **8** is not commercially available, nor could the second route (Scheme 2) since the iodine would likely be sensitive to the first oxidation step. Therefore, we designed a new route (Scheme 3). The starting point was the advanced intermediate **28b** (Scheme 3), which was subjected to an aromatic

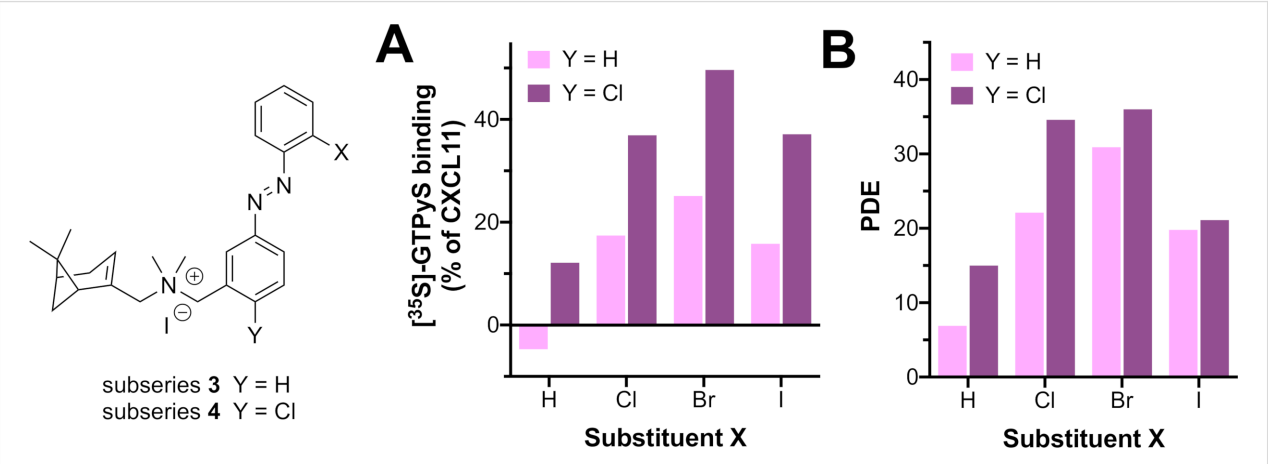
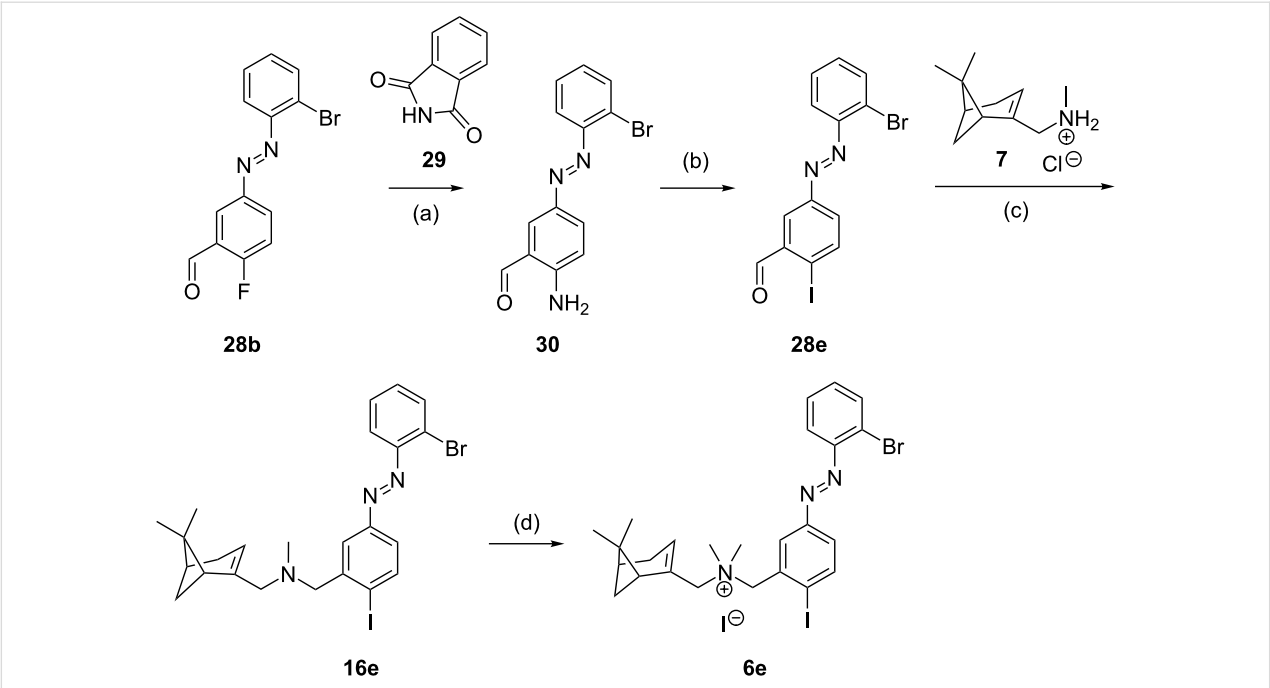


Figure 3: Comparison of compounds belonging to the subseries **3** or **4** with a halogen substitution on the *ortho*-position of the outer ring (X). (A) Activities of *cis*-isomers at 10 µM on CXCR3-mediated G protein activation. (B) PDE values at 10 µM.



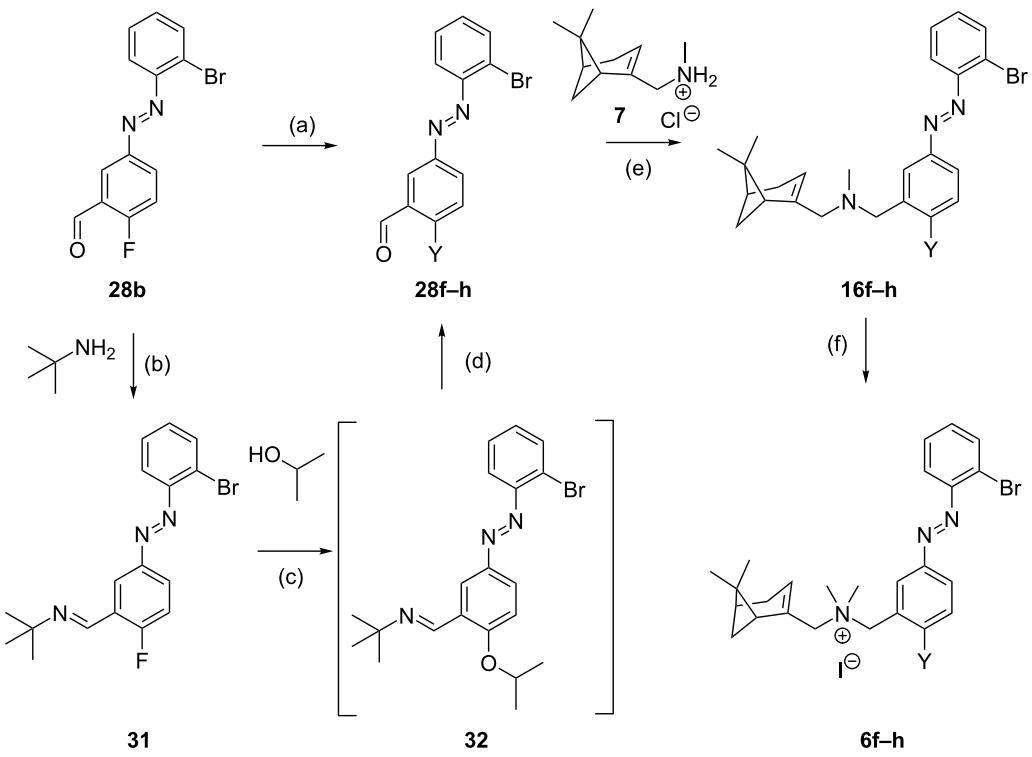
Scheme 3: Synthetic strategy for compound **6e**. Reagents and conditions: (a) i) K_2CO_3 (2.0 equiv), DMF, μW, 65 °C, 3 h; ii) AcOH, reflux, 1 h, 67%; (b) i) *p*TsOH·H_2O (3.0 equiv), MeCN, 10–15 °C; ii) $NaNO_2$ (2.0 equiv), KI (2.5 equiv), H_2O, 10–15 °C to rt, 2 h, 13%; (c) i) Et_3N (1.2 equiv), DCM, rt, 30 min; ii) $NaBH(OAc)_3$ (1.6 equiv), rt, 16 h, 54%; (f) MeI (20 equiv), DCM, rt, 20 h, 57%.

nucleophilic substitution with potassium phthalimide prepared in situ from **29** and K_2CO_3. Presumably due to the alkaline medium, the phthalimide ring was partially opened as detected by HPLC–MS. Upon attempted re-closing under reflux in AcOH, completely deprotection took place and, after purification, aniline **30** was obtained with high purity. Compound **30** was used to introduce the iodine atom through a Sandmeyer reaction to give **28e** albeit in low yield. Reductive amination with **7** afforded amine **16e** followed by methylation to give *trans*-**6e** as an orange solid with 97% purity.

The synthesis of compounds **6f–h** was performed following a nucleophilic aromatic substitution route on **28b** (Scheme 4) since precursors **8** or **17** with the required substituent Y were not available. We performed nucleophilic aromatic substitutions with the corresponding sodium salts of MeOH, 2-PrOH and MeSH under μW irradiation. Both **28f** (Y = OMe) and **28h** (Y = SMe) were formed in high yields, but the conversion of the reaction with NaOiPr was very low and partially gave reduction of the benzaldehyde. An alternative route utilized a method from Engle et al. proceeding through a *tert*-butylimine intermediate (**31**) formed under Dean–Stark conditions [32]. This imine was reacted with NaOiPr to form the ether **32**, which was subsequently hydrolyzed to obtain the desired aldehyde **28g** in high yield. Reductive amination of the aldehydes **28f–h** with **7** furnished amines **16f–h** which was followed by methylation to afford **6f–h** as orange solids with ≥98% *trans*-isomer.

The synthetic strategies for the synthesis of compound **6i** were reported in our previous communication [7].

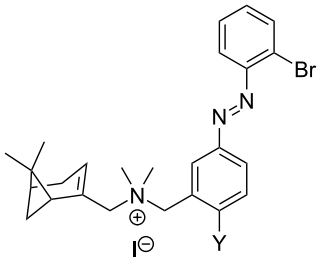
In the subseries depicted in Table 3, several notable differences in both the UV–vis spectra (Figure S1, Supporting Information File 1) and the photoisomerization are observed. When the substituent Y is a halogen atom, we observe a slight bathochromic shift of the π–π* band to higher wavelengths with increasing size of the heteroatom, from 323 nm for Y = H (**3e**) to 339 nm for Y = I (**6e**) (Table 3, Figure 4A). When the group Y is OMe (**6f**), this shift is larger due to the higher EDG properties of MeO (λ_{max} = 352 nm) and this is slightly increased with Y = OiPr (**6g,** λ_{max} = 355 nm). The shift is highest for Y = NMe_2 (**6i**, λ_{max} = 387 nm). When the oxygen atom of **6f** is replaced by a sulfur atom, the bathochromic shift of the π–π* band is also increased (**6h**, λ_{max} = 373 nm, Table 3, Figure 4A). This high capacity of sulfur substituents to induce a bathochromic effect has already been reported in the azobenzene field [33]. The *trans–cis* photoisomerization for **3e**, **4d**, **6b** and **6d–h** in general gives a high percentage of *cis*-isomer (89–93%) with two exceptions. Compound **6h** shows a PSS of only 65% *cis*-isomer due to a poor separation of the π–π* and n–π* bands as a result of the red-shifting by the SMe group (Figure S1A,B, Supporting Information File 1), whereas **6i** decomposes upon irradiation with 360 nm light (as previously reported by us [7]) leading to its exclusion from further characterization. The PSS_{360} forms of exemplary compounds **4d**, **6e**



Scheme 4: Synthetic strategies for compounds **6f–h** (Y = OMe, OiPr, SMe). Reagents and conditions: (a) NaOMe or NaSMe (1.0–1.2 equiv), MeOH or DMF, 65 °C, 30–60 min, 88–90%. (b) PhMe, 110 °C, Dean–Stark, 20 h, 99%; (c) NaH (1.0 equiv), DMSO, 100 °C, 1 h; (d) THF/H_2O/AcOH 50:15:1, rt, 16 h, 79% (two steps); (e) i) Et_3N (1.3–1.4 equiv), DCM, rt, 10–30 min; ii) $NaBH(OAc)_3$ (1.6 equiv), rt, 6–16 h, 84–95%; (f) MeI (20 equiv), DCM, rt, 20 h, 86–90%.

and **6f** have thermal half-lives of 55 [7], 28 and 29 [7] days, respectively, at 10 μM in HEPES (4-(2-hydroxyethyl)-1-piperazineethanesulfonic acid) buffer with 1% DMSO at 25 °C and we consider this to be in line with the expectations (vide supra). The binding affinity of *trans*-**3e, 4d, 6b** and **6d–h** (Table 3) is in the low micromolar range with a low PAS value upon illumination. Initial pilot studies on [^{35}S]-GTPγS binding after CXCR3 stimulation with single concentrations of subseries **6**

Table 3: Structure and results of photochemical and binding characterization of compounds **3e**, **4d**, **6b** and **6d–i**.



3e, 4d, 6b, 6d–i

		Photochemistry				*CXCR3 binding affinity*				
Compound	Y	λ_{max} *trans* π–π*[a]	λ_{max} *cis* n–π*[a]	PSS_{360} (% area *cis*)[b]	SEM	pK_i *trans*[c]	SEM	pK_i PSS_{360}[c]	SEM	PAS[d]
3e[e]	H	323	421	88.9	0.4	6.3	0.0	5.7	0.1	4.0
6b[e]	F	325	417	92.7	0.1	6.0	0.0	5.4	0.0	4.0

Table 3: Structure and results of photochemical and binding characterization of compounds **3e**, **4d**, **6b** and **6d–i**. (continued)

4d[e]	Cl	328	422	92.6	0.2	5.9	0.0	5.6	0.0	2.0
6d[e]	Br	333	420	92.6	0.2	5.8	0.0	5.4	0.0	2.5
6e	I	339	424	90.5	1.0	5.5	0.1	5.5	0.0	1.0
6f[e]	OMe	352	424	92.1	0.1	5.4	0.0	5.0	0.0	2.5
6g	OiPr	355	424	89.0	0.4	5.1	0.2	5.0	0.0	1.3
6h	SMe	373	≈425[f]	64.5	1.7	5.3	0.0	5.5	0.1	0.6
6i[e]	NMe_2	387	dec.[g]	dec.[g]						

[a]The absorbance maxima were extracted from UV–vis spectra at 25 μM in PBS buffer with 1% DMSO. [b]% of *cis*-isomer at the photostationary state (PSS_{360}) in 68% TRIS buffer and 32% DMSO (1 mM) measured after being pre-irradiated at 360 nm as obtained by LC–MS integration of the *cis* and *trans*-isomer signals at 265 nm. The mean and SEM of at least two experiments are shown. [c]Binding affinity of *trans*-isomer or PSS_{360} as measured using [^{3}H]-VUF11211 displacement. The mean and SEM of at least three experiments are shown. [d]The photoinduced affinity shift (PAS) is calculated as the ratio of the K_i PSS_{360} and K_i *trans*. [e]Compound was previously described by us [7]. [f]Could not be determined accurately due to partial overlapping of the π–π* and n–π* bands. [g]Compound decomposes under illumination.

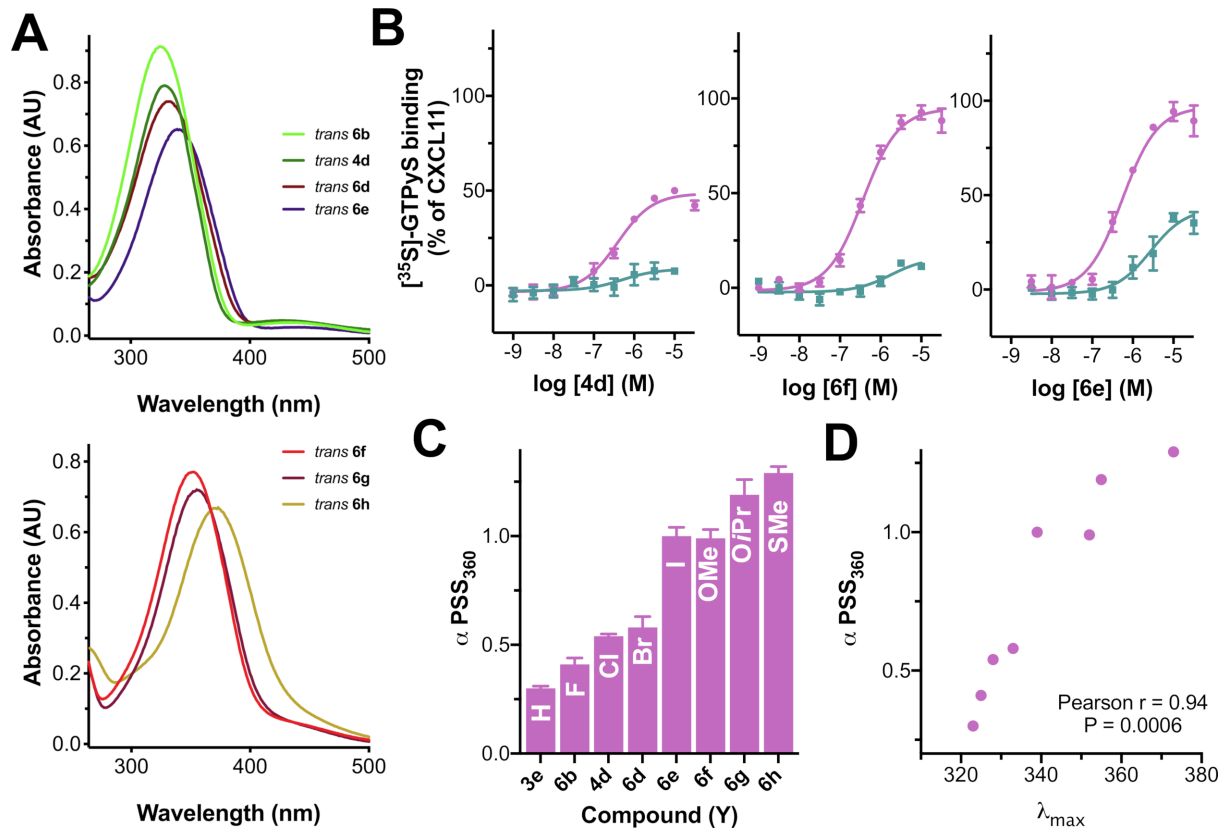
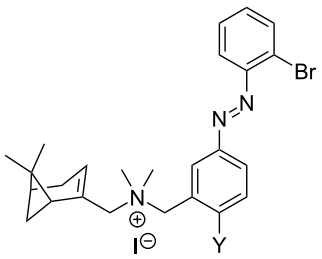


Figure 4: Properties of subseries **3e**, **4d**, **6b** and **6d-h**. (A) UV–vis absorption spectra of (top) *trans*-isomers of **6b**, **4d**, **6d** and **6e** (having substituent Y = F, Cl, Br and I, respectively) and (bottom) **6f**, **6g** and **6h** (having Y = OMe, OiPr and SMe, respectively). (B) Functional dose-response curves using [^{35}S]-GTPγS assay exemplified for **4d**, **6f** and **6e**, respectively. (C) Summary of the efficacies of compounds **3e, 4d, 6b** and **6d–h** at PSS_{360}. (D) Correlation between the bathochromic shifting of the π–π* band and the intrinsic activity of PSS_{360} for the compounds in Table 4.

(data not shown) showed substantial levels of CXCR3 agonism in this group of compounds. For subseries **6** (and associated **3e** and **4d**) we therefore generated dose-response curves for the *trans* and PSS_{360} forms (Figure S4, Supporting Information File 1) using the same [^{35}S]-GTPγS functional assay and calculated the intrinsic activity (α) and potency (EC_{50}). As reported in our previous communication for some of these compounds [7], the PSS_{360} forms give agonism with high nanomolar potencies while most *trans* compounds are antagonists or partial agonists with very low efficacies (Table 4). However, when the

Table 4: Structure and results of functional characterization of compounds **3e**, **4d**, **6b** and **6d–h**.



3e, 4d, 6b, 6d–h

Compound	Y	pEC_{50} *trans*[a]	SEM	pEC_{50} PSS_{360}[b]	SEM	α *trans*[c]	SEM	α PSS_{360}[d]	SEM	PDE[e]
1d	–	6.9	0.0	6.9	0.0	1.04	0.08	1.03	0.07	−0.01
3e[f]	H	n.m.[g]	n.m.[g]	6.5	0.1	0.05	0.03	0.30	0.01	0.25
6b[f]	F	n.m.[g]	n.m.[g]	6.2	0.1	0.12	0.00	0.41	0.03	0.29
4d[f]	Cl	n.m.[g]	n.m.[g]	6.3	0.1	0.11	0.01	0.54	0.01	0.43
6d[f]	Br	n.m.[g]	n.m.[g]	6.2	0.1	0.14	0.02	0.58	0.05	0.44
6e	I	5.5	0.3	6.3	0.2	0.49	0.04	1.00	0.04	0.51
6f[f]	OMe	n.m.[g]	n.m.[g]	6.4	0.1	0.16	0.01	0.99	0.04	0.83
6g	OiPr	n.m.[h]	n.m.[h]	6.0	0.0	n.m.[h]	n.m.[h]	1.19	0.07	n.m.[h]
6h	SMe	5.7	0.3	6.1	0.1	0.85	0.08	1.29	0.03	0.44

[a]Potency of *trans*-isomer in the dark. n.m. = not measurable. The mean and SEM of at least three experiments are shown. [b]Potency of a sample pre-irradiated at 360 nm to reach the photostationary state. The mean and SEM of at least three experiments are shown. [c]Intrinsic activity of *trans*-isomer in the dark (CXCL11 efficacy set at α = 1). The mean and SEM of at least three experiments are shown. [d]Intrinsic activity of a sample pre-irradiated at 360 nm to reach the photostationary state (CXCL11 efficacy set at α = 1). The mean and SEM of at least three experiments are shown. [e]The photoinduced difference of efficacy (PDE) is obtained by subtracting α *trans* from α PSS_{360}. [f]Compound was previously described by us [7]. [g]Too low window. [h]The curve for *trans*-**6g** shows anomalous behavior at 10^{-5} M and higher.

size and/or EDG properties of Y increase, remarkably partial agonism with substantial efficacies appears even for the *trans*-isomers, such as for **6e**, **6g** and **6h**. The compounds illuminated to PSS_{360} follow a similar qualitative trend: when the Y substituent is H or F (**3e** and **6b**), the *cis*-isomer behaves as a partial agonist with medium efficacy (α = 0.30–0.41), but when the Y substituent increases in size and/or EDG properties, the efficacy increases to full efficacy with compounds **6e–h** (Y = I, OMe, OiPr and SMe). The *trans*-form of **6g** shows anomalous behavior at 10^{-5} M and higher (Figure S4, Supporting Information File 1), preventing the extraction of accurate functional values. The PDE value, which reflects efficacies of both the *trans* and PSS form, appears to have an optimum for **6f** (Figure 4B). Figure 4B also shows more subtle behavior for compounds **4d** and **6e**, which harbor a PDE value of 0.43 and 0.51, respectively, but in different parts of the efficacy window.

The results reveal that the electron density of the aryl rings, especially of the inner one, plays a key role in inducing agonism in CXCR3. In general, the *cis*-isomers of the series **2–6** are better CXCR3 agonists. Indeed, the *cis*-isomers are generally assumed to have an intrinsically higher electron density due to the disruption of the conjugation between the two rings of the azobenzene through the N=N bond. Moreover, the electronic properties of the inner substituent Y have been proven to be of strategic use in increasing the intrinsic activity (α) of the *cis*-isomers (Figure 4C). This capacity of the Y substituent to alter the electron density is conceivably also related to its capacity to induce a bathochromic shift of the π–π* band of the *trans*-isomer. Potential evidence for this can be extracted from the significant correlation between the bathochromic shift and intrinsic activity of PSS_{360} (Figure 4D) for the subseries **3e, 4d, 6b** and **6d–h**, which only differ in the nature of Y group (Figure 4C, Table 4).

Conclusion

We report a toolbox of 31 photochromic small-molecule CXCR3 receptor ligands based on the modeling-assisted azologization of a biaryl series reported previously by us [24]. All compounds show affinity for CXCR3 from the high nanomolar to the low micromolar range. Our efforts, however, were focused on exploring the landscape in functional efficacy. To this end, the scaffold was subjected to positional and substitu-

tion changes in structure, necessitating extensive synthetic efforts through multiple routes. The presence of halogen substituents on the *ortho*-position of the outer ring (substituent X) provides partial agonism for the *cis*-isomer with a Br atom being the major exponent, while *trans*-isomers preserve antagonist behavior. The presence of a substituent on the *para*-position of the central ring (substituent Y) capable of delocalizing π-electrons increases the efficacy of the *cis*-isomer. The *cis*-isomers of compounds with Y = I, OMe, OiPr or SMe are all full agonists of CXCR3, however, the corresponding *trans*-isomers also activate the receptor to varying degrees. In all, our efforts deliver a spectrum of (subtle) efficacy differences. Notable tool compounds are VUF15888 (**4d**) switching from antagonism to partial agonism (PDE = 0.43), VUF16620 (**6e**) switching from partial agonism to full agonism (PDE = 0.51), and VUF16216 (**6f**), which represents the optimum balance and provides a CXCR3 photoswitch with a PDE value of 0.83, i.e., from antagonism to full agonism. Based on the pharmacological properties of these three compounds and the long half-lives of their PSS states, they will be valuable tools for future photopharmacological studies on the dynamic signaling of the chemokine receptor CXCR3.

Supporting Information

Supporting Information File 1

Experimental part.
[https://www.beilstein-journals.org/bjoc/content/supplementary/1860-5397-15-244-S1.pdf]

Acknowledgements

All authors acknowledge the Netherlands Organization for Scientific Research for financial support (TOPPUNT, “7 ways to 7TMR modulation (7-to-7)”, 718.014.002). We thank Danny Scholten, Chris de Graaf, and Luc Roumen for helpful discussions, Hans Custers for recording HRMS spectra and Mounir Andaloussi for providing key building block **7**.

ORCID® iDs

Xavier Gómez-Santacana - https://orcid.org/0000-0001-8830-0494
Tamara A. M. Mocking - https://orcid.org/0000-0001-6490-4429
Niels J. Hauwert - https://orcid.org/0000-0002-1217-1670
Prashanna Vijayachandran - https://orcid.org/0000-0002-1047-538X
Henry F. Vischer - https://orcid.org/0000-0002-0184-6337
Maikel Wijtmans - https://orcid.org/0000-0001-8955-8016
Rob Leurs - https://orcid.org/0000-0003-1354-2848

Preprint

A non-peer-reviewed version of this article has been previously published as a preprint doi:10.3762/bxiv.2019.69.v1

References

1. Hüll, K.; Morstein, J.; Trauner, D. *Chem. Rev.* **2018,** *118,* 10710–10747. doi:10.1021/acs.chemrev.8b00037
2. Hoorens, M. W. H.; Szymanski, W. *Trends Biochem. Sci.* **2018,** *43,* 567–575. doi:10.1016/j.tibs.2018.05.004
3. Hauwert, N. J.; Mocking, T. A. M.; Da Costa Pereira, D.; Kooistra, A. J.; Wijnen, L. M.; Vreeker, G. C. M.; Verweij, E. W. E.; De Boer, A. H.; Smit, M. J.; De Graaf, C.; Vischer, H. F.; de Esch, I. J. P.; Wijtmans, M.; Leurs, R. *J. Am. Chem. Soc.* **2018,** *140,* 4232–4243. doi:10.1021/jacs.7b11422
4. Donthamsetti, P. C.; Winter, N.; Schönberger, M.; Levitz, J.; Stanley, C.; Javitch, J. A.; Isacoff, E. Y.; Trauner, D. *J. Am. Chem. Soc.* **2017,** *139,* 18522–18535. doi:10.1021/jacs.7b07659
5. Lachmann, D.; Konieczny, A.; Keller, M.; König, B. *Org. Biomol. Chem.* **2019,** *17,* 2467–2478. doi:10.1039/c8ob03221a
6. Westphal, M. V.; Schafroth, M. A.; Sarott, R. C.; Imhof, M. A.; Bold, C. P.; Leippe, P.; Dhopeshwarkar, A.; Grandner, J. M.; Katritch, V.; Mackie, K.; Trauner, D.; Carreira, E. M.; Frank, J. A. *J. Am. Chem. Soc.* **2017,** *139,* 18206–18212. doi:10.1021/jacs.7b06456
7. Gómez-Santacana, X.; de Munnik, S. M.; Vijayachandran, P.; Da Costa Pereira, D.; Bebelman, J. P. M.; de Esch, I. J. P.; Vischer, H. F.; Wijtmans, M.; Leurs, R. *Angew. Chem., Int. Ed.* **2018,** *57,* 11608–11612. doi:10.1002/anie.201804875
8. Morstein, J.; Awale, M.; Reymond, J.-L.; Trauner, D. *ACS Cent. Sci.* **2019,** *5,* 607–618. doi:10.1021/acscentsci.8b00881
9. Hartley, G. S. *Nature* **1937,** *140,* 281. doi:10.1038/140281a0
10. Ricart-Ortega, M.; Font, J.; Llebaria, A. *Mol. Cell. Endocrinol.* **2019,** *488,* 36–51. doi:10.1016/j.mce.2019.03.003
11. Hauwert, N. J.; Mocking, T. A. M.; Da Costa Pereira, D.; Lion, K.; Huppelschoten, Y.; Vischer, H. F.; De Esch, I. J. P.; Wijtmans, M.; Leurs, R. *Angew. Chem., Int. Ed.* **2019,** *58,* 4531–4535. doi:10.1002/anie.201813110
12. Hauser, A. S.; Attwood, M. M.; Rask-Andersen, M.; Schiöth, H. B.; Gloriam, D. E. *Nat. Rev. Drug Discovery* **2017,** *16,* 829–842. doi:10.1038/nrd.2017.178
13. Schönberger, M.; Trauner, D. *Angew. Chem., Int. Ed.* **2014,** *53,* 3264–3267. doi:10.1002/anie.201309633
14. Pittolo, S.; Gómez-Santacana, X.; Eckelt, K.; Rovira, X.; Dalton, J.; Goudet, C.; Pin, J.-P.; Llobet, A.; Giraldo, J.; Llebaria, A.; Gorostiza, P. *Nat. Chem. Biol.* **2014,** *10,* 813–815. doi:10.1038/nchembio.1612
15. Bahamonde, M. I.; Taura, J.; Paoletta, S.; Gakh, A. A.; Chakraborty, S.; Hernando, J.; Fernández-Dueñas, V.; Jacobson, K. A.; Gorostiza, P.; Ciruela, F. *Bioconjugate Chem.* **2014,** *25,* 1847–1854. doi:10.1021/bc5003373
16. Levitz, J.; Pantoja, C.; Gaub, B.; Janovjak, H.; Reiner, A.; Hoagland, A.; Schoppik, D.; Kane, B.; Stawski, P.; Schier, A. F.; Trauner, D.; Isacoff, E. Y. *Nat. Neurosci.* **2013,** *16,* 507–516. doi:10.1038/nn.3346
17. Rovira, X.; Trapero, A.; Pittolo, S.; Zussy, C.; Faucherre, A.; Jopling, C.; Giraldo, J.; Pin, J.-P.; Gorostiza, P.; Goudet, C.; Llebaria, A. *Cell Chem. Biol.* **2016,** *23,* 929–934. doi:10.1016/j.chembiol.2016.06.013
18. Zussy, C.; Gómez-Santacana, X.; Rovira, X.; De Bundel, D.; Ferrazzo, S.; Bosch, D.; Asede, D.; Malhaire, F.; Acher, F.; Giraldo, J.; Valjent, E.; Ehrlich, I.; Ferraguti, F.; Pin, J.-P.; Llebaria, A.; Goudet, C. *Mol. Psychiatry* **2018,** *23,* 509–520. doi:10.1038/mp.2016.223

19. Agnetta, L.; Bermudez, M.; Riefolo, F.; Matera, C.; Claro, E.; Messerer, R.; Littmann, T.; Wolber, G.; Holzgrabe, U.; Decker, M. *J. Med. Chem.* **2019,** *62,* 3009–3020. doi:10.1021/acs.jmedchem.8b01822
20. Rustler, K.; Maleeva, G.; Bregestovski, P.; König, B. *Beilstein J. Org. Chem.* **2019,** *15,* 780–788. doi:10.3762/bjoc.15.74
21. Broichhagen, J.; Podewin, T.; Meyer-Berg, H.; von Ohlen, Y.; Johnston, N. R.; Jones, B. J.; Bloom, S. R.; Rutter, G. A.; Hoffmann-Röder, A.; Hodson, D. J.; Trauner, D. *Angew. Chem., Int. Ed.* **2015,** *54,* 15565–15569. doi:10.1002/anie.201506384
22. Broichhagen, J.; Johnston, N. R.; von Ohlen, Y.; Meyer-Berg, H.; Jones, B. J.; Bloom, S. R.; Rutter, G. A.; Trauner, D.; Hodson, D. J. *Angew. Chem., Int. Ed.* **2016,** *55,* 5865–5868. doi:10.1002/anie.201600957
23. Gómez-Santacana, X.; Pittolo, S.; Rovira, X.; Lopez, M.; Zussy, C.; Dalton, J. A. R.; Faucherre, A.; Jopling, C.; Pin, J.-P.; Ciruela, F.; Goudet, C.; Giraldo, J.; Gorostiza, P.; Llebaria, A. *ACS Cent. Sci.* **2017,** *3,* 81–91. doi:10.1021/acscentsci.6b00353
24. Wijtmans, M.; Scholten, D. J.; Roumen, L.; Canals, M.; Custers, H.; Glas, M.; Vreeker, M. C. A.; de Kanter, F. J. J.; de Graaf, C.; Smit, M. J.; de Esch, I. J. P.; Leurs, R. *J. Med. Chem.* **2012,** *55,* 10572–10583. doi:10.1021/jm301240t
25. Wijtmans, M.; Scholten, D.; Mooij, W.; Smit, M. J.; de Esch, I. J. P.; de Graaf, C.; Leurs, R. Exploring the CXCR3 Chemokine Receptor with Small-Molecule Antagonists and Agonists. In *Chemokines: Chemokines and Their Receptors in Drug Discovery;* Tschammer, N., Ed.; Topics in Medicinal Chemistry; Springer International Publishing: Cham, Switzerland, 2015; pp 119–185. doi:10.1007/7355_2014_75
26. *MOE,* Version 2016.0802; Chemical Computing Group, Inc.: Chemical Computing Group, Inc, 2016.
27. Fliegl, H.; Köhn, A.; Hättig, C.; Ahlrichs, R. *J. Am. Chem. Soc.* **2003,** *125,* 9821–9827. doi:10.1021/ja034433o
28. Wijtmans, M.; Verzijl, D.; Bergmans, S.; Lai, M.; Bosch, L.; Smit, M. J.; de Esch, I. J. P.; Leurs, R. *Bioorg. Med. Chem.* **2011,** *19,* 3384–3393. doi:10.1016/j.bmc.2011.04.035
29. García-Amorós, J.; Velasco, D. *Beilstein J. Org. Chem.* **2012,** *8,* 1003–1017. doi:10.3762/bjoc.8.113
30. Bandara, H. M. D.; Burdette, S. C. *Chem. Soc. Rev.* **2012,** *41,* 1809–1825. doi:10.1039/c1cs15179g
31. Scholten, D. J.; Wijtmans, M.; van Senten, J. R.; Custers, H.; Stunnenberg, A.; de Esch, I. J. P.; Smit, M. J.; Leurs, R. *Mol. Pharmacol.* **2015,** *87,* 639–648. doi:10.1124/mol.114.095265
32. Engle, K. M.; Luo, S.-X.; Grubbs, R. H. *J. Org. Chem.* **2015,** *80,* 4213–4220. doi:10.1021/acs.joc.5b00563
33. Nishioka, H.; Liang, X.; Kato, T.; Asanuma, H. *Angew. Chem., Int. Ed.* **2012,** *51,* 1165–1168. doi:10.1002/anie.201106093

License and Terms

This is an Open Access article under the terms of the Creative Commons Attribution License (http://creativecommons.org/licenses/by/4.0). Please note that the reuse, redistribution and reproduction in particular requires that the authors and source are credited.

The license is subject to the *Beilstein Journal of Organic Chemistry* terms and conditions: (https://www.beilstein-journals.org/bjoc)

The definitive version of this article is the electronic one which can be found at: doi:10.3762/bjoc.15.244

BEILSTEIN JOURNAL OF ORGANIC CHEMISTRY

A photochemical determination of luminescence efficiency of upconverting nanoparticles

Baptiste Amouroux[1,2], Clément Roux[1], Jean-Claude Micheau[1], Fabienne Gauffre[2] and Christophe Coudret[*1]

Full Research Paper

Open Access

Address:
[1]Laboratoire des IMRCP, Université de Toulouse, CNRS UMR 5623, Université Toulouse III - Paul Sabatier,118 route de Narbonne, 31062 Toulouse, France and [2]Université de Rennes, CNRS, UMR6226, ISCR, F-35000 Rennes, France

Email:
Christophe Coudret[*] - coudret@chimie.ups-tlse.fr

* Corresponding author

Keywords:
actinometry; diarylethene; lanthanide; photochemistry; upconverting nanoparticle

Beilstein J. Org. Chem. **2019,** *15,* 2671–2677.
doi:10.3762/bjoc.15.260

Received: 19 July 2019
Accepted: 24 October 2019
Published: 11 November 2019

This article is part of the thematic issue "Molecular switches".

Guest Editor: W. Szymanski

© 2019 Amouroux et al.; licensee Beilstein-Institut.
License and terms: see end of document.

Abstract

Upconverting nanoparticles are a rising class of non-linear luminescent probes burgeoning since the beginning of the 2000's, especially for their attractiveness in theranostics. However, the precise quantification of the light delivered remains a hot problem in order to estimate their impact on the biological medium. Sophisticated photophysical measurements under near infrared excitation have been developed only by few teams. Here, we present the first attempt towards a simple and cheap photochemical approach consisting of an actinometric characterization of the green emission of $NaYF_4$:Yb,Er nanoparticles. Using the recently calibrated actinometer 1,2-bis(2,4-dimethyl-5-phenyl-3-thienyl)-3,3,4,4,5,5-hexafluoro-1-cyclopentene operating in the green region of the visible spectra, we propose a simple photochemical experiment to get an accurate estimation of the efficiency of these green-emitting "nanolamps". The agreement of the collected data with the previous published results validates this approach.

Introduction

The photophysical property of converting low-energy light, typically near infrared (NIR), into high energy one thanks to noncoherent photon absorption is called "upconversion". This phenomenon is exemplified by the lanthanide-based materials [1]. With the rapid developments of nanotechnology, upconverting Ln^{3+}-based nanoparticles (UCNPs) have been reported for promising bio-applications [2].

The popularity of this family of photoactive nanocrystals comes from the spectral window that can be used to operate them. Excited at 976 nm or 808 nm, they re-emit over a large range from far-red (802 nm) up to UV in the form of a line spectrum typical of the emissive lanthanides used. The main application foreseen for these nanomaterials is as a substitute of quantum dots [3], since the combination of anti-Stokes emission and

noncoherent absorption prevent any luminescence background. Their extreme photostability [4] make them also ideal candidates for single particle tracking. More interestingly, because of the very large range of possible re-emitted energies, UCNPs are now identified as convenient secondary sources of light to trigger locally photoreactions [5,6]. Indeed, the anti-Stokes emission allows bypassing the usual restrictions (power, penetration depth) imposed by the combination of medium composition (organic compound absorbing mostly in the UV–vis range) and the Beer–Lambert law. Moreover, the NIR excitation wavelengths used are much less damaging when biological applications are in sight [7]. "NIR photochemistry", based on the upconversion phenomenon can find applications in material sciences such as photopolymerization [8], or micellization photocontrol [9], since the excitation wavelength lies in the first transparency window of most biological media, a spectacular range of use in biological sciences has been explored from drug release [10], drug uncaging [11] to photodynamic therapy [12] and optogenetics [13,14]. Inorganic lanthanide based-UCNPs are classically formulated as a mixed fluoride $NaREF_4$. Here, RE stands for a cocktail of trivalent rare-earth metal ions containing mostly photophysically inert metals (Y, Gd) and a few percent of "optically active" ions: a sensitizer (often ytterbium) and an emitter ("activator") such as thulium (UV and blue emissions), holmium (red) or erbium (mostly green). In this solid solution, energy collected by ytterbium at 976 nm is transferred to the less abundant emitting ions. Thanks to lanthanides' spectroscopic properties (regular level spacing and long excited states lifetimes), one emitting ion can undergo several energy transfer processes before relaxing radiatively [15], making the overall process fundamentally different form second harmonic generation or two-photon absorption. Furthermore, it has the following consequences: (i) the intensity of each line is power-dependent upon the excitation laser power, this latter point being made clear upon plotting each line intensities vs laser power in a log–log plot, (ii) the intensities of the upconversion emission lines are less and less intense as the emitted energy increases, (iii) the intensities of the emission lines but not their wavelength vary with the UCNP size, as the surface quenching becomes the most efficient deactivation path for small nanoparticles. Therefore, the assessment of the upconversion quantum yields (UCQY) is a hot topic as these depend on the size, the excitation power and the formulation of the nanocrystal.

This issue is classically addressed using physical measurements, therefore requiring complex equipment. Most of these assessments are achieved via the use of integration spheres [16-19]. The challenges are to cope with a large spectral range, the variable excitation power and, because UCQY are usually very small, to handle a large energy contrast between incident beam and collected emission. Fully built equipment to carry out UCQY determination are only starting to be developed commercially (Jasco, Hamamatsu). A more sophisticated approach involves microscopic techniques, enabling one to determine UCQY even at the single NP scale. A seminal report was published in 2013 by Nadort et al. [20] describing the measurement of the luminescence of Er-doped UCNPs at the single NP or cluster level after identification by TEM. Yet, this type of work has remained isolated. Moreover, in these conditions, the nanoparticles do not work in conditions close to their foreseen applications. As we became interested in the design of such nanoparticles [21], we envisioned a "chemical approach" of this measurement problem.

The chemical measurement of light intensity is called actinometry and relies on the exposure of a fully standardized photosensitive compound to the light to be measured [22]. The rate of the photochemical transformation is then used to retrieve the light intensity of the beam exciting the solution. Compared to physical radiometry, actinometry is directly transposable to the monitoring of photochemical transformations as it originates from the very same concept and can be performed in the same experimental conditions. It is also adapted to turbid mixtures and can be extended to polychromatic sources. Since the recent renewal of photochemistry caused by the use of LEDs and microfluidic devices, actinometry has become a convenient tool to parameterize the performances of photoreactors [23-25]. Actinometer choice is guided by the operating conditions and by the spectral overlap between the compound and the source. The emission of erbium-containing UCNPs (Er-UCNPs) is dominated by a pair of green (520 nm and 540 nm) and red band (655 nm). In this part of the electromagnetic spectrum, very few actinometers are available. Beside inorganic compounds such as Reinecke salt (ammonium diamminetetrakis(thiocyanato)chromate(III)), photochromic dyes have been proposed for such a purpose, mainly from the azobenzene, fulgide or diarylethene families [22]. The latter two are particularly attractive for visible light wavelengths above 400 nm. However, their use is conditioned by their availability and reliability. Recently, an accurate determination of photochemical quantum yields (QY) [26] was achieved for a commercially available diarylethene 1,2-bis(2,4-dimethyl-5-phenylthien-3-yl)-3,3,4,4,5,5-hexafluoro-1-cyclopentene, labelled **1**. Since then, this dye has been used as actinometer in the visible range (Figure 1) [25,27].

Switching of such diarylethene dyes in both directions (ring closure/coloration or ring opening/discoloration) by UCNPs has been documented for years, with a seminal work reported in 2009 by the team of Branda [28]. In the following we will show how this photochromic compound can be used to give a reasonable quantitative estimation of the upconversion phenomenon.

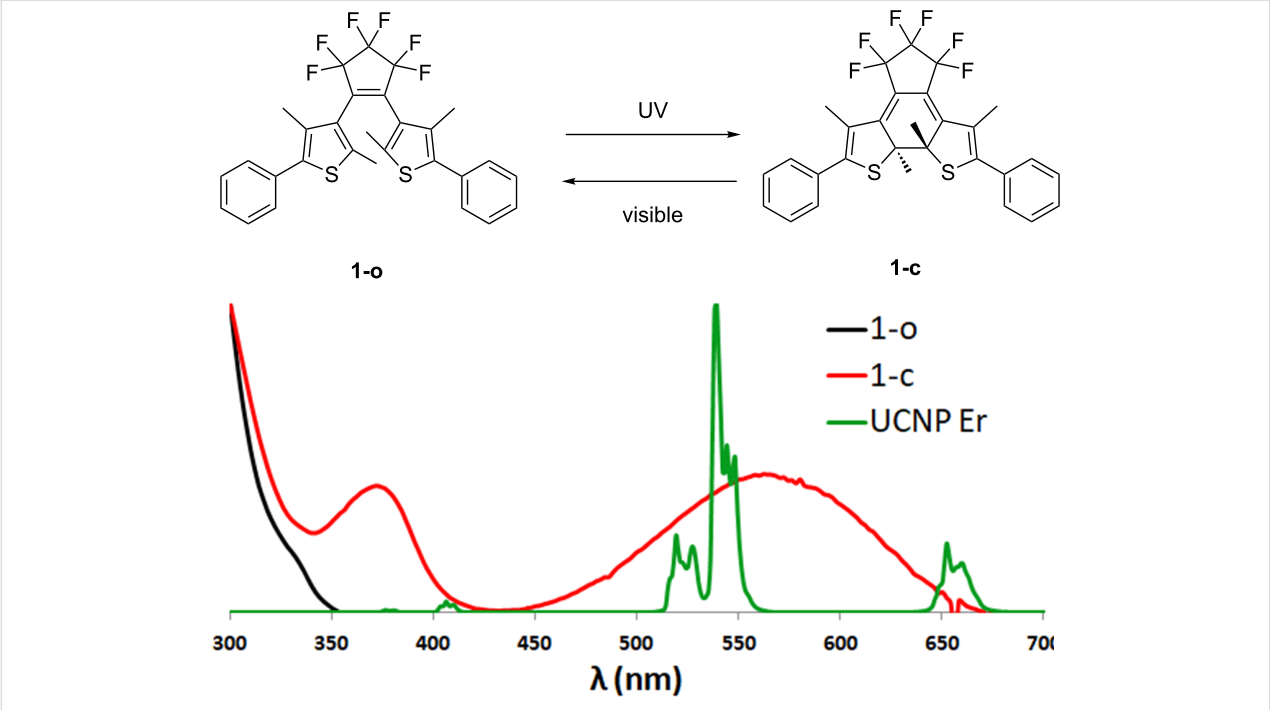


Figure 1: Top: photoisomers of diarylethene **1**, bottom: spectral overlaps between the **1-o** (black line), **1-c** (red line) UV–vis absorption spectra and the Er-UCNP emission spectrum (green line).

In particular, we will exploit the ring-opening reaction since only the closed form **1-c** presents a good spectral overlap with the visible emissions of the Er-UCNPs.

In order to achieve a "user friendly" quantitative measurement of the light emitted by the nanoparticles, we have chosen to mix together the nanoparticles and the actinometer.

Results and Discussion

Upconverting nanoparticles

Hydrophobic nanoparticles were prepared by adapting the standard reported procedure of Li and Zhang (details in Supporting Information File 1) [29]. Briefly, key points are: (i) the in situ preparation of metal oleate from their corresponding chloride, (ii) the introduction of the sodium and fluoride ions as two methanol solutions of respectively NaOH and NH_4F via separate syringe pumps (according to Zhai et al. [30]) and, after volatile solvents removal, (iii) the high temperature crystallization step for 90 minutes. Spherical nanoparticles of 21.8 ± 1.3 nm were collected. Crystal quality was assayed by XRD and only the hexagonal β-phase could be detected (Supporting Information File 1). These particles are kept well dispersed in cyclohexane.

Photolysis experiments

The description of the setup is summarized in Figure 2. The sample in a thermostated quartz cuvette was irradiated with a fibered, collimated CW 976 nm-laser beam. The transmitted laser intensity was measured using a calibrated power-meter. This measurement informed us about the fraction of light effectively absorbed by the medium and also the possibility of particle sedimentation. All this set-up was placed inside a UV–visible spectrophotometer (Figure 2).

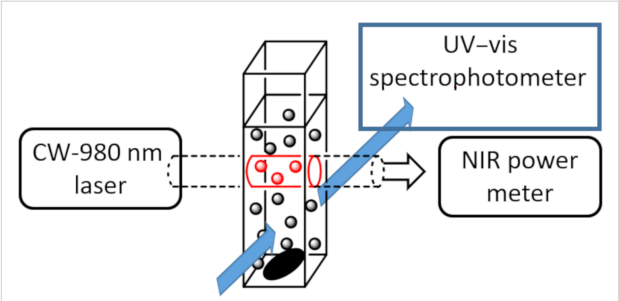


Figure 2: UCNPs (black dots) are irradiated inside the cylindrical CW 976 nm laser beam. Absorbed laser power is recorded with a power-meter. The UV–vis spectrophotometer axis is perpendicular to the laser beam.

Using cyclohexane as a common solvent for both diarylethene **1** and UCNPs, we have chosen to work on mixtures of the freshly prepared actinometer **1-c** and nanoparticles. Practically, the preparation of the **1-o/c** solution was achieved using bench-top UV source (TLC lamp), either on the UCNP-**1** mixture or before mixing the dye with the UCNPs. Concentrations were

standardized prior the photolysis experiments using published data (ε(**1-c**) 562 nm = 10900 L mol^{-1} cm^{-1} [26] and ε(**Yb**)976nm = 3.1 L mol^{-1} cm^{-1}). All the parameters used are gathered in Table 1. Actinometer absorbance changes were continuously monitored by the spectrophotometer [31]. Care has been taken to assess that the cuvette was sufficiently stirred [32], and that the actinometer was neither sensitive to the spectrophotometer measuring beam (laser off) nor to the NIR laser beam in the absence of UCNPs (see Supporting Information File 1).

Upon 976 nm irradiation, a clear-cut decrease of the absorbance in the visible range can be monitored. Typical kinetic traces were recorded at 650 nm and the data was processed in order to obtain the initial rate of the photoreaction (Figure 3).

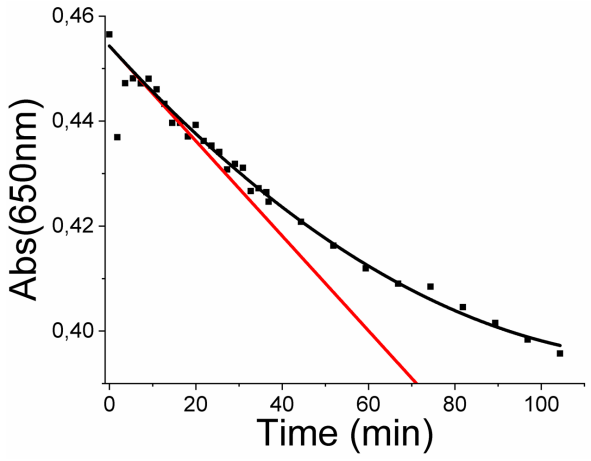


Figure 3: Kinetic trace at 650 nm under CW 976 nm laser at 4.71 W. Initial slope (red line) was determined on the 2nd order polynomial fit of experimental points (dark curve).

Beside these experiments, controls were made to rule out the possibility of thermal effect (irradiation of the actinometer alone with the 976 nm laser) or the possible effects of the spectrometer light source (no laser applied). Lower laser powers were not attempted in order to keep sufficient sensitivity and/or a reasonable reaction time. Data are gathered in Table 2 (vide infra) and in Supporting Information File 1.

Data treatment

The upconversion light source

Unlike two-photon excitation that requires very high local power density, the upconversion process is based on multiple, noncoherent, "single photon" successive absorptions. As the molar extinction coefficient of the sensitizer ytterbium is weak (ca. 3 mol L^{-1} cm^{-1}), the exciting beam is moderately attenuated as it crosses the colloidal suspension. Therefore, UCNPs are excited over the entire portion of the 976 nm laser beam that crosses the sample: the resulting visible light source can be considered as a cylinder having for base, the laser section, and for length, the laser path through the cuvette (Figure 2). To compute the number of "active" nanoparticles, we measured the absorbance A_{976} of the colloidal suspension at 976 nm by measuring the laser intensity that crosses the sample holder, with and without the NP's suspension. This absorbance is solely due to the ytterbium ions, therefore one can compute the number of Yb atoms n_{Yb} inside the beam volume v as:

$$n_{Yb} = \frac{v}{\varepsilon_{Yb} l} N_A \mathrm{Abs}_{976} \quad (1)$$

where ε_{Yb} is the ytterbium atomic molar extinction coefficient at 976 nm (3.1 L mol^{-1} cm^{-1}), l the optical path crossed by the laser beam (1 cm), N_A is Avogadro's number. The number of nanoparticles inside the laser beam n_{NP} can be determined knowing N_{Yb} the number of ytterbium per nanoparticle:

$$n_{NP} = n_{Yb} / N_{Yb}$$

N_{Yb} and N_{Er} (N_{Er}: number of erbium atom per particles) can be derived from the number of RE atoms per NP, itself computed from TEM and XRD measurements taking into account the

Table 1: Parameters of UCNP used in the photolysis experiment.

parameter	symbol	unit	value
1-c concentration	[**1-c**]	mol L^{-1}	2.12 × 10^{-4}
UCNP concentration	[UCNP]	NP L^{-1}	1.18 × 10^{16}
volume of the solution	V	L	1.96 × 10^{-3}
1-c Absorbance at 540 nm (irradiation)	Abs_{540}	–	2.07
absorbance of UCNP solution at 976 nm	Abs_{976}	–	0.0014
laser power at 976 nm (NIR)	*P*	W	4.7
laser beam section		cm^2	9.6 × 10^{-2}
laser power density at 976 nm (NIR)		W cm^{-2}	49

nanoparticles size (volume ≈ 5400 ± 1000 nm^3), unit cell volume (107.6 $Å^3$) and number of $NaREF_4$ per unit cell (Z = 1.5).

The DAE photobleaching experiments

From the spectral overlap one can notice that only the 540 nm erbium line will be the useful one: the UCNP-emission can be considered as quasi-monochromatic within the closed DAE (**1-c**) spectral range. At this wavelength, the value of the ring-opening QY Φ_{co} of actinometer **1** is taken as 0.02, using the calibration curve by Sumi et al. [26].

Monochromatic actinometry is typically ran in a continuously stirred reactor and relies on the following equation:

$$-\frac{\mathrm{d}[\mathbf{1\text{-}c}]}{\mathrm{d}t} = \Phi_{co} I_a \tag{2}$$

where d[**1-c**]/dt is the rate of consumption of the DAE closed form in mol L^{-1} s^{-1}, Φ_{co} is the ring opening quantum yield, i.e., the number of events divided by the number of photons absorbed and I_a is the rate of photon absorption, in mol L^{-1} s^{-1}, i.e., the photon flux per volume of solution to be measured. Note that for a given reactor of volume V, the photon flux per volume of solution is related to the photon flux J by a simple multiplication $J = I \times V$. The difficulty is then to relate the rate of absorbed photons I_a to the incident photon flux J_0 emitted by the UCNPs. A way to circumvent this issue is to adapt actinometer solution absorbance to the reactor used. Indeed, a light-absorbing solution is characterized by its "optical thickness" [23] L defined from the rewritten Beer–Lambert law (Equation 3)

$$I = I_0 10^{-\frac{l}{L}} \tag{3}$$

as

$$L = \frac{1}{\varepsilon_{540}[\mathbf{1\text{-}c}]} \tag{4}$$

L is therefore the inverse of the absorbance measured for an optical path of 1 cm (Equation 4). For $l = L$, $I = 0.01 \times I_0$: more than 99% of light is thus absorbed. In our case, we have chosen to use a sufficiently concentrated **1-c** solution so that all the emitted photons are supposedly absorbed. Indeed, an absorbance at 540 nm of 2.07 (over 1 cm) gives a characteristic length of 0.48 cm, comparable to the dimensions of the cuvette: practically no green light escapes the photoreactor.

Under these conditions the actinometric equation becomes

$$-\frac{\mathrm{d}[\mathbf{1\text{-}c}]}{\mathrm{d}t} \approx \Phi_{co} I_0 \tag{5}$$

so the flux in photon per second emitted by the source is:

$$J_0 = -\frac{N_A}{\Phi_{co}} v \frac{\mathrm{dAbs}_{650}}{\varepsilon_{650}\mathrm{d}t} \tag{6}$$

where V is the total volume of the DAE solution and the monitoring optical path is 1 cm. Finally, the average upconversion-QY, Φ_{UC} can be estimated by the ratio

$$\Phi_{UC} = \frac{J_0}{J_a^{NIR}} \tag{7}$$

where J_0 is the above measured photon flux and J_a^{NIR} is 976 nm laser photon flux absorbed by the nanoparticles:

$$J_a^{NIR} = J_0^{NIR}(1-10^{-\mathrm{Abs}_{976}}) = P\frac{\lambda_{976}}{hc}(1-10^{-\mathrm{Abs}_{976}}) \tag{8}$$

where P is the laser power in Watts and J_0^{NIR} the NIR photon flux. Additionally, one can access the number of emitted photons per particles J_0/n_{NP} (in photon s^{-1}), or, using the energy of a 540 nm photon, to the emitting power of a single nanoparticle

$$\wp^{NP} = \frac{J_0 hc}{n_{NP}\lambda_{540}} \text{ (in Watt)} \tag{9}$$

and the number of emitted photons per erbium atom J_0/n_{Er} in photon s^{-1}.

All of these numbers are gathered in Table 2, more detailed calculations are provided in Supporting Information File 1.

The as-determined quantum yield is in good agreement with measurements obtained on bulk samples by using integrating spheres [33], and the order of magnitude of the emissive power of a single NP is close to what was achieved by microscopy on nanoparticles of similar composition but at a higher laser power (49×10^{-16} W under 976 nm irradiation at 260 W cm^{-2}) and with a larger size (70 nm instead of 21.8) [20]. One can be surprised by the rather low number of photon emitted per second and per NP: one erbium center emits in average one photon every four seconds. This can be understood as lanthanides' excited states are long lived and also because the production of one green photon requires three energy transfer

Table 2: Obtained results.

parameter	symbol	unit	value
1-c bleaching rate	-d[**1-c**]/d*t*	mol L^{-1} s^{-1}	6.78×10^{-9}
1-c consumption		**molecule s^{-1}**	**8.00×10^{12}**
upconversion photon flux at 540nm	J_0	photon s^{-1}	4.00×10^{14}
incident NIR photon flux	J_0^{NIR}	photon s^{-1}	2.31×10^{19}
absorbed NIR photon flux	J_a^{NIR}	photon s^{-1}	7.45×10^{16}
up-conversion QY	Φ_{UC}	–	**0.54%**
number of NPs inside the laser beam	n_{Yb}	NP	1.14×10^{12}
number of emitted photons per erbium atom	J_0/N_{Er}	photon s^{-1}	0.24
number of emitted photons per NP's	J_0/n_{NP}	**photon s^{-1}**	**350**
power per NP's	$\wp^{NP}$	**W**	**1.29×10^{-16}**

steps from excited ytterbium ions. Despite this very weak emission rate, such nanoparticles can be used to induce local photochemistry. Thus, the group of Zvyagin has developed an in situ photodynamic therapy using quite large particles (70 nm) [34] and recruiting the flavin-containing coenzymes as $^1O_2$ sensitizers. In the skin, typical number of dyes per femtoliter is expected to be 750. This would correspond to an absorbance of 0.0014 in 1 cm of pure water according to a molar extinction coefficient of ca. 11300 L mol^{-1} cm^{-1}. To mimic such a situation, we have designed an experiment with larger nanoparticles (35 nm) and dilute **1-c** dye: an absorbance at 540 nm of 0.11 ([**1-c**] = 1.14×10^5 mol L^{-1}) corresponds to number of dyes of 6800 molecules per femtoliter. The photoswitching of the actinometer **1-c** was clearly observed (Supporting Information File 1) and an initial "bleaching activity" of 20 dyes per NP and per second could be calculated by dividing the bleaching rate by the number of particles within the laser beam. However, is it very difficult to derive the emitted flux J_0 for this reactor geometry: with a characteristic length L of 9 cm, most of the light escapes the cuvette and no simplification can be done. Thus, privileging the spectral information (clear UV–vis spectra are indeed monitored) lead to a loss of information; another photoreactor design would then be necessary.

Conclusion

We have demonstrated that the chemical approach of a light flux measurement could also be employed for assessing the efficiency of unusual light sources as small as the nanolamps that are upconverting nanoparticles. The observed results are in agreement with published data which is remarkable as the heredescribed methodology can been run with limited lab equipment. The technique is robust and simple to operate. Concerning the use of single-UCNP as nanolight sources, the emitted flow of photon is rather sparse but yet relevant biological signals could be triggered. This study shows the interest to use P-photochromic dyes as actinometer. Extension to blue emitting UCNPs would however require a suitable dye for the 400–500 nm spectral window, to be found probably in the "inverse DTE" family [35] or in the photodissociable family [36].

Supporting Information

Supporting Information File 1

Experimental details about the UCNPs syntheses, characterizations, photolysis experiments and detailed calculations.
[https://www.beilstein-journals.org/bjoc/content/supplementary/1860-5397-15-260-S1.pdf]

Acknowledgements

The *Agence Nationale de la Recherche* (ANR-15-CE09-0020 BLINK) is acknowledged for funding and the CNRS and Université Paul Sabatier for support. Anaïs Robillard and Carla Orlandi are acknowledged for their assistance on preliminary experiments.

ORCID® iDs

Baptiste Amouroux - https://orcid.org/0000-0001-8379-4878
Clément Roux - https://orcid.org/0000-0001-5707-4471
Jean-Claude Micheau - https://orcid.org/0000-0002-1193-4306
Christophe Coudret - https://orcid.org/0000-0001-7334-5112

Preprint

A non-peer-reviewed version of this article has been previously published as a preprint doi:10.3762/bxiv.2019.73.v1

References

1. Zhou, J.; Liu, Q.; Feng, W.; Sun, Y.; Li, F. *Chem. Rev.* **2015,** *115,* 395–465. doi:10.1021/cr400478f

2. Dong, H.; Du, S.-R.; Zheng, X.-Y.; Lyu, G.-M.; Sun, L.-D.; Li, L.-D.; Zhang, P.-Z.; Zhang, C.; Yan, C.-H. *Chem. Rev.* **2015,** *115,* 10725–10815. doi:10.1021/acs.chemrev.5b00091
3. Himmelstoß, S. F.; Hirsch, T. *Methods Appl. Fluoresc.* **2019,** *7,* 022002. doi:10.1088/2050-6120/ab0bfa
4. Wu, S.; Han, G.; Milliron, D. J.; Aloni, S.; Altoe, V.; Talapin, D. V.; Cohen, B. E.; Schuck, P. J. *Proc. Natl. Acad. Sci. U. S. A.* **2009,** *106,* 10917–10921. doi:10.1073/pnas.0904792106
5. Lederhose, P.; Chen, Z.; Müller, R.; Blinco, J. P.; Wu, S.; Barner-Kowollik, C. *Angew. Chem., Int. Ed.* **2016,** *55,* 12195–12199. doi:10.1002/anie.201606425
6. Wu, S.; Butt, H.-J. *Phys. Chem. Chem. Phys.* **2017,** *19,* 23585–23596. doi:10.1039/c7cp01838j
7. He, S.; Krippes, K.; Ritz, S.; Chen, Z.; Best, A.; Butt, H.-J.; Mailänder, V.; Wu, S. *Chem. Commun.* **2015,** *51,* 431–434. doi:10.1039/c4cc07489k
8. Xie, Z.; Deng, X.; Liu, B.; Huang, S.; Ma, P.; Hou, Z.; Cheng, Z.; Lin, J.; Luan, S. *ACS Appl. Mater. Interfaces* **2017,** *9,* 30414–30425. doi:10.1021/acsami.7b09124
9. Yan, B.; Boyer, J.-C.; Branda, N. R.; Zhao, Y. *J. Am. Chem. Soc.* **2011,** *133,* 19714–19717. doi:10.1021/ja209793b
10. Yan, B.; Boyer, J.-C.; Habault, D.; Branda, N. R.; Zhao, Y. *J. Am. Chem. Soc.* **2012,** *134,* 16558–16561. doi:10.1021/ja308876j
11. Fedoryshin, L. L.; Tavares, A. J.; Petryayeva, E.; Doughan, S.; Krull, U. J. *ACS Appl. Mater. Interfaces* **2014,** *6,* 13600–13606. doi:10.1021/am503039f
12. Cui, S.; Yin, D.; Chen, Y.; Di, Y.; Chen, H.; Ma, Y.; Achilefu, S.; Gu, Y. *ACS Nano* **2013,** *7,* 676–688. doi:10.1021/nn304872n
13. Chen, S.; Weitemier, A. Z.; Zeng, X.; He, L.; Wang, X.; Tao, Y.; Huang, A. J. Y.; Hashimotodani, Y.; Kano, M.; Iwasaki, H.; Parajuli, L. K.; Okabe, S.; Teh, D. B. L.; All, A. H.; Tsutsui-Kimura, I.; Tanaka, K. F.; Liu, X.; McHugh, T. J. *Science* **2018,** *359,* 679–684. doi:10.1126/science.aaq1144
14. Wang, Y.; Lin, X.; Chen, X.; Chen, X.; Xu, Z.; Zhang, W.; Liao, Q.; Duan, X.; Wang, X.; Liu, M.; Wang, F.; He, J.; Shi, P. *Biomaterials* **2017,** *142,* 136–148. doi:10.1016/j.biomaterials.2017.07.017
15. Auzel, F. *Chem. Rev.* **2004,** *104,* 139–174. doi:10.1021/cr020357g
16. Balabhadra, S.; Debasu, M. L.; Brites, C. D. S.; Ferreira, R. A. S.; Carlos, L. D. *J. Lumin.* **2017,** *189,* 64–70. doi:10.1016/j.jlumin.2017.03.054
17. Boyer, J.-C.; van Veggel, F. C. J. M. *Nanoscale* **2010,** *2,* 1417–1419. doi:10.1039/c0nr00253d
18. May, P. S.; Baride, A.; Hossan, M. Y.; Berry, M. *Nanoscale* **2018,** *10,* 17212–17226. doi:10.1039/c8nr03538e
19. Kaiser, M.; Würth, C.; Kraft, M.; Hyppänen, I.; Soukka, T.; Resch-Genger, U. *Nanoscale* **2017,** *9,* 10051–10058. doi:10.1039/c7nr02449e
20. Nadort, A.; Sreenivasan, V. K. A.; Song, Z.; Grebenik, E. A.; Nechaev, A. V.; Semchishen, V. A.; Panchenko, V. Y.; Zvyagin, A. V. *PLoS One* **2013,** *8,* e63292. doi:10.1371/journal.pone.0063292
21. Amouroux, B.; Roux, C.; Marty, J.-D.; Pasturel, M.; Bouchet, A.; Sliwa, M.; Leroux, O.; Gauffre, F.; Coudret, C. *Inorg. Chem.* **2019,** *58,* 5082–5088. doi:10.1021/acs.inorgchem.9b00143
22. Kuhn, H. J.; Braslavsky, S. E.; Schmidt, R. *Pure Appl. Chem.* **2004,** *76,* 2105–2146. doi:10.1351/pac200476122105
23. Aillet, T.; Loubiere, K.; Dechy-Cabaret, O.; Prat, L. *Int. J. Chem. React. Eng.* **2014,** *12,* 257–269. doi:10.1515/ijcre-2013-0121
24. El Achi, N.; Bakkour, Y.; Chausset-Boissarie, L.; Penhoat, M.; Rolando, C. *RSC Adv.* **2017,** *7,* 29815–29820. doi:10.1039/c7ra01237c
25. Roibu, A.; Fransen, S.; Leblebici, M. E.; Meir, G.; Van Gerven, T.; Kuhn, S. *Sci. Rep.* **2018,** *8,* 5421. doi:10.1038/s41598-018-23735-2
26. Sumi, T.; Takagi, Y.; Yagi, A.; Morimoto, M.; Irie, M. *Chem. Commun.* **2014,** *50,* 3928–3930. doi:10.1039/c4cc00396a
27. Gurke, J.; Budzák, Š.; Schmidt, B. M.; Jacquemin, D.; Hecht, S. *Angew. Chem., Int. Ed.* **2018,** *57,* 4797–4801. doi:10.1002/anie.201801270
28. Carling, C.-J.; Boyer, J.-C.; Branda, N. R. *J. Am. Chem. Soc.* **2009,** *131,* 10838–10839. doi:10.1021/ja904746s
29. Li, Z.; Zhang, Y. *Nanotechnology* **2008,** *19,* 345606. doi:10.1088/0957-4484/19/34/345606
30. Zhai, X.; Wang, Y.; Liu, X.; Liu, S.; Lei, P.; Yao, S.; Song, S.; Zhou, L.; Feng, J.; Zhang, H. *ChemPhotoChem* **2017,** *1,* 369–375. doi:10.1002/cptc.201700013
31. Deniel, M. H.; Lavabre, D.; Micheau, J. C. Photokinetics under Continuous Irradiation. *Organic Photochromic and Thermochromic Compounds;* Topics in Applied Chemistry; Kluwer Academic Publishers: Boston, MA, U.S.A.; pp 167–209. doi:10.1007/0-306-46912-x_4
32. Conrad, R. H. *Anal. Chem. (Washington, DC, U. S.)* **1967,** *39,* 1039. doi:10.1021/ac60252a023
33. Kraft, M.; Würth, C.; Muhr, V.; Hirsch, T.; Resch-Genger, U. *Nano Res.* **2018,** *11,* 6360–6374. doi:10.1007/s12274-018-2159-9
34. Khaydukov, E. V.; Mironova, K. E.; Semchishen, V. A.; Generalova, A. N.; Nechaev, A. V.; Khochenkov, D. A.; Stepanova, E. V.; Lebedev, O. I.; Zvyagin, A. V.; Deyev, S. M.; Panchenko, V. Ya. *Sci. Rep.* **2016,** *6,* 35103. doi:10.1038/srep35103
35. Irie, M.; Fukaminato, T.; Matsuda, K.; Kobatake, S. *Chem. Rev.* **2014,** *114,* 12174–12277. doi:10.1021/cr500249p
36. Filevich, O.; Zayat, L.; Baraldo, L. M.; Etchenique, R. Long Wavelength Phototriggering: Ruthenium-Based Caged Compounds. *Luminescent and Photoactive Transition Metal Complexes as Biomolecular Probes and Cellular Reagents;* Springer, 2014; pp 47–68. doi:10.1007/430_2014_169

License and Terms

This is an Open Access article under the terms of the Creative Commons Attribution License (http://creativecommons.org/licenses/by/4.0). Please note that the reuse, redistribution and reproduction in particular requires that the authors and source are credited.

The license is subject to the *Beilstein Journal of Organic Chemistry* terms and conditions: (https://www.beilstein-journals.org/bjoc)

The definitive version of this article is the electronic one which can be found at: doi:10.3762/bjoc.15.260

BEILSTEIN JOURNAL OF ORGANIC CHEMISTRY

A combinatorial approach to improving the performance of azoarene photoswitches

Joaquin Calbo[1], Aditya R. Thawani[2], Rosina S. L. Gibson[2], Andrew J. P. White[2] and Matthew J. Fuchter[*2]

Full Research Paper

Open Access

Address:
[1]Department of Materials, Imperial College London, London SW7 2AZ, United Kingdom and [2]Department of Chemistry, Molecular Sciences Research Hub, White City Campus, Imperial College London, W12 0BZ, United Kingdom

Email:
Matthew J. Fuchter[*] - m.fuchter@imperial.ac.uk

* Corresponding author

Keywords:
arylazopyrazoles; azobenzenes; molecular switches; *ortho*-substitution; photoswitches; thermal half-life

Beilstein J. Org. Chem. **2019,** *15,* 2753–2764.
doi:10.3762/bjoc.15.266

Received: 30 July 2019
Accepted: 28 October 2019
Published: 14 November 2019

This article is part of the thematic issue "Molecular switches".

Guest Editor: W. Szymanski

© 2019 Calbo et al.; licensee Beilstein-Institut.
License and terms: see end of document.

Abstract

Azoarenes remain privileged photoswitches – molecules that can be interconverted between two states using light – enabling a huge range of light addressable multifunctional systems and materials. Two key innovations to improve the addressability and *Z*-isomer stability of the azoarenes have been *ortho*-substitution of the benzene ring(s) or replacement of one of the benzenes for a pyrazole (to give arylazopyrazole switches). Here we study the combination of such high-performance features within a single switch architecture. Through computational analysis and experimental measurements of representative examples, we demonstrate that *ortho*-benzene substitution of the arylazopyrazoles drastically increases the *Z*-isomer stability and allows further tuning of their addressability. This includes the discovery of new azopyrazoles with a *Z*-isomer thermal half-life of ≈46 years. Such results therefore define improved designs for high performance azo switches, which will allow for high precision optically addressable applications using such components.

Introduction

Photoswitches are molecules that are capable of being reversibly interconverted between (at least) two states by means of light irradiation. The incorporation of photoswitches into multifunctional systems has huge relevance to next-generation materials, with a plethora of applications that range from photopharmacology [1,2] and optochemical genetics [3] to data storage [4]. Numerous classes of photochromic molecules exist, each with their own unique characteristics. For example, spiropyrans [5,6] may exhibit significant changes in solubility upon photoswitching, whilst the photoswitching of diarylethenes [7] is accompanied by large variations in their absorption spectra. However, azobenzenes remain one of the most popular photoswitches owing to their stability, reliability and tunability: azobenzenes provide high extinction coefficients and quantum

yields, allowing switching between *Z*- and *E*-isomers with low-intensity light, and are stable to repeated switching cycles. Of the several performance metrics that can be used to judge azo switches, however, there are two predominant ones that can prove problematic for azoarenes: 1) the completeness of switching at a given wavelength of light, and 2) the thermal stability of the *Z*-isomer.

Despite the huge body of structure–property relationship studies known for substituted azobenzenes [8,9], it is still common to observe azo photoswitches that undergo incomplete photoswitching and/or possess low *Z*-isomer thermal stability. Perhaps the most important advancement to tackle these limitations in recent times has been the discovery that tetra-*ortho* substitution of the azobenzene unit can lead to a significant improvement of the photoswitching properties (Figure 1a). Specifically, *o*-methoxy [10,11] and *o*-thio [12] analogues reported by Woolley and co-workers demonstrate slow thermal *Z*–*E* relaxation and the potential to switch with red light, while the *o*-fluoro compounds reported by Hecht and co-workers [13,14] offer excellent two-way isomerization with visible light and the longest thermal half-life reported for an azobenzene molecule (≈700 days at 25 °C) to date.

An emerging alternative approach to tune the properties of azoarene photoswitches is to replace one or both of the benzene

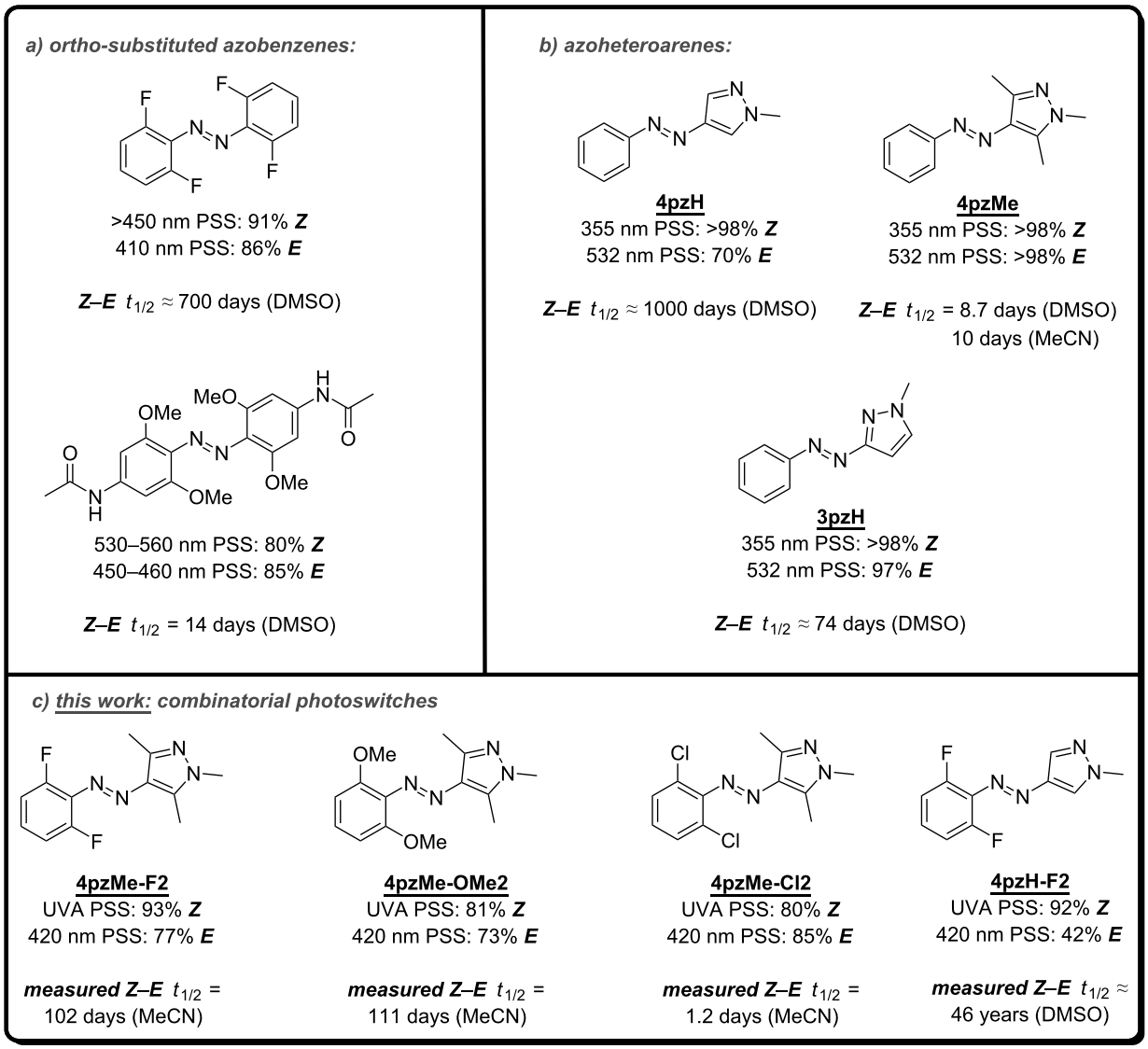


Figure 1: a) Tetra *ortho*-substituted azobenzenes represent a significant advance in terms of *Z*-isomer stability and completeness of photoswitching over azobenzene. b) Azoheteroarenes, developed by Fuchter and co-workers, offer quantitative, bidirectional photoswitching and long *Z*-isomer half-lives. c) This work seeks to understand the impact of these two approaches, when combined.

rings with a heteroaromatic ring [15,16]. While several useful heteroaromatic azo scaffolds have been reported, we previously identified such photoswitches containing a pyrazole ring, so-called arylazopyrazoles, which have excellent potential against the current state of the art (Figure 1b) [17,18]. Specifically, arylazopyrazole **4pzMe** can be near quantitatively (>98%) photoswitched in both directions, and **4pzH** demonstrated an exceptionally long thermal *Z*-isomer half-life (≈1000 days at 25 °C); one of the most stable azo photoswitches reported to date. We further extended the family of arylazopyrazoles with the help of theoretical modelling and discovered **3pzH** to be near quantitatively (>98%) switched back and forth between isomers, with a long thermal isomerization half-life ($t_{1/2}$ = 74 days at 25 °C). The photochemical addressability of the azopyrazoles can further be complemented by other stimuli, for example chemical switching using acid [19]. Given their excellent performance, arylazopyrazoles are replacing azobenzenes in optically addressable applications including imaging applications [20], photopharmacology [21], supramolecular chemistry [22,23], responsive foams [24], coordination chemistry [25] and DNA nanotechnology [26,27].

Whilst the azopyrazoles have excellent properties for use in a variety of photo-addressable applications, it remains frustrating that in order to improve the photochemical addressability of the *Z*-isomer of these molecules (as is observed in **4pzMe** and **3pzH**) we needed to sacrifice thermal stability (**4pzH** vs **4pzMe** and **3pzH**), (Figure 1b) [17,18]. One parameter that was not explored in our previous structure–property relationship study, was substitution on the benzene ring [18]. Since our work, Venkataramani and co-workers [28] have explored how substitution on the benzene ring of azopyrazoles can impact their properties. However, in their study they focused on dimethylpyrazoles not methylated on the pyrazole ring N–H; compounds which have fast thermal *Z*–*E* conversion through mechanisms such as tautomerization. Furthermore, the study of Venkataramani and co-workers did not particularly focus on substitution patterns known to give high performance in azobenzene switches. We therefore considered whether specifically combining the two high performance designs of state-of-the-art azo photoswitches – *N*-methylated pyrazole plus an *o*-substituted benzene – would be advantageous for further improving the properties of the azopyrazoles (Figure 1c). It is important to note that Jan Ravoo and co-workers [23] have reported a bis-*ortho*-fluoroazopyrazole as part of their study of the supramolecular chemistry of these systems. Irradiating their compound at 365 nm enables near quantitative *E*→*Z* conversion, however, the 520 nm PSS provides 55% of the *E*-isomer. In water, this compound possesses a thermal half-life of >11 days. Herein, we present theoretical and representative experimental data concerning the performance for **4pzH** and **4pzMe** derivatives upon aryl mono- and di-*ortho*-substitution. Both computational and experimental measurements indicate the addition of *ortho*-substituents to the benzene ring of arylazopyrazoles has the potential to drastically increase the isomerization half-life (to months or years) and allow further tuning of the photoaddressability of each isomer. We believe that the structure–property relationships described will guide further development of azoheteroarene photoswitches (particularly arylazopyrazoles), and their use in a wide array of light-addressable applications.

Results and Discussion

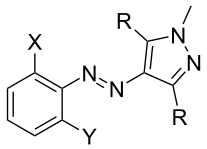
The effect of *ortho*-substitution on half-life

We first assessed the theoretical half-lives for a series of compounds with *ortho*-substitution on the benzene ring of previously reported azopyrazoles **4pzH** and **4pzMe** (Table 1). Electron-poor (F and Cl) and electron-rich moieties (methoxy and pyrrolidine abbreviated as OMe and Pyr, respectively) were considered to analyze the effect of these *ortho*-groups on the thermal stability of *Z*-arylazopyrazoles (Table 1). Such substitution has proved useful in the improvement of azobenzene performance: *o*-F [13,14], *o*-Cl [8,29,30], *o*-OMe [10,29,31], or *o*-Pyr [32]. For the sake of comparison, both mono- and di-*ortho*-substitutions were considered.

Theoretical half-lives ($t_{1/2}$) were calculated within the density functional theory (DFT) framework, according to the protocol reported in our prior paper [18]. Briefly, the different possible pathways for thermal *Z*–*E* isomerization were calculated, and each process was weighted by the relative *Z*-isomer ground state energy and transition state (TS) energy barrier for all possible conformers (see Experimental for details). Focusing first on the **4pzH** scaffold, the theoretical calculations at the PBE0-D3/6-31G** level indicate that an insertion of electron-poor fluorine atoms in the *ortho*-position of the aryl ring (**4pzH-F1** and **4pzH-F2**) leads to an increase in the half-life from ca. 1000 days in **4pzH** to 2000 days in **4pzH-F1** and to 4000 days in **4pzH-F2** (Table 1). In contrast, chloro-substituted analogues present a significant decrease in the computed half-lives: 90 days for **4pzH-Cl1** and 5 days for **4pzH-Cl2**. The inclusion of methoxy and pyrrolidine groups in the *ortho*-position leads to an enhanced *Z*-isomer thermal stability compared to unsubstituted **4pzH**, with $t_{1/2}$ = 2000 and 15000 days for **4pzH-OMe1** and **4pzH-OMe2**, respectively, and 34000 days for **4pzH-Pyr1** (Table 1). Unexpectedly, the inclusion of two bulky pyrrolidine groups in *ortho* (**4pzH-Pyr2**) leads to a decrease in $t_{1/2}$ (76 days).

For the arylazopyrazole scaffold **4pzMe**, in line with the trend above, theoretical calculations indicate that the addition of *ortho*-fluoro atoms leads to higher *Z*-isomer stability, whereas

Table 1: Theoretical half-lives ($t_{1/2,\ theor}$ in hours and days) calculated at the PBE0-D3/6-31G** level of theory for *ortho*-substituted arylazopyrazoles **4pzH-X** and **4pzMe-X**. Experimental $t_{1/2,\ exp}$ values are indicated.



R	X	Y	Compound	$t_{1/2,\ theor}$ (h)	$t_{1/2,\ theor}$ (d)	$t_{1/2,\ exp}$
H	H	H	**4pzH**	**31000**	**1300**	**≈1000 d**[a,b]
H	H	F	**4pzH-F1**	55000	2300	
H	F	F	**4pzH-F2**	97000	4100	46 y[b]
H	H	Cl	**4pzH-Cl1**	2200	92	
H	Cl	Cl	**4pzH-Cl2**	120	5.1	
H	H	OMe	**4pzH-OMe1**	54000	2200	
H	OMe	OMe	**4pzH-OMe2**	350000	15000	
H	H	Pyr	**4pzH-Pyr1**	810000	34000	
H	Pyr	Pyr	**4pzH-Pyr2**	1800	76	
Me	H	H	**4pzMe**	**9.1**	**0.38**	**10 d**[a,c]
Me	H	F	**4pzMe-F1**	94	3.9	
Me	F	F	**4pzMe-F2**	620	26	102 d[c]
Me	H	Cl	**4pzMe-Cl1**	2.1	0.087	
Me	Cl	Cl	**4pzMe-Cl2**	0.025	0.0010	1.2 d[c]
Me	H	OMe	**4pzMe-OMe1**	160	6.5	
Me	OMe	OMe	**4pzMe-OMe2**	630	26	111 d[c]
Me	H	Pyr	**4pzMe-Pyr1**	200	8.3	
Me	Pyr	Pyr	**4pzMe-Pyr2**	380	16	

[a]Previously reported value [17]. [b]Measured in DMSO-d_6 at elevated temperatures and then extrapolated to 25 °C using an Eyring plot. [c]Measured in MeCN-d_3. d = days, y = years.

the opposite effect is found upon chlorine *ortho*-substitution (Table 1). The insertion of one and two electron-donating OMe and Pyr groups systematically improve the *Z*-isomer stability compared to **4pzMe**, with $t_{1/2}$ = 7 and 26 days for **4pzMe-OMe1** and **4pzMe-OMe2**, and $t_{1/2}$ = 8 and 16 days for **4pzMe-Pyr1** and **4pzMe-Pyr2**, respectively.

It is important to note that, consistent with our previous results [18] and other recent reports [33], thermal *Z*–*E* isomerization for **4pzH-X** and **4pzMe-X** derivatives are predicted to occur through a transition state in which the N atom next to the benzene ring linearizes in an inversion mechanism (see B-type transition states in Figure 2 for **4pzH-F2** and **4pzMe-F2**, and Figure S1 in Supporting Information File 1 for the rest of di-*ortho*-substituted photoswitches). The inversion mechanism through linearization of the N atom next to the heteroring (H-type) is computed with a larger energy barrier in all cases (Figure 2 and Figure S1, Supporting Information File 1), and no low-energy rotation mechanism is predicted, in agreement with other reports [34]. Also consistent with our previous studies on **4pzH** compared to **4pzMe** [18], significantly larger half-lives are predicted for **4pzH-X** derivatives compared to the dimethylated **4pzMe-X** derivatives, which can be rationalized by the stabilizing short CH···π interactions in the T-shaped conformation of *Z*-**4pzH-X** (Figure 2).

In order to confirm our predictions of the *ortho*-substitution effect on the thermal *Z*–*E* isomerization process, photoswitches **4pzMe-F2**, **4pzMe-Cl2**, **4pzMe-OMe2** and **4pzH-F2** were synthesized (see Supporting Information File 1). Following irradiation to the PSS (see further details below), the thermal *Z*–*E* conversion was monitored by ^{1}H NMR spectroscopy (Table 1). While the results do not quantitatively match the theoretical predictions (as found previously [18]), the trends are faithfully reproduced: **4pzMe-F2** ($t_{1/2}$ = 102 days), and **4pzMe-OMe2** ($t_{1/2}$ = 111 days) have increased thermal stability over **4pzMe** ($t_{1/2}$ = 10 days), whereas **4pzMe-Cl2** ($t_{1/2}$ ≈ 1 day) exhibits a reduction in half-life. Additionally, **4pzH-F2** boasts a vastly increased thermal half-life of 46 years over **4pzH** ($t_{1/2}$ = 1000 days) making it the longest-lived azoheteroarene

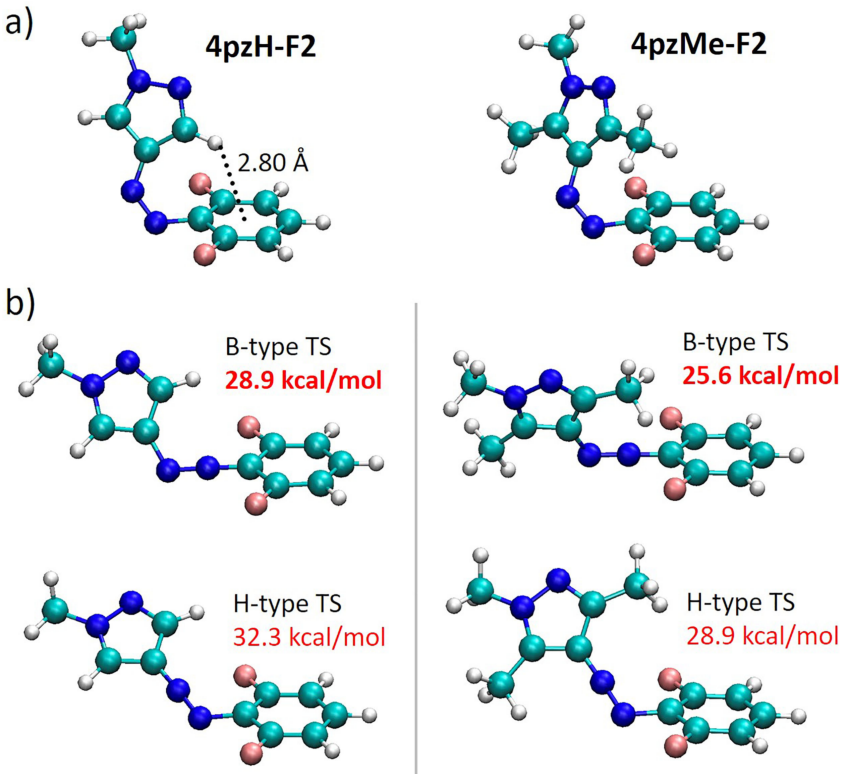


Figure 2: Minimum-energy geometry calculated for a) the *Z*-isomer ground state and b) the transition states with inversion of the N atom next to benzene (B-type) or the N atom next to heteroring (H-type) moiety, in arylazopyrazoles **4pzH-F2** (left) and **4pzMe-F2** (right). Free energy barriers calculated with respect to the corresponding ground-state *Z*-isomer are shown in red. Atom color coding: C in cyan, H in white, N in blue and F in pink.

photoswitch reported in the literature to date. This result demonstrates that it is indeed possible to combinatorially integrate two high performing azo switch fragments to discover switches with very long thermal half-lives (i.e., months to years).

We sought to further explain the trends observed through theoretical analysis of the minimum-energy geometries and noncovalent interactions. The energy-minimized structures for the *Z*-isomer of representative photoswitches are shown in Figure S2 (Supporting Information File 1). The proximity of the *ortho*-benzene substituents to the heteroaryl ring in the *Z*-isomer either stabilizes the *Z*-isomer ground state via noncovalent interactions, or destabilizes it, via steric clashes. In contrast, these effects are significantly diminished for the transition state geometry (Figure S3 in Supporting Information File 1), at which the pyrazole moiety and the *ortho* groups remain far apart. A particularly interesting case in point are the **4pzH-Pyr** compounds: the inclusion of one pyrrolidine group in the *ortho*-position (**4pzH-Pyr1**) is predicted to lead to a massively enhanced *Z*-isomer thermal stability (≈92 years), whereas two bulky pyrrolidine groups (**4pzH-Pyr2**) decrease stability, with a comparably modest $t_{1/2}$ = 76 d (Table 1). Theoretical calculations of the noncovalent index (NCI) surfaces indicate that dispersion forces exist between pyrrolidine groups and the heteroaromatic ring (green surfaces in Figure 3). The inclusion of one pyrrolidine (**4pzH-Pyr1**) promotes weak but stabilizing noncovalent interactions between the *ortho* group and the pyrazole moiety, causing a tilting of the heteroring away from orthogonality with respect to the benzene plane (from θ = 90° in **4pzH** to 114° in **4pzH-Pyr1**), and therefore supporting the long theoretical half-life through *Z*-ground state stabilization (Table 1). However, for the highly congested doubly substituted **4pzH-Pyr2**, a perfect T-shape conformation is predicted as the minimum-energy structure (θ = 90°; Figure 3). The steric interaction between the second pyrrolidine group with the azo group (CH···azo-N distance of only 2.2 Å) prevents the favorable tilting observed for **4pzH-Pyr1**. For the ***Z*-4pzMe-X** analogues (Figure 3), their twisted arrangements allow for a large array of weak and stabilizing noncovalent interactions between the *ortho*-groups and the methyl-substituted pyrazole ring (θ ca. 135°), potentially explaining the increase in $t_{1/2}$ upon systematic introduction of pyrrolidine moieties (Table 1).

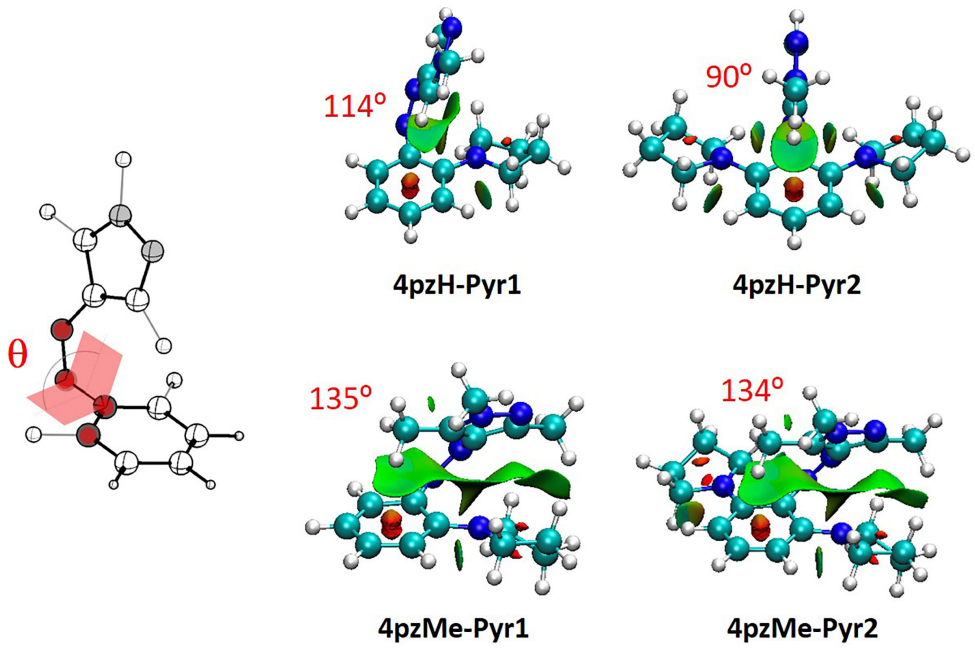


Figure 3: Noncovalent index (NCI) surfaces calculated for representative pyrrolidine-based *ortho*-substituted arylazopyrazoles. The definition of the CCNN dihedral angle between the aryl group and the heteroring moiety (θ) is shown, and the corresponding values for the derivatives are displayed in red.

The *ortho*-halogen-substituted photoswitches also present an unexpected behavior, where very large differences in half-lives are predicted depending on the nature of the halogen atom (from 5 days in **4pzH-Cl2** to ca. 4000 days in **4pzH-F2**, or from 2 minutes in **4pzMe-Cl2** to 26 days in **4pzMe-F2**, Table 1). The analysis of the NCI surfaces indicates that inclusion of F atoms in the *ortho*-position promotes stabilizing dispersion interactions with the pyrazole ring, provoking a tilting of the heteroring from 92° in **4pzH** to 118° in **4pzH-F1** and to 121° in **4pzH-F2** (Figure 4). Stabilizing F···pyrazole noncovalent forces are also predicted in the twisted *Z*-isomers of the **4pzMe-X** family, for which θ remains approximately

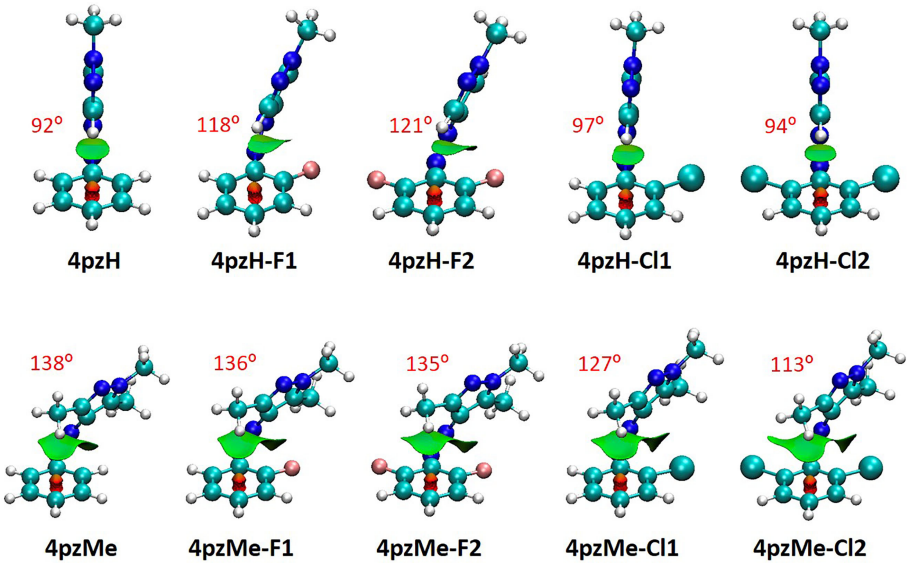


Figure 4: Noncovalent index (NCI) surfaces and θ dihedral angles (in red) calculated for the minimum-energy geometry of *ortho*-halogenated *Z*-arylazopyrazoles.

constant. Furthermore, the atomic charge of fluorine is calculated to be ca. −0.30*e*, which allows for electrostatic interactions with positively charged C atoms (ca. +0.40*e*) of the pyrazole ring in both **4pzH-X** and **4pzMe-X** families (Figure S7, Supporting Information File 1). These favorable dispersion and electrostatic interactions stabilize the *Z*-isomer ground state compared to the corresponding transition state, which in part explains the increase in energy barriers and in turn half-lives upon *ortho*-F substitution. In sharp contrast, the insertion of bulkier chlorine atoms at the *ortho* position(s) induces destabilizing steric clashes, as well as negligible electrostatic forces (chlorine atomic charge of +0.04*e*; Figure S8 in Supporting Information File 1). Somewhat similar to the **4pzH-Pyr** compounds, the destabilizing nature of the Cl···pyrazole interaction is evidenced by the absence of heteroring tilting in the T-shaped *Z*-isomers of the **4pzH-X** family (θ = 97° and 94° for **4pzH-Cl1** and **4pzH-Cl2**), and the systematic decrease in θ for the **4pzMe-X** series in going from **4pzMe** (138°) to **4pzMe-Cl1** (127°) and to **4pzMe-Cl2** (113°; Figure 4).

The effect of *ortho*-substitution on photoconversion efficiency

To a first approximation, in order to achieve high *Z*–*E* photoconversion efficiency, the two isomers of an azo photoswitch must offer well-separated absorption bands. Most frequently, *E*–*Z* photoisomerization is achieved by irradiating in the region of the high-energy π–π* band for the *E*-isomer, whereas *Z*–*E* photoisomerization occurs through irradiation in the low-energy *n*–π* band of the *Z*-isomer. However, an overlap in the absorbances between *E*/*Z* isomers causes incomplete photoswitching.

Table 2 summarizes the theoretical excitation energy separation (in nm) between the characteristic *n*–π* and π–π* transitions in the *ortho*-substituted arylazopyrazoles under study. Theoretical TD-DFT calculations indicate that the family of *ortho*-substituted **4pzH-X** presents well-separated *n*–π* transitions between *Z* and *E* (>30 nm), with the exception of pyrrolidine derivatives (Table 2). As such, the addition of *ortho*-substitution may provide a means to improve the addressability of the longer half-live **4pzH** compounds. In contrast, most of the **4pzMe-X** analogues show a relatively small band separation of the *n*–π* transition between the *Z*- and *E*-isomers, for which a less efficient *Z*-to-*E* photoconversion is expected. Note that the lowest-lying *n*–π* transition in the *Z*-isomer originates from a HOMO to LUMO monoelectronic excitation (Figure 5). The energy gap between these two molecular orbitals highly depends on the molecular conformation, significantly increasing for T-shaped structures (**4pzH-X**) compared to twisted arrangements (**4pzMe-X**), and thus leading to larger *n*–π* band separation for the **4pzH-X** series [18]. On the other hand, the intense π–π* transition of the *Z*-isomer is generally found higher in energy and lower in intensity compared to the *E*-isomer (Tables S1 and S2 in Supporting Information File 1), which is common for azo switches. For the **4pzH-X** family, large π–π* band separations of >50 nm are predicted between *Z* and *E*, whereas smaller values (>30 nm) are calculated for **4pzMe-X** (Table 2). In both series, di-*ortho*-chlorination is predicted to provide the higher overlap in π–π* bands between *Z* and *E*, for which a less efficient *E*-to-*Z* photoconversion is therefore expected.

Table 2: Theoretical energy separation (in nm) and oscillator strength (*f*, in au) of the characteristic electronic excitations in *ortho*-substituted arylazopyrazoles **4pzH-X** and **4pzMe-X**.[a]

	n–π* (*E*–*Z*)	π–π* (*E*–*Z*)	*n*–π* *f* (*Z*)	*n*–π* *f* (*E*)
4pzH	38	58	0.0020	0.0000
4pzH-F1	33	64	0.0129	0.0000
4pzH-F2	44	58	0.0157	0.0000
4pzH-Cl1	51	62	0.0024	0.0074
4pzH-Cl2	46	43	0.0018	0.0129
4pzH-OMe1	35	81	0.0110	0.0000
4pzH-OMe2	46	66	0.0069	0.0204
4pzH-Pyr1	−26	118	0.0309	0.0290
4pzH-Pyr2	−10	81	0.0038	0.0575
4pzMe	−15	30	0.0404	0.0000
4pzMe-F1	4	34	0.0420	0.0008
4pzMe-F2	26	33	0.0426	0.0025
4pzMe-Cl1	5	35	0.0371	0.0085
4pzMe-Cl2	5	23	0.0314	0.0147
4pzMe-OMe1	12	53	0.0404	0.0000
4pzMe-OMe2	29	47	0.0371	0.0124
4pzMe-Pyr1	−34	94	0.0557	0.0728
4pzMe-Pyr2	−36	59	0.0407	0.0865

[a]Excitation energies and intensities are averaged over the different conformers (see Tables S1 and S2 in Supporting Information File 1).

In addition to the band separation, the *n*–π* transition is required to be relatively intense for the *Z*-isomer compared to *E* to allow for efficient *Z*–*E* photoswitching. Theoretical calculations indicate that the family of *ortho*-substituted **4pzH-X** photoswitches provide a weak *n*–π* transition, with oscillator strengths $f < 0.020$. In contrast, **4pzMe-X** derivatives show a relatively intense *n*–π* excitation, with $f > 0.035$. The intensity of the *n*–π* transition is directly related with the dihedral angle between the benzene moiety and the heteroring (Figure S9, Supporting Information File 1), as we have shown previously [18]. The *n*–π* excitation is symmetry-forbidden for a complete (θ = 90°) T-shape conformation. Thus, a tilting of the pyrazole moiety away from orthogonality with respect to the plane generated by the aryl ring leads the *n*–π* excitation to be

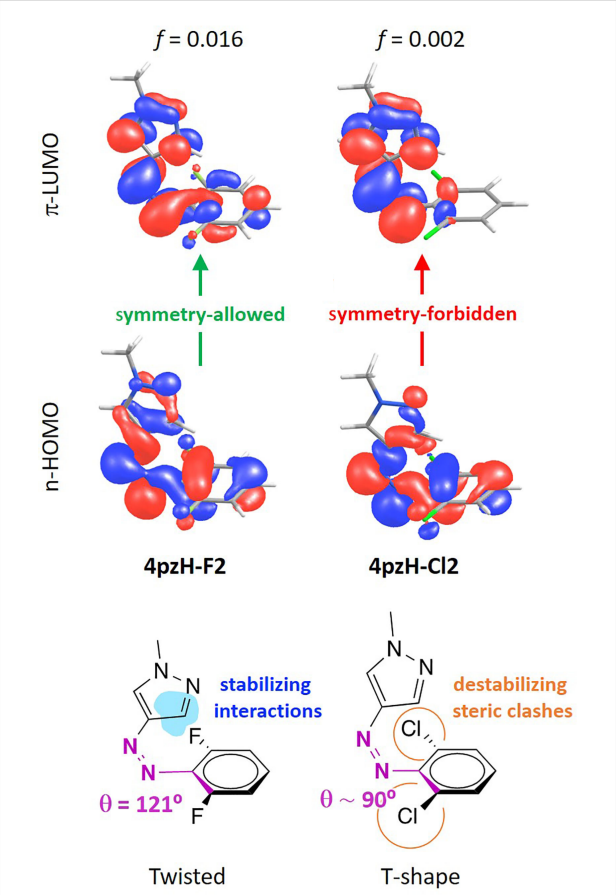


Figure 5: Description of the lowest-lying *n*–π* excitation for the *Z*-isomers of halogenated **4pzH-F2** and **4pzH-Cl2** photoswitches.

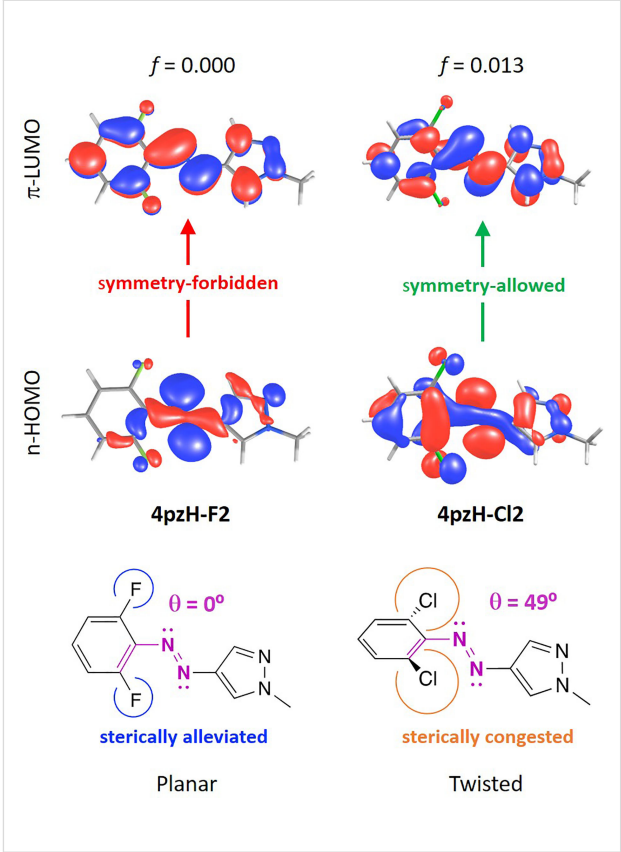


Figure 6: Description of the lowest-lying *n*–π* excitation for the *E*-isomers of halogenated **4pzH-F2** and **4pzH-Cl2** photoswitches.

symmetry-allowed, with the corresponding increase in intensity. For example, the heteroring in fluorine-substituted **4pzH-F2** photoswitch is tilted with a θ = 121°, and presents a moderately intense *n*–π* transition (*f* = 0.016), whereas the *n*–π* intensity in T-shaped *Z*-**4pzH-Cl2** is practically zero (Figure 5). On the other hand, methyl-based **4pzMe-X** derivatives show a twisted-like conformation for the minimum-energy geometry of the *Z*-isomer (Figure S2, Supporting Information File 1), promoting intense, symmetry-allowed *n*–π* excitations (Table 2).

The *n*–π* excitation in *E*-isomers is also symmetry-forbidden for a completely planar conformation in which the heteroring, the azo group and the benzene moiety are coplanar. Bulky groups introduced in the *ortho*-position of the benzene ring, such as methoxy, pyrrolidine or chlorine, promote steric interactions that disrupt planarity, with the corresponding increase in the *n*–π* transition intensity for the *E*-isomer of these compounds (*f* = 0.013, 0.020 and 0.058 for **4pzH-Cl2**, **4pzH-OMe2** and **4pzH-Pyr2**, and *f* = 0.015, 0.012 and 0.087 for **4pzMe-Cl2**, **4pzMe-OMe2** and **4pzMe-Pyr2**, respectively; see Figure 6 for **4pzH-F2** and **4pzH-Cl2**).

To experimentally compare the conformations of the *E*-isomers, we were able to characterize **4pzMe-F2**, **4pzMe-Cl2** and **4pzH-F2** by X-ray crystallography (Figure 7). In agreement with the calculations, the *E*-isomer of **4pzMe-F2** possesses a fully coplanar structure. Unexpectedly, for **4pzMe-OMe2** the pyrazole and benzene rings occupy two separate planes. Thus, in the solid state, the structure of the *E*-isomer **4pzMe-OMe2** becomes even more twisted (calculated dihedral angle of 49° versus 78° in the crystal structure). We attribute this to a packing effect in the solid state. To the best of our knowledge, an *E*-isomer azo photoswitch with this type of solid state packing is unprecedented and may open new possibilities in solid state photoswitchable materials applications. The benzene ring in **4pzH-F2** is also twisted away from the pyrazole ring with a calculated dihedral angle of approximately 42°. This is reminiscent of the *o*-methoxyazobenzenes, reported by Woolley and co-workers [10,11], where steric repulsion forces the *E*-isomer into a nonplanar mode. However, given the small size of the fluorine atoms, sterics are unlikely to play a role for **4pzH-F2** and we would expect a planar *E*-isomer, as noted by Hecht and co-workers in their *o*-fluoroazobenzenes [13,14]. Thus, once again, solid state packing of these derivatives is surprising.

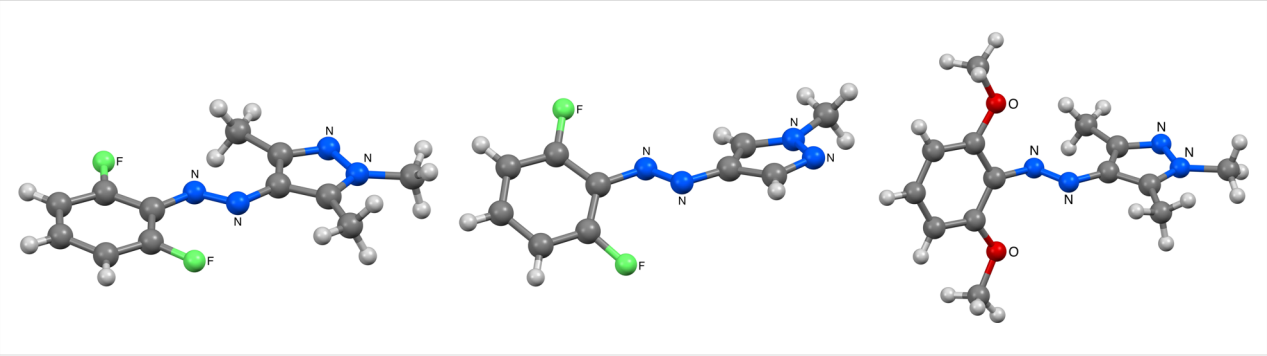


Figure 7: X-ray structures of **4pzMe-F2** (left), **4pzH-F2** (middle) and **4pzMe-OMe2** (right).

The experimental photoswitching performance of the synthesized **4pzMe-F2, 4pzMe-Cl2** and **4pzMe-OMe2** photoswitches was assessed and compared to the computational work (see Figure 8 and Table 3). In all cases, 420 nm light was used to promote *Z*–*E* switching and access a photostationary state (PSS) enriched with the *E*-isomer, whereas UVA light was used to obtain the *Z*-isomer-enriched PSS. Theoretical π–π* band separations for the *E*-isomers of **4pzMe-F2** and **4pzMe-Cl2** (Table 2) match very closely with the experimental data (Table 3), with the exception of the methoxy **4pzMe-OMe2** analogue. A large conformational space is expected for the twisted **4pzMe-OMe2** (vide supra) due to the *ortho*-methoxy groups, which likely explains the inaccuracy of the computational predictions for this compound. The experimental π–π* band for all compounds undergoes a blue shift upon isomerization *E* to *Z*, also in good accord with the theoretical predictions (Figure 8,

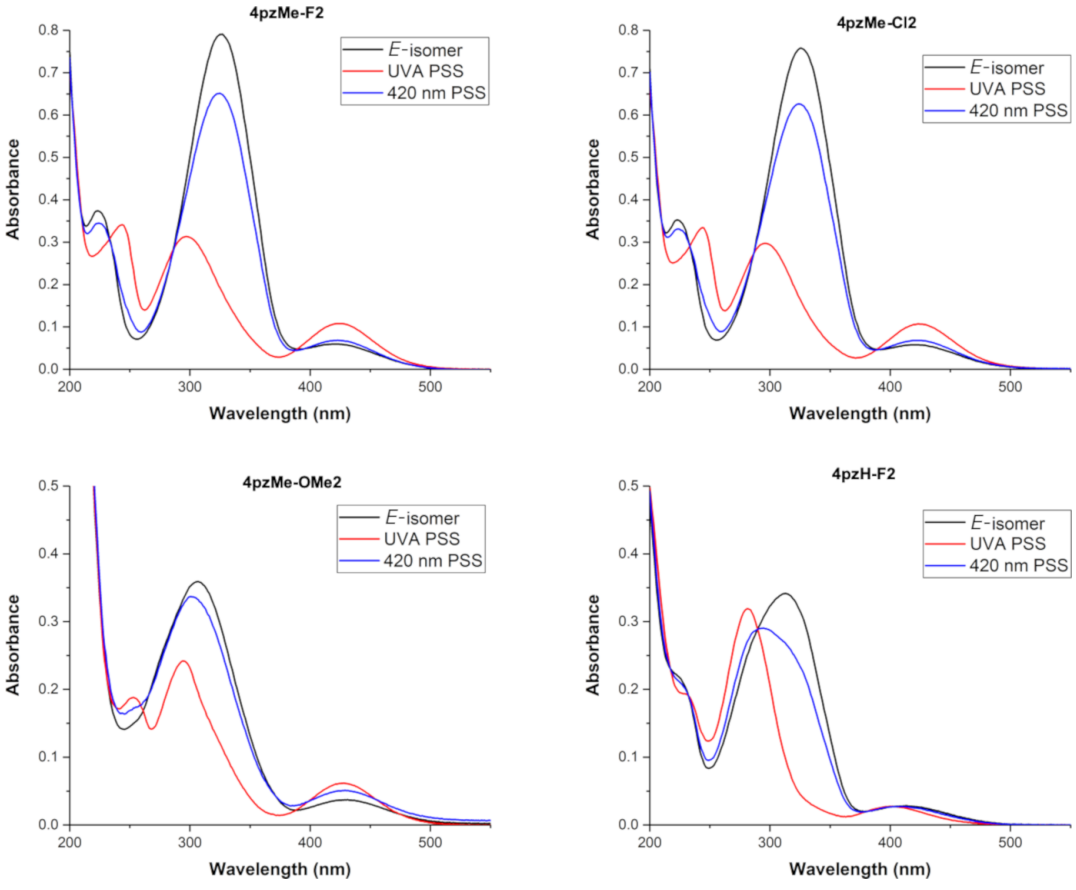


Figure 8: Experimental UV–vis spectra of **4pzMe-F2**, **4pzMe-Cl2**, **4pzMe-OMe2** and **4pzH-F2** in MeCN at 25 μM.

Table 3: Experimental band separation (in nm) of the characteristic UV–vis absorption bands, calculated as the λ_{max} subtraction between *E* and *Z*-isomers, and photostationary-state-conversion efficiency (PSS in %).

	n–π* (*E*–*Z*)	π–π* (*E*–*Z*)	PSS (% *E*)[a]	PSS (% *Z*)[b]
4pzH[c]	14	53	70	>98
4pzH-F2	13	33	42	92
4pzMe[c]	−16	39	>98	>98
4pzMe-F2	−3	30	77	93
4pzMe-Cl2	−1	29	85	80
4pzMe-OMe2	−3	13	73	81

[a]Irradiation wavelength = 420 nm. [b]UVA irradiation. [c]Data extracted from reference [18].

Table S1 and S2 in Supporting Information File 1). Compared to **4pzMe**, photoswitches **4pzMe-Cl2** and **4pzMe-OMe2** show smaller π–π* band separations, which supports the reduced *E*–*Z* photoisomerization efficiency (80 and 81%, respectively) upon *E*–*Z* switching (Table 3). In contrast, **4pzMe-F2** and **4pzH-F2** still provide excellent *E*–*Z* photoisomerization of 93% and 92%, respectively, despite the relatively small π–π* band separation (30 and 33 nm, respectively).

Conversely, the experimental *n*–π* band separation is very small (near complete band overlap) for the **4pzMe-X** family (Figure 8), in contrast to the theoretical predictions. We note that we previously found much better correlation for the heteroazoaryl switches without *ortho*-substituents [18]. Although the computed *n*–π* band separations do not quantitatively reproduce the experimental data, they do qualitatively predict an increased band overlap in the **4pzMe-X** family compared to **4pzH** (Table 2). Furthermore, the comparably intense *n*–π* band of the Z-**4pzMe-X** analogues, a function of the twisted (i.e., non-T-shaped) conformation of these compounds, is in agreement between theory and experiment (Supporting Information File 1, Figure S9). A significant *n*–π* band overlap directly impacts the *Z*–*E* photoconversion efficiency, and thus lower PSSs of 77, 85 and 73% are recorded for **4pzMe-F2, 4pzMe-Cl2** and **4pzMe-OMe2**, respectively, versus >98% for **4pzMe**. Similarly, **4pzH-F2** possesses a lower PSS versus **4pzH** (42% versus 70%). While inaccuracies in the DFT calculations may explain the differences observed, differences in the excited-state profiles and quantum yields for the photoisomerization pathway may also contribute to the lack of correlation between band overlap and photoisomerization efficiency [35].

Conclusion

We aimed to combine two features now known to significantly improve the performance of azoarene photoswitches – *ortho*-substitution of the benzene ring(s) and replacement of one of the benzenes for a pyrazole (to give an arylazopyrazole) – into a single switch unit. We show that *ortho*-benzene substitution of the arylazopyrazoles drastically increases the *Z*-isomer stability and allows further tuning of their addressability. This in turn has enabled us to discover **4pzH-F2**; a novel azoheteroarene photoswitch with the longest reported thermal half-life in the literature to date of ≈46 years. Many of the molecular features that we previously determined to be important for arylazopyrazole light absorption and *Z*-isomer half-life, such as the key role of conformation, hold true for these new derivatives. We believe our data provide important results for the further development of high-performance azo switches, which will open up possibilities in a large range of applications.

Experimental

Computational details. Theoretical calculations were performed using the Gaussian 16 (revision A03) suite of programs [36]. Several rotational conformers of the studied compounds are available due to free rotation of the aromatic rings along single bonds linked to the azo bridge. All the possible conformers both in the *Z*- and *E*-forms were fully optimized by using the hybrid exchange-correlation PBE0 functional [37] including the Grimme's dispersion correction in its latest version (D3) [38]. The split-valence Pople's basis set 6-31G** was used throughout [39]. Transition states were optimized by using the Berny algorithm at the same level of theory [40]. Theoretical calculations were carried out in the gas phase. Theoretical kinetic studies were carried out at the PBE0-D3/6-31G** level of theory by considering all possible transition states and minimum-energy conformers for the *Z*-isomer. All the transition states were characterized by one imaginary frequency of approximately (440–520)i cm^{-1}. The reliability of the single-determinant Kohn–Sham DFT approach to describe correctly the transition state energy/geometry was assessed by calculating the energy difference between the lowest-lying singlet excited state and the ground state at the transition state geometry for **4pzH** and **4pzMe**. Theoretical calculations at the PBE0-D3/6-31G** level indicate that the lowest-lying S1 state lies >1 eV above in energy with respect to the ground state, and therefore the DFT approach is accurate enough for TS analysis. We refer to our prior publication [18] for details of the theoretical protocol used to compute half-lives. The Boltzmann distribution was applied to the energy barriers [18] and to the relative energy differences between all possible *Z*-conformers. Note that half-lives are inversely proportional to the rate constant, and this is exponentially dependent on the free-energy barrier according to Eyring theory. Thus, a small variation in the energy barrier of <1 kcal/mol leads to a change of few orders of magnitude in half-life. Vertical electronic transition energies for the ground state geometries of both *Z*- and *E*-isomers were computed under the time-dependent density functional theory

(TDDFT) approach [41,42]. The 20 lowest-lying singlet excited states were calculated in all conformers at the TD-PBE0/6-31G** level of theory in the gas phase. Solvent effects in conformational stability, half-life times and excitation energies, were analyzed under the polarizable continuum model (PCM) and acetonitrile as solvent (Tables S3 and S4 in Supporting Information File 1). Theoretical calculations indicate that, although the solvent model impacts quantitatively in the parameters analyzed, qualitative rankings are maintained. Atomic charges were calculated by performing a natural bond orbital (NBO) analysis [43]. Wiberg bond indeces (WI) were calculated by using the Gaussian NBO version 3.1 [44] as implemented in Gaussian 16 (revision A03) through the analysis of the SCF density calculated at the PBE0/6-31G** level of theory. The noncovalent index (NCI) for the different compounds was computed using the NCIPLOT program [45,46].

Synthesis and characterization. Details for the synthesis and experimental characterization of **4pzMe-F2, 4pzMe-Cl2, 4pzMe-OMe2** and **4pzH-F2** can be found in Supporting Information File 1.

Supporting Information

Raw data can be found at doi:10.14469/hpc/6203

Supporting Information File 1

Theoretical calculations, synthetic methods, experimental characterization and X-ray crystallography data.
[https://www.beilstein-journals.org/bjoc/content/supplementary/1860-5397-15-266-S1.pdf]

Supporting Information File 2

CIF files for **4pzMe-F2**, **4pzMe-OMe2**, **4pzMe-OMe2_diethylether** and **4pzH-F2**.
[https://www.beilstein-journals.org/bjoc/content/supplementary/1860-5397-15-266-S2.cif]

Acknowledgements

J.C. acknowledges the Generalitat Valenciana for the postdoctoral APOSTD/2017/081 fellowship. R.S.L.G would like to thank the Faculty of Natural Sciences at Imperial College London for the Schrödinger Scholarship. M.J.F. would like to thank the EPSRC for an Established Career Fellowship (EP/R00188X/1).

ORCID® iDs

Joaquin Calbo - https://orcid.org/0000-0003-4729-0757
Aditya R. Thawani - https://orcid.org/0000-0003-0388-9055
Rosina S. L. Gibson - https://orcid.org/0000-0002-9621-565X
Andrew J. P. White - https://orcid.org/0000-0001-6175-1607
Matthew J. Fuchter - https://orcid.org/0000-0002-1767-7072

References

1. Velema, W. A.; Szymanski, W.; Feringa, B. L. *J. Am. Chem. Soc.* **2014,** *136,* 2178–2191. doi:10.1021/ja413063e
2. Broichhagen, J.; Frank, J. A.; Trauner, D. *Acc. Chem. Res.* **2015,** *48,* 1947–1960. doi:10.1021/acs.accounts.5b00129
3. Fehrentz, T.; Schönberger, M.; Trauner, D. *Angew. Chem., Int. Ed.* **2011,** *50,* 12156–12182. doi:10.1002/anie.201103236
4. Gindre, D.; Boeglin, A.; Fort, A.; Mager, L.; Dorkenoo, K. D. *Opt. Express* **2006,** *14,* 9896–9901. doi:10.1364/oe.14.009896
5. Lee, H.-i.; Wu, W.; Oh, J. K.; Mueller, L.; Sherwood, G.; Peteanu, L.; Kowalewski, T.; Matyjaszewski, K. *Angew. Chem., Int. Ed.* **2007,** *46,* 2453–2457. doi:10.1002/anie.200604278
6. Sendai, T.; Biswas, S.; Aida, T. *J. Am. Chem. Soc.* **2013,** *135,* 11509–11512. doi:10.1021/ja4060146
7. Tian, H.; Yang, S. *Chem. Soc. Rev.* **2004,** *33,* 85–97. doi:10.1039/b302356g
8. Dong, M.; Babalhavaeji, A.; Samanta, S.; Beharry, A. A.; Woolley, G. A. *Acc. Chem. Res.* **2015,** *48,* 2662–2670. doi:10.1021/acs.accounts.5b00270
9. Bandara, H. M. D.; Burdette, S. C. *Chem. Soc. Rev.* **2012,** *41,* 1809–1825. doi:10.1039/c1cs15179g
10. Beharry, A. A.; Sadovski, O.; Woolley, G. A. *J. Am. Chem. Soc.* **2011,** *133,* 19684–19687. doi:10.1021/ja209239m
11. Dong, M.; Babalhavaeji, A.; Collins, C. V.; Jarrah, K.; Sadovski, O.; Dai, Q.; Woolley, G. A. *J. Am. Chem. Soc.* **2017,** *139,* 13483–13486. doi:10.1021/jacs.7b06471
12. Samanta, S.; McCormick, T. M.; Schmidt, S. K.; Seferos, D. S.; Woolley, G. A. *Chem. Commun.* **2013,** *49,* 10314–10316. doi:10.1039/c3cc46045b
13. Bléger, D.; Schwarz, J.; Brouwer, A. M.; Hecht, S. *J. Am. Chem. Soc.* **2012,** *134,* 20597–20600. doi:10.1021/ja310323y
14. Knie, C.; Utecht, M.; Zhao, F.; Kulla, H.; Kovalenko, S.; Brouwer, A. M.; Saalfrank, P.; Hecht, S.; Bléger, D. *Chem. – Eur. J.* **2014,** *20,* 16492–16501. doi:10.1002/chem.201404649
15. Crespi, S.; Simeth, N. A.; König, B. *Nat. Rev. Chem.* **2019,** *3,* 133–146. doi:10.1038/s41570-019-0074-6
16. Harris, J. D.; Moran, M. J.; Aprahamian, I. *Proc. Natl. Acad. Sci. U. S. A.* **2018,** *115,* 9414–9422. doi:10.1073/pnas.1714499115
17. Weston, C. E.; Richardson, R. D.; Haycock, P. R.; White, A. J. P.; Fuchter, M. J. *J. Am. Chem. Soc.* **2014,** *136,* 11878–11881. doi:10.1021/ja505444d
18. Calbo, J.; Weston, C. E.; White, A. J. P.; Rzepa, H. S.; Contreras-García, J.; Fuchter, M. J. *J. Am. Chem. Soc.* **2017,** *139,* 1261–1274. doi:10.1021/jacs.6b11626
19. Gibson, R. S. L.; Calbo, J.; Fuchter, M. J. *ChemPhotoChem* **2019,** *3,* 372–377. doi:10.1002/cptc.201900065
20. Devi, S.; Gaur, A. K.; Gupta, D.; Saraswat, M.; Venkataramani, S. *ChemPhotoChem* **2018,** *2,* 806–810. doi:10.1002/cptc.201800146
21. Weston, C. E.; Krämer, A.; Colin, F.; Yildiz, Ö.; Baud, M. G. J.; Meyer-Almes, F.-J.; Fuchter, M. J. *ACS Infect. Dis.* **2017,** *3,* 152–161. doi:10.1021/acsinfecdis.6b00148
22. Lamping, S.; Stricker, L.; Ravoo, B. J. *Polym. Chem.* **2019,** *10,* 683–690. doi:10.1039/c8py01496e
23. Stricker, L.; Fritz, E.-C.; Peterlechner, M.; Doltsinis, N. L.; Ravoo, B. J. *J. Am. Chem. Soc.* **2016,** *138,* 4547–4554. doi:10.1021/jacs.6b00484

24. Schnurbus, M.; Stricker, L.; Ravoo, B. J.; Braunschweig, B. *Langmuir* **2018,** *34,* 6028–6035. doi:10.1021/acs.langmuir.8b00587
25. Ghebreyessus, K.; Cooper, S. M., Jr. *Organometallics* **2017,** *36,* 3360–3370. doi:10.1021/acs.organomet.7b00493
26. Haydell, M. W.; Centola, M.; Adam, V.; Valero, J.; Famulok, M. *J. Am. Chem. Soc.* **2018,** *140,* 16868–16872. doi:10.1021/jacs.8b08738
27. Adam, V.; Prusty, D. K.; Centola, M.; Škugor, M.; Hannam, J. S.; Valero, J.; Klöckner, B.; Famulok, M. *Chem. – Eur. J.* **2018,** *24,* 1062–1066. doi:10.1002/chem.201705500
28. Devi, S.; Saraswat, M.; Grewal, S.; Venkataramani, S. *J. Org. Chem.* **2018,** *83,* 4307–4322. doi:10.1021/acs.joc.7b02604
29. Samanta, S.; Beharry, A. A.; Sadovski, O.; McCormick, T. M.; Babalhavaeji, A.; Tropepe, V.; Woolley, G. A. *J. Am. Chem. Soc.* **2013,** *135,* 9777–9784. doi:10.1021/ja402220t
30. Konrad, D. B.; Frank, J. A.; Trauner, D. *Chem. – Eur. J.* **2016,** *22,* 4364–4368. doi:10.1002/chem.201505061
31. Samanta, D.; Gemen, J.; Chu, Z.; Diskin-Posner, Y.; Shimon, L. J. W.; Klajn, R. *Proc. Natl. Acad. Sci. U. S. A.* **2018,** *115,* 9379–9384. doi:10.1073/pnas.1712787115
32. Ahmed, Z.; Siiskonen, A.; Virkki, M.; Priimagi, A. *Chem. Commun.* **2017,** *53,* 12520–12523. doi:10.1039/c7cc07308a
33. Crespi, S.; Simeth, N. A.; Bellisario, A.; Fagnoni, M.; König, B. *J. Phys. Chem. A* **2019,** *123,* 1814–1823. doi:10.1021/acs.jpca.8b11734
34. Yin, T.-T.; Zhao, Z.-X.; Zhang, H.-X. *New J. Chem.* **2017,** *41,* 1659–1669. doi:10.1039/c6nj03095e
35. Wang, Y.-T.; Liu, X.-Y.; Cui, G.; Fang, W.-H.; Thiel, W. *Angew. Chem., Int. Ed.* **2016,** *55,* 14009–14013. doi:10.1002/anie.201607373
36. *Gaussian 16,* Revision A.03; Gaussian, Inc.: Wallingford, CT, 2016, https://gaussian.com/gaussian16/.
37. Adamo, C.; Barone, V. *J. Chem. Phys.* **1999,** *110,* 6158–6170. doi:10.1063/1.478522
38. Grimme, S.; Antony, J.; Ehrlich, S.; Krieg, H. *J. Chem. Phys.* **2010,** *132,* 154104. doi:10.1063/1.3382344
39. Francl, M. M.; Pietro, W. J.; Hehre, W. J.; Binkley, J. S.; Gordon, M. S.; DeFrees, D. J.; Pople, J. A. *J. Chem. Phys.* **1982,** *77,* 3654–3665. doi:10.1063/1.444267
40. Schlegel, H. B. *J. Comput. Chem.* **1982,** *3,* 214–218. doi:10.1002/jcc.540030212
41. Jamorski, C.; Casida, M. E.; Salahub, D. R. *J. Chem. Phys.* **1996,** *104,* 5134–5147. doi:10.1063/1.471140
42. Petersilka, M.; Gossmann, U. J.; Gross, E. K. U. *Phys. Rev. Lett.* **1996,** *76,* 1212–1215. doi:10.1103/physrevlett.76.1212
43. Glendening, E. D.; Landis, C. R.; Weinhold, F. *Wiley Interdiscip. Rev.: Comput. Mol. Sci.* **2012,** *2,* 1–42. doi:10.1002/wcms.51
44. *NBO,* Version 3.1; University of Wisconsin: Madison, WI, http://nbo6.chem.wisc.edu/.
45. Johnson, E. R.; Keinan, S.; Mori-Sanchez, P.; Contreras-Garcia, J.; Cohen, A. J.; Yang, W. *J. Am. Chem. Soc.* **2010,** *132,* 6498–6506. doi:10.1021/ja100936w
46. Contreras-García, J.; Johnson, E. R.; Keinan, S.; Chaudret, R.; Piquemal, J.-P.; Beratan, D. N.; Yang, W. *J. Chem. Theory Comput.* **2011,** *7,* 625–632. doi:10.1021/ct100641a

License and Terms

This is an Open Access article under the terms of the Creative Commons Attribution License (http://creativecommons.org/licenses/by/4.0). Please note that the reuse, redistribution and reproduction in particular requires that the authors and source are credited.

The license is subject to the *Beilstein Journal of Organic Chemistry* terms and conditions: (https://www.beilstein-journals.org/bjoc)

The definitive version of this article is the electronic one which can be found at:
doi:10.3762/bjoc.15.266

BEILSTEIN JOURNAL OF ORGANIC CHEMISTRY

A chiral self-sorting photoresponsive coordination cage based on overcrowded alkenes

Constantin Stuckhardt[1,2], Diederik Roke[1], Wojciech Danowski[1], Edwin Otten[1], Sander J. Wezenberg[*3] and Ben L. Feringa[*1]

Full Research Paper

Open Access

Address:
[1]Stratingh Institute for Chemistry, University of Groningen, Nijenborgh 4, 9747 AG, Groningen, The Netherlands, [2]Organisch-Chemisches Institut, University of Münster, Corrensstrasse 40, 48149 Münster, Germany and [3]Leiden Institute of Chemistry, Leiden University, Einsteinweg 55, 2333 CC, Leiden, The Netherlands

Email:
Sander J. Wezenberg[*] - s.j.wezenberg@lic.leidenuniv.nl;
Ben L. Feringa[*] - b.l.feringa@rug.nl

* Corresponding author

Keywords:
coordination cages; molecular motors; molecular switches; overcrowded alkene; palladium

Beilstein J. Org. Chem. **2019,** *15,* 2767–2773.
doi:10.3762/bjoc.15.268

Received: 05 July 2019
Accepted: 11 October 2019
Published: 15 November 2019

This article is part of the thematic issue "Molecular switches".

Guest Editor: W. Szymanski

© 2019 Stuckhardt et al.; licensee Beilstein-Institut.
License and terms: see end of document.

Abstract

In recent years, increasing efforts have been devoted to designing new functional stimuli-responsive supramolecular assemblies. Here, we present three isomeric supramolecular coordination complexes consisting of a Pd_2L_4 stoichiometry. As shown by NMR, CD and X-ray studies, as well as DFT calculations, these complexes form cage-like structures by chiral self-sorting. Photochromic ligands derived from first generation molecular motors enable light-driven interconversion between the three isomers. Two of the isomers were able to form host–guest complexes opening up new prospects toward stimuli-controlled substrate binding and release.

Introduction

Supramolecular coordination complexes (SCCs) represent a promising class of compounds which have been used in a variety of molecular systems [1-6]. Taking advantage of the vacant cavity inside these complexes, SCCs have been applied in drug delivery [6-8], supramolecular catalysis [9-12], X-ray structure determination [13,14] and stabilization of reactive species [15-17]. The use of reversible metal–ligand coordination bonds gives rise to systems that allow for adaption to external stimuli such as pH, anions, electric potential, concentration and light [4,8,18-21]. Using light to dynamically control the shape and function of SCCs is a very promising strategy as it is a noninvasive stimulus that can be easily applied with high spatiotemporal control, without producing any waste. Systems have been reported where photoisomerization of azobenzene-derived anions encapsulated in supramolecular palladium complexes caused immediate crystallization [22]. Moreover, azobenzenes have been used to functionalize both the interior [23] and exterior [24] of SCCs to photochemically control guest binding and release. Furthermore, incorporation of dithienylethene into the ligands connecting the metal centers has been used to control host–guest interactions [25-28], structural composition [29], and sol–gel transition [30]. However,

dithienylethene undergoes a limited structural change upon photoisomerization and, up to now, photoswitchable ligands based on other types of photochromic switches have not been reported in the literature.

In chiral self-sorting SCCs, either homo- or heterochiral complexes are formed exclusively through high fidelity recognition of the components within the complex [31-33]. The formation of such complexes with high selectivity and well-defined chirality is essential for the application of SCCs towards chiral recognition and sensing [34-37]. To the best of our knowledge no self-sorted responsive SCCs have been reported so far.

Molecular motors based on overcrowded alkenes are unique photoswitches that are able to undergo unidirectional rotation upon irradiation with light [38-40]. Moreover, they can be used as chiroptical multistate switches to control various functions in areas such as catalysis [41-43], soft materials [43-45] and supramolecular chemistry [46,47]. Employing molecular motors as ligands in SCCs provides an interesting strategy to form responsive coordination complexes, as they feature a large geometric change upon switching [47].

Herein, we report a photoresponsive coordination cage with ligands based on a first generation molecular motor (Figure 1). Cages with a Pd_2L_4 composition are formed from bidentate bispyridyl ligands and Pd(II) ions with a square planar geometry, which have been widely studied [6,48-50]. The photochromic ligands can be switched between three states, forming separate discrete cage complexes, allowing cage-to-cage transformations (Scheme 1). Interestingly, only homochiral cages are formed revealing that a chiral self-sorting process takes place. In addition, two of the cage isomers can bind a tosylate anion in solution by formation of a host–guest complex.

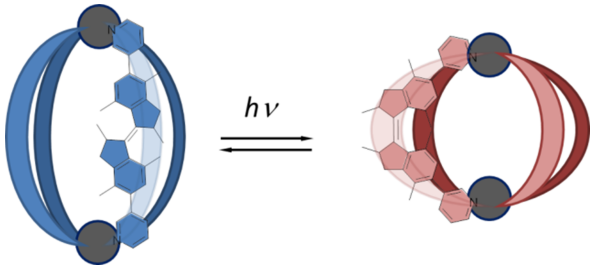
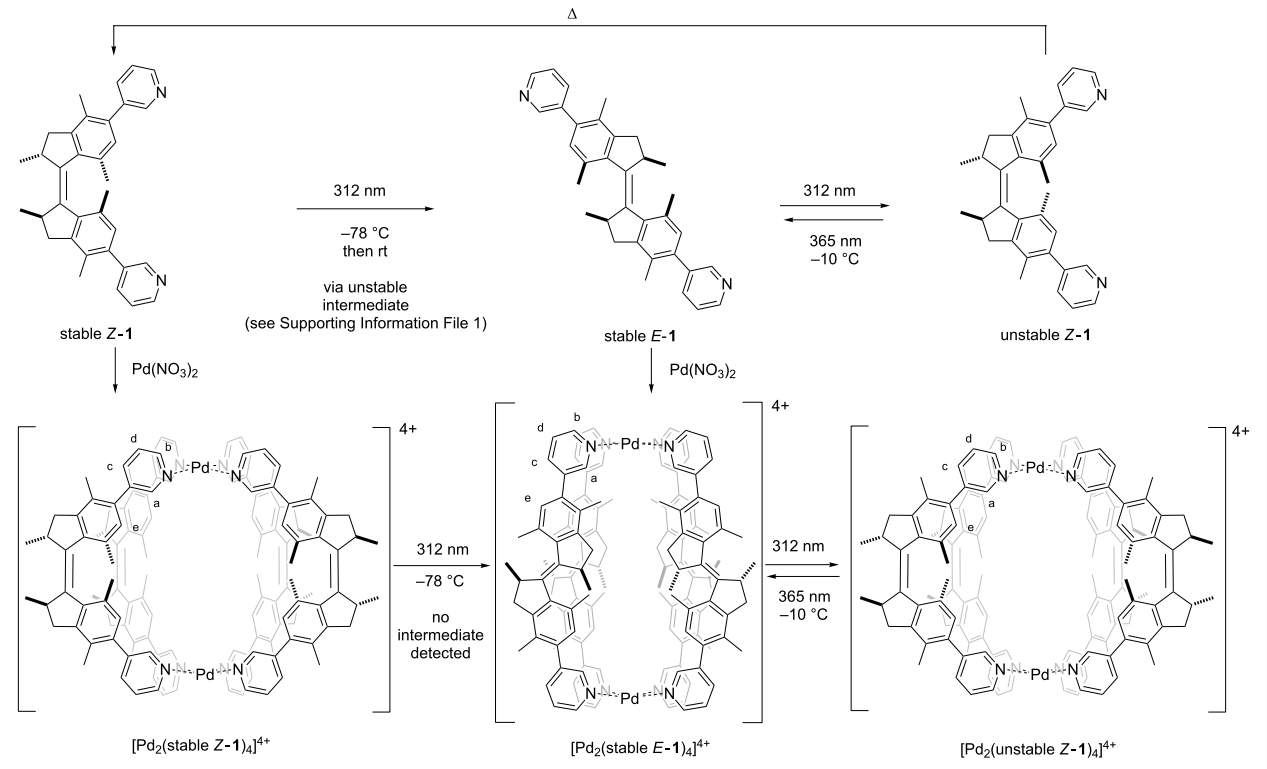


Figure 1: Schematic representation of a photoresponsive cage with ligands based on overcrowded alkenes.

Results and Discussion

Ligands *Z*-**1** and *E*-**1** (Scheme 1) were synthesized by a Suzuki cross-coupling reaction of 3-pyridinylboronic acid with an *E*/*Z*



Scheme 1: Cage formation of overcrowded alkene switches *E*/*Z*-**1** and their isomerization behavior. Note that the intermediate unstable *E*-**1** is not shown; due to the low barrier of thermal helix inversion and therefore fast isomerization to the corresponding stable isomer.

mixture of reported overcrowded alkene precursors [51] (see Supporting Information File 1 for full experimental details). Heating a 2:1 mixture of ligands (*S,S*)-*Z*-**1** or (*S,S*)-*E*-**1** with $Pd(NO_3)_2$ in acetonitrile at reflux led to the quantitative formation of cage Pd_2(stable *Z*-**1**)$_4$ or Pd_2(stable *E*-**1**)$_4$, respectively, as evidenced by ^{1}H NMR, DOSY and HRMS. The ^{1}H NMR signals of the pyridine moieties of the ligands ($H_{a–d}$) in the assembled cages are shifted downfield compared to those of the free ligands, as expected due to metal coordination (Figure 2) [28]. As the ligand exchange in Pd_2L_4 complexes is slow on the NMR timescale, the discrete signals do not represent an average of quickly interconverting isomers [52,53]. The formation of cage complexes using a racemic mixture of ligands stable *Z*-**1** or stable *E*-**1**, resulted in the exact same ^{1}H NMR spectrum as was obtained with the enantiopure ligands. Using a racemic mixture of ligands, four different diastereomeric cages can be formed ((*S*,*S*)$_4$, (*S*,*S*)$_3$(*R*,*R*), (*S*,*S*)$_2$(*R*,*R*)$_2$ and (*S*,*S*)(*R*,*R*)(*S*,*S*)(*R*,*R*) and their enantiomeric pairs). However, in both cases, only one set of signals is observed, which is a strong indication that only one species with high symmetry is formed by chiral self-sorting without any sign of the formation of diastereomeric mixtures. To further confirm the self-sorting behavior of these cage structures, CD spectroscopy was performed. A linear dependence of CD amplitude on the ee of ligand stable *Z*-**1** was found, which can be expected when the homochiral enantiomers of cage structure Pd_2(stable *Z*-**1**)$_4$ are the only optically active species in solution (Figure S1, Supporting Information File 1).

Additionally, DOSY NMR spectroscopy revealed that the signals correspond to a single type of assembly in each case (see Supporting Information File 1, section 2). The measured diffusion coefficients (D = 8.7 × 10^{-10} m^2 s^{-1} for Pd_2(stable *Z*-**1**)$_4$ and D = 7.9 × 10^{-10} m^2 s^{-1} for cage Pd_2(stable *E*-**1**)$_4$ in CD_3CN at 23 °C) can be translated into hydrodynamic radii of r_H = 7.2 Å for Pd_2(stable *Z*-**1**)$_4$ and r_H = 8.0 Å for Pd_2(stable *E*-**1**)$_4$ by using the Stokes–Einstein equation [54]. By means of ESI high-resolution mass spectrometry, we were able to verify the Pd_2L_4 constitution of both cages. The HRMS spectrum of Pd_2(stable *Z*-**1**)$_4$ shows the signals for the cations [Pd_2(stable *Z*-**1**)$_4$$(NO_3)_3]^+$, [$Pd_2$(stable *Z*-**1**)$_4$$(NO_3)_2]^{2+}$, [$Pd_2$(stable *Z*-**1**)$_4$$(NO_3)]^{3+}$, [$Pd_2$(stable *Z*-**1**)$_4]^{4+}$ (Figure 3). For Pd_2(stable *E*-**1**)$_4$, the peaks corresponding to the cations [Pd_2(stable *E*-**1**)$_4$$(NO_3)_2]^{2+}$ and [Pd_2(stable *E*-**1**)$_4$$(NO_3)]^{3+}$ were observed (Figure 3). For both isomers, the experimental isotopic patterns and exact *m*/*z* values match the simulated patterns.

A single crystal of Pd_2(stable *E*-**1**)$_4$ formed from a racemic mixture of ligand *E*-**1** suitable for X-ray structure determination was grown by vapor diffusion of a 1:1 mixture of benzene and diethyl ether into a solution of the cage in a 1:1 mixture of acetonitrile and chloroform. The crystal structure shows cage structures with a Pd_2L_4 stoichiometry with one NO_3^- counterion and one molecule of acetonitrile located inside each cage. In addition, a chloride ion is located close to the metal centers outside of the cage. This counterion most likely originates from the solvent, as chloroform can contain considerable amounts of HCl. The additional anions required to balance the charge of the tetracationic Pd_2L_4 cage could not be unambiguously located in the difference Fourier map (see Supporting Information File 1 for details). The structure belongs to the *P*4/*n* space group and the unit cell is occupied by a pair of enantiomeric cages in

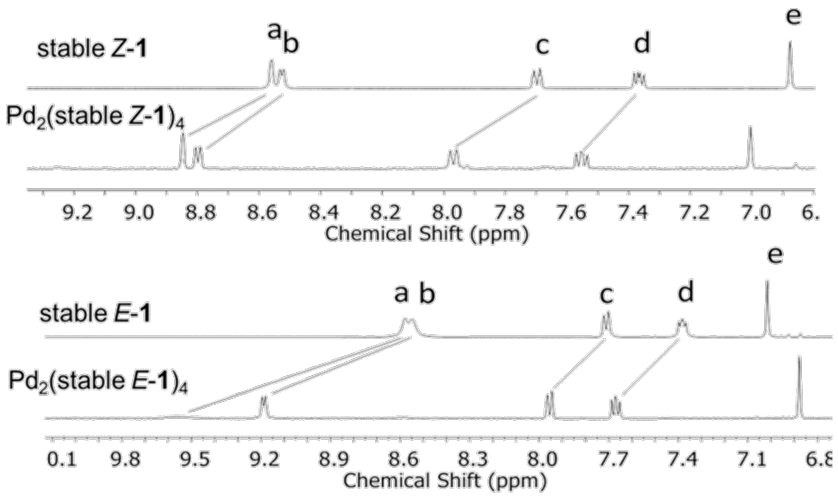


Figure 2: Aromatic region of stacked ^{1}H NMR spectra (in CD_3CN) of stable *Z*-**1** and cage complex Pd_2(stable *Z*-**1**)$_4$ (top) and *E*-**1** and cage complex Pd_2(stable *E*-**1**)$_4$ (bottom).

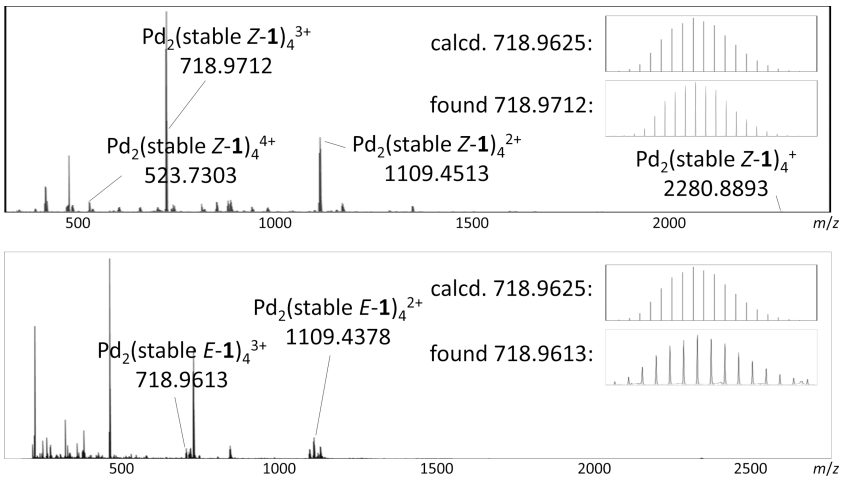


Figure 3: HRMS spectra of cage complex Pd_2(stable *Z*-**1**)$_4$ (top) and cage complex Pd_2(stable *E*-**1**)$_4$ (bottom); Insets: comparison of simulated and measured isotopic patterns of $Pd_2L_4(NO_3)^{3+}$ ions.

which the Pd–Pd axis of each cage is located at the 4-fold rotation axis. This means that the cage structure is made up with exclusively (*R,R*) or (*S,S*) enantiomer of the ligand and that the elementary cell is built from the racemic pair of cages.

DFT calculations were performed to gain insight in the self-sorting behavior of cages Pd_2(stable *Z*-**1**)$_4$ and Pd_2(stable *E*-**1**)$_4$. The structures of all possible cage diastereomers were optimized using B3LYP/6-31G(d) for C,H,N and LANL2DZ with ECP for Pd in the gas phase without counter ions. The optimized structure of Pd_2(stable *E*-**1**)$_4$ is in good agreement with the solved X-ray structure (Figure 4). Moreover, the calculations revealed that the homochiral cage Pd_2((*S,S*)-stable *E*-**1**)$_4$ (and its enantiomer) are energetically favored by at least 61 kJ mol^{-1} compared to the other possible diastereomers (Table S1, Supporting Information File 1). Similar calculations on the diastereomers of Pd_2(stable *Z*-**1**)$_4$ revealed that the homochiral cage diastereomers Pd_2((*S,S*)-stable *Z*-**1**)$_4$ are energetically favored as well, by at least 19 kJ mol^{-1} (Table S2, Supporting Information File 1). These calculations support that these cages are formed by chiral narcissistic self-sorting.

Next, we were interested in the guest binding abilities of cages Pd_2(stable *Z*-**1**)$_4$ and Pd_2(stable *E*-**1**)$_4$. The tosylate anion was chosen as it has the appropriate size to fit inside the cages. A Job plot analysis revealed a 1:1 binding stoichiometry between both cage isomers and OTs^- (Figures S3–S5, Supporting Information File 1), which corresponds to the model in which OTs^- serves as a guest molecule which is encapsulated inside the cages [55,56]. ^{1}H NMR titrations with tetrabutylammonium tosylate revealed that both cages are able to bind OTs^-, showing similar binding strengths (K_B = 1604 ± 39 M^{-1} for Pd_2(stable *Z*-1)$_4$; K_B = 1758 ± 39 M^{-1} for Pd_2(stable *E*-**1**)$_4$ at 293 K).

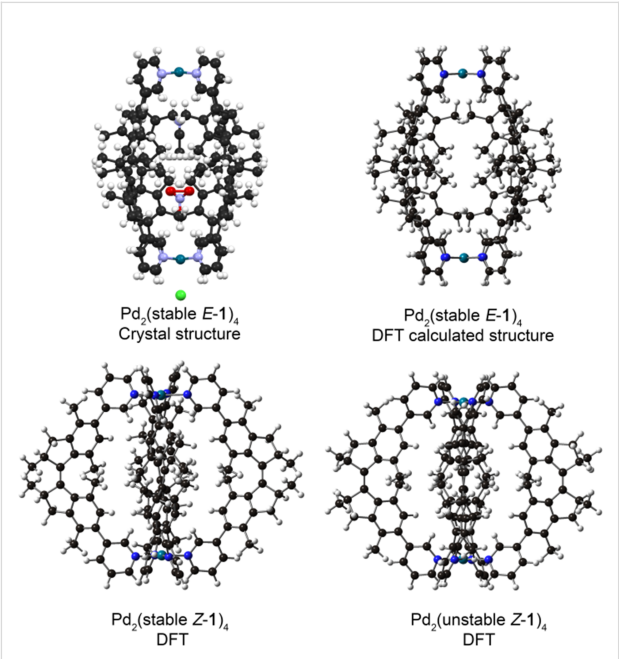


Figure 4: Crystal structure of cage complex Pd_2(stable *E*-**1**)$_4$ (top left) and DFT optimized structures of cage complexes Pd_2(stable *E*-**1**)$_4$, Pd_2(stable *Z*-**1**)$_4$ and Pd_2(unstable *Z*-**1**)$_4$. For clarity only one of the enantiomeric cages was depicted on the figure (carbon – black, nitrogen – blue, oxygen – red, palladium – cyan, chlorine – green, hydrogen – white).

Finally, the photochemical and thermal isomerization behavior of the complexes was studied. Initially, the behavior of ligand **1** was studied by UV–vis and NMR spectroscopy, showing similar behavior as related first generation molecular motors (see Supporting Information File 1 for full details). Irradiation with 312 nm light at −70 °C isomerizes stable *Z*-**1** to unstable *E*-**1**, which undergoes a thermal helix inversion (THI) when warmed

to room temperature to form stable *E*-**1**. The second half of the rotation cycle is similar, as irradiation with 312 nm light isomerizes stable *E*-**1** to unstable *Z*-**1**, which undergoes THI to form stable *Z*-**1** when left for several days at room temperature.

Subsequently, the photochemical and thermal isomerizations of cages Pd_2(stable *Z*-**1**)$_4$ and Pd_2(stable *E*-**1**)$_4$ were followed by ^{1}H NMR studies (Figure 5). Irradiation of Pd_2(stable *Z*-**1**)$_4$ in a CD_3CN/CD_2Cl_2 1:1 mixture at 312 nm at −70 °C was performed to isomerize ligand stable *Z*-**1** to unstable *E*-**1** (vide infra), followed by allowing the sample to warm to room temperature to form stable *E*-**1** (Figure 5ii). The ^{1}H NMR spectrum of this newly formed complex is identical to the spectrum of Pd_2(stable *E*-**1**)$_4$ prepared directly from *E*-**1** (Figure 5iii), showing that cage Pd_2(stable *Z*-**1**)$_4$ is effectively converted to Pd_2(stable *E*-**1**)$_4$. An intermediate complex containing unstable *E*-**1** ligands was not observed, even at low temperatures, most likely due to the low barrier for THI of this isomer. Conversion of cage Pd_2(stable *E*-**1**)$_4$ to Pd_2(unstable *Z*-**1**)$_4$ by photochemical *E*/*Z* isomerization of ligand stable *E*-**1** to unstable *Z*-**1** was performed by irradiation of a sample of Pd_2(stable *E*-**1**)$_4$ at 312 nm at −20 °C (Figure 5iv). Signals of cage Pd_2(stable *Z*-**1**)$_4$ disappeared and the formation of a new set of signals was observed. DOSY NMR confirmed the formation of an assembly with a hydrodynamic radius which was similar to that of the cage Pd_2(stable *Z*-**1**)$_4$. Precipitation of the metal centers in this assembly using tetrabutylammonium glutarate liberates the ligands and they were identified as unstable *Z*-**1**. Combined, these results confirm that the photogenerated complex is indeed Pd_2(unstable *Z*-**1**)$_4$. Subsequent irradiation of this sample containing Pd_2(unstable *Z*-**1**)$_4$ at −20 °C at 365 nm converts the unstable *Z*-**1** ligands back to stable *E*-**1**, reforming Pd_2(stable *E*-**1**)$_4$ (Figure 5v). These experiments highlight the reversible formation of Pd_2(unstable *Z*-**1**)$_4$ through photochemical *E*/*Z* isomerization of the ligands.

On the other hand, allowing the THI of ligands unstable *Z*-**1** in cage Pd_2(unstable *Z*-**1**)$_4$ to take place by leaving the solution at room temperature for 5 d did not lead to the formation of Pd_2(stable *Z*-**1**)$_4$, but to disassembly of the cage and formation of ill-defined complexes. Precipitation of the metal centers in these complexes identified the ligands as a mixture of both stable *Z*-**1** and stable *E*-**1** (originating from the PSS mixture), indicating that the THI does take place. A possible explanation could be that the mixture of stable *Z*-**1** and stable *E*-**1** does not form separate well-defined cage structures, but forms mixed complexes.

Conclusion

In summary, a new photoresponsive supramolecular coordination complex based on overcrowded alkenes is presented, allowing switching between three different cage structures. Interestingly, the cage structures with Pd_2L_4 constitution were shown to be homochiral, forming single diastereomers as evident from NMR, CD and X-ray analysis, supported by DFT calculations. Additionally, the cage structures were able to bind OTs^- inside their cavity. Although photoswitching affords a large geometric change of the ligands, only minor changes were observed in binding constants of the different cage structures. These results show that by incorporation of overcrowded alkenes into SCCs the geometry of cage structures can be controlled by light. Different designs might be considered to translate these geometrical changes to changes in properties such as guest binding affinity and selectivity.

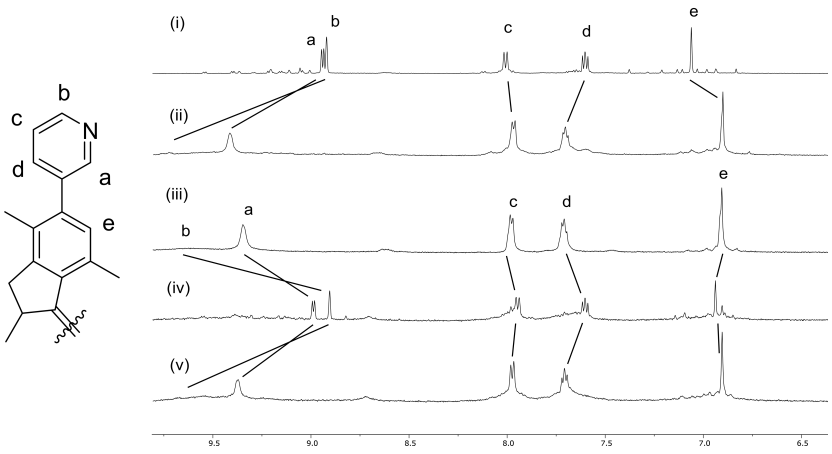


Figure 5: Aromatic region of stacked ^{1}H NMR spectra (CD_3CN/CD_2Cl_2 1:1) of i) Pd_2(stable *Z*-**1**)$_4$; ii) Pd_2(stable *E*-**1**)$_4$ generated by irradiation of Pd_2(stable *Z*-**1**)$_4$ at 312 nm; iii) Pd_2(stable *E*-**1**)$_4$ prepared directly from ligand stable *E*-**1**; iv) Pd_2(unstable *Z*-**1**)$_4$ generated by irradiation of Pd_2(stable *E*-**1**)$_4$ at 312 nm and v) Pd_2(stable *E*-**1**)$_4$ generated by irradiation of Pd_2(unstable *Z*-**1**)$_4$ at 365 nm.

Supporting Information

Supporting Information File 1

Experimental procedures, compound characterization, CD spectroscopy, binding studies, NMR studies of the photochemical and thermal isomerizations, X-ray crystallography, computational details and Cartesian coordinates of DFT optimized structures.
[https://www.beilstein-journals.org/bjoc/content/supplementary/1860-5397-15-268-S1.pdf]

Acknowledgements

Financial support from the Ministry of Education, Culture and Science (Gravitation program 024.001.035) and European Research Council (Advanced Investigator Grant No. 694345 to B.L.F.) are gratefully acknowledged. We would like to thank the Center for Information Technology of the University of Groningen for their support and for providing access to the Peregrine high performance computing cluster.

ORCID® iDs

Edwin Otten - https://orcid.org/0000-0002-5905-5108
Ben L. Feringa - https://orcid.org/0000-0003-0588-8435

References

1. Cook, T. R.; Zheng, Y.-R.; Stang, P. J. *Chem. Rev.* **2013,** *113,* 734–777. doi:10.1021/cr3002824
2. Smulders, M. M. J.; Riddell, I. A.; Browne, C.; Nitschke, J. R. *Chem. Soc. Rev.* **2013,** *42,* 1728–1754. doi:10.1039/c2cs35254k
3. Cook, T. R.; Stang, P. J. *Chem. Rev.* **2015,** *115,* 7001–7045. doi:10.1021/cr5005666
4. Harris, K.; Fujita, D.; Fujita, M. *Chem. Commun.* **2013,** *49,* 6703–6712. doi:10.1039/c3cc43191f
5. Han, M.; Engelhard, D. M.; Clever, G. H. *Chem. Soc. Rev.* **2014,** *43,* 1848–1860. doi:10.1039/c3cs60473j
6. Schmidt, A.; Casini, A.; Kühn, F. E. *Coord. Chem. Rev.* **2014,** *275,* 19–36. doi:10.1016/j.ccr.2014.03.037
7. Ma, Z.; Moulton, B. *Coord. Chem. Rev.* **2011,** *255,* 1623–1641. doi:10.1016/j.ccr.2011.01.031
8. Lewis, J. E. M.; Gavey, E. L.; Cameron, S. A.; Crowley, J. D. *Chem. Sci.* **2012,** *3,* 778–784. doi:10.1039/c2sc00899h
9. Vriezema, D. M.; Comellas Aragonès, M.; Elemans, J. A. A. W.; Cornelissen, J. J. L. M.; Rowan, A. E.; Nolte, R. J. M. *Chem. Rev.* **2005,** *105,* 1445–1490. doi:10.1021/cr0300688
10. Pluth, M. D.; Bergman, R. G.; Raymond, K. N. *Acc. Chem. Res.* **2009,** *42,* 1650–1659. doi:10.1021/ar900118t
11. Yoshizawa, M.; Klosterman, J. K.; Fujita, M. *Angew. Chem., Int. Ed.* **2009,** *48,* 3418–3438. doi:10.1002/anie.200805340
12. Kaphan, D. M.; Levin, M. D.; Bergman, R. G.; Raymond, K. N.; Toste, F. D. *Science* **2015,** *350,* 1235–1238. doi:10.1126/science.aad3087
13. Inokuma, Y.; Yoshioka, S.; Ariyoshi, J.; Arai, T.; Hitora, Y.; Takada, K.; Matsunaga, S.; Rissanen, K.; Fujita, M. *Nature* **2013,** *495,* 461–466. doi:10.1038/nature11990
14. Yan, K.; Dubey, R.; Arai, T.; Inokuma, Y.; Fujita, M. *J. Am. Chem. Soc.* **2017,** *139,* 11341–11344. doi:10.1021/jacs.7b06607
15. Ziegler, M.; Brumaghim, J. L.; Raymond, K. N. *Angew. Chem., Int. Ed.* **2000,** *39,* 4119–4121. doi:10.1002/1521-3773(20001117)39:22<4119::aid-anie4119>3.0.co;2-1
16. Kawano, M.; Kobayashi, Y.; Ozeki, T.; Fujita, M. *J. Am. Chem. Soc.* **2006,** *128,* 6558–6559. doi:10.1021/ja0609250
17. Mal, P.; Breiner, B.; Rissanen, K.; Nitschke, J. R. *Science* **2009,** *324,* 1697–1699. doi:10.1126/science.1175313
18. McConnell, A. J.; Wood, C. S.; Neelakandan, P. P.; Nitschke, J. R. *Chem. Rev.* **2015,** *115,* 7729–7793. doi:10.1021/cr500632f
19. Mahata, K.; Frischmann, P. D.; Würthner, F. *J. Am. Chem. Soc.* **2013,** *135,* 15656–15661. doi:10.1021/ja4083039
20. Scherer, M.; Caulder, D. L.; Johnson, D. W.; Raymond, K. N. *Angew. Chem., Int. Ed.* **1999,** *38,* 1587–1592. doi:10.1002/(sici)1521-3773(19990601)38:11<1587::aid-anie1587>3.0.co;2-r
21. Mal, P.; Schultz, D.; Beyeh, K.; Rissanen, K.; Nitschke, J. R. *Angew. Chem., Int. Ed.* **2008,** *47,* 8297–8301. doi:10.1002/anie.200803066
22. Clever, G. H.; Tashiro, S.; Shionoya, M. *J. Am. Chem. Soc.* **2010,** *132,* 9973–9975. doi:10.1021/ja103620z
23. Murase, T.; Sato, S.; Fujita, M. *Angew. Chem., Int. Ed.* **2007,** *46,* 5133–5136. doi:10.1002/anie.200700793
24. Park, J.; Sun, L.-B.; Chen, Y.-P.; Perry, Z.; Zhou, H.-C. *Angew. Chem., Int. Ed.* **2014,** *53,* 5842–5846. doi:10.1002/anie.201310211
25. Feringa, B. L.; Browne, W. R. *Molecular Switches,* 2nd ed.; Wiley-VCH Verlag GmbH & Co. KGaA: Weinheim, Germany, 2011; Vol. 1.
26. Irie, M.; Fukaminato, T.; Matsuda, K.; Kobatake, S. *Chem. Rev.* **2014,** *114,* 12174–12277. doi:10.1021/cr500249p
27. Tian, H.; Yang, S. *Chem. Soc. Rev.* **2004,** *33,* 85–97. doi:10.1039/b302356g
28. Han, M.; Michel, R.; He, B.; Chen, Y.-S.; Stalke, D.; John, M.; Clever, G. H. *Angew. Chem., Int. Ed.* **2013,** *52,* 1319–1323. doi:10.1002/anie.201207373
29. Han, M.; Luo, Y.; Damaschke, B.; Gómez, L.; Ribas, X.; Jose, A.; Peretzki, P.; Seibt, M.; Clever, G. H. *Angew. Chem., Int. Ed.* **2016,** *55,* 445–449. doi:10.1002/anie.201508307
30. Wei, S.-C.; Pan, M.; Fan, Y.-Z.; Liu, H.; Zhang, J.; Su, C.-Y. *Chem. – Eur. J.* **2015,** *21,* 7418–7427. doi:10.1002/chem.201406517
31. Safont-Sempere, M. M.; Fernandez, G.; Würthner, F. *Chem. Rev.* **2011,** *111,* 5784–5814. doi:10.1021/cr100357h
32. He, Z.; Jiang, W.; Schalley, C. A. *Chem. Soc. Rev.* **2015,** *44,* 779–789. doi:10.1039/c4cs00305e
33. Jędrzejewska, H.; Szumna, A. *Chem. Rev.* **2017,** *117,* 4863–4899. doi:10.1021/acs.chemrev.6b00745
34. Huang, W.-H.; Zavalij, P. Y.; Isaacs, L. *Angew. Chem., Int. Ed.* **2007,** *46,* 7425–7427. doi:10.1002/anie.200702189
35. Haino, T.; Shio, H.; Takano, R.; Fukazawa, Y. *Chem. Commun.* **2009,** 2481–2483. doi:10.1039/b900599d
36. Xuan, W.; Zhang, M.; Liu, Y.; Chen, Z.; Cui, Y. *J. Am. Chem. Soc.* **2012,** *134,* 6904–6907. doi:10.1021/ja212132r
37. Gidron, O.; Ebert, M.-O.; Trapp, N.; Diederich, F. *Angew. Chem., Int. Ed.* **2014,** *53,* 13614–13618. doi:10.1002/anie.201406585
38. Koumura, N.; Zijlstra, R. W. J.; van Delden, R. A.; Harada, N.; Feringa, B. L. *Nature* **1999,** *401,* 152–155. doi:10.1038/43646

39. Kassem, S.; van Leeuwen, T.; Lubbe, A. S.; Wilson, M. R.; Feringa, B. L.; Leigh, D. A. *Chem. Soc. Rev.* **2017,** *46,* 2592–2621. doi:10.1039/c7cs00245a
40. Roke, D.; Wezenberg, S. J.; Feringa, B. L. *Proc. Natl. Acad. Sci. U. S. A.* **2018,** *115,* 9423–9431. doi:10.1073/pnas.1712784115
41. Wang, J.; Feringa, B. L. *Science* **2011,** *331,* 1429–1432. doi:10.1126/science.1199844
42. Zhao, D.; Neubauer, T. M.; Feringa, B. L. *Nat. Commun.* **2015,** *6,* 6652. doi:10.1038/ncomms7652
43. Chen, J.; Leung, F. K.-C.; Stuart, M. C. A.; Kajitani, T.; Fukushima, T.; van der Giessen, E.; Feringa, B. L. *Nat. Chem.* **2018,** *10,* 132–138. doi:10.1038/nchem.2887
44. Li, Q.; Fuks, G.; Moulin, E.; Maaloum, M.; Rawiso, M.; Kulic, I.; Foy, J. T.; Giuseppone, N. *Nat. Nanotechnol.* **2015,** *10,* 161–165. doi:10.1038/nnano.2014.315
45. Foy, J. T.; Li, Q.; Goujon, A.; Colard-Itté, J.-R.; Fuks, G.; Moulin, E.; Schiffmann, O.; Dattler, D.; Funeriu, D. P.; Giuseppone, N. *Nat. Nanotechnol.* **2017,** *12,* 540–545. doi:10.1038/nnano.2017.28
46. van Leeuwen, T.; Heideman, G. H.; Zhao, D.; Wezenberg, S. J.; Feringa, B. L. *Chem. Commun.* **2017,** *53,* 6393–6396. doi:10.1039/c7cc03188b
47. Zhao, D.; van Leeuwen, T.; Cheng, J.; Feringa, B. L. *Nat. Chem.* **2017,** *9,* 250–256. doi:10.1038/nchem.2668
48. McMorran, D. A.; Steel, P. J. *Angew. Chem., Int. Ed.* **1998,** *37,* 3295–3297. doi:10.1002/(sici)1521-3773(19981217)37:23<3295::aid-anie3295>3.0.co;2-5
49. Chand, D. K.; Biradha, K.; Fujita, M. *Chem. Commun.* **2001,** 1652–1653. doi:10.1039/b104853h
50. Su, C.-Y.; Cai, Y.-P.; Chen, C.-L.; Smith, M. D.; Kaim, W.; zur Loye, H.-C. *J. Am. Chem. Soc.* **2003,** *125,* 8595–8613. doi:10.1021/ja034267k
51. Neubauer, T. M.; van Leeuwen, T.; Zhao, D.; Lubbe, A. S.; Kistemaker, J. C. M.; Feringa, B. L. *Org. Lett.* **2014,** *16,* 4220–4223. doi:10.1021/ol501925f
52. Clever, G. H.; Shionoya, M. *Chem. – Eur. J.* **2010,** *16,* 11792–11796. doi:10.1002/chem.201002013
53. Sato, S.; Ishido, Y.; Fujita, M. *J. Am. Chem. Soc.* **2009,** *131,* 6064–6065. doi:10.1021/ja900676f
54. Macchioni, A.; Ciancaleoni, G.; Zuccaccia, C.; Zuccaccia, D. *Chem. Soc. Rev.* **2008,** *37,* 479–489. doi:10.1039/b615067p
55. Performed with the use of Bindfit software – http://supramolecular.com
56. Thordarson, P. *Chem. Soc. Rev.* **2011,** *40,* 1305–1323. doi:10.1039/c0cs00062k

License and Terms

This is an Open Access article under the terms of the Creative Commons Attribution License (http://creativecommons.org/licenses/by/4.0). Please note that the reuse, redistribution and reproduction in particular requires that the authors and source are credited.

The license is subject to the *Beilstein Journal of Organic Chemistry* terms and conditions: (https://www.beilstein-journals.org/bjoc)

The definitive version of this article is the electronic one which can be found at: doi:10.3762/bjoc.15.268

BEILSTEIN JOURNAL OF ORGANIC CHEMISTRY

Photoreversible stretching of a BAPTA chelator marshalling Ca^{2+}-binding in aqueous media

Aurélien Ducrot, Arnaud Tron*, Robin Bofinger, Ingrid Sanz Beguer, Jean-Luc Pozzo and Nathan D. McClenaghan*

Full Research Paper

Open Access

Address:
Institut des Sciences Moléculaires, CNRS UMR 5255, Univ. Bordeaux, 351 cours de la Libération, 33405 Talence, France

Email:
Arnaud Tron* - arnaud.tron@u-bordeaux.fr;
Nathan D. McClenaghan* - nathan.mcclenaghan@u-bordeaux.fr

* Corresponding author

Keywords:
azobenzene; BAPTA; calcium binding; photorelease; photoswitch

Beilstein J. Org. Chem. **2019,** *15,* 2801–2811.
doi:10.3762/bjoc.15.273

Received: 28 July 2019
Accepted: 08 November 2019
Published: 21 November 2019

This article is part of the thematic issue "Molecular switches".

Guest Editor: W. Szymanski

© 2019 Ducrot et al.; licensee Beilstein-Institut.
License and terms: see end of document.

Abstract

Free calcium ion concentration is known to govern numerous biological processes and indeed calcium acts as an important biological secondary messenger for muscle contraction, neurotransmitter release, ion-channel gating, and exocytosis. As such, the development of molecules with the ability to instantaneously increase or diminish free calcium concentrations potentially allows greater control over certain biological functions. In order to permit remote regulation of Ca^{2+}, a selective BAPTA-type synthetic receptor / host was integrated with a photoswitchable azobenzene motif, which upon photoirradiation would enhance (or diminish) the capacity to bind calcium upon acting on the conformation of the adjacent binding site, rendering it a stronger or weaker binder. Photoswitching was studied in pseudo-physiological conditions (pH 7.2, [KCl] = 100 mM) and dissociation constants for azobenzene *cis*- and *trans*-isomers have been determined (0.230 μM and 0.102 μM, respectively). Reversible photoliberation/uptake leading to a variation of free calcium concentration in solution was detected using a fluorescent Ca^{2+} chemosensor.

Introduction

In terms of synthetic calcium binding molecules, since the 1,2-bis(*o*-aminophenoxy)ethane-*N*,*N*,*N*',*N*'-tetraacetic acid (BAPTA) scaffold was first described by Tsien, it has been widely used in biological systems and has given rise to a wealth of derivatives [1]. Key to the wide interest in this cation binder are its high specificity for Ca^{2+} ions over Mg^{2+} ions, and relative insensitivity to pH in biological media due to the relatively low pK_a of the electron-poor aniline nitrogens [1]. BAPTA-type molecules complex Ca^{2+} in an octacoordinated fashion, involving the two aniline functions, the two central ether oxygens and the four carboxylates, as elucidated by the crystallographic structure of a 1:1 host–guest BAPTA system [2]. This moiety has been exploited in the development of various fluorescent supramolecular chemosensor systems and even molecular logic systems [3-11].

Equally, the incorporation of photochemically active groups has been used to trigger the decrease of the ligand's affinity for

calcium ions leading to photorelease [12-14], and as such has proved an alternative to C–N-bond photocleavage [15,16]. A molecular prototype for the photodecaging of calcium was Nitr-5, where an electron-withdrawing carbonyl function is generated from a secondary alcohol adjacent to the BAPTA binding site upon photoirradiation, which proved sufficient to lower the binding affinity 40-fold and liberate calcium in biological media [17]. This design was subsequently improved in a symmetrical variant and indeed a wealth of successful variants for photodecaging calcium have been described including examples whose photochemical quantum yield approaches unity [18-24].

While photorelease of calcium can be efficiently achieved in micro-to-millimolar concentration and has led to new insights in neurobiology, reversible uptake and release could give rise to calcium fluxes which would give greater control over cellular function or ultimately provide new information on the role of calcium. With this long-term objective in mind, photochromic groups have been integrated with BAPTA (or structurally related EDTA) such that photoswitching would enhance or lower Ca^{2+} binding based on the state of the adjacent photoswitch. Photogeneration of a positive charge proximal to the BAPTA site is undoubtedly the most robust approach to provoke calcium cation release, while diminishing electron density on the chelating groups would also have a significant effect. Some groups reported BAPTA-diarylethene and EDTA-spiropyran conjugates, while noting limitations for implementation in terms of fatigue, solubility and relatively small affinity changes [25,26]. We further highlight a structurally elegant design integrating a spiroamidorhodamine with a BAPTA, whose anticipated switching remains to be proven [27]. Further, interesting approaches are currently being developed on interfacing calmodulin, a messenger protein ionophore, with photochromes [28].

The use of steric effects to decrease binding offers an alternative approach to generate calcium release, where deforming an ion-binding site would render it less well-adapted to bind a guest. Photoisomerization of the azobenzene moiety has previously been successfully used to modulate the affinity of crown ethers [29], lariats [30], and foldamers [31] for various ions and switch between complexes of different molecularity, albeit largely in organic solvents [32]. Azobenzene is generally considered relatively resistant to fatigue and has been employed to evoke changes in different biological systems, including ion channels based on changes of properties between *cis* and *trans*-forms [33,34]. Herein we describe a BAPTA host molecule **1**, with an azobenzene moiety integrated in the tether linking both aromatic rings, as illustrated in Figure 1. The principle goal of the current work, with a long-term view of interfacing biological systems, was the development of a water-soluble molecule which has a high affinity and selectivity for calcium, allowing binding of physiological levels of calcium, whose binding can be switched reversibly as efficiently as possible both in terms of affinity and quantum yield. In principle this would offer real-time regulation of free calcium levels. In the current design, the elongated **1*E*** form of azobenzene in the synthetic BAPTA podand can adopt the preferred binding geometry to sequester Ca^{2+}, while the metastable **1*Z*** is anticipated to deform the chelating site separating the binding groups, leading to a lowered guest affinity. Herein we describe the synthesis of **1**, its photoswitching, and affinity changes between both forms in pseudo-physiological conditions, further rationalized by energy-minimized molecular modelling structures.

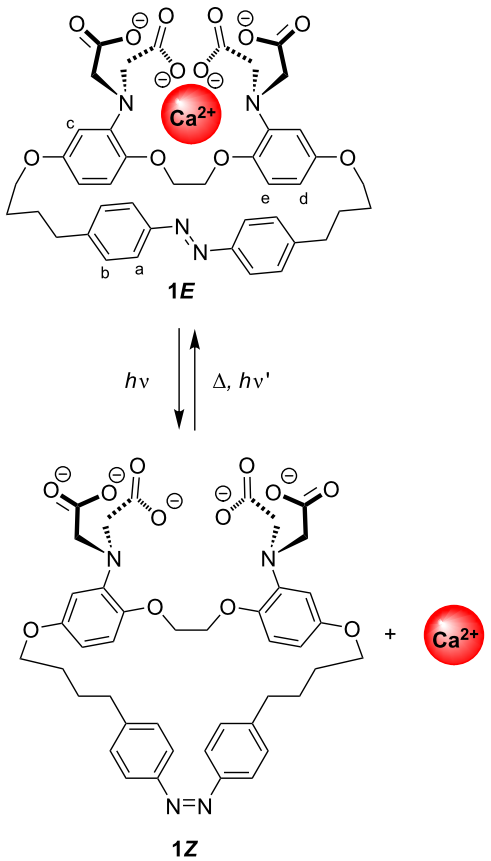
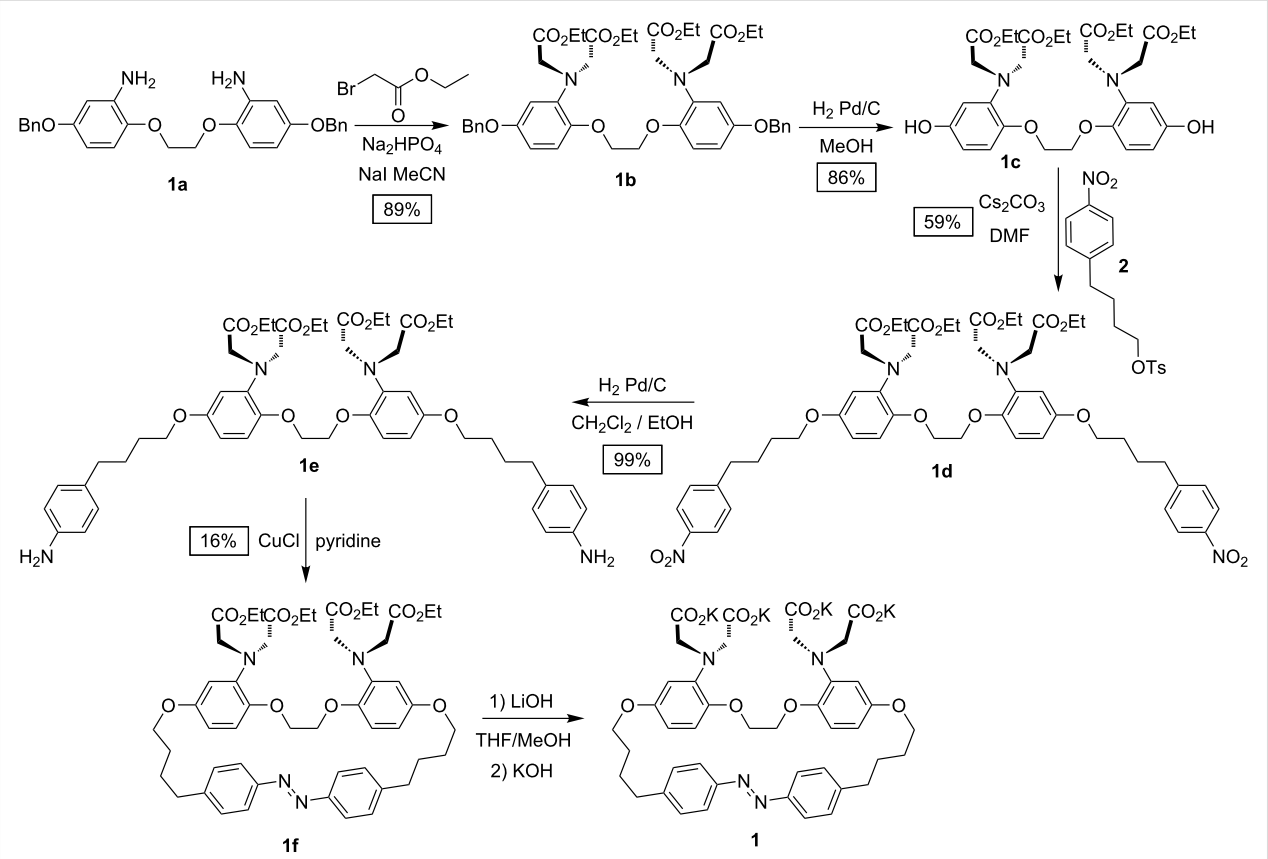


Figure 1: Azobenzene-BAPTA **1*E*** and **1*Z*** (a, b, c, d and e denote specific protons), showing idealized Ca^{2+} uptake and release. Counter ions omitted for clarity.

Results and Discussion

The synthetic pathway for the preparation of molecule **1** is shown in Scheme 1 and detailed synthetic procedures are given below. Briefly, the synthesis of **1** started with the preparation of a BAPTA core via a multistep route adapting the synthetic route



Scheme 1: Synthesis of azobenzene-tethered BAPTA **1**.

developed by Crossley et al. [35]. 1,4-Hydroquinone was benzylated and subsequently nitrated. This intermediate then underwent a regioselective monodeprotection to generate a lone phenol group. The phenolate was reacted with 1,2-dibromoethane and the nitrobenzene groups were reduced to the corresponding anilines giving **1a**. The double aniline **1a** was alkylated using ethyl bromoacetate under basic conditions in acetonitrile, forming the BAPTA precursor **1b**. The palladium-catalyzed benzyl cleavage was followed by a double alkylation with **2**, reactant **2** being synthesized from 4-(4-nitrophenyl)butanoic acid. The 4-nitrobenzene groups of the pendant arms were subsequently reduced yielding the corresponding anilines (**1e**). A cyclization reaction yielding the corresponding azobenzene **1f** was performed using a Cu(I) catalyst generated in situ [36]. Finally, the esters were hydrolyzed under mild conditions resulting in the azobenzene-BAPTA macrocycle **1**.

To gain some insight into the possible structures of the **1*E*** and **1*Z*** chelators and differences between them, which may have consequences on the chelation, energy-minimized (PM6) structures were determined (Figure 2). The *trans*-form was found to be the lowest energy structure, as is generally observed for azobenzenes [37]. In the *trans*- versus *cis*-chelates the following bond lengths were noted: N–Ca^{2+}: 2.35 and 2.49 Å cf. 3.24 and 3.03 Å. Smaller differences were noted considering the COO^-–Ca^{2+}: 2.20, 2.19, 2.29 and 2.70 Å cf. 2.21, 2.21, 2.23 and 2.23 Å or the ether linkage O–Ca^{2+}: 2.44 and 2.49 Å cf. 2.46 and 2.51 Å. Most significantly, the aniline N–N distance is stretched from 4.71 Å for the *trans*-form to 5.96 Å for the *cis*-form, which, taken in conjunction with the lengthened N–Ca^{2+} bond lengths tends to suggest a less tight calcium binding in the photogenerated *cis*-form as compared to the *trans*-form, consistent with photo-promoted guest release.

Exclusively *E*-isomers are observed in the ^{1}H NMR spectra of the azobenzene-containing macrocycles **1f** and **1** at 25 °C (Supporting Information File 1, Figures S13 and S14). Next, in the absence of Ca^{2+} ions, **1*E*** was subjected to irradiation into the π–π* band (λ_{max} = 362 nm) and photoisomerization of **1*E*** to **1*Z*** took place, as evidenced by the decrease of the π–π* absorption in the range 330-440 nm and the increase of the *n*–π* absorption above 440 nm (Figure 3), equally observed for **1f*E*** to **1f*Z*** (Figure S1 in Supporting Information File 1). The NMR analysis of photoirradiated samples of macrocyles **1** showed that the photostationary state (PSS) for the E→Z photoisomerization at 365 nm was 88:12 in favor of the *cis*-form (Figure 4).

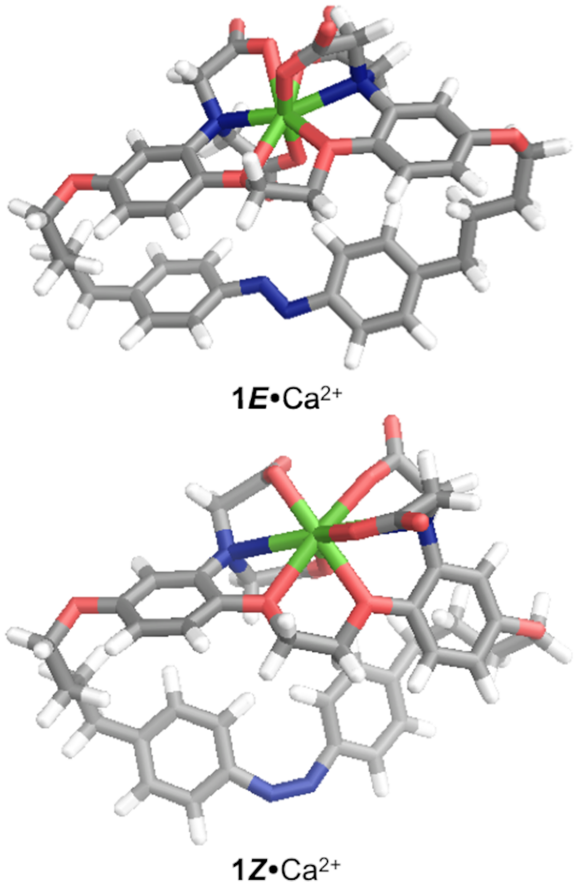


Figure 2: Energy-minimized molecular modelling structures of **1*E***•Ca^{2+} and **1*Z***•Ca^{2+} (PM6).

The reversibility of the photoswitching of the supramolecular host was tested over several isomerization cycles with little evidence of fatigue (Figure 5). Thermal isomerization $Z \rightarrow E$ resulted in the restoration of the electronic absorption band attributed to the π–π* transition at 30 °C (Figure 5), the rate constant (k) was estimated at 5.4×10^{-5} s^{-1}. Photoisomerization was also recorded in electron-absorption spectroscopy in the presence of calcium (see Figure S2 in Supporting Information File 1). The presence of the ion has the effect of reducing the reversibility of the isomerization cycles due to an apparent accelerated degradation, which may be attributed to rendering an unwanted photochemical pathway more competitive. The fatigue study showed that more than 90% of **1*E*** were recovered after each cycle (Figure S3, Supporting Information File 1). On repeating this cycle, slow decomposition was observed, estimated at 14% after 3 cycles.

Calcium binding by hosts **1*E*** and **1*Z*** was investigated by spectrophotometry, specifically monitoring aromatic ring chromophores which give rise to absorption bands observed in the UV, assigned to n–π* and π–π* transitions [38]. The calcium complexation studies of **1*E*** and **1*Z*** were performed under pseudo-intracellular conditions (100 mM KCl, 30 mM MOPS, pH 7.2). In the absence of ions, the spectra of **1*E*** (Figure 6a) comprised absorption bands at 298 nm (ε: 5815 M^{-1} cm^{-1}) and 359 nm (ε: 6728 M^{-1} cm^{-1}). The complexation of Ca^{2+} (Figure 6a) induced a blue-shifting and a decrease of the absorption bands of **1*E*** at 291 nm (ε: 4748 M^{-1} cm^{-1}) and 355 nm (ε: 5230 M^{-1} cm^{-1}). The spectrum of **1*Z*** (Figure 6b) exhibited two absorption bands at 303 nm (ε: 5450 M^{-1} cm^{-1})

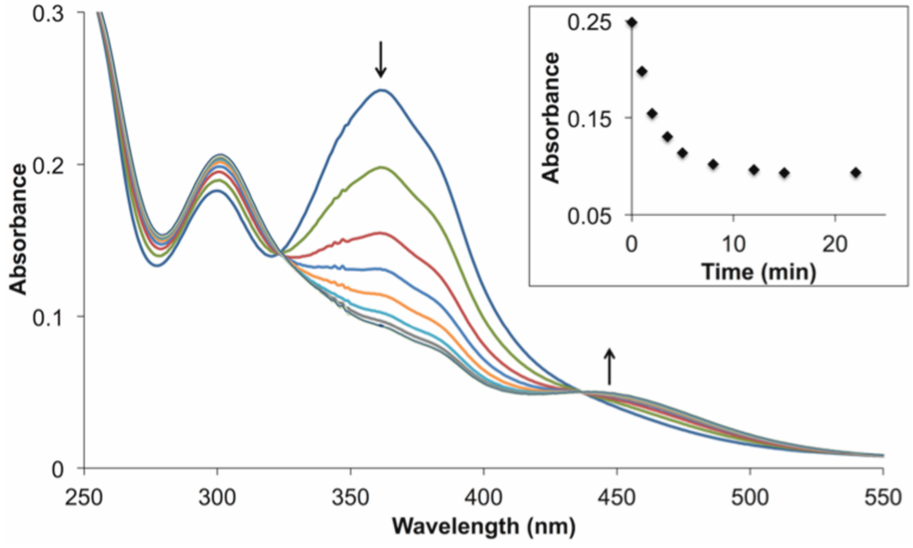


Figure 3: Electronic absorption spectra showing changes associated with photoisomerization of **1*E*** (40 μM) to **1*Z*** in aqueous 0.03 M MOPS buffer at pH 7.2 in the presence of KCl (0.1 M) and EGTA (0.011 M). Inset: Absorbance at 362 nm as a function of irradiation time.

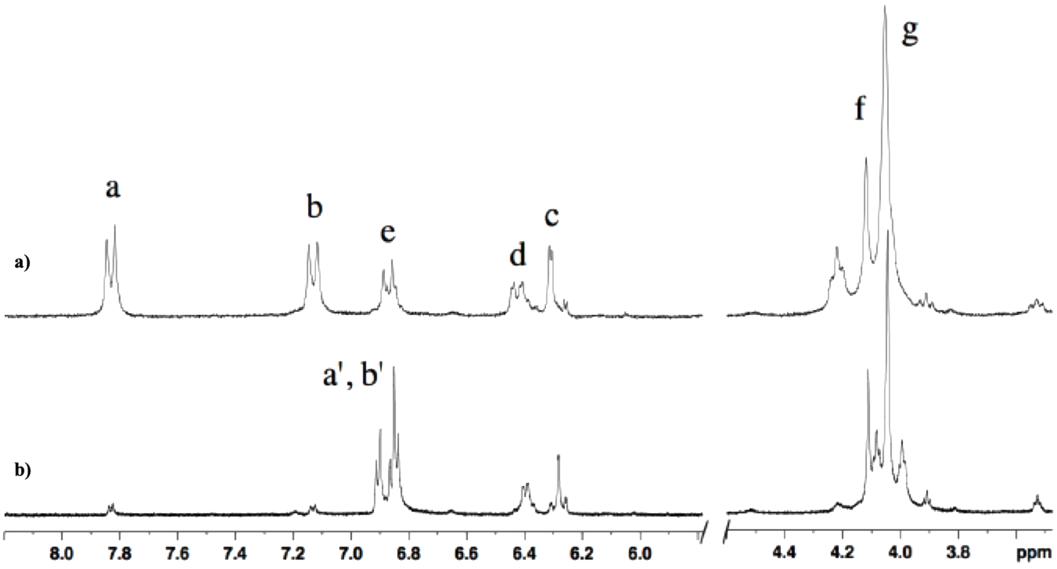


Figure 4: ^{1}H NMR spectra (300 MHz) recorded at room temperature (298 K) in D_2O of a) the thermodynamically stable *trans*-**1*E*** and b) at the photostationary state (PSS) after irradiation at 365 nm (88% of **1*Z*** and 12% of **1*E*** at PSS).

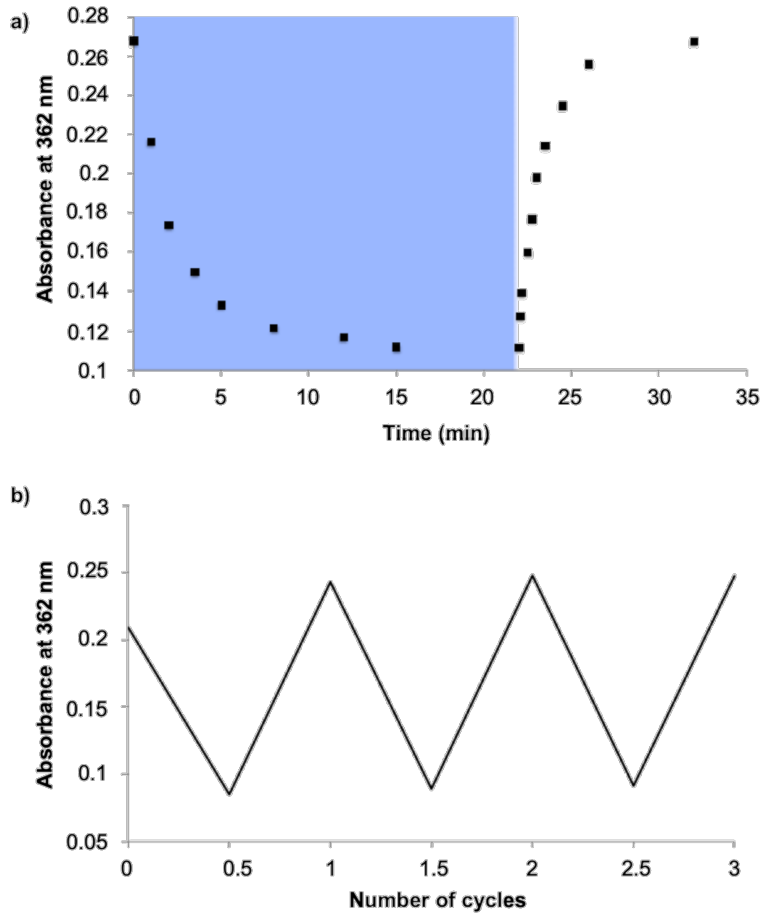


Figure 5: a) Multiple *trans–cis* cycles of **1*E*** (40 μM) indicated by absorption changes at 362 nm in aqueous 0.03 M MOPS buffer at pH 7.2 in presence of KCl (0.1 M) and EGTA (0.011 M). Each cycle corresponds to irradiation at 365 nm (blue), followed by thermal return at room temperature (white). b) Fatigue study of **1*E*** (40 μM) after 3 cycles.

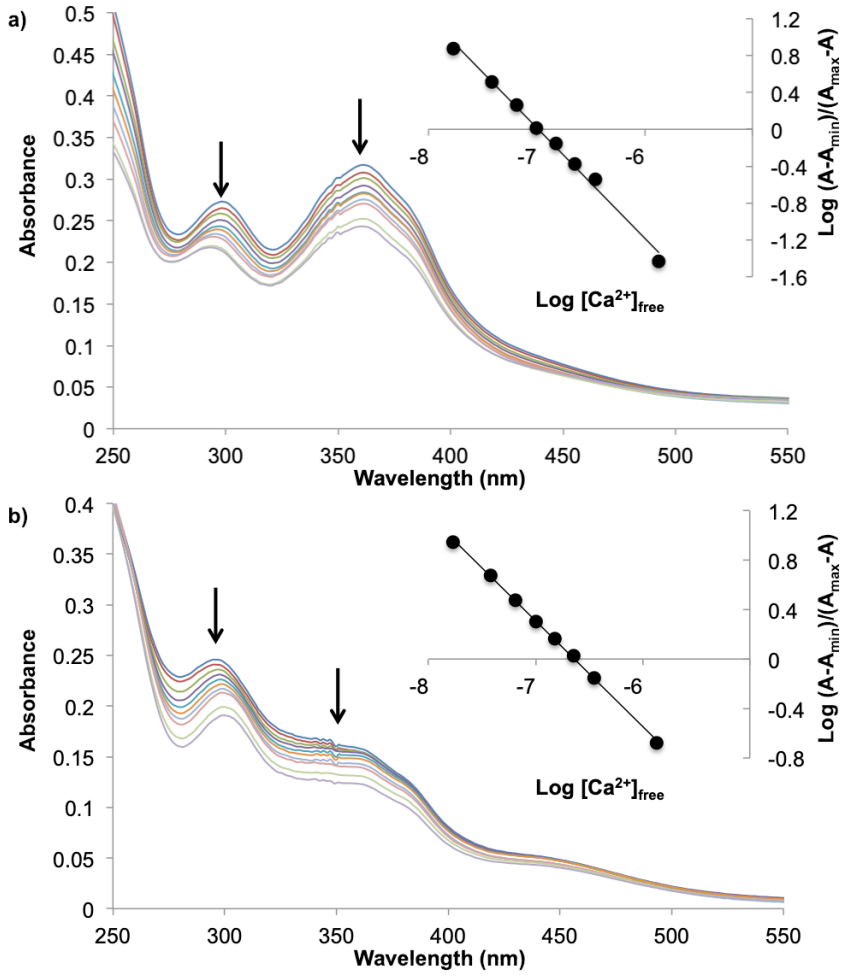


Figure 6: Electronic absorption spectra changes of **1*E*** (42 μM) (a) and **1*Z*** (43 μM) (b) in aqueous 0.03 M MOPS buffer at pH 7.2 in presence of KCl (0.1 M), and EGTA (0.010 M) upon Ca^{2+} addition (free Ca^{2+} concentration = 0.017, 0.038, 0.065, 0.100, 0.150, 0.225, 0.35, 1.35 and 39 μM). Insets: Hill plots for the absorbance change at 305 nm as a function of free Ca^{2+}, affording log K_d (*x*-axis intercept).

and 348 nm (ε: 2700 M^{-1} cm^{-1}). The complexation of Ca^{2+} (Figure 6b) induced blue-shifting and a decrease of the absorption band intensities of **1*E*** at 297 nm (ε: 4900 M^{-1} cm^{-1}) and 345 nm (ε: 3000 M^{-1} cm^{-1}). After linearizing the spectral changes via a Hill plot, a 1:1 binding with a K_d of 0.102 μM in the case of **1*E*** and 0.230 μM for **1*Z*** were determined. The value for **1*E*** is similar to the K_d value reported for BAPTA (K_d = 0.110 μM) and importantly calcium binding by the *cis*-form was circa 2.5-fold less than that of the *trans*-form [39]. This is conducive to photopromoted ion release.

Chemical actinometry afforded the quantum yield of the photoisomerization reaction (λ_{ex} = 365 nm) [40]. For solutions of **1*E*** in the absence and presence of Ca^{2+}, the measured quantum yields were identical (0.08) suggesting that the ion does not influence the efficiency of the photoreaction.

In order to unambiguously prove the liberation of Ca^{2+} upon photexcitation in solution, azobenzene macrocyle **1** was used as a reversible Ca^{2+} photoejector in the presence of a Ca^{2+}-selective "turn-on" fluorescent probe (**3**, Figure 7) [41]. The fluorescence of BODIPY dye **3** in the absence of calcium, is quenched by an intramolecular photoinduced electron-transfer reaction, while ion binding blocks this quenching pathway restoring emission. Thus, ion liberation from **1** and transfer to **3** would result in a fluorescence off–on switching of the latter.

To perform the ion-transfer experiment, the fluorescent dye is loaded with one equivalent of Ca^{2+}, giving rise to a highly fluorescent species upon excitation at 485 nm. The fluorescence is greatly diminished after the addition of 10 equivalents of **1*E***, as the azobenzene macrocycle abstracts the Ca^{2+} ion from fluorophore **3**. Upon irradiation of the ensemble at 365 nm at these

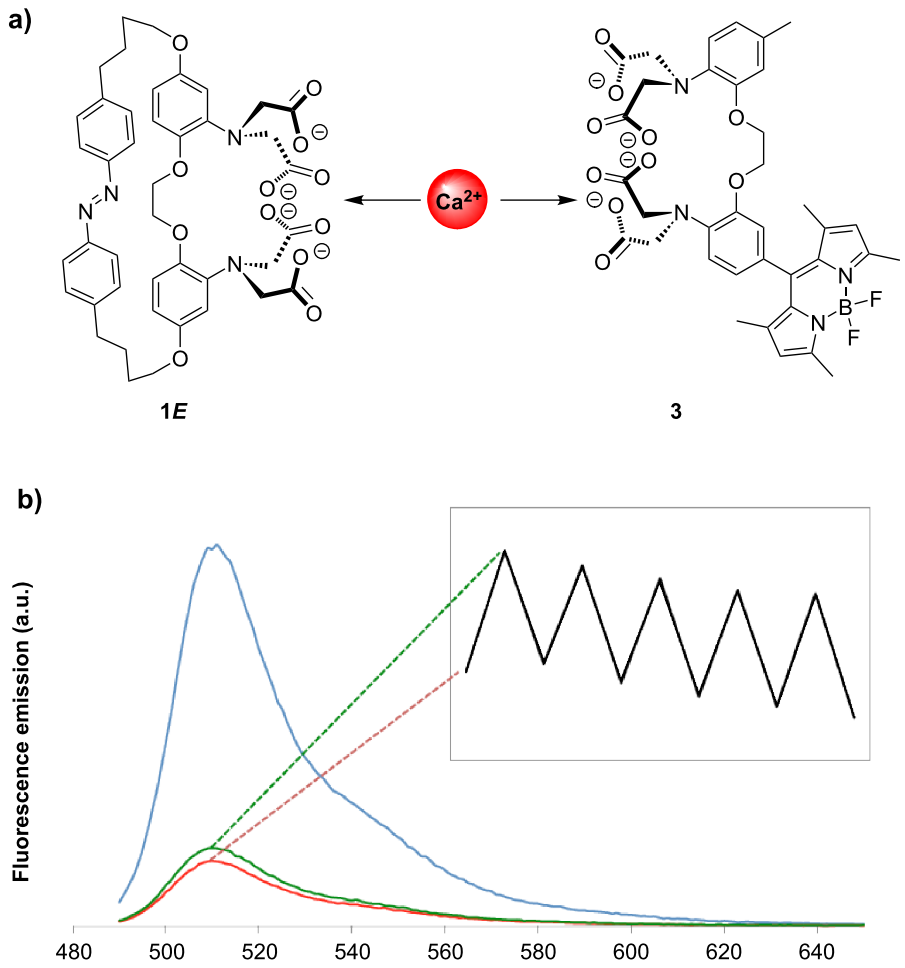


Figure 7: a) Reversible Ca^{2+} exchange between photoregulated host **1** and turn-"on" fluorescent probe **3**. b) Blue: **3** (5 μM) in 0.1 M KCl and added Ca^{2+} (5 μM) in aqueous 0.03 M MOPS buffer at pH 7.2, red: after the addition of 50 μM **1*E***, green: after photoirradiation at 365 nm. Inset: fluorescent response over 5 cycles.

low concentrations, a small but reproducible increase in fluorescence intensity can be observed, directly corresponding to the lower complexation/release of the Ca^{2+} ions in the PSS (Figure 7b). Furthermore, several irradiation cycles were successfully completed with this reversible system. The fatigue study showed that more than 90% of the fluorescence enhancement was recovered after each cycle despite a slight decrease of fluorescence intensity due to some photoinstability estimated at 20% after 5 cycles (inset Figure 7b).

The aforementioned experiment is simply a demonstration that calcium can be reversibly taken up and released in solution, dilute solutions being convenient to simultaneously monitor the state of the azobenzene and the fluorescence. In terms of possible applications for reversible photodecaging in biological systems, the amount of calcium required to be released to evoke a change is very system dependent and as such it is impossible to generalize precise quantities (although they would invariably involve higher concentrations). However, we can take skeletal muscle fibers as a representative example, where an increased free calcium concentration promotes muscular contraction [16]. It is noted that 5 μM of free calcium is in principle sufficient to induce a contraction (resting concentration of Ca^{2+} being 0.19–0.28 μM), but that the effective concentration should be much higher as the fibers themselves can buffer free calcium. This was effectively achieved (non-reversibly) with mM concentrations of the calcium-cage nitrophenyl-EGTA (K_d of 0.080 μM on excitation at 350 nm with a quantum yield of 0.23) [16]. For comparison, molecule **1** has a similar K_d and the quantum yield is in the same order of magnitude as nitrophenyl-EGTA but is around 3 times lower, thus in principle it could sequester calcium sufficiently well and show sufficient photoactivity in this situation. However, the modest 2.5-fold difference of binding affinity between complexing and non-complexing forms, while comparable to the best-known photochromic variants [25,26], would need to be significantly increased (at least

by an order of magnitude) to have sufficiently efficient ion release and free calcium increase for biological application. Indeed, this is the major challenge for photoswitchable variants, efficient release being more dramatic and readily achieved in versions with photodegradable, and hence non-switchable binding sites.

Conclusion

In conclusion, a photochromic BAPTA-based calcium ion host (**1**) incorporating an azobenzene photochrome is described. This chelating molecule showed high affinity for Ca^{2+} under pseudo-physiological conditions (K_d = 0.102 μM) and showed efficient photochemical *trans*-to-*cis* switching in terms of quantum yields (0.08) and PSS composition (88% *cis*). The calcium binding affinity of the *cis*-form was diminished by circa 2.5-fold with respect to the *trans*-form as the chelator was stretched rendering the binding pocket ill-adapted to accommodate the calcium, as suggested by molecular modelling. Reversible Ca^{2+} liberation and subsequent uptake was evidenced using a fluoroionophore. While the simultaneous observation of fluorescence and absorption was conveniently followed at low concentration, any future biological practical use would undoubtedly require use at much higher concentrations. In this regard a higher release efficiency would equally undoubtedly be required than that shown by prototype **1** described herein. To this end, shortening/rigidification of the hydrocarbon azobenzene-BAPTA linkages in **1** may be anticipated to lead to an exalted difference in *trans*/*cis*-binding affinity. However, in our hands, the synthesis of such architectures using protocols similar to those described herein proved inefficient in these more sterically challenging variants.

Experimental

Materials and methods

All synthetic steps were performed under a dry nitrogen atmosphere using standard techniques. Commercially available reagents and solvents were used as received unless otherwise stated. THF and diethyl ether were distilled over sodium/benzophenone. Acetonitrile and dichloromethane were distilled over calcium hydride immediately before use. Compounds **1a** and **2** were synthesized according to literature procedures [35,42]. The progress of all reactions was monitored by thin layer chromatography on silica gel 40 F254. Column chromatography was performed on silica gel 40 (0.230–0.400 mm or 40–63 μm,). ^1H and ^{13}C NMR experiments were performed at 295 K on the following spectrometers: Bruker DPX 200 (^1H: 200 MHz) or an Avance 300 (^1H: 300 MHz, ^{13}C: 75 MHz) spectrometer. Chemical shifts are reported in ppm (δ) and are referenced to the NMR solvent residual peaks. Abbreviations used are s = singlet, d = doublet, t = triplet, q = quartet, m = multiplet. Reagent grade tetrahydrofuran (THF) was distilled under argon over sodium benzophenone ketyl. CH_2Cl_2 was distilled over CaH_2 under argon. Mass spectrometry was performed at the CESAMO analytical center (University of Bordeaux, France) on a QStar Elite mass spectrometer (Applied Biosystems). The instrument is equipped with an electrospray ion (ESI) source and spectra were recorded in the positive mode. High-resolution mass spectrometry (HRMS) measurements were performed with an ESI source on a Q-TOF mass spectrometer with an accuracy tolerance of 2 ppm (Fédération de Recherche CBM/ICOA (FR2708) platform). The electrospray needle was maintained at 5000 V and operated at room temperature. Samples were introduced by injection through a 20 μL sample loop into a 4500 μL/min flow of methanol from the LC pump. Electronic absorption spectra were measured on a Varian Cary 5000 UV–vis–NIR spectrophotometer. Steady-state emission spectra were recorded on a spectrofluorometer fitted with a PMT detector and exciting with a 450 W Xe lamp across a double monochromator, and were corrected for instrumental response. Photoreaction quantum yields were determined upon excitation at 365 nm using the couple potassium ferrioxalate–phenanthroline as a chemical actinometer on an optical bench equipped with a 150 W Hg–Xe lamp and a monochromator [40]. Samples (40 μM) were stirred during the irradiation and the amount of converted material was determined at 2 min intervals by UV–vis spectroscopy following the disappearance of the band at 362 nm. The error in the photoreaction quantum yield determination was estimated at ±15%. Calcium titration: Two calcium calibration stock solutions were prepared, one containing 10 mM EGTA (0 μM Ca^{2+} buffer) and another with 10 mM CaEGTA (39 μM Ca^{2+} buffer). In addition, both buffers were charged with 100 mM KCl and 30 mM 3-(*N*-morpholino)-propanesulfonic acid (MOPS) adjusted at pH 7.2. In both buffers an equivalent amount of the Ca^{2+}-binding probe was dissolved with a final concentration between 1–10 μM. In order to determine the dissociation constant (K_d), spectra have been recorded after having adjusted the free Ca^{2+} concentration to 0.017 μM, 0.038 μM, 0.065 μM, 0.100 μM, 0.150 μM, 0.225 μM, 0.35 μM, 1.35 μM and 39 μM. Therefore, 2 mL of the 0 μM Ca^{2+} sample was placed in a cuvette and the spectra were recorded. Then, 200 μL of the sample were discarded and replaced with 200 μL of the 39 μM Ca^{2+} sample. In that fashion a concentration of 0.017 μM Ca^{2+} can be obtained without changing the concentration of the analyte. The aforementioned Ca^{2+} concentrations were then adjusted by discarding 250, 222, 250, 286, 333, 400, 500, 667 and 1000 μL and replacing the removed volume with an equivalent volume of the 39 μM Ca^{2+} sample. For the calculation of the free Ca^{2+} concentration a constant room temperature of 21 °C was assumed. The spectral change at a given wavelength is then introduced into Hill plot, where $\log (A - A_{min})/(A_{max} - A)$ is plotted against the logarithm of the free Ca^{2+} concentration as obtained from the Ca^{2+}

buffers and A is the absorption at a certain wavelength. The x-intercept gives the log K_d. Molecular modelling: The molecular structure of **1*E***·Ca^{2+} and **1*Z***·Ca^{2+} were built with AMPAC 10.1. A geometry optimization was performed by energy minimization using the PM6 method; solvation was not considered.

Synthetic procedures

Tetraethyl 2,2',2'',2'''-(1,2-ethanediylbis{oxy[5-(benzyloxy)-2,1-phenylene]nitrilo})tetraacetate (1b). A mixture of 2,2'-[1,2-ethanediylbis(oxy)]bis[5-(benzyloxy)aniline] [20] (**1a**, 3 g, 6.57 mmol), ethyl bromoacetate (9 mL, 78.87 mmol), Na_2HPO_4 (4.72 g, 33.25 mmol) and NaI (0.66 g, 4.37 mmol) in 90 mL acetonitrile was heated under reflux conditions and the reaction was followed by TLC (SiO_2, pentane/AcOEt 7:3, v/v). After 48 h, the reaction was allowed to cool to room temperature and the solvent was removed in vacuo. To the residue, 200 mL water was added and the aqueous solution extracted with toluene (3 × 100 mL). A final crystallization from EtOH yielded the title compound (4.69 g, 89%). ^{1}H NMR ($CDCl_3$, 200 MHz) δ 7.30–7.42 (m, 10H, CH_{Ar}), 6.75 (d, J = 9.2 Hz, 2H, CH_{Ar}), 6.43–6.48 (m, 4H, CH_{Ar}), 4.97 (s, 4H, CH_2), 4.18 (s, 4H, CH_2), 4.14 (s, 8H, CH_2), 4.06 (q, J = 7.2 Hz, 8H, CH_2), 1.16 (t, J = 7.2 Hz, 12H, CH_3) ppm; ^{13}C NMR ($CDCl_3$, 75 MHz) δ 170.5, 152.8, 143.9, 139.7, 136.4, 127.6, 126.9, 126.6, 113.8, 106.4, 105.6, 69.6, 67.1, 59.9, 52.6, 13.2 ppm; HRMS–ESI (m/z): [M + Na]$^+$ calculated for $C_{44}H_{52}N_2O_{12}Na$, 823.3429; found, 823.3412.

Tetraethyl 2,2',2'',2'''-{1,2-ethanediylbis[oxy(5-hydroxy-2,1-phenylene)nitrilo]tetraacetate (1c). A solution of **1b** (4.13 g, 5.16 mmol) in methanol (150 mL) and 10% Pd/C (0.5 g) was stirred vigorously under a H_2 atmosphere for 24 h at room temperature. The reaction mixture was subsequently filtered over celite and the celite pad was washed with hot EtOAc. Column chromatography (SiO_2, EtOAc/petroleum ether 7:3, v/v) yielded the title compound (2.76 g, 86%). ^{1}H NMR ($CDCl_3$, 300 MHz) δ 6.51 (d, J = 8.6 Hz, 2H, CH_{Ar}), 6.33 (d, J = 2.7 Hz, 2H, CH_{Ar}), 6.24 (dd, J = 8.6 Hz, J = 2.7 Hz, 2H, CH_{Ar}), 5.86 (br. s, 2H, OH), 4.04–4.16 (m, 20H, CH_2), 1.17 (t, J = 7.2 Hz, 12H, CH_3) ppm; ^{13}C NMR ($CDCl_3$, 75 MHz) δ 171.9, 150.9, 144.0, 140.4, 115.7, 108.0, 106.7, 68.0, 61.1, 53.7, 14.2 ppm; HRMS–ESI (m/z): [M + Na]$^+$ calcd for $C_{30}H_{40}N_2O_{12}Na$, 643.2468; found, 643.2573.

Tetraethyl 2,2',2'',2'''-[1,2-ethanediylbis(oxy{5-[4-(4-nitrophenyl)butoxy]-2,1-phenylene}nitrilo)]tetra acetate (1d). A solution of **1c** (0.60 g, 0.97 mmol), Cs_2CO_3 (1.26 g, 3.87 mmol) and **2** (1.35 g, 3.87 mmol) in 10 mL DMF was heated overnight at 110 °C. After allowing the solution to cool to room temperature, the solvent was removed in vacuo and the residue redissolved in DCM. The organic layer was washed with 20 mL H_2O and subsequently dried over $MgSO_4$. Column chromatography (SiO_2, 1: DCM/EtOAc 95:5 → 85:15, v/v; 2: petroleum ether/EtOAc 1:1, v/v) yielded the title compound (0.55 g, 59%). ^{1}H NMR ($CDCl_3$, 300 MHz) δ 8.15 (d, J = 8.9 Hz, 4H, CH_{Ar}), 7.37 (d, J = 8.9 Hz, 4H, CH_{Ar}), 6.79 (d, J = 8.5 Hz, 2H, CH_{Ar}), 6.38–6.46 (m, 4H, CH_{Ar}), 4.20 (s, 4H, CH_2), 4.18 (s, 8H, CH_2), 4.10 (q, J = 7.1 Hz, 8H, CH_2), 3.88–3.94 (m, 4H, O-CH_2), 2.76–2.83 (m, 4H, CH_2), 1.74–1.88 (m, 8H, CH_2), 1.18 (t, J = 7.1 Hz, 12H, CH_3) ppm; ^{13}C NMR ($CDCl_3$, 75 MHz) δ 171.4, 153.9, 150.2, 146.4, 144.7, 140.6, 129.2, 123.6, 123.2, 115.0, 107.1, 106.1, 68.1, 67.8, 60.7, 53.5, 35.5, 28.9, 27.5, 14.1 ppm; HRMS–FD (m/z): [M]$^+$ calcd for $C_{50}H_{62}N_4O_{16}$ 974.4161; found, 974.4144.

Tetraethyl 2,2',2'',2'''-[1,2-ethanediylbis(oxy{5-[4-(4-aminophenyl)butoxy]-2,1-phenylene}nitrilo)]tetraacetate (1e). A mixture of **1d** (0.18 g, 0.23 mmol), 10% Pd/C (0.02 g) and a few drops of triethylamine in 100 mL DCM/EtOH 1:1 (v/v) was stirred vigorously under a hydrogen atmosphere for 48 h. The reaction mixture was filtered over celite and the celite pad washed with hot EtOAc. Column chromatography (SiO_2, EtOAc) yielded the title compound (0.17 g, 99%). ^{1}H NMR ($CDCl_3$, 300 MHz) δ 7.02 (d, J = 8.2 Hz, 4H, CH_{Ar}), 6.80 (d, J = 8.8 Hz, 2H, CH_{Ar}), 6.65 (d, J = 8.2 Hz, 4H, CH_{Ar}), 6.39–6.47 (m, 4H, CH_{Ar}), 4.06–4.23 (m, 20H, CH_2-X), 3.87–3.93 (m, 4H, CH_2), 3.60 (br. s, 4H, NH_2), 2.56–2.63 (m, 4H, CH_2), 1.67–1.68 (m, 8H, CH_2), 1.21 (t, J = 7.6 Hz, 12H, CH_3) ppm; ^{13}C NMR ($CDCl_3$, 75 MHz) δ 171.4, 154.0, 144.6, 144.3, 140.6, 132.3, 129.2 115.2, 114.9, 107.0, 106.2, 68.3, 68.1, 60.8, 53.5, 34.8, 28.9, 28.1, 14.1 ppm; HRMS–FD (m/z): [M]$^+$ calcd for $C_{50}H_{66}N_4O_{12}$, 914.4677; found, 914.4668.

Azobenzene-BAPTA tetraester (1f). To a solution of **1e** (238 mg, 0.26 mmol) in 128 mL pyridine was added CuCl (260 mg, 2.62 mmol), the flask was left open to the air and the resulting mixture was stirred at room temperature for 48 h. Then, the solvent was removed in vacuo and column chromatography (SiO_2, EtOAc/petroleum ether 2:8, v/v) yielded the cyclized azobenzene (37 mg, 16%). ^{1}H NMR ($CDCl_3$, 300 MHz) δ 7.88 (d, J = 8.0 Hz, 4H, CH_{Ar}), 7.37 (d, J = 9.0 Hz, 4H, CH_{Ar}), 6.80 (d, J = 8.7 Hz, 2H, CH_{Ar}), 6.38–6.48 (m, 4H, CH_{Ar}), 4.21 (s, 4H, CH_2), 4.19 (s, 8H, CH_2), 4.12 (q, J = 7.2 Hz, CH_2), 3.87–3.97 (m, 4H, CH_2), 2.74–2.83 (m, 4H, CH_2), 1.87–1.92 (m, 8H, CH_2), 1.21 (t, J = 7.2 Hz, 12H) ppm; ^{13}C NMR ($CDCl_3$, 75 MHz) δ 171.4, 154.0, 151.2, 145.6, 144.6, 140.6, 129.1, 122.8, 115.0, 107.1, 106.2, 68.1, 60.8, 53.5, 35.5, 29.7, 29.0, 27.8, 14.1 ppm; HRMS–FD (m/z): [M]$^+$ calcd for $C_{50}H_{62}N_4O_{12}$, 910.4364; found, 910.4368.

Hydrolyzed azobenzene-BAPTA (1). To a solution of **1f** (87 mg, 0.040 mmol) in 11 mL THF/MeOH 5:1 (v/v),

$LiOH·H_2O$ (51 mg, 1.21 mmol) was added and the reaction mixture stirred overnight at room temperature. The solvent was removed in vacuo (at 30 °C) and the residue was sonicated briefly in 10 mL DCM/EtOAc 1:1 (v/v) and filtered. The solid is solubilized in Milli-Q water and acidified with HCl. The resulting suspension was centrifuged, the supernatant removed and the precipitate washed with a small volume of water. Then, the precipitate was redissolved by adding a small volume of a KOH solution and the solvent removed. ^{1}H NMR (DMSO-d_6, 300 MHz) δ 8.09 (d, J = 3 Hz, 2H, CH_{Ar}), 7.82 (dd, J = 9 Hz and 3 Hz, 2H, CH_{Ar}), 7.70 (d, J = 9 Hz, 4H, CH_{Ar}), 7.40 (d, J = 9 Hz, 2H, CH_{Ar}), 6.89 (d, J = 9.0 Hz, 4H, CH_{Ar}), 4.52 (s, 4H, CH_2), 4.27 (s, 8H, CH_2), 3.63 (t, J = 7 Hz, 4H, CH_2), 3.41 (t, J = 7 Hz, 4H, CH_2), 1.75 (m, 4H, CH_2), 1.51 (m, 4H, CH_2) ppm.

Supporting Information

Supporting Information File 1

Electronic absorption spectra, NMR and mass spectra.
[https://www.beilstein-journals.org/bjoc/content/supplementary/1860-5397-15-273-S1.pdf]

Acknowledgements

Financial support from the European Research Council (ERC, FP7-2008-2013, grant no. 208702), Région Aquitaine; University of Bordeaux; CNRS and Ministère de la Recherche et de l'Enseignement Supérieur (A.D.; A.T.) are gratefully acknowledged.

ORCID® iDs

Jean-Luc Pozzo - https://orcid.org/0000-0001-9156-8483
Nathan D. McClenaghan - https://orcid.org/0000-0003-0285-1741

References

1. Tsien, R. Y. *Biochemistry* **1980,** *19,* 2396–2404. doi:10.1021/bi00552a018
2. Gerig, J. T.; Singh, P.; Levy, L. A.; London, R. E. *J. Inorg. Biochem.* **1987,** *31,* 113–121. doi:10.1016/0162-0134(87)80056-9
3. Grynkiewicz, G.; Poenie, M.; Tsien, R. Y. *J. Biol. Chem.* **1985,** *260,* 3440.
4. de Silva, A. P.; Gunaratne, H. Q. N.; Maguire, G. E. M. *J. Chem. Soc., Chem. Commun.* **1994,** 1213–1214. doi:10.1039/c39940001213
5. de Silva, A. P.; McClenaghan, N. D. *J. Am. Chem. Soc.* **2000,** *122,* 3965–3966. doi:10.1021/ja994080m
6. de Silva, A. P.; McClenaghan, N. D. *Chem. – Eur. J.* **2002,** *8,* 4935–4945. doi:10.1002/1521-3765(20021104)8:21<4935::aid-chem4935>3.0.co;2-2
7. Gunnlaugsson, T.; Nieuwenhuyzen, M.; Richard, L.; Thoss, V. *J. Chem. Soc., Perkin Trans. 2* **2002,** 141–150. doi:10.1039/b106474f
8. Dhingra, K.; Maier, M. E.; Beyerlein, M.; Angelovski, G.; Logothetis, N. K. *Chem. Commun.* **2008,** 3444. doi:10.1039/b801975d
9. Liu, Q.; Bian, W.; Shi, H.; Fan, L.; Shuang, S.; Dong, C.; Choi, M. M. F. *Org. Biomol. Chem.* **2013,** *11,* 503–508. doi:10.1039/c2ob26888d
10. Egawa, T.; Hanaoka, K.; Koide, Y.; Ujita, S.; Takahashi, N.; Ikegaya, Y.; Matsuki, N.; Terai, T.; Ueno, T.; Komatsu, T.; Nagano, T. *J. Am. Chem. Soc.* **2011,** *133,* 14157–14159. doi:10.1021/ja205809h
11. Bhattacharyya, K. X.; Boubekeur-Lecaque, L.; Tapsoba, I.; Maisonhaute, E.; Schöllhorn, B.; Amatore, C. *Chem. Commun.* **2011,** *47,* 5199. doi:10.1039/c1cc11081k
12. Tsien, R. Y.; Zucker, R. S. *Biophys. J.* **1986,** *50,* 843–853. doi:10.1016/s0006-3495(86)83525-1
13. Gurney, A. M.; Tsien, R. Y.; Lester, H. A. *Proc. Natl. Acad. Sci. U. S. A.* **1987,** *84,* 3496–3500. doi:10.1073/pnas.84.10.3496
14. Adams, S. R.; Lec-Ram, V.; Tsien, R. Y. *Chem. Biol.* **1997,** *4,* 867–878. doi:10.1016/s1074-5521(97)90119-8
15. McCray, J. A.; Fidler-Lim, N.; Ellis-Davies, G. C. R.; Kaplan, J. H. *Biochemistry* **1992,** *31,* 8856–8861. doi:10.1021/bi00152a023
16. Ellis-Davies, G. C. R.; Kaplan, J. H. *Proc. Natl. Acad. Sci. U. S. A.* **1994,** *91,* 187–191. doi:10.1073/pnas.91.1.187
17. Adams, S. R.; Kao, J. P. Y.; Grynkiewicz, G.; Minta, A.; Tsien, R. Y. *J. Am. Chem. Soc.* **1988,** *110,* 3212–3220. doi:10.1021/ja00218a034
18. Cui, J.; Gropeanu, R. A.; Stevens, D. R.; Rettig, J.; del Campo, A. *J. Am. Chem. Soc.* **2012,** *134,* 7733–7740. doi:10.1021/ja2115184
19. Agarwal, H. K.; Janicek, R.; Chi, S.-H.; Perry, J. W.; Niggli, E.; Ellis-Davies, G. C. R. *J. Am. Chem. Soc.* **2016,** *138,* 3687–3693. doi:10.1021/jacs.5b11606
20. Ellis-Davies, G. C. R. *Chem. Rev.* **2008,** *108,* 1603–1613. doi:10.1021/cr078210i
21. Natali, M.; Giordani, S. *Chem. Soc. Rev.* **2012,** *41,* 4010. doi:10.1039/c2cs35015g
22. Kumar, S.; Hernandez, D.; Hoa, B.; Lee, Y.; Yang, J. S.; McCurdy, A. *Org. Lett.* **2008,** *10,* 3761–3764. doi:10.1021/ol801406b
23. Cui, S.; Tian, Z.; Pu, S.; Dai, Y. *RSC Adv.* **2016,** *6,* 19957–19963. doi:10.1039/c5ra26910e
24. Ushakov, E. N.; Nazarov, V. B.; Fedorova, O. A.; Gromov, S. P.; Chebun'kova, A. V.; Alfimov, M. V.; Barigelletti, F. *J. Phys. Org. Chem.* **2003,** *16,* 306–309. doi:10.1002/poc.619
25. Dozova, N.; Pousse, G.; Barnych, B.; Mallet, J.-M.; Cossy, J.; Valeur, B.; Plaza, P. *J. Photochem. Photobiol., A* **2018,** *360,* 181–187. doi:10.1016/j.jphotochem.2018.04.029
26. Sakata, T.; Jackson, D. K.; Mao, S.; Marriott, G. *J. Org. Chem.* **2008,** *73,* 227–233. doi:10.1021/jo7019898
27. Wu, L.; Dai, Y.; Marriott, G. *Org. Lett.* **2011,** *13,* 2018–2021. doi:10.1021/ol200408j
28. Shishido, H.; Yamada, M. D.; Kondo, K.; Maruta, S. *J. Biochem.* **2009,** *146,* 581–590. doi:10.1093/jb/mvp107
29. Shinkai, S.; Minami, T.; Kusano, Y.; Manabe, O. *J. Am. Chem. Soc.* **1983,** *105,* 1851–1856. doi:10.1021/ja00345a029
30. Ducrot, A.; Verwilst, P.; Scarpantonio, L.; Goudet, S.; Kauffmann, B.; Denisov, S.; Jonusauskas, G.; McClenaghan, N. D. *Supramol. Chem.* **2012,** *24,* 462–472. doi:10.1080/10610278.2012.678851
31. Hua, Y.; Flood, A. H. *J. Am. Chem. Soc.* **2010,** *132,* 12838–12840. doi:10.1021/ja105793c
32. Marchi, E.; Baroncini, M.; Bergamini, G.; Van Heyst, J.; Vögtle, F.; Ceroni, P. *J. Am. Chem. Soc.* **2012,** *134,* 15277–15280. doi:10.1021/ja307522f
33. Beharry, A. A.; Woolley, G. A. *Chem. Soc. Rev.* **2011,** *40,* 4422. doi:10.1039/c1cs15023e

34. Szymański, W.; Beierle, J. M.; Kistemaker, H. A. V.; Velema, W. A.; Feringa, B. L. *Chem. Rev.* **2013,** *113,* 6114–6178. doi:10.1021/cr300179f
35. Crossley, R.; Goolamali, Z.; Sammes, P. G. *J. Chem. Soc., Perkin Trans. 2* **1994,** 1615. doi:10.1039/p29940001615
36. Kinoshita, K. *Bull. Chem. Soc. Jpn.* **1959,** *321,* 777.
37. Siewertsen, R.; Neumann, H.; Buchheim-Stehn, B.; Herges, R.; Näther, C.; Renth, F.; Temps, F. *J. Am. Chem. Soc.* **2009,** *131,* 15594–15595. doi:10.1021/ja906547d
38. Birks, J. B. *Photophysics of Aromatic Molecules;* John Wiley and Sons, 1970.
39. Ellis-Davies, G. C. R.; Barsotti, R. J. *Cell Calcium* **2006,** *39,* 75–83. doi:10.1016/j.ceca.2005.10.003
40. Montalti, M.; Credi, A.; Prodi, L.; Gandolfi, M. T. *Handbook of Photochemistry,* 3rd ed.; CRC Press: Boca Raton, FL, U.S.A., 2006; p 601. doi:10.1201/9781420015195
41. Batat, P.; Vives, G.; Bofinger, R.; Chang, R.-W.; Kauffmann, B.; Oda, R.; Jonusauskas, G.; McClenaghan, N. D. *Photochem. Photobiol. Sci.* **2012,** *11,* 1666. doi:10.1039/c2pp25130b
42. Porter, R. A. Pyrimidinyl-piperazine derivatives and their use as medicaments. WO Pat. Appl. WO/1994/014779 A1, July 7, 1994.

License and Terms

This is an Open Access article under the terms of the Creative Commons Attribution License (http://creativecommons.org/licenses/by/4.0). Please note that the reuse, redistribution and reproduction in particular requires that the authors and source are credited.

The license is subject to the *Beilstein Journal of Organic Chemistry* terms and conditions: (https://www.beilstein-journals.org/bjoc)

The definitive version of this article is the electronic one which can be found at: doi:10.3762/bjoc.15.273

BEILSTEIN JOURNAL OF ORGANIC CHEMISTRY

Chemical tuning of photoswitchable azobenzenes: a photopharmacological case study using nicotinic transmission

Lorenzo Sansalone‡, Jun Zhao‡, Matthew T. Richers and Graham C. R. Ellis-Davies*

Full Research Paper

Open Access

Address:
Department of Neuroscience, Mount Sinai School of Medicine, New York, NY 10029, USA

Email:
Graham C. R. Ellis-Davies* - graham.davies@mssm.edu

* Corresponding author ‡ Equal contributors

Keywords:
acetylcholine receptors; bidirectional; photoswitchable drug; tetrafluoroazobenzene; visible light

Beilstein J. Org. Chem. **2019,** *15,* 2812–2821.
doi:10.3762/bjoc.15.274

Received: 28 August 2019
Accepted: 11 November 2019
Published: 21 November 2019

This article is part of the thematic issue "Molecular switches".

Guest Editor: W. Szymanski

© 2019 Sansalone et al.; licensee Beilstein-Institut.
License and terms: see end of document.

Abstract

We have developed photochromic probes for the nicotinic acetylcholine receptor that exploit the unique chemical properties of the tetrafluoroazobenzene (4FAB) scaffold. Ultraviolet light switching and rapid thermal relaxation of the metastable *cis* configuration are the main drawbacks associated with standard AB-based switches. We designed our photoprobes to take advantage of the excellent thermodynamic stability of the *cis*-4FAB configuration (thermal half-life > 12 days at 37 °C in physiological buffer) and *cis–trans* photostationary states above 84%. Furthermore, the well-separated n–π* absorption bands of *trans*- and *cis*-4FAB allow facile photoswitching with visible light in two optical channels. A convergent 11-step synthetic approach allowed the installation of a trimethylammonium (TA) head onto the 4FAB scaffold, by means of an alkyl spacer, to afford a free diffusible 4FABTA probe. TAs are known to agonize nicotinic receptors, so 4FABTA was tested on mouse brain slices and enabled reversible receptor activation with cycles of violet and green light. Due to the very long-lived metastable *cis* configuration, 4FAB in vivo use could be of great promise for long term biological studies. Further chemical functionalization of this 4FAB probe with a maleimide functionality allowed clean cross-linking with glutathione. However, attempts to conjugate with a cysteine on a genetically modified nicotinic acetylcholine receptor did not afford the expected light-responsive channel. Our data indicate that the 4FAB photoswitch can be derivatized bifunctionally for genetically-targeted photopharmacology whilst preserving all the favorable photophysical properties of the parent 4FAB scaffold, however, the tetrafluoro motif can significantly perturb pharmacophore–protein interactions. In contrast, we found that the freely diffusible 4FABTA probe could be pre-set with green light into an OFF state that was biologically inert, irradiation with violet light effectively "uncaged" agonist activity, but in a photoreversible manner. Since the neurotransmitter acetylcholine has fully saturated heteroatom valences, our photoswitchable 4FABTA probe could be useful for physiological studies of this neurotransmitter.

Introduction

Starting in 1937, azobenzenes (ABs) have attracted much attention because they undergo a photoreversible chemical transformation of the thermodynamically favored *trans* configuration into the corresponding *cis* configuration [1]. The reverse reaction can be initiated with a different wavelength. In a biological context, this photochromism was exploited first by Erlanger and colleagues for enzyme inhibitors in 1968 [2], and ion channels in 1971 [3]. Their ingenious approach was utilized further in collaboration with Lester [4-6], but the power of AB photochemistry for biochemistry and cell physiology was then largely forgotten until 2000, when it was revived by Woolley and co-workers in a seminal paper [7]. Since that time, AB photochromes have been exploited by many research groups to control a wide variety of biological process photoreversibly [8,9]. Furthermore, chemists have paid attention to spectral tuning of the AB chromophore [10,11].

Recently, an improved set of fluorine-substituted AB photochromes was developed by Hecht and co-workers [12,13]. ABs with two or four fluorines and electron-withdrawing groups at the *para* substituents all maintained the superb chemical properties of the parent tetrafluoro-(4F)AB chromophore [12]. Mild electron donation effectively destroys the beautiful separation of absorption bands of the n–π* transitions, and with it the excellent high isomeric content of both photostationary states (PSSs). For example, with *para*-diamide substituents the PSS can be either 85% *trans* and 69% *cis* (nitrogen attached to ring [12]) or 96% *trans* and 92% *cis* (carbonyl attached to ring [13]).

Since many modern neurobiological applications of AB-based photoprobes require asymmetric substitution of the photochrome, we decided to explore the effects of changing one *para* substituent of 4FAB so as to allow the attachment of different substituents from our first 4FAB photoprobe [14]. Specifically, we were attracted by the application [15] of a regular AB-based photoswitch called "MAHoCh" [16]. The MAHoCh probe was originally designed [16] to activate nicotinic acetylcholine receptors in vivo. However, it was found that the trimethylammonium (TA) head group blocked acetylcholine binding when the photoprobe was cross-linked to the channel near the neurotransmitter binding site, via a (still) mysterious mechanism [15,16]. Normally, TA-based drugs can activate nicotinic acetylcholine receptors, as shown, for example, by Trauner and co-workers [17] (azo-choline, Scheme 1).

Here we explore the effects of addition of the tetrafluoro motif onto such regular AB photoprobes. We have developed a synthetic route that allows the production of asymmetrically substituted 4FAB photoprobes (**1** and **2**, Scheme 1). Importantly, the *cis* and *trans* PSS are both >84%, and the thermal half-life of the *cis* configuration is 12 days in physiological buffer and temperature. The maleimide-substituted compound **1** reacted with the cysteine of glutathione, however, we found that this "4FAB version" of MAHoCh (Scheme 1) did not enable significant perturbation of nicotinic acetylcholine receptor currents used with MAHoCh [16]. However, when 4FABTA analog **2** was tested as a freely-diffusible photoprobe, photopharmacological control of native nicotinic acetylcholine receptors (shown schematically in Scheme 1) with neurons on the medial habenula was possible.

Results and Discussion

Acetylcholine receptors (AChR) are expressed in many organs, and these receptors fall into two fundamentally different categories which were defined, historically, using pharmacology. The neurotransmitter-gated ion channels are activated by the drug nicotine, and these are called nicotinic (n)AChR. The G-protein-coupled receptors are activated by the drug muscarine, and these are called muscarinic (m)AChR. The structural difference between the native acetylcholine and nicotine are striking, and their diversity reflects the complexity of structure–activity relationships of ligands for nicotinic acetylcholine receptors. For example, the drug homocholine phenyl ether (HoChPE) is an agonist of the nicotinic acetylcholine receptors, but the drug MG-624 is an antagonist (Scheme 1).

In our design of photochromes for the nicotinic acetylcholine receptor we were determined to preserve all the excellent chemical properties of the parent 4FAB whilst incorporating this new AB into a "4FAB version" of MAHoCh. Since the latter has an oxygen atom *para* to the azo group we tested the feasibility of adding such a strong electron donor to an analog of a difluoro-(2F)AB Hecht photochrome [13] by making "MeO-2FAB" (Figure 1, see Supporting Information File 1 for synthesis). Since 2FAB and 4FAB photochromes with electron-withdrawing groups at the *para* positions consistently show a separation of the n–π* transitions of the *trans* and *cis* configuration [13], we concluded the presence of one methoxy group in MeO-2FAB effectively destroyed this beautiful separation (a representative example of a 4FAB spectrum is shown in Figure 1). Our data is similar to that recently reported by Gorostiza and co-workers for a monofluorinated AB photochrome [18] (core structure shown in Figure 1 as "1FAB"). This monofluoro-(1)FAB chromophore is much less electron rich than MeO-2FAB, so it is perhaps not surprising that 2FAB cannot tolerate such strong electron-donating group. Hecht and co-workers had shown in their original paper that two amides connected to 2FAB and 4FAB via nitrogen atoms also lost much of the excellent features of the parent 4FAB chromophore [12]. (Note, "1FAB" also has a very short thermal half-life of the *cis* config-

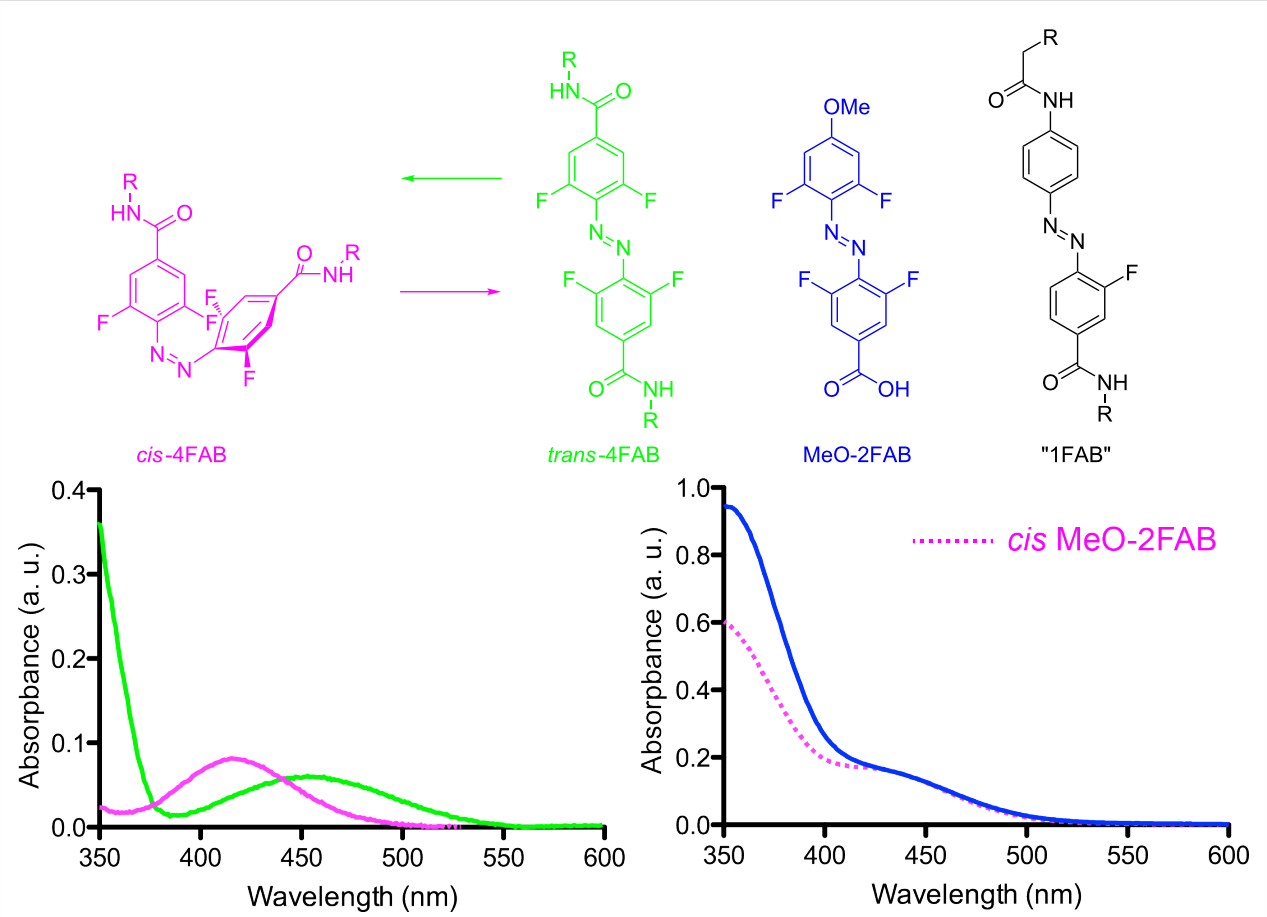
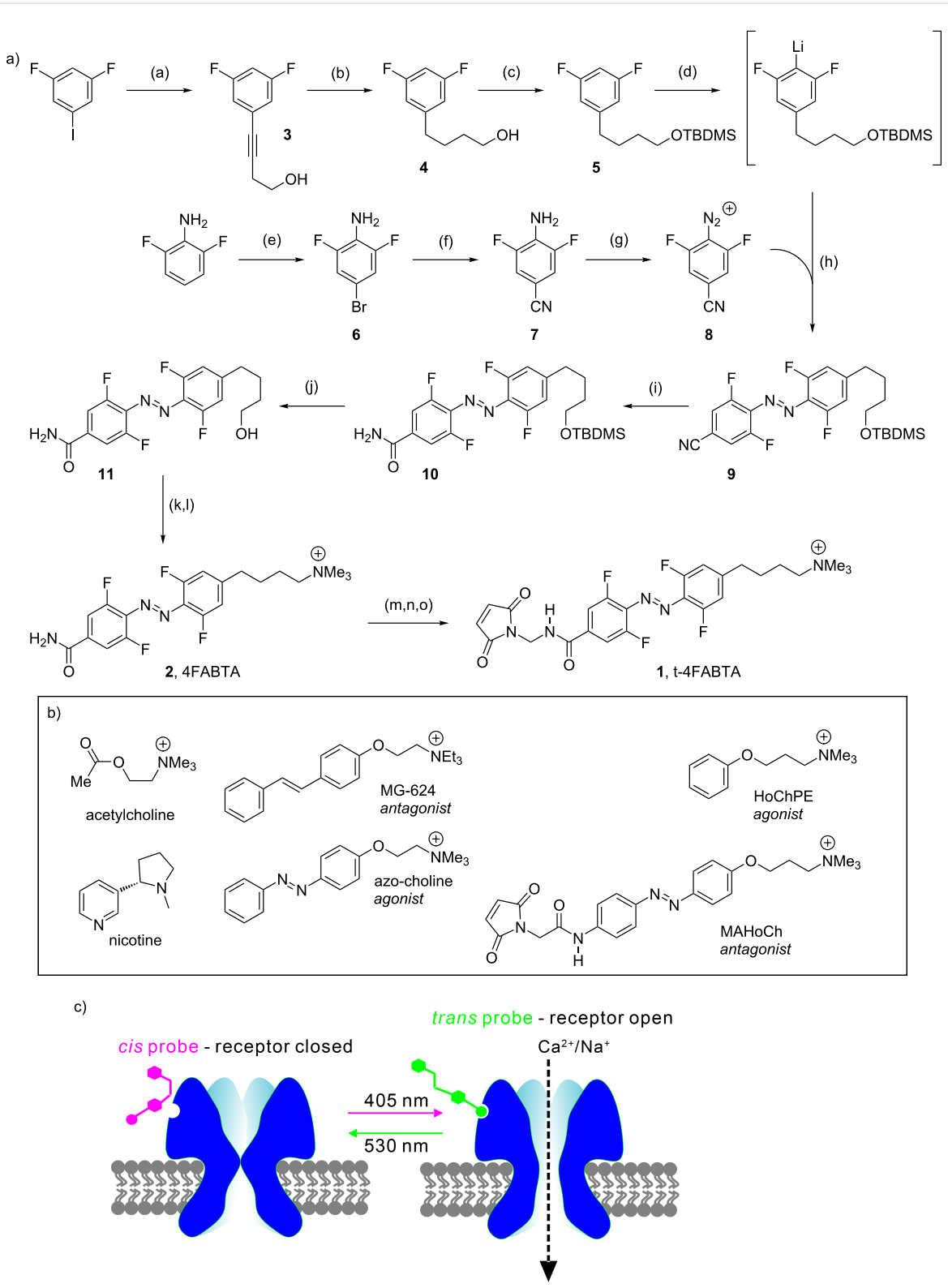


Figure 1: Fluoro-AB derivatives and spectra. Structures of 4FAB-diamides [13] *cis* and *trans* configurations, and the associated absorption spectra of these compounds (left). Note, the analogous difluoro-ABs have similar spectra to 4FABs [13]. Effect of electron donation on the fluoro-AB absorption spectra, the *cis*-MeO-2FAB (pink dots) is the green photostationary state of the photochrome (right). Structure of the photochrome core of a mono-fluoro-AB (1FAB) [18]. Spectra in HEPES, pH 7.4 at rt.

uration of 10 min at rt [18], compared to 2 years for 4FAB, implying that mild electron donating also destroys the other distinctive property of 4FAB.) Next, we tested if the mildly electron-donating methyl group could be tolerated better by Hecht photochromes [13]. We found that such a derivative did not perturb all the excellent chemical properties of 2FAB (data not shown). Thus, we synthesized a "4FAB version" of MAHoCh (i.e., **1**) as shown in Scheme 1.

The synthesis of photochromes **1** and **2** is outlined in Scheme 1. Sonogashira coupling of difluoroiodobenzene and 3-butynol gave **3**, which was reduced by catalytic hydrogenation to **4** followed by protection with TBDMS to give **5** in 63% yield for three steps. The synthesis of the other half of the photochrome started with bromination of difluorinated aniline to give **6** followed by copper-catalyzed cyanation to **7** in 62% overall yield. Diazonization of **7** with nitrosonium tetrafluoroborate gave **8** (54% yield). The two parts of the chromophore were coupled starting by treatment of **5** with *n*-butyllithium at −78 °C, which was coupled in situ with **8** to AB **9** (17% yield). Copper-catalyzed hydration of **9** gave amide **10**, which was treated with TBAF to alcohol **11** in 42% overall yield. Installation of the cationic head was performed in two steps: first bromination of **11** via Appel reaction, followed by treatment with trimethylamine to give **2** in 35% overall yield. Photoswitch **2** is the first example of a bifunctional, asymmetrically substituted 4FAB chromophore that actually maintains the near-ideal chemical properties of Hecht's 4FAB chromophores [12,13] (see below). The final synthetic challenge was the installation of a maleimide onto chromophore **2**. The original AB photoswitchable probes which were cross-linked to cysteine mutants had amides with a reverse orientation [19,20] compared to **2**, so a simple one-step route can be used to install the maleimides. It is this functionality that allows coupling (often called "tethering", symbolized as "t" for tetherable in Scheme 1) of the probe with mutant proteins. In our case, we developed a three-step route to install the maleimide using hydroxymethylation with formaldehyde, followed by treatment with thionyl chloride to give a



Scheme 1: Synthesis of 4FABTA. a) Reagents and conditions: (a) 3-Butynol, $PdCl_2(PPh_3)_2$, CuI, THF, rt, 93%; (b) H_2, PtO_2, EtOH, rt, 71%; (c) TBDMS-Cl, imidazole, DCM, rt, 96%; (d) *n*-BuLi, THF, −78 °C to −50 °C; (e) NBS, ACN, rt, 89%; (f) CuCN, NMP, 202 °C, 70%; (g) $NOBF_4$, EtOAC, −10 °C, 54%; (h) THF, −78 °C, 17%; (i) Et_2NOH, $Cu(OAc)_2$, MeOH, rt, 49%; (j) TBAF, THF, rt, 71%; (k) PPh_3, CBr_4, THF, rt, 64%; (l) $N(CH_3)_3$, THF, rt, 53% (m) CH_2O, K_2CO_2, H_2O, 50 °C, 95%; (n) $SOCl_2$, THF, −10 °C; (o) maleimide, DIPEA, THF, rt. Counter anion not shown for clarity. b) Structures of nicotinic acetylcholine receptor ligands. c) Illustration of how *cis* and *trans* agonists interact with ligand-gated ion channels.

chloromethyl intermediate, which was reacted in situ with maleimide to give **1** in 6% overall yield. Crucially, photochrome **1** also maintained the near-ideal photochemical properties of Hecht's 4FABs [12,13], specifically the spectral separation of the n–π* transitions of the *trans* and *cis* configurations.

Since the maleimide functionality of **1** is quite hydrolytically sensitive at neutral pH, we characterized precursor **2**. This photochrome underwent the expected *trans–cis* isomerization (Figure 2a). The absorption spectrum of the all *trans*-**2** in aqueous solution (HEPES, pH 7.4, no organic co-solvent, Figure 2a) is very similar to the parent 4FAB chromophore (Figure 1). Irradiation with a 532 nm laser gave the *cis* PSS having the expected hypsochromically shifted n–π* band (Figure 2b, full spectra Figure S1, Supporting Information File 1) containing 91% of *cis*-**2** (Figure S2, Supporting Information File 1). Irradiation of this mixture with a 405 nm laser generated the *trans* PSS containing 84% *trans*-**2** (Figure S2, Supporting Information File 1). As already noted, *cis*-4FAB is remarkably thermodynamically stable, some photochromes have a thermal half-life at rt of about 2 years [12]. We used UPLC to measure the thermal half-life of *cis*-**2** under physiological conditions, namely 37 °C and pH 7.4. We found, under these conditions, that *cis*-**2** decayed with a half-life of >12 days (Figure 2c). This datum suggests that even though the electron donor effect of the methylene substituent decreases the thermodynamic stability of the *cis* form compared to that report by Hecht [13], protein conjugates of **1** would be highly stable in vivo over the course of a typical daily mouse behavioral experiment [15]. *cis*-MAHoCh has a significantly shorter thermal half-life of about 75 min at rt [16], a value that would be much lower at physiological temperatures

Next we tested the chemical reactivity and stability of **1** in physiological buffer. First, we tested the thermal stability of **1** in physiological buffer (HEPES, pH 7.4). We found that in absence of any thiol, the maleimide functionality was reasonably stable, with 80% hydrolysis occurring over 22 h (Figure S3, see also LC–MS in Supporting Information File 1). Reassured by these data, **1** was mixed with a stoichiometric amount of glutathione, at 37 °C rapid reaction gave peak with a shorter retention time on UPLC (Figure 3). LC–MS analysis revealed a molecular ion confirming the addition product **12**. Under the conditions we used for this chemical reaction it was complete within a few minutes. It has been reported that maleimide–peptide conjugates undergo hydrolysis of the succinimide to give a more flexible product of type **13** (Figure 3a) [21]. Thus, we monitored the stability of **12** by UPLC at 37 °C and pH 7.4 and found that it was converted to two new peaks (**13**) in about 5 h (Figure 3b). To our knowledge this is the first report of the stability of a tethered photoswitch

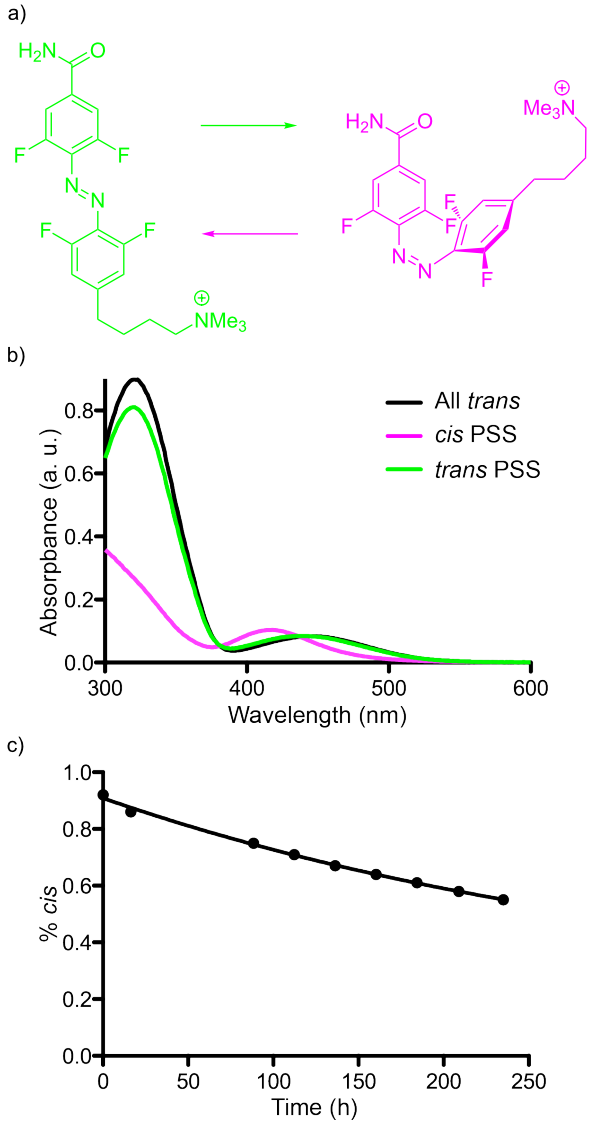


Figure 2: Photochemistry of 4FABTA (**2**), and thermodynamic stability in physiological buffer. a) *Trans–cis* photochemical reaction of **2**. b) Absorption spectra of all *trans*-**2** (black), *cis*-**2** PSS (from 532 nm laser), and *trans*-**2** PSS (from 405 nm laser) in HEPES (pH 7.4) at rt. c) Time course of thermal decay of *cis*-**2** PSS in HEPES (pH 7.4) at 37 °C.

[22] under physiological conditions. The broad success [22] of this strategy since 2004 [19] suggests that even though careful in silico modeling is a standard step in photoprobe development [22], this is always performed with unhydrolyzed conjugates. Perhaps for long-term use in vivo an additional modeling step involving hydrolyzed succinimides could be useful.

Our data (Figure 2 and Figure 3) suggested that t-4FABTA (**1**) could be used to replace MAHoCh in the labeling of genetically tagged nicotinic acetylcholine receptors on living cells. Thus, we co-transfected the nicotinic acetylcholine receptors α4

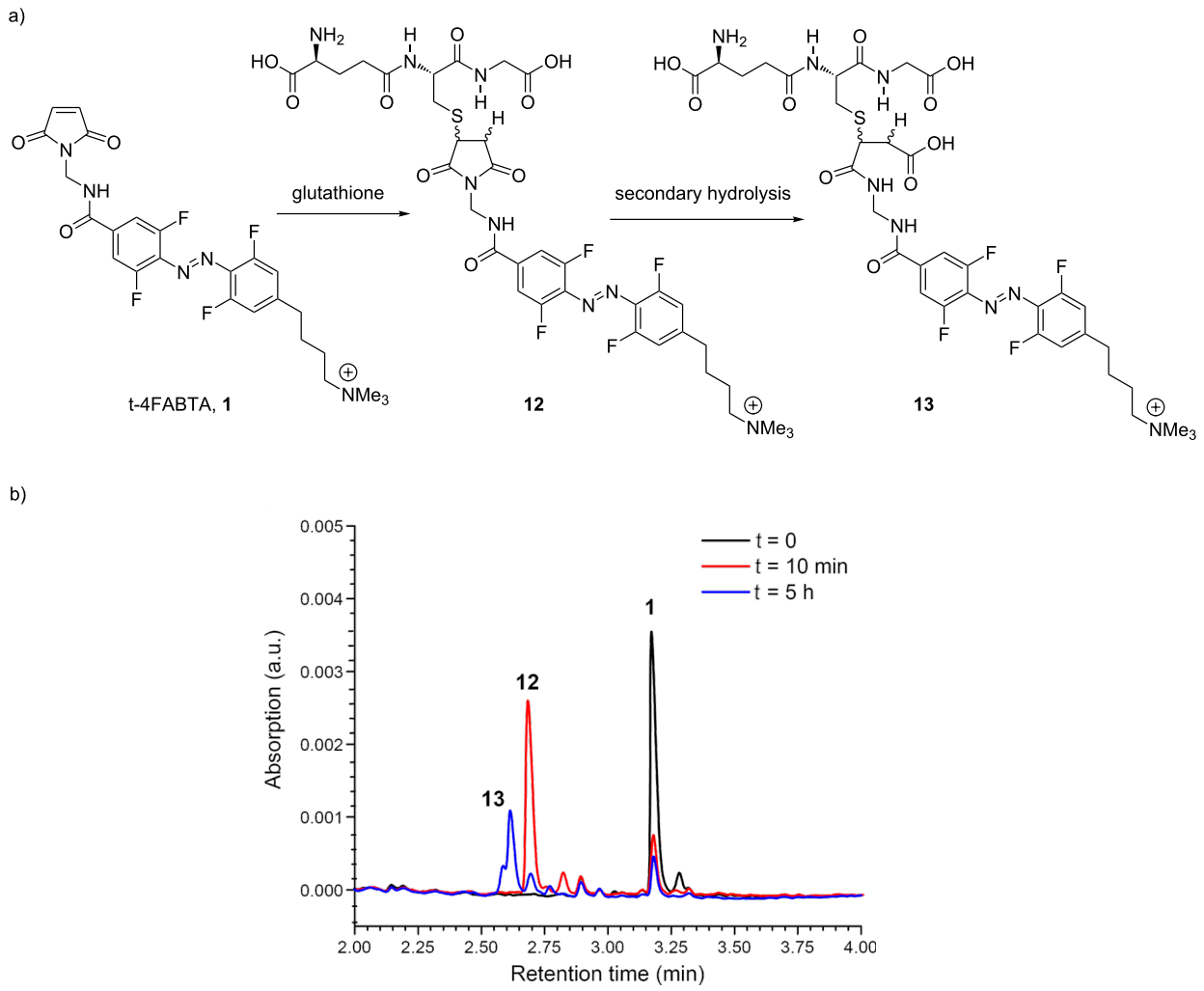


Figure 3: Reaction of t-4FABTA (**1**) with thiols, and thermal stability of initial conjugate. a) Chemical reaction of **1** with glutathione in HEPES (pH 7.4) at 37 °C to coupled conjugate **12**, and hydrolysis to **13**. b) UPLC chromatograms of chemical reactions shown in (a). Elution 0.75 to 1 mL/min, 2–100% acetonitrile in water for 4 min.

subunit with β2E61C mutant or β2 wild-type (as a control) subunits in HEK293 cells. Cells were treated with **1** for 20 min in the dark, then washed with normal artificial cerebral spinal fluid. First, we compared the basic biophysical properties of cells with mutant and WT β2 subunits, the values were as follows: the resting membrane potential (R_p) = 29.3 ± 3.9 mV and 28.3 ± 7.6 mV; holding currents at −40 mV were 77.65 ± 30.0 pA, and 76.96 ± 38.9 pA; and the input resistance (R_{Input}) = 215.2 ± 36.1 MΩ and 209.1 ± 40.7 MΩ (mutant vs WT, n = 5 cells each). These data show treatment with **1** does not change the electrical activity and health of cells.

Next we examined if **1** could serve as a photoswitchable antagonist of nicotinic acetylcholine receptors having α4β2E61C mutant as predicted from previous results [16]. After labeling HEK293 cells as described above, we recorded the currents evoked by puffing the agonist carbachol (CCh) for 1 s under three conditions: no light, or full field irradiation with green or violet light. Both wild-type and mutant channels were tested. Wild-type channels showed substantial inward currents (Figure 4a, grey) which were not perturbed by light (Figure 4a, green and violet, summary Figure 4b). This result was expected as these receptors have no cysteine available for drug conjugation. Surprisingly, similar results were seen with α4β2E61C mutant receptors (Figure 4c,d). We surmise from these data that the mysterious antagonism of *cis*-MAHoCh when conjugated to same mutant receptor is unfortunately perturbed. Since MAHoCh was initially predicted to be a tethered activator in the *trans* configuration, we would conclude the presence of the 4F substituents or the lack of oxygen atom in our version of this photoswitchable probe disturbs crucial drug–protein interactions essential for allosteric inhibition. It is noteworthy to

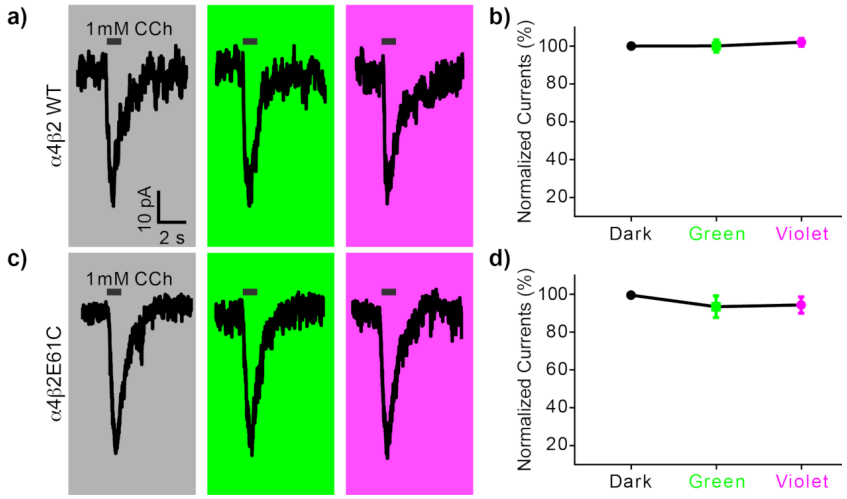


Figure 4: Testing photo-antagonism of **1** with genetically tagged nicotinic acetylcholine receptors. Currents from HEK293 cells were measured using the whole-cell patch-clamp method. Cell were transfected with either wild-type (WT) α4β2 or mutant (E61C) nicotinic acetylcholine receptors [16]. Cells with successful ion channel expression co-expressed YFP visualized using epi-fluorescence microscopy. Cover slips were treated with all *trans*-**1** (0.05 mM in physiological buffer) for 20 min in the dark. The cellular bathing solution was then exchanged for normal buffer before patch clamping. Currents were evoked by local puffing of the agonist carbachol (CCh, 1 mM, black bar). a) Representative currents from WT receptors before illumination (grey), followed by green light (530 nm, 3 mW, 2 min) or violet light (405 nm, 10 mW, 2 min). Irradiation started 100 s prior to puffing and ended 20 s after puffing. b) Summary of four experiments as in (a). Current amplitudes were normalized to the currents in the dark. Data are the mean ± s.e.m, *n* = 4 cells. c) Representative currents recordings from identical experiments to those on WT channels carried out on mutant receptors. d) Summary of the currents from six cells. Current amplitudes were normalized to the currents in the dark. Data are the mean ± s.e.m, *n* = 6 cells.

mention that without puffing any CCh agonist, irradiation of green or violet light did not evoke any detectable currents in patch-clamped cells.

Finally, we tested the synthetic precursor of our tetherable t-4FABTA probe (i.e., photochrome **2**) as a potential, freely diffusible optical probe of nicotinic acetylcholine receptors in situ. We chose neurons in the medial habenula brain region, as these cells endogenously express a very high density of acetylcholine receptors (mainly α3β4, but also α6, β2, β3 and α4 [23]). First, we puffed all *trans*-**2** (0.2 mM) onto a neuron and recorded excitatory postsynaptic currents (EPSCs) from nicotinic acetylcholine receptors in whole-cell voltage clamp mode. We isolated these currents by including TTX (blocker of voltage-dependent Na^+ channels), APV and CNQX (antagonists of NMDA and non-NMDA receptors), bicuculline and gabazine (GABAergic antagonists), and atropine (muscarinic acetylcholine receptor antagonist) in the artificial cerebral spinal fluid bathing solution. Thus, puffing all *trans*-**2** for 1 s evoked large EPSCs (ca. 40 pA). In contrast, puffing *cis*-**2** (0.2 mM) in the green PSS (i.e., 91% *cis*) did not evoke any detectable currents (Figure 5a). Next we identified whether *cis*-**2** could be photoswitched quickly to *trans*-**2** to function as an agonist in real time. We puffed *cis*-**2** (0.2 mM) in the green PSS onto a patch-clamped neuron for 1 s, and irradiated the full field of the microscope with violet light. We found that currents were evoked almost as quickly (Figure 5b, right) as those detected from use of all *trans*-**2** (Figure 5a, top). Thus, under these conditions the green PSS functions effectively like a "caged agonist", with violet irradiation rapidly producing an "uncaging-like" biological response. Since the neurotransmitter acetylcholine seems impossible to derivatize with a photochemical protecting group, a biologically inert photo-activatable agonist such **2** could be useful for neurophysiological studies. The long-term thermal stability of the 4FAB core allows a "stock" of the biologically inert *cis* PSS to be made. Since thermal decay is slow at 37 °C, frozen [14] such solutions could be used for many days without any change in pharmacological efficacy.

Our final set of biological experiments with photochrome **2** examined its ability to work as a dynamic, bidirectional photoswitchable drug for nicotinic acetylcholine receptors (Scheme 1c). To test this, we puffed all *trans*-**2** for 1 s onto a patch-clamped medial habenula neuron. As expected this drug configuration evoked an inward current (Figure 5c, upper trace). Irradiation of the application pipette during a subsequent puff with either green or violet light caused rapid photoswitching of **2** (Figure 5c, colored traces). The time between these sweeps was 3 min. Since we used full field illumination

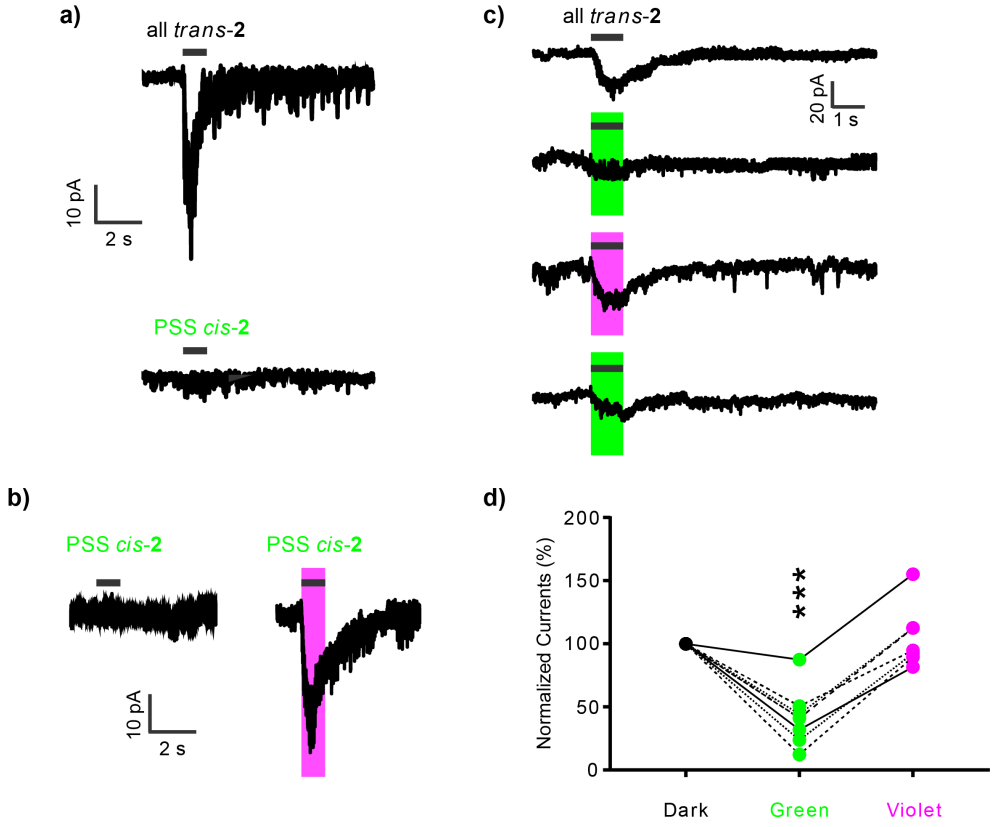


Figure 5: Photopharmacology with 4FABTA (**2**). Currents from neurons in the medial habenula in acutely isolated brain slices were measured using the whole-cell patch-clamp method. Signals from nicotinic acetylcholine receptors were isolated by blocking voltage-dependent Na^+ channels, muscarinic, GABAergic, and glutamatergic receptors. Photochrome **2** was puffed locally for 1 s (0.2 mM, black bar). LEDs centered at 405 and 530 nm were used for photoswitching. a) Representative responses evoked by all *trans*-**2** and cis-**2** in the green PSS. b) Representative responses evoked by *cis*-**2** in the green PSS without and with violet light (10 mW). c) Sequential responses from the same neuron when all *trans*-**2** was applied without irradiation (top) or with either green or violet light. The interval between sweeps was 3 min. d) Summary of the responses in the first three sweeps (dark-green-violet) from experiments shown in (c). The amplitudes of currents were normalized to the 1st dark response for each cell, $n = 7$ cells, *** indicates $P < 0.001$ in paired t-test.

through the epi-fluorescence port of the microscope for our experiments, the light not only illuminates an area around the cell, but much of the volume of the puffer pipette reservoir (illustrated in Figure S4, Supporting Information File 1). Figure 5d summarizes 7 independent experiments showing that irradiation of green light significantly decreased the evoked currents (42.8 ± 8.6% of *trans*-evoked currents), while irradiation with violet light reverted evoked currents back to the initial level (106.7 ± 9.1% of initial *trans*-**2**). Taken together, our studies suggest that photochromic drug **2** acts as a fast, reversible photoswitch for modulating the activity of nicotinic acetylcholine receptors on neurons in living brain slices.

Conclusion

Acetylcholine is one of the two major excitatory neurotransmitters. We have synthesized a photoswitchable tetrafluoroazobenzene (4FAB) agonist of nicotinic acetylcholine receptors that is biologically inert at sub-millimolar levels in the *cis* AB configuration. Photoswitching of the chromophore on neurons with violet light rapidly activates inward currents. We designed our photoprobe to take full advantage of high thermodynamic stability of the *cis* configuration of 4FAB, thus our probe can be pre-set to ON or OFF and used for extended periods without change of function.

Experimental

Chemical synthesis

Full experimental synthetic details can be found in Supporting Information File 1.

Absorption spectroscopy

UV–vis spectra were recorded using a Cary 50 spectrophotometer (Agilent, Santa Clara, CA, USA) at rt in quartz cuvettes with a 1 cm path length in HEPES buffer at pH 7.4.

UPLC

Chromatography was performed using a Waters Acuity Arc using Cortecs C-18 column (4.6 × 50 mm, 2.7 μm) monitored at 443 nm. Elution was isocratic (Figure S2 and Figure S3, Supporting Information File 1), or used a linear gradient (Figure 3), as specified. Both solvents contained 0.1% TFA.

Cell culture and electrophysiology

HEK293 cells were split and maintained in 0.1% gelatin-coated coverslips in a 12-well plate with the culture media (DMEM + 10% FBS + 1x Pen Strep). When the confluence reached ≈60%, 0.3 μg NACHO, 0.3 μg α4+eGFP and 0.3 μg β2E61C+eGFP or β2+eGFP WT were co-transfected into cells by Lipofectamine 3000 reagents (Thermo Fisher Scientific, USA) in each well. 2–4 days after transfection, cells simultaneously expressed nACh receptors and eGFP separately due to IRES elements in the vectors were used for photoswitch experiments.

Cells which were labeled in a recording chamber with compound **1** for 20 min, were then washed with external solution. Before and after labeling, labeling solutions were checked by UPLC. The external solution was (in mM): 140 NaCl, 2.8 KCl, 2 $CaCl_2$, 2 $MgCl_2$, 10 HEPES, 12 glucose (pH 7.3 with NaOH). Compound **1** (0.05 mM) was dissolved in external solution and sonicated for 5 min.

HEK293 cells with green fluorescence were chosen for recording. Patch pipettes were filled with an internal solution containing (in mM): 135 potassium gluconate, 4 $MgCl_2$, 10 HEPES, 4 Na_2-ATP, 0.4 Na_2-GTP, 10 Na_2-phosphocreatine, pH 7.35. Good recordings were identified only when resting membrane potential (R_p) < −20 mV, holding current < 200 pA at −40 mV, and Rs 10–20 MΩ. When recording nACh receptor currents, cells were held at −60 mV. Carbachol (1 mM) was puffed into the cells with a patch pipette for 1 second. For photoswitch, cells were irradiated with green LED (530 nm, 3 mW, 2 min) or violet LED (405 nm, 10 mW, 2 min). Irradiation started 100 s prior to puffing and ended 20 s after puffing.

All animal studies were approved by Mount Sinai IACUC review. C57BL/6J mice (2–3 month old) were anaesthetized with isoflurane and the brain was quickly removed. Coronal brain sections (300 μm) were made in ice-cold cutting solution containing (in mM): 60 NaCl, 2.5 KCl, 1.25 NaH_2PO_4, 7 $MgCl_2$, 0.5 $CaCl_2$, 26 $NaHCO_3$, 10 glucose, 100 sucrose, 3 sodium pyruvate, 1.3 sodium ascorbate equilibrated with 95% O_2/5% CO_2 (pH 7.3–7.4). The brain slices were then incubated for 15 min at 33 °C in artificial cerebrospinal fluid (ACSF, mM: 125 NaCl, 2.5 KCl, 1.25 NaH_2PO_4, 1 $MgCl_2$, 2 $CaCl_2$, 26 $NaHCO_3$, 10 glucose, 3 sodium pyruvate, 1.3 sodium ascorbate; 95% O_2/5% CO_2, pH 7.3–7.4) and held at room temperature.

Brain slices were then transferred to the recording chamber of a BX-61 microscope (Olympus, PennValley, PA, USA) and superfused with ACSF at room temperature. Medial habenula neurons were visualized under a 60× objective (Olympus) and infrared differential interference contrast optics. Whole-cell recordings were made with an EPC-10 amplifier using Patchmaster (Heka Instruments, Bellmore, NY, USA) in voltage-clamp mode (V_{hold} = −60 mV). Patch pipettes were filled with an internal solution containing (in mM): 135 potassium gluconate, 4 $MgCl_2$, 10 HEPES, 4 Na_2-ATP, 0.4 Na_2-GTP, 10 Na_2-phosphocreatine, pH 7.35. The red fluorescent dye Alexa 594 (0.05 mM, ThermoFisher Scientific, Waltham, MA, USA) was added to visualize the morphology of the neurons. Normal ACSF was added with the drug cocktails during photoswitch experiments. The cocktail is 10 μM CNQX, 100 μM APV, 1 μM TTX, 20 μM bicuculline, 20 μM gabazine and 2 μM atropine. For each photoswitch experiment, 0.2 mM 4FABTA (**2**) was locally puffed into a cell concurrently without irradiation or with either 1 s green (530 nm, 3 mW) or 1 s violet light (405 nm, 10 mW).

Data were analyzed in Patchmaster software (Heka). The amplitudes of currents were calculated as the difference of the peak and baseline. All data were present as the mean ± SEM. One-way ANOVA was used to determine whether there are any statistically significant differences between the means of the three groups (i.e., dark, green and violet), and paired t-test was used for post hoc comparisons. $P < 0.05$ indicates statistically significant.

Supporting Information

Supporting Information File 1

Additional figures, full synthetic details and NMR spectra, LC–MS of compounds **12** and **13** and LC–MS of the hydrolysis of compound **1**.
[https://www.beilstein-journals.org/bjoc/content/supplementary/1860-5397-15-274-S1.pdf]

Acknowledgements

This work was supported by grants from the NIH (USA) to GCRE-D. We thank Alex Mourot for providing acetylcholine receptor plasmids.

Conflicts of Interest

None.

Author Contributions

LS and JZ contributed equally to the work. LS made all the photochemical probes. JZ performed the biological experi-

ments. MTR first made some model photoprobes. GCRE-D supervised the work and wrote the paper. All authors commented on the paper and approved the final submitted version.

ORCID® iDs

Lorenzo Sansalone - https://orcid.org/0000-0002-7215-0783
Jun Zhao - https://orcid.org/0000-0003-3663-1595
Matthew T. Richers - https://orcid.org/0000-0002-2036-8262
Graham C. R. Ellis-Davies - https://orcid.org/0000-0003-4179-5455

References

1. Bandara, H. M. D.; Burdette, S. C. *Chem. Soc. Rev.* **2012,** *41,* 1809–1825. doi:10.1039/c1cs15179g
2. Kaufman, H.; Vratsanos, S. M.; Erlanger, B. F. *Science* **1968,** *162,* 1487–1489. doi:10.1126/science.162.3861.1487
3. Bartels, E.; Wassermann, N. H.; Erlanger, B. F. *Proc. Natl. Acad. Sci. U. S. A.* **1971,** *68,* 1820–1823. doi:10.1073/pnas.68.8.1820
4. Lester, H. A.; Krouse, M. E.; Nass, M. M.; Wassermann, N. H.; Erlanger, B. F. *Nature* **1979,** *280,* 509–510. doi:10.1038/280509a0
5. Lester, H. A.; Krouse, M. E.; Nass, M. M.; Wassermann, N. H.; Erlanger, B. F. *J. Gen. Physiol.* **1980,** *75,* 207–232. doi:10.1085/jgp.75.2.207
6. Nargeot, J.; Lester, H. A.; Birdsall, N. J.; Stockton, J.; Wassermann, N. H.; Erlanger, B. F. *J. Gen. Physiol.* **1982,** *79,* 657–678. doi:10.1085/jgp.79.4.657
7. Kumita, J. R.; Smart, O. S.; Woolley, G. A. *Proc. Natl. Acad. Sci. U. S. A.* **2000,** *97,* 3803–3808. doi:10.1073/pnas.97.8.3803
8. Fehrentz, T.; Schönberger, M.; Trauner, D. *Angew. Chem., Int. Ed.* **2011,** *50,* 12156–12182. doi:10.1002/anie.201103236
9. Lerch, M. M.; Hansen, M. J.; van Dam, G. M.; Szymanski, W.; Feringa, B. L. *Angew. Chem., Int. Ed.* **2016,** *55,* 10978–10999. doi:10.1002/anie.201601931
10. Dong, M.; Babalhavaeji, A.; Samanta, S.; Beharry, A. A.; Woolley, G. A. *Acc. Chem. Res.* **2015,** *48,* 2662–2670. doi:10.1021/acs.accounts.5b00270
11. Bléger, D.; Hecht, S. *Angew. Chem., Int. Ed.* **2015,** *54,* 11338–11349. doi:10.1002/anie.201500628
12. Bléger, D.; Schwarz, J.; Brouwer, A. M.; Hecht, S. *J. Am. Chem. Soc.* **2012,** *134,* 20597–20600. doi:10.1021/ja310323y
13. Knie, C.; Utecht, M.; Zhao, F.; Kulla, H.; Kovalenko, S.; Brouwer, A. M.; Saalfrank, P.; Hecht, S.; Bléger, D. *Chem. – Eur. J.* **2014,** *20,* 16492–16501. doi:10.1002/chem.201404649
14. Passlick, S.; Richers, M. T.; Ellis-Davies, G. C. R. *Angew. Chem., Int. Ed.* **2018,** *57,* 12554–12557. doi:10.1002/anie.201807880
15. Durand-de Cuttoli, R.; Mondoloni, S.; Marti, F.; Lemoine, D.; Nguyen, C.; Naude, J.; d'Izarny-Gargas, T.; Pons, S.; Maskos, U.; Trauner, D.; Kramer, R. H.; Faure, P.; Mourot, A. *eLife* **2018,** *7,* e37487. doi:10.7554/elife.37487
16. Tochitsky, I.; Banghart, M. R.; Mourot, A.; Yao, J. Z.; Gaub, B.; Kramer, R. H.; Trauner, D. *Nat. Chem.* **2012,** *4,* 105–111. doi:10.1038/nchem.1234
17. Damijonaitis, A.; Broichhagen, J.; Urushima, T.; Hüll, K.; Nagpal, J.; Laprell, L.; Schönberger, M.; Woodmansee, D. H.; Rafiq, A.; Sumser, M. P.; Kummer, W.; Gottschalk, A.; Trauner, D. *ACS Chem. Neurosci.* **2015,** *6,* 701–707. doi:10.1021/acschemneuro.5b00030
18. Cabré, G.; Garrido-Charles, A.; Moreno, M.; Bosch, M.; Porta-de-la-Riva, M.; Krieg, M.; Gascón-Moya, M.; Camarero, N.; Gelabert, R.; Lluch, J. M.; Busqué, F.; Hernando, J.; Gorostiza, P.; Alibés, R. *Nat. Commun.* **2019,** *10,* 907. doi:10.1038/s41467-019-08796-9
19. Banghart, M.; Borges, K.; Isacoff, E.; Trauner, D.; Kramer, R. H. *Nat. Neurosci.* **2004,** *7,* 1381–1386. doi:10.1038/nn1356
20. Volgraf, M.; Gorostiza, P.; Numano, R.; Kramer, R. H.; Isacoff, E. Y.; Trauner, D. *Nat. Chem. Biol.* **2006,** *2,* 47–52. doi:10.1038/nchembio756
21. Wu, D.; Dong, M.; Collins, C. V.; Babalhavaeji, A.; Woolley, G. A. *Adv. Opt. Mater.* **2016,** *4,* 1402–1409. doi:10.1002/adom.201600362
22. Hüll, K.; Morstein, J.; Trauner, D. *Chem. Rev.* **2018,** *118,* 10710–10747. doi:10.1021/acs.chemrev.8b00037
23. Shih, P.-Y.; Engle, S. E.; Oh, G.; Deshpande, P.; Puskar, N. L.; Lester, H. A.; Drenan, R. M. *J. Neurosci.* **2014,** *34,* 9789–9802. doi:10.1523/jneurosci.0476-14.2014

License and Terms

This is an Open Access article under the terms of the Creative Commons Attribution License (http://creativecommons.org/licenses/by/4.0). Please note that the reuse, redistribution and reproduction in particular requires that the authors and source are credited.

The license is subject to the *Beilstein Journal of Organic Chemistry* terms and conditions: (https://www.beilstein-journals.org/bjoc)

The definitive version of this article is the electronic one which can be found at: doi:10.3762/bjoc.15.274

BEILSTEIN JOURNAL OF ORGANIC CHEMISTRY

Design, synthesis and investigation of water-soluble hemi-indigo photoswitches for bioapplications

Daria V. Berdnikova

Full Research Paper

Open Access

Address:
Department Chemie–Biologie, Organische Chemie II, Universität Siegen, Adolf-Reichwein-Str. 2, 57076 Siegen, Germany

Email:
Daria V. Berdnikova - berdnikova@chemie-bio.uni-siegen.de

Keywords:
hemi-indigo; molecular switches; photochromism; photoswitching; visible light; water solubility

Beilstein J. Org. Chem. **2019,** *15,* 2822–2829.
doi:10.3762/bjoc.15.275

Received: 31 August 2019
Accepted: 07 November 2019
Published: 22 November 2019

This article is part of the thematic issue "Molecular switches".

Guest Editor: W. Szymanski

© 2019 Berdnikova; licensee Beilstein-Institut.
License and terms: see end of document.

Abstract

A series of hemi-indigo derivatives was synthesized and their photoswitching properties in aqueous medium were studied. The dimethoxy hemi-indigo derivative with the best photochromic performance in water was identified as a promising platform for the development of photoswitchable binders for biomolecules. The synthetic approach towards the introduction of the alkylamino pendant to the dimethoxy hemi-indigo core was developed that allowed to obtain an RNA-binding hemi-indigo derivative with photoswitchable fluorescent properties.

Introduction

The application of organic photochromes in biological systems is fraught with their poor solubility and reduced photoswitching efficiency in aqueous medium. In many cases, approaches to improve the water solubility by chemical modification of the photochromic scaffolds are not straightforward because the introduction of substituents often interferes with the desired photochemical properties. Along these lines, special efforts have been devoted to design, for example, water-soluble derivatives of spiropyran [1-3], azobenzene [4,5], diarylethene [6-8], or chromene [9] that keep efficient photochromism in aqueous medium. Although a significant progress has been made in the development of water-soluble photochromes, there is still an emerging search for new types of photochromic compounds for applications in biological systems. In particular, nowadays the development of photopharmacology is based mainly on azobenzene chemistry [10,11] and, therefore, finding of new biocompatible photochromes with complementary properties is highly desirable to speed up the progress in this important field. In this context, an emerging class of hemi-indigo photoswitches attracted special attention [12-17]. Despite the fact that the hemi-indigo dyes are known for more than 100 years [18], their photochemical properties are still underexplored and no targeted studies on their photoswitching in aqueous media were performed. The hemi-indigo scaffold exists in two forms that can be photoswitched reveresibly. In most cases, the *Z*-isomer of hemi-indigo is thermodynamically stable whereas the *E*-isomer is metastable. However, if the indoxyl nitrogen is substituted with alkyl or aryl groups, both

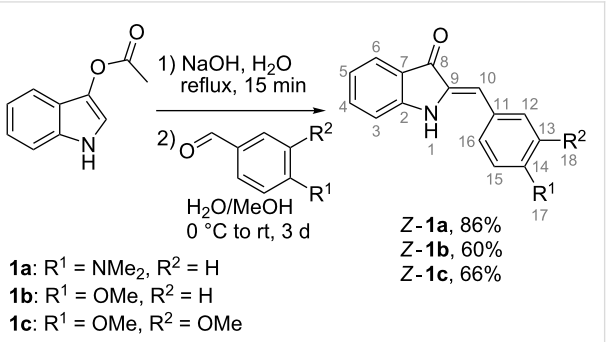
isomers of hemi-indigo have very close energies and none of them is clearly preferred thermodynamically [13]. The absorption spectrum of the *E*-isomer is bathochromically shifted relative to the one of the *Z*-isomer. Depending on the substitution pattern, the thermal lifetimes of metastable *E*-isomers at 25 °C vary from hours to days and sometimes even years [12-14]. Remarkably, for sterically hindered hemi-indigo derivatives, thermal lifetimes of the metastable states beyond 3000 years have been achieved [14]. Unlike most of the widely applied photochromes (spiropyrans, spirooxazines, chromenes, dithienylethenes, etc.), both forms of hemi-indigo absorb in the visible light region. Therefore, photochemical switching does not require the use of the UV light, which is of high importance for biological applications.

Herein, the synthesis and adjustment of the substitution pattern of hemi-indigo derivatives for the efficient photoswitching in aqueous medium are described. Detailed characterization of the photoinduced isomerization of hemi-indigo derivatives in water is provided. Additionally, synthetic peculiarities of the introduction of an RNA-affine alkylamino substituent to the hemi-indigo scaffold are discussed.

Results and Discussion

Synthesis of hemi-indigo derivatives *Z*-1a–c

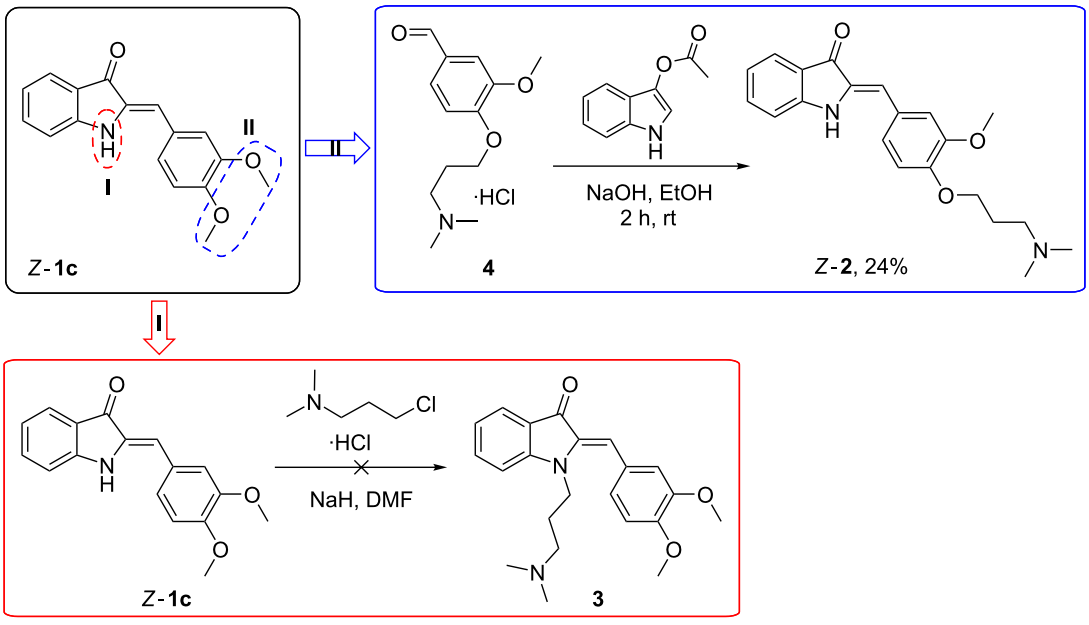
The synthesis of hemi-indigo derivatives *Z*-**1a**–**c** with different substitution patterns of the phenyl ring was performed through the aldol condensation of indoxyl-3-acetate with the corresponding benzaldehydes under alkaline conditions (Scheme 1) [13]. All compounds **1a**–**c** were obtained in good yields as pure *Z*-isomers as supported by the NMR data (Figures S5–S13 in Supporting Information File 1).



Scheme 1: Synthesis of hemi-indigo derivatives *Z*-**1a**–**c**.

Introduction of an alkylamino substituent to the hemi-indigo scaffold

Based on the data on photoswitching in water (vide supra), the dimethoxy-substituted hemi-indigo *Z*-**1c** was selected as a core structure for the design of RNA binders with photoswitchable properties [12]. To increase the solubility in aqueous medium and potential RNA-binding properties, the dimethylaminopropyl substituent [19] was introduced to hemi-indigo *Z*-**1c**. Two synthetically straightforward approaches of the alkylamino group introduction were considered: (i) *N*-alkylation of the indoxyl core and (ii) *O*-alkylation of the dimethoxyphenyl residue (Scheme 2).



Scheme 2: Synthetic routes to alkylamino-substituted dimethoxy hemi-indigo *Z*-**1c**.

Surprisingly, compound **3** (method I) could not be obtained due to the cleavage of the C–C double bond in the course of the reaction followed by extensive destruction of the heterocyclic fragment. Variation of the reaction conditions, e.g., reduction of the reaction temperature and time, changing the ratio of the reactants and addition of NaI as a catalyst, did not suppress this decomposition to a significant extent. A possible reason for this side process is the reactivity of the double bond carbon atom (Michael acceptor) [20]. The intramolecular nucleophilic attack of the introduced alkylamino group can possibly lead to the immediate double-bond cleavage in **3**. This results in formation of unstable indoxyl that undergoes further destruction and veratraldehyde that is detected in the reaction mixture by NMR. This assumption is supported by the observation that only one hemi-indigo derivative bearing an alkylamino substituent of a shorter length on the indoxyl N atom has been reported so far [20].

Modification of the phenyl ring by method II was successful and allowed to obtain the desired hemi-indigo **2** as a pure *Z*-isomer with 24% yield (Scheme 2) [12]. Importantly, the synthesis of *Z*-**2** required milder conditions and shorter reaction times than that of derivatives *Z*-**1a**–**c**. Thus, the use of the water/methanol mixture as a solvent, heating and extended reaction times of more than 2 h resulted in the destruction of the desired product *Z*-**2**. At the same time, performing the reaction at room temperature in pure ethanol allowed to increase the yield of *Z*-**2** and to reduce the number of side-products. Purification of hemi-indigo *Z*-**2** by conventional column chromatography was not efficient. However, pure product *Z*-**2** could be obtained by gel filtration chromatography on sephadex (MeOH); the isolated compound *Z*-**2** is stable in its free base form whereas its hydrochloride salt slowly decomposes.

Optical properties and photoswitching in aqueous medium

Hemi-indigo derivatives *Z*-**1a**–**c** display intense long-wavelength absorption bands, whose maxima are clearly dependent on the strength of the electron-donating substituent in the 4-position of the phenyl ring (Figure 1, Table 1). Thus, the exchange

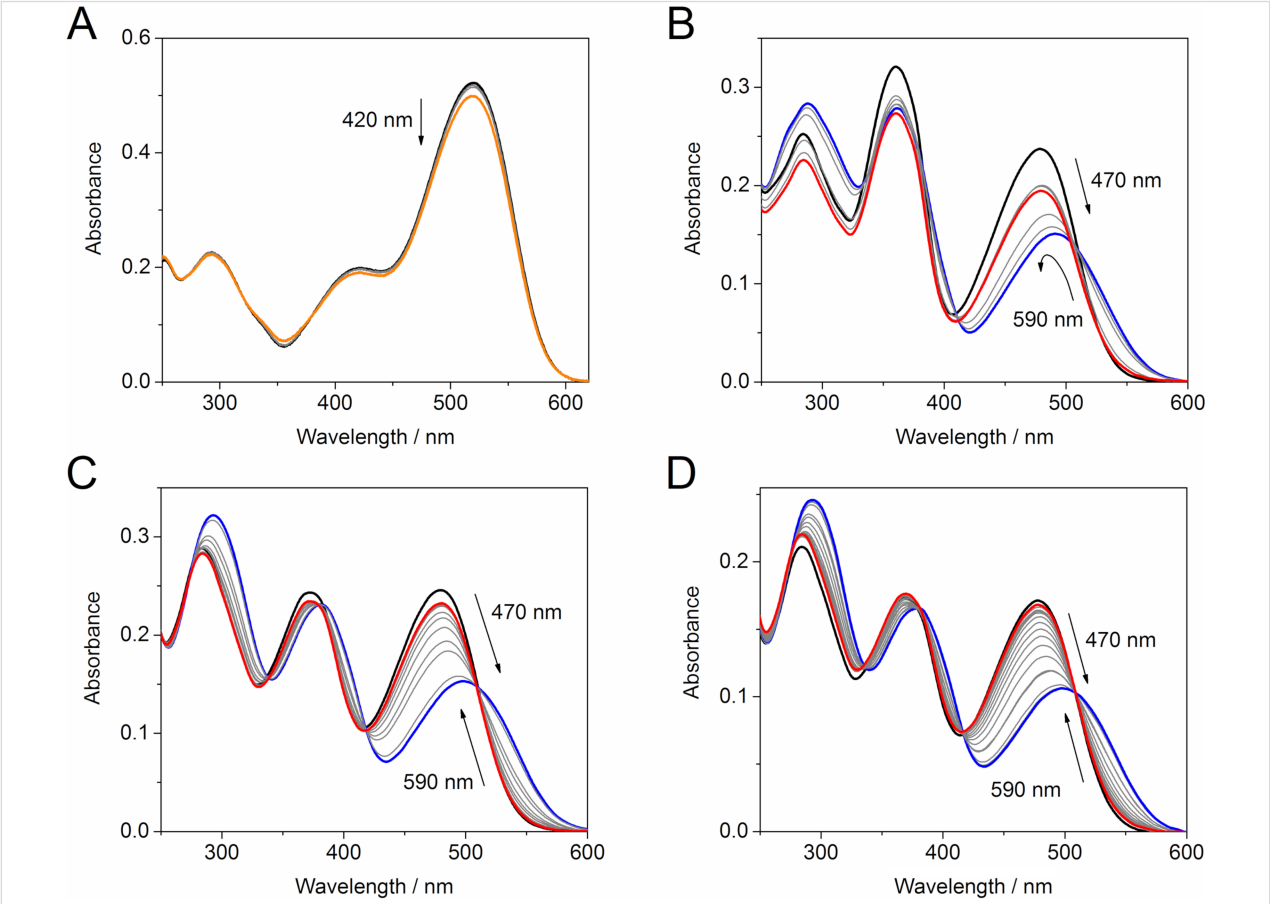


Figure 1: Photoswitching of hemi-indigo derivatives: (A) *Z*-**1a**, *c* = 20 μM in H_2O with 10% (v/v) DMSO, λ_{ex} = 420 nm; (B) *Z*-**1b**, *c* = 20 μM in H_2O with 2% (v/v) EtOH, λ_{ex} = 470 nm (forward reaction) and 590 nm (backward reaction); (C) *Z*-**1c**, *c* = 20 μM in H_2O with 2% (v/v) EtOH, λ_{ex} = 470 nm (forward reaction) and 590 nm (backward reaction); (D) *Z*-**2**, *c* = 15 μM in H_2O, λ_{ex} = 470 nm (forward reaction) and 590 nm (backward reaction), 20 °C. Spectra of the initial *Z*-isomers: black; PSS^{420}: orange; PSS^{470}: blue; PSS^{590}: red.

Table 1: Photochemical and photophysical properties of hemi-indigo derivatives **1a–c** and **2** in water.

Species	λ_{abs} (*Z*)/nm	ε (*Z*)/ L mol^{-1} cm^{-1}	λ_{abs} (*E*)/ nm[a]	ε (*E*)/ L mol^{-1} cm^{-1}[a]	PSS^{470}/ (% *Z*/*E*)[a]	PSS^{590}/ (% *Z*/*E*)[a]	$\Phi_{Z\text{-}E}/\Phi_{E\text{-}Z}$ / 10^{-2} [b]	$\Delta G^{\ddagger}$/ kcal mol^{-1} [c]	$t_{1/2}$ 25 °C[d]
1a[e]	521	26039	n.d.[f]	n.d.[f]	n.d.[f]	n.d.[f]	n.d.[f]	n.d.[f]	n.d.[f]
1b	479	11922	508	6727	28/72	n.d.[g]	3.8/n.d.[g]	26.5	47 d
1c	479	12086	515	7127	21/79	93/7	2.6/0.2	26.2	31 d
2	478	10549	515	6368	24/76	97/3	2.4/0.1	26.1	25 d
2[h]	478	10456	514	6289	20/80	97/3	2.7/0.2	23.7	11 h

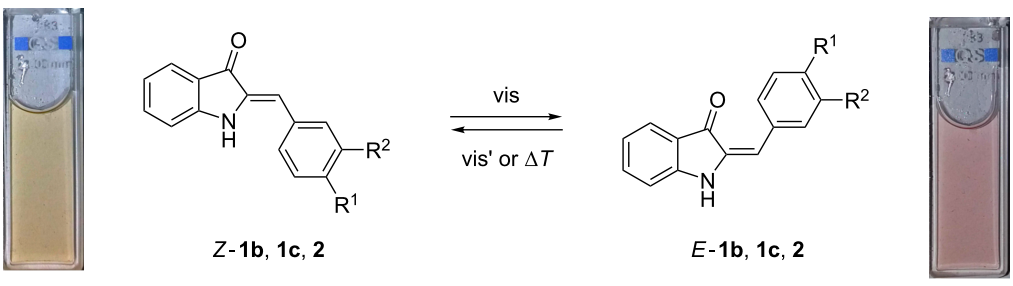
[a]Calculated according to Fischer [21]. [b]Photoisomerization quantum yields of the forward $\Phi_{Z\text{-}E}$ (at 470 nm) and backward $\Phi_{E\text{-}Z}$ (at 590 nm) reactions. [c]Free activation enthalpies for the thermal *E*–*Z* isomerization. [d]Half-lifes of the *E*-form at 25 °C. [e]In water containing 10% (v/v) DMSO. [f]Compound shows very weak photochromism in aqueous medium. [g]The backward switching was not complete due to precipitation of the compound after 2 h of irradiation. [h]The data were obtained in aqueous 10 mM Na-phosphate buffer containing 0.1 M NaCl, pH 7.0 [12].

of the 4-dimethylamino group in *Z*-**1a** for a 4-methoxy group in *Z*-**1b** resulted in a significant blue shift of the absorption maximum (Δλ = 42 nm). Notably, the introduction of a second methoxy group to the 3-position of the phenyl ring in *Z*-**1c** did not shift the absorption maximum and just slightly affected the extinction (Table 1). Hemi-indigo derivatives *Z*-**1a–c** are not fluorescent in aqueous solution.

To assess the potential applicability of hemi-indigo derivatives *Z*-**1a–c** in biological systems, photoswitching of these compounds was tested in aqueous medium (Scheme 3). The forward reaction was performed upon irradiation at 360 (UV), 420 nm (violet), 470 nm (blue) and 520 nm (green) light (Figure 1 and Figures S1 and S2 in Supporting Information File 1).

Surprisingly, almost no switching of the dimethylamino-substituted hemi-indigo *Z*-**1a** was observed in water with 10% DMSO, i.e., only irradiation with violet light (420 nm) led to the residual isomerization (Figure 1A). Additionally, the hemi-indigo *Z*-**1a** was hardly soluble in aqueous medium and rather fast precipitation took place even in the presence of the co-solvent. The comparison with the reported data on *Z*-**1a** [13] and related hemi-indigo derivatives containing a 4-amino group in the phenyl ring [13] allowed to conclude that this substitution pattern is unfavorable for photoswitching in aqueous medium. Thus, a higher content of organic co-solvents (20–30% of DMSO, DMF or THF) or/and the presence of triethylamine was required to stimulate the photoswitching of the reported compounds with a 4-amino group in the phenyl ring [13]. Considering the limitations imposed on the nature and content of organic co-solvents used in biological studies, the dimethylamino derivative *Z*-**1a** was excluded from further studies.

In contrast, mono- and dimethoxy-substituted hemi-indigo derivatives *Z*-**1b** and *Z*-**1c** showed pronounced spectral changes upon irradiation indicating an efficient *Z*–*E* isomerization of the C–C-double bond (Figure 1B and Figure 1C). The most complete *Z*–*E* conversion for both compounds *Z*-**1b** and *Z*-**1c** was achieved upon irradiation with blue light (470 nm) (cf. Figures S1 and S2, Supporting Information File 1). The photoreactions proceeded rather fast and the photostationary state PSS^{470} was reached within 2.5 min for compound *Z*-**1b** and within 3.0 min for compound *Z*-**1c**. The backward *E*–*Z* conversion from PSS^{470} was performed by irradiation with 590 nm (amber) light and occurred much slower (Table 1). In the case of monomethoxy derivative *E*-**1b**, the backward reaction from PSS^{470} proceeded successfully during ca. 2 h of irradiation after



Scheme 3: Photoswitching of hemi-indigo derivatives.

which the isosbestic point was lost and the absorption intensity started decreasing due to slow precipitation of the compound from the aqueous solution (Figure 1B). The presence of the second methoxy group ensured a better stability of aqueous solutions of the dimethoxy derivative *Z*-**1c**. In this case, the backward *E*–*Z* isomerization of *E*-**1c** from PSS^{470} took place within 5 h resulting in almost complete restoration of the initial absorbance of *Z*-**1c** in the PSS^{590} (Figure 1C). Investigation of the photostationary mixtures by fluorescence spectroscopy revealed that the photoinduced isomers *E*-**1b** and *E*-**1c** are not fluorescent in aqueous medium. The analysis of the isomeric compositions of the photostationary states was performed by the Fischer method [21] because NMR-spectroscopic analysis was precluded by insufficient solubility or/and possible aggregation at higher concentrations. Thus, the Fischer method allowed to calculate the absorption spectra of pure *E*-isomers of **1b** and **1c** in water (Figure 2) as well as to evaluate the extent of the *Z*–*E* conversion in PSS^{470} and PSS^{590} (Table 1).

The dimethoxy derivative *Z*-**1c** showed better *Z*–*E* conversion in PSS^{470} and a larger difference between the absorption maxima of the *Z*- and *E*-forms. At the same time, the introduction of the second methoxy group to the phenyl ring resulted in a decrease of the *Z*–*E* isomerization quantum yield and reduced the thermal half-life of *E*-**1c** in comparison to *E*-**1b** (Table 1). Nevertheless, the dimethoxy-substituted hemi-indigo *Z*-**1c** was selected as a core structure for the design of photoswitchable RNA binders due to its higher conversion and better solubility in water.

The introduction of the alkylamino group provided compound *Z*-**2** with much better solubility in water. At the same time, the presence of the alkylamino substituent only slightly influenced the photochemical and photophysical characteristics of the hemi-indigo *Z*-**2** in comparison with the parent compound *Z*-**1c** (Figure 1D, Figure 2C, Table 1). Thus, the positions of the absorption maxima of both, the *Z*- and *E*-forms, the extent of conversion in PSSs, the photoisomerization quantum yields as well as the half-lifes of the photoinduced forms appeared to be almost independent of the presence of the alkylamino substituent. Interestingly, a comparison with the data obtained for *Z*-**2** in aqueous 10 mM Na-phosphate buffer containing 0.1 M NaCl, pH 7.0 [12], showed that the increase in the ionic strength of the medium resulted in a drastic decrease of the half-life of the photoinduced form *E*-**2** whereas other characteristics remained almost unaffected (Table 1). This indicates that the highly ionic medium reduces the energy barrier in the ground state that is responsible for the rate of thermal *E*–*Z* isomerization pointing out the importance of the Coulomb interactions between hemi-indigo and buffer components. A possible explanation of this observation can be provided by the comparison with structurally related hemi(thio)indigo dyes [22]. Thus, in the case of hemi(thio)indigo, the energy maximum in the ground state corresponds to the 90° rotation about the central double bond resulting in formation of a state with biradical-like character that is polarized along the molecule's long axis [22]. The close structural similarity allows to expect a similar character of the transition state for the hemi-indigo derivatives. Therefore, a highly ionic medium can stabilize the transition state of the hemi-indigo leading to the decrease of the energy barrier between *Z*- and *E*-isomers and, therefore, reducing the half-life of the *E*-form. However, further studies are required to provide detailed explanation of this effect.

Recently, a proof-of-principle for the application of hemi-indigo derivative *Z*-**2** as a binder for the human immunodeficiency virus type 1 (HIV-1) RNA with photoswitchable fluorescent properties was provided [12]. It was shown that hemi-indigo *Z*-**2** associates with the regulatory elements of HIV-1 genome RNA with high affinity ($K_b \approx 10^5\ M^{-1}$) while keeping its photoswitching properties. Both, the initial *Z*-**2** and photoinduced *E*-**2** forms remain bound to RNA. Most notably, the

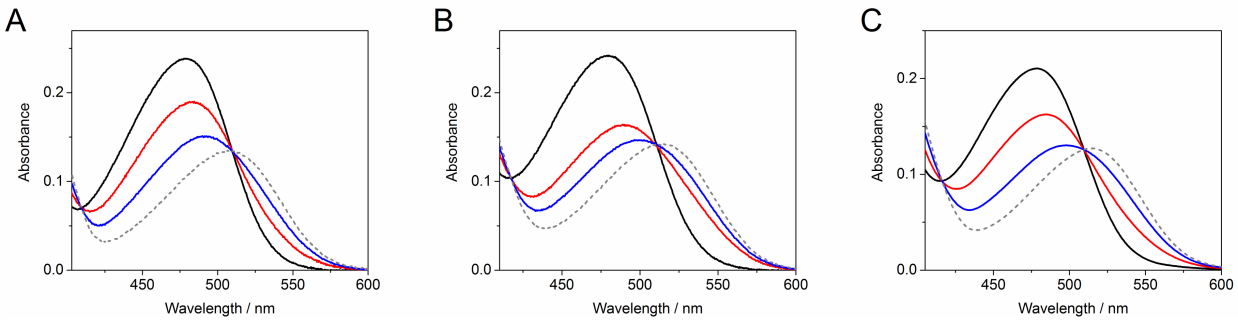


Figure 2: Absorption spectra of the *Z*-isomer (black), two photostationary states obtained upon irradiation with 520 nm (red) and 470 nm (blue) light for (A) **1b**, (B) **1c**, (C) **2** in water, *c* = 20 μM, 20 °C. Grey dashed line represents the spectra of the corresponding *E*-isomers calculated by the Fischer method.

interaction of *Z*-**2** with HIV-1 RNA produces a remarkable light-up effect whose extent depends on the particular sequence of RNA. Photoswitching of the RNA-bound hemi-indigo *Z*-**2** to the *E*-form results in emission quenching. The ON–OFF fluorescence switching of *Z*-**2**–RNA complexes can be performed reversibly by repeated irradiation with blue (470 nm) and amber (590 nm) light.

Conclusion

To sum up, hemi-indigo derivatives with different substitution patterns in the phenyl ring were synthesized and their photochemical behavior in aqueous medium was studied. The presence of a methoxy group in the 4-position of the phenyl ring was identified as a necessary condition for the efficient photoswitching of hemi-indigo in water. At the same time, the presence of a strong electron-donating dimethylamino group at this position is unfavorable for the photoswitching in water. It was also shown that the introduction of a second methoxy group in the 3-position of the phenyl ring improves the water solubility of the photoswitch and increases the red shift of the absorption maximum of the *E*-isomer. As a further step, the synthetic approach towards the attachment of the RNA-affine alkylamino substituent was developed. Overall, the hemi-indigo derivatives were introduced as promising photoswitches for aqueous media possessing valuable properties for bioapplications.

Experimental

Materials and equipment

Reagents and solvents were obtained from commercial sources (Acros, Merck, Fischer) and used as received. Reactions were monitored on POLYGRAM® SIL G/UV$_{254}$ (Macherey-Nagel) TLC plates with detection by UV light irradiation (254 nm or 366 nm). Column chromatography was performed on Sephadex® columns. ^{1}H NMR and ^{13}C NMR spectra were recorded on a JEOL ECZ 500 spectrometer at 25 °C using 5 mm tubes. Chemical shifts were determined with accuracy of 0.01 ppm and 0.1 ppm for ^{1}H and ^{13}C spectra, respectively, and are given relative to the residual signal of the solvent that was used as internal standard (DMSO-d_6: δ_H = 2.50 ppm, δ_C = 39.5 ppm). Spin–spin coupling constants for the proton spectra were determined with accuracy of 0.2 Hz. The proton NMR signal assignments were performed using COSY and ROESY 2D NMR techniques. The carbon NMR signal assignments were performed by means of HSQC and HMBC 2D NMR techniques. Mass spectra (ESI) were recorded on a Finnigan LCQ Deca mass spectrometer. Elemental analysis was performed with a HEKAtech EUROEA combustion analyser by Mr. Rochus Breuer (Universität Siegen, Organische Chemie I). Melting points were measured with a BÜCHI 545 (BÜCHI, Flawil, CH) melting point apparatus in open capillaries and are uncorrected. Electronic absorption spectra were measured on a Cary 100 Bio two-beam spectrophotometer and a Specord 600 (Analytik Jena AG) diode-array spectrophotometer. Fluorescence spectra were recorded on a Cary Eclipse spectrofluorimeter. Optical spectroscopy measurements were performed in thermostated quartz sample cells of 10 mm pathlength. Preparation and handling of the solutions were carried out under red light. Photochemical reactions were performed using the following LED light sources: LUMOS (360 nm); Roithner H2A1-H420 130 mW (420 nm); Roschwege HighPower-LED Blau (470 nm); Roschwege HighPower-LED Grün (520 nm); Roschwege HighPower-LED Amber (590 nm).

Synthesis

The synthesis and characterization of hemi-indigo derivative *Z*-**2** are described in detail in [12].

General procedure for the synthesis of hemi-indigo derivatives *Z*-**1a–c**

Under argon gas atmosphere, a solution of indoxyl-3-acetate (200 mg, 1.14 mmol) in aqueous NaOH (1.5 M, 6.2 mL, degassed) was heated at 100 °C for ca. 15 min. Then, the mixture was cooled to 0 °C and a solution of the corresponding aldehyde in 1–2 mL MeOH (Ar degassed) was added upon vigorous stirring (for compound *Z*-**1a**: 4-(dimethylamino)benzaldehyde (170 mg, 1.14 mmol); for compound *Z*-**1b**: *p*-anisaldehyde (155 mg, 1.14 mmol); for compound *Z*-**1c**: veratraldehyde (189 mg, 1.14 mmol)). After the addition of the aldehyde, the mixture was warmed to ambient temperature and stirred for 3 days. Then, the mixture was neutralized with 1 M aq HCl and extracted with EtOAc. The combined organic layers were dried with Na_2SO_4 and the solvent was removed in vacuo. The obtained solid was redissolved in EtOH and filtered to remove the insoluble precipitate of indigo side-product. After filtration, the solvent was partially removed and the pure *Z*-isomer of the corresponding product was crystallized at −20 °C.

(Z)-2-(4-(Dimethylamino)benzylidene)indolin-3-one (Z-**1a**)

Deep violet needles, yield 86% (259 mg, 0.98 mmol); mp 232–234 °C (lit. [13]: 235–236 °C); R_f 0.67 (hexane/EtOAc 1:1, v/v); ^{1}H NMR (500 MHz, DMSO-d_6) δ 3.00 (s, 6H, H-17), 6.64 (s, 1H, H-10), 6.78 (d, *J* = 9.0 Hz, 2H, H-13, H-15), 6.88 (ddd, *J* = 7.8, 7.0, 0.7 Hz, 1H, H-5), 7.14 (d, *J* = 8.1 Hz, 1H, H-3), 7.47 (ddd, *J* = 8.3, 7.1, 1.3 Hz, 1H, H-4), 7.55 (d, *J* = 8.3. Hz, 1H, H-6), 7.61 (d, *J* = 8.8 Hz, 2H, H-12, H-16), 9.55 (s, 1H, H-1) ppm; ^{13}C NMR (126 MHz, DMSO-d_6) δ 39.7 (2C, C-17), 112.1 (2C, C-13, C-15), 112.5 (1C, C-3), 112.6 (1C, C-10), 119.1 (1C, C-5), 120.5 (1C, C-7), 121.3 (1C, C-11), 123.7 (1C, C-6), 131.72 (2C, C-12, C-16), 131.68 (1C, C-9), 135.3 (1C, C-4), 150.3 (1C, C-14), 153.3 (1C, C-2), 185.2 (1C, C-8); Anal. calcd for $C_{17}H_{16}N_2O$: C, 77.25; H, 6.10; N, 10.60; found: C,

77.05; H, 6.13; N, 10.39 %; ESIMS (MeOH, *m/z*): 263 [*Z*-**1a** − H]$^-$, 264 [*Z* − **1a**]$^+$, 265 [*Z*-**1a** + H]$^+$.

(Z)-2-(4-Methoxybenzylidene)indolin-3-one (Z-**1b**)

Brownish-golden powder, yield 60% (172 mg, 0.68 mmol); mp 180–181 °C (lit. [20]: 180–181 °C); R_f 0.75 (hexane/EtOAc 1:1, v/v); ^{1}H NMR (500 MHz, DMSO-d_6) δ 3.82 (s, 3H, H-17), 6.65 (s, 1H, H-10), 6.90 (t, , *J* = 7.8 Hz, 1H, H-5), 7.04 (d, *J* = 8.8 Hz, 2H, H-13, H-15), 7.14 (d, *J* = 8.1 Hz, 1H, H-3), 7.51 (ddd, *J* = 8.4, 7.1, 1.1 Hz, 1H, H-4), 7.57 (d, *J* = 7.6 Hz, 1H, H-6), 7.71 (d, *J* = 8.8 Hz, 2H, H-12, H-16), 9.68 (s, 1H, H-1) ppm; ^{13}C NMR (126 MHz, DMSO-d_6) δ 55.3 (1C, C-17), 110.5 (1C, C-10), 112.6 (1C, C-3), 114.6 (2C, C-13, C-15), 119.5 (1C, C-5), 120.2 (1C, C-7), 123.9 (1C, C-6), 126.6 (1C, C-11), 131.7 (2C, C-12, C-16), 133.1 (1C, C-9), 136.0 (1C, C-4), 153.9 (1C, C-2), 159.6 (1C, C-14), 186.0 (1C, C-8) ppm); Anal. calcd for $C_{16}H_{13}NO_2$: C, 76.48; H, 5.21; N, 5.57; found: C, 76.31 H, 5.15; N, 5.50 %; ESIMS (MeOH, *m/z*): 250 [*Z*-**1b** − H]$^-$.

(Z)-2-(3,4-Dimethoxybenzylidene)indolin-3-one (Z-**1c**)

Orange crystals, yield 66% (211 mg, 0.75 mmol); mp 191–192 °C; R_f 0.56 (hexane/EtOAc 1:1, v/v); ^{1}H NMR (500 MHz, DMSO-d_6) δ 3.82 (s, 3H, H-18), 3.85 (s, 3H, H-17), 6.66 (s, 1H, H-10), 6.91 (t, *J* = 7.8 Hz, 1H, H-5), 7.06 (d, *J* = 8.4 Hz, 1H, H-15), 7.14 (d, *J* = 8.1 Hz, 1H, H-3), 7.29 (d, *J* = 2.0 Hz, 1H, H-12), 7.35 (dd, *J* = 8.7, 2.0 Hz, 1H, H-16), 7.51 (ddd, *J* = 8.3, 6.9, 1.1 Hz, 1H, H-4), 7.58 (d, *J* = 7.6 Hz, 1H, H-6), 9.66 (s, 1H, H-1) ppm; ^{13}C NMR (126 MHz, DMSO-d_6) δ 55.6 (1C, C-18), 55.7 (1C, C-17), 111.1 (1C, C-10), 112.0 (1C, C-15), 112.7 (1C, C-3), 113.8 (1C, C-12), 119.6 (1C, C-5), 120.4 (1C, C-7), 123.3 (1C, C-16), 123.9 (1C, C-6), 126.8 (1C, C-11), 133.3 (1C, C-9), 136.0 (1C, C-4), 148.9 (1C, C-14), 149.5 (1C, C-13), 154.0 (1C, C-2), 186.0 (1C, C-8) ppm; Anal. calcd for $C_{17}H_{15}NO_3$: C, 72.58; H, 5.37; N, 4.98; found C, 72.80; H, 5.27; N, 4.89 %; ESIMS (MeOH, *m/z*): 280 [*Z*-**1c** − H]$^-$.

Supporting Information

Supporting Information File 1

Additional spectral data, detailed description of the experiments performed, NMR of compounds *Z*-**1a–c** and LED characteristics.
[https://www.beilstein-journals.org/bjoc/content/supplementary/1860-5397-15-275-S1.pdf]

Acknowledgements

This project has received funding from the European Union's Horizon 2020 research and innovation programme, Marie Skłodowska-Curie actions (MSCA), under grant agreement No 749788 – PHOTORNA. I thank Prof. Dr. Heiko Ihmels (Universität Siegen, Germany) for fruitful discussions and valuable advices.

ORCID® iDs

Daria V. Berdnikova - https://orcid.org/0000-0002-0787-5753

Preprint

A non-peer-reviewed version of this article has been previously published as a preprint doi:10.3762/bxiv.2019.95.v1

References

1. Özçoban, C.; Halbritter, T.; Steinwand, S.; Herzig, L.-M.; Kohl-Landgraf, J.; Askari, N.; Groher, F.; Fürtig, B.; Richter, C.; Schwalbe, H.; Suess, B.; Wachtveitl, J.; Heckel, A. *Org. Lett.* **2015,** *17,* 1517–1520. doi:10.1021/acs.orglett.5b00397
2. Kohl-Landgraf, J.; Braun, M.; Özçoban, C.; Gonçalves, D. P. N.; Heckel, A.; Wachtveitl, J. *J. Am. Chem. Soc.* **2012,** *134,* 14070–14077. doi:10.1021/ja304395k
3. Kaiser, C.; Halbritter, T.; Heckel, A.; Wachtveitl, J. *ChemistrySelect* **2017,** *2,* 4111–4123. doi:10.1002/slct.201700868
4. Bergen, A.; Rudiuk, S.; Morel, M.; Le Saux, T.; Ihmels, H.; Baigl, D. *Nano Lett.* **2016,** *16,* 773–780. doi:10.1021/acs.nanolett.5b04762
5. Zhang, Z.; Burns, D. C.; Kumita, J. R.; Smart, O. S.; Woolley, G. A. *Bioconjugate Chem.* **2003,** *14,* 824–829. doi:10.1021/bc0340161
6. Tong, Z.; Pu, S.; Xiao, Q.; Liu, G.; Cui, S. *Tetrahedron Lett.* **2013,** *54,* 474–477. doi:10.1016/j.tetlet.2012.11.056
7. Pu, S.; Liu, H.; Liu, G.; Chen, B.; Tong, Z. *Tetrahedron* **2014,** *70,* 852–858. doi:10.1016/j.tet.2013.12.037
8. Zou, Y.; Yi, T.; Xiao, S.; Li, F.; Li, C.; Gao, X.; Wu, J.; Yu, M.; Huang, C. *J. Am. Chem. Soc.* **2008,** *130,* 15750–15751. doi:10.1021/ja8043163
9. Paramonov, S. V.; Lokshin, V.; Ihmels, H.; Fedorova, O. A. *Photochem. Photobiol. Sci.* **2011,** *10,* 1279–1282. doi:10.1039/c1pp05094j
10. Velema, W. A.; Szymanski, W.; Feringa, B. L. *J. Am. Chem. Soc.* **2014,** *136,* 2178–2191. doi:10.1021/ja413063e
11. Hüll, K.; Morstein, J.; Trauner, D. *Chem. Rev.* **2018,** *118,* 10710–10747. doi:10.1021/acs.chemrev.8b00037
12. Berdnikova, D. V. *Chem. Commun.* **2019,** *55,* 8402–8405. doi:10.1039/c9cc04270a
13. Petermayer, C.; Thumser, S.; Kink, F.; Mayer, P.; Dube, H. *J. Am. Chem. Soc.* **2017,** *139,* 15060–15067. doi:10.1021/jacs.7b07531
14. Petermayer, C.; Dube, H. *J. Am. Chem. Soc.* **2018,** *140,* 13558–13561. doi:10.1021/jacs.8b07839
15. Ikegami, M.; Arai, T. *Bull. Chem. Soc. Jpn.* **2003,** *76,* 1783–1792. doi:10.1246/bcsj.76.1783
16. Ikegami, M.; Arai, T. *Chem. Lett.* **2005,** *34,* 492–493. doi:10.1246/cl.2005.492
17. Petermayer, C.; Dube, H. *Acc. Chem. Res.* **2018,** *51,* 1153–1163. doi:10.1021/acs.accounts.7b00638
18. Baeyer, A. *Ber. Dtsch. Chem. Ges.* **1883,** *16,* 2188–2204. doi:10.1002/cber.188301602130
19. Thomas, J. R.; Hergenrother, P. J. *Chem. Rev.* **2008,** *108,* 1171–1224. doi:10.1021/cr0681546

20. Velezheva, V. S.; Brennan, P. J.; Marshakov, V. Y.; Gusev, D. V.; Lisichkina, I. N.; Peregudov, A. S.; Tchernousova, L. N.; Smirnova, T. G.; Andreevskaya, S. N.; Medvedev, A. E. *J. Med. Chem.* **2004,** *47,* 3455–3461. doi:10.1021/jm030479g
21. Fischer, E. *J. Phys. Chem.* **1967,** *71,* 3704–3706. doi:10.1021/j100870a063
22. Wiedbrauk, S.; Dube, H. *Tetrahedron Lett.* **2015,** *56,* 4266–4274. doi:10.1016/j.tetlet.2015.05.022

License and Terms

This is an Open Access article under the terms of the Creative Commons Attribution License (http://creativecommons.org/licenses/by/4.0). Please note that the reuse, redistribution and reproduction in particular requires that the authors and source are credited.

The license is subject to the *Beilstein Journal of Organic Chemistry* terms and conditions: (https://www.beilstein-journals.org/bjoc)

The definitive version of this article is the electronic one which can be found at: doi:10.3762/bjoc.15.275

BEILSTEIN JOURNAL OF ORGANIC CHEMISTRY

Synthesis and characterization of bis(4-amino-2-bromo-6-methoxy)azobenzene derivatives

David Martínez-López[1], Amirhossein Babalhavaeji[2], Diego Sampedro[1] and G. Andrew Woolley[*2]

Full Research Paper

Open Access

Address:
[1]Departamento de Química, Universidad de La Rioja, Centro de Investigación en Síntesis Química (CISQ), Madre de Dios, 53, 26006 Logroño, Spain and [2]Department of Chemistry, University of Toronto, 80 St. George St., Toronto, M5S 3H6, Canada

Email:
G. Andrew Woolley[*] - andrew.woolley@utoronto.ca

* Corresponding author

Keywords:
azobenzene; azonium; molecular switches; *ortho* substitution; photoisomerization; photoswitch; visible light

Beilstein J. Org. Chem. **2019,** *15,* 3000–3008.
doi:10.3762/bjoc.15.296

Received: 19 August 2019
Accepted: 04 December 2019
Published: 30 December 2019

This article is part of the thematic issue "Molecular switches".

Guest Editor: W. Szymanski

© 2019 Martínez-López et al.; licensee Beilstein-Institut.
License and terms: see end of document.

Abstract

Aminoazobenzene derivatives with four *ortho* substituents with respect to the N–N double bond are a relatively unexplored class of azo compounds that show promise for use as photoswitches in biology. Tetra-*ortho*-methoxy-substituted aminoazobenzene compounds in particular can form azonium ions under physiological conditions and exhibit red-light photoswitching. Here, we report the synthesis and characterization of two bis(4-amino-2-bromo-6-methoxy)azobenzene derivatives. These compounds form red-light-absorbing azonium ions, but only under very acidic conditions (pH < 1). While the low pK_a makes the azonium form unsuitable, the neutral versions of these compounds undergo *trans*-to-*cis* photoisomerization with blue-green light and exhibit slow ($\tau_{1/2}$ ≈ 10 min) thermal reversion and so may find applications under physiological conditions.

Introduction

The application of photoswitches to control biological targets has been a driving force for the development of photoswitches that operate at wavelengths that are compatible with cells and tissues. While many classes of photoswitches are known [1,2], few of these are easily adaptable to controlling targets, such as proteins [3], while simultaneously exhibiting robust photochemistry in the red or near-infrared (NIR) regions of the spectrum [4-7]. Azonium ions – protonated forms of azobenzenes – have recently been found to exhibit photoswitching properties suitable for in vivo use [8-10]. Typically, the formation of azonium ions from aminoazobenzenes occurs at pH < 3.5 [11,12], however, the pK_a of the *trans*-azonium ion **1** is ca. 7.5 in aqueous solution (Figure 1) [9,10]. The elevated pK_a of **1** has been attributed to resonance stabilization of the azonium cation together with intramolecular H-bonding between the azonium proton and methoxy groups in *ortho*-position to the azo double bond [10]. Since the azonium ion **1** forms under physiological conditions, i.e., at neutral pH value in an aqueous solution, it is useful as a

photoswitch for the photocontrol of biomolecules [6]. It absorbs red light, undergoes *trans*-to-*cis* photoisomerization, and relaxes to the *trans* isomer in the dark on the timescale of seconds so that pulses of red light can be used to drive multiple isomerization cycles [10]. Efforts to apply **1** to photocontrol protein–protein interactions have recently been reported [13].

Despite the usefulness of **1** as a photoswitch, compounds undergoing photoisomerization at longer wavelengths (>700 nm) would be valuable since the penetration of light through tissue is enhanced in the NIR window [7]. Longer-wavelength absorption is achieved by compounds **2**, **3**, and related derivatives (Figure 1) [9]. However, the lifetime of thermal reversion of the *cis* isomer of **2** is only ≈1 ms at a neutral pH value, and the pK_a for *trans*-azonium ion formation is ca. 2.6. The low pK_a was attributed to a steric clash between the methoxy groups in *meta*-position to the azo double bond and the six-membered morpholino ring [9]. The rapid thermal reversion was attributed to the removal of two *ortho*-methoxy groups, leading to diminished steric strain in the transition state for reversion [9]. In compound **3**, all four *ortho*-positions are substituted, and the *meta*-oxygen substituents are part of dioxane rings so that the steric clash with the *para*-amino substituents is reduced. Compound **3** and derivatives with pyrrolidino groups in the *para*-positions were shown to be effective NIR switches, undergoing isomerization with 720 nm light under physiological conditions [8]. While the photoswitching properties of **3** are suitable for the use in biological systems, the overall size of **3** may limit the possibilities for the use as a component of photopharmaceutical agents. Currently, most photopharmaceutical agents are constructed by adding a photoswitchable unit to a pharmacophore [14,15], thereby significantly increasing the size of the compound and decreasing its potential as a drug. Therefore, we were interested in exploring other substitution patterns for these aminoazobenzene derivatives. To allow for the possibility of intramolecular H-bond formation, we wished to retain at least one methoxy group. To reduce the rate of thermal reversion, only derivatives with substituents in all four *ortho*-positions were considered. Time-dependent density functional theory (TD-DFT) calculations were used to predict the absorption wavelengths of possible derivatives. Based on these considerations, we carried out the synthesis and photochemical characterization of compounds **4** and **5**.

Results and Discussion

Computational chemistry

Calculations were performed using density functional theory (DFT) methods (B3LYP/6-31+G**) to optimize geometry, and TD-DFT with a Solvation Model based on Density (SMD) to calculate absorption wavelength maxima. These computational methods have been used successfully with related compounds [16,17]. The relative stability of different conformations of the molecule was calculated, i.e., with the methoxy substituents on the same or on the opposite side of the N–N double bond. The conformation where both methoxy groups were on the opposite side was found to be the most stable one, although the conformation where both methoxy groups were on the same side was also predicted to be significantly populated at 20 °C (see Supporting Information File 1). Calculating the effect of the substitution pattern on the pK_a value is problematic [18] and was not

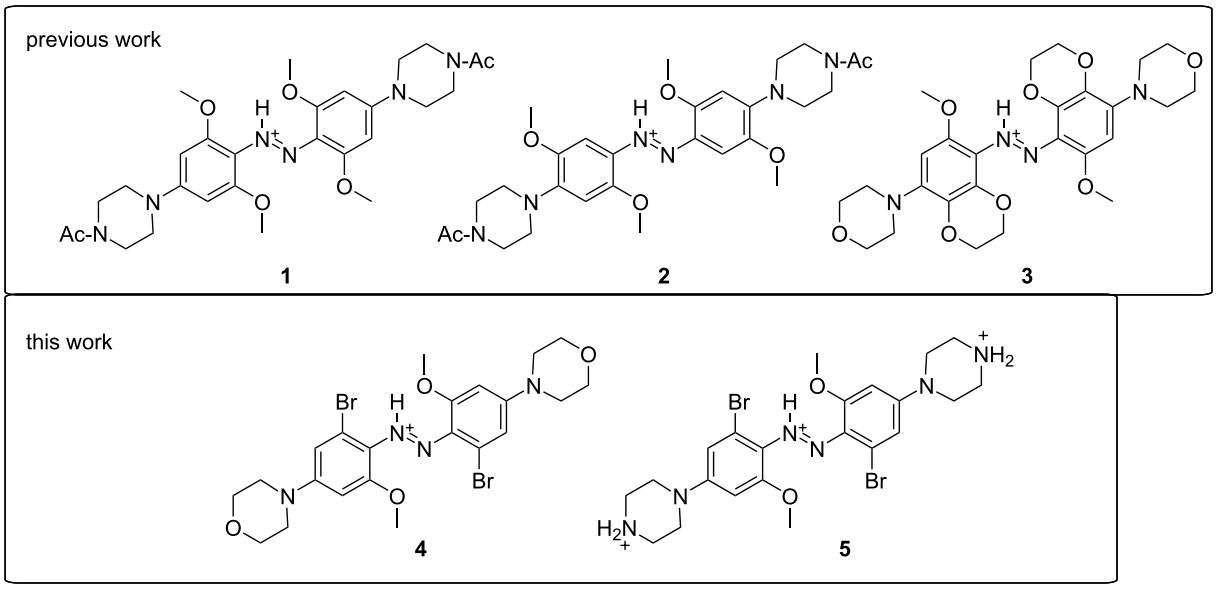


Figure 1: Structures of azonium ions studied.

attempted here. Figure 2 shows calculated structures and spectra of the neutral forms of simplified models of **4** and **5**, with either a pyrollidino or piperidino substituent in *para*-position, as well as the corresponding azonium ions. Calculations indicated that the nature of the respective amino substituent did not have a large effect on the positions of wavelength maxima. These models predicted that compounds **4** and **5** should absorb at longer wavelengths than **1** [10]. Figure 2 also shows experimental spectra, which are discussed below.

Synthesis

The overall synthetic route that was taken is shown in Scheme 1. The azo compound **8**, carrying two *ortho*-methoxy groups, was prepared from **7** using an oxidative coupling approach [19]. The *para*-chloro substituents were then replaced by amino substituents using a Buchwald–Hartwig coupling [20]. Since calculations predicted that 5- and 6-membered rings would have similar effects on the positions of the absorption maxima, we opted to use 6-membered rings, specifically a morpholino substituent and a piperazino substituent in an attempt to enhance water solubility. Late-stage functionalization of the *ortho*-position was carried out through a palladium(II)-catalyzed C–H activation, resulting in *ortho*-brominated azobenzenes [21].

Photochemical characterization

Despite the morpholino substituent, compound **4** was found to be insoluble in water. We therefore dissolved **4** in DCM to obtain the UV–vis spectrum of the neutral form. Addition of TFA to this solution produced the corresponding azonium ion, and the spectra of the neutral and azonium forms of **4** are shown as solid lines in Figure 2. Observed absorption maxima were at 426 (neutral form) and 640 nm (azonium form). While the observed absorption maximum wavelength was close to that predicted for the neutral form, the observed absorption maximum wavelength of the azonium ion was significantly higher than predicted, although the signal's tail was less pronounced. The absorption maximum wavelength of the azonium ion was also higher than that observed for compound **1** [10], as predicted.

We confirmed that the neutral form of **4** underwent photoisomerization. Exposure of a solution of **4** in DCM to 440 nm light led to a photostationary state (PSS) in which the absorbance at 440 nm was diminished and that at 330 nm slightly enhanced (Figure 3). An estimated PSS of ca. 60% *Z*-isomer was calculated as described in the Experimental section. Thermal relaxation from the PSS was monitored by UV–vis spectroscopy, recording a spectrum every minute. As shown in Figure 3, a half-life of 6.5 minutes was obtained at room temperature.

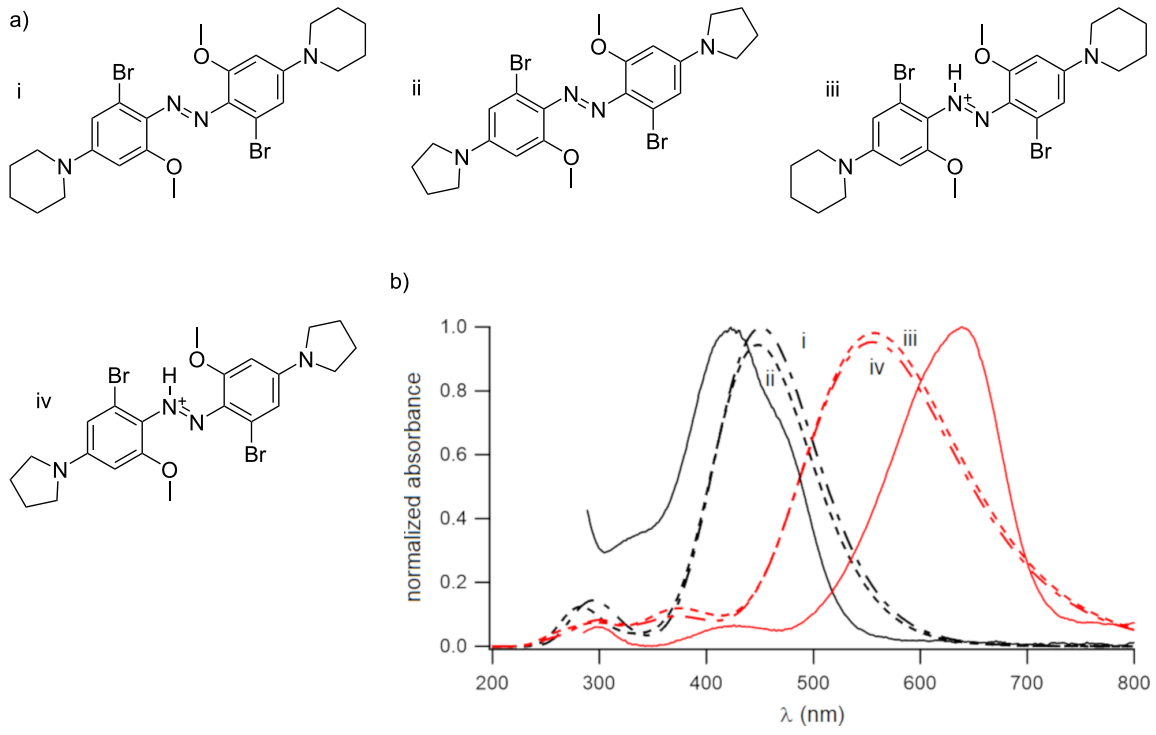
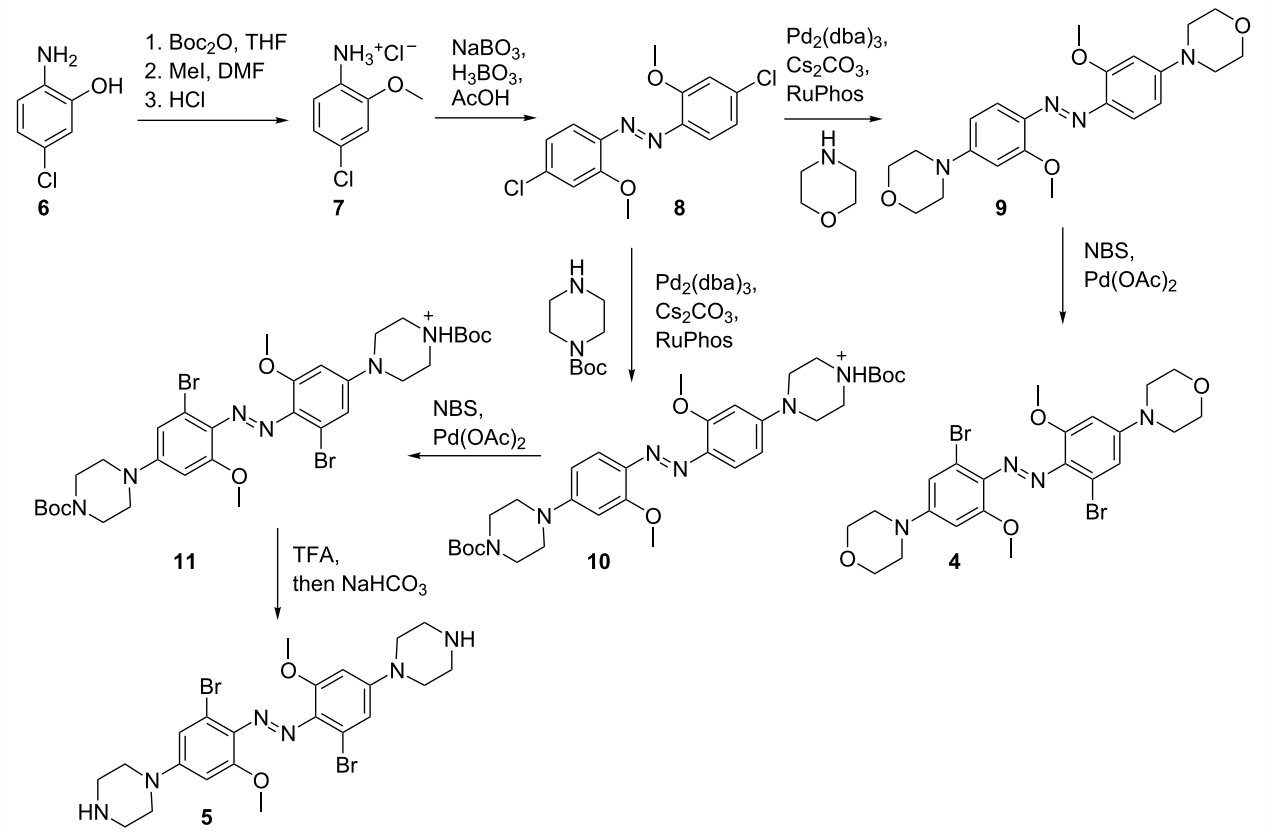


Figure 2: a) Structures of model compounds used for computations (see Experimental section; in calculations, water was set as the solvent). b) Calculated spectra of neutral forms i and ii (black spectra) and azonium forms iii and iv (red spectra), carrying either *para*-piperidino (i and iii, dashed lines) or *para*-pyrrolidino (ii and iv, dash-dotted lines) substituents. Solid lines show experimental spectra of **4** in DCM ($c \approx 15$ µM) without (black) or with TFA added (red).



Scheme 1: Synthesis of bis(4-amino-2-bromo-6-methoxy)azobenzene compounds.

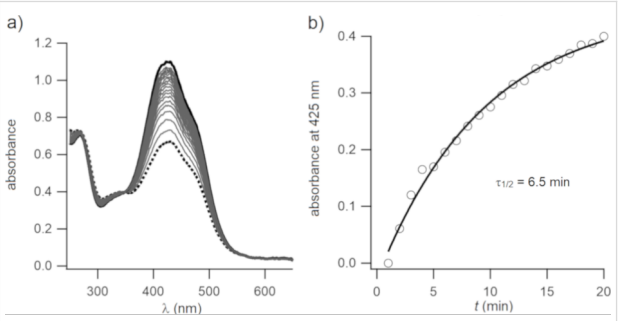


Figure 3: a) UV–vis spectra of **4** in DCM (ca. 15 μM) at the PSS and 440 nm irradiation (thick dotted line; ca. 60% *Z*-isomer), and during thermal reversion to the dark-adapted state (solid black line). b) Time course of thermal reversion at 22 °C. Data were fitted to a single exponential decay equation (solid line).

To enhance the compounds' water solubility, the morpholino substituents were replaced by piperazino groups because the secondary amino groups on the piperazino units were expected to have pK_a values near 10 [22], and so should be protonated at neutral pH, creating a doubly charged species. As anticipated, compound **5** was found to be much more water-soluble than **4**.

The UV–vis spectrum of **5** at a neutral pH value is shown in Figure 4. Irradiation with blue light at 440 nm produced the PSS (dotted line). Thermal reversion from the *cis* isomer was monitored by UV–vis spectroscopy, recording a UV–vis spectrum every 3 minutes, and a half-life of 12.6 minutes was obtained.

The formation of the azonium ion of **5** in aqueous solution was explored thereafter. Addition of hydrochloric acid to a neutral solution of **5** was carried out. Spectra at different pH values are shown in Figure 4c. As can be seen, the formation of the azonium ion of compound **5** required strongly acidic conditions. Even at pH ≈ 0.1, a substantial fraction of the neutral species was still present, implying that the pK_a value of the azonium ion was below ca. 0.2. This pK_a value was at least 7 pH units lower than for the tetra-*ortho*-methoxy compound **1**. As noted above, the presence of the piperazino amino groups made compound **5** doubly positively charged at a neutral pH value. This feature was expected to reduce the pK_a value of the azonium ion through electrostatic effects [23]. The first pK_a value of substituted piperazines falls in the range ca. 4–6 (vs 9–10 for the second pK_a value) [22]. In addition, the electron-withdrawing bromine atoms were also expected to lower the azonium ion's pK_a value (the pK_a values of 2-bromobenzoic acid and unsubstituted benzoic acid are 2.85 and 4.2, respectively [24]). While electrostatic effects on the pK_a value could be ameliorated

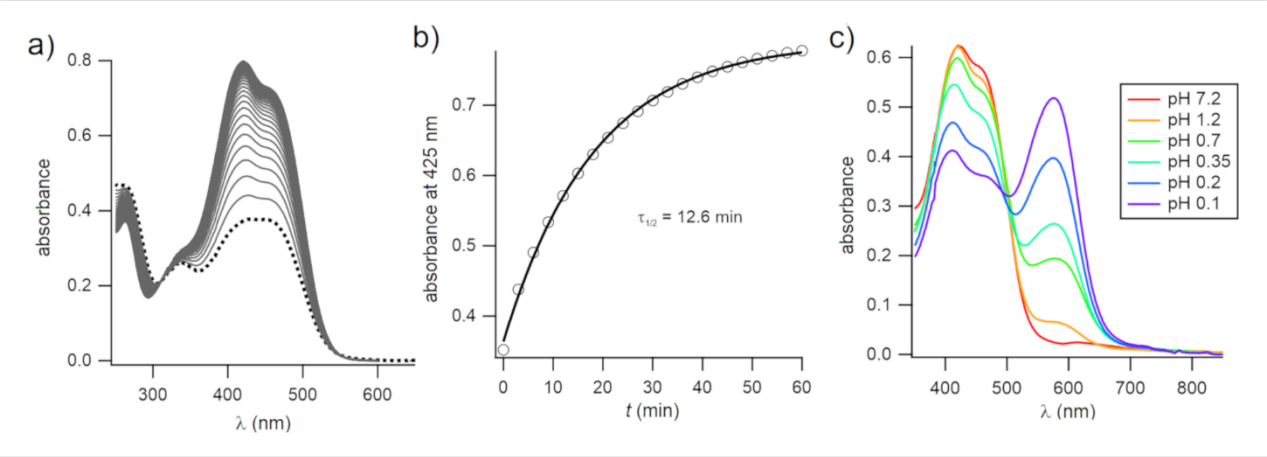


Figure 4: a) UV–vis spectra of **5** in aqueous solution ($c \approx 15$ µM, 5% methanol, pH 7) at the PSS and 440 nm irradiation (thick dotted line; ca. 60% *Z*-isomer) and during thermal reversion to the dark-adapted state (solid black line). b) Time course of thermal reversion at 22 °C. Data were fitted to a single exponential decay equation (solid line). c) Spectra of an aqueous solution of **5** upon addition of hydrochloric acid, as indicated by pH values. The wavelength of the absorption maximum of the azonium ion was 575 nm.

(i.e., by adding negatively charged groups), this would place additional constraints on the general applicability of the compounds. In addition, unlike compound **4**, the wavelength of the absorption maximum of the azonium ion of **5** was not red-shifted relative to that of **1**. Conceivably, the wavelength of maximum absorbance was affected by the charged piperazino groups; calculations were done with uncharged piperidino substituents, as shown in Figure 2. Nevertheless, the lack of a red-shift, combined with the significantly lowered pK_a value, made **5** unsuitable as an azonium photoswitch under physiological conditions.

Despite this undesired effect on the pK_a value, the steric bulk introduced by the bromine substituents did appear to slow thermal relaxation of the neutral (unprotonated) azo forms of these compounds. Species **5** could be switched with blue and green light under physiological conditions and be thermally relaxed with a half-life of 12 minutes. This relaxation rate was substantially lower than other blue-green-absorbing azo compounds without substituents in all four *ortho*-positions relative to the azo unit, which showed half-lives ranging from 50 ms [25] to a few seconds [26,27]. Instead, compounds **4** and **5** exhibited photoswitching properties similar to those reported for tetra-*ortho*-thiol-substituted azobenzenes [17].

Conclusion

Substitution of *p*-aminoazobenzene with *ortho*-bromo and *ortho*-methoxy groups (i.e., a 2-bromo-6-methoxy substitution pattern) was found to lower the pK_a of the azonium ion such that it fell outside the normal physiological range. The neutral version of this compound nevertheless underwent *trans*-to-*cis* photoisomerization in the presence of blue-green light and exhibited slow thermal relaxation ($\tau_{1/2}$ ca. 10 min).

Experimental

General

All commercial materials (solvents, reagents, and substrates) were used as received. SilicaFlash silica gel, P60, 40–63 µm particle size (SiliCycle) was used for column chromatography. High-performance liquid chromatography was performed on a PerkinElmer Series 200 pump with a Waters 2487 Dual λ Absorbance Detector connected to an eDAQ PowerChrom 280 recorder. One-dimensional ^{1}H and ^{13}C NMR spectra were recorded on a Varian UnityPlus 500 MHz or Varian Mercury 400 MHz spectrometer. Chemical shifts are reported in ppm, and the signals were referenced to residual undeuterated solvent signals. Mass spectra were recorded using an Agilent 6538 mass spectrometer with a Q-TOF ionization source or a JEOL AccuTOF mass spectrometer with a DART ionization source.

Synthesis and characterization

4-Chloro-2-methoxyanilinium chloride (7): (1) 2-Amino-5-chlorophenol (**6**, 3.5 mmol, 500 mg) was dissolved in THF at room temperature. Then, Boc_2O (7 mmol, 1.52 g) was added and the resulting mixture was stirred for 18 h at room temperature. The reaction progress was monitored by TLC. When the reaction was complete, the solvent was removed under reduced pressure, resulting in a yellowish oil. This was purified by column chromatography using hexane/ethyl acetate, 4:1, v/v as eluent. The product, phenol *tert*-butyl (4-chloro-2-hydroxyphenyl)carbamate, was used directly in the next step. (2) *tert*-Butyl (4-chloro-2-hydroxyphenyl)carbamate (2 mmol, 500 mg) was dissolved in DMF. Then, an aqueous solution of K_2CO_3 (6 mmol, 828 mg) was added, together with methyl iodide (Caution: toxic, potential carcinogen; 6 mmol, 851 mg). The mixture was stirred for 18 h until the starting reagent was consumed. Then, the solvent was removed under reduced pressure,

resulting in a brown oil. This was poured into water and extracted three times with DCM. The organic fractions were collected and evaporated under reduced pressure. The product, *tert*-butyl (4-chloro-2-methoxyphenyl)carbamate, was used directly in the next step. (3) *tert*-Butyl (4-chloro-2-methoxyphenyl)carbamate (400 mg, 1.16 mmol) was dissolved in 3 mL of ethyl acetate. Then, 9 mL of fuming hydrochloric acid were added dropwise to the reaction mixture with vigorous stirring. The resulting mixture was stirred for 1 hour. Then, the solvent was evaporated under reduced pressure, giving a brown oil. This was added to 30 mL of hexane in an ice bath to precipitate the title compound. Finally, the product **7** (420 mg, 77% over three steps) was isolated by filtration. ^{1}H NMR (400 MHz, methanol-d_4) δ 7.36 (d, J = 8.4 Hz, 1H), 7.30 (d, J = 2.1 Hz, 1H), 7.11 (dd, J = 8.4, 2.1 Hz, 1H), 3.99 (s, 3H).

(*E*)-1,2-Bis(4-chloro-2-methoxyphenyl)diazene (8): 4-Chloro-2-methoxyanilinium chloride (**7**, 2.5 mmol, 400 mg) was dissolved in acetic acid (2 mL), and boric acid (2.11 mmol, 135 mg) was added to the mixture, followed by sodium perborate (2.5 mmol, 680 mg) in three portions over 15 minutes. Then, the reaction mixture was heated at 70 ºC for 18 hours. The reaction progress was monitored by TLC, and when the reaction was complete, the solvent was removed under reduced pressure. The resulting oil was poured into water and extracted with DCM three times. The organic fractions were collected, and the solvent was removed. The resulting oil was purified by column chromatography using hexane/ethyl acetate, 4:1, v/v as eluent. This way, 250 mg (32%) of **8** could be obtained. ^{1}H NMR (300 MHz, chloroform-*d*) δ 7.59 (d, J = 8.6 Hz, 2H), 7.07 (d, J = 2.1 Hz, 2H), 6.98 (dd, J = 8.6, 2.1 Hz, 2H), 4.01 (s, 6H); ^{13}C NMR (75 MHz, chloroform-*d*) δ 157.4, 141.4, 138.3, 121.2, 118.5, 113.3, 56.7; HRMS (*m*/*z*): [M + H]$^+$ calcd for $C_{14}H_{15}N_2O_2Cl_2$, 311.0349; found, 311.0341.

(*E*)-1,2-Bis(2-methoxy-4-morpholinophenyl)diazene (9): (*E*)-1,2-Bis(4-chloro-2-methoxyphenyl)diazene (**8**, 100 mg, 0.32 mmol) was dissolved in toluene in an Ace pressure tube (10.2 cm × 8 mm). Then, morpholine (84 mg, 0.96 mmol), tris(dibenzylideneacetone)dipalladium(0) (29.3 mg, 0.032 mmol), RuPhos (29.8 mg, 0.064 mmol), and cesium carbonate (302.4 mg, 0.96 mmol) were added. The mixture was heated at 100 ºC in the pressure tube for 24 hours. The reaction progress was monitored by TLC until the starting reagent was consumed. The solvent was evaporated under reduced pressure, and the resulting oil was extracted with DCM three times. The resulting crude product was purified by column chromatography using hexane/ethyl acetate, 1:4, v/v as eluent to obtain 95 mg (72%) of **9**. ^{1}H NMR (400 MHz, chloroform-*d*) δ 7.71 (s, 2H), 6.48 (m, 4H), 4.01 (s, 6H), 3.87 (m, 8H), 3.28 (m, 8H); ^{13}C NMR (101 MHz, chloroform-*d*) δ 158.1, 154.0, 136.7, 118.5, 107.7, 98.9, 66.9, 56.7, 48.6; HRMS (*m*/*z*): [M + H]$^+$ calcd for $C_{22}H_{29}N_4O_4$, 413.2189; found, 413.2186.

(*E*)-1,2-Bis(2-bromo-6-methoxy-4-morpholinophenyl)diazene (4): (*E*)-1,2-Bis(2-methoxy-4-morpholinophenyl)diazene (**9**, 30 mg, 0.07 mmol) was dissolved in DCM. To this solution, palladium acetate (1.6 mg, 0.007 mmol) was added, and the resulting mixture was stirred for 15 minutes. Then, *N*-bromosuccinimide (28.6 mg, 0.16 mmol) was added to the reaction. The reaction mixture was stirred for additional 30 minutes until completed. The solvent was evaporated under reduced pressure, and the resulting oil was purified by column chromatography using hexane/ethyl acetate, 1:2, v/v as eluent to obtain 29 mg (70%) of **4**. ^{1}H NMR (300 MHz, chloroform-*d*) δ 7.91 (s, 2H), 6.67 (s, 2H), 4.03 (s, 6H), 3.89 (m, 8H), 3.17 (s, 8H); ^{13}C NMR (101 MHz, chloroform-*d*) δ 157.3, 153.7, 138.8, 122.6, 110.8, 104.9, 67.0, 58.6, 51.9; HRMS (*m*/*z*): [M + H]$^+$ calcd for $C_{22}H_{27}Br_2N_4O_4$, 569.0393; found, 569.0393.

Di-*tert*-butyl 4,4'-(diazene-1,2-diyl)bis(3-methoxy-4,1-phenylene)-(*E*)-bis(1λ^4-piperazine-1-carboxylate) (10): (*E*)-1,2-Bis(4-chloro-2-methoxyphenyl)diazene (**8**, 100 mg, 0.32 mmol) was dissolved in toluene in a pressure tube. Then, 1-Boc-piperazine (180 mg, 0.96 mmol), tris(dibenzylideneacetone)dipalladium(0) (29.3 mg, 0.032 mmol), RuPhos (29.8 mg, 0.064 mmol), and cesium carbonate (302.4 mg, 0.96 mmol) were added. The mixture was heated at 100 ºC in a pressure tube for 36 hours. The reaction progress was monitored by TLC until the starting reagent was consumed. The solvent was evaporated under reduced pressure, and the resulting oil was extracted with DCM three times. The final mixture was purified by column chromatography using hexane/ethyl acetate, 1:3, v/v as eluent to obtain 130 mg (65%) of the product **10**. ^{1}H NMR (400 MHz, DCM-d_2) δ 7.57 (m, 2H), 6.50 (m, 4H), 3.99 (s, 6H), 3.58 (m, 8H), 3.29 (m, 8H), 1.47 (s, 18H).

Di-*tert*-butyl 4,4'-(diazene-1,2-diyl)bis(3-bromo-5-methoxy-4,1-phenylene)-(*E*)-bis(1λ^4-piperazine-1-carboxylate) (11): Di-*tert*-butyl 4,4'-(diazene-1,2-diyl)bis(3-methoxy-4,1-phenylene)-(*E*)-bis(1λ^4-piperazine-1-carboxylate) (**10**, 30 mg, 0.04 mmol) was dissolved in DCM, palladium acetate (1 mg, 0.004 mmol) was added, and the resulting mixture was stirred for 15 minutes. Then, *N*-bromosuccinimide (22 mg, 0.1 mmol) was added to the reaction. The reaction mixture was stirred for additional 30 minutes until completion. The solvent was evaporated under reduced pressure and the resulting oil was purified by column chromatography using hexane/ethyl acetate, 1:1, v/v as eluent to obtain 19 mg (50%) of the product **11**. ^{1}H NMR (400 MHz, DCM-d_2) δ 7.74 (s, 2H), 6.61 (s, 2H), 3.93 (s, 6H), 3.53 (m, 8H), 3.00 (m, 8H), 1.39 (s, 18H); ^{13}C NMR (126 MHz, DCM-d_2) δ 152.9, 150.2, 149.4, 134.1, 117.5, 106.2,

75.1, 52.1, 47.0, 23.7; HRMS (*m*/*z*): $[M + H]^+$ calcd for $C_{32}H_{45}Br_2N_6O_6$, 767.1767; found, 767.1762.

(*E*)-1,2-Bis(2-bromo-6-methoxy-4-(piperazin-1-yl)-phenyl)diazene (5): Di-*tert*-butyl 4,4'-(diazene-1,2-diyl)bis(3-bromo-5-methoxy-4,1-phenylene)-(*E*)-bis(1λ^4-piperazine-1-carboxylate) (**11**, 15 mg, 0.02 mmol) was dissolved in 5 mL of DCM, and 0.25 mL of TFA was added. The resulting mixture was stirred for 16 hours. 1 mL of a 10% aqueous solution of sodium bicarbonate was added to neutralize the compound. Then, the solvent was evaporated to produce the product **5** (90%) without further purification needed. ^{1}H NMR (400 MHz, DCM-d_2) δ 7.92 (s, 2H), 6.97 (s, 2H), 4.11 (s, 6H), 3.45 (m, 8H), 3.00 (m, 8H); ^{13}C NMR (126 MHz, DCM-d_2) δ 158.9, 154.0, 140.2, 123.0, 111.5, 107.2, 66.9, 57.3, 45.1; HRMS (*m*/*z*): $[M + H]^+$ calcd for $C_{22}H_{29}Br_2N_6O_2$, 567.0719; found, 567.0713.

UV–vis spectroscopy

UV–vis spectra were recorded on a PerkinElmer LAMBDA 35, Shimadzu UV-2401PC, or an Ocean Optics USB4000 diode array spectrophotometer. The temperature was maintained at 22 °C for all measurements (Quantum Northwest temperature controller), and 10 mm or 1.5 mm quartz cuvettes (Hellma Analytics) were used. Samples were prepared in sodium phosphate buffer, pH 7.0, or in DCM, as described, at nominal concentrations of 15 μM. The pH value was adjusted by adding microliter volumes of aq HCl or NaOH (as to not change the total volume of the sample solutions significantly). The pH values were measured directly in the samples using a combination pH electrode.

Photoisomerization

UV irradiation was performed by placing a 365 nm LED (897-LZ440U610; LED Engin) operating at 68 mW/cm^2 above the sample tube for 1 minute. For blue light irradiation, a 440 nm LED (Luxeon III Star LED Royal Blue Lambertian; Luxeon Star LEDs) operating at 40 mW/cm^2 at 700 mA was used in the experiments.

Estimates of the percentage of *cis*/*trans* isomers in PSSs

Based on NMR spectra, we assumed that the fraction of *Z*-isomer present at equilibrium in the dark was negligible. Since UV–vis spectra obtained during thermal reversion exhibited an isosbestic point, we assumed that only *E*- and *Z*-isomers contributed to the spectrum at any time. An estimate for the spectrum of pure *Z*-isomer could therefore be obtained simply by subtracting the contribution of the *E*-isomer from the spectrum of the PSS, with the restriction that the absorbance of the *Z*-isomer could not be less than zero at any wavelength. With this approach, estimated PSS values of 60% (±10%) *Z*-isomer were obtained.

Thermal relaxation rates

The cuvette was irradiated with blue light for 1 minute, gently mixed by pipetting, then immediately capped with Parafilm to prevent evaporation, and placed inside the spectrophotometer. The sample was periodically scanned (250 to 600 nm for each scan; integration time: 2s; scan speed: 480 nm/min) in 2-minute intervals. Absorbance data vs time were then fitted to a single exponential equation to obtain thermal relaxation half-lives using Equation 1.

$$\mathrm{Abs} = \mathrm{Abs_f} - \Delta\mathrm{Abs} \cdot e^{-k \cdot t} \quad (1)$$

Computational methods

DFT calculations were performed using the Gaussian 09 suite of programs at the B3LYP level of theory using a 6-31+G(d,p) basis set [28]. Optimizations were followed by harmonic oscillator frequency calculations at the same level of theory to verify the absence of imaginary frequencies. Though an exhaustive conformational search was not performed for any of the species, the following calculations were performed: To ensure that the conformation shown in Figure 2 was the thermodynamically most stable arrangement around the azo moiety, free energies for two alternative arrangements – conformer 2: with both bromine atoms on the same side of the N–N double bond and conformer 3: with a bromine atom in the position of the methoxy group that H-bonded with the azonium proton (see Supporting Information File 1) – were calculated for each compound at 298.15 K. Both alternate conformers were predicted to have higher energies in vacuo (conformer 2: 1.1 kJ/mol for the 6-membered ring and 2.2 kJ/mol for the 5-membered ring; conformer 3: 20 kJ/mol for the 6-membered ring and 19 kJ/mol for the 5-membered ring). Thus, conformer 2 was slightly higher in energy than conformer 1 and should be populated at room temperature. However, we did not carry out TD-DFT calculations for conformer 2. Second, for the neutral species, the N=N–C–C dihedral angles in the optimized structures were manually set to 20° to generate new input files. Reoptimization yielded the same structures and free energies. The optimized geometries of all structures were subjected to TD-SCF calculations using the same functionals and basis set, assuming the first 15 singlet excitations, and by applying a SMD (assuming water as the solvent) to implicitly approximate the effect of the solvent [29]. TD-SCF data were used to generate the simulated UV–vis spectra by applying a Gaussian function with 0.333 eV peak half-width at half-height to each transition. For the lowest-energy conformer of both protonated species, single point calculations were performed at B3LYP/6-31+G(d,p) with a

SMD (assuming water as the solvent), and molecular orbitals corresponding to HOMO and LUMO were visualized using GaussView, with the isovalue set to 0.02. HOMO-to-LUMO transitions correspond to the longest wavelength with high oscillator strength. In general, HOMOs were found to be more delocalized than LUMOs (see Supporting Information File 1).

Supporting Information

Supporting Information File 1

NMR spectra and further computational data.
[https://www.beilstein-journals.org/bjoc/content/supplementary/1860-5397-15-296-S1.pdf]

Funding

We are grateful to the Natural Sciences and Engineering Research Council of Canada and MINECO/FEDER (CTQ2017-87372-P) for financial support. D. M.-L. thanks the U. de La Rioja for a fellowship.

ORCID® iDs

Diego Sampedro - https://orcid.org/0000-0003-2772-6453
G. Andrew Woolley - https://orcid.org/0000-0002-3446-2639

Preprint

A non-peer-reviewed version of this article has been previously published as a preprint doi:10.3762/bxiv.2019.88.v1

References

1. García-Iriepa, C.; Marazzi, M.; Frutos, L. M.; Sampedro, D. *RSC Adv.* **2013,** *3,* 6241–6266. doi:10.1039/c2ra22363e
2. Szymański, W.; Beierle, J. M.; Kistemaker, H. A. V.; Velema, W. A.; Feringa, B. L. *Chem. Rev.* **2013,** *113,* 6114–6178. doi:10.1021/cr300179f
3. Kumita, J. R.; Flint, D. G.; Smart, O. S.; Woolley, G. A. *Protein Eng., Des. Sel.* **2002,** *15,* 561–569. doi:10.1093/protein/15.7.561
4. Bléger, D.; Hecht, S. *Angew. Chem., Int. Ed.* **2015,** *54,* 11338–11349. doi:10.1002/anie.201500628
5. Samanta, S.; Qin, C.; Lough, A. J.; Woolley, G. A. *Angew. Chem., Int. Ed.* **2012,** *51,* 6452–6455. doi:10.1002/anie.201202383
6. Dong, M.; Babalhavaeji, A.; Samanta, S.; Beharry, A. A.; Woolley, G. A. *Acc. Chem. Res.* **2015,** *48,* 2662–2670. doi:10.1021/acs.accounts.5b00270
7. Lentes, P.; Stadler, E.; Röhricht, F.; Brahms, A.; Gröbner, J.; Sönnichsen, F. D.; Gescheidt, G.; Herges, R. *J. Am. Chem. Soc.* **2019,** *141,* 13592–13600. doi:10.1021/jacs.9b06104
8. Dong, M.; Babalhavaeji, A.; Collins, C. V.; Jarrah, K.; Sadovski, O.; Dai, Q.; Woolley, G. A. *J. Am. Chem. Soc.* **2017,** *139,* 13483–13486. doi:10.1021/jacs.7b06471
9. Dong, M.; Babalhavaeji, A.; Hansen, M. J.; Kálmán, L.; Woolley, G. A. *Chem. Commun.* **2015,** *51,* 12981–12984. doi:10.1039/c5cc02804c
10. Samanta, S.; Babalhavaeji, A.; Dong, M.-x.; Woolley, G. A. *Angew. Chem., Int. Ed.* **2013,** *52,* 14127–14130. doi:10.1002/anie.201306352
11. Stoyanov, S.; Antonov, L.; Stoyanova, T.; Petrova, V. *Dyes Pigm.* **1996,** *32,* 171–185. doi:10.1016/0143-7208(96)00016-2
12. Stoyanova, T.; Stoyanov, S.; Antonov, L.; Petrova, V. *Dyes Pigm.* **1996,** *31,* 1–12. doi:10.1016/0143-7208(95)00095-x
13. Yasuike, N.; Blacklock, K. M.; Lu, H.; Jaikaran, A. S. I.; McDonald, S.; Uppalapati, M.; Khare, S. D.; Woolley, G. A. *ChemPhotoChem* **2019,** *3,* 431–440. doi:10.1002/cptc.201900016
14. Hüll, K.; Morstein, J.; Trauner, D. *Chem. Rev.* **2018,** *118,* 10710–10747. doi:10.1021/acs.chemrev.8b00037
15. Velema, W. A.; Hansen, M. J.; Lerch, M. M.; Driessen, A. J. M.; Szymanski, W.; Feringa, B. L. *Bioconjugate Chem.* **2015,** *26,* 2592–2597. doi:10.1021/acs.bioconjchem.5b00591
16. Bléger, D.; Schwarz, J.; Brouwer, A. M.; Hecht, S. *J. Am. Chem. Soc.* **2012,** *134,* 20597–20600. doi:10.1021/ja310323y
17. Samanta, S.; McCormick, T. M.; Schmidt, S. K.; Seferos, D. S.; Woolley, G. A. *Chem. Commun.* **2013,** *49,* 10314–10316. doi:10.1039/c3cc46045b
18. Alongi, K. S.; Shields, G. C. *Annu. Rep. Comput. Chem.* **2010,** *6,* 113–118. doi:10.1016/s1574-1400(10)06008-1
19. Merino, E. *Chem. Soc. Rev.* **2011,** *40,* 3835–3853. doi:10.1039/c0cs00183j
20. Maiti, D.; Fors, B. P.; Henderson, J. L.; Nakamura, Y.; Buchwald, S. L. *Chem. Sci.* **2011,** *2,* 57–68. doi:10.1039/c0sc00330a
21. Konrad, D. B.; Frank, J. A.; Trauner, D. *Chem. – Eur. J.* **2016,** *22,* 4364–4368. doi:10.1002/chem.201505061
22. Khalili, F.; Henni, A.; East, A. L. L. *J. Chem. Eng. Data* **2009,** *54,* 2914–2917. doi:10.1021/je900005c
23. Borisenko, V.; Sansom, M. S. P.; Woolley, G. A. *Biophys. J.* **2000,** *78,* 1335–1348. doi:10.1016/s0006-3495(00)76688-4
24. Woolley, E. M.; Tomkins, J.; Hepler, L. G. *J. Solution Chem.* **1972,** *1,* 341–351. doi:10.1007/bf00715992
25. Chi, L.; Sadovski, O.; Woolley, G. A. *Bioconjugate Chem.* **2006,** *17,* 670–676. doi:10.1021/bc050363u
26. Beharry, A. A.; Sadovski, O.; Woolley, G. A. *Org. Biomol. Chem.* **2008,** *6,* 4323–4332. doi:10.1039/b810533b
27. Sadovski, O.; Beharry, A. A.; Zhang, F.; Woolley, G. A. *Angew. Chem., Int. Ed.* **2009,** *48,* 1484–1486. doi:10.1002/anie.200805013
28. *Gaussion 09,* Revision B.01; Gaussian, Inc.: Wallingford, CT, 2009.
29. Marenich, A. V.; Cramer, C. J.; Truhlar, D. G. *J. Phys. Chem. B* **2009,** *113,* 6378–6396. doi:10.1021/jp810292n

License and Terms

This is an Open Access article under the terms of the Creative Commons Attribution License (https://creativecommons.org/licenses/by/4.0). Please note that the reuse, redistribution and reproduction in particular requires that the authors and source are credited.

The license is subject to the *Beilstein Journal of Organic Chemistry* terms and conditions: (https://www.beilstein-journals.org/bjoc)

The definitive version of this article is the electronic one which can be found at: doi:10.3762/bjoc.15.296

BEILSTEIN JOURNAL OF ORGANIC CHEMISTRY

Light-controllable dithienylethene-modified cyclic peptides: photoswitching the in vivo toxicity in zebrafish embryos

Sergii Afonin[1], Oleg Babii[1], Aline Reuter[2], Volker Middel[3], Masanari Takamiya[3], Uwe Strähle[3], Igor V. Komarov[*4,5] and Anne S. Ulrich[*1,2]

Full Research Paper

Open Access

Address:
[1]Institute of Biological Interfaces (IBG-2), Karlsruhe Institute of Technology (KIT), POB 3640, 76021 Karlsruhe, Germany, [2]Institute of Organic Chemistry (IOC), KIT, Fritz-Haber-Weg 6, 76131 Karlsruhe, Germany, [3]Institute of Toxicology and Genetics (ITG), KIT, POB 3640, 76021 Karlsruhe, Germany, [4]Taras Shevchenko National University of Kyiv, vul. Volodymyrska 60, 1601 Kyiv, Ukraine and [5]Lumobiotics GmbH, Auerstr. 2, 76227 Karlsruhe, Germany

Email:
Igor V. Komarov* - Igor.Komarov@lumobiotics.com; Anne S. Ulrich* - Anne.Ulrich@kit.edu

* Corresponding author

Keywords:
diarylethene photoswitch; gramicidin S; membrane-active peptides; photopharmacology; zebrafish embryotoxicity model

Beilstein J. Org. Chem. **2020,** *16,* 39–49.
doi:10.3762/bjoc.16.6

Received: 31 July 2019
Accepted: 17 December 2019
Published: 07 January 2020

This article is part of the thematic issue "Molecular switches".

Guest Editor: W. Szymanski

© 2020 Afonin et al.; licensee Beilstein-Institut.
License and terms: see end of document.

Abstract

This study evaluates the embryotoxicity of dithienylethene-modified peptides upon photoswitching, using 19 analogues based on the β-hairpin scaffold of the natural membranolytic peptide gramicidin S. We established an in vivo assay in two variations (with ex vivo and in situ photoisomerization), using larvae of the model organism *Danio rerio,* and determined the toxicities of the peptides in terms of 50% lethal doses (LD_{50}). This study allowed us to: (i) demonstrate the feasibility of evaluating peptide toxicity with *D. rerio* larvae at 3–4 days post fertilization, (ii) determine the phototherapeutic safety windows for all peptides, (iii) demonstrate photoswitching of the whole-body toxicity for the dithienylethene-modified peptides in vivo, (iv) re-analyze previous structure–toxicity relationship data, and (v) select promising candidates for potential clinical development.

Introduction

Biologically-active peptides as a class of chemotherapeutic compounds are uniquely positioned between traditional small organic molecule drugs and high-molecular weight biologics [1,2]. Since recent breakthroughs in peptide synthesis technology [3,4] have enabled peptide production at industrial scales, the exploration of therapeutic peptides as potential drugs is rapidly developing [4-6]. It has been shown that peptide drugs are less immunogenic than biologics and can hit the “undruggable” space of molecular targets [2,7,8]. As a result, the market for peptide drugs (e.g., hormones, receptor antagonists, anticancer, or antibiotic agents) grows faster than that of many other chemotherapeutics [9]. Significant general disadvantages

of peptides as pharmacological agents are their poor oral bioavailability, low plasma stability in vivo, limited understanding of their mechanisms of action, and high in vivo toxicity. The former two drawbacks are being adequately resolved [9] (e.g., by modifying the peptide backbone [10], macrocyclization [11], or by use of unnatural amino acids [12]), and mechanistic understanding of the relevant molecular mechanisms is gradually improving [13]. However, the safety consideration still poses a considerable challenge. Hence, the understanding and decreasing of the in vivo toxicity of peptides is of paramount importance for their development as drugs.

In recent years, photopharmacology [14-16] has emerged as a successful approach to enhance spatiotemporal selectivity of chemotherapeutics, decreasing the overall toxicity and increasing the safety of drugs. Various compound classes are currently being explored as photopharmacology agents [16-21], including peptides [19-21]. The idea behind photopharmacology is based on the design and use of drugs containing a reversibly photoisomerizable fragment ("molecular photoswitch") as part of their structure. Importantly, the photoisomerizable fragment should – in one of its photoforms – destroy or mask the pharmacophore (the drug is "switched OFF"), whereas the other photoform should restore the biological activity of the active element (the drug is "switched ON"). Correspondingly, an inactive drug (the OFF photoform) can be safely administered, and subsequently it can be locally activated for the therapy (converted to the ON photoform) by applying light of a specific wavelength, precisely at the desired site of action. Spatiotemporal resolution of such light-mediated drug delivery is limited mainly by the technical characteristics of the medical devices used for light application and by the light propagation in tissues.

Among several known photoswitches [18] that are being used in peptides [19-23], diarylethenes (DAE) have increasingly attracted attention in recent years [22,23]. Photoswitchable DAE-derived molecules offer several advantages for medical applications, as their photoforms are thermally irreversible and highly fatigue resistant [24-26]. Light-induced reversible pericyclic reactions toggle the structure of DAE between a flexible ring-open isomer and a planar rigidified ring-closed form (Figure 1A). Irradiation of the ring-open isomer with UV light (<400 nm) generates the ring-closed isomer, while irradiation with visible light (>400 nm) converts the ring-closed isomer back to the ring-open photoform (Figure 1B), thereby affecting the structure and flexibility of the immediate molecular surrounding.

We have constructed a number of DAE-containing peptides by incorporating a DAE photoswitch into the backbone of gramicidin S (**1**, GS), which is an intrinsically biostable cyclic peptide, as exemplified by one of our first prototypes compound **2** (Figure 1C). This natural antimicrobial agent has an amphipathic structure, whose functional mechanism is attributed to the permeabilization of bacterial membranes, with considerable side-effects also on eukaryotic cell membranes

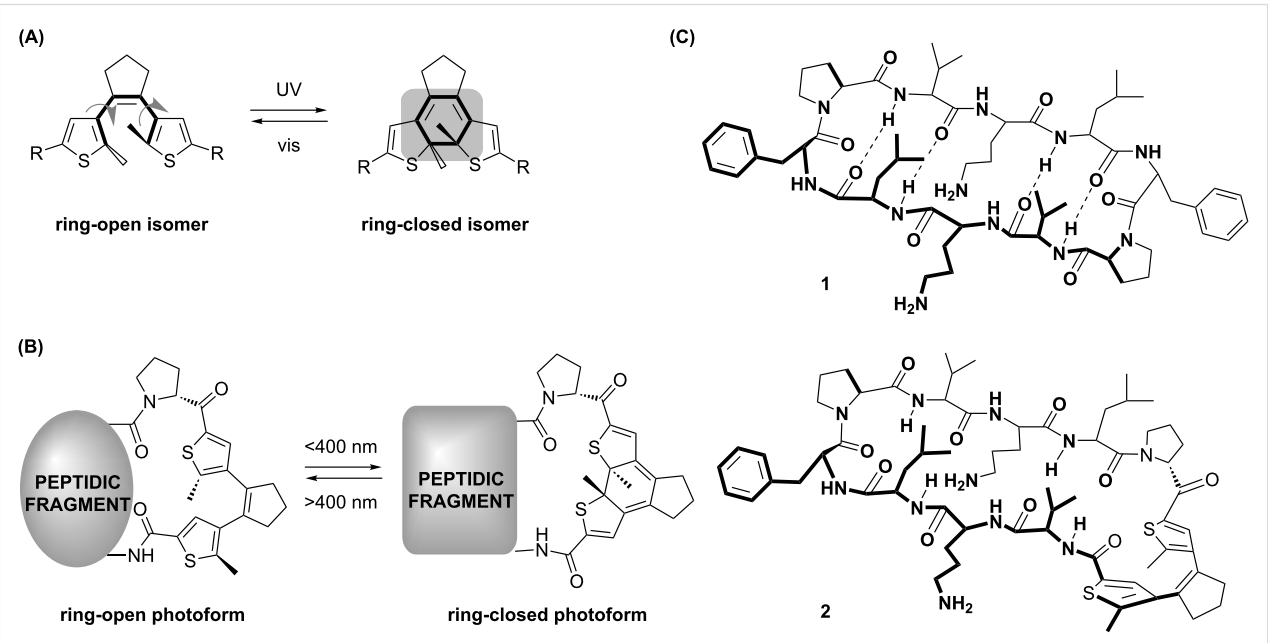


Figure 1: DAE photoswitch and photoswitchable peptides explored in this study. (A) The reversible photoisomerization of the dithienylethene photoswitch core. (B) Photoconversion between ring-open and ring-closed photoforms of DAE-derived peptides. (C) Structures of the non-photoswitchable cytotoxic peptide GS (**1**), and one of our first photoswitchable prototypes **2** in the ring-open photoform.

[27,28]. Compared to the ring-closed (deactivated, OFF) photoform, the ring-open (active, ON) isomer of **2** indeed displayed a much stronger in vitro toxicity against several tumor cell lines [29,30]. Using the photoswitchable analogue **2** in an allograft mouse model, the first in vivo photopharmacology application for a DAE-derived peptide as an anticancer agent has been demonstrated [29]. In order to optimize **2**, we have recently performed a structure–activity relationship (SAR) study using a library of photoswitchable derivatives of **2** [30]. The library contained 29 compounds grouped into several series: with natural amino acid mutations affecting the amphipathicity (series i), with point mutations that modulate polarity and conformational stability of the β-structural elements (series ii), with backbone *N*-alkylation and side-chain hydroxylation modifications (series iii), with macrocycle ring-size variations (series iv), and with macrocycle homodimerization (series v). We systematically screened the ring-open and ring-closed photoforms of all 29 compounds in vitro, using a range of cellular toxicity assays (against Gram-positive bacteria, Gram-negative bacteria, HeLa cells, and human erythrocytes) and were able to rationalize the specific impact of our modifications onto cell selectivity indices. Though all compounds demonstrated distinctly different cell toxicities in the ring-open and the ring-closed photoforms, we noticed that there was generally a poor correlation between the antibacterial activity on the one side, and the cytotoxicity against HeLa cells on the other side, and erythrocytes as a third scenario. Different compounds could thus be regarded as potential leads for chemotherapy of either infectious diseases caused by Gram-positive or -negative bacteria, or for anticancer applications. We hypothesized that the lack of correlation between cell types might not only reflect different mechanisms of killing (possibly even within any pair of isomers), but that it may also be due to unique differences of erythrocytes compared to other somatic cells. Although easily measured, hemolytic activity gives only a rough estimate of toxicity for peptide therapeutics. Erythrocytes are terminally differentiated non-adherent organelle-free cells, densely packed with oxygen-carrying proteins; their homeostasis and pharmacokinetics are highly specialized, and many molecular targets are absent in them [31].

Aiming at applications of photoisomerizable drugs in human healthcare, investigators cannot be limited to in vitro toxicity assays. Furthermore, preclinical drug development programs specifically require the inclusion of in vivo toxicity studies using vertebrate animal models. (For example, toxicity studies of anticancer chemotherapeutics are requested by the International Council for Harmonisation of Technical Requirements for Pharmaceuticals for Human Use (ICH) to include at least two mammalian species, whereby one of them must be a non-rodent [32]). Comprehensive in vivo toxicity studies are obviously lengthy, significantly more expensive than in vitro assays, and are hampered by strict bioethics regulations. We therefore looked for an alternative toxicity assay that would be as technically simple as hemolysis, and at the same time would make the data more relevant to human toxicity. Hence, we selected the zebrafish embryotoxicity assay as a potential compromise. Due to their small size, cheap husbandry and maintenance, fast embryogenesis, extracorporeal development, known genome and accessibility of several thousand transgenic lines [33], zebrafish (*Danio rerio*) is an excellent model for developmental biology and phenotypic genetics [34]. The zebrafish species are attractive to utilize them in toxicity studies due to several reasons. Optimum maintenance and breeding conditions for *D. rerio* are well described in the literature [35], as well as complete details of its embryogenesis [34]. Furthermore, the vertebrate body plan of the zebrafish is, in its basic structure, similar to mammals [36,37], and up to 80% of the known human drug targets are present in the *D. rerio* genome [38]. Since 2005, a zebrafish embryotoxicity test is used as a standardized ISO assay for sewage water testing in Germany [39,40]. Due to its manifold advantages, zebrafish larvae could be used as a cost-effective vertebrate animal model, yet sophisticated enough for pharmacological toxicity evaluations, especially for preclinical drug candidate screenings. However, to the best of our knowledge, such applications for therapeutic peptides are still sparse [41-45]. Notably, zebrafish embryos are transparent, which makes them ideal for in vivo manipulation of photosensitive compounds [46]. This has been advantageously used by other authors in studies of azobenzene-containing photoswitchable bioactive agents [47-50]. Finally, according to the recent edition of EU directive 2010/63/EU, zebrafish embryos of up to 5 days post fertilization (dpf), as the larvae are still feeding on the yolk [51], are excluded from the legislation governing animal testing, i.e., experiments do not require ethical approval.

In this study, we selected 19 photoswitchable DAE-modified cytotoxic peptides from our previous SAR evaluation [30] and established with them the *D. rerio* embryotoxicity assay. For each photoswitchable peptide, we determined the lethal dose of both photochromic forms, using two assay variations, and these in vivo toxicity values could then be compared with the known in vitro cytotoxicities.

Results and Discussion

All peptides (Table 1) were synthesized as was previously described [30] and initially handled as ring-open photoforms under ambient (visual, vis) light conditions. Each of the ring-open photoforms was converted into the ring-closed photoforms by UV irradiation in a solution of denaturing agents, reproducing previously documented results [29,30,52]. All

Table 1: Nomenclature, sequences, molecular masses of the peptides synthesized and explored in this study. The photoswitchable peptides are grouped in series (i–v) according to their original design [30].

Peptide	Linear sequence[a]	Molecular mass, *m*/*z* calculated	measured
1	fPVOLfPVOL	1141.4	1141.2
2	DAE-VOLfPVOL	1280.7	1280.1
	analogues with point mutations affecting amphipathicity (series i)		
3	DAE-VOLfPVOA	1238.6	1238.1
4	DAE-AOLfPVOA	1210.6	1210.1
5	DAE-OOLfPVOL	1295.7	1295.1
	mutations affecting polarity and stability of β-structures (series ii)		
6	DAE-TOVfPVOV	1254.6	1254.1
7	DAE-Asn^{iPr}-OVfPVOV	1309.7	1309.3
8	DAE-Dab^{iBu}-OVfPVOV	1323.7	1323.3
9	DAE-lOLpPlOL	1258.7	1258.5
	analogues with *N*-alkylation and hydroxylation modifications (series iii)		
10	DAE-lOlf-Leu$^{N\text{-}Me}$-LOI	1338.8	1338.8
11	DAE-lOLf-Leu$^{N\text{-}Bu}$-lOL	1380.9	1380.4
12	DAE-Leu^{OH}-OVfPVOV	1282.7	1282.3
13	DAE-VOVfP-Leu^{OH}-OV	1282.7	1282.4
14	DAE-VOVfPVO-Leu^{OH}	1282.7	1282.4
15	DAE-Leu^{OH}-OVfP-Leu^{OH}-OV	1312.7	1312.4
	analogues with extended macrocycles (series iv)		
16	DAE-VKLKVfPLKVKL	1777.4	1776.2
17	DAE-VKLKVfPLkVKV	1763.3	1762.2
18	DAE-VKLKVfPKLVKV	1763.3	1762.2
	"click"-chemistry connected homodimers (series v)		
19	DAE-Leu^{OH}-OLf-Orn$N_3^{N\text{-}Me}$-VOL[b]	2773.5[c]	2773.1[c]
20	DAE-OrnN_3-OLfPVOL[b]	2681.4[c]	2681.0[c]

[a]Canonical amino acids and ornithine (designated O) are given in one-letter code. Lower case letters are for amino acids with D-configuration. Non-canonical amino acids are presented by three-letter code. Superscript indices *N*-Me and *N*-Bu, next to a three-letter abbreviation, indicate *N*-methylation and *N*-butylation, respectively. Leu^{OH} = (2*S*,3*R*)-β-hydroxyleucine; Asn^{iPr} = N^{γ}-isopropylasparagine; Dab^{iBu} = N^{γ}-isobutyryldiaminobutyric acid; OrnN_3 = L-δ-azidoornithine; DAE photoswitching fragment = 4-(2-(5-((L-prolyl-2-methylthiophene-3-yl)cyclopent-1-en-1-yl)-5-methylthiophene-2-carboxyl); [b]monomers (as listed here) were dimerized through azides of the azidoornithines via propargyl ether by means of Cu(I)-catalyzed "click" reaction [29]; [c]molecular masses are for final ether-conjugated dimers.

studied compounds were prepared in >95% purity using preparative-scale high-performance liquid chromatography (HPLC).

To establish the assay for screening the photoswitchable peptides, we first studied the toxicity of our prototype **2** by varying the assay conditions. The parent peptide GS **1** was used as a control. Although the parent **1** does not contain a photoswitchable moiety, it was treated throughout the assay in the same fashion as **2**, in order to account for both (i) the light application effects as well as (ii) the expected [53] developmental changes of the embryos during the experiment. We measured the doses causing the death of 50% embryos (LD_{50}). We tested two different assay variations: in one version, the LD_{50}(open) was determined after direct application of **1** or of the ring-open form of **2**. In the other variant, the photoswitchable peptide was applied in the ring-closed photoform in the darkness, its LD_{50}(closed) was recorded, and then in situ illumination ("photoactivation") was applied to switch into the ring-open photoform and obtain the respective LD_{50}(opened) values (see Figure 2 for the study design and the killing curves).

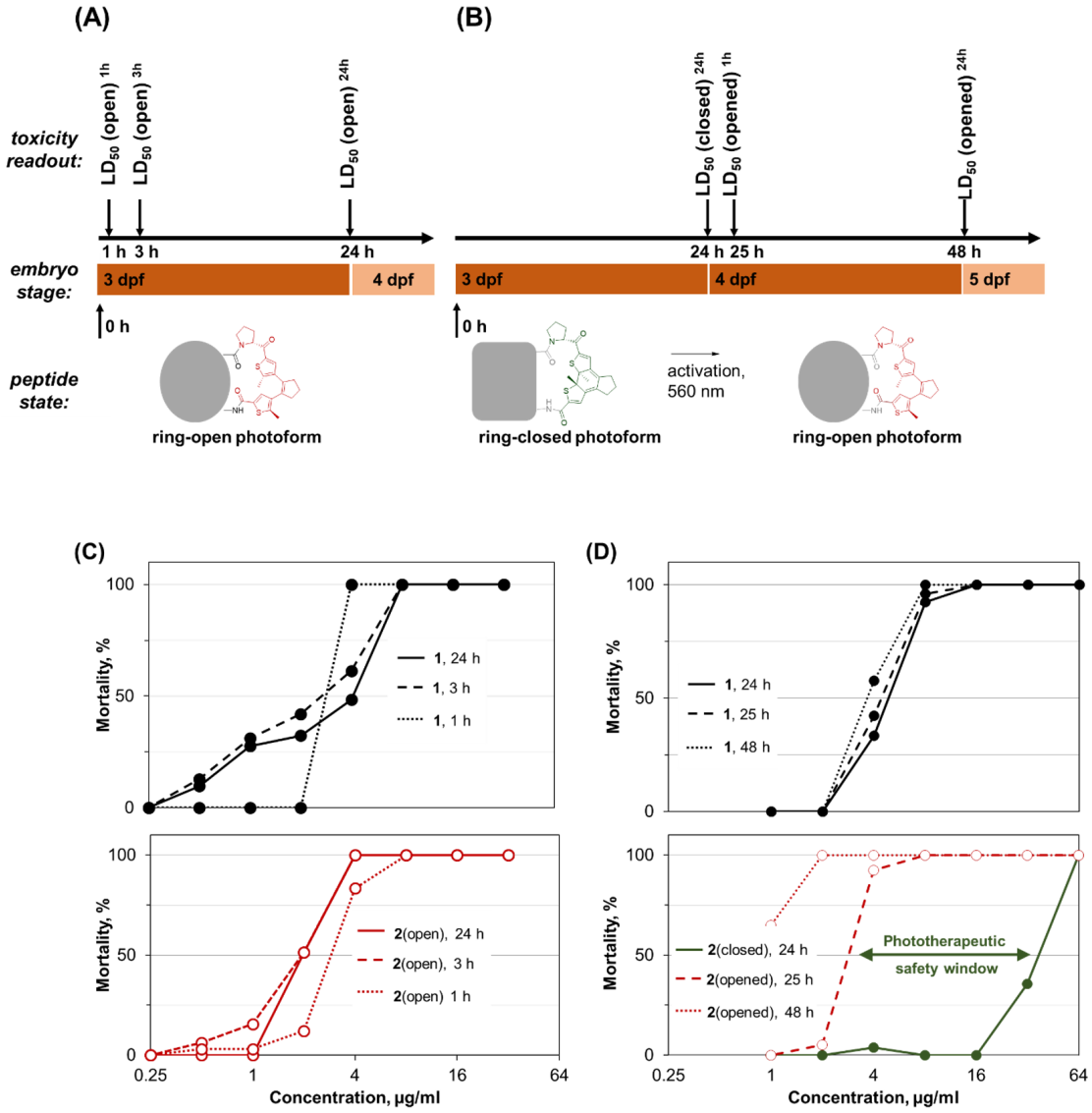


Figure 2: Two versions of the *D. rerio* embryotoxicity assay for DAE-modified peptides: timelines, peptide photostates, ages of larvae, and definitions of the measured characteristics. (A) Direct application of the non-photoswitchable parent GS **1** or of the ring-open photoform of our prototype **2**, and the corresponding killing curves for **1** (C, top, black) and **2** (C, bottom, red). (B) "Photoactivation" assay: initial application of the ring-closed photoform, incubation in darkness, followed by in situ photoconversion into the ring-open(ed) photoform, with the corresponding killing curves for **1** (D, top) and **2** (D, bottom, green for ring-closed, red for ring-open isomers). The latter panel illustrates the "phototherapeutic safety window" (green arrow) as the difference in toxicity between the ring-closed and the ring-open isomers upon photoactivation.

Each time, 12–15 or 18–20 zebrafish embryos at 3 dpf were treated by applying the corresponding peptide dissolved in dimethyl sulfoxide (final dimethyl sulfoxide concentration was 0.2%). Double-concentrated peptide stock solutions (64–512 µg/mL) were prepared by weighing lyophilized peptides, dissolving in 10% dimethyl sulfoxide and constructing two-fold dilution series with ten–eleven dilution steps. In the photoconversion experiments, in order to prevent spontaneous photoswitching of the ring-closed peptides by vis light, zebrafish embryos and peptides were kept in the dark before the first readout, and the vials were sealed to avoid evaporation of the embryonic medium (E3) at prolonged incubation times. After the first screen, without exchanging any solution, the vials with embryos and ring-closed photoforms were exposed to intense illumination for 10 min (LUMATEC Superlite 410 light source, λ = 570 nm, irradiance approximately 20 mW/cm^2). Mortality was then determined under ambient light conditions at 1 h and 24 h after the illumination procedure.

As shown in Figure 2C, the control **1** (non-switchable parent) and the ring-open isomer of our first prototype **2** displayed very similar LD_{50} values upon direct application. After 24 h, 50% of

embryos had died at a concentration of 2.4 ± 0.2 μg/mL GS **1** and 2.1 ± 0.3 μg/mL ring-open **2**. With increasing incubation time, lower concentrations were expected to achieve comparable mortality; however, the difference between 1 h and 24 h incubation was low for both peptides (Table 2).

The photoactivation assay, in which two photoisomers of **2** were tested, shows the anticipated difference between the non-photoswitchable **1** and the photoswitchable **2** (Figure 2D and Table 2). For **1**, the dose-dependent mortality before and after illumination was very similar, with only marginal deviation caused by prolonged incubation time. In contrast, **2** displayed an about 16-fold decrease in the LD_{50} value after in situ photoactivation. This difference indicates that the ring-open isomer of **2** indeed possesses a higher toxicity than the ring-closed isomer, and it demonstrates in vivo photoswitching of the whole-body toxicity.

Since the determined LD_{50} values were practically identical in 3 independent experiments, both assays were used to evaluate the entire library of 19 photoswitchable peptides (see Table 2). Overall, the two assay versions gave comparable LD_{50} values for each of the tested peptide, namely $LD_{50}(open)^{1h}$ vs $LD_{50}(opened)^{1h}$, and $LD_{50}(open)^{24h}$ vs $LD_{50}(opened)^{24h}$. An

Table 2: Toxicities and $LD_{50}(closed)^{24h}/LD_{50}(open)^{24h}$ ratios for the photoswitchable peptides. The peptides are grouped in series (i–v) according to their original design in [30].

Peptide	Toxicities at different conditions, μg/mL ± STD[a]						$LD_{50}(closed)^{24h}/LD_{50}(open)^{24h}$ ratio
	LD_{50} $(open)^{1h}$	LD_{50} $(open)^{3h}$	LD_{50} $(open)^{24h}$	LD_{50} $(closed)^{24h}$	LD_{50} $(opened)^{1h}$	LD_{50} $(opened)^{24h}$	
1	2.8 ± 2.7	2.0 ± 3.0	2.4 ± 0.2	–	–	–	–
2	2.7 ± 1.0	1.7 ± 1.1	2.1 ± 0.3	34.2 ± 12.2	3.3 ± 0.7	0.7 ± 1.3	16.3
analogues with point mutations affecting amphipathicity (series i)							
3	9.3 ± 7.8	4.8 ± 3.9	4.7 ± 0.1	31.1 ± 4.2	9.5 ± 1.3	6.2 ± 0.6	6.6
4	69.8 ± 10.5	40.6 ± 11.2	19.0 ± 1.3	197.7[b]	51.0 ± 7.7	12.9 ± 1.9	10.4
5	4.8 ± 2.2	2.8 ± 1.9	3.3 ± 0.7	8.1 ± 1.0	8.1 ± 1.0	5.3 ± 0.5	2.5
mutations affecting polarity and stability of β-structures (series ii)							
6	30.8 ± 15.0	13.2 ± 13.3	8.6 ± 0.0	196.9[b]	20.6 ± 1.7	6.3 ± 2.3	22.9
7	15.9 ± 4.3	8.7 ± 9.1	5.8 ± 0.4	266.4[b]	18.2 ± 4.6	3.0 ± 2.5	45.9
8	12.0 ± 0.8	5.7 ± 0.4	3.9 ± 1.5	472.9[b]	9.6 ± 5.6	3.0 ± 2.7	121.2
9	2.0 ± 1.1	2.1 ± 0.8	1.6 ± 0.3	9.1 ± 2.7	2.2 ± 0.5	0.8 ± 0.1	5.7
analogues with *N*-alkylation and hydroxylation modifications (series iii)							
10	1.3 ± 1.5	1.0 ± 0.6	1.0 ± 0.6	9.5 ± 0.1	2.2 ± 1.0	1.3 ± 1.5	9.5
11	3.0 ± 1.8	2.4 ± 0.7	1.6 ± 0.1	4.4 ± 0.2	4.0 ± 0.3	3.0 ± 1.0	2.8
12	9.2 ± 1.1	6.7 ± 0.4	3.6 ± 0.5	77.0 ± 19.4	6.2 ± 0.0	2.1 ± 1.0	21.4
13	4.8 ± 3.8	4.3 ± 3.8	2.2 ± 1.0	45.0[b]	6.4 ± 0.4	3.4 ± 0.5	20.5
14	8.1 ± 2.0	6.2 ± 0.7	2.0 ± 0.0	50.4 ± 27.2	9.1 ± 4.2	4.6 ± 2.0	25.2
15	36.5 ± 2.1	14.1 ± 6.0	7.2 ± 3.8	56.1 ± 12.2	22.9 ± 0.2	7.2 ± 0.7	7.8
analogues with extended macrocycles (series iv)							
16	3.1 ± 1.0		1.6 ± 0.0	6.0 ± 0.1	5.6 ± 0.5	5.2 ± 0.5	3.8
17	10.5 ± 5.8		3.2 ± 0.2	9.9 ± 0.1	9.9 ± 0.1	9.4 ± 0.7	3.1
18	0.9 ± 0.4		0.4 ± 0.2	12.3 ± 1.5	12.3 ± 1.5	12.3 ± 1.5	30.8
“click”-chemistry connected homodimers (series v)							
19	2.7 ± 1.7		1.2 ± 0.3	4.8 ± 0.3	4.7 ± 0.5	4.3 ± 1.3	4.0
20	3.7 ± 1.9		1.5 ± 0.0	10.7 ± 0.1	8.4 ± 3.3	3.5 ± 0.6	7.1

[a]STD = standard deviation; [b]STD was not calculated, the measurement was performed once.

exception was noted for the elongated analogues **16**–**18**, where the light-generated ring-opened forms did not restore the activity levels observed in the direct application experiment. This behavior could be explained by a decreased proteolytic stability of these lysine-rich analogues. For the remaining 16 photoswitchable peptides, only minor differences in LD_{50} values between the two types of assays were found. These slight discrepancies are attributed to the different developmental stages of the embryos in the two assays. In the direct activation assay the zebrafish embryos were at 3 dpf, whereas in the photoactivation assay they were at 4 dpf when the ring-closed isomer was converted into the ring-open isomer and subsequently measured at 5 dpf. Also, shielding the embryos for 24 h from light exposure might affect embryogenesis and sensitivity of the larvae [53]. Furthermore, the uptake and accumulation of the ring-closed and ring-open isomer could be different in each case.

Due to photochemical properties of DAE, a realistic DAE-derived in vivo photopharmacology agent should have a low toxicity in the ring-closed form and a high activity in the ring-open form [29,30]. Therefore, analysis relating (undesired) toxicity of the closed form to the (desired) activity of the open form is crucial for the drug candidate assessment. To compare results from different assays and to visualize activity relations of the two photoforms, phototherapeutic indices (e.g., HC_{50}(closed)/IC_{50}(open) and correlation analysis scatter plots are convenient approaches [30]. Analyzing our data, it was interesting to see that the structure–toxicity relationships turned out to be more complicated than it had initially been anticipated and implemented in the original design of the peptide series. Nonetheless, except for the peptides in series iv (**16**–**18**, with increased charge densities) and one of the homodimers (**19**), the difference in activity between the ring-open and the ring-closed photoforms was significant. In all cases, the ring-open states were more active than the corresponding ring-closed photoforms. For approximately half of the peptides (**2**, **7**, **8**, **9**–**13**, and **20**), the ring-open photoforms were even more toxic than the non-switchable parent compound **1**. For our prototype peptide **2**, the ratio $LD_{50}(closed)^{24h}/LD_{50}(open)^{24h}$ was equal to 16.3. The largest drop in toxicity was observed for the inactive forms of peptides **4**, **6**, **7** and **8** ($LD_{50}(closed)^{24} \geq 200$ μg/mL), followed by the analogs with hydroxyleucine side chains **12**, **13**, **14**, and **15** (with values in the range of 50–80 μg/mL). This trend, naturally, translates into the safety windows being the largest for these compounds. Peptides **7**, **8**, and – surprisingly – **18**, significantly surpassed the safety window of the original prototype **2**.

The data in Table 2 reveals several structure–toxicity correlations. Both of the tested dimers (**19**, **20**) showed relatively inefficient photoactivation. Given that **19** and **20** were observed to photoisomerize readily between the ring-closed and ring-opened isomers, we can presume that homodimerization may affect the way in which the peptides interact with their molecular targets, or it may compromise their long-term biostability. Likewise, an elongation of the β-sheet core and an increase in cationic charge density (peptides **5**, **15**–**17**) was seen to decrease the photoactivation efficiency in vivo. The corresponding LD_{50} values indicate that an uncharged polar amino acid residue next to the DAE (compounds **6**, **7**, **8**) and the presence of hydroxyleucine residues (**12**, **13**, **14**) improve the photoactivation efficiency compared to compound **2**. Even though this prototype **2** already had quite a large phototherapeutic safety window (the ratio $LD_{50}(closed)^{24h}/LD_{50}(open)^{24h}$ is 16.3), the new mutants showed even higher safety, the best being peptide **8** (with a ratio $LD_{50}(closed)^{24h}/LD_{50}(open)^{24h}$ of 121).

We have also analyzed the correlation between the empirical low-pH hydrophobicity of the peptides (as assessed from the retention times in reversed-phase HPLC) and toxicity against zebrafish embryos. Independent on the photoisomeric state and the type of toxicity assay, decreasing polarity of the peptides is accompanied by an increase in toxicity against zebrafish embryos (compare Figure 3A and 3B). Within the different series of peptides (the series are marked with different colors in Figure 3 for clarity) we get almost linear toxicity–hydrophobicity correlations in most cases, and all the outliers are readily explainable. For instance, in Figure 3A the peptides **19** and **20** are from series v (homodimers), compounds **16**–**18** have larger (extended) macrocycles and together with **5** possess a higher net charge and charge density than the rest of the peptides. For the most hydrophobic peptide **11** in the ring-open form, which deviates from the general trend, we observed a very low water solubility and tendency to aggregate.

As can be seen from Figure 4, the toxicity against zebrafish embryos is higher than hemolysis for the majority of the ring-open isomers and for all ring-closed photoforms. This result suggests that the lysis of red blood cells may not be the leading cause of in vivo toxicity for these membranolytic peptides.

Based on the results described above, we wondered whether the cytotoxicity against epithelial cells should be considered as an important safety aspect for applications in humans, and whether it should be monitored in preclinical evaluation of this type of chemotherapeutics. It is known, that compounds from the surrounding media are absorbed by the zebrafish mainly through the skin and gills at embryonic stages and through the digestive system during later larval stages [54], which points to epithelial cells as the immediate target and should correspond to the dermal route of administration or other through-epithelium paths in human applications. Notably, it has been shown that

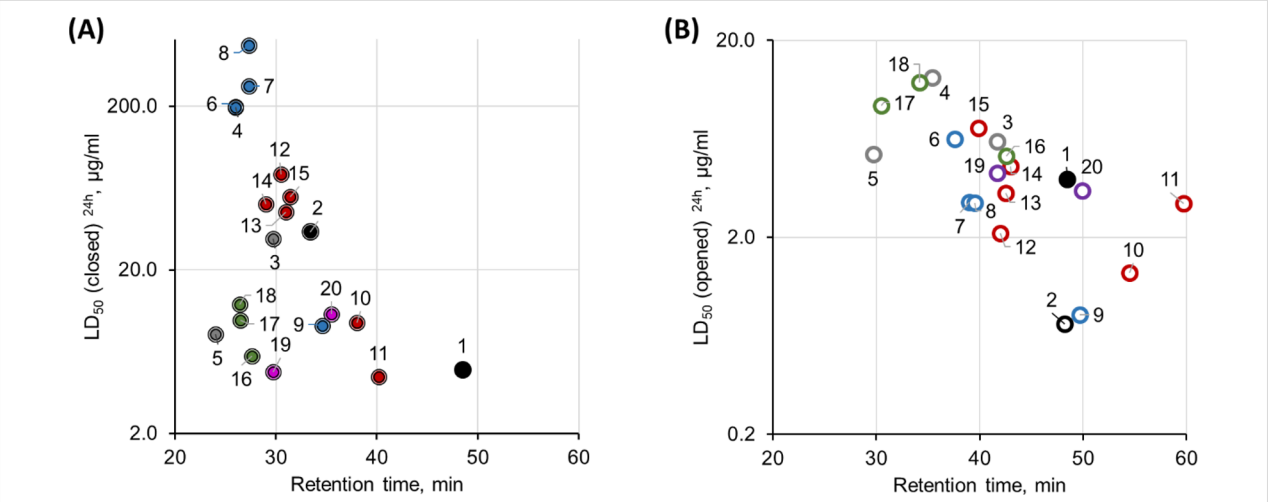


Figure 3: The in vivo toxicity against *D. rerio* embryos appears to be correlated with the empirical hydrophobicities of GS **1** and its photoswitchable analogues **2**–**20**. LD_{50} values are plotted against the HPLC (C_{18}) retention times upon elution with a standardized linear water/acetonitrile gradient: both, for the ring-closed photoforms (A, filled circles), as well as for the ring-open photoforms (B, open circles). The compound numbers are shown next to the data points. Values for the parent peptide **1** are shown as black filled circles; the original prototype **2** is color-coded in black; the data points for peptides of series i (**3**–**5**) are shown in grey, series ii (**6**–**9**) in blue, series iii (**10**–**15**) in red, series iv (**16**–**18**) in green, and series v (**19**, **20**) in purple.

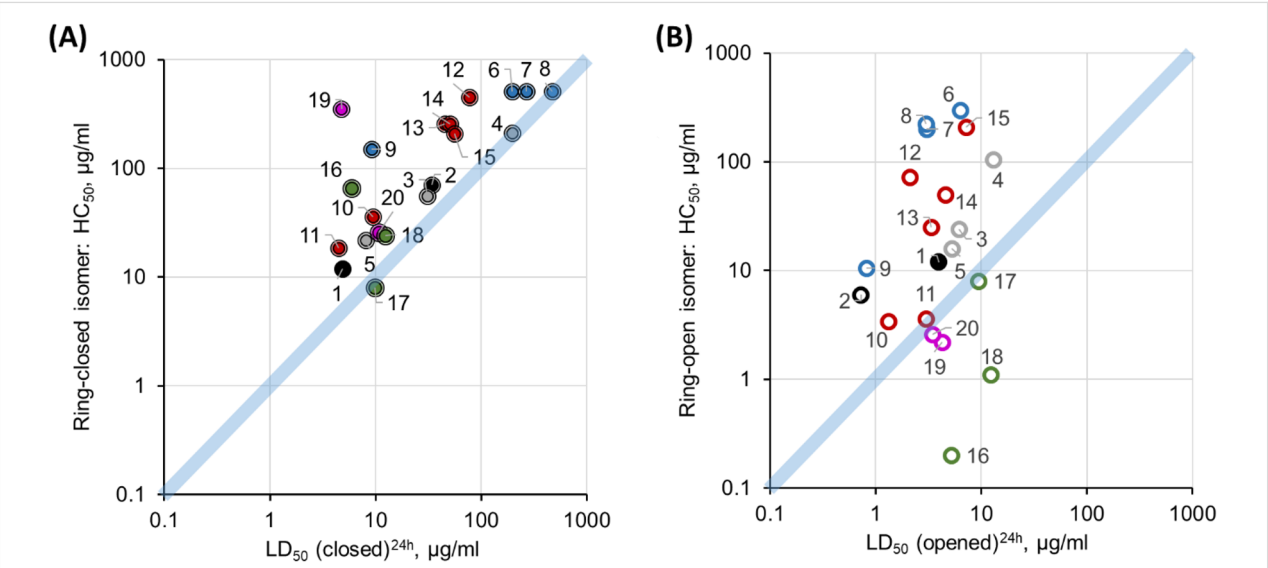


Figure 4: *D. rerio* embryotoxicity of GS **1** and the photoswitchable analogues **2**–**20** correlated with their in vitro hemolysis [30] for the ring-closed photoforms (A, filled circles), and for the ring-open photoforms (B, open circles). The compound numbers are shown next to the data points, and the color code is the same as in Figure 3.

toxicities against zebrafish larvae may correlate with rodent inhalational toxicities [55], but to the best of our knowledge, no such comparisons are known for peptides or peptidomimetics.

When plotting the *D. rerio* embryotoxicity LD_{50} values of the ring-open (activated, ON) photoforms against the in vitro HeLa cytotoxicity indicators, namely against IC_{50} [30] of the ring-closed (deactivated, OFF) photoforms (Figure 5A), the data points are correlated quite well along the diagonal. This correspondence is in contrast to the comparison between hemolysis and HeLa cytotoxicity (Figure 5B) that had been reported in our earlier study, where the whole data set shows a systematic deviation off the diagonal. Our new in vivo data, thus shows a much better correlation of the toxicities between the two tested targets – epithelial cells of the zebrafish embryo and human malignant epithelial cells. Erythrocytes, on the other hand, are clearly less suitable and constitute less representative cells to predict toxic effects in humans. We can therefore expect an even lower in

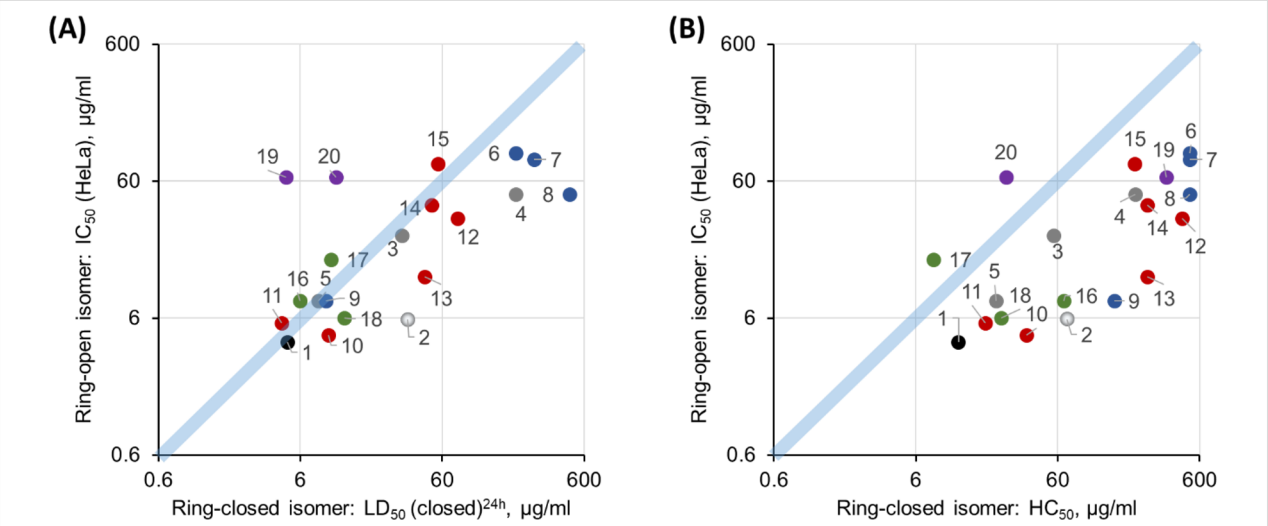


Figure 5: Phototherapeutic cytotoxic action against HeLa cells of GS **1** and its photoswitchable analogues **2**–**20**, correlated with the new in vivo results and earlier in vitro data. For each peptide, the HeLa cytotoxic concentrations of the ring-open photoforms (IC_{50}(open)) are plotted against the corresponding in vivo toxicities to *D. rerio* embryos (A, $LD_{50}(closed)^{24h}$), or against the in vitro hemolytic activities (B, HC_{50}(closed), i.e., 50% hemolysis]) of the ring-closed photoforms. The compound numbers are shown next to the data points. The in vitro data is from [30]. Values for the parent peptide **1** are marked black, and a white filling highlights the initial prototype **2**. Color codes for the remaining peptides are the same as in Figure 3.

vivo anticancer selectivity of our peptides than we had previously judged from the in vitro data on erythrocytes and HeLa cells. Thus, a further increase of the phototherapeutic indices by compound modifications is appropriate. Amongst the most selective compounds against cancer cells, the modifications implemented in series i, ii and iii are the most effective strategies so far to enhance the phototherapeutic indices. The present evaluation identifies peptides **2**, **4**, **7**, **8**, and **13** as the best candidates in terms of the phototherapeutic index.

Conclusion

In this study, we have synthesized 19 photoswitchable membranolytic peptides, derived from the cyclic parent gramicidin S. The two photoforms of these dithienylethene-modified peptides showed different retention times in reversed-phase HPLC, with the ring-open forms being more hydrophobic. An in vivo toxicity assay (using two approaches, giving essentially the same results) was established in order to study the in situ photoactivation of these peptides using a zebrafish embryo model. We systematically evaluated the toxicities of the two photoforms and found that the activated ring-open isomers of our peptides are more toxic than the inactivated ring-closed isomers, with up to two orders of magnitude difference. The most promising modifications of GS appear to be those where a single uncharged polar amino acid has been introduced on the hydrophilic face of the peptide.

Acknowledgements

We thank Dr. Wadhwani (KIT, Karlsruhe) for access to the peptide synthesis facility.

Funding

Financial support was provided by Helmholtz Association (Germany) via the program “BioInterfaces in Technology and Medicine” (BIF-TM). SA, OB, IVK, and ASU acknowledge EU funding by the EU H2020-MSCA-RISE-2015 through the PELICO project (grant 690973). This work was supported by the DFG-GRK 2039 (SA, OB, US, ASU) and by the BMBF VIP+ (OB, ASU).

ORCID® iDs

Sergii Afonin - https://orcid.org/0000-0002-2356-4226
Oleg Babii - https://orcid.org/0000-0001-7107-1402
Masanari Takamiya - https://orcid.org/0000-0002-6524-5813
Igor V. Komarov - https://orcid.org/0000-0002-7908-9145
Anne S. Ulrich - https://orcid.org/0000-0001-5571-9483

References

1. Craik, D. J.; Fairlie, D. P.; Liras, S.; Price, D. *Chem. Biol. Drug Des.* **2013,** *81,* 136–147. doi:10.1111/cbdd.12055
2. Uhlig, T.; Kyprianou, T.; Martinelli, F. G.; Oppici, C. A.; Heiligers, D.; Hills, D.; Calvo, X. R.; Verhaert, P. *EuPa Open Proteomics* **2014,** *4,* 58–69. doi:10.1016/j.euprot.2014.05.003
3. Verzele, D.; Madder, A. *ChemBioChem* **2013,** *14,* 1032–1048. doi:10.1002/cbic.201200775
4. Behrendt, R.; White, P.; Offer, J. *J. Pept. Sci.* **2016,** *22,* 4–27. doi:10.1002/psc.2836
5. Palomo, J. M. *RSC Adv.* **2014,** *4,* 32658–32672. doi:10.1039/c4ra02458c
6. Mäde, V.; Els-Heindl, S.; Beck-Sickinger, A. G. *Beilstein J. Org. Chem.* **2014,** *10,* 1197–1212. doi:10.3762/bjoc.10.118
7. Boehncke, W.-H.; Brembilla, N. C. *Expert Rev. Clin. Immunol.* **2018,** *14,* 513–523. doi:10.1080/1744666x.2018.1468753

8. Atangcho, L.; Navaratna, T.; Thurber, G. M. *Trends Biochem. Sci.* **2019,** *44,* 241–257. doi:10.1016/j.tibs.2018.11.008
9. Lau, J. L.; Dunn, M. K. *Bioorg. Med. Chem.* **2018,** *26,* 2700–2707. doi:10.1016/j.bmc.2017.06.052
10. Werner, H. M.; Cabalteja, C. C.; Horne, W. S. *ChemBioChem* **2016,** *17,* 712–718. doi:10.1002/cbic.201500312
11. White, C. J.; Yudin, A. K. *Nat. Chem.* **2011,** *3,* 509–524. doi:10.1038/nchem.1062
12. Qvit, N.; Rubin, S. J. S.; Urban, T. J.; Mochly-Rosen, D.; Gross, E. R. *Drug Discovery Today* **2017,** *22,* 454–462. doi:10.1016/j.drudis.2016.11.003
13. Henninot, A.; Collins, J. C.; Nuss, J. M. *J. Med. Chem.* **2018,** *61,* 1382–1414. doi:10.1021/acs.jmedchem.7b00318
14. Hüll, K.; Morstein, J.; Trauner, D. *Chem. Rev.* **2018,** *118,* 10710–10747. doi:10.1021/acs.chemrev.8b00037
15. Velema, W. A.; Szymanski, W.; Feringa, B. L. *J. Am. Chem. Soc.* **2014,** *136,* 2178–2191. doi:10.1021/ja413063e
16. Lerch, M. M.; Hansen, M. J.; van Dam, G. M.; Szymanski, W.; Feringa, B. L. *Angew. Chem., Int. Ed.* **2016,** *55,* 10978–10999. doi:10.1002/anie.201601931
17. Morstein, J.; Trauner, D. *Curr. Opin. Chem. Biol.* **2019,** *50,* 145–151. doi:10.1016/j.cbpa.2019.03.013
18. Pianowski, Z. L. *Chem. – Eur. J.* **2019,** *25,* 5128–5144. doi:10.1002/chem.201805814
19. Jankovic, B.; Gulzar, A.; Zanobini, C.; Bozovic, O.; Wolf, S.; Stock, G.; Hamm, P. *J. Am. Chem. Soc.* **2019,** *141,* 10702–10710. doi:10.1021/jacs.9b03222
20. Yeoh, Y. Q.; Yu, J.; Polyak, S. W.; Horsley, J. R.; Abell, A. D. *ChemBioChem* **2018,** *19,* 2591–2597. doi:10.1002/cbic.201800618
21. Albert, L.; Vázquez, O. *Chem. Commun.* **2019,** *55,* 10192–10213. doi:10.1039/c9cc03346g
22. Komarov, I. V.; Afonin, S.; Babii, O.; Schober, T.; Ulrich, A. S. *Chem. – Eur. J.* **2018,** *24,* 11245–11254. doi:10.1002/chem.201801205
23. Peddie, V.; Abell, A. D. *J. Photochem. Photobiol., C* **2019,** *40,* 1–20. doi:10.1016/j.jphotochemrev.2019.05.001
24. Matsuda, K.; Irie, M. *J. Photochem. Photobiol., C* **2004,** *5,* 169–182. doi:10.1016/j.jphotochemrev.2004.07.003
25. Irie, M.; Fukaminato, T.; Matsuda, K.; Kobatake, S. *Chem. Rev.* **2014,** *114,* 12174–12277. doi:10.1021/cr500249p
26. Zhang, J.; Tian, H. *Adv. Opt. Mater.* **2018,** *6,* 1701278. doi:10.1002/adom.201701278
27. Katsu, T.; Kobayashi, H.; Fujita, Y. *Biochim. Biophys. Acta, Biomembr.* **1986,** *860,* 608–619. doi:10.1016/0005-2736(86)90560-2
28. Semrau, S.; Monster, M. W. L.; van der Knaap, M.; Florea, B. I.; Schmidt, T.; Overhand, M. *Biochim. Biophys. Acta, Biomembr.* **2010,** *1798,* 2033–2039. doi:10.1016/j.bbamem.2010.07.001
29. Babii, O.; Afonin, S.; Garmanchuk, L. V.; Nikulina, V. V.; Nikolaienko, T. V.; Storozhuk, O. V.; Shelest, D. V.; Dasyukevich, O. I.; Ostapchenko, L. I.; Iurchenko, V.; Zozulya, S.; Ulrich, A. S.; Komarov, I. V. *Angew. Chem., Int. Ed.* **2016,** *55,* 5493–5496. doi:10.1002/anie.201600506
30. Babii, O.; Afonin, S.; Ishchenko, A. Y.; Schober, T.; Negelia, A. O.; Tolstanova, G. M.; Garmanchuk, L. V.; Ostapchenko, L. I.; Komarov, I. V.; Ulrich, A. S. *J. Med. Chem.* **2018,** *61,* 10793–10813. doi:10.1021/acs.jmedchem.8b01428
31. Cossum, P. A. *Biopharm. Drug Dispos.* **1988,** *9,* 321–336. doi:10.1002/bod.2510090402
32. ICH guideline S9 on the "Nonclinical Evaluation for Anticancer Pharmaceuticals".
33. Yang, L.; Ho, N. Y.; Alshut, R.; Legradi, J.; Weiss, C.; Reischl, M.; Mikut, R.; Liebel, U.; Müller, F.; Strähle, U. *Reprod. Toxicol.* **2009,** *28,* 245–253. doi:10.1016/j.reprotox.2009.04.013
34. Tsang, M. *Birth Defects Res., Part C* **2010,** *90,* 185–192. doi:10.1002/bdrc.20183
35. Tsang, B.; Zahid, H.; Ansari, R.; Lee, R. C.-Y.; Partap, A.; Gerlai, R. *Zebrafish* **2017,** *14,* 561–573. doi:10.1089/zeb.2017.1477
36. Kimmel, C. B.; Ballard, W. W.; Kimmel, S. R.; Ullmann, B.; Schilling, T. F. *Dev. Dyn.* **1995,** *203,* 253–310. doi:10.1002/aja.1002030302
37. Goldsmith, P. *Curr. Opin. Pharmacol.* **2004,** *4,* 504–512. doi:10.1016/j.coph.2004.04.005
38. Howe, K.; Clark, M. D.; Torroja, C. F.; Torrance, J.; Berthelot, C.; Muffato, M.; Collins, J. E.; Humphray, S.; McLaren, K.; Matthews, L.; McLaren, S.; Sealy, I.; Caccamo, M.; Churcher, C.; Scott, C.; Barrett, J. C.; Koch, R.; Rauch, G.-J.; White, S.; Chow, W.; Kilian, B.; Quintais, L. T.; Guerra-Assunção, J. A.; Zhou, Y.; Gu, Y.; Yen, J.; Vogel, J.-H.; Eyre, T.; Redmond, S.; Banerjee, R.; Chi, J.; Fu, B.; Langley, E.; Maguire, S. F.; Laird, G. K.; Lloyd, D.; Kenyon, E.; Donaldson, S.; Sehra, H.; Almeida-King, J.; Loveland, J.; Trevanion, S.; Jones, M.; Quail, M.; Willey, D.; Hunt, A.; Burton, J.; Sims, S.; McLay, K.; Plumb, B.; Davis, J.; Clee, C.; Oliver, K.; Clark, R.; Riddle, C.; Elliott, D.; Threadgold, G.; Harden, G.; Ware, D.; Begum, S.; Mortimore, B.; Kerry, G.; Heath, P.; Phillimore, B.; Tracey, A.; Corby, N.; Dunn, M.; Johnson, C.; Wood, J.; Clark, S.; Pelan, S.; Griffiths, G.; Smith, M.; Glithero, R.; Howden, P.; Barker, N.; Lloyd, C.; Stevens, C.; Harley, J.; Holt, K.; Panagiotidis, G.; Lovell, J.; Beasley, H.; Henderson, C.; Gordon, D.; Auger, K.; Wright, D.; Collins, J.; Raisen, C.; Dyer, L.; Leung, K.; Robertson, L.; Ambridge, K.; Leongamornlert, D.; McGuire, S.; Gilderthorp, R.; Griffiths, C.; Manthravadi, D.; Nichol, S.; Barker, G.; Whitehead, S.; Kay, M.; Brown, J.; Murnane, C.; Gray, E.; Humphries, M.; Sycamore, N.; Barker, D.; Saunders, D.; Wallis, J.; Babbage, A.; Hammond, S.; Mashreghi-Mohammadi, M.; Barr, L.; Martin, S.; Wray, P.; Ellington, A.; Matthews, N.; Ellwood, M.; Woodmansey, R.; Clark, G.; Cooper, J. D.; Tromans, A.; Grafham, D.; Skuce, C.; Pandian, R.; Andrews, R.; Harrison, E.; Kimberley, A.; Garnett, J.; Fosker, N.; Hall, R.; Garner, P.; Kelly, D.; Bird, C.; Palmer, S.; Gehring, I.; Berger, A.; Dooley, C. M.; Ersan-Ürün, Z.; Eser, C.; Geiger, H.; Geisler, M.; Karotki, L.; Kirn, A.; Konantz, J.; Konantz, M.; Oberländer, M.; Rudolph-Geiger, S.; Teucke, M.; Lanz, C.; Raddatz, G.; Osoegawa, K.; Zhu, B.; Rapp, A.; Widaa, S.; Langford, C.; Yang, F.; Schuster, S. C.; Carter, N. P.; Harrow, J.; Ning, Z.; Herrero, J.; Searle, S. M. J.; Enright, A.; Geisler, R.; Plasterk, R. H. A.; Lee, C.; Westerfield, M.; de Jong, P. J.; Zon, L. I.; Postlethwait, J. H.; Nüsslein-Volhard, C.; Hubbard, T. J. P.; Crollius, H. R.; Rogers, J.; Stemple, D. L. *Nature* **2013,** *496,* 498–503. doi:10.1038/nature12111
39. Braunbeck, T.; Böttcher, M.; Hollert, H.; Kosmehl, T.; Lammer, E.; Leist, E.; Rudolf, M.; Seitz, N. *ALTEX* **2005,** *22,* 87–102.
40. Nagel, R. *ALTEX* **2002,** *19,* S38–S48.
41. Shull, A. Y.; Hu, C.-A. A.; Teng, Y. *Amino Acids* **2017,** *49,* 1907–1913. doi:10.1007/s00726-017-2388-3
42. Chan, J. Y.-W.; Zhou, H.; Kwan, Y. W.; Chan, S. W.; Radis-Baptista, G.; Lee, S. M.-Y. *J. Biochem. Mol. Toxicol.* **2017,** *31,* e21964. doi:10.1002/jbt.21964
43. Morash, M. G.; Douglas, S. E.; Robotham, A.; Ridley, C. M.; Gallant, J. W.; Soanes, K. H. *Dis. Models Mech.* **2011,** *4,* 622–633. doi:10.1242/dmm.007310

44. Liao, Q.; Gong, G.; Siu, S. W. I.; Wong, C. T. T.; Yu, H.; Tse, Y. C.; Rádis-Baptista, G.; Lee, S. M. *Toxins* **2018,** *10,* 238. doi:10.3390/toxins10060238
45. Casciaro, B.; Lin, Q.; Afonin, S.; Loffredo, M. R.; de Turris, V.; Middel, V.; Ulrich, A. S.; Di, Y. P.; Mangoni, M. L. *FEBS J.* **2019,** *286,* 3874–3891. doi:10.1111/febs.14940
46. Beharry, A. A.; Wong, L.; Tropepe, V.; Woolley, G. A. *Angew. Chem., Int. Ed.* **2011,** *50,* 1325–1327. doi:10.1002/anie.201006506
47. Lam, P.-Y.; Mendu, S. K.; Mills, R. W.; Zheng, B.; Padilla, H.; Milan, D. J.; Desai, B. N.; Peterson, R. T. *Sci. Rep.* **2017,** *7,* 11839. doi:10.1038/s41598-017-11791-z
48. Rovira, X.; Trapero, A.; Pittolo, S.; Zussy, C.; Faucherre, A.; Jopling, C.; Giraldo, J.; Pin, J.-P.; Gorostiza, P.; Goudet, C.; Llebaria, A. *Cell Chem. Biol.* **2016,** *23,* 929–934. doi:10.1016/j.chembiol.2016.06.013
49. Berlin, S.; Szobota, S.; Reiner, A.; Carroll, E. C.; Kienzler, M. A.; Guyon, A.; Xiao, T.; Trauner, D.; Isacoff, E. Y. *eLife* **2016,** *5,* e12040. doi:10.7554/elife.12040
50. Gómez-Santacana, X.; Pittolo, S.; Rovira, X.; Lopez, M.; Zussy, C.; Dalton, J. A. R.; Faucherre, A.; Jopling, C.; Pin, J.-P.; Ciruela, F.; Goudet, C.; Giraldo, J.; Gorostiza, P.; Llebaria, A. *ACS Cent. Sci.* **2017,** *3,* 81–91. doi:10.1021/acscentsci.6b00353
51. Strähle, U.; Scholz, S.; Geisler, R.; Greiner, P.; Hollert, H.; Rastegar, S.; Schumacher, A.; Selderslaghs, I.; Weiss, C.; Witters, H.; Braunbeck, T. *Reprod. Toxicol.* **2012,** *33,* 128–132. doi:10.1016/j.reprotox.2011.06.121
52. Schweigert, C.; Babii, O.; Afonin, S.; Schober, T.; Leier, J.; Michenfelder, N. C.; Komarov, I. V.; Ulrich, A. S.; Unterreiner, A. N. *ChemPhotoChem* **2019,** *3,* 403–410. doi:10.1002/cptc.201900005
53. Villamizar, N.; Vera, L. M.; Foulkes, N. S.; Sánchez-Vázquez, F. J. *Zebrafish* **2014,** *11,* 173–181. doi:10.1089/zeb.2013.0926
54. Eimon, P. M.; Rubinstein, A. L. *Expert Opin. Drug Metab. Toxicol.* **2009,** *5,* 393–401. doi:10.1517/17425250902882128
55. Ducharme, N. A.; Reif, D. M.; Gustafsson, J.-A.; Bondesson, M. *Reprod. Toxicol.* **2015,** *55,* 3–10. doi:10.1016/j.reprotox.2014.09.005

License and Terms

This is an Open Access article under the terms of the Creative Commons Attribution License (https://creativecommons.org/licenses/by/4.0). Please note that the reuse, redistribution and reproduction in particular requires that the authors and source are credited.

The license is subject to the *Beilstein Journal of Organic Chemistry* terms and conditions: (https://www.beilstein-journals.org/bjoc)

The definitive version of this article is the electronic one which can be found at: doi:10.3762/bjoc.16.6

BEILSTEIN JOURNAL OF ORGANIC CHEMISTRY

Reversible photoswitching of the DNA-binding properties of styrylquinolizinium derivatives through photochromic [2 + 2] cycloaddition and cycloreversion

Sarah Kölsch[1], Heiko Ihmels[*1], Jochen Mattay[2], Norbert Sewald[2] and Brian O. Patrick[3]

Full Research Paper

Open Access

Address:
[1]Department of Chemistry and Biology, Organic Chemistry II, University of Siegen, Adolf-Reichwein-Str. 2, D-57068 Siegen, Germany, [2]Department of Chemistry, Organic and Bioorganic Chemistry, Bielefeld University, PO Box 100121, D-33501 Bielefeld, Germany and [3]Department of Chemistry, Structural Chemistry Facility, The University of British Columbia, 2036 Main Mall, V6T 1Z1, Vancouver, BC, Canada

Email:
Heiko Ihmels[*] - ihmels@chemie.uni-siegen.de

* Corresponding author

Keywords:
azoniahetarenes; DNA ligands; photodimerization; photoswitches

Beilstein J. Org. Chem. **2020,** *16,* 111–124.
doi:10.3762/bjoc.16.13

Received: 07 November 2019
Accepted: 08 January 2020
Published: 23 January 2020

This article is part of the thematic issue "Molecular switches" and is dedicated to Prof. Dr. Hans-Jörg Deiseroth, University of Siegen, on the occasion of his 75th birthday.

Guest Editor: W. Szymanski

© 2020 Kölsch et al.; licensee Beilstein-Institut.
License and terms: see end of document.

Abstract

It was demonstrated that styrylquinolizinium derivatives may be applied as photoswitchable DNA ligands. At lower ligand:DNA ratios (≤1.5), these compounds bind to duplex DNA by intercalation, with binding constants ranging from $K_b = 4.1 \times 10^4$ M to 2.6×10^5 M (four examples), as shown by photometric and fluorimetric titrations as well as by CD and LD spectroscopic analyses. Upon irradiation at 450 nm, the methoxy-substituted styrylquinolizinium derivatives form the corresponding *syn* head-to-tail cyclobutanes in a selective [2 + 2] photocycloaddition, as revealed by X-ray diffraction analysis of the reaction products. These photodimers bind to DNA only weakly by outside-edge association, but they release the intercalating monomers upon irradiation at 315 nm in the presence of DNA. As a result, it is possible to switch between these two ligands and likewise between two different binding modes by irradiation with different excitation wavelengths.

Introduction

The association of DNA-targeting drugs with nucleic acids [1-8] is considered one of the essential properties that determine their biological activity [9]. Specifically, a ligand may occupy particular binding sites of DNA or induce significant structural changes of the nucleic acid. In turn, both of these processes interfere with biologically relevant recognition processes between DNA and enzymes, e.g., topoisomerase [10]. Therefore, many potential lead structures of chemotherapeutic anticancer drugs exhibit DNA-binding properties [1-10]. Nevertheless, most DNA-binding ligands have an insufficient selec-

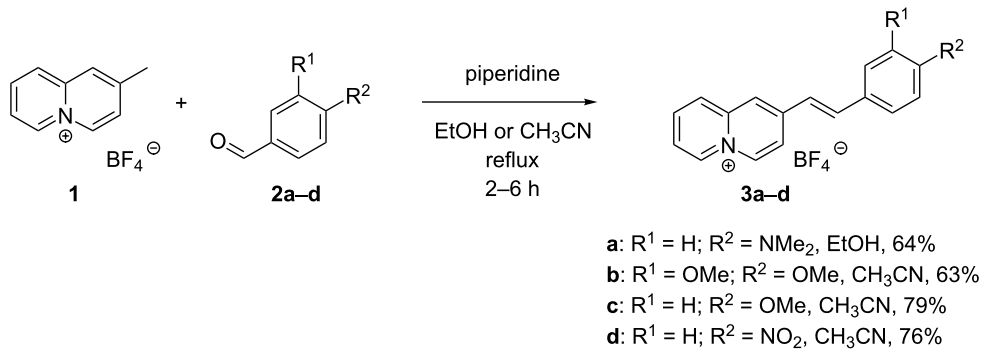
tivity towards the targeted nucleic acid, and they also accumulate in healthy tissue, so that the chemotherapeutic treatment of tumors with DNA-binding drugs still suffers from severe side effects because of the intrinsic toxicity of the employed drugs [11-13]. As a result, there is an urgent need for DNA-targeting chemotherapeutic reagents that can be activated with an external stimulus only at the desired point of action. In this context, light offers several distinct advantages to switch on the activity of an otherwise inactive substrate (prodrug) because light is noninvasive, traceless, and easy to apply, and it enables local and temporal control [14]. To this end, photochromic systems appear to be highly attractive as a basis for photocontrollable substrates because they allow to switch the biological activity on and off due to the reversibility of the photoreaction [15]. Indeed, the application of light to induce and control bioactivity of pharmaceuticals or bio(macro)molecules has been convincingly demonstrated in the emerging field of photopharmacology [16-18]. Consequently, several attempts have also been made to develop photochromic DNA binders. Thus, it has been shown with spiropyran [19-21], stilbene [22,23], azobenzene [24-28], dithienylethene [29-32], chromene [33], and spirooxazine [34] derivatives that specifically modified photochromic ligands bind to DNA only with one of the components of the photochromic equilibrium. Moreover, these ligand–DNA interactions can be photochemically switched between the binding and nonbinding form. Interestingly, the photochromic systems applied in this context are almost exclusively photoinduced electrocyclization or *E*-to-*Z* isomerization reactions, whereas the well-established photochromic cycloaddition–cycloreversion equilibrium to establish photoswitchable DNA binders has so far been widely neglected. In fact, there is only one reported example for the use of the reversible photoinduced dimerization of stilbene derivatives as photoswitchable DNA ligand [35], and in this case, the structure of the photoproduct was not fully identified. Also, it has been shown that a DNA-binding azoniatetracene may be generated by photoinduced [4 + 4] cycloreversion. However, this system was not applied for photoinduced switching of binding properties [36]. Apparently, styryl-substituted aromatic derivatives could fill this gap because the [2 + 2] photocyclization reaction of stilbenes and derivatives thereof is a well-established reversible photoreaction [37-46], and styryl dyes, in particular cationic ones, were shown to be efficient DNA binders [47-58]. Nevertheless, the photochromic nature of DNA-binding styryl dyes has not been applied to use them as photoswitchable DNA binders. Although, there is one reported example that demonstrates the deactivation of a stilbene tyrosine kinase inhibitor by a [2 + 2] photocycloaddition [59].

As the quinolizinium ion has been established as a versatile platform for the development of DNA intercalators [60], we identified styryl-substituted quinolizinium derivatives as a promising basis for the search for photoswitchable DNA binders based on the photocycloaddition–photocycloreversion equilibrium. In fact, some selected styrylquinolizinium derivatives have already been shown to bind to DNA [61-67], however, their photocycloaddition reaction and the propensity of the corresponding photodimers to release the DNA-binding ligand have not been reported so far. Herein, we report on the photochemical and DNA-binding properties of the selected styrylquinolizinium derivatives **3a–d** and demonstrate their ability to operate as photoswitchable DNA ligands.

Results and Discussion

Synthesis

2-Methylquinolizinium tetrafluoroborate (**1**) was synthesized according to published procedures [68]. The piperidine-catalyzed reaction of the latter with the benzaldehyde derivatives **2a–d** gave the 2-styrylquinolizinium derivatives **3a–d** in 63–79% yield (Scheme 1). The known products **3a** and **3c** were identified by comparison with literature data [69], and the new compounds **3b** and **3d** were fully characterized by NMR spectroscopy (^{1}H, ^{13}C, COSY, HSQC, and HMBC), elemental analyses, and mass spectrometry. In all cases, *E*-configuration



Scheme 1: Synthesis of styrylquinolizinium derivatives **3a–d**.

of the alkene double bonds in **3a–d** was indicated by characteristic coupling constants of the alkene protons ($^3J_{H–H}$ = 16 Hz) [70].

Absorption and emission properties

The photophysical properties of the styrylquinolizinium derivatives **3a** and **3c** have already been reported [69], while the ones of **3b** and **3d** were determined in this work (Table 1 and Figure 1). In acetonitrile, the derivatives **3b** and **3d** exhibited long-wavelength absorption maxima at λ_{abs} = 404 nm and 368 nm, with emission bands at λ_{fl} = 548 nm and 419 nm. Derivative **3d** was essentially nonfluorescent (Φ_{fl} < 0.01 in MeCN), whereas compound **3b** (Φ_{fl} = 0.17 in MeCN) had the largest fluorescence quantum yield in comparison to the derivatives **3a** (Φ_{fl} = 0.02 in MeCN) and **3c** (Φ_{fl} = 0.04 in MeCN). In aqueous solution, the compounds exhibited long-wavelength absorption maxima at 434 nm (**3a**), 389 nm (**3b**), 384 nm (**3c**), and 371 nm (**3d**) as well as weak emission bands at 630 nm (**3a**), 538 nm (**3b**), and 507 nm (**3c**). In contrast, the emission intensity of **3d** was too low to identify a maximum, as usually observed with nitro-substituted fluorophores. Unfortunately, the emission quantum yields of **3a–c** could not be determined in water because of the compounds' tendency to dimerize even at very low concentrations (see below). Overall, the absorption and emission data revealed a significantly less pronounced donor–acceptor interplay in the methoxy-substituted derivatives **3b** and **3c** as compared to the strong donor–acceptor system **3a**, as clearly indicated by the blue-shifted absorption and emission bands of **3b** and **3c**. Consequently, the absorption bands of the electron acceptor-substituted derivative **3d** were shifted to even shorter wavelengths.

Table 1: Absorption and emission data for styrylquinolizinium derivatives **3a–d** in MeCN and water.

	MeCN			H_2O	
	λ_{abs}/nm[a]	λ_{fl}/nm[b]	Φ_{fl}[c]	λ_{abs}/nm[a]	λ_{fl}/nm[b]
3a[d]	474	643	0.02	434	630
3b	404	548	0.17[e]	389	538
3c[d]	392	517	0.04	384	507
3d	368	419	<0.01[f]	371	–[g]

[a]Long-wavelength absorption maximum, *c*(**3b**/**3d**) = 20 µM. [b]Fluorescence maximum, λ_{ex} = 394 nm (**3b**) and 370 nm (**3d**). [c]Emission quantum yield, determined with Abs = 0.10 at λ_{ex}, estimated error of Φ_{fl}: ±10%. [d]Taken from [71]. [e]Relative to coumarin 152 (Φ_{fl} = 0.28) [71]. [f]Relative to coumarin 1 (Φ_{fl} = 1.00) [71]. [g]Too weak to be determined.

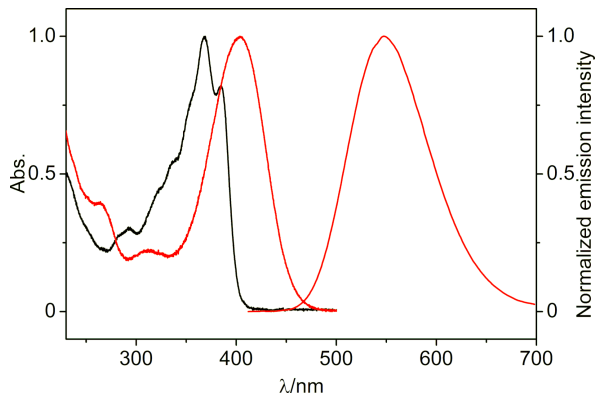


Figure 1: Absorption spectra and normalized emission spectrum (Abs. = 0.10, **3b**: λ_{ex} = 394 nm) of derivatives **3b** (red) and **3d** (black) in MeCN.

DNA-binding properties

The DNA-binding properties of the 2-styrylquinolizinium derivatives **3a–d** were investigated by spectrometric titrations of calf thymus DNA (ct DNA) to **3a–d** in a phosphate buffered solution at pH 7.0 (Figure 2). During the photometric titrations, the initial absorption maxima continuously decreased and new, bathochromically shifted absorption maxima arose at 464 nm (**3a**), 404 nm (**3b**), 399 nm (**3c**), and 378 nm (**3d**), respectively (Figure 2), which clearly indicated the association of these ligands with the nucleic acid [72]. In all cases, isosbestic points developed at the beginning of the titration and eventually became indistinct, which already indicated different binding modes at particular stages of the titration.

The data from the photometric titrations are presented as binding isotherms, and fitting of the experimental data to an established theoretical model [73] gave the corresponding binding constants K_b (cf. Supporting Information File 1). Thus, the largest binding constant was determined for the dimethylamino-substituted styrylquinolizinium derivative **3a** ($K_b = 2.6 \pm 0.1 \times 10^5$ M). The nitro-substituted derivative **3d** had a slightly lower affinity with $K_b = 8.2 \pm 0.2 \times 10^4$ M, and the methoxy-substituted derivatives had the lowest binding constants of $K_b = 4.8 \pm 0.1 \times 10^4$ M (**3b**) and $4.1 \pm 0.1 \times 10^4$ M (**3c**). Overall, these binding affinities resembled the ones of known DNA-intercalating benzoquinolizinium derivatives [60].

In addition, the changes of the emission properties upon the addition of ct DNA to 2-styrylquinolizinium derivatives **3a–d** were determined in fluorimetric titrations (Figure 3). The intensity of the rather weak emission bands of **3a**, **3b**, and **3c** increased significantly upon the addition of DNA. In the case of derivative **3b**, a blue-shift of the emission maximum by 10 nm was also observed. Notably, compound **3a** had the weakest emission intensity, i.e., it was essentially nonfluorescent in aqueous solution, but when it was bound to DNA, it showed a strong light-up effect of the emission with a factor of I/I_0 = 44.

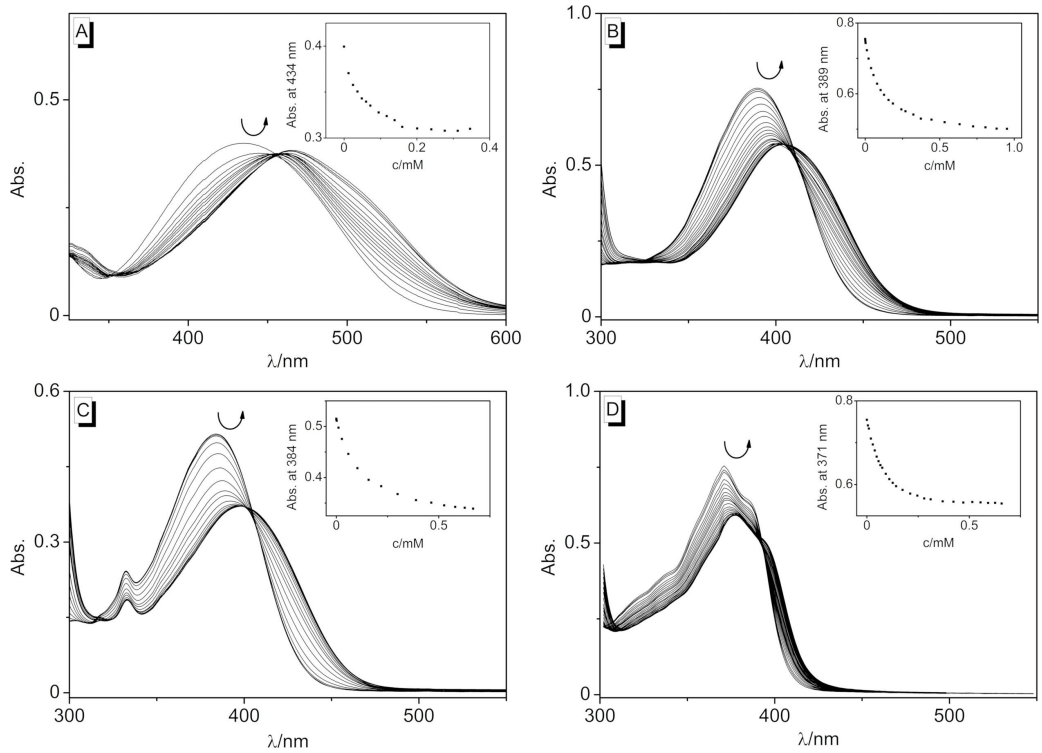


Figure 2: Spectrophotometric titration upon the addition of ct DNA to the styrylquinolizinium derivatives **3a** (A), **3b** (B), **3c** (C), and **3d** (D) in BPE [c_L = 20 μM, c_{DNA} = 1.45 mM (A–C), c_{DNA} = 2.45 mM (D), c_{DNA} in base pairs]. The insets show the plots of absorption vs DNA concentration. The arrows indicate the changes of absorption upon the addition of ct DNA.

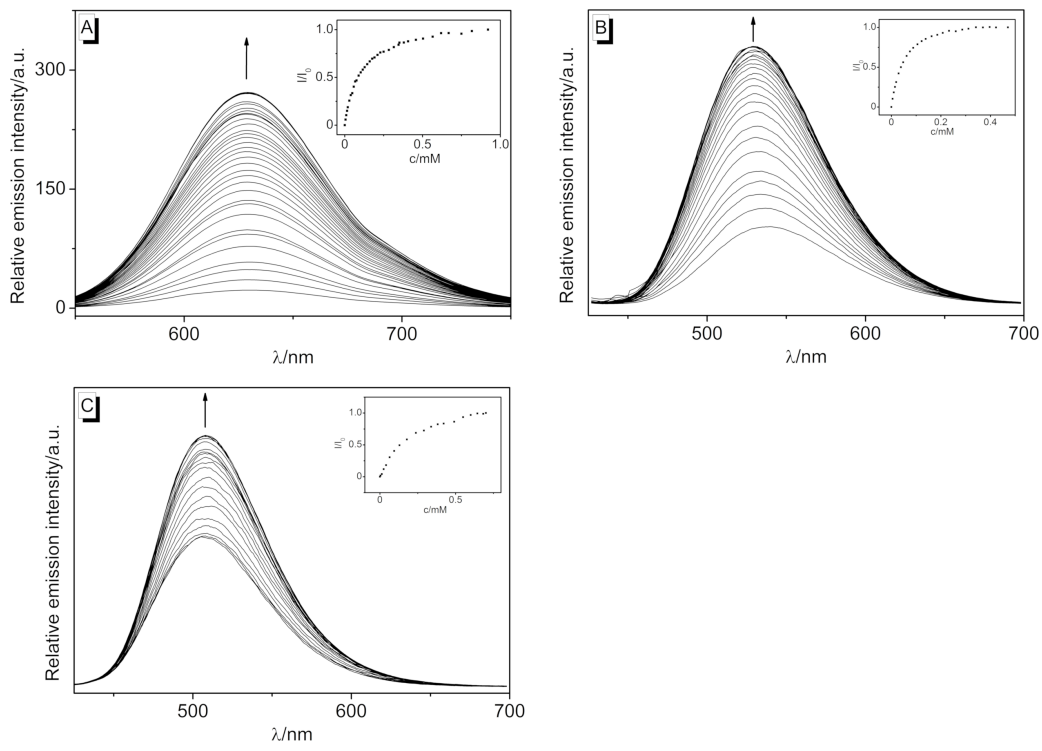


Figure 3: Spectrofluorimetric titration upon the addition of ct DNA to the styrylquinolizinium derivatives **3a** (A), **3b** (B) and **3c** (C) in BPE buffer [c_L = 5 μM (A, C), c_L = 1 μM (B), c_{DNA} = 1.45 mM, c_{DNA} in base pairs]. The insets show the plots of relative emission intensity vs DNA concentration. The arrows indicate the changes of emission intensity upon the addition of ct DNA.

For compounds **3b** and **3c**, significantly smaller light-up factors of I/I_0 = 3.3 and 1.6, respectively, were observed. In contrast, the very low emission intensity of **3d** did not change upon the addition of ct DNA. The fluorescence light-up effects of the ligands **3a–c** upon association with DNA resembled the ones observed for other styryl-substituted quinolizinium derivatives [62-67]. Accordingly, the emission enhancement most likely resulted from the accommodation of the ligand in the constrained binding site of the DNA, which led to a restricted conformational flexibility. As a result, conformational changes of the styryl substituent in the excited state that lead to radiationless deactivation in solution were significantly suppressed within the binding site so that emission became competitive.

The DNA-binding properties of the ligands **3a–d** were further investigated by circular dichroism (CD) and flow linear dichroism (LD) spectroscopy [74,75] in phosphate buffer at different ligand-to-DNA ratios (LDR). The mixtures of compounds **3a–d** with ct DNA showed clear induced circular dichroism (ICD) and LD bands in the absorption region of the ligands that further confirmed the binding of the ligands (Figure 4). In all cases, a positive ICD signal developed, and with increasing LDR, the characteristic CD bands of duplex DNA at 254 nm and 277 nm [76] increased slightly. Ligand **3a** exhibited a strong positive and a weak negative ICD signal at 473 nm and 583 nm, respectively, in the presence of DNA, along with a weaker positive signal at 346 nm (Figure 4A1). For LD spectroscopic analysis, the DNA molecules were oriented in a hydrodynamic field of a rotating couette (flow linear dichroism). The corresponding LD spectra were the result of the differential absorption of linearly polarized light, which was polarized parallel and perpendicular to a reference axis, respectively, thus indicating the orientation of the transition moment of the chromophores relative to the electric field vector of the light [75]. The LD spectrum of DNA-bound **3a** displayed a negative band in the absorption range of the ligand at small LDR (≤1.0) at 506 nm, whereas at higher values, a positive band developed, which led to a distorted bisignate band. In the case of ligands **3b** and **3c**, a similar development of LD bands was observed with increasing LDR, however, the effect was more pronounced with a strong positive LD signal at 397 nm (**3b**) and 382 nm (**3c**) at LDR = 0.5 (Figure 4B2 and Figure 4C2). Interestingly, the CD spectra of **3b** and **3c** did not resemble the ones of **3a**. Both ligands showed a clear positive ICD band at 400–407 nm (**3b**) and 382 nm (**3c**), but only in the case of **3b**, a weak blue-shifted ICD band also appeared at lower LDR (Figure 4B1 and Figure 4C1). Ligand **3d** exhibited positive ICD and negative LD signals at 382 nm upon binding to DNA (Figure 4D). Altogether, the CD and LD spectra of ligands **3a–c** at low LDR as well as the ones of **3d** in general showed the characteristic signatures of DNA intercalators. Namely, the negative LD bands of the bound ligands unambiguously revealed an intercalative mode [75,76], whereas the positive ICD bands indicated an essentially perpendicular alignment of the transition dipole moments of the ligands relative to the ones of the DNA base pairs [75,76]. Considering a dipole moment of the donor–acceptor systems **3a–c** along the long molecular axis, a binding mode in which the ligand is accommodated in the intercalation site with its long molecular axis perpendicular to the long axis of the binding site could be deduced. With increasing LDR, however, another binding mode became predominant for the ligands **3a–c**, as particularly indicated by the development of a positive LD band in the absorption range of the ligand that denoted groove binding [74-76]. It is proposed that with increasing ligand concentration, i.e., at larger LDR, the ligands tended to form aggregates, as commonly observed for donor–acceptor dyes, that stacked along the grooves of DNA.

Photocycloaddition reactions

The photochemical properties of the derivatives **3a–d** were investigated. Firstly, the substrates were irradiated in acetonitrile solution at 520–535 nm (**3a**), 420–470 nm (**3b** and **3c**), and >395 nm (**3d**), and the photoreaction was monitored photometrically. Notably, the amino-substituted derivative **3a** did not react under these conditions, as indicated by only marginal changes of the absorption spectrum (Figure 5A). Presumably, the strong donor–acceptor system in **3a** led to an intramolecular charge-transfer (ICT) state that did not lead to a subsequent photoreaction [77]. In contrast, the absorption bands of the substrates **3b–d** decreased relatively fast upon irradiation, but the maxima did not disappear completely (Figure 5B–D). Even after 4 h, compound **3b** exhibited a weak band at λ_{abs} = 404 nm, whereas the newly formed band at λ_{abs} = 332 nm did not increase further (Figure 5B). In this case, additional ^{1}H NMR spectroscopic analysis showed that the derivatives **3c** and **3d** were initially converted to the *Z*-isomer by irradiation at λ = 450 nm or λ = 360 nm in acetonitrile, as indicated by the upfield shift of the signals of the alkene double bonds and the characteristic coupling constants of Z-configured protons ($^3J_{H–H}$ = 12 Hz). Notably, the derivative **3c** did not react any further under these conditions (cf. Supporting Information File 1). However, it was observed that further irradiation of the nitro-substituted derivative **3d** furnished the dimer in acetonitrile, as shown by the development of the characteristic cyclobutane protons at 4.85–4.95 ppm. In contrast, the NMR-spectroscopic analysis in D_2O showed that the derivative **3b** gave the corresponding cycloaddition product much faster, i.e., within a few minutes under these conditions, and the formation of the corresponding *Z*-isomer proceeded only to a marginal extent.

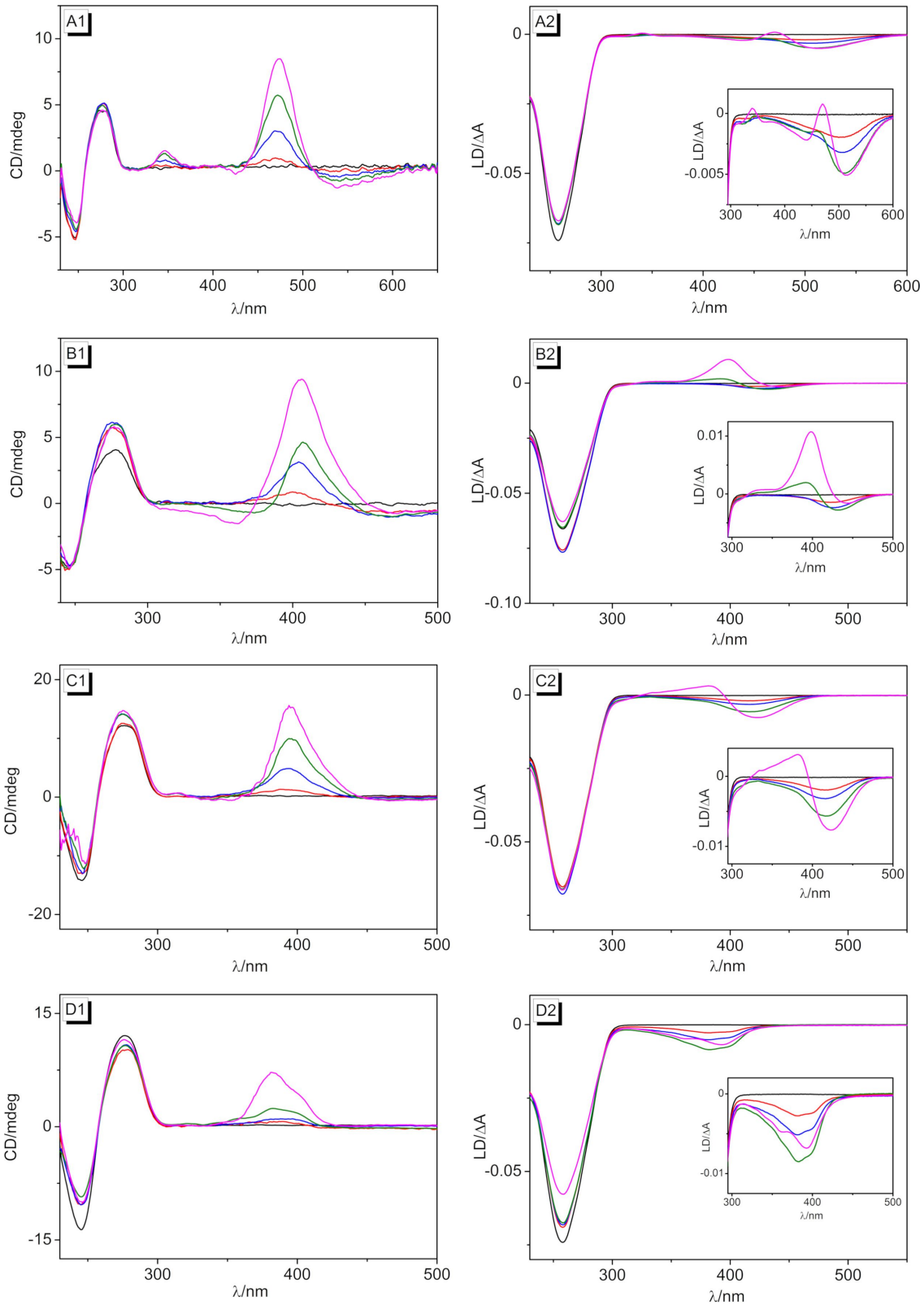


Figure 4: CD and LD spectra of the styryl derivatives **3a** (A), **3b** (B), **3c** (C), and **3d** (D) with ct DNA in BPE buffer [$c_{ct\ DNA}$ = 20 μM (A1, B1), $c_{ct\ DNA}$ = 50 μM (C1, D1), and $c_{ct\ DNA}$ = 500 μM (A2–D2), with *LDR* = 0 (black), 0.5 (red), 1.0 (blue), 1.5 (green), and 2.0 (magenta), $c_{ct\ DNA}$ in base pairs).

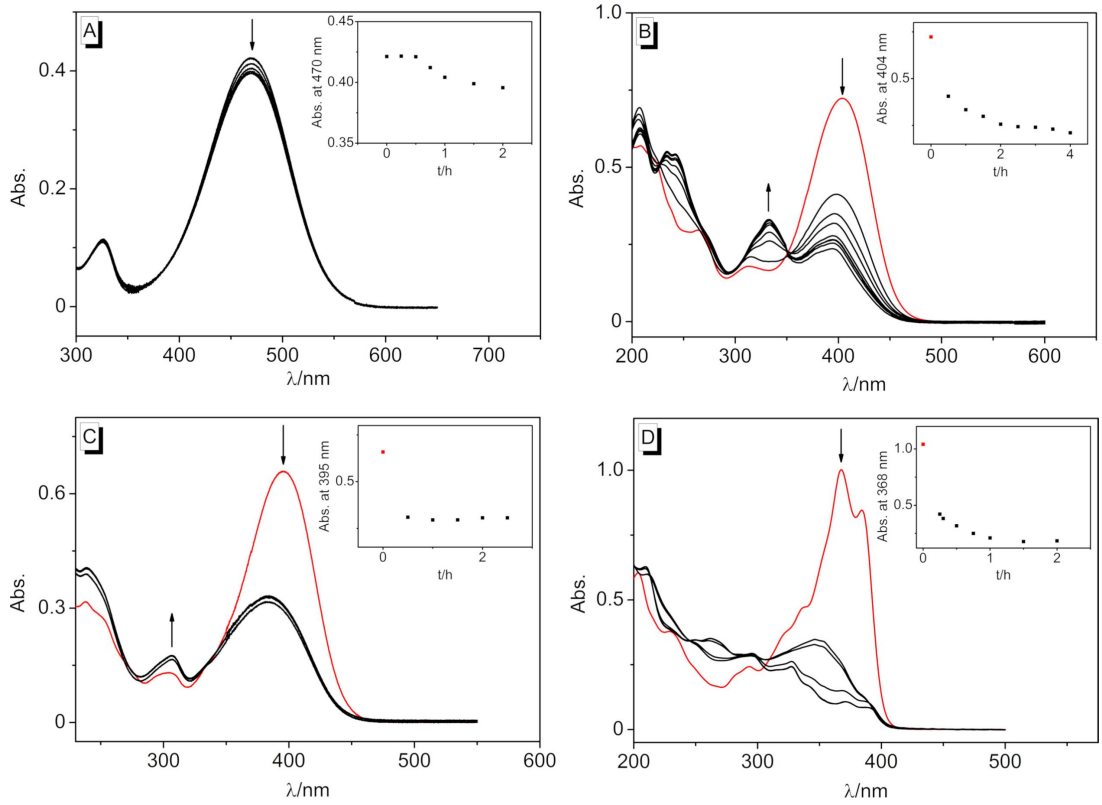


Figure 5: Spectrophotometric monitoring of the irradiation of styrylquinolizinium derivatives **3a** (A), **3b** (B), **3c** (C), and **3d** (D) in acetonitrile [c_L = 10 µM (A), c_L = 20 µM (B, C, D)]. The arrows indicate the changes of absorption upon irradiation.

In aqueous solution, the substrates **3a–d** showed essentially the same photochemical behavior, however, with different reaction times and conversions. Thus, the photoreaction of derivative **3b** was complete after 90 min (Figure 6A), whereas the reaction of derivative **3c** took more than 5 h. The early stages of the photoreaction of substrate **3b** in water were monitored in short time intervals (1 s) to identify possible primary photoprocesses (Figure 7A). The initial maximum of the monomer **3b** decreased substantially by approximately half within a second, whereas further reaction was indicated by the appearance of the absorption maximum of **4b** at 317–331 nm. Notably, no additional intermediate absorption band appeared, and three isosbestic points developed at 239 nm, 310 nm, and 337 nm after the initial steps. These observations provided evidence that the phototransformation of the styrylquinolizinium species **3b** to its photodimer **4b** was a two-step process.

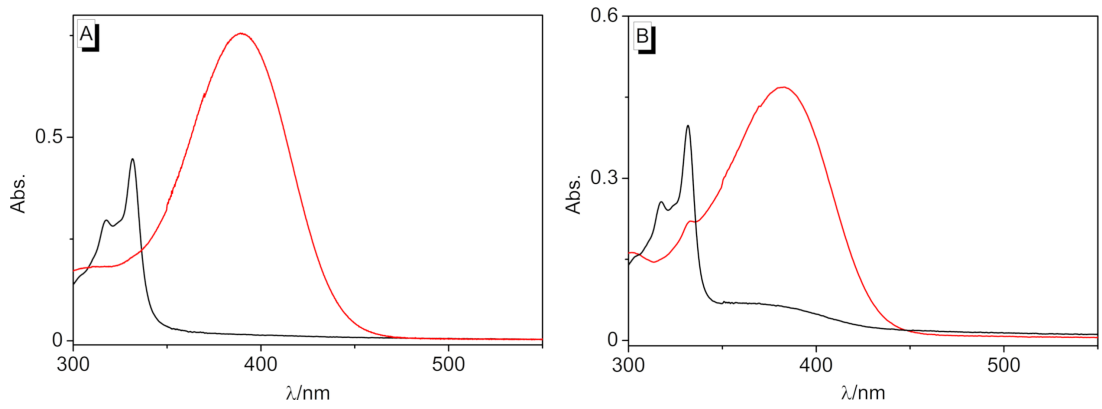


Figure 6: Absorption of the monomers (c = 20 µM, red) **3b** (A) and **3c** (B) and their dimers (black) **4b** and **4c** in H_2O after 1.5 h and 4 h, respectively, at ca. 450 nm.

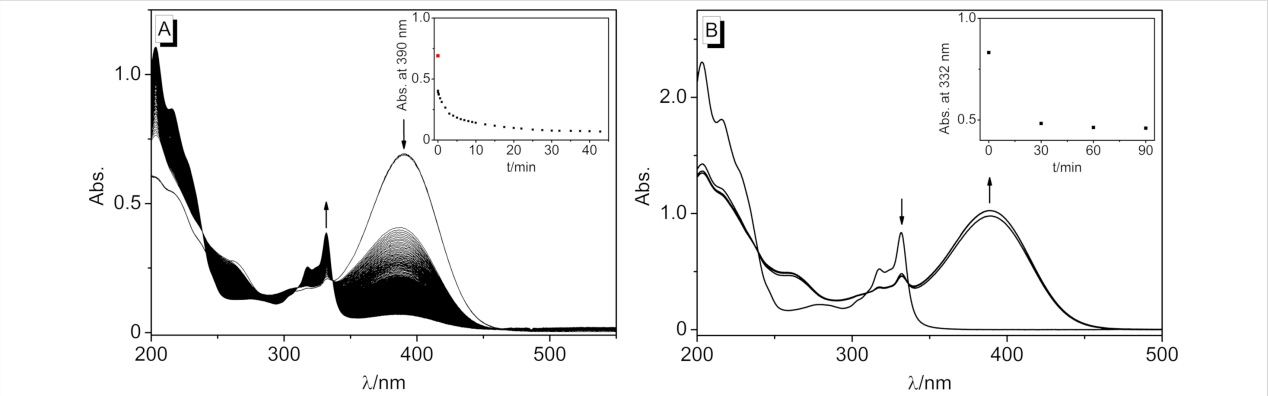


Figure 7: Photometric monitoring of the photoreaction of **3b** (c = 20 µM) to the dimer **4b** by irradiation at ca. 450 nm in H_2O (A) and of the photo-induced cycloreversion of **4b** (c = 20 µM) to the monomer **3b** at 315 nm in H_2O (B).

Preparative-scale photoreactions were performed with the methoxy-substituted derivatives **3b** and **3c** because the photometric studies (see above) indicated reasonable reaction times. Unfortunately, it turned out that due to the low solubility of these derivatives in water, the concentrations required for a bimolecular reaction could not be accomplished. However, it is well known that [2 + 2] photodimerizations can also be performed in the solid state or with a thoroughly stirred suspension [37,43,78]. Therefore, suspensions of **3b** und **3c** in water were irradiated with an LED lamp at 450–470 nm to give the 2,2'-(2,4-diphenyl-1,3-cyclobutanediyl)bisquinolizinium **4b** and **4c** as photoproducts in quantitative yield. The products **4b** and **4c** were fully characterized by NMR spectroscopy (^{1}H, ^{13}C, COSY, HSQC, HMBC, and ROESY) and mass spectrometry, which revealed a cyclobutane structure, specifically by the appearance of the characteristic NMR signals of the cyclobutane at 4.89–5.00 ppm [42-46]. Unfortunately, detailed 2D NMR and spectroscopic analyses did not allow a conclusive assignment of the configuration of the products. Even in the ROESY NMR spectra, only unspecific correlations were detected. However, as both products could be obtained as single crystals after slow evaporation, their structure was determined by single crystal X-ray diffraction (XRD) analysis (Figure 8, cf. Supporting Information File 1). The cyclobutane **4b** crystallized from water

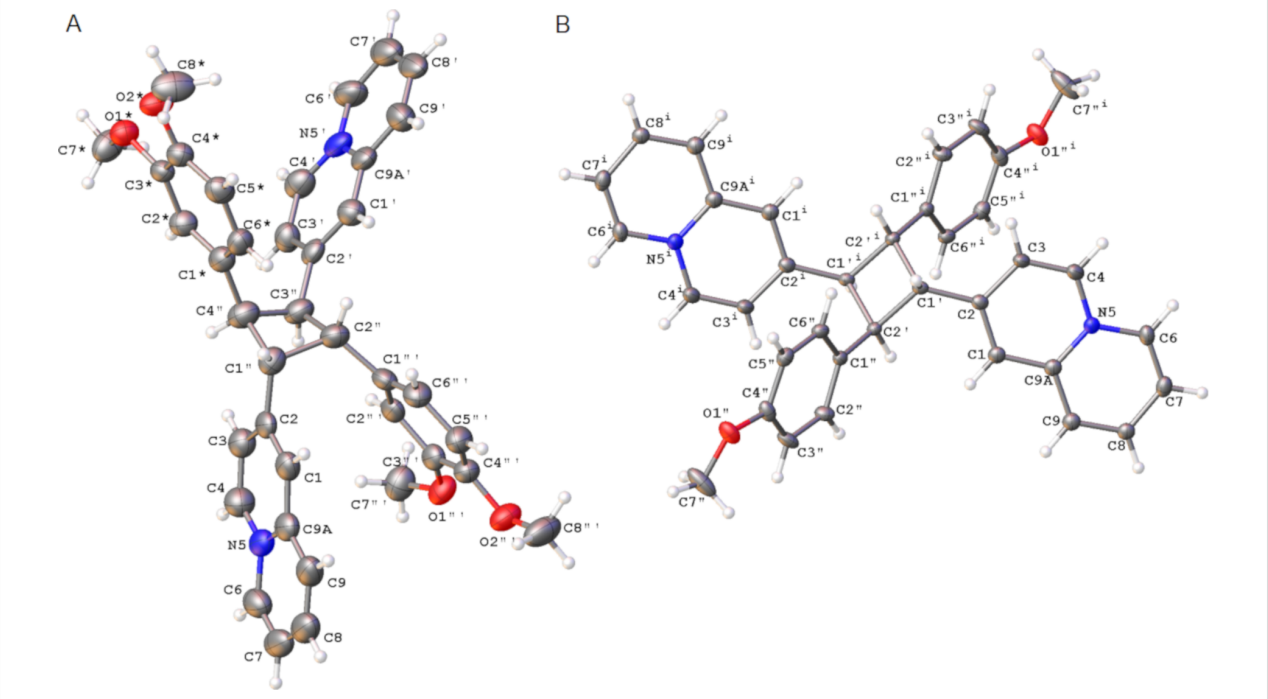


Figure 8: ORTEP drawings of cyclobutane derivatives **4b** (A) and **4c** (B) in the solid state (thermal ellipsoids indicate 50% probability). The tetrafluoroborate counterions were omitted for clarity.

in the monoclinic space group $P2_1/n$, and the derivative **4c** crystallized from water in the triclinic space group $P\bar{1}$. Both XRD analyses clearly showed that both cyclobutane products were formed as *rctt* configured dimers **4b** and **4c** (Figure 8).

The products **4b** and **4c** may have formed by a *syn* head-to-tail dimerization of the *E*-configured substrate **3a** and **3b** or by an *anti* head-to-tail photodimerization of the initially formed *Z*-isomers *Z*-**3a** and *Z*-**3b**, with both processes generally being possible starting from **3b** and **3c** (Scheme 2). On the one hand, the photometric monitoring as well as the ^{1}H NMR spectroscopic studies of the photoreaction of **3b** indicated a preceding *E*-to-*Z* isomerization (cf. Supporting Information File 1) that may have been followed by a [2 + 2] photodimerization (Scheme 2). However, it is difficult to explain why the photocycloaddition of the *Z*-isomers *Z*-**3b** and *Z*-**3c** led exclusively to the dimer, because such a selectivity has not been reported so far for (*Z*)-stilbenes. On the other hand, the reaction was performed using suspensions, so that the reaction may also have taken place with undissolved solid in which the *E*-to-*Z* isomerization was most likely suppressed due to the restricted space in the confined medium. Thus, the selective formation of the dimers **4b** and **4c** is reminiscent of the high stereoselectivity observed for [2 + 2] photodimerizations in organized media or in the solid state [37-41].

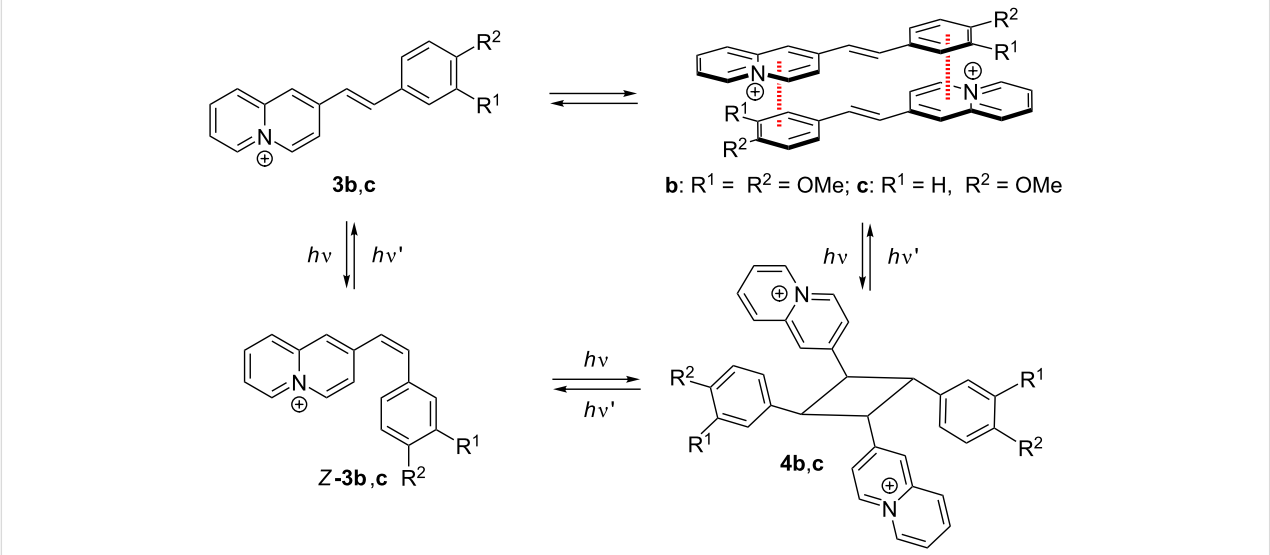
Considering the pronounced donor–acceptor interplay in **3b** and **3c** and the resulting strong dipole moment, it may be proposed that these compounds form dimeric aggregates in the solid state and even in solution through dipole–dipole interactions and directional π stacking (Scheme 2), as observed, for example, with donor-substituted benzoquinolizinium derivatives [79] or donor-substituted styrylpyridinium derivatives [80-82]. Hence, an ideal overlap of the π systems and antiparallel alignment of dipole moments is realized in a *syn* head-to-tail complex where irradiation would lead directly to the photodimers **4b** and **4c** in a topochemical reaction (Scheme 2).

Notably, the cyclobutane derivatives **4b** and **4c** were not persistent in solution for extended periods of time. As already shown for several cyclobutane derivatives, these compounds tend to isomerize to the corresponding *rttt* isomers [83-86].

With derivative **4b** as a representative example, it was demonstrated that the photodimers can be transformed back to the monomers. Thus, upon irradiation of cyclobutane **4b** at 315 nm in H_2O, the monomer **3b** formed, as indicated by the development of its characteristic absorption band (Figure 7B). After 30 min, the reaction was almost complete, however, dimer **4b** still remained in solution in the photostationary state.

Interactions of the photodimer **4b** with DNA

The interactions of dimer **4b** with DNA were investigated by photometric titrations as well as by CD and LD spectroscopy (Figure 9). Upon the addition of ct DNA to compound **4b** in buffered solution, the absorption maximum decreased slightly, but apart from a broadening of the band at the long-wavelength tail, the overall shape of the spectrum did not change (Figure 9). Furthermore, only a small positive ICD band in the absorption region of ligand **4b** appeared at 300–350 nm that developed into a significantly broader band with increasing LDR. At the same time, the signal of the DNA did not change in the presence of the ligand. Additionally, the LD experiment showed a small positive signal at 300–350 nm, and the negative band of the ct



Scheme 2: Possible pathways for the selective photodimerization of styrylquinolizinium derivatives **3b** and **3c**.

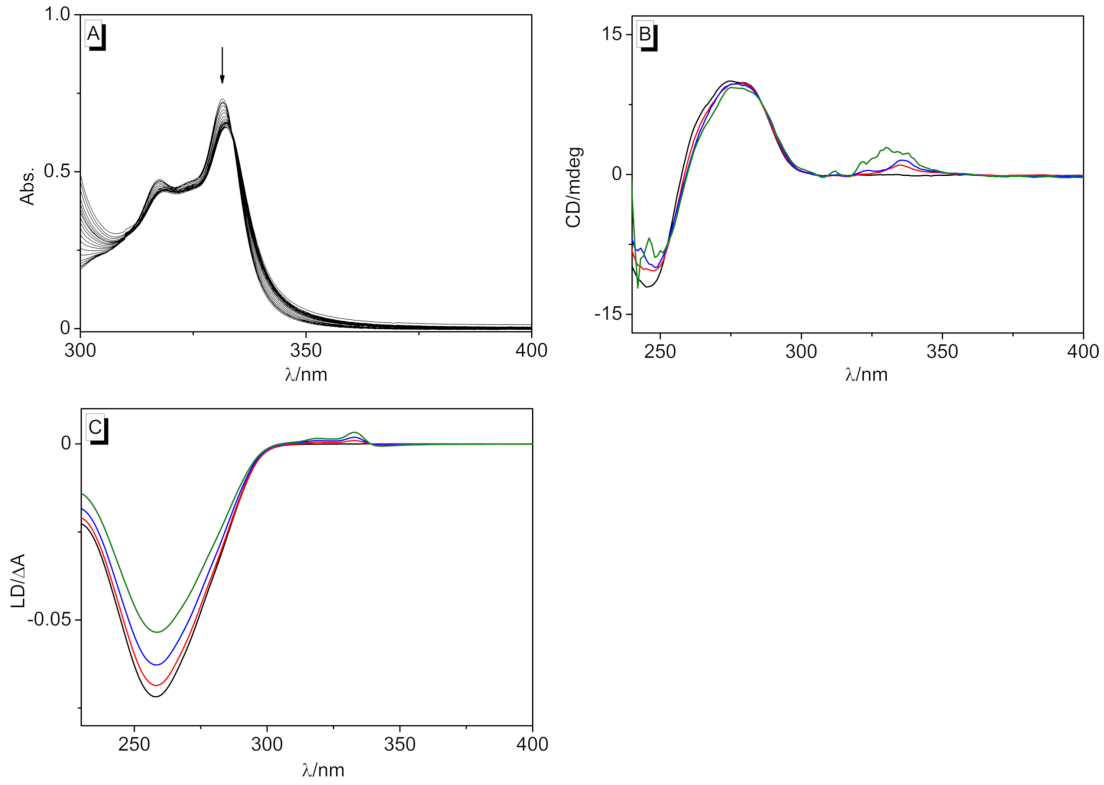


Figure 9: A) Spectrophotometric titration of ct DNA to dimer **4b** in BPE buffer (c_L = 20 μM, $c_{ct\ DNA}$ = 1.45 mM, $c_{ct\ DNA}$ in base pairs). The arrow indicates the changes of absorption upon the addition of ct DNA. B) CD spectra of the dimer **4b** with ct DNA (50 μM) in BPE buffer with LDR = 0 (black), 0.5 (red), 1.0 (blue), and 2.0 (green). C) LD spectra of dimer **4b** with ct DNA (c = 500 μM) in BPE buffer with LDR = 0 (black), 0.04 (red), 0.08 (blue), and 2.0 (green).

DNA at 254 nm decreased. These spectroscopic data indicated a very weak interaction of the substrate **4b** with DNA, and the band broadening in the absorption region already confirmed an aggregation of the molecules along the DNA backbone at very high ligand concentrations. Nevertheless, the CD and LD spectroscopic data revealed at least some specific binding interactions of **4b** with DNA that caused a distinct orientation of the aromatic units relative to the host DNA. In particular, the weak positive LD band indicated an alignment of the aromatic units along the DNA grooves. In addition, the close vicinity of the quinolizinium substituents to the DNA helix was further confirmed by the CD band in the absorption region of the quinolizinium moiety, as it resulted from the coupling of its transition dipole moment with the ones of the DNA bases. Overall, these data revealed a loose binding of the cyclobutane derivative **4b** to DNA through outside-edge binding of the ligand that enabled the association of one or two aromatic units in the DNA grooves.

Photoswitching of the DNA binding properties

Finally, it was tested whether the DNA-binding quinolizinium derivative **3b** could be released photochemically from cyclobutane **4b** in the presence of DNA. For that purpose, a mixture of the photodimer and DNA was irradiated at 315 nm using an LED, and the reaction was monitored by absorption and CD spectroscopy (Figure 10). In the course of the photoreaction, the formation of **3b** was indicated by the emergence of its characteristic long-wavelength absorption band, whose shape and shift matched its DNA-bound form. The association of the released monomer **3b** with DNA was also clearly demonstrated by the ICD band of the DNA-bound ligand. It should be noted, however, that the photoinduced conversion of the dimer was not complete, indicating a photostationary state. Noteworthy, irradiation of the bound ligand at ca. 450 nm using an LED regenerated the cyclobutane dimer, as shown unambiguously by the formation of the characteristic signature of its absorption and CD bands and by the disappearance of the monomer's signals (Figure 10). Although the sequence of photocycloreversion and photoaddition could be performed four times, a slight but steady photobleaching or photodecomposition was observed. It should be noted that the DNA-bound ligand did not dimerize upon irradiation because within the intercalation site, it could not approach another quinolizinium molecule that was required for the photoreaction. Instead, the photodimerization most likely

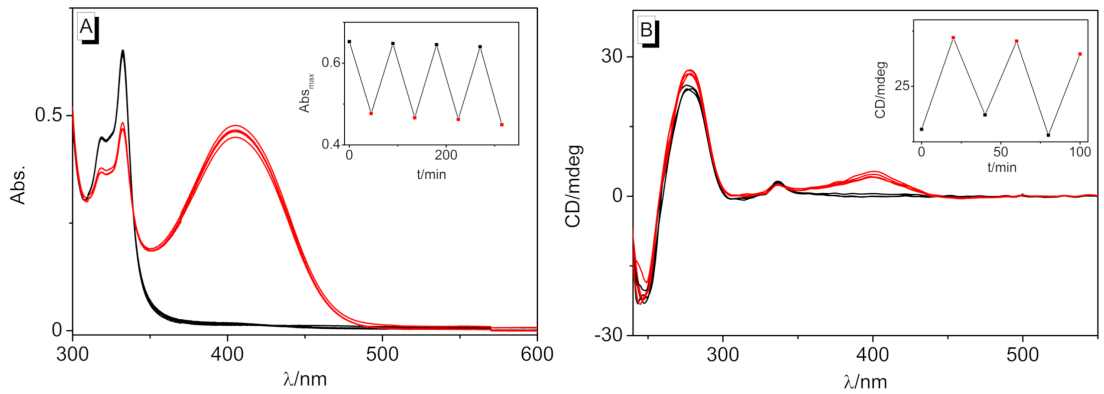
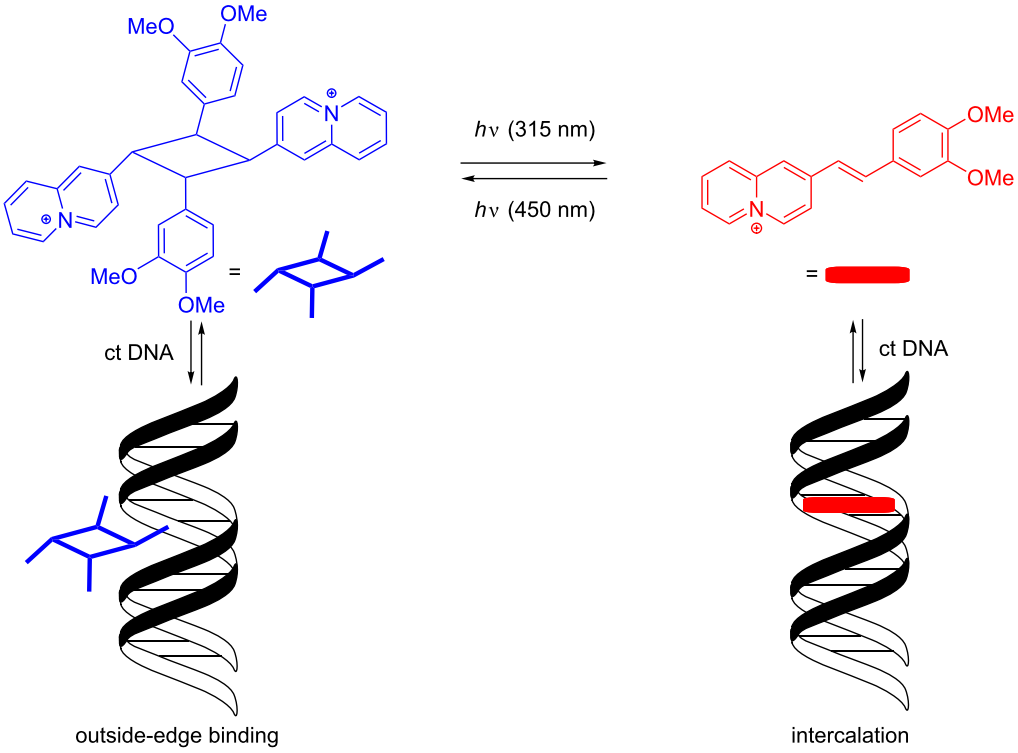


Figure 10: A) Photometric and B) CD spectroscopic monitoring of the photoinduced switching (**4b**: λ_{ex} = 315 nm, **3b**: λ_{ex} = 450 nm) between **4b** (c = 20 µM, black) and **3b** (red) in the presence of ct DNA (c = 20 µM) in BPE buffer. DNA concentration in base pairs.

involved the free or loosely backbone-associated ligands that were in a dynamic equilibrium with the respective intercalator–DNA complexes, as shown for aryl stilbazonium ligands [35]. At the same time, the photoinduced cycloreversion may have taken place both with the free or DNA-bound dimer. Specifically, the dimer is only loosely bound to the DNA backbone so that the cycloreversion reaction does not experience steric constrains that may hinder the photoreaction. Furthermore, it has been demonstrated that the photoinduced cycloreversion of quinolizinium dimers is even enhanced in the presence of DNA [36].

Conclusion

In summary, we have shown that appropriately substituted styrylquinolizinium derivatives constitute a new class of photoswitchable DNA ligands. It was shown that these ligands bind to duplex DNA mainly by intercalation and that their *syn* head-to-tail photodimers, obtained by selective [2 + 2] photocycloaddition, bind to DNA only weakly by outside-edge association. Most notably, it was possible to switch between those two binding modes by irradiation with different excitation wavelengths (Scheme 3). Although the system still has to be improved with respect to photostability, it may be considered as a



Scheme 3: Photoinduced switching of the DNA binding properties of styrylquinolizinium compound **3b**.

promising complementary approach toward the development of photoswitchable bioactive compounds.

Supporting Information

Supporting Information File 1

Additional spectroscopic data, detailed experimental procedures, ^{1}H NMR spectra, and crystallographic data.
[https://www.beilstein-journals.org/bjoc/content/supplementary/1860-5397-16-13-S1.pdf]

Acknowledgements

We thank Ms. Sandra Uebach, Ms. Jennifer Hermann, and Mr. Aboubakr Hamad for technical assistance.

Funding

Financial support by the Deutsche Forschungsgemeinschaft (DFG) is gratefully acknowledged.

ORCID® iDs

Heiko Ihmels - https://orcid.org/0000-0003-0969-0426
Jochen Mattay - https://orcid.org/0000-0002-1511-7960
Norbert Sewald - https://orcid.org/0000-0002-0309-2655

References

1. Rahman, A.; O'Sullivan, P.; Rozas, I. *Med. Chem. Commun.* **2019,** *10,* 26–40. doi:10.1039/c8md00425k
2. Bhaduri, S.; Ranjan, N.; Arya, D. P. *Beilstein J. Org. Chem.* **2018,** *14,* 1051–1086. doi:10.3762/bjoc.14.93
3. Wang, M.; Yu, Y.; Liang, C.; Lu, A.; Zhang, G. *Int. J. Mol. Sci.* **2016,** *17,* No. 779. doi:10.3390/ijms17060779
4. Rescifina, A.; Zagni, C.; Varrica, M. G.; Pistarà, V.; Corsaro, A. *Eur. J. Med. Chem.* **2014,** *74,* 95–115. doi:10.1016/j.ejmech.2013.11.029
5. Bolhuis, A.; Aldrich-Wright, J. R. *Bioorg. Chem.* **2014,** *55,* 51–59. doi:10.1016/j.bioorg.2014.03.009
6. Banerjee, S.; Veale, E. B.; Phelan, C. M.; Murphy, S. A.; Tocci, G. M.; Gillespie, L. J.; Frimannsson, D. O.; Kelly, J. M.; Gunnlaugsson, T. *Chem. Soc. Rev.* **2013,** *42,* 1601–1618. doi:10.1039/c2cs35467e
7. Pazos, E.; Mosquera, J.; Vázquez, M. E.; Mascareñas, J. L. *ChemBioChem* **2011,** *12,* 1958–1973. doi:10.1002/cbic.201100247
8. Ihmels, H.; Thomas, L. Intercalation of Organic Ligands as a Tool to Modify the Properties of DNA. In *Materials Science of DNA Chemistry;* Jin, J.-l.; Grote, J., Eds.; CRC Press: Boca Raton, FL, USA, 2011; pp 49–75.
9. Pett, L.; Hartley, J.; Kiakos, K. *Curr. Top. Med. Chem.* **2015,** *15,* 1293–1322. doi:10.2174/1568026615666150413155431
10. Pommier, Y. *ACS Chem. Biol.* **2013,** *8,* 82–95. doi:10.1021/cb300648v
11. Carelle, N.; Piotto, E.; Bellanger, A.; Germanaud, J.; Thuillier, A.; Khayat, D. *Cancer* **2002,** *95,* 155–163. doi:10.1002/cncr.10630
12. Sonis, S. T.; Elting, L. S.; Keefe, D.; Peterson, D. E.; Schubert, M.; Hauer-Jensen, M.; Bekele, B. N.; Raber-Durlacher, J.; Donnelly, J. P.; Rubenstein, E. B. *Cancer* **2004,** *100* (Suppl. 9), 1995–2025. doi:10.1002/cncr.20162
13. Ludwig, H.; Van Belle, S.; Barrett-Lee, P.; Birgegård, G.; Bokemeyer, C.; Gascón, P.; Kosmidis, P.; Krzakowski, M.; Nortier, J.; Olmi, P.; Schneider, M.; Schrijvers, D. *Eur. J. Cancer* **2004,** *40,* 2293–2306. doi:10.1016/j.ejca.2004.06.019
14. Albini, A.; Fagnoni, M. The Greenest Reagent in Organic Synthesis: Light. In *Green Chemical Reactions;* Tundo, P.; Esposito, V., Eds.; NATO Science for Peace and Security Series (Series C: Environmental Security); Springer: Dordrecht, Netherlands, 2008; pp 173–189. doi:10.1007/978-1-4020-8457-7_8
15. Pianowski, Z. L. *Chem. – Eur. J.* **2019,** *25,* 5128–5144. doi:10.1002/chem.201805814
16. Hüll, K.; Morstein, J.; Trauner, D. *Chem. Rev.* **2018,** *118,* 10710–10747. doi:10.1021/acs.chemrev.8b00037
17. Szymański, W.; Beierle, J. M.; Kistemaker, H. A. V.; Velema, W. A.; Feringa, B. L. *Chem. Rev.* **2013,** *113,* 6114–6178. doi:10.1021/cr300179f
18. Velema, W. A.; Szymanski, W.; Feringa, B. L. *J. Am. Chem. Soc.* **2014,** *136,* 2178–2191. doi:10.1021/ja413063e
19. Andersson, J.; Li, S.; Lincoln, P.; Andreasson, J. *J. Am. Chem. Soc.* **2008,** *130,* 11836–11837. doi:10.1021/ja801968f
20. Hammarson, M.; Nilsson, J. R.; Li, S.; Lincoln, P.; Andréasson, J. *Chem. – Eur. J.* **2014,** *20,* 15855–15862. doi:10.1002/chem.201405113
21. Brieke, C.; Heckel, A. *Chem. – Eur. J.* **2013,** *19,* 15726–15734. doi:10.1002/chem.201302640
22. Czerwinska, I.; Juskowiak, B. *Int. J. Biol. Macromol.* **2012,** *51,* 576–582. doi:10.1016/j.ijbiomac.2012.06.027
23. Fortuna, C. G.; Mazzucato, U.; Musumarra, G.; Pannacci, D.; Spalletti, A. *J. Photochem. Photobiol., A* **2010,** *216,* 66–72. doi:10.1016/j.jphotochem.2010.09.007
24. Dohno, C.; Uno, S.-n.; Nakatani, K. *J. Am. Chem. Soc.* **2007,** *129,* 11898–11899. doi:10.1021/ja074325s
25. Dohno, C.; Yamamoto, T.; Nakatani, K. *Eur. J. Org. Chem.* **2009,** 4051–4058. doi:10.1002/ejoc.200900323
26. Basak, A.; Mitra, D.; Kar, M.; Biradha, K. *Chem. Commun.* **2008,** 3067–3069. doi:10.1039/b801644e
27. Wang, X.; Huang, J.; Zhou, Y.; Yan, S.; Weng, X.; Wu, X.; Deng, M.; Zhou, X. *Angew. Chem.* **2010,** *122,* 5433–5437. doi:10.1002/ange.201002290
28. Bergen, A.; Rudiuk, S.; Morel, M.; Le Saux, T.; Ihmels, H.; Baigl, D. *Nano Lett.* **2016,** *16,* 773–780. doi:10.1021/acs.nanolett.5b04762
29. Linares, M.; Sun, H.; Biler, M.; Andréasson, J.; Norman, P. *Phys. Chem. Chem. Phys.* **2019,** *21,* 3637–3643. doi:10.1039/c8cp05326j
30. Mammana, A.; Carroll, G. T.; Areephong, J.; Feringa, B. L. *J. Phys. Chem. B* **2011,** *115,* 11581–11587. doi:10.1021/jp205893y
31. Pace, T. C. S.; Müller, V.; Li, S.; Lincoln, P.; Andréasson, J. *Angew. Chem., Int. Ed.* **2013,** *52,* 4393–4396. doi:10.1002/anie.201209773
32. Presa, A.; Barrios, L.; Cirera, J.; Korrodi-Gregório, L.; Pérez-Tomás, R.; Teat, S. J.; Gamez, P. *Inorg. Chem.* **2016,** *55,* 5356–5364. doi:10.1021/acs.inorgchem.6b00362
33. Paramonov, S. V.; Lokshin, V.; Ihmels, H.; Fedorova, O. A. *Photochem. Photobiol. Sci.* **2011,** *10,* 1279–1282. doi:10.1039/c1pp05094j
34. Ihmels, H.; Mattay, J.; May, F.; Thomas, L. *Org. Biomol. Chem.* **2013,** *11,* 5184–5188. doi:10.1039/c3ob40930a
35. Juskowiak, B.; Chudak, M. *Photochem. Photobiol.* **2004,** *79,* 137–144. doi:10.1111/j.1751-1097.2004.tb00003.x
36. Ihmels, H.; Otto, D.; Dall'Acqua, F.; Faccio, A.; Moro, S.; Viola, G. *J. Org. Chem.* **2006,** *71,* 8401–8411. doi:10.1021/jo0612271

37. Ramamurthy, V.; Sivaguru, J. *Chem. Rev.* **2016,** *116,* 9914–9993. doi:10.1021/acs.chemrev.6b00040
38. Bibal, B.; Mongin, C.; Bassani, D. M. *Chem. Soc. Rev.* **2014,** *43,* 4179–4198. doi:10.1039/c3cs60366k
39. MacGillivray, L. R.; Papaefstathiou, G. S.; Frišcic, T.; Hamilton, T. D.; Bucar, D.-K.; Chu, Q.; Varshney, D. B.; Georgiev, I. G. *Acc. Chem. Res.* **2008,** *41,* 280–291. doi:10.1021/ar700145r
40. Nagarathinam, M.; Peedikakkal, A. M. P.; Vittal, J. J. *Chem. Commun.* **2008,** 5277–5288. doi:10.1039/b809136f
41. Mishra, A.; Behera, R. K.; Behera, P. K.; Mishra, B. K.; Behera, G. B. *Chem. Rev.* **2000,** *100,* 1973–2012. doi:10.1021/cr990402t
42. Fedorova, O. A.; Saifutiarova, A. E.; Gulakova, E. N.; Guskova, E. O.; Aliyeu, T. M.; Shepel, N. E.; Fedorov, Y. V. *Photochem. Photobiol. Sci.* **2019,** *18,* 2208–2215. doi:10.1039/c9pp00028c
43. Wei, P.; Zhang, J.-X.; Zhao, Z.; Chen, Y.; He, X.; Chen, M.; Gong, J.; Sung, H. H.-Y.; Williams, I. D.; Lam, J. W. Y.; Tang, B. Z. *J. Am. Chem. Soc.* **2018,** *140,* 1966–1975. doi:10.1021/jacs.7b13364
44. Berdnikova, D. V.; Aliyeu, T. M.; Delbaere, S.; Fedorov, Y. V.; Jonusauskas, G.; Novikov, V. V.; Pavlov, A. A.; Peregudov, A. S.; Shepel', N. E.; Zubkov, F. I.; Fedorova, O. A. *Dyes Pigm.* **2017,** *139,* 397–402. doi:10.1016/j.dyepig.2016.11.053
45. Budyka, M. F.; Gavrishova, T. N.; Potashova, N. I.; Chernyak, A. V. *Mendeleev Commun.* **2015,** *25,* 106–108. doi:10.1016/j.mencom.2015.03.008
46. Ushakov, E. N.; Vedernikov, A. I.; Lobova, N. A.; Dmitrieva, S. N.; Kuz'mina, L. G.; Moiseeva, A. A.; Howard, J. A. K.; Alfimov, M. V.; Gromov, S. P. *J. Phys. Chem. A* **2015,** *119,* 13025–13037. doi:10.1021/acs.jpca.5b10758
47. Berdnikova, D. V.; Sosnin, N. I.; Fedorova, O. A.; Ihmels, H. *Org. Biomol. Chem.* **2018,** *16,* 545–554. doi:10.1039/c7ob02736b
48. Botti, V.; Cesaretti, A.; Ban, Ž.; Crnolatac, I.; Consiglio, G.; Elisei, F.; Piantanida, I. *Org. Biomol. Chem.* **2019,** *17,* 8243–8258. doi:10.1039/c9ob01186b
49. Wang, M.-Q.; Liu, S.; Tang, C.-P.; Raza, A.; Li, S.; Gao, L.-X.; Sun, J.; Guo, S.-P. *Dyes Pigm.* **2017,** *136,* 78–84. doi:10.1016/j.dyepig.2016.08.041
50. Narayanaswamy, N.; Narra, S.; Nair, R. R.; Saini, D. K.; Kondaiah, P.; Govindaraju, T. *Chem. Sci.* **2016,** *7,* 2832–2841. doi:10.1039/c5sc03488d
51. Berdnikova, D. V.; Fedorova, O. A.; Tulyakova, E. V.; Li, H.; Kölsch, S.; Ihmels, H. *Photochem. Photobiol.* **2015,** *91,* 723–731. doi:10.1111/php.12405
52. Narayanaswamy, N.; Das, S.; Samanta, P. K.; Banu, K.; Sharma, G. P.; Mondal, N.; Dhar, S. K.; Pati, S. K.; Govindaraju, T. *Nucleic Acids Res.* **2015,** *43,* 8651–8663. doi:10.1093/nar/gkv875
53. Xie, X.; Choi, B.; Largy, E.; Guillot, R.; Granzhan, A.; Teulade-Fichou, M.-P. *Chem. – Eur. J.* **2013,** *19,* 1214–1226. doi:10.1002/chem.201203710
54. Mazzoli, A.; Carlotti, B.; Consiglio, G.; Fortuna, C. G.; Miolo, G.; Spalletti, A. *Photochem. Photobiol. Sci.* **2014,** *13,* 939–950. doi:10.1039/c4pp00023d
55. Mazzoli, A.; Carlotti, B.; Bonaccorso, C.; Fortuna, C. G.; Mazzucato, U.; Miolo, G.; Spalletti, A. *Photochem. Photobiol. Sci.* **2011,** *10,* 1830–1836. doi:10.1039/c1pp05214d
56. Fortuna, C. G.; Barresi, V.; Berellini, G.; Musumarra, G. *Bioorg. Med. Chem.* **2008,** *16,* 4150–4159. doi:10.1016/j.bmc.2007.12.042
57. Fortuna, C. G.; Barresi, V.; Bonaccorso, C.; Consiglio, G.; Failla, S.; Trovato-Salinaro, A.; Musumarra, G. *Eur. J. Med. Chem.* **2012,** *47,* 221–227. doi:10.1016/j.ejmech.2011.10.060
58. Barresi, V.; Bonaccorso, C.; Consiglio, G.; Goracci, L.; Musso, N.; Musumarra, G.; Satriano, C.; Fortuna, C. G. *Mol. BioSyst.* **2013,** *9,* 2426–2429. doi:10.1039/c3mb70151d
59. Schmidt, D.; Rodat, T.; Heintze, L.; Weber, J.; Horbert, R.; Girreser, U.; Raeker, T.; Bußmann, L.; Kriegs, M.; Hartke, B.; Peifer, C. *ChemMedChem* **2018,** *13,* 2415–2426. doi:10.1002/cmdc.201800531
60. Granzhan, A.; Ihmels, H. *Synlett* **2016,** *27,* 1775–1793. doi:10.1055/s-0035-1561445
61. Ihmels, H.; Karbasiyoun, M.; Löhl, K.; Stremmel, C. *Org. Biomol. Chem.* **2019,** *17,* 6404–6413. doi:10.1039/c9ob00809h
62. Xie, X.; Zuffo, M.; Teulade-Fichou, M.-P.; Granzhan, A. *Beilstein J. Org. Chem.* **2019,** *15,* 1872–1889. doi:10.3762/bjoc.15.183
63. Das, A. K.; Ihmels, H.; Kölsch, S. *Photochem. Photobiol. Sci.* **2019,** *18,* 1373–1381. doi:10.1039/c9pp00096h
64. Chang, L.; Liu, C.; He, S.; Lu, Y.; Zhang, S.; Zhao, L.; Zeng, X. *Sens. Actuators, B* **2014,** *202,* 483–488. doi:10.1016/j.snb.2014.05.089
65. Yao, H.; Chang, L.; Liu, C.; Jiao, X.; He, S.; Liu, H.; Zeng, X. *J. Fluoresc.* **2015,** *25,* 1637–1643. doi:10.1007/s10895-015-1650-x
66. Zacharioudakis, E.; Cañeque, T.; Custodio, R.; Müller, S.; Cuadro, A. M.; Vaquero, J. J.; Rodriguez, R. *Bioorg. Med. Chem. Lett.* **2017,** *27,* 203–207. doi:10.1016/j.bmcl.2016.11.074
67. Maçoas, E.; Marcelo, G.; Pinto, S.; Cañeque, T.; Cuadro, A. M.; Vaquero, J. J.; Martinho, J. M. G. *Chem. Commun.* **2011,** *47,* 7374–7376. doi:10.1039/c1cc12163d
68. Richards, A.; Stevens, T. S. *J. Chem. Soc.* **1958,** 3067–3073. doi:10.1039/jr9580003067
69. Marcelo, G.; Pinto, S.; Cañeque, T.; Mariz, I. F. A.; Cuadro, A. M.; Vaquero, J. J.; Martinho, J. M. G.; Maçôas, E. M. S. *J. Phys. Chem. A* **2015,** *119,* 2351–2362. doi:10.1021/jp507095b
70. Pithan, P. M.; Decker, D.; Druzhinin, S. I.; Ihmels, H.; Schönherr, H.; Voß, Y. *RSC Adv.* **2017,** *7,* 10660–10667. doi:10.1039/c6ra27684a
71. Jones, G.; Jackson, W. R.; Choi, C.-y.; Bergmark, W. R. *J. Phys. Chem.* **1985,** *89,* 294–300. doi:10.1021/j100248a024
72. Sirajuddin, M.; Ali, S.; Badshah, A. *J. Photochem. Photobiol., B* **2013,** *124,* 1–19. doi:10.1016/j.jphotobiol.2013.03.013
73. Stootman, F. H.; Fisher, D. M.; Rodger, A.; Aldrich-Wright, J. R. *Analyst* **2006,** *131,* 1145–1151. doi:10.1039/b604686j
74. Šmidlehner, T.; Piantanida, I.; Pescitelli, G. *Beilstein J. Org. Chem.* **2018,** *14,* 84–105. doi:10.3762/bjoc.14.5
75. Norden, B.; Rodger, A.; Dafforn, T. *Linear Dichroism and Circular Dichroism;* Royal Society of Chemistry: Cambridge, U.K., 2010.
76. Nordén, B.; Kurucsev, T. *J. Mol. Recognit.* **1994,** *7,* 141–155. doi:10.1002/jmr.300070211
77. Holzmann, N.; Bernasconi, L.; Callaghan, K. M.; Bisby, R. H.; Parker, A. W. *Chem. Phys. Lett.* **2018,** *692,* 146–151. doi:10.1016/j.cplett.2017.12.028
78. Amjaour, H.; Wang, Z.; Mabin, M.; Puttkammer, J.; Busch, S.; Chu, Q. R. *Chem. Commun.* **2019,** *55,* 214–217. doi:10.1039/c8cc08017h
79. Ihmels, H.; Luo, J. *J. Photochem. Photobiol., A* **2008,** *200,* 3–9. doi:10.1016/j.jphotochem.2008.04.008
80. Mondal, B.; Zhang, T.; Prabhakar, R.; Captain, B.; Ramamurthy, V. *Photochem. Photobiol. Sci.* **2014,** *13,* 1509–1520. doi:10.1039/c4pp00221k
81. Yamada, S.; Azuma, Y.; Aya, K. *Tetrahedron Lett.* **2014,** *55,* 2801–2804. doi:10.1016/j.tetlet.2014.03.036
82. Mondal, B.; Captain, B.; Ramamurthy, V. *Photochem. Photobiol. Sci.* **2011,** *10,* 891–894. doi:10.1039/c1pp05070b
83. Hill, Y.; Linares, M.; Briceño, A. *New J. Chem.* **2012,** *36,* 554–557. doi:10.1039/c2nj20855e

84. Kole, G. K.; Tan, G. K.; Vittal, J. J. *J. Org. Chem.* **2011,** *76,* 7860–7865. doi:10.1021/jo201268p
85. Peedikakkal, A. M. P.; Peh, C. S. Y.; Koh, L. L.; Vittal, J. J. *Inorg. Chem.* **2010,** *49,* 6775–6777. doi:10.1021/ic100853h
86. Horner, M.; Hünig, S. *Liebigs Ann. Chem.* **1982,** 1183–1210. doi:10.1002/jlac.198219820619

License and Terms

This is an Open Access article under the terms of the Creative Commons Attribution License (https://creativecommons.org/licenses/by/4.0). Please note that the reuse, redistribution and reproduction in particular requires that the authors and source are credited.

The license is subject to the *Beilstein Journal of Organic Chemistry* terms and conditions: (https://www.beilstein-journals.org/bjoc)

The definitive version of this article is the electronic one which can be found at: doi:10.3762/bjoc.16.13

BEILSTEIN JOURNAL OF ORGANIC CHEMISTRY

Potent hemithioindigo-based antimitotics photocontrol the microtubule cytoskeleton in cellulo

Alexander Sailer, Franziska Ermer, Yvonne Kraus, Rebekkah Bingham, Ferdinand H. Lutter, Julia Ahlfeld and Oliver Thorn-Seshold*

Full Research Paper

Open Access

Address:
Department of Pharmacy, Ludwig Maximilian University of Munich, Butenandtstraße 5-13, Munich 81377, Germany

Email:
Oliver Thorn-Seshold* - oliver.thorn-seshold@cup.lmu.de

* Corresponding author

Keywords:
antimitotics; cytoskeleton; hemithioindigo; photopharmacology; photoswitch

Beilstein J. Org. Chem. **2020,** *16,* 125–134.
doi:10.3762/bjoc.16.14

Received: 31 July 2019
Accepted: 13 November 2019
Published: 27 January 2020

This article is part of the thematic issue "Molecular switches".

Guest Editor: W. Szymanski

© 2020 Sailer et al.; licensee Beilstein-Institut.
License and terms: see end of document.

Abstract

Background: Hemithioindigo is a promising molecular photoswitch that has only recently been applied as a photoswitchable pharmacophore for control over bioactivity in cellulo. Uniquely, in contrast to other photoswitches that have been applied to biology, the pseudosymmetric hemithioindigo scaffold has allowed the creation of both dark-active and lit-active photopharmaceuticals for the same binding site by a priori design. However, the potency of previous hemithioindigo photopharmaceuticals has not been optimal for their translation to other biological models.

Results: Inspired by the structure of tubulin-inhibiting indanones, we created hemithioindigo-based indanone-like tubulin inhibitors (**HITubs**) and optimised their cellular potency as antimitotic photopharmaceuticals. These **HITubs** feature reliable and robust visible-light photoswitching and high fatigue resistance. The use of the hemithioindigo scaffold also permitted us to employ a *para*-hydroxyhemistilbene motif, a structural feature which is denied to most azobenzenes due to the negligibly short lifetimes of their metastable *Z*-isomers, which proved crucial to enhancing the potency and photoswitchability. The **HITubs** were ten times more potent than previously reported hemithioindigo photopharmaceutical antimitotics in a series of cell-free and cellular assays, and allowed robust photocontrol over tubulin polymerisation, microtubule (MT) network structure, cell cycle, and cell survival.

Conclusions: HITubs represent a powerful addition to the growing toolbox of photopharmaceutical reagents for MT cytoskeleton research. Additionally, as the hemithioindigo scaffold allows photoswitchable bioactivity for substituent patterns inaccessible to the majority of current photopharmaceuticals, wider adoption of the hemithioindigo scaffold may significantly expand the scope of cellular and in vivo targets addressable by photopharmacology.

Introduction

The cytoskeletal scaffolding protein tubulin, a heterodimer consisting of α and β subunits, each of various isotypes, reversibly assembles into giant non-covalent polymeric microtubules (MTs), which play a pivotal role as a dynamic scaffold for a multitude of cellular processes. These include mechanostasis, the completion of mitosis, cell motility, and cargo trafficking in all cell types, as well as cell-type-specific roles, such as polarization, cargo sorting, and trafficking in neurons; the regulation and functioning of these processes is still not satisfactorily understood [1-4]. The MT cytoskeleton is a finely tuned complex system that is highly conserved through evolution. Direct genetic modifications of tubulin that affect its functions risk causing a diversity of effects, due to its many survival-critical roles, as well as non-functionality of the modified tubulin product. For example, knockout approaches have only been described for single isoforms of α/β-tubulin, and these cannot deliver the dynamic reversibility and effect-specificity that is required for understanding MT biology; and optogenetic modifications of tubulin have never succeeded. Instead, studies of the roles of MTs in these processes overwhelmingly rely on small molecule tubulin inhibitors [1].

Due to the non-invasiveness and high spatiotemporal precision with which optical stimulation can be applied, photopharmacology has drawn great interest for studies of crucial biological processes in a range of fields, from neuroscience [5,6] and G-protein-coupled receptor (GPCR) function [7,8] to antibiotic research [9]. Particularly in the context of MT biology, photopharmacology is an attractive development beyond classical small molecule inhibitors; since the spatiotemporal complexity inherent to the diversity of tubulin-dependent cellular processes may finally yield to studies that can leverage high-spatiotemporal-specificity optical control to deliver cell-specific, time-reversible modulation of native cytoskeleton function.

We and others have reported on photoswitchable azobenzene-based inhibitors of tubulin polymerisation [10-13] that have since been used in studies of neuronal trafficking [14] and embryonic development [15,16], and we have recently reported biologically robust heterostilbenes that deliver green fluorescent protein (GFP)-orthogonal MT photocontrol [17]. However, in both azobenzene and heterostilbene scaffolds, the steric properties of the *E*- and *Z*-isomer are so different that the protein binding site shape determines that the *Z*-isomer (the lit-form) is the more bioactive one, without the possibility of sign inversion by substituent shifts. To overcome this conceptual limitation, we recently reported on the first use of hemithioindigos (HTIs) as photoswitchable pharmacophores for optical control of tubulin dynamics in vitro (cell-free) and MT-dependent processes in cellulo [18]. We showed for the first time that the pseudosymmetry of hemithioindigos can be used to enable a priori design of HTI-based pharmacophores for a single binding site, with higher bioactivity as either the lit-form *E*- or the dark-

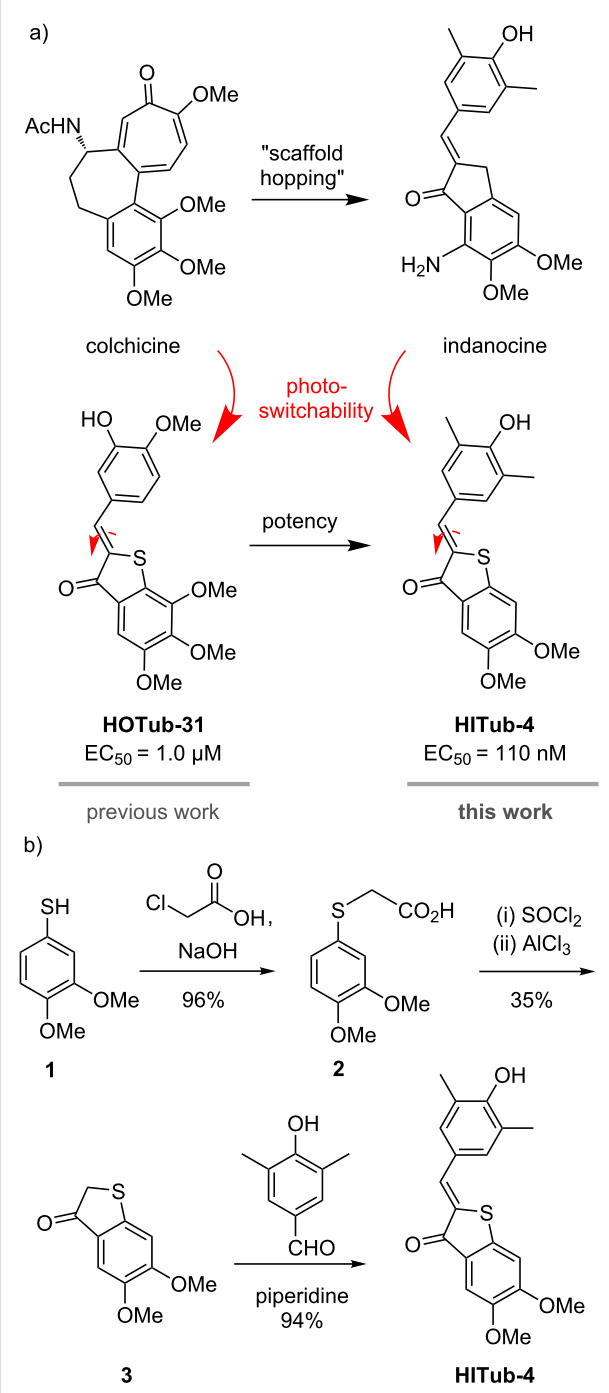


Figure 1: a) The potent tubulin inhibitor colchicine as a lead scaffold led to the development of the **HOTub** generation of HTI-based antimitotics (e.g., **HOTub-31**). Changing the lead scaffold to indanocine led to the development of up to ten times more potent **HITubs** (e.g., **HITub-4**). b) Straightforward, short, and high-yielding synthesis of **HITub-4**.

form *Z*-isomer, just by changing substituent patterns, and developed HTI-based antimitotics with cytotoxic potencies in the low micromolar range (Figure 1a) [18].

In this work, we wished to enhance the bioactivity of the distinctive dark-active HTI-based tubulin-binding antimitotics while retaining the benefits of the HTI scaffold, namely robust, fatigue-resistant, all-visible-light photoswitching.

Results and Discussion

Design strategy for HTIs

The HTI-based colchicinoid **HOTubs** (e.g., **HOTub-31**) that we previously explored had the HTI photoswitch embedded inside a methoxylation pattern, such that one isomer obeyed the structure–activity relationship (SAR) of colchicine or its analogue combretastatin A-4 and was bioactive, while the other isomer clashed with their SAR and was less active [18]. That approach of directly embedding a photoswitch motif inside the pharmacophore seemed to be more promising for photopharmacology than the synthetically more straightforward attachment of photoswitches on the pharmacophore periphery. We expected that embedding (which is referred to as azologization in the case of azobenzene-based photopharmaceuticals [19]) should in general lead to more significant alterations of the binding-relevant structure, and increase the differential potency between isomers of the resulting photopharmaceutical, than peripheral attachment (referred to as azo-extension in the case of azobenzenes [18]). We therefore desired to maintain the embedding strategy, yet to improve potency we chose to break with substitution patterns strictly based on colchicine. It is not the case that colchicine (or any other small-molecule inhibitor) represents an ideal structure that colchicine domain inhibitors (CDIs) should reproduce. Thus, our design focus was to introduce reversible photoresponse to a CDI rather than developing compounds with high similarity to colchicine per se, aiming at compounds where one isomer would be almost biologically inactive such that light can be used to effect a photoisomerisation-based switch-on/switch-off of bioactivity. The end-to-end distance of the HTI scaffold is significantly longer than that in either the biaryl colchicine or the stilbene combretastatin, and the torsion angle between the aryl blades of the HTI is nearly planar (up to 4°), while that between the rings of (*Z*)-combretastatin or colchicine is approximately 50–60° [20]. Thus, we assumed that the length and the near-planarity of the HTI could suit it to different substituent patterns to those of colchicine, and attempted to rationally determine these.

Firstly, since the HTI scaffold is longer than a biaryl motif but should occupy a similar volume in the pocket, we assumed that we would have to reduce the substituent bulk present on colchicine/combretastatin A-4. The middle methoxy group of colchicine's trimethoxy-substituted "south ring" (Figure 1a) makes a beneficial polar contact in the binding pocket via the oxygen atom, but upon demethylation, the potency is much reduced, presumably from insufficient desolvation in the colchicine site (which is known from work on podophyllotoxin derivatives [20]). We therefore chose to keep that methoxy group intact. However, colchicine's methoxy group on the "north ring" establishes a non-polar spacefilling interaction, which can be replaced equipotently by an ethyl group. Thus, we considered that the HTI scaffold could best be reduced in volume by "shortening" this substituent, maintaining the above-mentioned non-polar interaction.

Secondly, since the torsion angle of the HTI is far lower than that of (*Z*)-stilbenes or biaryl compounds, we considered that even with shortening, their SARs might not directly match. Mainly, we assumed that re-orientation of the substituent pattern on one or both rings (e.g., re-orientation of the archetypal 3,4,5-trimethoxyphenyl south ring pattern to a 4,5,6-trimethoxyaryl pattern) might be needed to occupy a similar space.

A wealth of CDIs have been reported, including scaffolds such as aurones that apparently reproduce the substituent pattern SAR of combretastatins [21] while having closely similar scaffold steric properties to HTIs. However, in light of the considerations above, we rather selected indanocine as a starting point for alternative substituent patterning (Figure 1a). Indanocine is a cytotoxic indanone-based CDI (EC_{50} ≈ 10–40 nM) [22] with similar cell culture potency to colchicine (EC_{50} ≈ 3–20 nM) [23] that likewise disrupts MTs, arrests cells in the G2/M phase, and induces apoptosis. Although the size and geometry of thioindoxyl and indanone rings differ because of the S/CH_2 replacement, we assumed that "mapping" the substitution pattern of indanocine onto a hemithioindigo core should result in a lead structure for tubulin-binding (*Z*)-HTIs, namely the class of **HITubs**.

The *para*-hydroxy substitution of indanocine suggested that HTI might be a more desirable photopharmaceutical scaffold than the widely used azobenzene motif. While *para*-hydroxyazobenzenes feature negligibly short *cis*-to-*trans* thermal relaxation half- lives in aqueous media in the range of µs [24,25], probably making them unsuitable for robust photoswitching applications against intracellular targets, data for *para*-hydroxy HTIs have not been reported so far. We considered that if the *para*-hydroxy-**HITubs** featured photoswitchable bioactivity in cellulo, implying suitable (*E*)-HTI stability under cellular conditions, this would more generally commend them as a scaffold of choice for cellular photo-

pharmaceutical use with strong electron-donating substituents, such as amino or hydroxy groups in *ortho*- or *para*-position, aiming at intracellular targets. This is an important scope of substituents to address, since these small polar groups often establish high-affinity ligand–target interactions, but otherwise represent an obstacle to photoswitchability with azobenzene compounds.

Preview: design of target **HITubs**

Our SAR-driven compound development path is described in full later in the section on bioactivity, but in brief, we began the series of indanocine-inspired HTI designs by replacing the south ring amino unit of indanocine (which is attached in *ortho*-position to the key south ring methoxy group) by a hydroxy function, giving **HITub-1** (Figure 2).

When **HITub-1** later proved less bioactive than we had wished, we explored steric and polarity changes to this south ring hydroxy group by methylation (**HITub-2**), methylation and shifting on the ring (**HITub-3**), or even its removal (**HITub-4**). We additionally controlled against our design logic of north ring substituent shortening (**HITub-5**). We also controlled for the SAR observation that CDIs should not tolerate a non-polar central north ring substituent (**HITub-6**), but can support removal of this substituent altogether, with only small potency loss (**HITub-7**) [20]. The progression and results of this SAR study are explained below in the section on bioactivity.

General synthetic access

Synthetic routes to HTIs are well established [26] and typically involve aldol condensation of benzaldehyde onto thioindoxyls. However, the key step is the formation (and where necessary, isolation) of the thioindoxyl species. In our studies, the electron-rich dimethoxy- and trimethoxy-substituted thioindoxyls were noted to be unstable to air, base, and silica gel during chromatography, so it was sought to minimise their exposure to these conditions during synthesis. In the end, we used two routes to the thioindoxyls: either Friedel–Crafts acylation of α-phenylthioacetic acids (which are easily accessible from thiophenols by alkylation using 2-chloroacetic acid, Figure 1b) or else, lithium diisopropylamide (LDA)-mediated cyclisation of 2-(methylthio)benzamides, which were obtained by directed *ortho*-metalation of the respective benzamides followed by quenching with dimethyl disulfide [27] (Supporting Information File 1, Scheme S1). In general, we found the LDA-mediated cyclisation more convenient, as it generated fewer side products and enabled faster, easier workup and purification. We used these routes to synthesise the **HITubs** typically in good (32% for **HITub-4**, Figure 1b) to excellent (93% for **HITub-7**, Scheme S5) overall yields from commercial building blocks (see Supporting Information File 1).

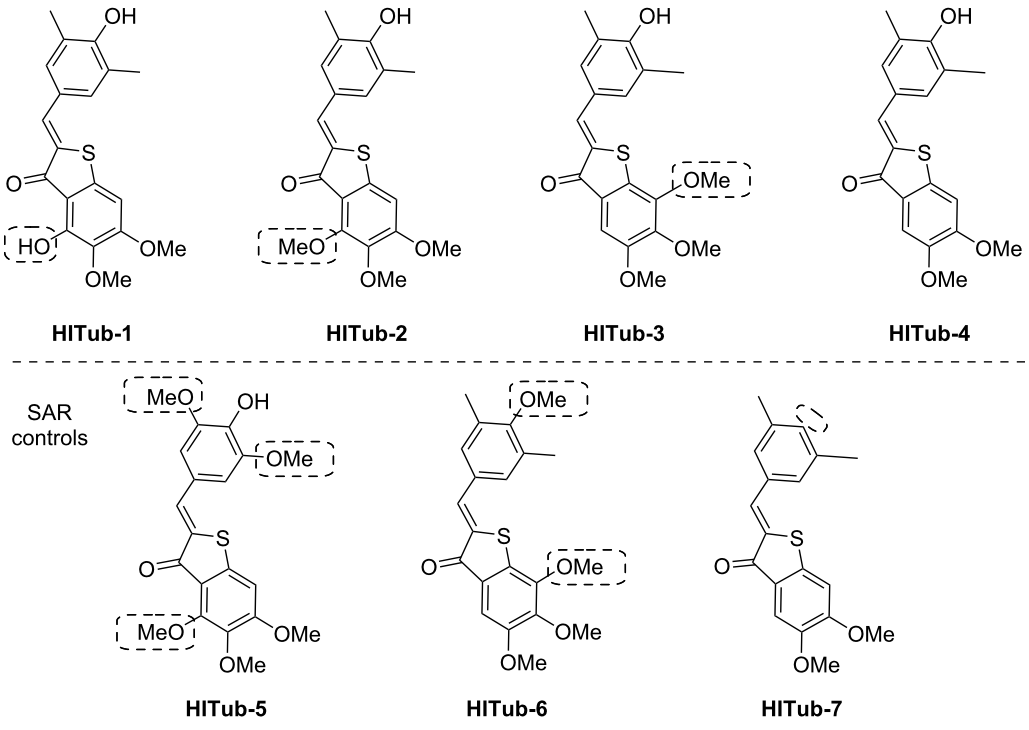


Figure 2: Chemical structures of **HITubs**. Key variations with respect to **HITub-4** are highlighted in dashed boxes.

Photocharacterisation

Although some *para*-hydroxy-substituted HTIs have been described [28,29], we are unaware of any report of the solvent- and pH-dependency of their photochromism and thermal relaxation. Dube and co-workers have reported that in general, increasing the electron-donating strength of groups in the hemistilbene *para*-position of HTIs correlates to (a) a bathochromic shift of the $S_0 \rightarrow S_1$ absorption band (up to $\lambda_{max} \approx 500$ nm with julolidine substitution) and (b) decreased thermal stability of the metastable *E*-isomer, i.e., faster thermal relaxation [30]. However, they also reported that introducing electron-donating groups (methoxy, dimethylamino) in *para*-position to the thioindoxyl sulfur atom restored *E*-stability while maintaining red-shifted absorption maxima. This *para*-position was occupied by the key methoxy group in all our **HITub** designs. With scant information available, we could not predict the thermal stability of (*E*)-**HITubs** in cellular conditions, so we turned to experimental measurement.

Since we found no substantial differences between the photochemical properties of the *para*-hydroxylated compounds (Figure 3 and Supporting Information File 1, Figure S1), we here describe the photocharacterisation of **HITub-4** as a representative example of the photoswitchable bioactive compounds (for more detailed analysis see Supporting Information File 1). In polar aprotic solvents, the **HITub-4** *Z*-isomer ($\lambda_{max} \approx 380$, 460 nm) showed robust, reliable, and fully reversible photoswitching (λ = 450 nm for $Z \rightarrow E$ and 530 nm for $E \rightarrow Z$ switching), with the high fatigue resistance characteristic of HTIs. The *E*-isomer's thermal half-life in EtOAc or DMSO was ca. 40 s (Figure 3 and Supporting Information File 1, Figure S3). Its absorption spectra and photoswitchability were unaltered by the addition of acid, however, addition of base led to a remarkable bathochromic and hyperchromic shifts of the absorption band at ca. 550 nm, and no observed photoswitchability (Supporting Information File 1, Figure S2). We assumed that this spectrum resulted from a quinoidal structure, formed after deprotonation of the hydroxy group, and that the lack of observable photoswitchability arose due to fast free rotation around the C–C single bond connecting the thioindigo and hemistilbene motifs. Interestingly, in neutral or acidic aqueous media where the quinoidal structure is not present (λ_{max} ca. 370, 480 nm), photoswitching could not be observed either, which we presumed to be due to fast thermal relaxation. However, noting that typical CDIs are substantially biolocalised into lipid environments within cells [31], we decided to explore photoswitching-based cellular assays with these compounds nonetheless (further discussion in Supporting Information File 1).

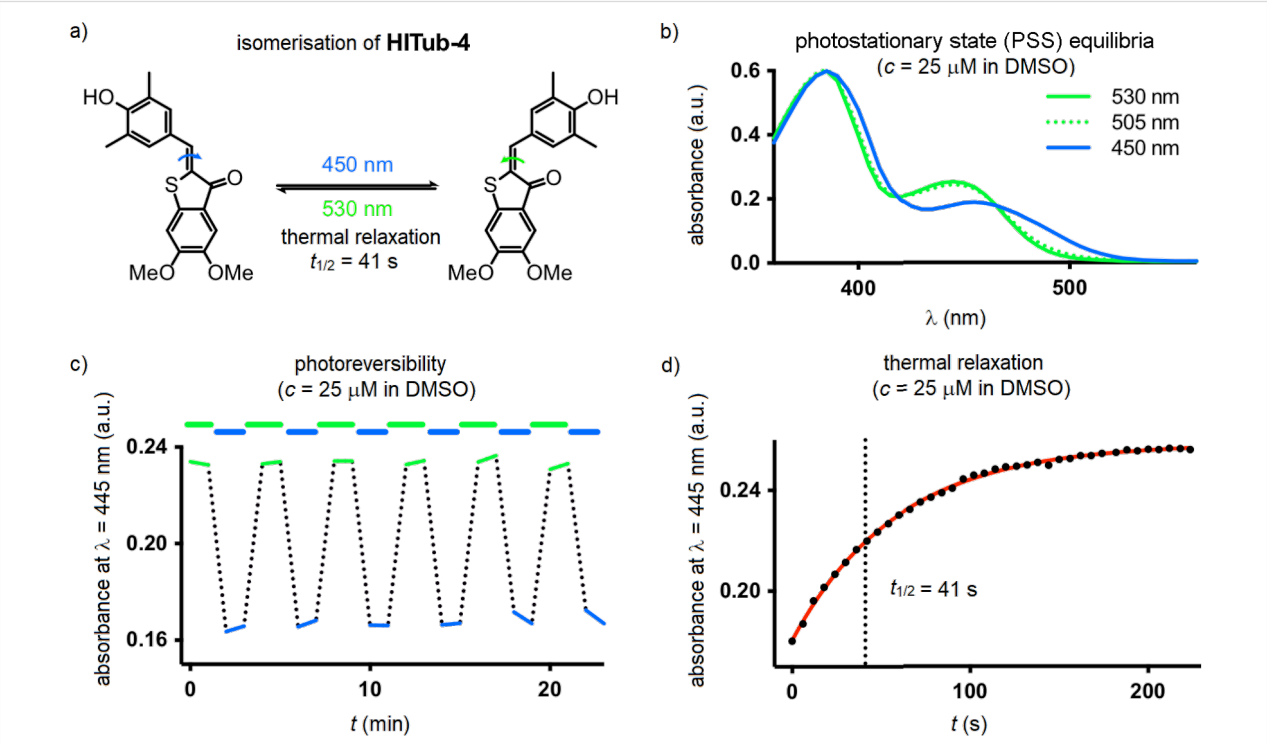


Figure 3: Photocharacterisation of **HITub-4**. a) Photochemical and thermal isomerisation. b) UV–vis spectra after saturating illumination at λ = 450, 505, and 530 nm, respectively. c) Photoreversible switching upon alternating illumination (λ = 450 and 530 nm). d) Thermal relaxation at room temperature after reaching the photostationary state at λ = 450 nm.

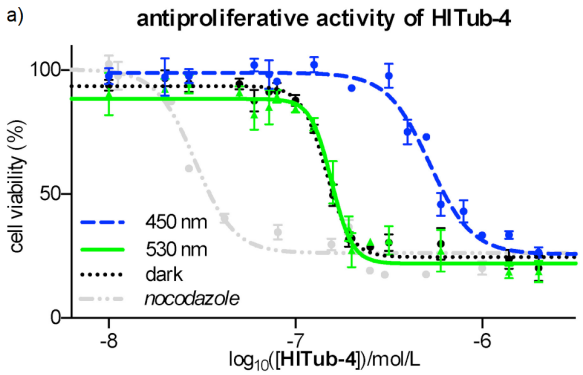
We found that the photochemical properties of the non-*para*-hydroxylated control **HITub-6** were similar to those of previously reported non-*para*-hydroxylated **HOTubs** [18], with satisfactory photoswitching in both DMSO and phosphate-buffered saline (PBS)/DMSO mixtures (Figure S1f,g in Supporting Information File 1).

Bioactivity: SAR study of **HITubs** in cellulo

To begin evaluating the isomer-dependent bioactivity of **HITub** photopharmaceuticals in cellulo, we first performed resazurin (resorufin *N*-oxide) antiproliferation assays under different lighting conditions (Figure 4). Inhibitors of tubulin polymerisation act as antimitotic cytotoxins in cell culture by preventing formation of a functional mitotic spindle, resulting in mitotic arrest and eventually cell death. The reduction of resazurin by viable cells serves as a fluorogenic proxy readout for antimitotic potency in cellulo, since the degree of resazurin turnover scales to the number of cells still viable after compound treatment, although the mechanism behind antiproliferative activity must later be determined using more specific assays. We used the HeLa human cervical cancer cell line to assess the biological activity of **HITubs** in all cellular experiments shown in this work. Since tubulin is a highly conserved protein target critical for survival in all cell types, we expected that, as for other colchicine domain tubulin inhibitors, trends in potency and in photoswitchability of potency determined in this representative mammalian cell line can be translated to other cell types, although their specific response (e.g., EC_{50} values) would need individual determination. Nocodazole was used as a benchmarking reference and mechanistic positive control in all in cellulo assays since it is a potent inhibitor of the colchicine binding site (EC_{50} ≈ 40 nM) with both appropriate solubility and straightforward handling.

Self-made low-intensity LED arrays with relatively narrow bandwidth were used for illumination of cells during assays, with a pulsing regime of 75 ms every 15 s to maintain photostationary state equilibria in cellulo [10]. We cross-checked different illumination wavelengths in cellular toxicity assays; in accordance with the DMSO photoswitching studies, we observed that 530 nm (ca. 97% *Z*-configuration, but additionally controls for non-specific phototoxicity) delivered results equivalent to dark conditions (exclusively *Z*-configuration), to which 450 nm (lit conditions, ca. 70% *E*-configuration) gave the greatest difference in antiproliferative potencies.

We began our studies with **HITub-1**. This is a HTI analogue of indanocine in which the indanocine amino function (in *ortho*-position to the key south ring methoxy group) has been replaced by a synthetically more accessible hydroxy group (delivered via demethylation of a trimethoxy precursor through BBr_3). The



b)

compound	dark EC_{50} (μM)	450 nm EC_{50} (μM)	lit/dark ratio
HITub-1	0.5	1.1	2.2
HITub-2	1.2	3.8	3.2
HITub-3	0.15	0.4	2.7
HITub-4	0.11	0.45	4.1
HITub-5	n.d. (>50)	n.d. (>50)	n.d.
HITub-6	n.d. (>10)	n.d. (>10)	n.d.
HITub-7	0.4	0.4	1.0

Figure 4: a) Resazurin reduction assay for **HITub-4** and nocodazole in HeLa cells (n = 3), demonstrating the difference in antiproliferative potencies at λ = 450 and 530 nm/dark conditions (75 ms pulsing every 15 s). b) EC_{50} values of **HITubs** from cellular antiproliferation assays under dark conditions and at λ = 450 nm. The ratio of lit/dark EC_{50} values shows the fold change in photoswitchable bioactivity.

hydroxy and amino groups have similar size and polarity, and can both act as H-bond donors or acceptors. Therefore, we expected **HITub-1** to allow reliable evaluation of the indanocine substituent pattern. (*Z*)-**HITub-1** was already strongly bioactive (EC_{50} ≈ 500 nM, Figure 4b), although one order of magnitude less so than indanocine (EC_{50} ≈ 10–40 nM, depending on the cell line). Pleasingly, although we had not observed its photoswitching in pure aqueous media, in the heterogeneous cellular environment, we found that its overall toxicity under lit conditions was reliably and reproducibly halved.

We then explored changes to the substituent pattern to determine whether we could improve both *Z*-isomer potency in an absolute sense and the overall photoswitchability of potency comparing *E*- and *Z*-isomers. We began by methylating the south ring hydroxy group (**HITub-2**) to see how changes in size and polarity affect the bioactivity; surprisingly, the potency loss was not dramatic (indicating that this position is not a key determinant of bioactivity), but the photoswitchability increased substantially (3-fold with regard to the lit/dark ratio). We took this as an encouraging indicator of the overall polarity

required for binding, and now examined re-orienting the south ring substituents by shifting the trimethoxy pattern on the ring (**HITub-3**), which improved the potency dramatically (EC_{50} ≈ 150 nM for the *Z*-isomer) while retaining the 3-fold photoswitchability of bioactivity.

Since comparison of **HITub-2** and **HITub-3** showed that the potency can be retained without substituents in *ortho*-position to either the carbonyl group or the sulfur atom, for maximal simplicity, we tested whether both substituents could be deleted simultaneously (**HITub-4**). This proved to be the strongest-performing compound of our studies, with the *Z*-isomer possessing an EC_{50} value of ca. 110 nM and a 4-fold difference of bioactivity between lit and dark conditions (λ = 450 nm). This difference was surprisingly high, given that even in aprotic media (e.g., lipid environment reservoirs within cells), there should be ca. 30% residual *Z*-isomer at photoequilibrium [18], and we had expected that any (*E*)-**HITub** entering the cytosol (aqueous environment) would quickly relax to its more bioactive *Z*-isomer before encountering its cytosolic protein target. We theorised that fast cytosolic relaxation of the *para*-hydroxy **HITubs** to their bioactive *Z*-isomer may actually be a decisive factor in preventing the simple equilibration of the extracellular **HITub** concentration (exclusively *Z*-configuration due to fast relaxation, irrespective of illumination conditions) with the cytosolic (*Z*)-**HITub** concentration available to bind to tubulin (and which all experiments show is reduced under λ = 450 nm illumination). Examining this in detail is beyond the scope of this study, however, see Supporting Information File 1 for a discussion on isomer-dependent subcellular biolocalisation effects.

We first controlled against our design logic of north ring substituent shortening by changing the north ring apolar-contact methyl groups to methoxy groups (**HITub-5**), and were satisfied when this abolished bioactivity. We also controlled for the result, known from extensive SAR work at the colchicine site [18,32], that CDIs should not tolerate a non-polar central north ring substituent (**HITub-6**) but can support removal of this substituent altogether, with only small potency loss (**HITub-7**). We considered that if the screened compounds obeyed this principle, it would reinforce our mechanistic understanding of them as CDIs. Indeed, **HITub-6** proved inactive until it reached its solubility limit, but (*Z*)-**HITub-7** was relatively potent and featured an only 4-fold reduction of bioactivity as compared to its hydroxylated parent (*Z*)-**HITub-4**. Interestingly, however, **HITub-7** displayed no difference between dark (all-*Z*) and lit (mostly *E*) conditions, and we were unable to rationalise this with reference to either polarity or structure, in light of our prior work on apolar **HOTubs** [18] (see also Supporting Information File 1). We were, however, overall satisfied by these findings (Supporting Information File 1, Figure S4), especially by the potency and photoswitchability of **HITub-4**.

These results indicated that indanocine-inspired HTI-based reagents are a potent, cellularly bioactive class of photoswitchably antiproliferative agents, with the most potent light-controlled antimitotic bioactivity reported for photoswitches designed for tubulin: 10-fold enhancement compared to the predecessor HTI generation **HOTubs** [18] and styrylbenzothiazole-based **SBTubs** [17], and 5-fold superior to azocombretastatins [10-12]. In view of the generally limited solubility of photopharmaceuticals (associated with their extended flat aromatic structures), this increase in potency renders the **HITub** compound class a promising addition to the toolbox of photoswitchable antimitotics, which might prove valuable for future in vivo studies.

We also noted that the *para*-hydroxy **HITubs** featured ca. 30% residual (*Z*)-**HITub** at PSS λ = 450 nm in cell-free measurements, and that for **HITub-2**–**4**, the PSS isomer mixture's cellular cytotoxicity at that wavelength was on average 3.3-fold lower than the cytotoxicity of the corresponding (*Z*)-**HITub** (Figure 4). This can be interpreted as indicative that the *E*-isomers are essentially biologically inactive, similar to what has been observed for heterostilbene **SBTubs** [17] and azobenzene photostatins (**PSTs**) [10]. If substantiated, HTI-like analogues for which photostationary state (PSS) with enhanced proportions of *E*-isomer can be photogenerated would represent an exciting advance: they could, in contrast to the other photoswitch types, allow all-visible, photoreversible, high-potency switching while reproducing similarly beneficial photoswitchability of bioactivity.

Mechanistic assessment of **HITub** action

We now determined to confirm the mechanism of action of the **HITub** compounds. To evaluate the biological mechanism of action behind the **HITubs**' photoswitchable antimitotic activity, we first checked their inhibition of polymerisation of purified tubulin in a cell-free assay. The results showed almost identical inhibition potency for **HITub-4** at c = 10 μM as for the archetypal CDI colchicine at c = 20 μM (Figure S5, Supporting Information File 1), which we took to indicate that (*Z*)-**HITub-4** exerted its bioactivity by specifically binding to tubulin directly in the cell-free system. This suggests that the same specific direct action can be reproduced in cellulo, and that effects on auxiliary cellular systems dependent upon the MT cytoskeleton can likely be downstream effects of MT depolymerisation. We next investigated the **HITubs**' isomer-dependent effects on the MT network inside cells, focusing on the active analogues **HITub-4** and **HITub-2** in comparison with inactive **HITub-5** as a control (Figure 5). By reducing tubulin polymerisation dy-

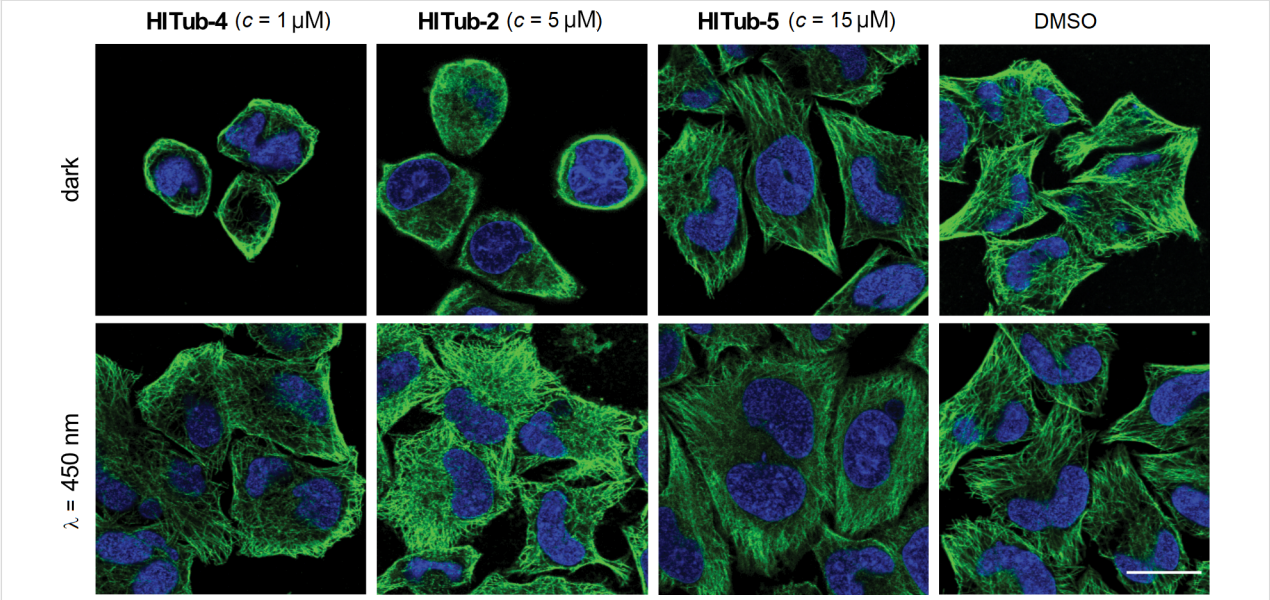


Figure 5: Confocal microscopy images of immunofluorescently labelled MT networks after treatment with **HITubs** for 24 h under lit (λ = 450 nm) and dark conditions. **HITub-4** and **HITub-2** caused light-dependent MT disruption at low concentrations (*c* = 1 and 5 µM, respectively) matching their cytotoxicities (EC_{50} = 1 and 5 µM, respectively). High concentrations of the structurally related negative control **HITub-5**, like the DMSO co-solvent control, produced no effects under either illumination condition. MTs (anti-α-tubulin) are visualized in green while the nuclear stain 4′,6-diamidino-2-phenylindole (DAPI) is visualized in blue. Scale bar length = 20 µm.

namics, CDI treatment should first disorganise and then depolymerise the cellular MT network. We performed immunofluorescence staining of the MT network within cells treated with **HITubs** and documented the resulting disruption of the physiological MT network integrity, and consequently also changes in cell morphology by confocal microscopy. Cells exposed to **HITub-4** (1 µM) in the dark or under λ = 530 nm illumination (to maintain exclusively *Z*-configuration) show near-complete disruption of MT structures after 24 h, while treatment with λ = 450 nm illumination caused no significant disruption of the MT network compared to an untreated dark control (Figure 5). Less potent **HITub-2** also showed similar light dependency of its biological effects at higher concentrations (Supporting Information File 1, Figure S6). Pleasingly, SAR control **HITub-5** showed no impact on MT integrity at the highest tested concentration under lit or dark conditions, which we took as a promising indication for the absence of phototoxicity or of other effects non-specific to tubulin disruption.

Lastly, to substantiate the causative link between the observations on MT disruption and cellular toxicity, we examined the impacts of **HITub-4** on the cell cycle. Tubulin-binding agents whose major cellular mechanism of toxic action is the disruption of MT dynamics or structure should cause cell cycle arrest in the G2/M phase by preventing the completion of mitosis [1]. We examined cell cycle repartition by quantification of cellular DNA content via propidium iodide (PI) incorporation, which was analysed by flow cytometry (Supporting Information File 1, Figure S7). HeLa cells were treated for 24 h with **HITub-4** under λ = 530 and 450 nm irradiation, respectively, with the synthetic tubulin-binding agent nocodazole (Noc) used as a reference. As expected, **HITub-4** showed highly light-dependent bioactivity with near-complete G2/M phase arrest at a concentration of 6 µM and λ = 530 nm irradiation (Figure 6a and Figure 6b), but nearly no cell cycle interference at the same concentration and λ = 450 nm irradiation (Figure 6c and Figure 6d).

Conclusion

Taken together, these results indicate that the **HITubs** had achieved their design aims, being a rationally-designed, potency-enhanced set of HTI-based tubulin-inhibiting photopharmaceuticals with photoswitchable bioactivity across cell biology assays, allowing reliable photocontrol over tubulin polymerisation, MT network structure, cell cycle, and cell survival. They feature mid-nanomolar potency in cellulo, the highest yet reported for photopharmaceutical tubulin inhibitors, as well as satisfactory photoswitchability of potency. We expect that due to the **HITubs**' potency of tubulin inhibition, they will prove a powerful reagent system for biological studies on MT, especially where dark-isomer activity (compared to the currently known, lit-active azobenzenes or styrylbenzothiazoles) is desirable, in particular for cell-free mechanistic studies [33]. More broadly, this work also shows that the HTI scaffold robustly enables the photoswitchable use of resonance-capable substituents that can establish high-affinity interactions (such as *para*-

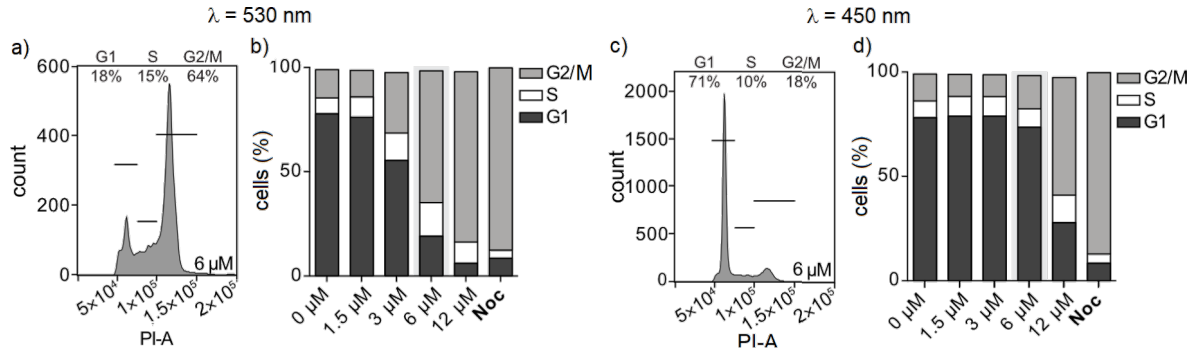


Figure 6: Cell cycle analysis of **HITub-4**-treated cells. a) and b) (*Z*)-**HITub-4** caused significant G2/M arrest already at a concentration of 6 μM (λ = 530 nm). c) and d) Under irradiation at λ = 450 nm, where a majority of (*E*)-**HITub-4** was present, no mitotic arrest could be observed at comparable concentrations. a) and c) Representative histograms showing cell cycle arrest, with population binning as indicated. In b) and d), nocodazole (Noc) was used as a positive control (*c* = 1 μM).

hydroxy groups), which are otherwise problematic for current photopharmaceutical scaffolds to tolerate without loss of photoswitchability. In the broader sense, this is of interest for cell biology and further highlights the potential of HTIs as a pharmacophore scaffold for expanding the scope of cellular photopharmacology.

Supporting Information

Supporting Information File 1

Full experimental protocols for chemical syntheses, photocharacterisation, biochemistry, and cell biology, including NMR spectra.
[https://www.beilstein-journals.org/bjoc/content/supplementary/1860-5397-16-14-S1.pdf]

Acknowledgements

This research was supported by funds from the German Research Foundation (DFG: SFB1032 *Nanoagents for Spatiotemporal Control* project B09, SFB TRR 152 project P24 number 239283807, and an Emmy Noether grant) and the Munich Centre for Nanoscience (CeNS) to O.T.-S. A.S. particularly thanks Linda Pettersson for her great assistance during photocharacterisation.

ORCID® iDs

Alexander Sailer - https://orcid.org/0000-0003-4140-9956
Rebekkah Bingham - https://orcid.org/0000-0001-5740-0353
Julia Ahlfeld - https://orcid.org/0000-0002-4879-4159
Oliver Thorn-Seshold - https://orcid.org/0000-0003-3981-651X

Preprint

A non-peer-reviewed version of this article has been previously published as a preprint doi:10.26434/chemrxiv.9176747

References

1. Peterson, J. R.; Mitchison, T. J. *Chem. Biol.* **2002,** *9,* 1275–1285. doi:10.1016/s1074-5521(02)00284-3
2. Guedes-Dias, P.; Nirschl, J. J.; Abreu, N.; Tokito, M. K.; Janke, C.; Magiera, M. M.; Holzbaur, E. L. F. *Curr. Biol.* **2019,** *29,* 268–282.e8. doi:10.1016/j.cub.2018.11.065
3. Armstrong, M. T.; Armstrong, P. B. *Exp. Cell Res.* **1979,** *120,* 359–364. doi:10.1016/0014-4827(79)90395-1
4. Kelliher, M. T.; Saunders, H. A.; Wildonger, J. *Curr. Opin. Neurobiol.* **2019,** *57,* 39–45. doi:10.1016/j.conb.2019.01.003
5. Banghart, M.; Borges, K.; Isacoff, E.; Trauner, D.; Kramer, R. H. *Nat. Neurosci.* **2004,** *7,* 1381–1386. doi:10.1038/nn1356
6. Caporale, N.; Kolstad, K. D.; Lee, T.; Tochitsky, I.; Dalkara, D.; Trauner, D.; Kramer, R.; Dan, Y.; Isacoff, E. Y.; Flannery, J. G. *Mol. Ther.* **2011,** *19,* 1212–1219. doi:10.1038/mt.2011.103
7. Riefolo, F.; Matera, C.; Garrido-Charles, A.; Gomila, A. M. J.; Sortino, R.; Agnetta, L.; Claro, E.; Masgrau, R.; Holzgrabe, U.; Batlle, M.; Decker, M.; Guasch, E.; Gorostiza, P. *J. Am. Chem. Soc.* **2019,** *141,* 7628–7636. doi:10.1021/jacs.9b03505
8. Agnetta, L.; Kauk, M.; Canizal, M. C. A.; Messerer, R.; Holzgrabe, U.; Hoffmann, C.; Decker, M. *Angew. Chem., Int. Ed.* **2017,** *56,* 7282–7287. doi:10.1002/anie.201701524
9. Velema, W. A.; van der Berg, J. P.; Hansen, M. J.; Szymanski, W.; Driessen, A. J. M.; Feringa, B. L. *Nat. Chem.* **2013,** *5,* 924–928. doi:10.1038/nchem.1750
10. Borowiak, M.; Nahaboo, W.; Reynders, M.; Nekolla, K.; Jalinot, P.; Hasserodt, J.; Rehberg, M.; Delattre, M.; Zahler, S.; Vollmar, A.; Trauner, D.; Thorn-Seshold, O. *Cell* **2015,** *162,* 403–411. doi:10.1016/j.cell.2015.06.049
11. Engdahl, A. J.; Torres, E. A.; Lock, S. E.; Engdahl, T. B.; Mertz, P. S.; Streu, C. N. *Org. Lett.* **2015,** *17,* 4546–4549. doi:10.1021/acs.orglett.5b02262
12. Sheldon, J. E.; Dcona, M. M.; Lyons, C. E.; Hackett, J. C.; Hartman, M. C. T. *Org. Biomol. Chem.* **2016,** *14,* 40–49. doi:10.1039/c5ob02005k
13. Müller-Deku, A.; Loy, K.; Kraus, Y.; Heise, C.; Bingham, R.; Ahlfeld, J.; Trauner, D.; Thorn-Seshold, O. *bioRxiv* **2019,** No. 778993. doi:10.1101/778993
14. Eguchi, K.; Taoufiq, Z.; Thorn-Seshold, O.; Trauner, D.; Hasegawa, M.; Takahashi, T. *J. Neurosci.* **2017,** *37,* 6043–6052. doi:10.1523/jneurosci.0179-17.2017

15. Zenker, J.; White, M. D.; Templin, R. M.; Parton, R. G.; Thorn-Seshold, O.; Bissiere, S.; Plachta, N. *Science* **2017,** *357,* 925–928. doi:10.1126/science.aam9335
16. Singh, A.; Saha, T.; Begemann, I.; Ricker, A.; Nüsse, H.; Thorn-Seshold, O.; Klingauf, J.; Galic, M.; Matis, M. *Nat. Cell Biol.* **2018,** *20,* 1126–1133. doi:10.1038/s41556-018-0193-1
17. Gao, L.; Kraus, Y.; Wranik, M.; Weinert, T.; Pritzl, S. D.; Meiring, J. C. M.; Bingham, R.; Olieric, N.; Akhmanova, A.; Lohmüller, T.; Steinmetz, M. O.; Thorn-Seshold, O. *bioRxiv* **2019,** No. 716233. doi:10.1101/716233
18. Sailer, A.; Ermer, F.; Kraus, Y.; Lutter, F. H.; Donau, C.; Bremerich, M.; Ahlfeld, J.; Thorn-Seshold, O. *ChemBioChem* **2019,** *20,* 1305–1314. doi:10.1002/cbic.201800752
19. Hüll, K.; Morstein, J.; Trauner, D. *Chem. Rev.* **2018,** *118,* 10710–10747. doi:10.1021/acs.chemrev.8b00037
20. Tron, G. C.; Pirali, T.; Sorba, G.; Pagliai, F.; Busacca, S.; Genazzani, A. A. *J. Med. Chem.* **2006,** *49,* 3033–3044. doi:10.1021/jm0512903
21. Lawrence, N. J.; Rennison, D.; McGown, A. T.; Hadfield, J. A. *Bioorg. Med. Chem. Lett.* **2003,** *13,* 3759–3763. doi:10.1016/j.bmcl.2003.07.003
22. Leoni, L. M.; Hamel, E.; Genini, D.; Shih, H.; Carrera, C. J.; Cottam, H. B.; Carson, D. A. *J. Natl. Cancer Inst.* **2000,** *92,* 217–224. doi:10.1093/jnci/92.3.217
23. Dose Response Curves for NSC 757. National Cancer Institute - Developmental Therapeutics Program: Rockville, MD, https://dtp.cancer.gov/services/nci60data/colordoseresponse/pdf/757 (accessed Nov 6, 2019).
24. Garcia-Amorós, J.; Sánchez-Ferrer, A.; Massad, W. A.; Nonell, S.; Velasco, D. *Phys. Chem. Chem. Phys.* **2010,** *12,* 13238–13242. doi:10.1039/c004340k
25. Dunn, N. J.; Humphries, W. H., IV; Offenbacher, A. R.; King, T. L.; Gray, J. A. *J. Phys. Chem. A* **2009,** *113,* 13144–13151. doi:10.1021/jp903102u
26. Wiedbrauk, S.; Dube, H. *Tetrahedron Lett.* **2015,** *56,* 4266–4274. doi:10.1016/j.tetlet.2015.05.022
27. Mukherjee, C.; De, A. *Synlett* **2002,** 325–327. doi:10.1055/s-2002-19752
28. Takeo, Y.; Takahiro, S.; Takashi, T.; Kunihiro, I. *Bull. Chem. Soc. Jpn.* **1992,** *65,* 649–656. doi:10.1246/bcsj.65.649
29. Eggers, K.; Fyles, T. M.; Montoya-Pelaez, P. J. *J. Org. Chem.* **2001,** *66,* 2966–2977. doi:10.1021/jo0056848
30. Kink, F.; Collado, M. P.; Wiedbrauk, S.; Mayer, P.; Dube, H. *Chem. – Eur. J.* **2017,** *23,* 6237–6243. doi:10.1002/chem.201700826
31. Bisby, R. H.; Botchway, S. W.; Hadfield, J. A.; McGown, A. T.; Parker, A. W.; Scherer, K. M. *Eur. J. Cancer* **2012,** *48,* 1896–1903. doi:10.1016/j.ejca.2011.11.025
32. Nguyen, T. L.; McGrath, C.; Hermone, A. R.; Burnett, J. C.; Zaharevitz, D. W.; Day, B. W.; Wipf, P.; Hamel, E.; Gussio, R. *J. Med. Chem.* **2005,** *48,* 6107–6116. doi:10.1021/jm050502t
33. Gaspari, R.; Prota, A. E.; Bargsten, K.; Cavalli, A.; Steinmetz, M. O. *Chem* **2017,** *2,* 102–113. doi:10.1016/j.chempr.2016.12.005

License and Terms

This is an Open Access article under the terms of the Creative Commons Attribution License (https://creativecommons.org/licenses/by/4.0). Please note that the reuse, redistribution and reproduction in particular requires that the authors and source are credited.

The license is subject to the *Beilstein Journal of Organic Chemistry* terms and conditions: (https://www.beilstein-journals.org/bjoc)

The definitive version of this article is the electronic one which can be found at:
doi:10.3762/bjoc.16.14